UNIVERSITY OF SOUTHAMPTON

THE SHELFWARD PENETRATION OF WESTERN BOUNDARY CURRENTS

by

KYUNG-IL CHANG

A dissertation submitted in candidature
for the degree of Doctor of Philosophy
at the University of Southampton

November 1993

To Elizabeth and Catherine

UNIVERSITY OF SOUTHAMPTON

ABSTRACT

FACULTY OF SCIENCE

OCEANOGRAPHY

Doctor of Philosophy

THE SHELFWARD PENETRATION OF WESTERN BOUNDARY CURRENTS

by KYUNG-IL CHANG

Penetration of the western boundary current onto a continental shelf, and a marginal sea is investigated numerically to understand the observed shelfward penetration of the Kuroshio in the East China and Japan Seas. The work described in this thesis is mainly divided into two parts.

The first is to study the response of the circulation on a continental shelf to a steady western boundary current forcing using a numerical model in a simple domain. The model domain consists of a rectangular shelf and a deep ocean with a step-like cross section. The model predicts an anticyclonic penetration of the WBC onto the shelf, which is driven by the meridional pressure gradient inherent in the WBC. A southward intensification of the on-shelf flow takes place due to a vorticity constraint. The fundamental features are insensitive to different numerical model assumptions including boundary conditions and the presence of a passive lower layer. The amount of penetration, however, depends on frictional parameterisation, location of the shelf on a β-plane, depth of the shelf, and latitudinal distance of the shelf.

Non-linear effects are found to be important in setting the shelf circulation. Inertial effects broaden the length scale of the penetration boundary layer, resulting in an increased on-shelf transport. This occurs due to vorticity advection, which reduces the frictional effects in the boundary layer by balancing part of the topographic vorticity tendency. Zonal and meridional penetration scales also significantly increase, compared with those in the linear models. Changes in the circulation pattern are also investigated as the inertial effects increase. It turns out that the inertial effects are of little importance for a shelf located to the western boundary of a subpolar gyre, while they are important for a shelf located to the western boundary of a subtropical gyre like the East China Sea.

The second part of the thesis is an investigation of the effects, which changes in the large scale circulation of the deep ocean have, on the influx to a marginal sea. Both simple domains and a more realistic domain modelling the East China and Japan Seas are used. Model results suggest that the Tsushima Current, a branch of the Kuroshio entering the Japan Sea, is generated by the pressure difference between the inshore part of the Kuroshio and the Tsugaru strait region through which the Tsushima Current exits to the Pacific. The model results indicate that the volume transport of the TC is dependent on the separation latitude of the Kuroshio and the strength of the Oyashio Current as well as the Kuroshio transport. The realistic model predicted that a 100 km change in the separation latitude of the Kuroshio corresponds to a 20 % change of the Kuroshio transport in determining the influx to the Japan Sea.

CONTENTS

LIST OF FIGURES

shaded region indicates a place where the current velocity is negative (from Kaneko et al., 1990).

Fig. 1-9. Absolute geostrophic velocity section on the G-line in Fig. 1-1 on August 1987 estimated from hydrographic data at N_{HYD} stations and surface current data at N_{SCV} stations. Positive value indicates the northeastward component of velocity in cm/s. The heavy line at the bottom represents the ocean bottom while the light line represents the maximum depth of the hydrographic casts. The solid circles at the surface indicate the location of the hydrographic stations. (from Ichikawa and Beardsley, 1993).

Fig. 1-10. Schematic picture of the Kuroshio Current System variability determined by a statistical analysis of temperature/depth data during the period from summer 1976 to spring 1980 (from Mizuno and White, 1983). The mean Kuroshio Current path is shown as a dashed line; the envelope of the maximum displacement that the Kuroshio Current experienced near the nodal point (solid points) is shown as solid lines.

Fig. 1-11. Horizontal distribution of temperature at a depth of 100 m during August 1970 around the Kuroshio Extension (from Kitano, 1975). Contour interval are 1°C. Two thermal fronts around 35°N ~ 36°N (AA) and 39°N ~ 40°N (BB) represent the Kuroshio and Oyashio fronts respectively. A warm eddy can be seen in the north of the Oyashio front.

Fig. 1-12. Histograms of latitude of the northern limit of the Kuroshio Extension based on hydrographic data for 1927-1969 (Kawai, 1972). The northern limit of the Kuroshio Extension was determined by 14°C isotherm at 200 m depth. Numbers inside the histogram denote the sample size.

Fig. 1-13. The model ocean considered by Minato and Kimura (1980). A sinusoidal curve in region A shows the distribution of wind stress.

Fig. 1-14. Generation of the Tsushima Current conjectured from the satellite images: (A) zone of mixing along the shelf-edge, (B) episodic intrusion from the Kuroshio, and (C) resultant Tsushima Current (from Huh, 1982b).

Fig. 1-15. Schematic map of regional currents round Cheju Island (Jeju-Do) in summer. The closed and broken arrows indicate a Yellow Sea Warm Current, and the surface plume of Changjiang River Diluted Water (from Kim et al., 1991).

Fig. 3-1. (A) Plane and (B) side views of model geometry and topography for two simple models used for numerical experiments. (a) SSM : simple shelf model, (b) SMSM : simple marginal sea model. SWEM and SPEM denote the linear two-layer model and primitive equation model used for numerical experiments respectively. Notations for the SWEM are : ρ_1 , H_1 represent the density and thickness of upper layer and ρ_2 , H_2 same quantities of lower layer, and η_1 , η_2 the free surface and interface perturbation respectively. Notations for the SPEM are : h represents the depth and ρ_0 constant water density.

Fig. 4-1. Temporal variation of (A) free surface and (B) meridional velocity in the upper layer at two points in the western (solid lines) and eastern (dotted lines) boundaries. The results are obtained from the deep channel model of the SWEM. Scales of solid and dotted lines are indicated to the left and right sides of the vertical axes respectively.

Fig. 4-2. (Upper panel) Contours of (A) free surface, (B) interface perturbation, and (C) meridional velocity in the upper layer at an equilibrium state of the deep channel model of the SWEM.
(Lower panel) Profiles of free surface (solid line) and meridional velocity in the upper layer (dotted line) along (A) a zonal section (J=120 in the above figure) and (B) the western boundary (I=2 in the above figure).

Fig. 4-3. Temporal variation of (A) free surface and (B) meridional velocity at two points in the western boundary of the shelf (solid lines, I=2 in the legend) and near the shelf-edge (dotted lines, I=20 in the legend). The results are obtained from the standard shelf model of the SWEM. Scales of solid and dotted lines are indicated to the left and right sides of the vertical axes respectively.

Fig. 4-4. Contours of free surface at an equilibrium state of the standard shelf model of the SWEM (A) in the whole domain, (B) in the shelf and adjacent deep channel area, and (C) only in the shelf. Continental slope lies between grid points I=21 (depth=200 m) and I=22 (depth=400 m). As the staggered grid was used (Fig. A-1), the depth of u-points at I=21 is 300 m. The zonal velocity along the shelf-edge referred to in the text indicates the zonal velocity along I=20 (depth=200 m).

Fig. 4-5. (A) Zonal velocity profile along the southern wall of the shelf (J=101 in Fig. 4-4). The distance is measured westwards from the shelf-edge (I=20). Dotted arrow indicates the ZPS as defined in the text. (B) Zonal velocity profile along the shelf-edge (I=20 in Fig. 4-4). The distance is measured northwards from the southernmost point (I=20 and J=101). Dotted arrow indicates the length scale of the SBL as defined in the text.

Fig. 4-5. (C) Meridional velocity profile along the western wall of the shelf (I=2 in Fig. 4-4). The distance is measured northwards from the southernmost point (I=2, J=101). Dotted arrow indicates the MPS as defined in the text. (D) Ratio between the on-shelf volume transport and the WBC transport along meridional sections as a function of the distance measured westwards from the shelf-edge (I=20 in Fig. 4-4).

Fig. 4-6. Contours of streamlines at an equilibrium state of the standard SPEM experiment (A) in the whole domain, (B) in the shelf and adjacent deep ocean area, and (C) only in the shelf. Contour intervals in (B) are 0.4 Sv in the shelf and 2.0 Sv in the deep ocean.

Fig. 4-7. Comparisons of (A) zonal velocity profile along the southern wall of the shelf (J=101 in Fig. 4-4 for the SWEM, and J=54 in Fig. 4-6 for the SPEM), and (B) zonal velocity profile along the shelf-edge (I=20 in Fig. 4-4 for the SWEM, and I=19 in Fig. 4-6 for the SPEM) between the standard case of the SWEM and the

SPEM.

Fig. 4-7. Comparisons of (C) meridional velocity profile along the western wall of the shelf (I=2 in Fig. 4-4 for the SWEM, and I=2 in Fig. 4-6 for the SPEM), and (D) meridional distribution of on-shelf volume transport between the standard case of the SWEM and the SPEM. The distance is measured from the southern wall to the north in (C), and measured from the shelf-edge to the west in (D).

Fig. 4-8. Selected sections along which the local vorticity balance was examined, superimposed on the contours of free surface in the shelf and adjacent deep channel region at an equilibrium state for the standard SWEM experiment.

Fig. 4-9. Zonal distribution of terms in the vorticity equation IV-2-7 at section a in Fig. 4-8. DIVE, BETA, BOTF, and LATF represent the topographic vorticity tendency, the planetary vorticity tendency, the dissipation of vorticity due to bottom friction, and the vorticity diffusion term respectively.

Fig. 4-10. Meridional distribution of terms in the vorticity equation IV-2-7 (A) at section c, and (B) at section b in Fig. 4-8. Legends are the same as in Fig. 4-9.

Fig. 4-11. Meridional distribution of terms in the vorticity equation IV-2-7 (A) along the shelf-edge (at section d in Fig. 4-8), and (B) at the same section as (A) but only in the off-shelf flow region.

Fig. 4-12. Meridional profile of the relative vorticity in the shelf boundary layer (SBL). The distance is measured from the southern wall of the shelf to north.

Fig. 4-13. Zonal profile of upper layer meridional velocity and relative vorticity at section e in Fig. 4-8.

Fig. 4-14. Meridional distribution of terms in the vorticity equation IV-2-8 at section f in Fig. 4-8.

Fig. 4-15. Zonal distribution of terms in the vorticity equation IV-2-7 at section e in Fig. 4-8, (A) from grid point I=2 to I=17, and (B) from I=18 to I=25.

Fig. 4-16. Distribution of terms in the momentum equations (A) (IV-2-4), and (B) (IV-2-5) along a meridional section in the western boundary layer (I=2 in the upper panel of Fig. 4-2) before introducing the shelf.

Fig. 4-17. Distribution of terms in the momentum equation (A) (IV-2-4), and (B) (IV-2-5) along the same section as in Fig. 4-16 (I=22 in Fig. 4-8) after introducing the shelf.

Fig. 4-18. Same as in Fig. 4-17 (B), but only shows the distribution of terms in the off-shelf flow region.

Fig. 4-19. Meridional distribution of terms in the momentum equation (A) (IV-2-4) , and (B) (IV-2-5) at section b in Fig. 4-8.

Fig. 4-20. Contours of free surface at an equilibrium state for the four experiments (A) r = 0.0, (B) r = 10^{-4}, (C) r = 5 × 10^{-4}, and (D) r = 10^{-3} (standard case), where r is the coefficient of bottom friction. All other parameters are the same as those in Table 4-1.

Fig. 4-21. Comparisons of (A) meridional velocity profile along the western wall of the shelf (I=2 in Fig. 4-20), (B) zonal velocity profile along the shelf-edge (I=20 in Fig. 4-20) for the four experiments with different coefficient of bottom friction. The distance is measured northward from the southernmost point in (A), and measured from the southern wall to the north in (B).

Fig. 4-21. Comparisons of (C) zonal velocity profile along the southern wall of the shelf (J=101 in Fig. 4-20), and (D) longitudinal distribution of the volume transport ratio between the WBC and the on-shelf flow with different coefficient of bottom friction. The distance is measured from the shelf-edge to the west.

Fig. 4-22. A comparison of terms in the vorticity equation IV-2-7 at section f in Fig. 4-8 (A) for the standard case with the coefficient of bottom friction r = 10^{-3}, and (B) for the lateral friction model without bottom friction.

Fig. 4-23. Comparisons of (A) meridional velocity components, and (B) relative vorticities at section e in Fig. 4-8 between the standard case with the coefficient of bottom friction r = 10^{-3}, and the lateral friction model without bottom friction.

Fig. 4-24. (Upper panel) Contours of streamlines at an equilibrium state in the shelf and adjacent deep ocean region (upper panel), and **(Lower panel)** only in the shelf (lower panel) for the three experiments with different eddy viscosity. For clarity, streamlines of negative values are not plotted in the upper panel. The coefficient of eddy viscosity increases from left (A_M = 10^3 m^2s^{-1}) to right (A_M = 10^4 m^2s^{-1}). All other parameters are the same as those for the standard SPEM experiment in Table 4-1.

Fig. 4-25. Comparisons of (A) zonal velocity profile along the shelf-edge (I=19 in Fig. 4-24), and (B) longitudinal distribution of on-shelf volume transports for the three experiments with different values for the eddy viscosity. The distance is measured (A) from the southern wall to the north, and (B) from the shelf-edge to the west.

Fig. 4-26. Dependence of the ratio between the maximum on-shelf transport and the WBC transport on five factors; 1. ratio between the shelf depth (d) and unperturbed upper layer depth in the deep ocean (h); 2. coefficient of bottom friction (r, m s^{-1}); 3. latitude of southern boundary of the shelf (θ); 4. coefficient of eddy viscosity (A_M, m^2 s^{-1}); 5. latitudinal size of the shelf (ℓ_y, km).

Fig. 4-27. Contours of free surface for three experiments where the southern boundaries of the shelf are placed at (A) 15°27', (B) 21°49', and (C) 28°11' on a β-plane.

Fig. 4-28 Contours of free surface for five experiments where depths of the shelf are

(A) 50 m, (B) 100 m, (C) 150 m, (D) 200 m, and (E) 250 m. The unperturbed upper layer thickness of the deep channel is 400 m for all the experiments.

Fig. 4-29. Log-log plot of the ratio between the maximum on-shelf transport along the shelf-edge and the prescribed transport of the WBC along the southern boundary of the deep channel as a function of the shelf depth.

Fig. 4-30. (Upper panel) Contours of free surface for two experiments of different longitudinal size of the shelf.
(Lower panel) Contours of free surface for two experiments of different latitudinal size of the shelf.

Fig. 4-31. Contours of streamlines in the whole domain for four experiments where the applied Sverdrup transports in the deep ocean are (A) 13.5 Sv, (B) 27.0 Sv, (C) 40.4 Sv, and (D) 53.9 Sv.

Fig. 4-31. Contours of streamlines in the shelf and continental slope area for four experiments where the applied Sverdrup transports in the deep ocean are (A) 13.5 Sv, (B) 27.0 Sv, (C) 40.4 Sv, and (D) 53.9 Sv.

Fig. 4-32. (Upper panel) Contours of free surface in the shelf and continental slope area for two experiments with different lateral boundary conditions, (A) free-slip boundary condition, and (B) no-slip boundary condition.
(Lower panel) Longitudinal variation of the ratio between the on-shelf transport and the prescribed WBC transport along the southern boundary of the deep channel for the above two experiments.

Fig. 4-33. (Upper panel) Contours of streamlines in the shelf area for two experiments with different grid resolution, (A) 20 km, and (B) 10 km.
(Lower panel) Longitudinal variation of the ratio between the on-shelf transport and the applied Sverdrup transport in the deep ocean for three experiments with different grid resolution (d in the legend).

Fig. 4-34. (Upper panel) Contours of streamlines in the shelf and adjacent deep ocean area for two experiments, (A) standard case, and (B) smoothed sharp corner.
(Lower panel) Longitudinal variation of the ratio between the on-shelf transport and the applied Sverdrup transport in the deep ocean for the above two experiments.

Fig. 4-35. Contours of streamlines in the shelf and adjacent deep ocean area for two experiments with different longitudinal size of the deep ocean, (A) narrower case, and (B) wider case.

Fig. 4-36. (A) Profiles of meridional velocity along the western wall of the shelf (I=2 in Fig. 4-35) for the two experiments in Fig. 4-35. (B) Longitudinal variation of the ratio between the on-shelf transport and the applied Sverdrup transport in the deep ocean for the two experiments in Fig. 4-35.

Fig. 4-37. (Upper panel) Contours of streamlines for two linear experiments (A) $p_y < 0$, $h_x > 0$ (ECS case), and (B) $p_y > 0$, $h_x > 0$ (MAB case).

(Lower panel) Contours of streamlines for two linear experiments (A) $p_y < 0$, $h_x < 0$, and (B) $p_y > 0$, $h_x < 0$. The p_y and h_x denote the meridional pressure gradient along the WBC and the zonal gradient of topography respectively. Applied Sverdrup transports are the same for both cases.

Fig. 4-38. **(Upper panel)** Contours of streamlines in the whole domain for (A) a linear, and (B) a non-linear experiments.
(Lower panel) Contours of streamlines only in the shelf and adjacent deep ocean area for (A) a linear, and (B) a non-linear experiments.

Fig. 4-39. Comparisons of (A) zonal velocity profile along the southern wall of the shelf (J=55 in Fig. 4-38), and (B) zonal velocity along the shelf-edge (I=19 in Fig. 4-38) between the linear and non-linear experiments in Fig. 4-38.

Fig. 4-39. Comparisons of (C) meridional velocity profile along the western wall of the shelf (I=2 in Fig. 4-38), and (D) Longitudinal variation of the ratio between the on-shelf transport and the applied Sverdrup transport in the deep ocean between the linear and non-linear experiments in Fig. 4-38.

Fig. 4-40. Contours of streamlines for two non-linear experiments (A) $p_y < 0$, $h_x > 0$ (ECS case), and (B) $p_y > 0$, $h_x > 0$ (MAB case). The p_y and h_x represent the meridional pressure gradient along the WBC and the zonal gradient of topography respectively. Applied Sverdrup transports are the same for both cases.

Fig. 4-41. Contours of streamlines from the barotropic lateral friction model of Böning (1986) for the case (A) $\delta_I / \delta_L = 0.2$, (B) $\delta_I / \delta_L = 0.5$, (C) $\delta_I / \delta_L = 0.8$, (D) $\delta_I / \delta_L = 1.0$, and (E) $\delta_I / \delta_L = 1.5$. δ_I and δ_L represent the non-dimensional inertial and diffusive scales of western boundary layer respectively, defined by the equation (II-3-8) in the text.

Fig. 4-42. Ratio between the maximum on-shelf transport along the shelf-edge and the applied Sverdrup transport for the linear experiments in Table 4-2, and the non-linear experiments in Table 4-4. ϵ in the figure indicates the ratio between the inertial boundary layer scale and the diffusive boundary layer scale (δ_I / δ_L).

Fig. 4-43. Contours of streamlines in the whole domain for the case (A) $\epsilon = 0.14$, (B) $\epsilon = 0.31$, and (C) $\epsilon = 0.70$.

Fig. 4-43. Contours of streamlines in the whole domain for the case (D) $\epsilon = 0.99$, (E) $\epsilon = 1.21$, and (F) $\epsilon = 1.40$.

Fig. 4-44. Contours of streamlines in the shelf and adjacent deep ocean for the case (A) $\epsilon = 0.14$, (B) $\epsilon = 0.31$, and (C) $\epsilon = 0.70$.

Fig. 4-44. Contours of streamlines in the shelf and adjacent deep ocean for the case (D) $\epsilon = 0.99$, (E) $\epsilon = 1.21$, and (F) $\epsilon = 1.41$.

Fig. 4-45. (A) Zonal velocity profiles along the southern wall (J=55 in Fig. 4-44), and (B) meridional velocity profiles along the western wall (I=2 in Fig. 4-44) for the

all experiments in Table 4-4.

Fig. 4-45. (C) Zonal velocity profiles along the shelf-edge (I=19 in Fig. 4-44), and (D) longitudinal variation of the ratio between the on-shelf transport and the applied Sverdrup transport in the deep ocean for the all experiments in Table 4-4.

Fig. 4-46. Meridional distribution of terms in the vorticity equation (II-2-13) (A) along the shelf-edge (I=19 and J=55~93 in Fig. 4-44), and (B) along the same section as (A), but J=65~93. DIVE, ADVE, LATF, and BETA represent the topographic vorticity tendency, relative vorticity advection, vorticity diffusion, and planetary vorticity tendency respectively.

Fig. 4-47. Distribution of relative vorticity near the southern part of the shelf (A) for a linear case (experiment C in Table 4-2), and for two non-linear cases of (B) ϵ = 1.2 (experiment E in Table 4-4), and (C) ϵ = 1.4 (experiment F in Table 4-4). Dotted areas represent the region of positive relative vorticity.

Fig. 4-48. Zonal distribution of terms in the vorticity equation (II-2-13) (A) along the southern wall of the shelf (J=56 and I=3~12 in Fig. 4-44), and (B) along the same section as (A), but I=13~19.

Fig. 4-49. Meridional distribution of terms in the vorticity equation (II-2-13) (A) along the western wall of the shelf (I=3 and J=55~93 in Fig. 4-44), and (B) along the mid-longitude of the shelf (I=10 and J=55~93 in Fig. 4-44).

Fig. 5-1 (A) Contours of streamlines for an antisymmetric double gyre circulation at an equilibrium state (left) driven by the applied antisymmetric zonal wind stress (right). The model ocean is homogeneous and flat with a depth of 400 m. (B) Locations of straits of each shallow basin for the experiments 2~4 in Table 5-1 superimposed on the meridional distribution of the surface pressure along the western boundary of the double gyre circulation before introducing the shallow basins. The surface pressure is computed assuming that the pressure at the southwestern corner is zero.

Fig. 5-2. Contours of streamlines for the experiments 2~4 from left to right (see Table 5-1). Positive and negative values of the streamlines within the shallow basins indicate that the penetration of the boundary currents takes place through the southern and northern straits of each basin respectively.

Fig. 5-3. Contours of streamlines for the two cases (A) without the MS, and (B) with the MS. Model parameters for both of the experiments are the same as those of experiment D in Table 4-3.

Fig. 5-4. A comparison of three model results ; (A) non-linear lateral friction model, (B) linear lateral friction model, and (C) non-linear bottom friction model. The applied Sverdrup transports are the same for the three experiments.

Fig. 5-5. As in Fig. 5-4 except the circulation in the shelf and the MS regions only with a contour interval of 0.2 Sv.

Fig. 5-6. Contours of streamlines in the shelf and the MS regions for the six experiments with the depth of the shelf and the MS varying from 50 m (top left) to 300 m (bottom right) at 50 m intervals. The depth of the deep ocean is 400 m.

Fig. 5-7. The maximum on-shelf transport and the influx to the MS as a function of the shelf depth. Two solid lines having a slope of 1 and 2 are also drawn.

Fig. 5-8. Three paths (thick solid lines) along which the pressure is calculated , superimposed on the contours of streamlines for the experiment 1 in Table 5-2. Contour intervals of the streamlines are arbitrary.

Fig. 5-9. The pressure along the path A in Fig. 5-8 for the six experiments with different depths of the shelf and the MS. Numerals denote the shelf depth, and locations of the two straits of the MS are also marked (KS and TS in the figure).

Fig. 5-10. The pressure along the path B in Fig. 5-8 for the two experiments with different depths of the shelf and without the MS. Numerals denote the shelf depth, and locations of the two straits of the MS in the marginal sea model are also marked (KS and TS in the figure).

Fig. 5-11. The pressure along the inshore part of the western boundary current (path C in Fig. 5-8) for the two experiments with different depths of the shelf and without the MS. Numerals denote the shelf depth, and the locations of the shelf is indicated inside the figure. The location of the TS in the marginal sea model is also marked (TS in the figure).

Fig. 5-12. The pressure along the inshore part of the western boundary current (path C in Fig. 5-8) for the six experiments with different depths of the shelf and the MS. Numerals denote the shelf depth, and locations of the shelf and the TS are indicated.

Fig. 5-13. Meridional profiles of the zonal wind stress used for the spin-up of the six experiments in Table 5-3. The y-axes represent the latitudinal grid points (grid J), and the location of the TS is indicated. Note that the location of vanishing curl of the wind stress moves to the south from left to right. The amplitude of the wind stress also decreases from left to right since the Sverdrup value is fixed.

Fig. 5-14. Plots of model kinetic energy as a function of time for the experiment 4 in Table 5-3 in the whole domain (labelled total), and in the deep ocean area from the offshore side of the WBC (grid J=30 in Fig. 5-18) to the eastern boundary (labelled ocean).

Fig. 5-15. As in Fig. 5-14 except in the ocean and the MS areas from 100 days to 200 days.

Fig. 5-16. Plots of the maximum on-shelf transport and the influx to the MS as a function of time. Marked on the solid line are the days of maximum or minimum influx to the MS.

Fig. 5-17. Plots of the influx to the MS and the kinetic energy in the MS as a

function of time.

Fig. 5-18. Snapshots of streamlines for the experiment 4 in Table 5-3 at days 120, 125, 131, 138, 146, 152, and 158 plotted on Fig. 5-16. The influx to the MS showed its minimum at (A) and (E), and its maximum at (C) and (G).

Fig. 5-19. The pressure along the inshore part of the western boundary current (path C in Fig. 5-8) at the different times plotted on Fig. 5-16. The influx to the MS showed its minimum at day 120, and its maximum at day 131. The southern and northern boundaries of the shelf are located at grid J=44 and J=84 respectively. The TS is located between the grid points J=124 and J=129.

Fig. 5-20. Contours of streamlines for the experiments 1~6 in Table 5-3 from (A) to (G) at the times when the influx to the MS for each case is nearly the same as its mean value.

Fig. 5-20. (continued)

Fig. 5-21 (A). The maximum on-shelf transport and the influx to the MS as a function of the distance between the centre of the TS and the latitude of vanishing curl.

Fig. 5-21 (B). The maximum on-shelf transport and the influx to the MS as a function of the ratio between the transports of the subtropical and subpolar gyres in the deep ocean.

Fig. 5-22 (A). The pressure along the inshore part of the western boundary current (path C in Fig. 5-8) for the experiments 2 and 4 in Table 5-3, but <u>without the MS</u>. The location of the TS in the marginal sea model is indicated (TS in the figure).

Fig. 5-22 (B). The pressure along the inshore part of the western boundary current (path C in Fig. 5-8) for the six experiments in Table 5-3. Numerals denote the number of the experiments in Table 5-3.

Fig. 5-23. Contours of streamlines for (A) experiment 2, and (B) experiment 4 in Table 5-3, but <u>without MSs</u>.

Fig. 5-24. Meridional profiles of the zonal wind stress used for the spin-up of the five experiments in Table 5-4. The y-axes represent the latitudinal grid points (grid J), and the location of the TS is indicated. Note that the location of vanishing curl of the wind stress is fixed. The amplitude of the wind stress of the subpolar gyre is intensified from left to right.

Fig. 5-25. Contours of streamlines for the experiments 4, and 7~10 in Table 5-4 from (A) to (E) at the times when the influx to the MS for each case is nearly the same as its mean value.

Fig. 5-25. (continued)

Fig. 5-26. The pressure along the inshore part of the western boundary current (path C in Fig. 5-8) for the experiments 4, 7, 9, and 10 in Table 5-4, but without the MS. The location of the TS in the marginal sea model is indicated (horizontal bar near the grid J=124 in the figure).

Fig. 5-27. Contours of streamlines for the three experiments in Table 5-5. The value for the lateral eddy viscosity are (A) 5000 m^2s^{-1}, (B) 10000 m^2s^{-1}, and (C) 20000 m^2s^{-1}.

Fig. 5-28. Contours of streamlines for experiments 2-1, and 4-1 in Table 5-6. The longitudinal distances of the deep ocean basins are extended to 2.4 times of those of experiments 2 and 4 in Table 5-3.

Fig. 5-29. Plan view of the realistic model domain with bottom topography. Contour intervals between isobaths are 20 m. The ECS, JS, KS, and TS denote the East China Sea, the Japan Sea, Korea Strait, and Tsugaru Strait respectively.

Fig. 5-30. Time series of the total kinetic energy and the influx to the Japan Sea obtained for every one day interval from the standard case in Table 5-7.

Fig. 5-31. Contours of streamlines for the standard case at an equilibrium state. Contour intervals are 2 Sv from a streamline 58.5 to a streamline 102.5, and the intervals of other streamlines are 1 Sv. The 1.0 Sv streamline is also marked. The thick solid line indicates a section on which the velocity component perpendicular to the line is plotted together with the topographic profile along the line in Fig. 32 (A).

Fig. 5-32 (A). Profiles of the velocity component perpendicular to the line P in Fig. 5-31, and bottom topography along the line. **(B).** Profiles of the meridional velocity component, and bottom topography along the western wall (I=2 in Fig. 5-31).

Fig. 5-33. Trajectories of three satellite tracking surface drifters released in July 17, 1991 in the area west of Kyushu (from KORDI, 1992).

Fig. 5-34. Contours of streamlines for **(A)** experiment 1, and **(B)** experiment 3 in Table 5-8 at an equilibrium state. Contour intervals are 2 Sv from a streamline 58.5 to a streamline 102.5 for experiment 1, and from a streamline 49.5 to a streamline 130.5 for experiment 3. The intervals of other streamlines are 1 Sv. The 1.0 Sv streamline is also marked.

Fig. A1. Horizontal arrangements of variables on an Arakawa C-grid. ● represents free surface (η_1), interface perturbation (η_2), and depth points, × meridional velocity points, and ◇ zonal velocity points. Δ indicates horizontal grid spacing and dotted lines indicate the placement of horizontal boundary.

Fig. B1. Time-latitude plot of free surface along the western boundary with open boundary conditions (A) case I, (B) case II, and (C) case III from initial state to 250 days (left panel) and from 250 days to 500 days (right panel). The direction of increasing grid point is due north. Contour intervals are 1 m (case I), and 0.5 cm (case II and case III).

Fig. B2. Time-latitude plot of upper layer meridional velocity along the eastern boundary with open boundary conditions (A) case I, (B) case II, and (C) case III from initial state to 50 days. The direction of increasing grid point is due north. Contour intervals are 1 cm/s. Dotted lines show the theoretical path of the inviscid internal Kelvin wave.

Fig. B3. Time-latitude plot of upper layer meridional velocity along the eastern boundary with open boundary conditions (A) case I, (B) case II, and (C) case III from initial state to 250 days. The direction of increasing grid point is due north. Contour intervals are 1 cm/s.

Fig. B4. Time-longitude plot of interface perturbation along the middle section with open boundary conditions (A) case I, (B) case II, and (C) case III from initial state to 250 days. The direction of increasing grid point is due east. Contour intervals are 4 m (case I), and 2 m (case II and case III). Dotted lines show the theoretical path of the long Rossby wave whose phase and group speeds are given by equation (II-4-6).

Fig. B5. Contours of (A) free surface, (B) interface perturbation, and (C) upper layer meridional velocity after 500 days for the case I. Contour intervals are (a) 1 m, (b) 2 m, and (c) 2 cm/s.

Fig. B6. Contours of (A) free surface, (B) interface perturbation, and (C) upper layer meridional velocity after 500 days for the case II **(upper panel)**, and case III **(lower panel)**. Contour intervals are (A) 1 m, (B) 2 m, and (C) 2 cm/s.

Fig. B7. Contours of free surface at an equilibrium state for the closed basin model covering the (A) whole domain, (B) shelf and adjacent deep ocean area, and (C) shelf area. Contour intervals are 2 cm (A and B), and 1 cm (C).

Fig. B8. Contours of free surface at an equilibrium state for the open channel model covering the (A) whole domain, (B) shelf and adjacent deep ocean area, and (C) shelf area. Contour intervals are 2 cm (A and B), and 1 cm (C).

Fig. B9. Meridional velocity profile along a zonal section (J=70 in Fig. B8).

Fig. B10. Latitudinal variation of northward volume transport ratio for the closed basin and open channel cases from the southern wall (left to the horizontal axis) to the northern wall (right to the horizontal axis) of the shelf.

Fig. B11. (A) Alongshore phase speed (Re(c)) and (B) temporal decay factor (-Im(c)) for the Kelvin wave versus Δ at selected values of ϵ for the C-grid with free-slip boundary (from Hsieh et al., 1983). Increasing Δ and ϵ implies worsening resolution and higher viscosity respectively. Re(c)=1 means the phase speed of the inviscid Kelvin wave in a continuum. The e-folding decay scale t_d is given by $t_d = (-\mathrm{Im}(c) \times \ell)$, where ℓ is the longshore wavenumber.

Fig. D-1. Plots of kinetic energies averaged over four different regions of the model domain of the experiment 4 in Table D-1 as a function of time. Numerals denote the

times when the total kinetic energy shows its maximum or minimum values.

Fig. D-2. Plots of total kinetic energies for the three experiments in Table D-1 as a function of time. Observed periods of oscillation are marked for each experiment. Numerals denote the times when the total kinetic energy shows its maximum or minimum values.

Fig. D-3. Contours of streamlines at 150 days for the three experiments in Table D-1.

Fig. D-4. Contours of streamlines at the different times of day 15, day 27, and day 41 (from left to right) marked in Fig. D-1.

Fig. D-4. Contours of streamlines at the different times of day 55, and day 69 (from left to right) marked in Fig. D-1.

Fig. D-5. Plots of normalised kinetic energies for the six experiments in Table 4-4 as a function of time **(A)** in the whole domain, and **(B)** only in the shelf. T=10.0 in the figure indicates the kinetic energy for the highly inertial case (experiment F in Table 4-4).

ACKNOWLEDGEMENTS

I am mostly grateful to my supervisors, Dr. Kelvin Richards and Prof. Steve Thorpe for their constant interest and valuable guidance. They also assisted me in completing the work in due course. Discussion with Dr. Kelvin Richards was very helpful, he offered encouragement or gave me an insight at times when I made slow progress through an awful amount of numerical results. I and my family members also would like to express our gratitude to their family members for their warm-heartedness.

I also wish to thank many members of the department who have helped me with my work and life, especially Dr. Wolfgang Barkmann, Julian Castaneda, and Peter Lancaster. Special thanks to Dr. Michael Dearnaley for providing his model codes at an earlier stage of this work.

My thanks also go to Korean colleagues in the University, who shared their experience of foreign life with me, and with whom it was my favourite relaxations to spend a evening every week at the pub. Dr. Kwang-Su Kim and Mr. Hang-Kyung Lee helped me with computing and preparing figures.

I am greatly indebted to my parents for their encouragement and support for three years.

I was partly supported by the British Embassy and the British Council in the Republic of Korea for the period of August 1990 - September 1992. The Korea Ocean Research and Development Institute (KORDI) helped me to complete this work.

Last but not least, I wish to thank my family from the bottom of my heart. Their thoughtful consideration made me give myself to study.

LIST OF ABBREVIATIONS

BVE : Barotropic Vorticity Equation

ECS : East China Sea

KS : Korea Strait

JS : Japan Sea

MAB : Middle Atlantic Bight

MS : Marginal Sea

SAB : South Atlantic Bight

SBL : Shelf Boundary Layer

SPEM: Semi-spectral Primitive Equation Model

SSM : Simple Shelf Model

SWEM: Shallow Water Equation Model

TC : Tsushima Current

TS : Tsugaru Strait

TWC : Taiwan Warm Current

YSWC: Yellow Sea Warm Current

WBC : Western Boundary Current

CHAPTER I. INTRODUCTION

I-1. INTRODUCTION

I-1-1. Shelf seas

The study of shelf seas is important scientifically because it is through shelf seas that materials are exchanged between oceans and continents. It has been suggested that continental shelves play an important role in the global carbon budget (Walsh et al., 1981).

The shelf seas are characterised by their intense spatial and temporal variability, partly due to river runoff from surrounding land masses and atmospheric forcing. Apart from these forcing effects, the shelf seas located in the western part of the ocean basin are also strongly affected by strong western boundary currents and associated meanders and synoptic/mesoscale eddies.

There have been attempts at quantifying cross-shelf exchange of sediments, pollutants, carbon, and nutrients from continental shelves to the open ocean from multidisciplinary oceanographic programs in recent years (Atkinson et al., 1985; Walsh et al., 1988; Liu et al., 1992). Various exchange processes between estuarine, nearshore, shelf, slope, and deep ocean were reviewed by Wroblewski and Hofmann (1989). Huthnance (1981) reviews the physical processes that can result in exchanges between shelf and oceanic waters mainly in the eastern boundary region.

A variety of processes operate. For example, in the South Atlantic Bight (SAB), the southeast U.S. continental shelf, low-frequency current and temperature variability along the outer shelf region where water depth ranges from 40 m to 75 m is primarily influenced by Gulf Stream frontal disturbances such as northward propagating wavelike meanders and cold cyclonic frontal eddies (Lee et al., 1981; Lee and Atkinson, 1983).

The Gulf Stream provides an almost continual supply of nutrient to the SAB through the mechanisms of Gulf Stream frontal eddies and associated shelf-break upwelling (Atkinson et al., 1985).

In the Middle Atlantic Bight (MAB), the northeast U.S. continental shelf, the mean southward component of the shelf flow is driven primarily by an alongshore pressure gradient imposed at the shelf break by the cyclonic gyre called the slope water region in the deep ocean found between the continental shelf and the Gulf Stream (Csanady, 1978; Beardsley and Boicourt, 1981; Beardsley and Winant, 1981).

The East China (ECS) and Japan Seas (JS), which form the principle areas of interest in the present study, are marginal seas of western North Pacific where the Kuroshio, the western boundary current in the North Pacific, flows along its oceanic boundary. The cross-shelf exchange in the ECS through mechanisms such as shelf break upwelling (Su and Pan, 1987; Liu et al., 1992), a filament of outpouring shelf water (Chern et al., 1990; Liu et al., 1992), and meanders of Kuroshio front (Sugimoto et al., 1988; Qiu et al., 1990) is responsible for the transport of nutrient-laden water to the shelf from the deep ocean and the seaward transport of particulate material. Because the ECS is one of the largest continental shelf in the world and receives a large amount of river run-off and sediment discharge mainly from China, the exchange processes are expected to be very important in terms of biogeochemical fluxes (Liu et al., 1992).

The region is also unique in that deep penetration of the Kuroshio into the JS occurs. A generally northward-flowing warm current system driven by the Kuroshio has been believed to exist in the ECS since Uda (1934) firstly proposed the general circulation pattern in this area. The three warm currents in the ECS originating from the Kuroshio are designated schematically in Fig. 1-1. This phenomena has been called the branching or penetration of the Kuroshio. There have been several theoretical and numerical investigations of the shelfward penetration of the Kuroshio since the 1980s'(e.g. Minato and Kimura, 1980; Ichiye, 1984; Qiu and Imasato, 1990; Chao, 1991; Oey and Chen, 1991). The branching mechanism and the interrelation between the branched currents are, however, still in contention.

I-1-2. Theoretical and numerical studies

There have been theoretical and numerical investigations of how bottom topography influences the ocean circulation (Holland, 1967; Holland, 1973; Liu, 1990; Salmon, 1992). These studies were mainly concerned for the effect of the continental slope on the nature of the western boundary current. The main objective of present study is, however, to be focused on the shelf circulation driven by the strong western boundary current.

The influence of deep ocean over the shelf has been investigated by a pameterisation of offshore currents by imposition of an alongshore pressure gradient at the shelf break (Csanady, 1978; Middleton, 1987; Lorenzzeti et al., 1988).

Csanady (1978) presented a simple linear model for the frictionally damped depth-averaged flow driven over a sloping and an unbounded shelf by a uniform alongshore pressure gradient externally imposed at the shelf break. He concluded that the open ocean imposed the mean pressure gradient along the outer edge of the MAB that was required to drive the observed mean southward flow on the shelf. The alongshore pressure for the MAB case slopes downward toward the south associated with southward flowing slope currents. According to his results the entire coastal zone experiences essentially the same along-shore pressure gradient imposed on the shelf break. His suggestion has been further supported by Beardsley and Winant (1979). Wang (1982), however, argued that open ocean pressure gradient effects are ineffective at driving the circulation observed on the MAB due to the insulating effect of the continental slope against the pressure field imposed by the deep ocean.

Atkinson et al. (1983) suggested that the alongshore pressure of oceanic origin which slopes downward toward the north may account for the observed northward flowing mean flow at midshelf in the SAB similar to that found for the MAB by Csanady (1978) and Beardsley and Winant (1979). Coastal circulation numerical models have been used to study the SAB circulation (Kantha et al., 1982; Blumberg and Mellor, 1983; Lorenzzeti et al., 1988). Lorenzzeti et al. (1988) investigated the isolated effect of

the alongshore pressure gradient of oceanic origin by applying the alongshore sea level slope along the shelf break open boundary of their linear two-layer model domain. They found that the alongshore pressure gradient is confined over the outer shelf region, while the alongshelf sea level slope is negligible at the coast. They pointed out that a nonlinear model should be used for the outer shelf region because of the dominant presence of the Gulf Stream, while their linear model seems to be appropriate for the wind-driven circulation of the inner and midshelf regions.

The steady response of the coastal ocean to alongshore pressure gradients imposed by the deep ocean was studied analytically by Middleton (1987) using a depth-averaged barotropic model. The governing equation of Middleton (1987) is identical to that found by Csanady (1978) on a f-plane. The alongshore pressure at the outer edge of the continental shelf entered the problem through the boundary condition having a spatially oscillatory structure in the alongshore direction. The on- and off-shelf flow is directly implied by the geostrophic relationship for this case. Middleton (1987) found that oceanic pressure fields penetrates shoreward more effectively on narrow continental margins than on a broad shelf inshore of the shelf break. The work of Middleton (1987) was further extended to a time-dependent problem by Power at al. (1989).

Effects of non-linearity and variable earth's rotation are neglected for most of the above theoretical studies. Both effects are expected to be important in studying the response of the continental shelf to the strong western boundary current as well as the frictional effect as pointed out by Lorenzzeti et al. (1988). Analytical models incorporating all of the above factors seem to be intractable, even when features of topography and geometry in the real ocean are neglected.

I-1-3. General objectives and outline

This study attempts to investigate the influence of the western boundary current on the circulation of the continental shelves by building upon simple numerical models. Particularly, the present study aims at understanding the underlying dynamics of penetration of the Kuroshio onto the ECS and JS, although parts of simple model results

may be applicable to other areas.

A general description of the ECS area, and a rather detailed review of observations and studies of the Kuroshio and its effect on ECS circulation form the remaining part of this chapter. As this study intends to investigate factors affecting the influx to the JS rather than the detailed circulation pattern within the JS, studies of the circulation within the JS are not reviewed. The first chapter concludes with a statement on the approach and aims of this study.

In chapter II, the barotropic vorticity equation (BVE), used as a main tool of explaining numerical model results, is presented. Non-dimensional numbers obtained from a non-dimensionalised BVE will be used for classifying numerical model runs. Some of the long-wave theories needed for understanding transients of initial spin-up experiments will also be brought together.

Two types of models are used; a two-layer shallow water equation model and a barotropic version of primitive equation model based on Haidvogel et al. (1991a). Chapter III describes both the models, together with numerical methods for solving the continuous equations, the boundary conditions, and the forcing.

Chapter IV and V present the analysis of numerical model results. Ocean models are configured to basically two types of simple model domains; ocean-shelf domain, and ocean-shelf-marginal sea domain. The results of the former are presented in chapter IV and the latter in chapter V.

Chapter IV splits into two main parts, linear and non-linear modelling results, to elucidate effects of non-linearity on the structure of penetration of the western boundary current. Interpretation of model results is mostly done by examining the local vorticity balance along selected sections.

Chapter V mainly presents the analysis of the simple shelf-marginal sea model results. Several numerical model results obtained from a realistic domain, which

represents the ECS area and a part of the JS are presented in the final part of the chapter.

Finally, a summary of this study together with a discussion of results are presented in chapter VI. Possible directions for future work in this field are also presented.

All figures referred to at each chapter are placed at the end of each chapter with figure captions in the left page of each figure.

I-2. GENERAL CIRCULATION IN THE NORTH PACIFIC

The anticyclonic subtropical gyre of the North Pacific consists of the North Equatorial Current on the south, the Kuroshio on the west, the Kuroshio Extension and the North Pacific Current on the north, and the California Current on the east (Fig. 1-2, from Wells (1986)). The Kuroshio is a narrow and swift western boundary current in the North Pacific Ocean originating from the North Equatorial Current. The Kuroshio enters the ECS through the passage east of Taiwan and flows northeast along the continental slope (see Fig. 1-1) roughly following bottom topography. It exits from the ECS through the Tokara Strait south of Kyushu Island and flows northeast along the east coast of Japan after being joined by transport outside the ECS. The Kuroshio separates from the Japan around 36° N ~ 37° N (Masuzawa, 1972 ; Kawai, 1972) and flows generally east. The eastward continuation of the Kuroshio beyond the separation location has been called the Kuroshio Extension by Sverdrup et al. (1942). The further continuation of the Kuroshio Extension is called the North Pacific Current. It is weak and broad current and reaches as far as 150° W (Kawai, 1972).

The subpolar region north of the subtropical gyre is occupied by the cyclonic subpolar (or subarctic) gyre. The Oyashio, the western boundary current of the subpolar gyre, flows southwest along the southern Kuril Islands and the southeast coast of

Hokkaido and encounters the Kuroshio east of Japan (see also Fig. 1-1).

I-3. DESCRIPTION OF THE STUDY AREA

The ECS lies on a broad continental shelf with depths less than 200 m and consists of an extension of the Yellow Sea (or Huanghae Sea) shelf with the 1,000-2,700 m Okinawa Trough along its southeastern margin (Fig. 1-3). Both the ECS and Yellow Sea form a large semi-enclosed shallow sea with a broad shallow continental shelf along the Chinese coast and a narrow shelf along the Korean coast. Water depths more than 100 m appear in the eastern part of the ECS, west of Kyushu Island. The Ryukyu Islands and the Okinawa trough define approximately the seaward boundary of the ECS. The deeper Pacific Ocean is located just outside of this island chain, while the core of the Kuroshio flows northward on the inside of the islands along the Okinawa Trough.

The ECS is connected to the adjacent abyssal depths of the Japan Sea in the northeast by narrow (about 100 km wide) and relatively shallow (maximum depth of 150 m) Korea Strait. It is also connected through Taiwan Strait to the South China Sea in the southwest.

The maximum width of the ECS shelf is off the Changjiang River where it reaches 450 km; farther southwest the shelf narrows to about 125 km west of Taiwan. The total area of the ECS including the Yellow Sea is about 9.0×10^5 km^2.

The JS is a marginal sea surrounded by the Japanese Islands and the Asian continent. It is connected to the ECS, the North Pacific, and the Okhotsk Sea through the Korea, Tsugaru, and Soya Straits respectively. A branch of the Kuroshio called the Tsushima Current (TC) enters the JS and forms the most energetic upper layer circulation within the JS. The TC enters the JS through the Korea Strait, and exits from the JS to the Pacific Ocean through the Tsugaru Strait located south of Hokkaido and to the Okhotsk Sea through the Soya Strait located north of Hokkaido as schematically

shown in Fig. 1-1. A recent review of the oceanographic condition of the above three straits related to the passage of the TC was made by Sugimoto (1990).

I-4. PHYSICAL OCEANOGRAPHY OF THE ECS

Hydrography and circulation of the ECS are influenced by the Kuroshio, the monsoon winds, and a large amount of fresh water discharge. The general circulation driven by the wind and buoyancy input, and the hydrography are briefly described in this section. The Kuroshio and its influence on the ECS circulation will be reviewed in the next three sections.

The monsoon regime prevails over the Yellow Sea and the ECS. In winter, strong cold and dry northerly winds dominate over the area. On the other hand, winds are southerly, light and variable through the summer season accompanied by strong solar heating (Huh, 1982a).

Strong northerly winds in winter induce southward flowing coastal currents of cold, low salinity and high turbidity waters along both the west coast of Korea and the China coast (Guan, 1983a, 1984; Huh, 1982a). A band of cold water along the China coast is frequently seen in surface temperature distributions derived from satellite images in winter (Huh, 1982a; Qiu et al., 1990). This cold coastal water not only extends farther south toward Taiwan Island but also protrudes over the central part of the ECS shelf. Numerical and analytical studies of wind-driven circulation of the ECS (Choi, 1982; Kang, 1984; Yuan and Su, 1983, 1984) also showed that northerly winds maintain a southward flow along both the China coast and along the west coast of Korea. There exist northward flows opposing the dominant northerly wind in winter in the central part of the Yellow Sea (Choi, 1982; Huh, 1982a; Yuan and Su, 1983, 1984).

A large amount of fresh water discharges into the ECS from rivers in the China and Korea especially during the summer. The Changjiang (or Yangtze) River in China is the largest one in this area. In terms of volume discharge, it is the largest river in Asia

and the fourth largest in the world (Wang and Aubrey, 1987). The annual discharge of the Changjiang River amounts to about 9.3×10^{11} m^3, and 70 % of its annual discharge occurs in the months from May to October with a maximum in July. The total discharge of all other rivers in China and Korea is less than 10 % of Changjiang River discharge.

The behaviour of the Changjiang discharge over the adjacent shelf is dependent on the amount of discharge. The spring and summer discharge is sufficient to form a surface plume of relatively fresh water called Changjiang River Diluted Water, CRDW (Guan, 1983a, 1984). The water tongue of the CRDW in summer may extend some 600 km into the ECS toward northeast direction (Guan, 1984). The surface plume of CRDW was observed in the sea area around Cheju Island 600 km away from the mouth of the Changjiang River in summer (Kim et al., 1991). During the low river runoff in winter, the Changjiang discharge turns right at the mouth of the river and flows southward along the Chinese coast (Beardsley et al., 1985).

Hydrography in the ESC shows marked seasonality. As an example, Fig. 1-4 shows the vertical distributions of temperature and salinity in the western channel of the Korea Strait in summer and winter (Moriyasu, 1972) through which the TC enters the JS. During the winter, shelf waters in the ECS become almost vertically homogeneous since atmospherically cooled surface waters are mixed downward by the cold and strong wind. However, thermohaline fronts are formed in the areas where the cold and fresh shelf-origin waters meet the warm and saline oceanic-origin waters. Therefore, the influence of the Kuroshio can be easily identified from the sea surface temperature distribution in winter. Fig. 1-5 shows winter SST (sea surface temperature) pattern in the ECS. Relatively warm tongues near A (28°N, 124°E), B (31°N, 129°E), and C (35°N, 122°E) in the figure represent the influence of the Kuroshio.

The opposite effect occurs during the summer and the water column is typified by strong vertical stratification due to the extensive precipitation, river runoff and solar heating. Water masses originating from the Kuroshio water cannot be easily identified from the surface distribution of water properties in summer since the warm and low salinity waters from different source areas cover the whole ECS area. However, the

influence of the Kuroshio, waters with salinity higher than 34.2 ‰ in Fig. 1-4, can still be seen below the seasonal thermocline during the summer.

I-5. KUROSHIO IN THE EAST CHINA SEA

The Kuroshio in the ECS referred here is defined as the section of the Kuroshio between the east of Taiwan in the south and the Tokara Strait south of Kyushu Island in the north.

Fig. 1-6 shows the mean surface velocity pattern in the ECS averaged from GEK (Geomagnetic ElectroKinetograph) observations between 1953 and 1984 (Qiu and Imasato, 1990). It can be seen from this figure and also Fig. 1-3 that the western edge of the Kuroshio approximately follows the 200 m isobath. The main axis of the Kuroshio in the ECS fluctuates by about 35 km (Nitani, 1972) and is relatively stable compared with variation in the Pacific Ocean (Guan, 1980). A narrow countercurrent flows southwestward between the main axis of the Kuroshio and Ryukyu Islands. The Kuroshio deflects eastward south of Kyushu and flows out into the Pacific Ocean through the Tokara Strait.

A large amount of GEK and hydrographic data has enabled estimates to be made of the variability of the Kuroshio in the ECS (Nitani, 1972; Guan, 1980; Nisizawa et al., 1982; Guan, 1983b; Ichikawa and Beardsley, 1993).

Guan (1980) reported the seasonal and interannual variations of the Kuroshio surface velocities using the GEK data obtained on a line in the ECS (section G in Fig. 1-1) during the period of 1956-1975. The mean monthly surface velocity of the Kuroshio on the section is shown in Fig. 1-7 (B). The main results are as follows: (1) The position of the main axis of the Kuroshio determined by the location where the maximum velocities were observed, its direction (which lay between 40-60° from the north to the clockwise direction), and its width (about 50-100 km) are quite stable. (2) The mean velocity at the main axis was 95 cm/sec and ranged from 45 cm/sec to 150

cm/sec. (3) Seasonal variation of the velocity at the main axis were quite large with a maximum in spring (March and May) and a minimum in fall (November). (4) Seasonal and annual fluctuations of the surface velocity seem to be related with the wind-stress curl field observed two months earlier on the Northern Subtropical Pacific Ocean adjacent to the Hawaiian Islands. (5) The seasonal variation of surface velocities of the Kuroshio countercurrent is in phase with the Kuroshio itself.

Several authors calculated the baroclinic transport of the Kuroshio in the ECS using long-term hydrographic data (Nitani, 1972; Nisizawa et al., 1982; Guan, 1983b). The magnitude of the transport is somewhat different for each calculation due to the difference in location, averaging period and reference level.

Nitani (1972) described the Kuroshio from its beginning based on scattered observations from 1942 to 1967. According to his estimation the volume transport of the Kuroshio varies meridionally and the calculated mean transports were 40 Sv east of Taiwan and 33 Sv (1 Sv = 10^6 m^3/s) at the entrance of the ECS northeast of Taiwan. The transport shows long periodic variations ranging between 20 - 40 Sv. The mean baroclinic transport of the Kuroshio countercurrent was also estimated to be approximately 5 Sv.

Guan (1983b) analysed a data set between 1955 and 1978 to calculate the baroclinic transport of the Kuroshio referred to the 700db surface on the section G in Fig. 1-1. The overall mean value was 21.3 Sv with a standard deviation of 5.36 Sv. The calculation by Guan (1983b) shows that the maximum volume transport of about 24-25 Sv occurred in spring season (April) with the secondary maximum in July and August, and the minimum of 19-20 Sv occurred in fall season (September). The trend of spring-maximum and fall-minimum is similar to that of the seasonal variations of surface current velocities in Fig. 1-7 (B).

The calculation by Nishizawa et. al. (1982), however, on the same section with same reference level as Guan (1983b) using the data between 1954-1980 shows no apparent seasonality, although the mean transport values is comparable to that of Guan

(1983b).

There are many uncertainties in the dynamic method, e.g. the choice of reference level, barotropic component, mesoscale phenomena and so on. It was not until the end of 1980s' that the assessment of the Kuroshio volume transport using directly measured currents was possible in the ECS.

A cross-stream survey of the Kuroshio was conducted with the fish-mounted ADCP (Acoustic Doppler Current Profiler) west of Okinawa in the ECS (line F in Fig. 1-8 (A)) during 29-30 October 1987.

Fig. 1-8 (B) shows a detailed velocity structure of the Kuroshio obtained from the ADCP measurement (Kaneko et al., 1990). The strongest current, over 80 cm/sec, was observed between stations F6 and F5. The maximum velocity of 112 cm/sec was observed at a depth of 90 m near station F6. There exists a countercurrent with velocities ranging from 0 and 20 cm/sec at the right side of the Kuroshio between stations F2 and F1. Kaneko et al. (1990) further showed that volume transport of the Kuroshio in the upper 700 m depth along the line F using the ADCP current, and also hydrographic data, was 27.2 Sv, which was about 35 % higher than the baroclinic transport based solely on the hydrographic data.

Temporal and spatial variability of absolute volume transport of the Kuroshio in the ECS was estimated for the period 1986-1988 from hydrographic data referenced to surface velocity data obtained by either GEK or ADCP (Ichikawa and Beardsley, 1993). Fig. 1-9 shows an example of absolute geostrophic sections on the G-line estimated from hydrographic and surface current observations. The strong velocity cores over 60 cm/s appear in the upper 400 m on the continental slope region. Weak countercurrent regions are also seen in the east of the Kuroshio core. According to their calculation the three-year mean value of the Kuroshio transport was 27.6 $\pm$ 3.7 Sv with a seasonal signal (maximum in summer) of 20 $\sim$ 30 Sv in range. They also found that the barotropic contribution (depth-averaged component) to both the average and the fluctuation of the Kuroshio transport greatly exceeds the baroclinic component. They also suggested that

the local wind forcing of the Kuroshio transport in the ECS is important rather than a large scale wind forcing implied by the Sverdrup relationship, which led to an annual transport cycle with a maximum in February and minimum in September according to Kutsuwada and Teramoto (1987).

The half-year mean transport of the Kuroshio was estimated to be 23 Sv with a standard deviation of 3 Sv by Mizuno et al. (1991) from the horizontal and vertical current profiles obtained from three mooring lines across the Kuroshio main stream.

The absolute volume transport of the Kuroshio estimated from the hydrographic and ADCP current data in the southwestern part of the Kyushu Island was 30.3 $\pm$ 2.0 Sv (Chen et al., 1992).

The transport of the Kuroshio inferred from the monthly sea level difference across the Tokara Strait downstream of the Kuroshio in the ECS shows a summer-maximum (Blaha and Reed, 1982; Kawabe, 1988). Blaha and Reed (1982) also showed that the fluctuations in seasonal transport of the Kuroshio are six months out of phase with those predicted by the Sverdrup relation. They speculated that the seasonal winds between 7° N ~ 15° N cause the seasonal fluctuations of the Kuroshio. Greatbatch and Goulding (1990) pointed out the importance of bottom topography in shifting the annual cycle of the Kuroshio from that predicted by Sverdrup relation to that observed by Blaha and Reed (1972) and Kawabe (1988).

Although the mean Kuroshio path in the ECS is largely controlled by the bottom topography and is relatively stable compared to that in the sea area south of Japan, recent observations have shown the presence of low-frequency fluctuations of the Kuroshio in shelf break and slope regions (Sugimoto et al., 1988; Qiu et al., 1990; Ichikawa and Beardsley, 1993). Based on a sequence of satellite IR images obtained during the springtime, Qiu et al. (1990) found meanders of the Kuroshio front, which appear along the western edge of the mean Kuroshio path determined by a long-term GEK data, with horizontal scales of 100 to 150 km and wave periods of 14 to 20 days propagating downstream. Ichikawa and Beardsley (1993) also noted fluctuations in the

Kuroshio transport with an amplitude of 5-10 Sv, period of 8-32 days, wavelength of 150-375 km, and downstream phase velocity of 8-19 km/day by comparing the transport between transects.

I-6. THE KUROSHIO CURRENT SYSTEM

The Kuroshio Current System referred here is defined as the Kuroshio south of Japan and the Kuroshio Extension, following the Mizuno and White (1983).

The Kuroshio Current System is characterised by a larger transport than the Kuroshio in the ECS (Nitani, 1972; Nishizawa et al., 1982; Kaneko et al., 1992; Clifford and Horton, 1992; Ichikawa and Beardsley, 1993) and a quasi-stationary meander pattern (Mizuno and White, 1983) as shown in Figs. 1-7 (D) and 1-10.

The volume transport of the Kuroshio Current System is two or three times larger than that of the Kuroshio in the ECS based solely on the hydrographic data (Nitani, 1972; Nishizawa et al., 1982; Clifford and Horton, 1992) and on the combined data of hydrographic measurements and currents (Kaneko et al., 1992; Ichikawa and Beardsley, 1993). The reason for the larger transport has been ascribed to the joining of the transport outside the ECS to the Kuroshio in the ECS, serving to increase the transport of the Kuroshio Current System (Nitani, 1972; Ichikawa and Beardsley, 1993) and/or the presence of recirculation gyre to the north and south of the Kuroshio (Qiu, 1992).

There are two thermal fronts at the sub-surface depths in the sea area east of Japan as shown in Fig. 1-11; the southern one is called the Kuroshio front, which represents the stream axis of the Kuroshio Extension; and the northern one is called as the Oyashio Front (Kawai, 1972). The area between the two fronts is called as the Perturbed Area (Kawai, 1972) or the confluence zone (Kitano, 1975).

The Perturbed Area is characterised by a high spatial and temporal variability

(Mizuno and White, 1983) due to the meso-scale phenomena such as the formation and decay of warm and cold rings associated with the meandering of the Kuroshio Extension and the intrusion of minor branches originating from the northern and southern parts of the area (Kawai, 1972; Kitano, 1975). A warm outflow from the Tsugaru Strait further complicates the oceanographic conditions in the Perturbed Area as schematically shown in Fig. 1-1.

Seasonal and interannual variability of the Kuroshio Current System has been reported based on hydrographic data (Kawai, 1972; Mizuno and White, 1983). Surface transports of the Kuroshio Current System based on the altimetry data were shown to have a seasonal cycle with a maximum in summer south of Japan and in autumn in the Kuroshio Extension (Qiu et al., 1991; Qiu, 1992) as shown in Fig. 1-7 (C) and (D) respectively. The autumn-maximum tendency was also found in the baroclinic transport of the Kuroshio Extension (Clifford and Horton, 1992), which is nearly 180° out of phase to the baroclinic transport of the Kuroshio in the ECS calculated by Guan (1983b).

Qiu et al. (1991) found that the large-scale fluctuation in the surface transport was significantly correlated with the current path fluctuations, with more northerly path positions coinciding with large surface transport values for the Kuroshio Extension. The meridional range of the long period fluctuation of the northern limit of the Kuroshio Extension determined from a long-term hydrographic data is about 400 km (Kawai, 1972), and the fluctuation mainly occurs between 36°N ~ 38°N as shown in Fig. 1-12.

I-7. SHELFWARD PENETRATION OF THE KUROSHIO

Not all of the Kuroshio water passing Taiwan flows out to the Pacific Ocean. Part of the Kuroshio water branches shelfward to become the Taiwan Warm Current (TWC), Tsushima Current (TC) and Yellow Sea Warm Current (or Hwanghae Sea Warm Current, YSWC) as shown schematically in Fig. 1-1.

I-7-1. Taiwan Warm Current

The first influence of the Kuroshio on the circulation of the ECS comes from the region northeast of Taiwan, where sudden expansion of shelf width causes the isobaths of the continental slope to become more zonal (Fig. 1-3), almost perpendicular to the axis of the Kuroshio. The major part of the Kuroshio follows isobaths northeastward, but a part of it overshoots and penetrates northward to become the TWC.

When the Kuroshio impinges on the continental shelf and turns northeastward, an upwelling of Kuroshio sub-surface water occurs above the shelf break. The existence of cold and nutrient-rich upwelled water to the northeast of Taiwan has been well documented and seems to be a permanent feature (Liu and Pai, 1987; Chern and Wang, 1990; Hsueh, 1992; Liu et al., 1992). Liu et al. (1992) showed that the upwelling north of Taiwan is intensified shortly after the onset of northeast monsoon as a consequence of the shelfward surface Ekman drift, and subsequently the intrusion of the subsurface Kuroshio water occurs along the shelf break farther north.

A part of the Kuroshio flows directly into the shelf along the northeast coast of Taiwan to the left of the upwelling core (Chern and Wang, 1990; Qiu and Imasato, 1990). Qiu and Imasato (1990) studied the generation mechanism of this branch of the Kuroshio, which they called the Kuroshio Branch Current, using a barotropic inflow-outflow numerical model with a simplified configuration and bottom topography of the ECS. They explained it as a western boundary current supported by the northern coast of Taiwan, hence the planetary β-effect and the existence of Taiwan Island are two indispensable factors in the formation of this branch.

To the northeast of the upwelling core, a part of Kuroshio surface water was observed to overrun the shelf break and penetrates northward as a shallow surface current (Hsueh, 1992). Using an analytical, and inviscid reduced-gravity model, Hsueh (1992) showed that the transport of this penetration ($\sim$ 25 % of the baroclinic Kuroshio transport) is equal to the product of depth ratio squared between the shelf depth and the upper layer depth of the Kuroshio, and the transport of the Kuroshio.

The definition of the TWC mainly used by Chinese Oceanographers (Su and Pan, 1987; Yuan and Su, 1988) is imprecise, but it appears that the northward or northeastward flowing current north of Taiwan which carries properties of the Kuroshio water is called the TWC. The above mentioned two branches of the Kuroshio, and the inflow from the Taiwan Strait originating from the South China Sea (Guo et al., 1987), contribute to the generation of the TWC (Su and Pan, 1987; Chao, 1991).

In winter, warm TWC water extending over the continental shelf north of Taiwan is clearly distinguished from the cold coastal water on satellite images (Liu and Pai, 1987; Qiu et al., 1990).

Two branches of the TWC have been documented (Su and Pan, 1987; Yuan and Su, 1988) as schematically represented in Fig. 1-1. The inshore branch of the TWC flows northward in the offshore area of China and the TWC water, characterised by high temperature and salinity, appears to the south of the mouth of the Changjiang River (Guan, 1983a). The western side of the TWC water is adjacent to the coastal water characterised by low salinity , and a sharp front is formed where these two waters meet. The offshore branch of the TWC has a tendency to turn to the east-southeast to rejoin the main stream of the Kuroshio after it flows onto the continental shelf north of Taiwan (Su and Pan, 1987; Yuan and Su, 1988). Some dynamical aspects of the TWC were discussed by Su and Pan (1987) using the similar equation to that of Csanady (1978), but on a β-plane and in a horizontally finite domain.

Chao (1991) developed a three-dimensional primitive equation model to study the regional circulation feature in the southern part of the ECS. His model was forced by a prescribed geostrophic jet at the southern boundary representing the Kuroshio, the steady wind field, inflow from the Taiwan Strait, and the buoyancy forcing from the Changjiang River. He showed how the atmospheric and buoyancy forcings, and the effect of stratification, enhance or weaken the intrusion of the Kuroshio into the ECS.

I-7-2. Tsushima Current

The second effect of the Kuroshio on the circulation of the ECS is the penetration of the TC into the JS. The TC originating from the Kuroshio transports warm and saline equatorial water into the Japan Sea through the Korea Strait. Most of its transport moves northward within the Japan Sea, returning to the Pacific through the Tsugaru Strait (70-90 %) and the Soya Strait (Moriyasu, 1972) as shown schematically in Fig. 1-1.

The baroclinic volume transport of the TC calculated by the dynamic method (Yi, 1970), and the surface current velocities of the TC determined by the sea level difference across the Korea Strait (Yi, 1966) show a seasonal cycle with a summer/fall maximum of about 2 Sv and a winter/spring minimum of about 0.3 Sv (Fig. 1-7 (A)). The annual cycle of both the volume transport and surface current velocities of the TC is almost 180° out of phase with that of the Kuroshio in the ECS determined by a long-term hydrographic (Guan, 1983b) and GEK data (Guan, 1980). However, the annual cycle of the TC is in phase with that of the Kuroshio Current System as shown in Fig. 1-7 (D). The total transport through the Korea Strait is less than 10 % of the Kuroshio transport in the ECS.

The wind-driven transport was supposed to contribute to the seasonal variation of the TC (Huh, 1982a; Icyiye, 1984; Kang, 1984); wind-driven currents in winter generally flow southwards opposite to that associated with the Kuroshio and, therefore, the transport through the Korea Strait is small in winter. In summer, however, both the wind-associated and the Kuroshio-associated currents flow in the same direction, hence, the transport through the Korea Strait is large.

It had long been believed that the TC was generated as branching from the Kuroshio south of Kyushu Island (Nitani, 1972), just like a river tributary since Uda (1934) first proposed the circulation pattern in the ECS and adjacent sea area. Water mass analysis in the ECS, however, indicates that the TC water is formed by mixing between the Kuroshio Surface Water and the ECS water along the continental margin

(Lim, 1971; Sawara and Hanzawa, 1979).

The amount of penetration of a western boundary current into a marginal sea which is connected to an open ocean by two narrow straits (Fig. 1-13) was estimated from a linear, steady and barotropic theoretical model by Kimura and Minato (1980). Their work was a first theoretical approach to explain the generation of the TC as a result of pressure difference between the Tsugaru and Korea Straits due to the wind-driven oceanic circulation. They obtained a relation between the volume transport into the marginal sea and various external parameters such as the coefficient of bottom friction, depth ratio between the marginal sea and deep ocean, width of straits, and the location of straits. They predicted that about 2 % of the volume transport of the Kuroshio penetrates into the Japan Sea.

Toba et al. (1982) suggested that the TC is driven by the sea level difference caused by the variation of the internal density structure between the ECS and east of Tsugaru Strait, and the annual cycle of the TC also results from the annual cycle of the sea level difference.

Ichiye (1984) suggested that the TC is formed through the lateral flow of the Kuroshio due to horizontal Reynolds stresses. He also argued that the pressure difference along the Kuroshio may be irrelevant in the generation of the TC as the annual trend of it is opposite to the seasonal cycle of the TC.

Ichiye and Li (1984) developed a barotropic inflow-outflow numerical model to investigate the generation of the TC in the sea area west of Kyushu. They concluded that the circulation in the area is mainly controlled by the bottom topography and the Coriolis effect is important in modifying the circulation.

Recently Wang and Su (1987) and Yuan and Su (1988) suggested that a part of the TWC becomes a source of the TC after rejoining with the Kuroshio around the shelfbreak north of 29°30′ N

Using a three-dimensional primitive equation model, Oey and Chen (1991) suggested that episodic large amplitude meanders resulting from the interaction between topographic waves and frontal disturbances propagating in opposite directions are responsible for the shelfward intrusion of the Kuroshio in the ECS.

Satellite data have provided useful information in understanding the circulation features and the distribution of water masses in the ECS, but mainly in winter (Huh, 1982a, 1982b; Zheng and Klemas, 1982; Qiu et al., 1990), because then cooling destratifies the water column, forcing oceanic thermal fronts between shallow and deep waters and waters of coastal versus oceanic origin. Analysing a series of spring season satellite images, Huh (1982b) mentioned that the source of warm TC water consists of the mixed water between the Kuroshio and shelf waters and the intermittent intrusion of the Kuroshio west of Kyushu as depicted in Fig. 1-14. He also suggested that branching of the Kuroshio in the area west of Kyushu is a transient event.

Qiu et al. (1990), also using satellite images, further showed that a warm eddy was formed southwest of Kyushu during a period when the volume transport of the Kuroshio in the ECS increased.

I-7-3. Yellow Sea Warm Current

It had long been believed that the Yellow Sea Warm Current was a branch of the Kuroshio flowing northward deep into the Yellow Sea (Uda, 1934; Nitani, 1972; Guan, 1983a).

There are, however, different views on the source of the YSWC. Nitani (1972) and Guan (1983a) mentioned that the YSWC separates from the TC somewhere around west of Kyushu and flows northwestwards towards the Yellow Sea. On the other hand, Yuan and Su (1988) suggested that the YSWC is primarily a result of the branching of the TWC guided by bottom topography.

Detailed hydrographic survey and current measurements in the sea area southwest

of Korean Peninsula show no evidence of deep penetration of the YSWC into the Yellow Sea (Kim and Lee, 1982; Lie, 1986; Park, 1986; Kim et al., 1991), contrary to previous studies. Instead, it is found that the YSWC flows eastward in the Cheju Strait after turning to the east at the western coast of Cheju Island as shown schematically in Fig. 1-15. Repeated hydrographic and a month-long current measurements further confirmed the existence of the warm current in the Cheju strait (Chang, 1983).

I-8. SUMMARY AND DISCUSSION

Knowledge of the Kuroshio and its penetration onto the ECS and the JS has been reviewed. The main feature identified is the existence of three warm currents originating from the Kuroshio. The review also highlights two questions that have not been resolved satisfactorily; the dynamics of the penetration mechanism, and the interrelation between branched currents.

The mean transport of the Kuroshio in the ECS (section I-5) seems to be within 20 ~ 30 Sv with an annual range of 40 % of the mean transport or less. The maximum velocity of the Kuroshio in the ECS reaches 1 m/s, and strong velocity core is confined to upper 400 m depth (Kaneko et al., 1990; Ichikawa and Beardsley, 1993). The seasonal variability of the Kuroshio in the ECS is inconclusive. Relative geostrophic transport and the surface velocity of the Kuroshio based on long-term hydrographic (Guan, 1983b) and GEK (Guan, 1980) data showed a maximum in spring and a minimum in autumn. On the other hand, the absolute transport for a relatively short period showed a maximum in summer (Ichikawa and Beardsley, 1993), and the transport of the Kuroshio through the Tokara Strait inferred from the sea level difference also showed a maximum in summer (Blaha and Reed, 1982; Kawabe, 1988).

The volume transport of the Kuroshio Current System (Kuroshio south of Japan and the Kuroshio Extension; section I-6) is 2 ~ 3 times larger than that of the Kuroshio in the ECS (Nitani, 1972; Nishizawa et al., 1982; Kaneko et al., 1992; Clifford and Horton, 1992; Ichikawa and Beardsley, 1993), and has an annual cycle with a maximum

in summer south of Japan (Qiu, 1992) and in autumn for the Kuroshio Extension (Qiu et al., 1991; Clifford and Horton, 1992). Sverdrup relation failed to account for this annual cycle (Blaha and Reed, 1982). The annual range of the volume transport of the Kuroshio Extension is less than 20 % of the mean transport according to Clifford and Horton (1992).

The Kuroshio separates from the coast of Japan around 36 °N ~ 37° N (Kawai, 1972), but the separation latitude varies meridionally about 400 km (Kawai, 1972) and it relates to the amount of the transport of the Kuroshio Extension (Qiu et al., 1991). The Kuroshio separates from the coast further north when the transport of the Kuroshio Extension is large and vice versa.

The shelfward penetration of the Kuroshio (section I-7) has been fairly well documented since Uda's early study (1934). The Kuroshio generates a branch (TWC) northeast of Taiwan immediately after entering the ECS. Another branch of the Kuroshio, the TC, enters the JS and most of its transport exits to the North Pacific through the Tsugaru Strait which is located in the southwestern part of the subpolar gyre. The YSWC exerts its influence on the southern sea area of the Korea.

To date there have been few analytical and numerical modelling studies of the shelfward penetration of the Kuroshio in the ECS (e.g. Minato and Kimura, 1980; Yuan and Su, 1983, 1984; Ichiye and Li, 1984; Su and Pan, 1987; Wang and Su, 1987; Qiu and Imasato, 1990; Chao, 1991; Oey and Chen, 1991; Hsueh, 1992). These studies contributed much to the understanding of the general circulation features and some specific processes occurred in this area. However, our understanding of the phenomena is still largely empirical and therefore unsatisfactory.

The generation mechanism of the TS has been the subject of much particular controversy. Uda (1934) and Nitani (1972) speculated that the TC is directly fed by the Kuroshio southwest of Kyushu, just like a river tributary, and that the YSWC separates from the TC. Recently Wang and Su (1987) and Yuan and Su (1988) suggested that the TC and the YSWC are a continuation of the TWC. Several other authors have also

suggested mechanism of the generation of the TC since 1980s'; meridional pressure difference along the Kuroshio (Minato and Kimura, 1980), internal density gradient between the ECS and the sea area near the Tsugaru Strait (Toba et al., 1982), lateral flow of the Kuroshio due to horizontal Reynolds stress (Ichiye, 1984), and interaction between the topography and the Kuroshio (Oey and Chen, 1991). The possible importance of the mesoscale phenomena southwest of Kyushu in driving the intrusion of the Kuroshio into the JS was also pointed out by Huh (1982b). We need to clarify the interrelation between the branched currents and to investigate further the generation mechanism of those currents.

I-9. APPROACH AND AIMS

I-9-1. Approach

Our knowledge of the dynamics of the circulation in the ECS driven by the Kuroshio is meagre. Much more observational efforts must be made. Recently process-oriented observational programmes are in operation in the ECS area (e.g. KORDI, 1992). It is also useful to address many of the unresolved issues with simple analytical and/or numerical models since these provide a basis for interpretation of disparate data and an understanding of the natural processes at work.

In this study a numerical modelling approach is adopted to study the penetration of the WBC onto the shelf and marginal sea. Although theoretical studies of shelf circulation driven by offshore forcing (Csanady, 1978; Middleton, 1987) have elucidated some fundamental features, our understanding of the phenomena seems to be poor. This is particularly true of strong boundary current forcing of the shelf circulation. In some numerical studies such as Blumberg and Mellor (1983), circulation of the shelf area is driven by a combination of various forcings, so that it is hard to identify which component of the circulation is driven by the boundary current. Effects of non-linearity and frictional forces are expected to be important in determining the circulation of the continental shelf, which is frictionally dominated environment, driven by a strong

western boundary current, itself likely to be inertial. Both effects can only be taken into consideration in numerical models. Salient features of topography and geometry in real ocean can also be incorporated into numerical models.

This study sets out to investigate the dynamics of the shelfward penetration of the Kuroshio in the ECS, but not to simulate the detailed circulation of the area. Primitive equation models driven by observed wind and buoyancy forcings are computationally costly. They may also obscure the understanding of underlying dynamics. The required model is one that can represent the pivotal features of the region and can be used to determine the effect of various parameters on those features.

A development of a quasi-geostrophic model is inadequate for the present problem since the corresponding Rossby number U_c / f L_c (for the Kuroshio, $U_c \sim 1$ m/sec, $L_c \sim 100$ km), where U_c and L_c are characteristic velocity and length scales respectively and f is the Coriolis parameter, is generally $O(10^{-1})$ or larger. Also, a condition of the quasi-geostrophic approximation is that bottom topography must be no more than 10 % of the water depth (Thompson and Schmitz, 1989). Such a condition is inappropriate for the present purpose.

In this study a two-layer shallow water equation model (SWEM) and a barotropic version of semi-spectral ocean model (SPEM) based on Haidvogel et al. (1991a) are used. Both models are described in chapter III.

In chapter IV, the fundamental features of the shelf circulation driven by the strong boundary current are studied using the both models in a simple model domain which consists of deep ocean and shelf. To understand the underlying dynamics, the hierarchy of the models is gradually built upon by incorporating a single physical process previously neglected. Using this approach, effects of various internal and external parameters on the features are investigated.

In chapter V, penetration of the boundary current into the marginal sea is investigated using the SPEM in a simple model domain which consists of a deep ocean,

a shelf, and a marginal sea. The problem is further investigated using the SPEM in a more realistic model domain which incorporates some pivotal topographic features of the study area.

I-9-2. Aims

(1) To study the shelf circulation driven by a strong western boundary current by using simple numerical models.

(2) To investigate factors controlling the flow predicted by the models.

(3) To study the penetration of the boundary current into the marginal sea using a simple and a more realistic models.

(4) To understand the underlying dynamics of the shelfward penetration of the Kuroshio in the ECS using a combination of simple and more realistic models.

Fig. 1-1. Schematic circulation pattern in the East China and Japan Seas. Heavy dotted line denotes the approximate path of the Kuroshio. Dotted lines in the northeast of Taiwan, in the southwest of Korea, and in the Japan Sea denote the approximate paths of the Taiwan Warm Current (TWC), Yellow Sea Warm Current (YSWC), and Tsushima Current (TC) respectively. Lines G, I, and U indicate transects on which the magnitude of the Kuroshio and Tsushima Current was examined on the basis of hydrographic, current, and satellite altimetry data.

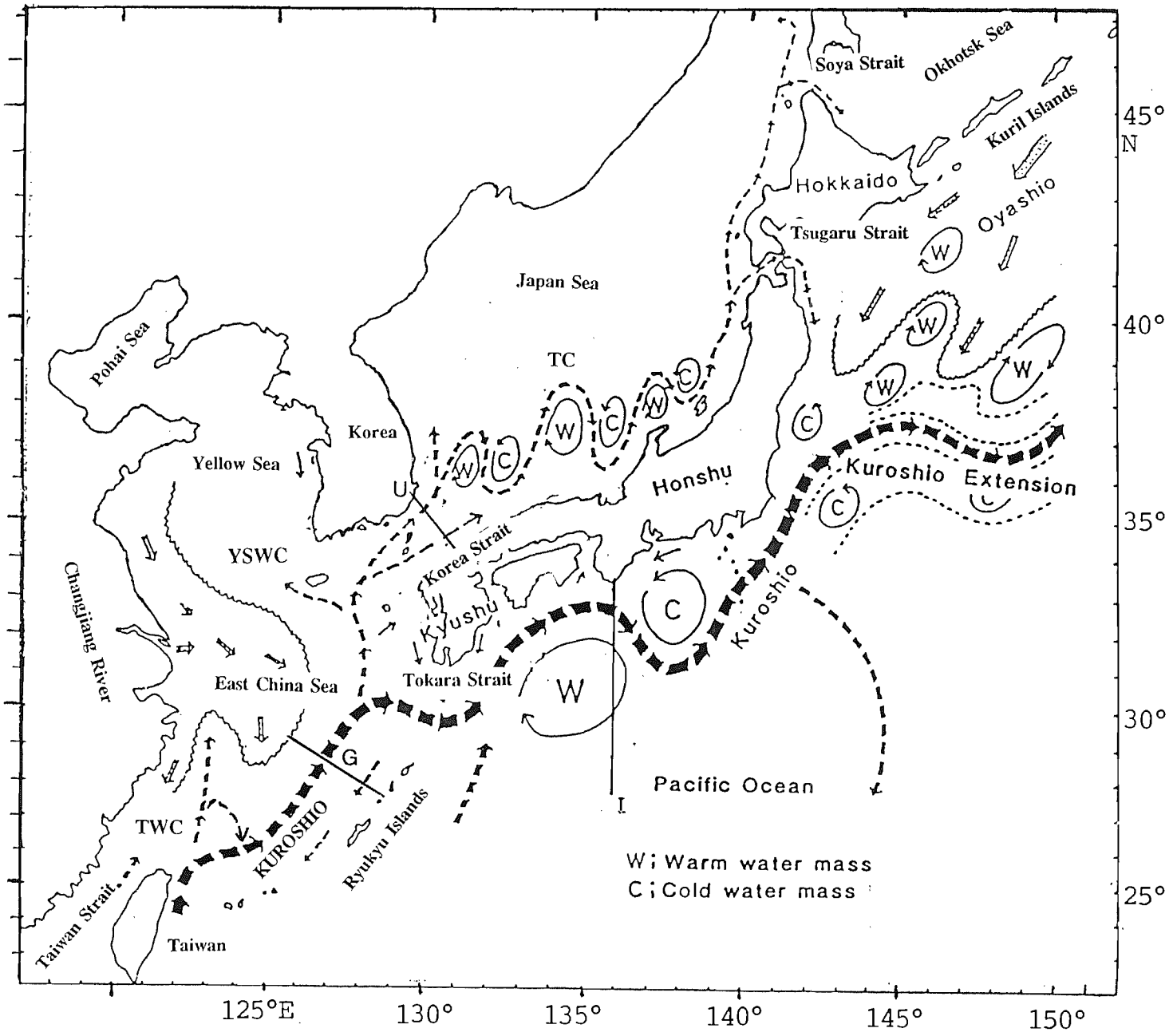
Soya Strait
Okhotsk Sea
Kuril Islands
Hokkaido
Tsugaru Strait
Oyashio
Japan Sea
Pohai Sea
TC
Korea
Yellow Sea
U
Honshu
Kuroshio Extension
YSWC
Korea Strait
Changjiang River
Kyushu
Kuroshio
East China Sea
Tokara Strait
G
Pacific Ocean
I
TWC
KUROSHIO
Ryukyu Islands
Taiwan Strait
Taiwan
W; Warm water mass
C; Cold water mass
45° N
40°
35°
30°
25°
125°E
130°
135°
140°
145°
150°

Fig. 1-2. General surface circulation of the world ocean in February-March (from Wells, 1986). Three marginal seas, South China Sea, East China Sea, and Japan Sea, in the northwest Pacific are indicated.

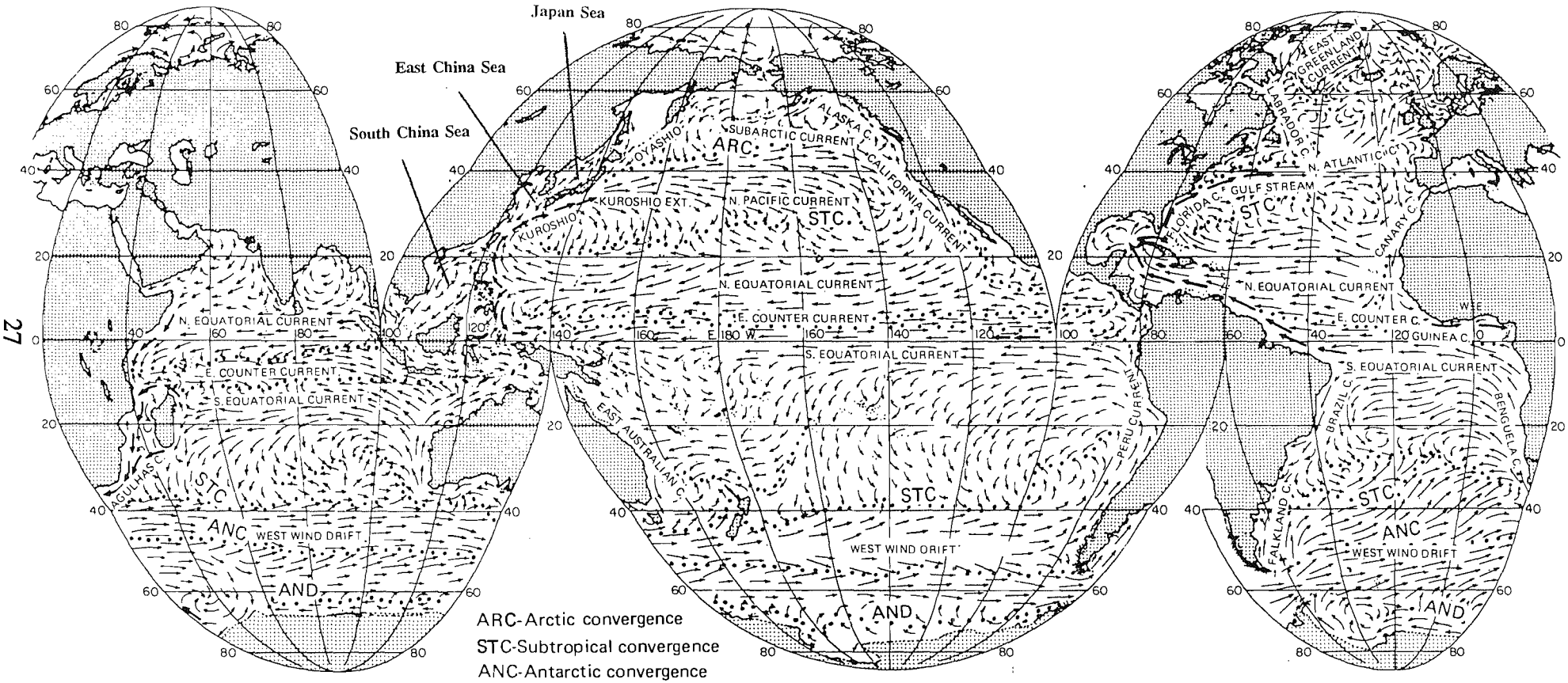

ARC-Arctic convergence
STC-Subtropical convergence
ANC-Antarctic convergence
AND-Antarctic divergence

Fig. 1-3. (Left) Bathymetry of the East China and Yellow Seas. Isobaths are in metres (from Huh, 1982b).

Fig. 1-4. (Right) Vertical sections of temperature (°C) and salinity (‰) in the western channel of Korea Strait (from Moriyasu, 1972). Upper and lower panels represent salinity and temperature respectively, left in February and right in July. The bottom panel shows the station positions.

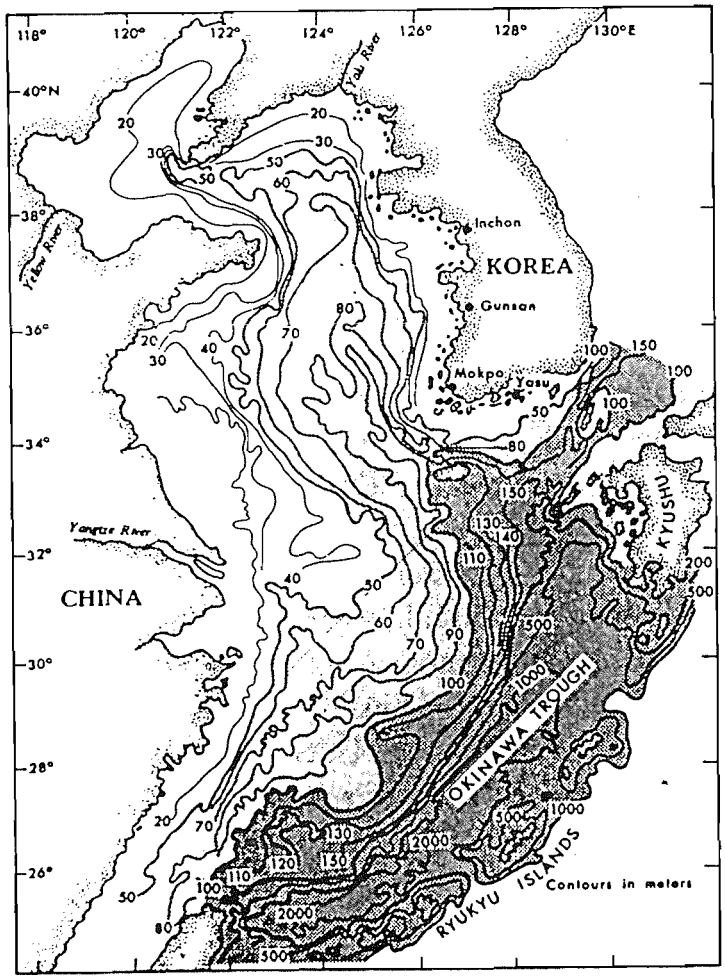
KOREA
CHINA
Inchon
Gunsan
Mokpo
Yosu
Yellow River
Yangtze River
Tsushima
KYUSHU
OKINAWA TROUGH
RYUKYU ISLANDS
Contours in meters

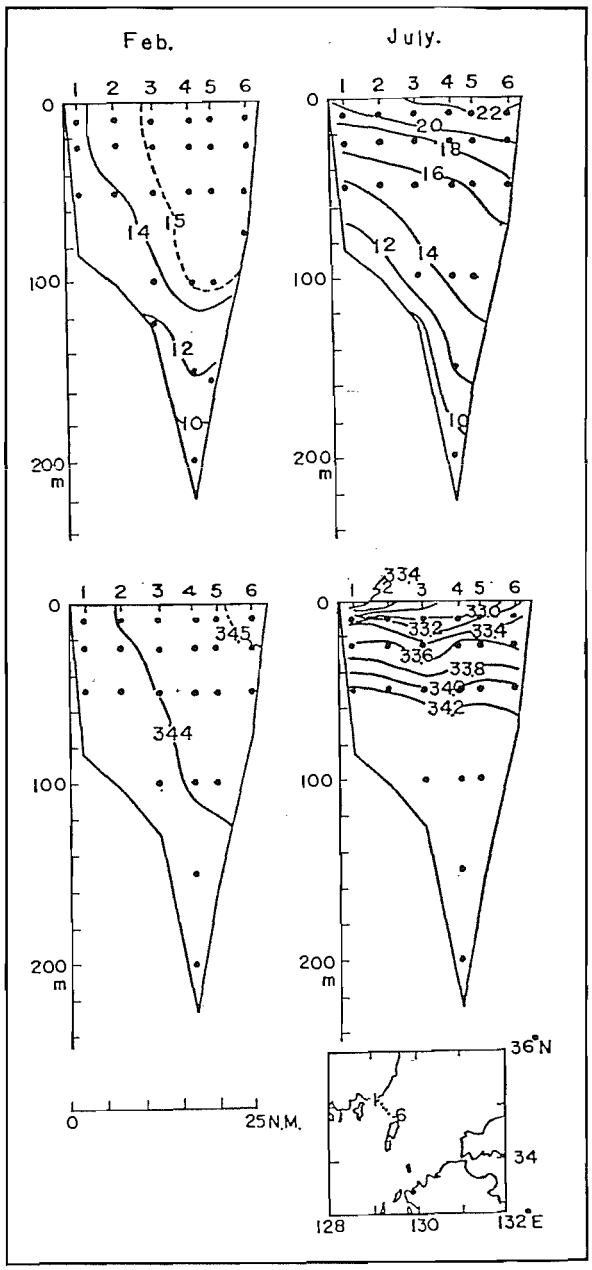
Feb.
July.
25N.M.
36°N
34
128
130
132°E

Fig. 1-5. Winter sea surface temperature pattern in the East China Sea derived from a satellite image on 7 January (from Zheng and Klemas, 1982).

Fig. 1-6. Surface flow pattern of the Kuroshio in the East China Sea derived from the long-term GEK observations from 1953 to 1984 (from Qiu and Imasato, 1990).

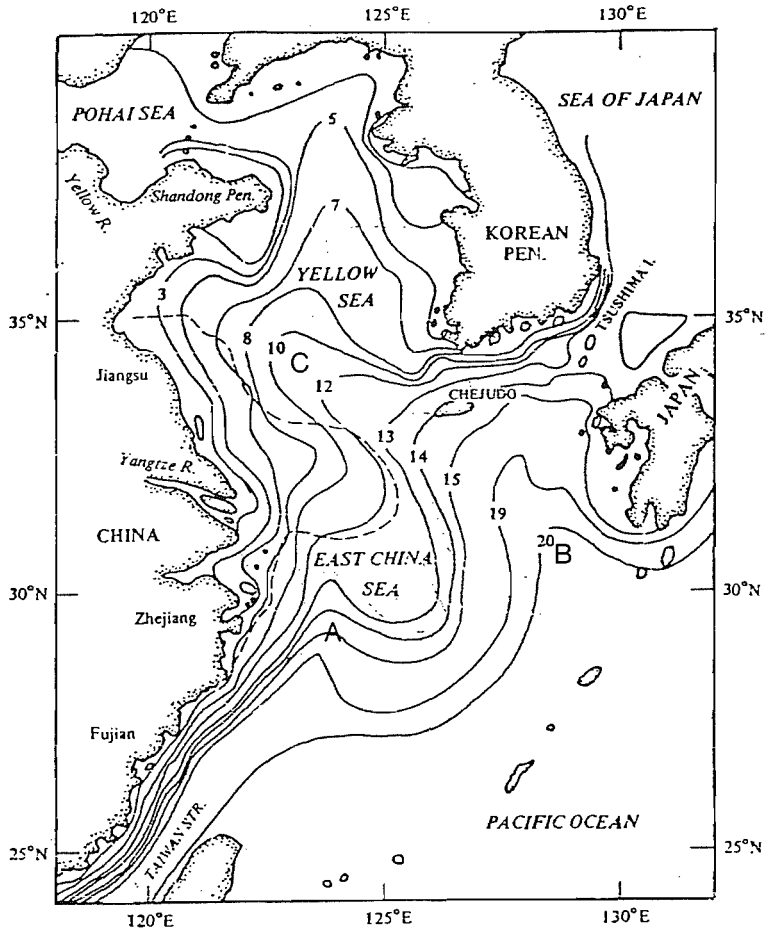
120°E
125°E
130°E
35°N
30°N
25°N
POHAI SEA
SEA OF JAPAN
Yellow R.
Shandong Pen.
KOREAN PEN.
YELLOW SEA
TSUSHIMA I.
Jiangsu
CHEJUDO
JAPAN
Yangtze R.
CHINA
EAST CHINA SEA
Zhejiang
Fujian
PACIFIC OCEAN
TAIWAN STR.
A
B
C
3
5
7
8
10
12
13
14
15
19
20

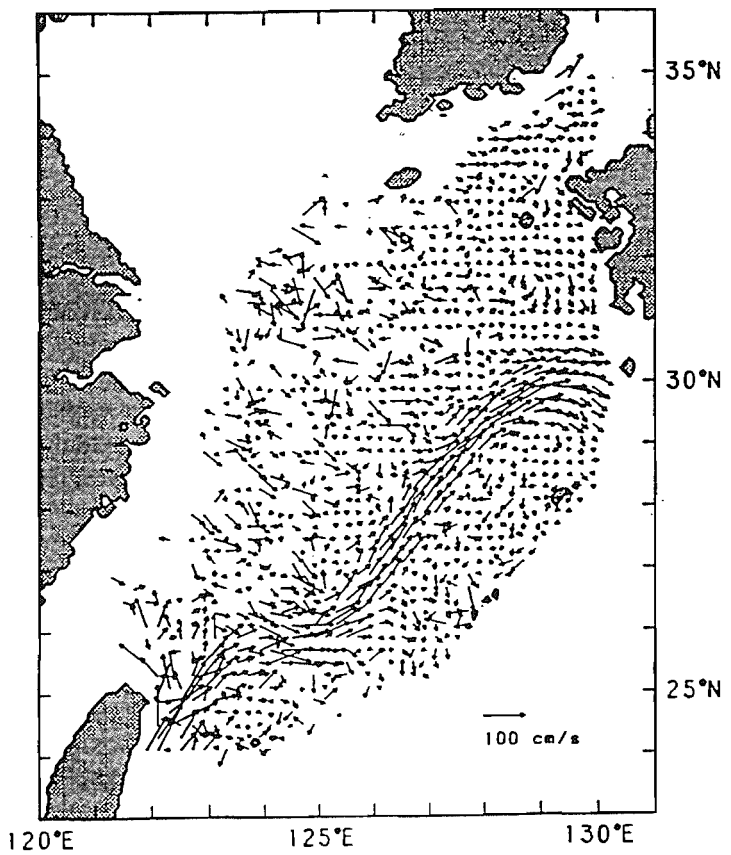
35°N
30°N
25°N
100 cm/s
120°E
125°E
130°E

Fig. 1-7. (A) Mean monthly surface current velocity based on sea level differences between two cross-strait locations in the Korea Strait by Yi (1966), and northward baroclinic transport of the Tsushima Current by Yi (1970) on line U in Fig. 1-1. (B) Mean monthly surface velocity of the Kuroshio on line G in Fig. 1-1 based on a long-term GEK data by Guan (1980). (C) Seasonal changes of the surface height differences across the Kuroshio south of Japan based on the altimetry data from the 2.5-year period of the Geosat ERM (Exact Repeat Mission, 17 day repeat cycle) by Qiu (1992). Squares and triangles denote value from two tracks running northwest-southwest from 26°N to the coast, close to line I in Fig. 1-1. Solid line denotes the 2-month running average and vertical bars denote a 95% confidence level. (D) Seasonal variation of longitudinally averaged baroclinic transports of the Kuroshio Extension between 141°E and 165°E relative to 500 dbar (squares), 800 dbar (triangles), 1000 dbar (plus signs), and 2000 dbar (circles) based on a climatology (Dynamic Generalized Digital Environmental Model, Dynamic GDEM) by Clifford and Horton (1992).

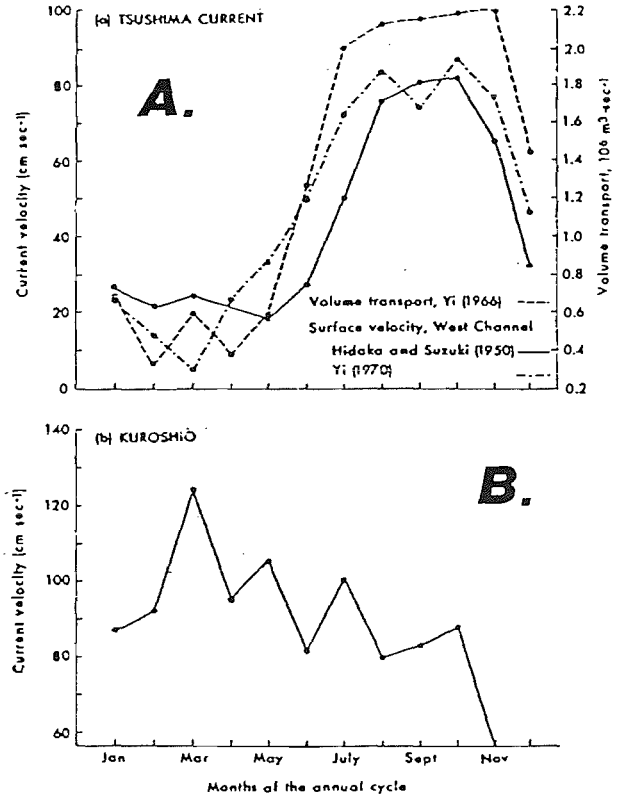
(a) TSUSHIMA CURRENT
A.
Current velocity (cm sec⁻¹)
Volume transport, 10⁶ m³ sec⁻¹
Volume transport, Yi (1966)
Surface velocity, West Channel
Hidaka and Suzuki (1950)
Yi (1970)
(b) KUROSHIO
B.
Current velocity (cm sec⁻¹)
Jan
Mar
May
July
Sept
Nov
Months of the annual cycle

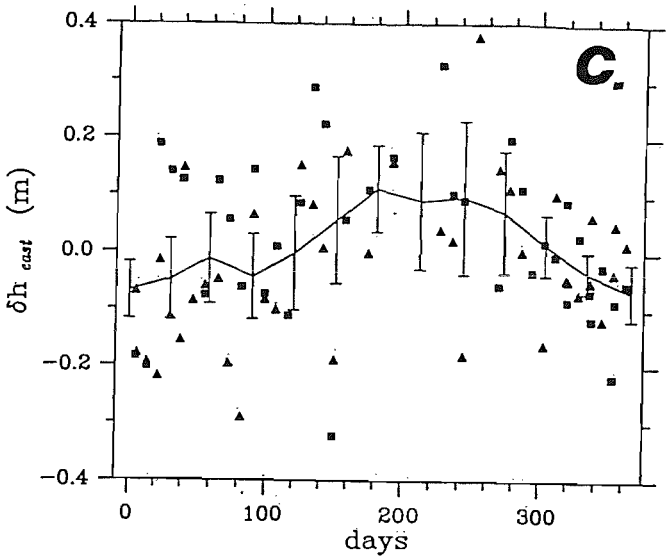
C.
δh east (m)
days

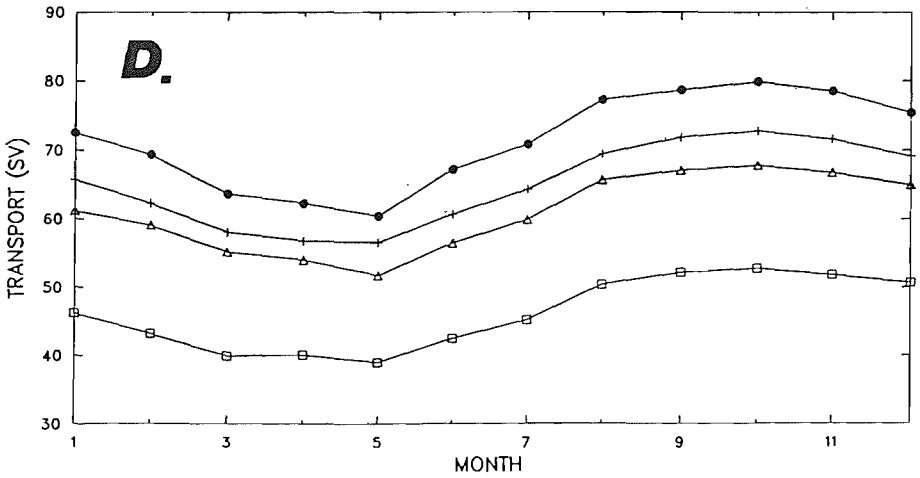
D.
TRANSPORT (SV)
MONTH

Fig. 1-8 (A). Map showing the location of ADCP observation lines. The traverse survey was conducted on the F-line located upstream of the G-line in Fig. 1-1 during 29-30 October 1987. The path of the Kuroshio and the position of a large cyclonic eddy are shown with arrows (from Kaneko, 1990).

(B) Contour plot of the velocity component normal to the F-line in Fig. 1-8(A). The shaded region indicates a place where the current velocity is negative (from Kaneko et al., 1990).

Fig. 1-9. Absolute geostrophic velocity section on the G-line in Fig. 1-1 on August 1987 estimated from hydrographic data at N_{HYD} stations and surface current data at N_{SCV} stations. Positive value indicates the northeastward component of velocity in cm/s. The heavy line at the bottom represents the ocean bottom while the light line represents the maximum depth of the hydrographic casts. The solid circles at the surface indicate the location of the hydrographic stations. (from Ichikawa and Beardsley, 1993).

A.

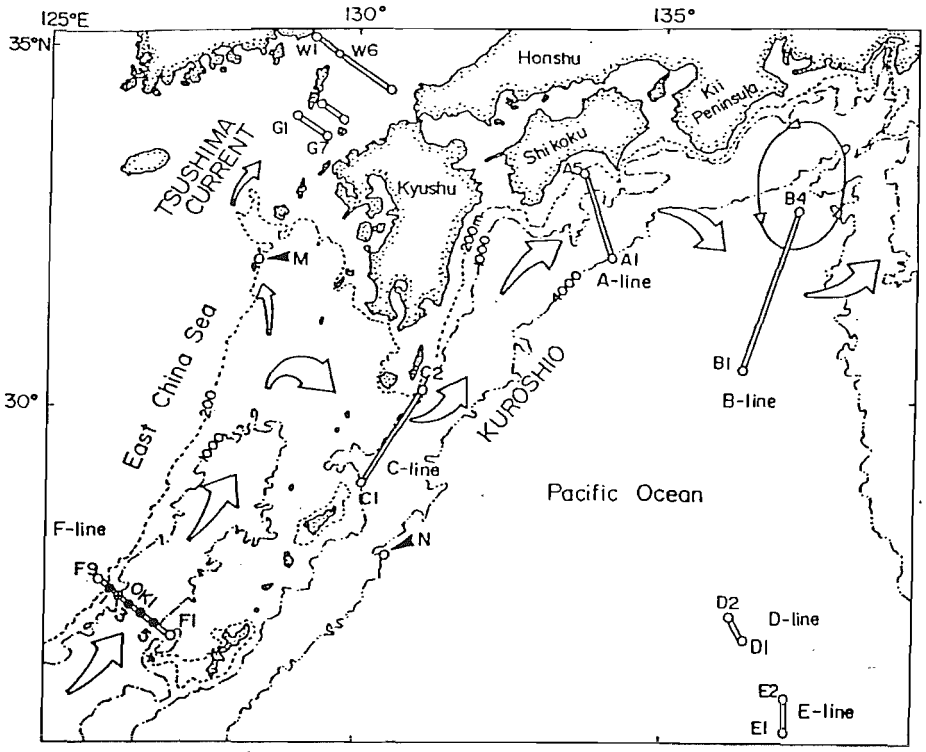
125°E
130°
135°
35°N
30°
W1
W6
Honshu
Kii Peninsula
G1
G7
TSUSHIMA CURRENT
Shikoku
Kyushu
A5
B4
M
A1
A-line
B1
B-line
East China Sea
KUROSHIO
C2
C-line
C1
Pacific Ocean
F-line
N
F9
OKI
F1
D2
D-line
D1
E2
E1
E-line

B.

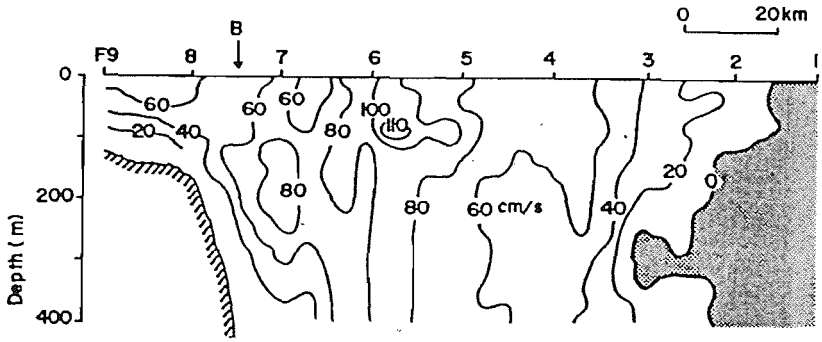
0
20km
B
F9
8
7
6
5
4
3
2
1
Depth (m)
0
200
400
60
20
40
80
100
IIG
60 cm/s
20
0

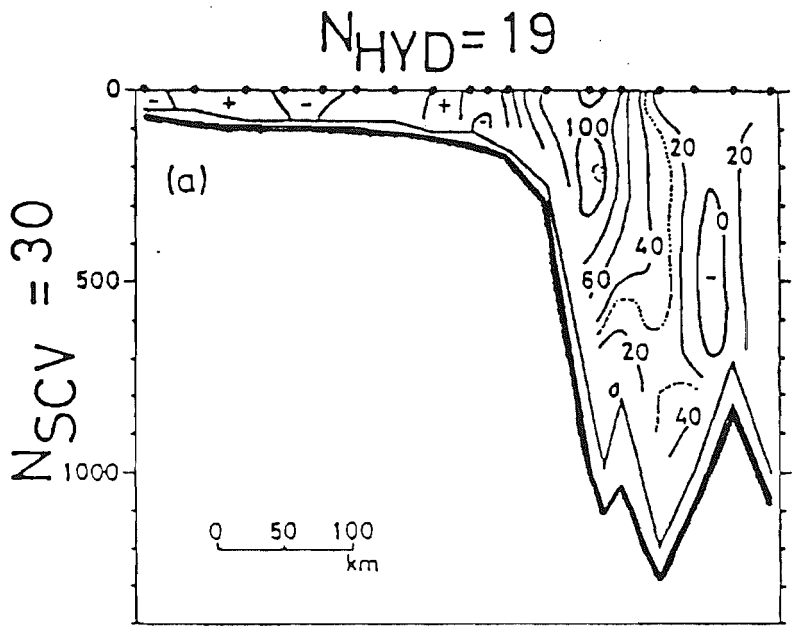
NHYD=19
NSCV=30
0
500
1000
(a)
100
20
40
60
0
0 50 100
km

Fig. 1-10. Schematic picture of the Kuroshio Current System variability determined by a statistical analysis of temperature/depth data during the period from summer 1976 to spring 1980 (from Mizuno and White, 1983). The mean Kuroshio Current path is shown as a dashed line; the envelope of the maximum displacement that the Kuroshio Current experienced near the nodal point (solid points) is shown as solid lines.

Fig. 1-11. Horizontal distribution of temperature at a depth of 100 m during August 1970 around the Kuroshio Extension (from Kitano, 1975). Contour interval are 1°C. Two thermal fronts around 35°N ~ 36°N (AA) and 39°N ~ 40°N (BB) represent the Kuroshio and Oyashio fronts respectively. A warm eddy can be seen in the north of the Oyashio front.

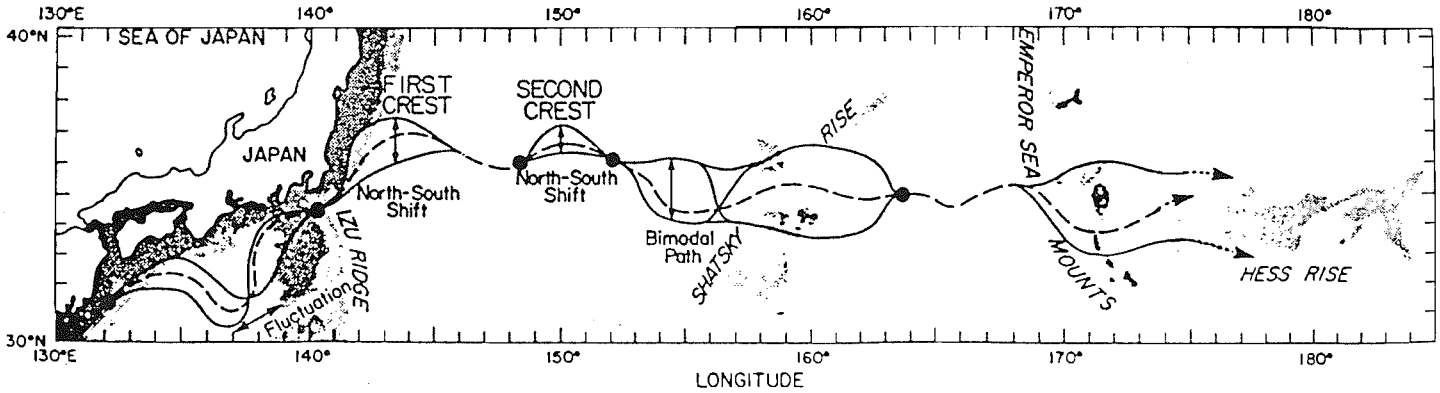
130°E
140°
150°
160°
170°
180°
40°N
30°N
SEA OF JAPAN
JAPAN
FIRST CREST
SECOND CREST
North-South Shift
North-South Shift
IZU RIDGE
Fluctuation
Bimodal Path
SHATSKY RISE
EMPEROR SEA MOUNTS
HESS RISE
LONGITUDE

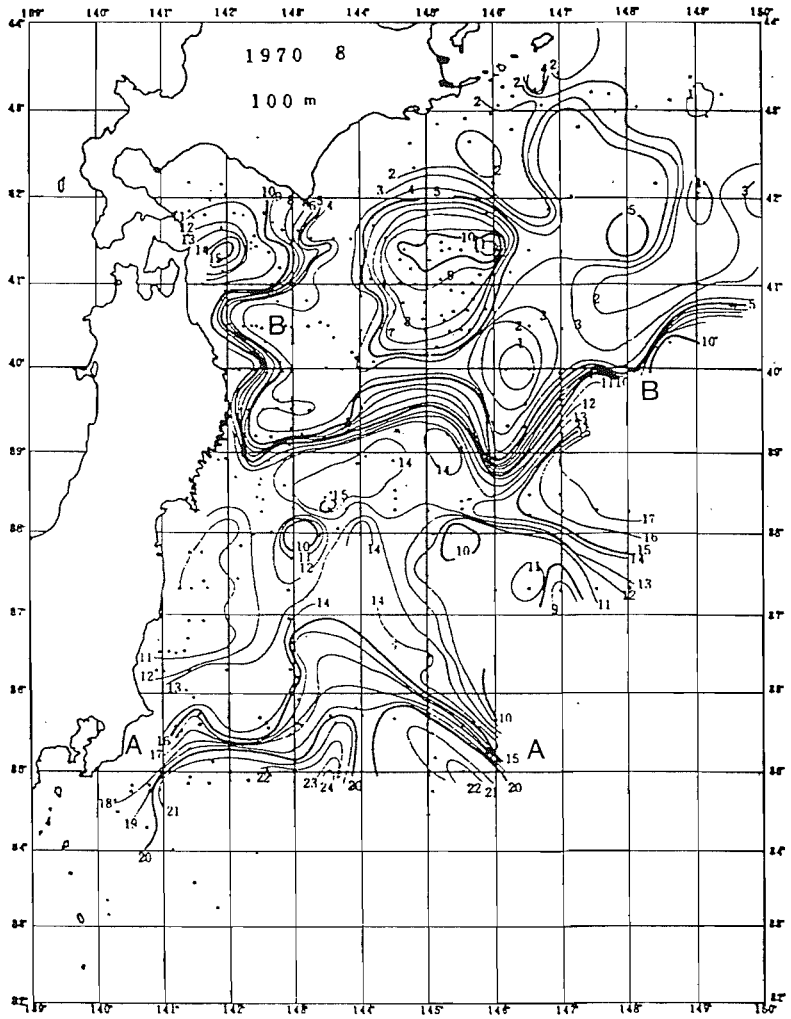
1970 8
100 m
A
B

Fig. 1-12. Histograms of latitude of the northern limit of the Kuroshio Extension based on hydrographic data for 1927-1969 (Kawai, 1972). The northern limit of the Kuroshio Extension was determined by 14°C isotherm at 200 m depth. Numbers inside the histogram denote the sample size.

Fig. 1-13. The model ocean considered by Minato and Kimura (1980). A sinusoidal curve in region A shows the distribution of wind stress.

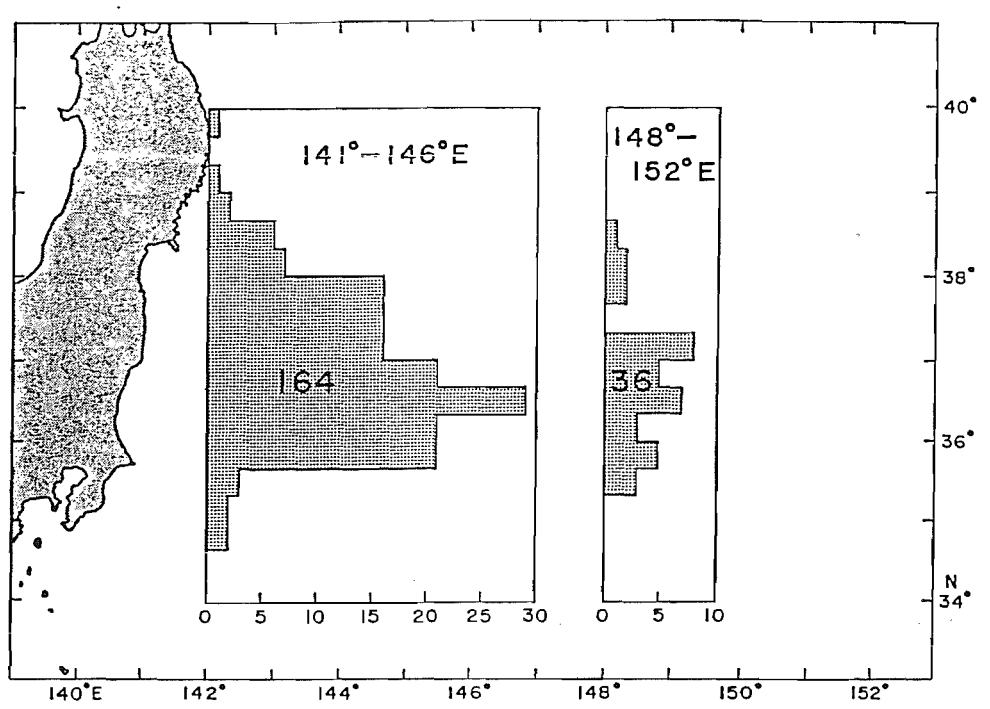

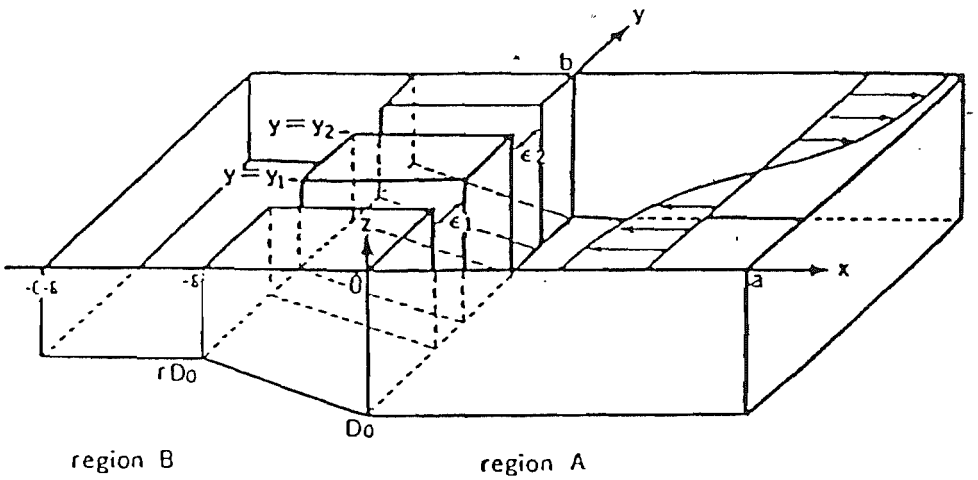

region B region A

Fig. 1-14. Generation of the Tsushima Current conjectured from the satellite images: (A) zone of mixing along the shelf-edge, (B) episodic intrusion from the Kuroshio, and (C) resultant Tsushima Current (from Huh, 1982b).

Fig. 1-15. Schematic map of regional currents round Cheju Island (Jeju-Do) in summer. The closed and broken arrows indicate a Yellow Sea Warm Current, and the surface plume of Changjiang River Diluted Water (from Kim et al., 1991).

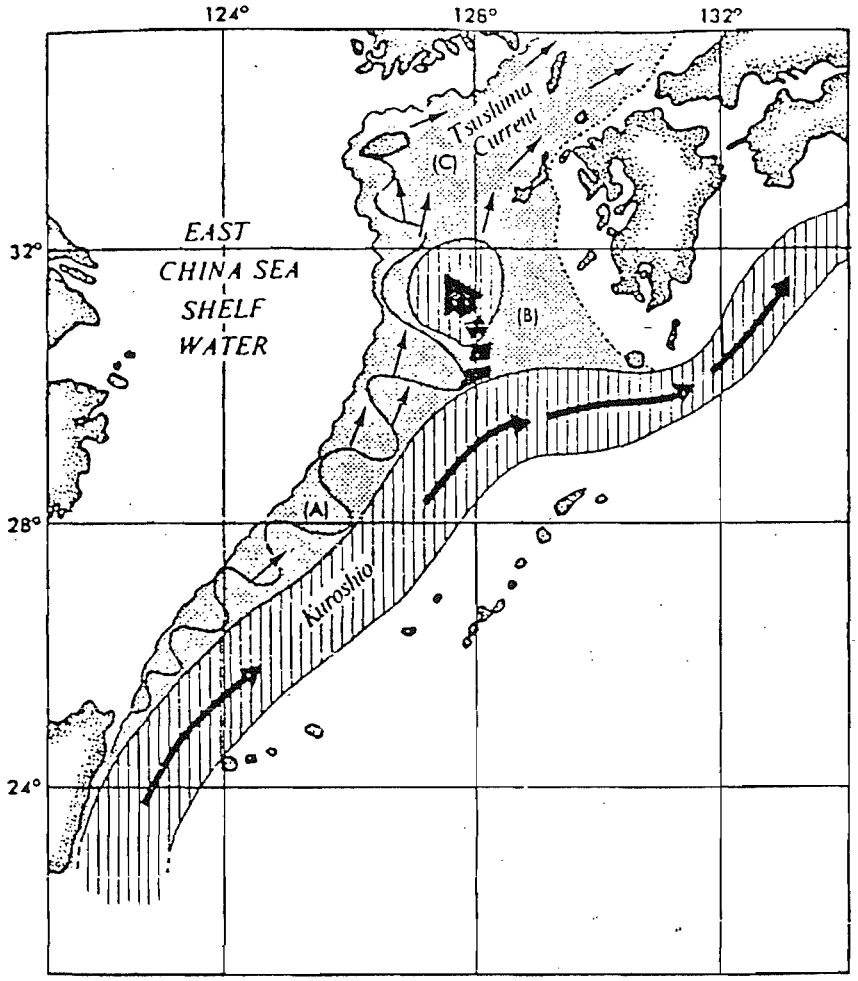
124°
126°
132°
32°
28°
24°
EAST
CHINA SEA
SHELF
WATER
Tsushima
Current
(C)
(B)
(A)
Kuroshio

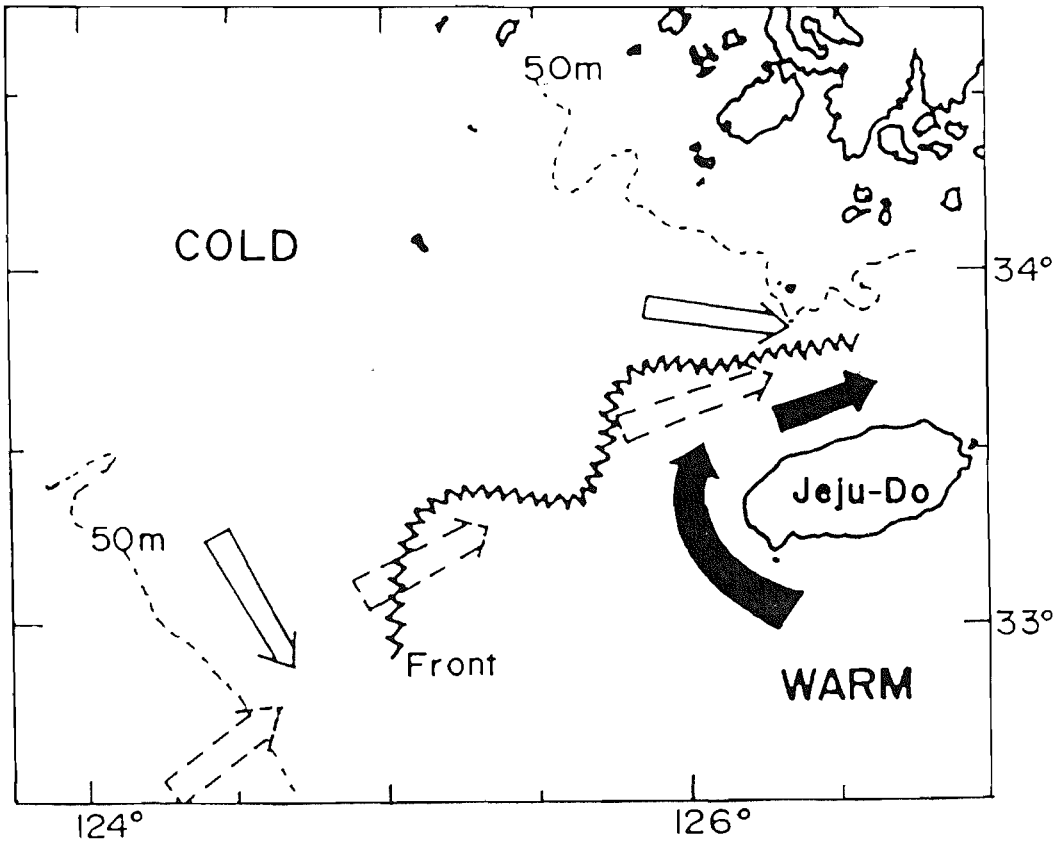
50m
COLD
34°
Jeju-Do
50m
Front
WARM
33°
124°
126°

CHAPTER II.
DYNAMICAL EQUATIONS

II-1. INTRODUCTION

In this chapter, a set of dynamical equations and the associated barotropic vorticity equation (BVE) applicable to a homogeneous ocean over arbitrary topography will be presented. Numerical model results will be mainly explained in terms of the vorticity balance in the BVE. The equations in this chapter will be frequently referred to in later chapters.

An idealised topographic regime was used for numerical experiments in building upon simple models, i.e., flat-bottomed deep ocean and shelf area, and a step-like or narrow continental slope region in between. The depth of the deep ocean in a realistic model was also set to be constant (see Fig. 3-1). Scaling of BVE in a flat-bottomed ocean will be performed to classify numerical experiments in terms of non-dimensional parameters and to study the dependence of shelf circulation on these deep ocean parameters.

The generation of the WBC in the model ocean can be explained in terms of free waves in the system. Long-wave theory relevant to the present study will be given briefly in this chapter.

II-2. BAROTROPIC VORTICITY EQUATION

We considered the momentum and continuity equations for the flow of a homogeneous fluid over arbitrary topography in a rotating frame driven by wind stress, and damped by both lateral friction and bottom stress :

$$\frac{Du}{Dt} - fv = -\frac{1}{\rho_0}p_x + A_M\nabla^2 u + A_V u_{zz} \qquad \text{(II-2-1)}$$

$$\frac{Dv}{Dt} + fu = -\frac{1}{\rho_0}p_y + A_M\nabla^2 v + A_V v_{zz} \qquad \text{(II-2-2)}$$

$$\frac{\partial u}{\partial x} + \frac{\partial v}{\partial y} + \frac{\partial w}{\partial z} = 0 \qquad \text{(II-2-3)}$$

$$\frac{1}{\rho_0}p_z = -g\ , \qquad \text{(II-2-4)}$$

where,

(u,v,w) = the (x,y,z) component of velocity vector v

(x,y,z) = Cartesian coordinates in the east-west, north-south, and vertical directions

ρ_0 = constant water density

p(x,y,z,t) = total pressure

$f = f_0 + \beta_0 y$, variable Coriolis parameter

A_M = horizontal diffusion coefficient

A_V = vertical diffusion coefficient, and

$$\frac{D}{Dt} = \frac{\partial}{\partial t} + u\frac{\partial}{\partial x} + v\frac{\partial}{\partial y}\ .$$

Subscripts x, y, z, and t denote the partial differentiation and other notations are standard. The rotation axis of the fluid coincides with the z-axis that is positive upwards.

Following approximations are made in writing above equations,

1. Mid-latitude β-plane approximation : the effect of earth's sphericity is represented by a linear variation of Coriolis parameter f. This is generally valid when

the horizontal scale of motion is less than the earth's radius ($\sim$6370 km).

2. Hydrostatic approximation : other terms in vertical momentum equation II-2-4 are neglected except the vertical pressure gradient and buoyancy force.

3. Incompressible approximation : changes in density with pressure are negligible or the velocity field is non-divergent. Equation II-2-3 is the continuity equation for the incompressible fluid.

The boundary conditions are

1) at $z = \eta(x,y,t)$

$$A_V u_z = \frac{\tau^x}{\rho_0} , A_V v_z = \frac{\tau^y}{\rho_0} , w = \eta_t + u\eta_x + v\eta_y$$

2) at $z = -h(x,y)$

$$A_V u_z = \frac{\tau^{bx}}{\rho_0} = ru , A_V v_z = \frac{\tau^{by}}{\rho_0} = rv , w = -(uh_x + vh_y) .$$

In the above, η is the free surface elevation, h is the depth of the ocean when there is no motion, and (τ^x,τ^y) represent the x- and y-components of surface wind stress. Bottom stresses (τ^{bx},τ^{by}) are taken to be proportional to the fluid velocity.

The vertical velocities at $z = \eta(x,y,t)$ and $z = -h(x,y)$ can be found as follows. The free surface and the variable topography are considered to be the material lines. A fluid particle in each surface will remain in that surface. Therefore, the following conditions

$$\frac{D'}{D't}(z-\eta) = 0 \qquad \text{(II-2-5)}$$

$$\frac{D'}{D't}(z+h) = 0 \,, \tag{II-2-6}$$

where

$$\frac{D'}{D't} = \frac{\partial}{\partial t} + u\frac{\partial}{\partial x} + v\frac{\partial}{\partial y} + w\frac{\partial}{\partial z} \,,$$

will determine the vertical velocities at z = η and z = -h (Gill, 1982). From equations (II-2-5) and (II-2-6),

$$\frac{D'z}{D't} = (w)_{z=\eta} = \frac{D'\eta}{D't} = \eta_t + u\eta_x + v\eta_y$$

$$\frac{D'z}{D't} = (w)_{z=-h} = -\frac{Dh}{Dt} = -uh_x - vh_y \,.$$

Integration of (II-2-4) from the surface to z yields,

$$p = \rho_0 g(\eta - z) + p_a \,,$$

where p_a is the atmospheric pressure acting on the free surface. Then,

$$p_x = \rho_0 \, g \, \eta_x \,, \; p_y = \rho_0 \, g \, \eta_y \,, \tag{II-2-7}$$

if there is no atmospheric pressure gradient.

The momentum equations (II-2-1) and (II-2-2) are integrated from z = -h to z = η after replacing p_x and p_y to η_x and η_y respectively using equation (II-2-7) to yield,

$$\frac{Du}{Dt} - fv = -g\eta_x + A_M\nabla^2 u + \frac{\tau^x}{\rho_0(h+\eta)} - \frac{ru}{h+\eta} \tag{II-2-8}$$

$$\frac{Dv}{Dt} + fu = -g\eta_y + A_M\nabla^2 v + \frac{\tau^y}{\rho_0(h+\eta)} - \frac{rv}{h+\eta} \tag{II-2-9}$$

In deriving the equations (II-2-8) and (II-2-9) from (II-2-1) and (II-2-2) the following relationships are used:

$$\int_{-h}^{\eta} u u_x \, dz = u \int_{-h}^{\eta} u_x \, dz = u \left[\frac{\partial}{\partial x} \int_{-h}^{\eta} u \, dz - u \, (h+\eta)_x \right]$$

$$= u[(h+\eta)u]_x - u^2(h+\eta)_x = (h+\eta)uu_x ,$$

$$\int_{-h}^{\eta} p_x \, dz = \frac{\partial}{\partial x} \int_{-h}^{\eta} p \, dz - (p)_{z=\eta} \, \eta_x - (p)_{z=-h} \, h_x$$

$$= \frac{\partial}{\partial x} \left[\rho_0 g \eta z - \frac{1}{2} \rho_0 g z^2 \right]_{-h}^{\eta} - \rho_0 g (h+\eta) h_x = \rho_0 g (h+\eta) \eta_x .$$

The vertically averaged continuity equation has the form

$$\eta_t + [u(h+\eta)]_x + [v(h+\eta)]_y = 0 ,$$

or alternatively,

$$u_x + v_y = - \frac{1}{h+\eta} \frac{D}{Dt}(h+\eta) \qquad \text{(II-2-10)}$$

Cross differentiation of equations (II-2-8) and (II-2-9) eliminates the pressure gradient terms to yield

$$\frac{D}{Dt}(\zeta+f) = -(\zeta+f)(u_x+v_y) + curl \frac{\vec{\tau}}{\rho_0(h+\eta)} + A_M \nabla^2 \zeta - curl \left(\frac{r\vec{u}}{h+\eta} \right) ,$$

(II-2-11)

where $\zeta = v_x - u_y$ is the relative vorticity.

Combining equations (II-2-10) and (II-2-11) provides the barotropic vorticity equation (BVE),

$$(h+\eta)\,\frac{D}{Dt}\left(\frac{f+\zeta}{h+\eta}\right) = curl\,\frac{\vec{\tau}}{\rho_0(h+\eta)} + A_M\nabla^2\zeta - curl\left(\frac{r\vec{u}}{h+\eta}\right) \tag{II-2-12}$$

For an inviscid case without forcing, the potential vorticity $(f+\zeta)/(h+\eta)$ is conserved along the streamlines.

Assuming that the ocean depth is much greater than the free surface elevation ($h+\eta \approx h$), and the applied wind-stress has a zonal structure, equation (II-2-12) has the form for steady flow,

$$u\zeta_x + v\zeta_y - \frac{(f+\zeta)}{h}(uh_x+vh_y) + \beta_0 v = -\frac{\tau^x_y}{\rho_0 h} + \frac{h_y}{\rho_0 h^2}\tau^x + A_M\nabla^2\zeta - \frac{r}{h}\left[\zeta - \frac{1}{h}(vh_x - uh_y)\right] \tag{II-2-13}$$

Equation (II-2-13) can be expressed in terms of a transport stream function, ψ, such that

$$J(\psi,\zeta) - \frac{(f+\zeta)}{h}J(\psi,h) + \beta_0\psi_x = -\frac{\tau^x_y}{\rho_0} + \frac{h_y}{\rho_0 h}\tau^x + h\,A_M\nabla^2\zeta - r\left[\zeta - \frac{1}{h^2}(\psi_x h_x + \psi_y h_y)\right] \tag{II-2-14}$$

where $hu = -\psi_y$, $hv = \psi_x$, $\zeta = \nabla\cdot(\nabla\psi/h)$, and $J(a,b) = a_x b_y - a_y b_x$.

The individual contributions to the equation (II-2-14) can be identified as follows; the first term on the left hand side (LHS) is the non-linear advection of relative vorticity , the second term on the LHS is the topographic vorticity tendency, the third term on the LHS represents the planetary vorticity tendency, the first and second terms on the right hand side (RHS) is the wind stress curl, and the remaining terms on the RHS are the dissipation of vorticity due to lateral and bottom friction respectively.

II-3. Scaling of the BVE

For a flat-bottomed ocean, equation (II-2-14) has the form

$$J(\psi,\zeta) + \beta_0\psi_x = -\frac{\tau^x_y}{\rho_0} + h\,A_M\nabla^2\zeta - r\zeta \qquad \text{(II-3-1)}$$

It is convenient to introduce non-dimensional numbers and to study the dependence of model results on these numbers. The model deep ocean basin was chosen to be rectangular with sides of length L^x and L^y, and depth d so that $0 \le x \le L^x$ and $0 \le y \le L^y$. The wind-stress is assumed to have the simple form used by Stommel (1948),

$$\tau^x = -T_0 \cos\left(\frac{\pi y}{L^y}\right), \text{ and } \tau^y = 0.$$

The non-dimensionalisation of the equation (II-3-1) is accomplished by the scaling

$$(x,y) = L\,(x^*,y^*),\ h = d\,h^*,\ \psi = \psi_0\,\psi^*,\ \tau = T_0\,\tau^*,\ \zeta = \frac{\psi_0}{dL^2}\,\zeta^*, \qquad \text{(II-3-2)}$$

where L is chosen to be min (L^x,L^y), and asterisks denote non-dimensional variables.

The possible maximum value of ψ_0 can be found in terms of other quantities using the Sverdrup balance. At a steady state the negative vorticity imparted by a negative wind-stress curl competes with the positive vorticity acquired by the southward flowing fluid particles in an ocean interior, where the frictional and inertial effects are of little importance. Then the vorticity balance is simply given by

$$\beta_0\psi_x = -\frac{\tau^x_y}{\rho_0} = -\frac{\pi T_0}{\rho_0 L^y}\sin\left(\frac{\pi y}{L^y}\right).$$

Scaling the above equation gives the maximum possible value of ψ_0,

$$\psi_0 = \frac{T_0 \pi}{\rho_0 \beta_0}\left(\frac{L^x}{L^y}\right) = \frac{T_0 \pi}{\rho_0 \beta_0}\lambda \ . \qquad \text{(II-3-3)}$$

To estimate the Sverdrup transport correctly for a non-square basin, λ ($=L^x/L^y$) is used.

The resulting non-dimensional equation using (II-3-2) and (II-3-3) takes the form after dropping asterisks

$$R\, J(\psi,\zeta) + \psi_x = - T_y + E_L\, h\, \nabla^2\zeta - E_B\, \nabla^2\psi \ , \qquad \text{(II-3-4)}$$

where the Rossby number R, horizontal and vertical Ekman numbers E_L and E_B, and T are given by

$$R = \frac{T_0\ \pi\ \lambda}{\rho_0\ \beta_0^2\ d\ L^3} \ , \quad E_L = \frac{A_M}{\beta_0\ L^3} \ , \quad E_B = \frac{r}{\beta_0\ d\ L} \ , \quad T = - \frac{1}{\pi}\cos(\pi y) \ . \qquad \text{(II-3-5)}$$

For typical values of wind stress $T_0 / \rho_0 = 0.5 \times 10^{-3}$ m^2s^{-1} and the planetary vorticity gradient $\beta_0 = 2 \times 10^{-11}$ $m^{-1}s^{-1}$ used for the experiments, the linear frictionless Sverdrup transport amounts to $(\pi\ T_0\ \lambda) / (\beta_0\ \rho_0) \sim 27.5$ Sv (1 Sv $= 10^6$ m^3s^{-1}).

The western boundary layer can be either frictionally or inertially dominated. For Munk's and Stommel's linear problem (R=0), the width of the western boundary current is found by assuming a balance between the planetary vorticity term and either the lateral friction or bottom friction terms in the boundary layer, that is,

$$\beta_0 \psi_x \sim h A_M \nabla^2\zeta \quad or \quad \beta_0 \psi_x \sim r\,\zeta \qquad \text{(II-3-6)}$$

from equation (II-3-1). For an inertially dominated flow a balance exists between the planetary vorticity tendency and the advection term in the boundary layer,

$$J(\psi,\zeta) \sim \beta_0\, \psi_x \ . \qquad \text{(II-3-7)}$$

The width of the non-dimensional inertial and frictional boundary layers can be found by scaling of equations (II-3-6) and (II-3-6) in terms of the boundary layer scale (ℓ), and

assuming $\ell = L\,\ell^*$, where ℓ^* is the non-dimensional boundary-layer scale (Pedloski, 1979). They are defined as

$$\delta_I = R^{\frac{1}{2}}, \quad \delta_L = E_L^{\frac{1}{3}}, \quad \delta_B = E_B, \tag{II-3-8}$$

where δ_I is the width of the non-dimensional inertial boundary layer, and δ_L and δ_B are the widths of the non-dimensional frictional boundary layers dominated by lateral and bottom frictional forces respectively. Note that the magnitude of the streamfunction in the boundary layer is of the same order as the magnitude of the interior streamfunction.

II-4. LONG-WAVE THEORY

In this section properties of linear free waves in a flat-bottomed ocean are presented briefly. Those properties will be used later in describing the initial response of the model ocean.

There are three kinds of free waves with long wavelengths in our model ocean : long gravity waves (or Poincaré waves), planetary waves (or Rossby waves), and Kelvin waves. Discussion will be limited to planetary and Kelvin waves through which the establishment of the westward intensification of the circulation can be understood.

Formulation and physical implication of the long-wave theory are well summarised in Leblond and Mysak (1978), Pedlosky (1979), Hendershott(1981) and Gill (1982).

II-4-1. Rossby waves

The Rossby waves are very low-frequency ($\sigma \ll f$) waves which exist due to the presence of β. In a two-layer fluid the dispersion relations for the zonally propagating Rossby waves are given by

$$\sigma_n = - \frac{\beta k}{k^2 + \frac{1}{r_n^2}} \quad (n=0,1) \ , \tag{II-4-1}$$

where σ_0 and σ_1 represent the frequency of the barotropic and baroclinic modes respectively, k is the wavenumber in the zonal direction, and r_0 and r_1 represent the external and internal radii of deformation respectively. The r_o and r_1 are defined as

$$r_0 = \frac{(gH)^{\frac{1}{2}}}{f} \ , \ r_1 = \frac{\left(\frac{g' H_1 H_2}{H} \right)^{\frac{1}{2}}}{f} \ , \tag{II-4-2}$$

where g′ is the reduced gravity, H_1 and H_2 are the unperturbed upper and lower layer depths respectively, and $H = H_1 + H_2$.

Phase and group velocities are then given by

$$C_{nx} = - \frac{\beta}{k^2 + \frac{1}{r_n^2}} \tag{II-4-3}$$

$$C_{ngx} = \frac{\beta \left(k^2 - \frac{1}{r_n^2} \right)}{\left(k^2 + \frac{1}{r_n^2} \right)^2} \tag{II-4-4}$$

For short waves ($r_n k \gg 1$), i.e., waves short compared with the Rossby radius, the dispersion relation can be approximated by $\sigma_n = - \beta / k$, and the phase and group velocities are given by

$$C_{nx} = - \frac{\beta}{k^2} \ , \quad C_{ngx} = \frac{\beta}{k^2} \tag{II-4-5}$$

respectively. Hence, these waves are dispersive and the energy propagation is eastward.

Barotropic planetary waves belong to these type of waves as the external Rossby radius is the order of 10^3 km. The phase and group velocities for the non-divergent flow are also given by (II-4-5).

For long waves ($r_n k \ll 1$), i.e., waves long compared with the Rossby radius, the dispersion relation is approximated in this case by $\sigma_n = -\beta k r_n^2$. The phase and group velocities are given by

$$C_{nx} = C_{ngx} = -\beta r_n^2 . \qquad \text{(II-4-6)}$$

These waves are non-dispersive and the energy propagation is westwards the same as the phase propagation. The formula (II-4-6) is particularly appropriate for baroclinic waves in the ocean since the internal Rossby radius is small, typically order of 10^2 km, so equation (II-4-6) applies to any baroclinic waves with large scale.

In a bounded basin, the planetary wave motion occurs in the form of characteristic modes, each of which is composed of a number of component waves produced by reflections from the basin's wall. Planetary oscillations in a stratified rectangular basin of uniform depth and of finite horizontal extent can be described by following dispersion relation (LeBlond and Mysak, 1978),

$$\sigma_n^{lm} = \frac{\beta}{2\left(\frac{l^2\pi^2}{a^2} + \frac{m^2\pi^2}{b^2} + \frac{f^2}{gh_n}\right)^{\frac{1}{2}}} , \qquad \text{(II-4-7)}$$

where $0 \le x \le b$, $0 \le y \le b$, ℓ and m refer to the horizontal mode numbers in the x- and y- directions respectively, and n is the vertical mode number.

II-4-2. Rossby waves and westward intensification

A common feature of the oceanic circulation for various dynamical models is the westward intensification although the treatment of the boundary layer is considerably

different each other (e.g. Stommel, 1948; Munk, 1950).

A simple physical explanation for the westward intensification can also be found by considering the character of Rossby waves (Pedlosky, 1979). The group velocity of a Rossby wave in the x-direction is given by equation (II-4-4). Energy with small x-scales ($k^2 > 1/r_n^2$) will be transmitted eastward, while energy with large x-scales ($k^2 < r_n^2$) will move to the west. Thus information from the eastern boundary is carried westwards by the long wave, while information from the western boundary is carried eastward by relatively short wave.

The westward intensification can be understood as the concentration or trapping of small scale energy on the western side of the ocean basin. A relatively long wave whose energy is rapidly propagating westwards, will be transformed into a relatively short and slowly propagating wave upon reflection from a meridional boundary (Pedlosky, 1979; Leblond and Mysak, 1981). The western boundary thus acts as a source of small-scale energy. The reflected short wave is likely to be damped and trapped at the western boundary when friction is taken into account.

Let us consider Munk's model, where lateral friction is dominant in the boundary layer. The characteristic time for the decay of small scale energy produced at the western boundary will be the viscous dissipation time T_d, i.e., $T_d = O\ (1 / A_M k^2)$, in which time the energy has moved eastward a distance $L = C_{gx}\ T_d = T_d\ \beta / k^2$, since for the short Rossby waves $C_{gx} \sim \beta / k^2$. The wave energy will be trapped at the western boundary for scales sufficiently short that the distance is of the same order as the wave-length, i.e., $k \sim L^{-1}$. Combining above three leads to the estimate $L = (A_M / \beta)^{1/3}$, which can also be derived from equation (II-3-8) by setting δ_L to be 1.

II-4-3. The Kelvin wave

In the presence of rotation, propagating waves can be trapped at a vertical wall with their amplitude decaying away from the wall. The Kelvin wave is a solution of the wave propagation problem in the presence of a vertical side wall.

In a two-layer system, there are two modes of the Kelvin wave, external and first baroclinic modes. The dispersion relation, phase speed, and offshore decay scale of each mode are given by,

$$\sigma_n^2 = c_n k^2 \ , \ c_n = (g h_n)^{1/2} \ , \ r_n = \frac{c_n}{f} \ ,$$

$$n=0 \ (external\ mode) : h_0 = H_1 + H_2 \qquad \text{(II-4-8)}$$

$$n=1 \ (first\ baroclinic\ mode) : h_1 = \frac{\rho_2 - \rho_1}{\rho_2} \frac{H_1 H_2}{H_1 + H_2} \ ,$$

where H_1, ρ_1 are the thickness and density of the upper layer, and H_2, ρ_2 the same quantities in the lower layer.

CHAPTER III. OCEAN MODELS

III-1. INTRODUCTION

The main approach of this study is to build on simple models and to culminate in a realistic model to understand the underlying dynamics. In this chapter model configurations, model equations, and numerical methods to solve the equations will be presented.

Two kinds of ocean models are used in this study and are introduced in sections III-2 and III-3. The first one is a linearised two-layer shallow water equation model with free surface (SWEM), the other is a barotropic version of the three dimensional primitive equation model (SPEM). The purpose of using the two modelling approaches is to show the lack of sensitivity to the model assumptions made. Comparisons are made between the two modelling approaches in the next chapter.

Description of dynamical equations used for the experiments, discretization of the continuous equation, boundary conditions, and the results of spin-up experiments will be mentioned for each model.

The model geometry and topography used to configure the numerical models is presented in section (III-4).

III-2. TWO-LAYER MODEL (SWEM)

III-2-1. Model equations

The model ocean consists of two basins ; a deep ocean and a shallow continental shelf (see Fig. 3-1). The deep ocean consists vertically of two fluids of different density that are immiscible, and the shelf is vertically homogeneous. The well-known two layer

shallow water equations are used for the SWEM.

With the same assumptions as those in chapter II-2, the model equations for the SWEM in the deep ocean are,

$$u_{1t} - fv_1 = -g\eta_{1x} + A_M\nabla^2 u_1 \tag{III-2-1}$$

$$v_{1t} + fu_1 = -g\eta_{1y} + A_M\nabla^2 v_1 \tag{III-2-2}$$

$$(\eta_1 - \eta_2)_t + (u_1 H_1)_x + (v_1 H_1)_y = 0 \tag{III-2-3}$$

$$u_{2t} - fv_2 = -\frac{\rho_1}{\rho_2} g\eta_{1x} - g'\eta_{2x} + A_M\nabla^2 u_2 \tag{III-2-4}$$

$$v_{2t} + fu_2 = -\frac{\rho_1}{\rho_2} g\eta_{1y} - g'\eta_{2y} + A_M\nabla^2 v_2 \tag{III-2-5}$$

$$\eta_{2t} + (u_2 H_2)_x + (v_2 H_2)_y = 0 \ , \tag{III-2-6}$$

where subscripts 1 and 2 denote the upper and lower layer variables respectively and subscripts t, x, and y denote partial differentiation as before. $H_1(x)$, and H_2 represent the unperturbed upper and lower depths respectively. η_1 and η_2 denote the free surface and interface perturbation respectively. Combining equation III-2-3 with III-2-6 yields

$$\eta_{1t} + (u_1 H_1)_x + (v_1 H_1)_y + (u_2 H_2)_x + (v_2 H_2)_y = 0 \ . \tag{III-2-7}$$

There are no surface, interfacial, and bottom stresses in the deep ocean.

In the shelf area a bottom friction term is included that is proportional to the fluid velocity (proportionality r). Model equations in the shelf area are

$$u_{1t} - fv_1 = -g\eta_{1x} + A_M\nabla^2 u_1 - \frac{r}{H_1}u_1 \qquad \text{(III-2-8)}$$

$$v_{1t} + fu_1 = -g\eta_{1y} + A_M\nabla^2 v_1 - \frac{r}{H_1}v_1 \qquad \text{(III-2-9)}$$

$$\eta_{1t} + (u_1 H_1)_x + (v_1 H_1)_y = 0 \qquad \text{(III-2-10)}$$

The upper and lower depths of the deep ocean are taken to be 400 m and 1100 m respectively. The main stream of the Kuroshio in the ECS occupies the upper 400 m depth approximately.

III-2-2. Numerical methods

The dynamical equations (III-2-1) ~ (III-2-2) and (III-2-4) ~ (III-2-10) are solved numerically on the staggered Arakawa C-grid. The explicit numerical scheme used is a mid-latitude version of Dearnley (1990). The time differencing is leapfrog, but a forward scheme is used every one day (1,728 time steps) to prevent development of the time splitting associated with the leapfrog scheme. Friction terms are lagged in time for computational stability. Details of the finite difference equations can be found in Appendix A.

Grid spacing and timestep length were determined considering the scale and the phase speed of free waves in the system. There are two phases to the transitory motions, the very rapid passing of the surface mode and the slowly varying internal disturbances. With the standard upper and lower depths, the phase speed of the external (C_0) and internal (C_1) gravity waves are given by equation III-2-11. The external and internal radii of deformation at the central latitude (30° N) are 1663 km and 39 km respectively.

$$C_0 = [g(H_1+H_2)]^{1/2} = 121.24\ ms^{-1},$$

$$C_1 = \left(g' \frac{H_1 H_2}{H_1+H_1}\right)^{1/2} = 3.14\ ms^{-1}, \qquad \text{(III-2-11)}$$

The grid size in both directions is 20 km which is about a half of the internal radius of deformation. A timestep of 50 seconds was used which is less than half that is required to fulfil the most restrictive CFL condition $\Delta t < \Delta x / C_0 \sim 165$ s.

III-2-3. Boundary conditions and forcing

Eastern and western boundaries of the model domain are rigid walls, and northern and southern boundaries of the deep ocean are open.

A slip boundary condition, $u_n = 0$ and $\partial v / \partial n = 0$, is applied at the rigid walls where n refers to the normal direction to the wall. The slip boundary condition is used because the walls in the model do not necessarily correspond to the actual coastal lines.

The model is forced by a prescribed velocity in the upper layer at the southern boundary. The velocity in the lower layer was set to be zero in all experiments. The normal velocity component along the northern boundary is self-determined using a Orlanski radiation condition and the integral constraint such that the inflow volume transport exactly matches the outflow at every time step (Thompson and Schmitz, 1990). A viscous boundary layer was also applied near the northern boundary in an effort to damp the free surface oscillations due to the integral constraint. The tangential velocity at grid points just outside the domain is assumed to be zero for calculating lateral friction terms. The model was spun-up with an e-folding time of one day. Details of the open boundary condition specifications including a spin-up experiment are given in Appendix B.

III-2-4. Experimental procedure

A two-stage modelling approach was adopted for the experiments. First, a western boundary current was generated in a deep channel of rectangular cross section by the prescribed inflow from the southern boundary with the outflow self-determined (deep channel model). Establishing a stable circulation pattern in the deep channel, an initially quiescent shallow shelf is introduced at the western boundary of the deep channel (shelf model). The shelf model driven by the result of the deep channel model was integrated again until field variables show no further change.

This approach is extremely useful and economic as it takes three or four times longer for the deep channel model to reach the equilibrium state than the shelf model. Therefore, once we have the result of the deep channel model it is quick and easy to make changes to the shelf model as and when required.

III-3. PRIMITIVE EQUATION MODEL (SPEM)

The other dynamical model employed for the experiments described in subsequent chapters is a semi-spectral model (SPEM) of Haidvogel et al. (1991a). It has been designed for regional and basin-scale modelling problems featuring irregular basin geometry, finite amplitude bottom topography, and/or wind and thermohaline forcing. A complete description of the model and its solution procedure is given by Haidvogel et al. (1991a) and Hedström (1990). Application of the SPEM to physical oceanographic studies can be found in Gawarkiewicz and Chapman (1991), Haidvogel et al. (1991b), and Chapman and Haidvogel (1992).

In the following section, the governing equations in a topography-following σ-coordinate system is presented. Although the SPEM was originally written in the σ- and horizontal orthogonal coordinate system, a simple rectangular geometry was used in this study as shown in Fig. 3-1.

A summary of the numerical solution technique, forcing and boundary conditions used will then be presented.

III-3-1. Model equations

The SPEM solves the fully non-linear, and hydrostatic primitive equations of motion. A topography-following σ-coordinates is used in the vertical to allow for arbitrary bottom topography. The topography-following variable is defined as

$$\sigma = 1 + 2\left(\frac{z}{h}\right), \tag{III-3-1}$$

where h(x,y) is the local depth of the fluid. In the σ-coordinate system, the vertical coordinate spans the range $-1 \leq \sigma \leq 1$. Details of the σ-coordinate transformation is given in Appendix C.

The same approximations as those in the chapter II-2 are used in the SPEM with two additional approximations, rigid-lid and Boussinesq approximations. With the Boussinesq approximation density variations are neglected in the horizontal momentum equations except in their contribution to the buoyancy force in the vertical momentum equation. With the rigid-lid approximation the displacement of the ocean surface is not allowed so that the vertical velocity at the ocean surface is zero ($\Omega = 0$ at $\sigma=1$). However, there exists surface pressure variations which have the same effect as that of the free surface. This approximation greatly improves the efficiency in numerical computation by filtering out surface gravity waves.

The resulting equations of motion in the σ-coordinates are,

$$u_t + \vec{v}\cdot\nabla u - fv = -\phi_x + (1-\sigma)\left(\frac{g\rho}{2\rho_0}\right)h_x + F_u + D_u \tag{III-3-2}$$

$$v_t + \vec{v}\cdot\nabla v + fu = -\phi_y + (1-\sigma)\left(\frac{g\rho}{2\rho_0}\right)h_y + F_v + D_v \tag{III-3-3}$$

$$\phi_\sigma = -\frac{gh\rho}{2\rho_0} \tag{III-3-4}$$

$$\rho_t + \vec{v}\cdot\nabla\rho = F_\rho + D_\rho \tag{III-3-5}$$

$$(hu)_x + (hv)_y + h\Omega_\sigma = 0 \ , \tag{III-3-6}$$

where, in standard notation :

(u,v,Ω) = the (x,y,σ) component of the vector velocity v

ρ_0 = reference density

$\rho(x,y,\sigma,t)$ = perturbation density

$\phi(x,y,\sigma,t)$ = dynamic pressure (p/ρ_0)

$f = f_0 + \beta_0 y$, Coriolis parameter

$$\vec{v}\cdot\nabla = u\frac{\partial}{\partial x} + v\frac{\partial}{\partial y} + \Omega\frac{\partial}{\partial\sigma} \ , \tag{III-3-7}$$

and subscripts x, y, σ, and t indicate the partial differentiation.

The vertical velocity in σ-coordinates is given by

$$\Omega(x,y,\sigma,t) = \frac{1}{h}[(1-\sigma)u\,h_x + (1-\sigma)v\,h_y + 2w] \ , \tag{III-3-8}$$

where w is vertical velocity components in Cartesian coordinates.

The functions F_u, F_v, and F_ρ represent Laplacian momentum mixing terms needed for numerical stability and are applied along σ-coordinate surfaces. The functions D_u, D_v, and D_ρ represent forcing terms.

III-3-2. Numerical methods

The SPEM uses finite differences in the horizontal and a spectral expansion in the vertical with modified Chebyshev polynomials as basis functions.

The vertical (σ) dependence of the model variable is represented as an expansion in a finite polynomial basis set $P_k(\sigma)$;

$$b(x,y,\sigma) = \sum_{k=0}^{N} P_k(\sigma)\hat{b}_k(x,y)$$

where the arbitrary variable b is any of u, v, ρ, ϕ, or Ω. The only restriction placed on the form of the basis polynomials is that

$$\frac{1}{2}\int_{-1}^{1} P_k(\sigma)d\sigma = \delta_{ok} ,$$

i.e., only the lowest-order polynomial has a nonzero vertical integral. This isolates the external mode (or depth-averaged component of the field) in the amplitude of the k = 0 polynomial. To avoid the expensive computations of the convolution sums of the non-linear terms, the semi-spectral technique does not explicitly solve for the polynomial coefficients b_k but rather for the actual variable values at "collocation" points (or equivalent grid points) σ_n chosen to correspond to the location of the extrema of the highest order polynomial. The Chebyshev polynomials have the advantage of increased vertical resolution at the surface and the bottom boundaries.

In the horizontal, a centred, second order finite difference approximation is adopted. The variables are arranged on the staggered Arakawa C-grid, the same as in the SWEM. The resulting spatial discretization exactly conserves the volume-averaged budgets of momentum and density. Kinetic energy and the square of the density can be also strictly conserved optionally using special forms of the vertical advective terms. A horizontal spacing of 20 km in both directions is used for all SPEM experiments, the same as in the SWEM.

Although the rigid lid approximation allows a more efficient calculation, it complicates the solution of the time dependent equations. Time-stepping of internal and external modes of velocity distribution was made (Bryan, 1969; Semtner, 1986; Hedström, 1990) as follows :

Vertical integration of the hydrostatic equation III-3-4 yields,

$$\phi = \phi^s - \int_\sigma^1 \left(\frac{gh\rho}{2\rho_0} \right) d\sigma \ , \qquad \text{(III-3-9)}$$

where $\phi^s(x,y,t)$ is the surface pressure. Replacing the horizontal pressure gradient in equations III-3-2 and III-3-3 with III-3-9 yields,

$$u_t = R_u - \phi_x^s \qquad \text{(III-3-10)}$$

$$v_t = R_v - \phi_y^s \qquad \text{(III-3-11)}$$

where R_u and R_v represent the sum of all other terms in the u and v equations respectively except surface pressure gradient. Performing a vertical average

$$\left(\frac{1}{2} \int_{-1}^{1} d\sigma \right) ,$$

the equations III-3-10, III-3-11, and III-3-6 become:

$$\bar{u}_t = \overline{R_u} - \phi_x^s \qquad \text{(III-3-10)}$$

$$\bar{v}_t = \overline{R_v} - \phi_y^s \qquad \text{(III-3-11)}$$

$$(h\bar{u})_x + (h\bar{v})_y = 0 \qquad \text{(III-3-12)}$$

Note that the vertical velocity (Ω) is zero at the top ($\sigma=1$) and the bottom ($\sigma=-1$) in σ-coordinates.

By virtue of equation III-3-12, the depth-averaged flow is horizontally non-divergent enabling us to define the streamfunction, ψ (x,y,t), such that

$$\bar{u} = -\frac{\Psi_x}{h} , \bar{v} = \frac{\Psi_y}{h} . \qquad \text{(III-3-13)}$$

Taking the curl of equations III-3-10 and III-3-11 yields a vorticity equation for the depth-averaged flow,

$$\zeta_t = \left(\bar{v}_x - \bar{u}_y\right)_t = \left(\overline{R}_v\right)_x - \left(\overline{R}_u\right)_y \equiv R_\zeta , \qquad \text{(III-3-14)}$$

or using (III-3-13),

$$\left[\left(\frac{\Psi_x}{h}\right)_x + \left(\frac{\Psi_y}{h}\right)_y\right]_t = R_\zeta . \qquad \text{(III-3-15)}$$

The total velocity components u and v may be decomposed into an external (vertically averaged) mode plus internal mode. Thus

$$(u,v) = (\bar{u},\bar{v}) + (u',v') \text{ , where } \int_{-1}^{1} u' d\sigma = \int_{-1}^{1} v' d\sigma = 0 .$$

By ignoring the unknown contribution made by the surface pressure ϕ^s, equations for preliminary velocities u^* and v^* at time $t+\Delta t$ are obtained using the following equations,

$$u_t^* = R_u$$

$$v_t^* = R_v .$$

These preliminary velocities are in error by amounts that are independent of depth, so

that no final error occurs in calculating u´ by setting

$$(u',v') = (u^* - \overline{u^*}, v^* - \overline{u^*}) \ .$$

The depth-averaged velocity is determined by the following procedure : firstly the barotropic vorticity is directly time-stepped using equation (III-3-14), secondly the associated value of streamfunction is determined from the generalised elliptic equation,

$$\left(\frac{\psi_x}{h}\right)_x + \left(\frac{\psi_y}{h}\right)_y = \zeta \ ,$$

Once the ψ is determined the depth-averaged velocity components are obtained using equation III-3-13.

The surface pressure is not computed directly since the SPEM has a rigid lid. However, the surface pressure gradient may be diagnostically inferred using equations III-3-2 and III-3-3 after the total velocity components are determined.

III-3-3. Forcing and boundary conditions

The most important simplification in the present model study with the SPEM is the neglect of the stratification. The total density was set equal to the constant value. The depth of the deep ocean was set to 400 m for most cases assuming implicitly that the energetic boundary current is confined to the upper 400 m.

The model ocean was spun-up using a simple Stommel type wind-stress distribution in a closed basin,

$$\tau^x = -\tau_0 \cos\left(\frac{\pi y}{L}\right) \ , \ \tau^y = 0 \ , \quad \textit{where } 0 \le y \le L \ .$$

To examine the component of the shelf circulation driven by the WBC, the wind-stress was applied only over the deep ocean in a depth-independent manner like a body force. The retarding, linear bottom drag, if used, was also treated as a body force and applied only over the shelf area. The bottom boundary layer, therefore, is not explicitly resolved. Since the fluid is homogeneous, and forced and/or dissipated in a depth-independent manner, it is expected that the flow will remain depth-independent at all times. This was observed to be the case to machine accuracy. A free-slip condition was used for the velocity at all boundaries. Spin-up of the SPEM is discussed in Appendix D.

III-4. MODEL GEOMETRY AND TOPOGRAPHY

Two types of simple model geometry are used for the numerical experiments as shown in Fig. (3-1).

The simple shelf model (SSM) consists of two basins (Fig. 3-1 (a)). The large and small basins represent a deep ocean and a shallow continental shelf respectively. The depth of each basin is constant. The depth change between two basins takes place over one grid spacing so that it has a step-like character. Both the SWEM and the SPEM are configured to this domain.

For the SWEM the vertical water column in the deep ocean consists of two immiscible fluids of different density. The interface intersects the deep ocean so that the shelf area remains homogeneous at all time. For the SPEM the lower layer in the SWEM is removed so that the model ocean now consists of a deep ocean and a continental shelf with the same density, and a step-like continental slope in between. As will be shown later, the limited depth and neglect of stratification used for the SPEM has little effect on the circulation of the shelf.

Neglecting all the details of topography and coastlines in Fig. 1-3, the idealised shelf area in Fig. 3-1 (a) may be regarded as a crude picture of the ECS if the

orientation of the northeastward-running continental slope in the real ocean rotates 45 ° counterclockwise. With this simple configuration we investigate the response of the ECS to the WBC forcing.

The second simple model is designed to be an intermediate stage towards the final more realistic model by adding a bit more complexity to the SSM domain (Fig. 3-1 (b)). Basically, it consists of a deep ocean, a continental shelf, and a marginal sea. The marginal sea is connected to the shelf and the deep ocean through two narrow straits (~ 100 km). The continental shelf and the marginal sea may be regarded as the ECS and the JS respectively in a crude manner. The depth of the marginal sea is set to be constant, the same as the depth of the shelf. As will be shown later the circulation within the marginal sea is sensitive to the topography in it. However, the inflow to the marginal sea is not expected to be affected by the existence of the topography within the marginal sea. This study is focused on the amount of inflow to the marginal sea rather than the detailed circulation pattern within the Japan Sea. The main purpose of building the second model is to investigate the factors affecting the influx to the marginal sea.

Fig. 3-1. (A) Plane and (B) side views of model geometry and topography for two simple models used for numerical experiments. (a) SSM : simple shelf model, (b) SMSM : simple marginal sea model. SWEM and SPEM denote the linear two-layer model and primitive equation model used for numerical experiments respectively. Notations for the SWEM are : ρ_1 , H_1 represent the density and thickness of upper layer and ρ_2 , H_2 same quantities of lower layer, and η_1 , η_2 the free surface and interface perturbation respectively. Notations for the SPEM are : h represents the depth and ρ_0 constant water density.

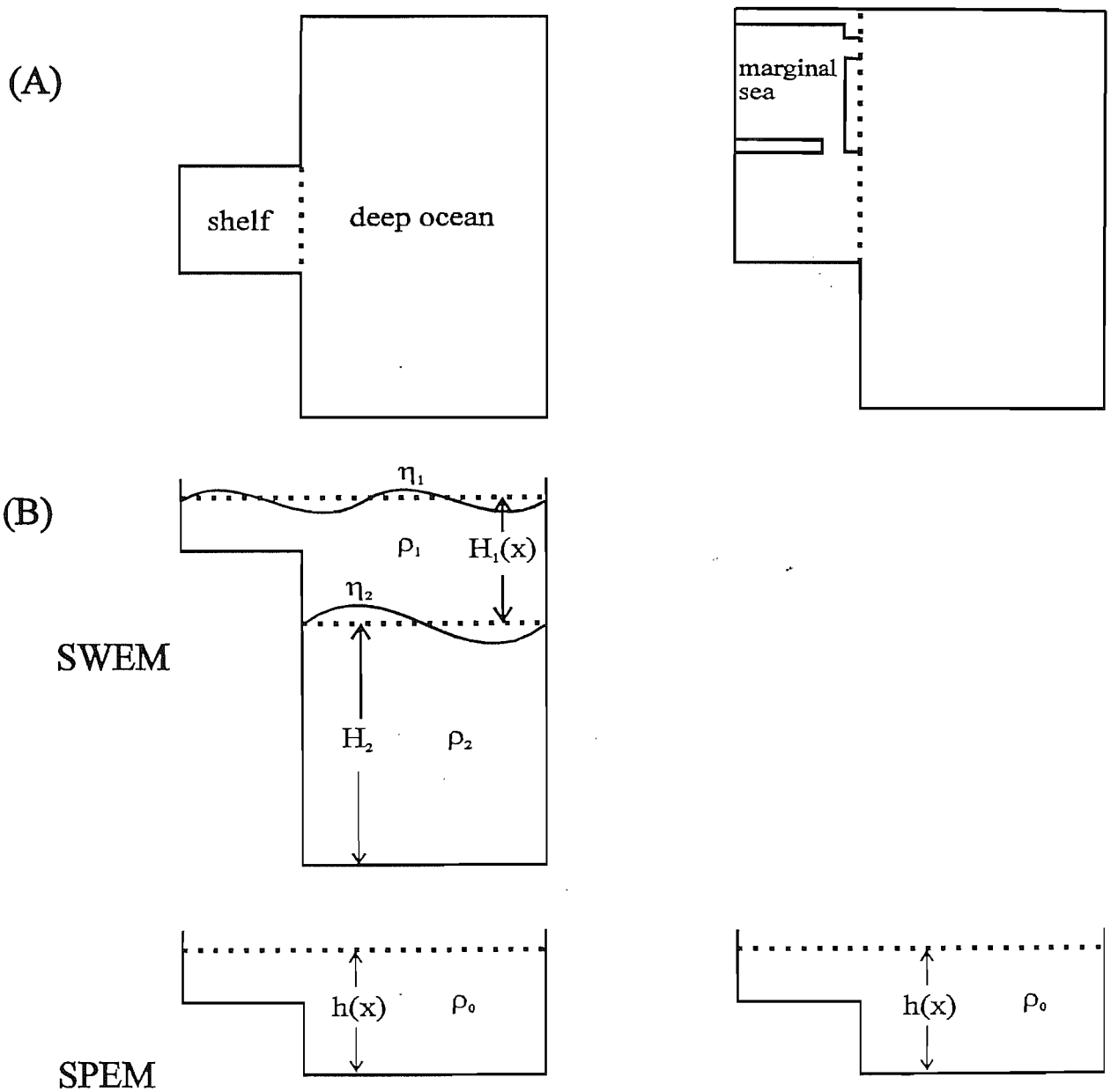
(A)
shelf
deep ocean
marginal
sea
(B)
η1
ρ1
H1(x)
η2
SWEM
H2
ρ2
h(x)
ρ0
SPEM
h(x)
ρ0

(a) SSM (b) SMSM

CHAPTER IV.

RESULTS - SIMPLE SHELF MODEL

IV-1. INTRODUCTION

In this chapter numerical model results obtained in a simplified basin geometry and topography (Fig. 3-1(a)) will be presented. The main objectives of numerical experiments are to investigate the response of the shelf to the WBC forcing and to examine the factors affecting the response. Specifically we are interested in the penetration of the Kuroshio in the ECS that is located in the western part of the North Pacific subtropical gyre. The model results may be, however, applicable to other shelf areas, e.g. South Atlantic Bight in the North Atlantic, counterpart of the ECS, where the Gulf Stream flows northward along the continental slope.

The shelf area located to the west of the subpolar gyre can be similarly investigated by establishing a southward flowing boundary current along the continental slope region. We will compare the response of continental shelves located to the west of subtropical and subpolar gyres to the boundary current forcing in a later part of this chapter.

In the SWEM experiments, the interface always intersects the deep ocean (Fig. 3-1) so that the shelf area remains vertically homogeneous at all time which may corresponds to the winter condition of the ECS. The lower layer was assumed to be motionless. In the SPEM experiments, the lower layer in the SWEM was taken out (Fig. 3-1) so that the model ocean consists of a homogeneous shelf and deep ocean which are connected to each other by a step-like continental slope.

The finite difference form of the dynamical equations was integrated until there was no further change to field variables with time. Results at an equilibrium state will be mainly presented and discussed. Numerical model results are presented in term of contours of free surface and streamlines for the SWEM and SPEM respectively. For the steady flow, contours of the free surface can be regarded as quasi-streamlines for the upper layer flow.

This chapter is mainly divided into three sections. Section IV-2 describes the linear modelling results using both the SWEM and SPEM. Section IV-3 discusses the effect of non-linearity using the results of the SPEM. Section IV-4 summarises the chapter and discusses the results.

The plan of describing the linear modelling results using two different models is as follows. Comparisons between the results of both models are made first for the standard case in section IV-2-2 followed by general description of the standard case in section IV-2-1. Results will be shown to be insensitive to the way the problem is studied such as boundary conditions and model assumptions. Linear modelling results in section IV-2 have been obtained with either SWEM or SPEM and are compatible with each other. In section IV-2-3 term balances of both momentum and vorticity equations are discussed. Effects of different frictional parameterisation are then given in sections IV-2-4 and IV-2-5. Section IV-2-6 examines other factors affecting the on-shelf transport and the sensitivity of model results to the lateral boundary condition, model geometry, and grid resolution. Section IV-2-7 compares the response of continental shelves located to the west of subtropical and subpolar gyres to the boundary current forcing.

IV-2. LINEAR MODELLING RESULTS

IV-2-1. Standard case (SWEM)

Model parameters for the standard case are given in Table 4-1. The linearised version of equation (II-3-1) without wind forcing takes the form,

$$\beta_0 \psi_x = h A_M \nabla^2 \zeta - r\zeta \ . \tag{IV-2-1}$$

The vorticity balance in the flat-bottomed shelf area is governed by the above equation. Non-dimensionalisation of the above equation using scales,

$$(x\ ,\ y) = \ell\ (x^*\ ,\ y^*),\quad h = d\ h^*,\quad \psi = U\ \ell\ \psi^*,\quad \zeta = U/\ell\ \ \zeta^*,$$

where ℓ is the length scale of the shelf, d is the depth of the shelf, and U is the typical velocity scale in the shelf, yields

$$\psi_x = E_L^s\ h\ \nabla^2\zeta - E_B^s\ \nabla^2\psi\ , \tag{IV-2-2}$$

after dropping asterisks. In the above E_L^s and E_B^s are horizontal and vertical Ekman numbers given by

$$E_L^s = \frac{A_M}{\beta_0\ l^3}\ ,\quad E_B^s = \frac{r}{\beta_0\ d\ l}\ . \tag{IV-2-3}$$

For the standard case both the lateral and bottom frictional effects are included as shown in Table 4-1. The horizontal and vertical Ekman numbers are 4×10^{-3} and 6 respectively for the standard case, so that the major vorticity sink on the shelf is the dissipation by bottom friction.

As mentioned in chapter III-2-4 the deep channel model is initially spun-up

without a shelf by a prescribed velocity at the southern boundary. Fig. 4-1 shows the temporal variation of free surface and meridional velocity in the upper layer (v_1) at two points in the eastern and western boundaries of model deep channel. The velocity at the western boundary reaches its maximum after about 200 days corresponding to the timescale for the long Rossby wave to cross the model basin ($\sim$ 180 days). Model variables show no significant change after 1 year. We integrated the deep channel model for 2 years.

Fig. 4-2 shows the fields of the deep channel model at an equilibrium state, and zonal and meridional profiles of free surface and meridional velocity in the upper layer. A strong northward flowing WBC ($\sim$ 115 cm/s) and adjacent weaker ($\sim$ -20 cm/s) return flow are the dominant features of the flow field away from the northern sponge layer. The contours are spreading out in the northern boundary region and the jet structure is disintegrated to a more uniform flow due to the high friction applied to the northern boundary. The speed of the WBC in the north-south direction is nearly constant, and the free surface linearly decreases northwards with a gradient of $\sim 10^{-7}$, i.e., 1 cm / 100 km. The shelf was introduced at the western part of the deep channel where there is a linear meridional pressure gradient with constant WBC flowing northward. Refer the Appendix B for more details of the spin-up experiment and open boundary conditions.

Fig. 4-3 shows a result of shelf model, temporal variation of free surface and meridional velocity at two points in the shelf. There are no virtual changes to shelf variables after 100 days. Results of the shelf model after 200 days will be presented for the SWEM.

Fig. 4-4 shows contour plots of free surface at an equilibrium state. Shelfward penetration of part of the WBC can be clearly seen and it takes place in the southern part of the shelf. The penetrated water rejoins the WBC after turning anticyclonically and leaving cyclonic recirculation cell in the northern part of the shelf. It can also be seen from the Fig. 4-4 that the fluid particles turn cyclonically before leaving the shelf and rejoining the WBC.

Table 4-1. Model parameters for the standard case of the SWEM and for the SPEM used for the comparison with the SWEM

parameters	SWEM	SPEM
f_0 (s^{-1})	7.29×10^{-5}	7.29×10^{-5}
f_1 (s^{-1})	6.89×10^{-5}	6.89×10^{-5}
β_0 (m^{-1} s^{-1})	1.98×10^{-11}	1.98×10^{-11}
L^x, L^y (km)	550, 4360	550,2180
ℓ^x, ℓ^y (km)	390, 780	390,780
H_1, H_2 (m)	400, 1100	h = 400 m
d (m)	200	200
g (m s^{-2})	9.81	9.81
g'(m s^{-2})	0.0336	
A_M (m^2 s^{-1})	5000	5000
r (m s^{-1})	10^{-3}	10^{-3}
$\Delta x,\Delta y$ (km)	20, 20	20, 20
Δt	50 sec	20 min

where,

f_0 : Coriolis parameter at a central latitude
f_1 : Coriolis parameter at a southern boundary of the shelf
β_0 : latitudinal variation of Coriolis parameter
L^x : width of the deep channel
L^y : length of the deep channel
ℓ^x : width of the shelf
ℓ^y : length of the shelf
H_1 : unperturbed upper layer thickness of deep channel
H_2 : unperturbed lower layer thickness of deep channel
h : depth of deep ocean
D : unperturbed shelf depth
g : acceleration of gravity
g' : reduced gravity
A_M : lateral viscosity
r : bottom friction coefficient
$\Delta x,\Delta y$: grid spacings
Δt : timestep length.

Fig. 4-5(B) shows a zonal velocity profile along a outermost meridional section of the shelf (I=20 in Fig. 4-4, referred to as shelf-edge hereafter). Shelfward penetration is confined to a relatively thin layer (referred to as a shelf boundary layer, SBL hereafter) with broad off-shelf flow. The length scale of the SBL is defined as a e-folding distance over which the negative zonal velocity drops to e^{-1} of its maximum value at the southern wall along this section.

Fig. 4-5(A) shows a zonal velocity profile along the southern wall of the shelf. The negative zonal velocity reduces exponentially from the maximum value near the continental slope towards the western wall of the shelf. For a flat-bottomed shelf, part of the penetrated water always reaches the western wall along the southern boundary of the shelf however small as it is. The zonal penetration is only restricted by the geographic location of the western wall. The zonal penetration scale (ZPS), however, is arbitrarily defined as the distance along the southern wall of the shelf over which the negative zonal velocity decreases to e^{-1} of its maximum value.

The penetrated water does not reach the northern wall of the shelf. Instead, it separates from the western wall at some latitude. The meridional penetration scale (MPS) is defined as the distance from the southern wall over which the meridional velocity has positive value along the western wall of the shelf (Fig. 4-5(C)).

The above length scales are defined to describe and compare various model results in terms of scale of penetration. The ZPS, MPS, and the length scale of the SBL for the standard case are 54.4 km, 720 km, and 41.6 km respectively. It indicates that the energetic penetration is confined within 100 km from the source region of the penetration although the sluggish flow reaches far north. Note that the maximum velocity scale in Fig. 4-5(C) is less than 5 % of the maximum velocity scale in Fig. 4-5(A) and Fig. 4-5(B).

The on-shelf volume transport along a meridional section on the shelf was computed by integrating the magnitude of the zonal velocity component multiplied by the shelf depth from the southern wall to the first zero-crossing point of the zonal

velocity component. Fig. 4-5(D) shows the ratio of the on-shelf transport as estimated above to the volume transport of the WBC as a function of distance from the shelf-edge. The volume transport of the WBC (29.5 Sv) was estimated using the prescribed velocity profile at the southern boundary of the deep channel. The maximum ratio that occurs along the shelf-edge is about 15 % (4.5 Sv), about one-seventh of the WBC water penetrating into the shelf region. The on-shelf transport decreases rapidly with distance up to 100 km from the shelf-edge, and then decreases linearly. More than half of the penetrated transport rejoins the WBC within the 100 km distance from the shelf-edge.

IV-2-2. Comparison between SWEM and SPEM results

The SPEM was configured to the basin geometry and topography shown in Fig. 3-1. Model parameters for the SPEM used for the comparison with the SWEM are given in Table 4-1.

The purpose of the comparison between the results of two different models is to investigate any effect of stratification in deep ocean on the shelfward penetration of the WBC and to test the robustness of the results obtained from the SWEM.

Differences between the two models are as follows : i) the SWEM is a finite difference layer model, on the other hand , the SPEM uses finite differences in the horizontal and a spectral expansion in the vertical, ii) there is no lower layer in the SPEM configuration so that both the deep ocean and the shelf are vertically homogeneous, iii) the model ocean was spun-up by the applied wind-stress in a closed basin in the SPEM, and iv) rigid-lid approximation was used in the SPEM but there exists surface pressure variations which have the same effect as that of the free surface. As mentioned in chapter III-3-3, the surface stress is applied only over the deep ocean and the bottom stress only over the shelf region in a depth-independent manner. Apart from the above differences, the factors affecting the amount of on-shelf transport such as the depth ratio between the shelf and deep ocean, the location of the shelf on a β-plane, both the meridional and zonal lengths of the shelf, and frictional coefficients are set to be equal in the two models. The zonal size of the deep ocean is same for the two

experiments, but the meridional size is different, which is thought to be little importance in affecting the amount and the scale of the penetration.

Transient phenomena in the SPEM are expected to be quite different from those in the SWEM. There are no gravity and internal Kelvin waves since the rigid lid approximation was used and the ocean is homogeneous. Possible waves in the system are the dispersive barotropic planetary wave whose phase and group velocities are given by the equation (II-4-5) and topographic wave. Refer the Appendix D for the spin-up of the SPEM. All the wave motions are effectively damped by lateral friction within 150 days. Model results presented in this chapter are those at 150 days.

Fig. 4-6 shows the streamfunction fields for the standard case of the SPEM at an equilibrium state. The SPEM also predicts the anticyclonic penetration of the WBC. Comparing Fig. 4-6 with Fig. 4-4, the flow pattern in the shelf is quite similar to that of the SWEM. To compare the model results quantitatively, velocity profiles along the same sections as in Fig. 4-5 and the ratio of on-shelf transport to the WBC transport are presented in Fig. 4-7. The ZPS and the length scale of the SBL agree quite well with each other (Figs. 4-7 (A) and (B)). The MPS is about 100 km smaller for the SPEM than that for the SWEM, but the location of the maximum speed coincides with each other. The maximum ratio of on-shelf transport shows also good agreement though the ratio is slightly higher for the SWEM than for the SPEM systematically away from the shelf-edge. The volume transport of the WBC in the SPEM was estimated using the applied wind-stress and Sverdrup balance.

By and large the steady state results of both models show good agreement with each other quantitatively as well as qualitatively although the transients are different. It then turns out that the stratification in the deep channel is of little significance in determining the penetration of the WBC for the linear case when the lower layer is motionless.

IV-2-3. Momentum and vorticity balances

Momentum and vorticity balances were examined based on the final steady state model results of the SWEM. Such an examination is useful in understanding the dynamics of the model results. Both balances in the upper layer is presented below.

According to equations (III-2-8) ~ (III-2-10), momentum and continuity equations in the upper layer at a steady state have the form,

$$-g\eta_{1x} + fv_1 + A_M\nabla^2 u_1 - \frac{r}{H_1}u_1 = 0 \,, \tag{IV-2-4}$$

$$-g\eta_{1y} - fu_1 + A_M\nabla^2 v_1 - \frac{r}{H_1}v_1 = 0 \,, \tag{IV-2-5}$$

$$(u_1 H_1)_x + (v_1 H_1)_y = 0 \,, \tag{IV-2-6}$$

where $H_1 = H_1(x)$ is the depth of the upper layer as before. From equations (IV-2-4) and (IV-2-5), continuous form of the vorticity equation is derived,

$$-\beta_0 v_1 - f(u_{1x}+v_{1y}) + A_M\nabla^2\zeta - \frac{r}{H_1}\left(\zeta - \frac{H_{1x}}{H_1}v\right) = 0 \,, \tag{IV-2-7}$$

where $\zeta = v_{1x} - u_{1y}$. Combining equations (IV-2-6) and (IV-2-7) yields,

$$-\beta_0 v_1 + f\frac{H_{1x}}{H_1}u_1 + A_M\nabla^2\zeta - \frac{r}{H_1}\left(\zeta - \frac{H_{1x}}{H_1}v\right) = 0 \,. \tag{IV-2-8}$$

Equation (IV-2-8) is a linearised version of equation (II-2-13) if there is no wind forcing and the depth h in equation (II-2-13) is only a function of x. Terms on the LHS of equation (IV-2-8) represent the planetary vorticity tendency (referred to as BETA hereafter), divergence term (or topographic tendency term, referred to as DIVE hereafter), vorticity diffusion term (referred to as LATF hereafter), and dissipation of vorticity due to bottom friction (referred to as BOTF hereafter). There are two

contributions to the dissipation due to bottom friction, the first is proportional to the relative vorticity and the other one emerges due to the variable topography.

A finite difference form of equation (IV-2-7) was derived from the discrete form of upper layer momentum equations A7 and A8 in Appendix A. Any spurious terms which have no counterpart in the continuous equation do not arise in the finite difference form of the resulting vorticity equation with our choice of Coriolis terms (Foreman and Benenett, 1989). However, it is important to derive the finite form of the vorticity equation from that of the momentum equations since there can be alternative ways in converting the continuous equation to a finite difference form directly. The discrete form of each term in equation (IV-2-7) is given in Appendix E.

IV-2-3-1. Vorticity balance

The local rate of change of relative vorticity was observed to be nearly zero after 200 days, and a balance exists among the various terms on the LHS of (IV-2-7). The local vorticity balance was examined along selected sections shown in Fig. 4-8.

Fig. 4-9 shows the vorticity balance along a zonal section in the deep channel (section a in Fig. 4-8). The balance is between the planetary vorticity tendency (BETA) and the vorticity diffusion term (LATF). In the western boundary layer, the BETA term acts as a source of negative relative vorticity since a fluid particle having a negligible relative vorticity enters the boundary layer and moves northward. The LATF term acts as a source of positive vorticity by diffusing the negative vorticity in the boundary layer into the surroundings.

For the standard case, estimation of two Ekman numbers using the length scale of the shelf indicates the dominance of the BOTF term in the shelf area. Fig. 4-10 (B) shows the vorticity balance along the middle longitude of the shelf (section b in Fig. 4-8). It clearly shows the balance between the BOTF and BETA. The region where the sign of the BETA changes to positive is the cyclonic recirculation area in the northern part of the shelf. Along the western wall of the shelf (section c in Fig. 4-8), both the

BOTF and LATF balance the BETA term as shown in Fig. 4-10 (A).

Fig. 4-11 shows the balance along the shelf-edge (section d in Fig. 4-8). The main balance in the on-shelf flow region (or SBL, I=102 ~ 104 in the figure) is between the divergence term (DIVE) and the LATF with a minor contribution of the dissipation due to bottom friction (BOTF) to the LATF. The DIVE term tends to increase the negative vorticity while both the LATF and BOTF tend to decrease it. A fluid column entering the shallow shelf acquires negative vorticity due to the shrinking of a water column. As the topographic β-effect is about ten times as large as the planetary β-effect ($\beta_0 / f < \Delta H / H$), where H and ΔH are the mean depth and depth gradient between the shelf and deep channel respectively, frictional forces must act as a source of positive vorticity at a steady state.

The southern intensification of currents predicted by the model is consistent with the vorticity balance in the SBL for both bottom and lateral frictions to balance the stretching term.

If the flow is frictionally dominated due to bottom friction, negative vorticity should be generated in order that the vorticity dissipation term due to bottom friction acts as a source of positive vorticity. This is only consistent with the strongest flow at the southern boundary and slow flow far out from the boundary when the fluid moves westward along the wall. Fig. 4-11 shows that the sign of the BOTF is positive in the SBL.

The sign of the LATF is also positive in the SBL. Fig. 4-12 shows a meridional profile of the relative vorticity in the SBL. As the free slip boundary condition was used, the relative vorticity at the boundary is zero. Maximum negative vorticity appears just north of the boundary and the vorticity rapidly increases between points B and C. The maximum negative vorticity value over the whole shelf region occurs at point A. This negative vorticity is diffused into surroundings due to the action of vorticity diffusion term so that the LATF term acts also as a source of positive vorticity. If the shelfward penetration would take place at the northern boundary of the shelf, the sign of both

BOTF and LATF would be negative resulting in a vorticity imbalance.

Re-estimation of both Ekman numbers of (IV-2-3) using the length scale of the SBL ($\ell = 10$ km) yields,

$$E_L^s = \frac{A_M}{\beta_0 l^3} \sim 250 \ , \ E_B^s = \frac{r}{\beta_0 d l} \sim 25 \ .$$

Therefore, the LATF term is a dominant dissipation mechanism in the narrow SBL although the major vorticity sink in the remaining shelf area is the BOTF term.

Along the broad off-shelf flow region (Fig. 4-11 (B)), the sign of both DIVE and LATF terms is positive, while the sign of BOTF is negative. The sign of the DIVE term is determined by the sign of the zonal velocity. For the off-shelf flow having a positive zonal velocity, the sign of the DIVE is positive. Fig. 4-13 shows profiles of meridional velocity and the relative vorticity along a middle latitude in the shelf (section e in Fig. 4-8). The inshore part of the WBC is a source of positive vorticity due to the large velocity shear. The BOTF, therefore, acts as a source of negative vorticity and balances both the DIVE and LATF terms.

Fig. 4-14 shows the vorticity balance along a meridional section located 40 km west of the shelf-edge. The DIVE term is now nearly zero since the shelf is flat. Near the southern wall where the zonal velocity is negative, the BOTF term balances the BETA and LATF terms. The main balance in the broad off-shelf flow region is between BOTF and LATF. The BOTF term acts as a source of negative vorticity by destroying the positive vorticity, while the LATF term acts as a source of positive vorticity implying that positive vorticity is diffused into it out of some source region, I=20 in Fig. 4-13.

The vorticity balance investigated above may be summarised by looking at the balance along a middle latitude of the shelf (section e in Fig. 4-8) as is shown in Fig. 4-15. In most parts of the shelf area the balance is between BETA and BOTF. In the western part of shelf-edge the vorticity diffusion term (LATF) is mainly balanced by the

BOTF. At the shelf-edge (I=20 in the figure) the BOTF is balanced by both DIVE and LATF.

At grid point I=21 just east of the shelf-edge where the depth change takes place, the balance is given by

$$-A_M \nabla^2 \zeta \sim f\frac{H_{1x}}{H_1}u_1 - \frac{r}{H_1}\left(\zeta - \frac{H_{1x}}{H_1}v_1\right).$$

Off-shelf flow acquires positive vorticity due to the vortex tube stretching. Therefore, the DIVE term tends to increase the positive vorticity. The LATF term then acts as a source of negative vorticity by diffusing the positive vorticity into surroundings. Note that the maximum positive vorticity occurs at this point (Fig. 4-13) and this point is a source place from which positive vorticity is diffused into surroundings. The sign of the BOTF is not negative but positive though the sign of the relative vorticity is positive since the second term in the BOTF, $r\, H_{1x}\, v_1 / H_1^2$, is now larger than $-r\,\zeta / H_1$. The fluid flow in the deeper region experiences less retardation due to bottom frictional force than the flow in the shallow region, which results in the generation of positive vorticity.

The examination of the local vorticity balance along the selected sections implies following balances in various geographic area,

$$\beta_0 v_1 \sim A_M \nabla^2 \zeta \quad (WBC \ \ region),$$

$$\beta_0 v_1 \sim -\frac{r}{H_1}\zeta \quad (interior\ shelf\ region),$$

$$\frac{r}{H_1}\zeta \sim A_M \nabla^2 \zeta \quad (inshore\ part\ of\ the\ shelf\text{-}edge),$$

$$\frac{r}{H_1}\zeta \sim f\frac{H_{1x}}{H_1}u_1 + A_M \nabla^2 \zeta \quad (shelf\text{-}edge\ ,\ off\text{-}shelf\ flow\ region),$$

$$-f\frac{H_{1x}}{H_1}u_1 \sim A_M \nabla^2 \zeta \quad (shelf\text{-}edge\ ,\ on\text{-}shelf\ flow\ region).$$

IV-2-3-2. Momentum balance

The term balance in the upper-layer momentum equations (IV-2-4) and (IV-2-5) was also examined along selected sections with the model generated current velocities and free surface at a steady state.

In the deep channel model the zonal momentum balance along the western boundary layer (refer to Fig. 4-2) is geostrophic, while the meridional momentum balance is between the pressure gradient force and lateral friction term as shown in Fig. 4-16. Northward-flowing WBC balances the free surface tilting in the zonal direction, and the meridional gradient of the free surface inherent in the WBC balances the frictional force.

Fig. 4-17 shows the momentum balance along the same section after introducing the shelf area. The zonal momentum balance remains geostrophic. On the other hand, the Coriolis force becomes important in the meridional balance after removing the western wall and introducing the shelf. Especially, the balance is highly geostrophic near the region where shelfward penetration takes place (J=102 and J=103 in the lower panel of Fig. 4-17). Coriolis and pressure gradient forces are balanced to within only a few percent, with the horizontal friction term making up the difference. Westward on-shelf flow is therefore highly correlated with the meridional free surface sloping downward to the south. Along the off-shelf flow region both the Coriolis force and the lateral friction term balance the pressure gradient force as shown in Fig. 4-18. The magnitude of the Coriolis force is about two times larger than that of the lateral friction.

Shelfward penetration of the WBC can be understood by considering the change in the term balance in the meridional direction before and after introducing the shelf along the section described above. The meridional gradient of the free surface inherent in the WBC balances the lateral friction without the shelf. However, the balance changes to be approximately geostrophic after introducing the shelf. Then a broad off-shelf flow is induced since the free surface slopes downward to the north. Shelfward penetration

must take place to compensate this off-shelf flow. Otherwise, the shelf would be emptied and the steady state could not be attained. The penetration takes place at the southern part of the shelf forming a narrow frictional boundary layer (SBL) to meet the vorticity tendency requirement as the fluid particles cross the topography as was examined in the vorticity balance.

In most parts of the inner shelf region, the balance of terms in both directions is geostrophic as shown in Fig. 4-19. The flow field is only weakly damped and the anticyclonic circulation in the shelf is not dictated at leading order by the chosen frictional mechanisms. The frictional forces only enter the momentum balance as a secondary importance near the region where strong velocity gradient exists and also along the wall.

IV-2-4. Role of bottom friction

The effect of bottom friction was examined by reducing the coefficient of bottom friction from 10^{-3} (standard case) to zero. As a matter of convenience, the latter will be referred to as a lateral friction model. As mentioned before, the dynamical effects of bottom friction are present in a bulk sense, and the bottom boundary layer is not explicitly resolved.

Fig. 4-20 shows the standard run of Fig. 4-4 together with experiments where the coefficient of bottom friction ranges from 0 to 5×10^{-4}. Without bottom friction the shelf circulation is dominated by strong cyclonic recirculation in the north. Anticyclonic penetration of the WBC is only confined to the southeastern part of the shelf. As the coefficient of bottom friction increases, the recirculation cell is reduced in its size and strength accompanied by more broader spreading of the WBC water penetrated onto the shelf. The bottom friction, therefore, acts to destroy the recirculation cell, and allow fluid particles to make a larger meridional excursion.

In order to examine the scale and strength of the penetration for the experiments, velocity profiles along selected sections, and longitudinal variation of on-shelf transport

are plotted in Fig. 4-21 as was done in section IV-2-1. Reduction of size and strength of the recirculation cell can be clearly seen in the meridional velocity profile along the western wall of the shelf (Fig. 4-21 (A)). The length scale of the SBL and the ZPS seem to be insensitive to changes in the coefficient of bottom friction although the maximum on-shelf velocity decreases significantly as the coefficient increases. The length scale of the SBL increases slightly as the coefficient increases. The maximum on-shelf transport tends to decrease as the coefficient increases as can be expected. The maximum transport for the standard case ($r=10^{-3}$) is only about 70 % of that for the lateral friction model. However, the transport beyond 100 km distance from the shelf-edge shows larger values as the coefficient increases despite the lower speed at the southern wall, which indicates the broader on-shelf current as the coefficient increases.

The length scale of frictional boundary layers dominated by either the bottom friction or the lateral friction is given by

$$\frac{r}{\beta_0 d}, \quad or \quad \left(\frac{A_M}{\beta_0}\right)^{\frac{1}{3}},$$

according to equation (IV-2-3). For typical values of r($= 10^{-3}$ ms^{-1}), β_0, A_M, and d used in the experiment (see Table 4-1), estimates of the both length scales yield

$$\frac{r}{\beta_0 d} \sim 250\ km, \quad \left(\frac{A_M}{\beta_0}\right)^{\frac{1}{3}} \sim 50\ km.$$

When the bottom friction is a dominant sink of relative vorticity, the resulting length scale of the boundary layer is much larger than the case where the lateral friction is dominant.

The result of lateral friction model (Fig. 4-20 (A)) is characterised by a large and strong cyclonic recirculation cell in the north. The generation of this recirculation cell may be understood by considering the difference in the vorticity balance between the lateral friction model and the standard case. There must be a source of positive vorticity for this recirculation cell to be formed and maintained. As mentioned before, the inshore part of the WBC has a source of positive vorticity due to the zonal gradient of

meridional velocity. This velocity gradient results from the fact that only a part of the WBC penetrates into the shelf, while most of the WBC flows northward along the western part of the deep channel. The maximum positive vorticity appears near the shelf-edge (Fig. 4-13).

Fig. 4-22 shows the vorticity balance for the two cases along a latitudinal section located 40 km west of the shelf-edge. The vorticity diffusion term (LATF) is exactly balanced by the BETA in the lateral friction model. Fluid particles moving northward acquire negative vorticity due to the increase of planetary vorticity. The positive vorticity is, then, supplied through diffusion from the shelf-edge in the lateral friction model, resulting in the cyclonic recirculation cell. In the bottom friction model, the vorticity diffusion is balanced by the dissipation of the vorticity due to bottom friction, and the β-effect is of little significance. It implies that the bottom friction is now prohibiting the positive vorticity diffusion resulting in no appreciable recirculation cell in the standard case. The maximum positive vorticity is smaller in the lateral friction model than in the standard case as a consequence of vorticity diffusion as shown in Fig. 4-23. However, the vorticity value is higher and the sign of the vorticity is positive in the interior region of the shelf in the lateral friction model, while the vorticity value is negative and weaker in the standard bottom friction model. The local maximum of the positive vorticity near the western wall of the shelf in the lateral friction model is also due to diffusion of the positive vorticity from the boundary. The southward flowing current along the western wall acquires positive vorticity and then excess positive vorticity must be diffused into the surroundings.

IV-2-5. Lateral friction model

The lateral friction model was further examined by varying the eddy viscosity. The two stage modelling approach with the SWEM was not used in this case since the model deep channel is only damped by lateral friction so that the integration with different eddy viscosities requires spinning up the deep channel model in each case. Instead, the SPEM was used for this examination, which is relatively quick to reach an

equilibrium state.

Fig. 4-24 shows the results of the lateral friction model with different values of eddy viscosity. There is no bottom friction in all of three cases in the figure. All other parameters are same as those of standard SPEM case (Table 4-1) except different eddy viscosity. The applied frictionless Sverdrup transport is about 27.6 Sv.

The characteristic length scale of the WBC is given by $(A_M/\beta)^{1/3}$. It can be clearly seen from the figure that the trapping scale of the WBC reduces as the eddy viscosity decreases. The maximum gyre transports of the experiments increase as the eddy viscosity decreases.

The shelf circulation (lower panel in Fig. 4-24) is dominated by large cyclonic recirculation cell, and the shelfward penetration of the WBC is confined only to the southeastern part of the shelf. The trapping scale of the currents along the inshore part of the WBC, and along the western and northern walls is also reduced as the eddy viscosity decreases. The maximum transport of the recirculation cell increases as the eddy viscosity decreases. It is also interesting to note that the streamlines become more zonally-oriented as the eddy viscosity decreases since the flow tends to follow f/H contour, which is parallel to the latitudinal lines within the flat-bottomed shelf, as the frictional effect becomes less important. Consequently, the zero streamline intersects the southern part of the western wall when the value of $A_M=1000\ m^2s^{-1}$, while it intersects the southwestern corner for the two other cases.

The maximum on-shelf flow speed increases significantly as the eddy viscosity decreases as shown in Fig. 4-25 (B). However, the length scale of the SBL increases as the eddy viscosity increases. The negative zonal velocity component occurs only at one grid point when the eddy viscosity $A_M=1000\ m^2s^{-1}$. Comparing Fig. 4-25 (A) with Fig. 4-21 (B), the length scale of the SBL is more sensitive to the change to the eddy viscosity. A ten times increase in the coefficient of the bottom friction increases the length scale of the SBL by 3.5 km, while a similar increase in the eddy viscosity broadens the SBL by 33 km. Simple scaling analysis of the vorticity balance in the SBL

(LATF vs DIVE) gives an approximate length scale of the SBL as $(A_M/f_1)^{1/2}$, where f_1 is the Coriolis parameter at the southern wall of the shelf. Further reduction of the eddy viscosity below 1000 m^2s^{-1} led to an instability probably due to the inability of the model grid size to resolve the SBL. As a consequence of the reduction in the length scale of the SBL, the model predicts less penetration when the eddy viscosity is small as shown in Fig. 4-25 (B), contrary to the result of the bottom friction model. Further increase in the coefficient from A_M=5000 m^2s^{-1} to A_M=20000 m^2s^{-1}, however, resulted in the reduction of the maximum on-shelf transport (see Fig. 4-26).

IV-2-6. Other factors affecting on-shelf transport

A series of experiments are now described that examines the dependence of on-shelf transport of various parameters other than the coefficients of bottom friction and lateral viscosity. Results of various experiments are compared with the standard SWEM or SPEM results where both frictional parameterisation are present. Contour plots of free surface (SWEM) or streamlines (SPEM) in the shelf and adjacent deep channel region are presented for each case. Standard model parameters are the same as those tabulated in Table 4-1. Fig. 4-26 shows the dependence of the ratio between the WBC transport and the maximum on-shelf transport on three major parameters examined in this section, and coefficients of bottom friction and lateral viscosity. A ten times increase in the coefficient of bottom friction results in the 10 % decrease in the ratio. The ratio is relatively insensitive to the change of the coefficient of lateral viscosity compared to the sensitivity of the ratio to that of bottom friction.

IV-2-6-1. Location of the shelf

The dependence of the circulation and on-shelf transport on the location of the shelf on a β-plane is shown in Fig. 4-27. More penetration of the WBC takes place into the shelf located in the lower latitude as shown in Fig. 4-26. As was examined in section IV-2-3-2, the off-shelf flow is in a crude geostrophic balance and the on-shelf flow is highly geostrophic. For the geostrophically balanced flow, the flow speed is inversely proportional to the Coriolis parameter f. The on-shelf transport is, therefore,

dependent on the location of the shelf on a β-plane. The increase in the latitude by 13° reduces the maximum on-shelf transport ratio by about 7 % as shown in Fig. 4-26.

IV-2-6-2. Depth of the shelf

Fig. 4-28 shows the results of five experiments varying the depth of the shelf 50 m ~ 250 m with other parameters set to be equal. As the depth of the shelf is getting closer to the upper layer depth of the deep channel, more penetration occurs as shown Fig. 4-26. The ratio of maximum on-shelf transport to the volume transport of the WBC tends to be proportional to the square of the ratio of shelf depth to the upper layer depth of deep channel as shown in Fig. 4-29. The reason for this trend is not clear.

IV-2-6-3. Size of the shelf

Dependence on width (longitudinal size of the shelf) and length (latitudinal size of the shelf) of the on-shelf transport was investigated by doubling the size of the shelf in each direction (Fig. 4-30). The amount of penetration is insensitive to the width of the shelf but sensitive to the length of the shelf. As the length of the shelf increases, the off-shelf transport also increases as shown in Fig. 4-26 since the volume transport is proportional to the length scale of the off-shelf flow, while the meridional gradient of free surface remains same. Consequently, the on-shelf transport also increases.

IV-2-6-4. Effect of the WBC transport

Table 4-2 summarise four experiments to investigate the effect of WBC transports on the amount and scale of penetration. The WBC transport was made increase by increasing the applied wind-stress. All other parameters are same for all experiments and there is no bottom friction on the shelf. The maximum gyre transports for all experiments are about 10 % larger than the Sverdrup value.

For the linear case, the flow field in the shelf region remains same regardless of the WBC transport as shown in Fig. 4-31. Shelfward penetration is confined to the

southeastern part of the shelf and the large recirculation cells are dominant feature as already examined in section IV-2-5. The scale of penetration including the length scale of the SBL remains same as shown in Table 4-2. The amount of penetration increases as the WBC transport increases. However, the ratio between the on-shelf transport and the WBC transport (either Sverdrup value or maximum gyre transport) remains same. For the non-linear case, results are very different as will be shown in the next section.

IV-2-6-5. Lateral boundary condition

A free-slip boundary condition was used for all experiments in this study partly because of simplicity in interpretation of results and partly because the model boundary does not necessarily correspond to the actual coastlines. Changes in lateral boundary condition in numerical model studies have shown to affect the separation of the WBC (Haidvogel et al., 1992 ; Dengg, 1992).

Sensitivity of model results to the lateral boundary condition was tested by applying a no-slip boundary condition to the case in Fig. 4-20 (C), where the WBC water penetrated onto the shelf separates from the western wall of the shelf near the mid-latitude of the shelf and rejoins the WBC leaving a cyclonic recirculation cell in the north. As shown in Fig. 4-32, the model results such as the separation latitude of the WBC water penetrated onto the shelf and the strength of recirculation cell are little affected by the change in lateral boundary condition. The source region of positive vorticity needed to form the recirculation cell in the model is the inshore part of the WBC not the solid wall. The no-slip boundary condition reduces the maximum on-shelf transport by about 1 % of the prescribed WBC transport (~ 0.3 Sv).

IV-2-6-5. Grid resolution

Any effects of grid spacing on the model results were examined by halving and doubling the grid spacings of the standard SPEM case. The result of finer resolution model is much the same as the result of the standard 20 km resolution model as shown in Fig. 4-33. The maximum on-shelf transport observed at the outermost grid point of

the shelf (shelf-edge) decreases as the grid resolution becomes poorer. The difference in the on-shelf transport between the results of the 10 km and 20 km resolutions is negligible, while the difference between the 10 km and 40 km resolutions reaches up to 10 % (about 2 % of the applied total Sverdrup transport). We believe that the 20 km grid resolution is enough to predict the correct penetration of the WBC quantitatively as well as qualitatively.

Table 4-2. Summary of four linear experiments with different applied Sverdrup transport in the deep ocean.

Experiment		A	B	C	D
T ($\times 10^{-4}$)		2.5	5.0	7.5	10.0
$\nabla \times \tau$ (Sv)		13.5	27.0	40.4	53.9
ψ_{max} (Sv)		14.4	28.8	43.2	57.6
OSVT	I=19	23.90	23.80	23.90	23.90
(%)	I=10	1.57	1.56	1.57	1.57
SBL (km)		40.6	40.6	40.6	40.5
ZPS (km)		55.4	55.3	55.3	55.2
MPS (km)		0.0	0.0	0.0	0.0
U_{max} (cm/s)		45.6	91.3	137.0	183.0

where
T (τ_0/ρ_0 , N·m/kg) : applied wind-stress
$\nabla \times \tau$: applied Sverdrup transport in equation (II-3-3)
ψ_{max} : resulting maximum gyre transport in deep ocean
OSVT : ratio between the on-shelf transport and applied Sverdrup transport
U_{max} : maximum shelfward zonal velocity in the SBL

IV-2-6-6. Effect of sharp corner

A part of the WBC penetrates onto the shelf around a right-angled corner in the model. Smoothed corner results a decrease in the maximum on-shelf

transport by 10 % (about 2 % of the applied Sverdrup transport) as shown in Fig. 4-34.

IV-2-6-7. Effect of width of the deep ocean

Any effect of the size of the deep ocean was examined by changing the width of the deep ocean of the SPEM configuration (Fig. 4-35). The applied frictionless Sverdrup transport (~ 29.5 Sv) in both cases is same. The maximum gyre transports in both cases are different : 27 Sv for the narrow width case and 30 Sv for the broad width case. The amount of penetration or the ratio between the on-shelf transport and applied Sverdrup value, however, remains same irrespective of the longitudinal size of the deep ocean as shown in Fig.4-36. The latitudinal size of the deep ocean is thought to be of little significance in affecting the amount of penetration.

IV-2-7. Other experiments

The rectangular shelf has been assumed to be located at the western boundary of the subtropical gyre in all the previous experiments, i.e., $p_y < 0$ and $h_x > 0$, where p_y is the meridional pressure gradient along the WBC and h_x is the zonal gradient of topography. Let us consider a case where the p_y is positive. This case may be referred to as the MAB (Middle Atlantic Bight) case where the mean southward component of the flow of shelf is driven primarily by an alongshore pressure gradient imposed at the shelf break by the cyclonic gyre called slope water region in the deep ocean, which is found between the continental shelf and the Gulf Stream (Beardsley and Boicourt, 1981).

Fig. 4-37 (A) compares the shelf circulation located west of subtropical and subpolar gyres for the linear case. The flow pattern is symmetric for the linear case in that only the sign of contour lines is reversed for the MAB case compared with the ECS case. The model result shows a broad southwestward on-shelf flow and the off-shelf flow is confined to a narrow boundary layer for the MAB case.

Let us consider a case where h_x is negative, i.e. the shelf is deeper than the deep ocean. This is unrealistic, but may be justifiable in the context of a process-oriented study to understand the dynamics. In this case northern intensification of currents takes place as shown in Fig. 4-37 (B). For the ECS case ($p_y < 0$) the model result shows a broad and sluggish on-shelf flow and a narrow and strong off-shelf flow and vice versa for the MAB case.

We sum up the picture by considering the linear vorticity equation,

$$\frac{D}{Dt}\left(\frac{f}{h}\right) = A_M \nabla^2 \zeta \ .$$

Table 4-3 summarises the results of four experiments in Figs. 4-37 (A) and (B). The sign of the Df/Dt (BETA) is determined by the meridional pressure gradient along the boundary currents (p_y) since the shelf current is driven by the offshore pressure gradient. For the on-shelf and off-shelf flows, the sign of the $D(h^{-1})/Dt$ (DIVE) is positive and negative respectively. If the sign of both terms is the same, the vorticity diffusion term (LATF) should increase in size. If both terms have opposite signs, the size of the LATF term decreases. The intensification of currents takes place either in the south or in the north depending upon the sign of the h_x such that the velocity profile in the boundary layer is consistent with the generation of acquired relative vorticity when fluid particles cross the topography.

Table 4-3. Summary of four experiments with different combination of p_y and h_x in terms of the vorticity balance.

case	1	2	3	4	5	6	7	8
	$p_y < 0$				$p_y > 0$			
	ECS case				MAB case			
	$h_x > 0$		$h_x < 0$		$h_x > 0$		$h_x < 0$	
	on-shelf	off-shelf	on-shelf	off-shelf	on-shelf	off-shelf	on-shelf	off-shelf
BETA	+	+	+	+	-	-	-	-
DIVE	+	-	-	+	+	-	-	+
LATF	large & +	small	small	large & +	small	large & -	large & -	small
zonal velocity profile in the SBL	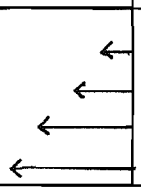			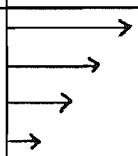		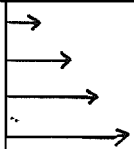	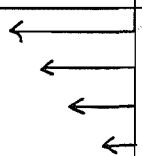	
flow pattern in the shelf	northward current & southern intensification		northward current & northern intensification		southward current & southern intensification		southward current & northern intensification	

where,

p_y : meridional pressure gradient along the boundary current,

h_x : zonal gradient of bottom topography,

BETA : Df/Dt,

DIVE : $D(h^{-1})/Dt$,

LATF : $A_M \nabla^2 \zeta$,

IV-3. NON-LINEAR MODELLING RESULTS

IV-3-1. Introduction

The effects of non-linearity will be investigated in this section entirely with the SPEM. The only difference between the non-linear and linear models is the inclusion of the advective terms in the momentum equations.

The results of a standard case with and without the advective terms is presented firstly in the next section (section IV-3-2) to grasp the significance of the non-linearity. Section IV-3-2 also compares the ECS and MAB cases in section IV-2-7 again with a non-linear model. Results of a non-linear lateral friction model are then presented to investigate the changes to the amount and scale of WBC penetration onto the shelf as the WBC becomes more inertial (section IV-3-3). Section IV-3-4 describes the local vorticity balance for a non-linear model.

IV-3-2. Comparisons between linear and non-linear experiments

The non-linear advective terms are included in the momentum equations of the linear experiment B in Table 4-2, and the model equations are integrated up to 150 model days as was done in the linear experiments. The non-linear model also reaches an equilibrium state at 150 days (see Appendix D).

For the non-linear case the eastward jet builds up at the northern boundary of the deep ocean, while the flow is symmetric for the linear case as shown in Fig. 4-38. The non-linear model also predicts the anticyclonic penetration of the WBC onto the shelf, and the penetration takes place at the southeastern part of the shelf the same as for the linear case. However, the amount and scale of the penetration are dramatically increased for the non-linear case. The on-shelf flow

clearly splits into two regimes for the non-linear case : one rejoins the WBC in a tight anticyclonic turn (referred to as an offshore branch hereafter) and the other one penetrates deep into the shelf (referred to as an inshore branch hereafter). The inshore branch moves anticyclonically in the southern half of the shelf and then rejoins the WBC after sharply turning to north near the shelf-edge. Meandering of the flow can also be seen along the inshore part of the WBC and it is prominent in the southern part of the shelf. The strength and the horizontal scale of the northern recirculation cell are reduced to about half of those for the linear case.

Velocity profiles along selected sections clearly show an increase in the penetration scale as shown in Fig. 4-39. The maximum negative zonal velocity in the SBL is larger for the linear case than for the non-linear case. However, the ZPS and the length scale of the SBL are about two times and 1.5 times larger respectively for the non-linear case than for the linear case resulting in the larger on-shelf transport along every longitudinal sections as shown in Fig. 4-39 (D). For example, the on-shelf transport estimated along a mid-longitude of the shelf (I=10 in Fig. 4-39 (D)) is about 50 % of the maximum transport along the shelf-edge for the non-linear case, while it is only about 10 % for the linear case.

We examined the case where the meridional pressure gradient along the western boundary is positive (MAB case) in section IV-2-7 (see Fig. 4-37 (A)). The ECS and MAB cases are re-examined with the non-linear model.

Inertial effects are expected to be of little significance for the MAB case since the on-shelf flow is sluggish and extends over a broad area. This is confirmed by the results of the non-linear model (Fig. 4-40), which shows a flow pattern similar to that of the linear case. However, the inertial effects radically change the flow pattern for the ECS case. On-shelf flow for the ECS case is likely to be inertial since the strong flow is confined to a narrow boundary layer. Meridional extent of the recirculation cell is increased for the non-linear MAB case, contrary to the ECS case.

IV-3-3. Non-linear lateral friction model

In this section results of six non-linear experiments without bottom friction on the shelf are presented (Table 4-4). The main purpose of these experiments is to investigate any changes in the amount and scale of WBC penetration onto the shelf as the WBC becomes more inertial from a diffusive state. The characteristic of the WBC in our flat-bottomed deep ocean may be described in terms of two non-dimensional numbers R and E_L in equation (II-3-5) or δ_I and δ_L defined in equation (II-3-8). As the R or δ_I increases the WBC becomes more inertial.

Wind-driven ocean circulation in an idealised basin has been fairly well documented since the early papers on the theoretical linear problem of Stommel (1948) and Munk (1950). The complete non-linear problem with different frictional parameterisation was also studied numerically (Veronis, 1966 ; Böning, 1986).

Fig. 4-41 shows the results of a series of numerical experiments using a model with lateral friction and free-slip boundary conditions of Böning (1986). It demonstrates how the flow fields evolve as the inertial boundary layer width (δ_I) increases.

Regardless of the frictional parameterisation, both the bottom friction model of Veronis (1966) and the lateral friction model examined by Böning (1986) show common features of a northward shift of the gyre centre compared to the symmetrical linear flow as the flow becomes weakly non-linear (compare Figs. 4-40 (A) and (B)).

In an 'intermediate' range of the R where the inertial boundary layer width (δ_I) is comparable to the frictional scale (δ_L or δ_B), details of both the bottom friction and the lateral friction model results greatly differ, while a northern boundary current emerges in common with an eastward penetration scale depending on the R. In the lateral friction model, a strong recirculating sub-gyre

emerges in the northwestern corner of the basin associated with an increase in the maximum gyre transport to values larger than the Sverdrup value as can be seen in Fig. 4-41 (C) and (D).

When the inertial scale is 1.5 times the diffusive scale (Fig. 4-41 (E)), the model ocean is dominated by the sub-gyre. The result at this limit is quite similar to that of the highly inertial case of the bottom friction model (Veronis, 1966).

Six experiments in Table 4-4 are classified in terms of the Rossby (R^d in Table 4-4) and horizontal Ekman (E_L^d in Table 4-4) numbers or the ratio between inertial and diffusive scales of boundary layer (ϵ in Table 4-4) in the deep ocean as was done by Böning (1986). The Ekman number is held constant at a value of 3.83×10^{-4} which is equivalent to an eddy viscosity A_M=5000 m^2s^{-1}. The western boundary layer is made more and more inertial by increasing the wind stress from 0.1 dyne/cm^2 (T=0.1×10^{-4} in Table 4-4) to 10 dyne/cm^2 (T=10.0×10^{-4} in Table 4-4). The corresponding Sverdrup transport ranges from 0.54 Sv to 53.9 Sv. The maximum volume transport of the Kuroshio in the ECS is less than 50 Sv (Nitani, 1972 ; Guan, 1983b ; Ichikawa and Beardsley, 1993). The maximum current speed of the WBC resulting from the experiment F is about 90 cm/s, which is also comparable to the observed one (Kaneko et al., 1990).

With the steady value of wind stress applied only in the deep ocean the whole system gradually evolved from an initial state until a steady state was achieved. The flow eventually became steady in the parameter range we examined. Eddies did not develop in all experiments probably due to a rather higher eddy viscosity used.

Non-dimensional numbers in the SBL will be of interest. Rossby, Ekman, and Reynolds numbers in the SBL are defined as

$$R^s = \frac{U}{\beta_0 l^2} \quad , \quad E_L^s = \frac{A_M}{\beta_0 l^3} \quad , \quad Re^s = \frac{Ul}{A_M} \, , \qquad \text{(IV-3-1)}$$

Table 4-4. Summary of six non-linear experiments.

Experiment		A	B	C	D	E	F
T ($\times 10^{-4}$)		0.1	0.5	2.5	5.0	7.5	10.0
$\nabla \times \tau$ (Sv)		0.54	2.70	13.5	27.0	40.4	53.9
ψ_{max} (Sv)		0.58	2.91	14.5	27.4	40.3	82.6***
R^d ($\times 10^{-4}$)		1.03	5.17	25.8	51.7	77.5	103.0
E_L^d ($\times 10^{-4}$)		3.83	3.83	3.83	3.83	3.83	3.83
$\epsilon = \delta_I/\delta_L$		0.14	0.31	0.70	0.99	1.21	1.40
R^s		0.56	2.63	8.94	10.39	11.19	9.79
E_L^s		3.69	3.41	2.06	1.13	0.69	0.41
Re^s		0.15	0.77	4.34	9.19	16.22	23.88
OSVT	I=19	24.68	24.85	28.15	31.07	33.66	35.44
(%)	I=10	2.26	2.69	9.33	15.74	14.85	6.42
SBL (km)		40.9	42.0	49.7	60.7	71.4	85.0
ZPS (km)		57.0	60.0	90.8	123.6	81.3	47.1
MPS (km)		80.0	100.0	260.0	400.0	520.0	440.0
U_{max} (cm/s)		1.87	9.18	43.7	75.8	113.0	140.0
ζ_{max} ($\times 10^{-5}$)		0.032	0.159	0.667	1.19	1.77	2.36

where

T (τ_0/ρ_0 , N·m/kg) : applied wind-stress

$\nabla \times \tau$: applied Sverdrup transport in equation (II-3-3)

ψ_{max} : resulting maximum gyre transport in deep ocean

R^d : Rossby number in equation (II-3-5)

E_L^d : horizontal Ekman number in equation (II-3-5)

δ_I : inertial boundary layer in equation (II-3-8)

δ_L : frictional boundary layer in equation (II-3-8)

$\epsilon = \delta_I / \delta_L$

R^s : Rossby number in the SBL in equation (IV-3-1)

E_L^s : Ekman number in the SBL in equation (IV-3-1)

Re^s : Reynolds number in the SBL in equation (IV-3-1)

OSVT : ratio between the on-shelf transport and applied Sverdrup transport

U_{max} : maximum shelfward zonal velocity in the SBL

ζ_{max} : maximum negative relative vorticity in the SBL.

*** : The maximum WBC transport is 52.7 Sv.

where U is the maximum shelfward zonal velocity in the SBL and ℓ is the length scale of the SBL. The numbers were estimated for each case using the model generated velocity values and are given in Table 4-4.

Fig. 4-42 shows the ratio between maximum on-shelf transport along the shelf-edge and the Sverdrup value for the six experiments. The linear model results with the same range of applied wind stress are also plotted for comparison. For the linear experiments, the ratio remains the same as was found before. On the other hand, for the non-linear case, the ratio increases as the Sverdrup value increases or the inertial boundary layer width in the deep ocean becomes more prominent.

Figs. 4-43 and 4-44 show the contours of streamlines for the six experiments in Table 4-4 at 150 days. Fig. 4-45 shows the velocity profiles along the same sections as before, and the longitudinal variation of the ratio between the on-shelf transport and the applied Sverdrup transport. As a matter of convenience, experiments (A) and (B) will be referred to as weakly inertial cases ($\epsilon < 0.5$), (C) ~ (E) as moderately inertial cases, and (F) as a highly inertial case.

Although flow fields in the deep ocean tend to evolve according to the ϵ value as in Fig. 4-41, the difference between with and without shelf is perceptible especially when the inertial scale is comparable and larger than the diffusive scale. The recirculating flow in the northwestern corner of the deep ocean seems to develop at a larger value of ϵ when there exists a shallow shelf. When the inertial scale is greater than the frictional scale, two recirculating flows emerge in the deep ocean in the with-shelf case, while only the northern recirculating flow is a dominant feature in the without-shelf case. For the experiment E, the transports of both recirculating flows are same. The transport of northern recirculating flow is 1.5 times larger than the southern one for the experiment F.

As this study is focused on the effect of deep ocean on the shelf circulation rather than the effect of the shelf on the wind-driven circulation in the deep ocean, further investigation of the difference between two cases in Fig. 4-41 and Fig. 4-43 was not made.

For the weakly non-linear cases, the shelf circulation features are almost the same as for the linear cases (Figs. 4-44 (A) and (B)), and the amount and scale of penetration is only slightly larger than that for the linear cases as shown in Fig. 4-45. The local Reynolds number in the SBL are less than one in this parameter range of the deep ocean suggesting the vorticity diffusion is the major term to balance the vortex tube shrinking, the same as for the purely linear cases.

As the ϵ increases further, the inshore branch becomes more prominent until the inertial scale is 1.2 times the diffusive scale. In association with this strengthening of inshore branch the horizontal scale of the recirculation cell in the northern part of the shelf becomes reduced. The on-shelf transport along the mid-longitude of the shelf (I=10 in Table 4-4) increases to about half of the maximum on-shelf transport when ϵ is about 1 (experiment D).

For the highly inertial case, the inshore branch becomes less prominent and most of the water penetrated onto the shelf rejoins the WBC in a tight anticyclonic turn. When the inertial scale is 1.4 times the diffusive scale, the transport along the mid-longitude of the shelf (I=10) is less than those for the moderately inertial cases as shown in Fig. 4-45 (D) (Exp. F) and Table 4-4.

The ZPS reaches the maximum when ϵ is 1, and then decreases as the inertial scale further increases. The MPS increases as the inertial scale increases until $\epsilon = 1.2$ and then it is reduced for experiment F. The length scale of the SBL continuously increases as ϵ increases. The maximum shelfward velocity in the SBL increases as ϵ increases. The maximum velocity is located on the southern rim of the on-shelf flow for $\epsilon < 1$, but it is found at one grid point north of the rim when the inertial scale is greater than the diffusive scale as can be seen in Fig. 4-45 (C).

As the inertial scale increases, there is a noticeable meandering of the zonal velocity component along the shelf-edge as shown in Fig. 4-45 (C). The meandering feature is recognizable from the case of $\epsilon = 0.7$ (Exp. C in Fig. 4-45 (C)). The amplitude is reduced northwards. For experiment F, the meandering of the offshore

branch is a dominant feature, while the inshore branch weakens considerably as shown in Figs. 4-43 (F) and 4-44 (F). Snapshots of streamlines for every ten days after 150 days for experiment F indicated that the meandering pattern shown in Fig. 4-44 (F) is stationary (not shown).

The local Rossby number in the SBL increases as the inertial scale in the deep ocean increases. On the other hand, the local Ekman number decreases due to the increase in the length scale of the SBL. The meandering along the shelf-edge rather than the deep penetration becomes predominant when the local Reynolds number is greater than 20.

In summary, as the inertial boundary layer width in deep ocean increases until the value of ϵ is around 1, the amount and the scale of penetration increases. However, further increase in the value of ϵ leads to the weakening of deep penetration and the meandering along the inshore part of the WBC becomes dominant for the highly inertial case.

IV-3-4. Local vorticity balance

Each term in the vorticity tendency equation (II-2-13) was calculated for a moderately inertial case (experiment E in Table 4-4) using a model generated velocity field. The actual finite difference form of the vorticity equation was derived from the finite difference forms of momentum equations as before rather than directly from the equation (II-2-13). The local vorticity balance along selected sections only in the shelf area will be presented. The regional vorticity balance in a barotropic, flat-bottomed wind-driven ocean model was investigated by Veronis (1966) and Böning (1986).

Fig. 4-46 shows the balance along the shelf-edge. Relative vorticity advection term (ADVE) is of primary importance in balancing the stretching term (DIVE) for the on-shelf flow in the SBL. Consequently, vorticity diffusion term (LATF) makes less

contribution to the balance than for the linear case. For the outgoing offshore branch (J=59~63 in the figure), the balance is primarily between the DIVE and the ADVE, i.e., D (ζ/h) / Dt = 0, suggesting that the offshore branch behaves like an inviscid inertial flow. The ADVE term becomes less important in the remaining part of the shelf-edge and the balance for the outgoing inshore branch is between the DIVE and LATF, BETA, the same as the balance for the linear case.

Note that the sign of the LATF is negative at a southernmost point 20 km north of the southern boundary of the shelf (J=55 in Fig. 4-46), while it is positive at other points in the SBL. The relative vorticity in the region of on-shelf flow along the shelf-edge and continental slope is negative for the linear case as shown in Fig. 4-47 (A). For the non-linear case, there exists a zone of positive relative vorticity in the SBL, along a southern boundary of the shelf, and just north of the corner in the continental slope. The maximum value of the positive vorticity is located at the north of the corner (I=20 and J=55 in Fig. 4-47). The positive vorticity is generated due to the fact that the zonal velocity gradient between two points close to the boundary is smaller than the meridional velocity gradient (see Fig. 4-45 (C)), so that the sign of the vorticity is mainly determined by the meridional velocity gradient which has a positive sign. The positive relative vorticity is advected to the SBL and southern boundary of the shelf for the non-linear case. Consequently, the maximum negative zonal velocity is located on the southern rim of the on-shelf flow, but it is found at one grid point north of the rim as the inertial effects increase as shown in Fig. 4-45 (C). At other points in the SBL, the sign of relative vorticity is negative. As can be seen in Fig. 4-47 (C), the region of positive relative vorticity is enlarged for experiment F, where any energetic inshore branch does not exist and the meandering of the offshore branch is a dominant feature.

The effect of inertial processes in a flat-bottomed, homogeneous ocean is to broaden the boundary layer thickness and to weaken the role of the dissipation due to bottom friction in the region of inflow (Veronis, 1966 ; Veronis, 1981). The same idea may be applicable to the present lateral friction model. In the SBL, the vorticity balance is given by

$$f\frac{D}{Dt}\left(\frac{1}{h}\right) + \frac{1}{h}\frac{D\zeta}{Dt} = A_M\nabla^2\zeta \ .$$

The planetary vorticity tendency gives little contribution to the above balance in the SBL. Since the two terms on the LHS of the above equation (DIVE and ADVE terms respectively) mainly balances for the non-linear case, the frictional term (LATF term) on the RHS must consequently decrease in size than for the linear case, where the LATF term solely balances the DIVE term. The LATF term ($\nabla^2\zeta$) will decrease if the relative vorticity (or velocity) decreases or if the horizontal scale increases. The inertial effects, therefore, weaken the flow in the SBL by broadening the length scale of the SBL as shown by comparing the experiments A~D in Table 4-2 with the experiments C~F in Table 4-4. The increase in the maximum on-shelf transport is associated with this broadening of the SBL.

Along the southern wall of the shelf the ADVE balances the LATF as shown in Fig. 4-48. It can be seen from the Fig. 4-44 that the width of the inshore branch along the southern wall (ℓ_w) increases as the distance from the SBL (L_b) increases. The scale of ℓ_w may be determined using a vorticity balance between the ADVE and the LATF,

$$U\frac{\partial\zeta}{\partial x} = A_M\frac{\partial^2\zeta}{\partial y^2} \ , \ i.e., l_w \propto \left(\frac{L_b \times A_M}{U}\right)^{\frac{1}{2}} \ .$$

A Munk type balance holds along the western wall of the shelf as shown in Fig. 4-49 (A). Along the mid-longitude of the shelf three terms of the ADVE, the BETA, and the LATF balance each other in different regions. Close to the southern boundary the balance is between the ADVE and the LATF as shown before. The magnitude of the BETA term increases northward from the wall. In other words as the width of the inshore branch broadens due to the vorticity diffusion, the BETA term becomes dominant due to the increase in the magnitude of the meridional velocity component. Across the separated inshore branch from the western wall (J=70~76 in Fig. 4-49 (B)) the ADVE balances both the BETA and the LATF terms. In the recirculation region the LATF term balances both the ADVE and the BETA terms.

IV-4. SUMMARY OF THE CHAPTER AND DISCUSSION

Response of a continental shelf to the WBC forcing was investigated in an idealised basin numerically keeping in mind the circulation driven by the Kuroshio in the ECS. Due to the steep topography, most of the WBC flows northwards and only a part of the transport penetrates onto the shelf. The circulation pattern of the shelf driven by the subtropical WBC is independent of the particular choice of model parameters. The model predicts an anticyclonic penetration of the WBC onto the shelf, and the penetration is confined to a narrow boundary layer (SBL) formed at a southern part of the shelf.

The momentum balance indicates that the meridional pressure sloping downward to the north inherent in the WBC drives a broad off-shelf flow along the inshore part of the WBC. Continuity then requires shelfward penetration of the WBC to compensate for this off-shelf flow.

Changes in the structure of the SBL to the frictional parameterisation and the inclusion of inertial effects can be understood by examining the local vorticity balance in the SBL;

$$f\frac{D}{Dt}\left(\frac{1}{h}\right) = A_M\nabla^2\zeta \ , \quad \textit{linear lateral friction model}$$

$$f\frac{D}{Dt}\left(\frac{1}{h}\right) = A_M\nabla^2\zeta - \frac{r}{h} \ , \quad \textit{linear bottom friction model}$$

$$f\frac{D}{Dt}\left(\frac{1}{h}\right) + \frac{1}{h}\frac{D\zeta}{Dt} = A_M\nabla^2\zeta \ , \quad \textit{non-linear lateral friction model} \ .$$

The planetary vorticity tendency gives little contribution to the above balances in the SBL.

For the linear and weakly non-linear cases which we examined, the major balance in the SBL is between the stretching term and the vorticity diffusion term. The negative vorticity acquired by fluid particles crossing the topography is diffused from the boundary by the action of vorticity diffusion. The sign of relative vorticity in the SBL should be negative in order for the frictional term to act as a source of positive vorticity. This can only be achieved by the southward intensification of the flow. The on-shelf flow turns sharply to the left of the WBC, and the maximum on-shelf velocity is located on the southern rim of the shelf boundary. For the highly inertial cases, the relative vorticity advection term is of primary importance in balancing the stretching term. The maximum on-shelf velocity is, however, found at one grid point north of the southern rim of the shelf boundary for the highly inertial case since the fluid inertia attempts to advect the on-shelf flow to the right to conserve the negative vorticity induced by shrinking of the water column.

Results of the lateral friction model are characterised by a strong recirculation cell in the northern part of the shelf. This cyclonic cell is formed by the diffusion of positive vorticity from the inshore part of the WBC.

For the linear bottom friction model, the size of the vorticity diffusion term is reduced since the viscous bottom torque partly balances the stretching term. This is achieved by the reduction of the on-shelf velocity, while the length scale of the SBL changes little compared to that for the lateral friction model. Inclusion of bottom friction, therefore, reduces the amount of penetration. Additional effects of the bottom friction result in the broad spreading of the on-shelf flow and act to destroy the recirculation cell in the north of the shelf.

The advection terms also act to reduce the size of the vorticity diffusion term by balancing part of the stretching term for the non-linear lateral friction model. This occurs by broadening the length scale of the SBL for the inertially dominated flow which carries its own momentum. The increase in the maximum on-shelf transport for the non-linear model is associated with the broadening of the boundary layer. Inclusion of advection terms also increases the zonal and meridional penetration scales significantly. The ratio

between the on-shelf transport and the WBC transport increases as the transport of the WBC increases, while it remains the same for the linear model.

For the moderately non-linear case, on-shelf flow splits into two distinct regimes : one rejoins the WBC in a tight anticyclonic turn and meanders along the inshore part of the WBC (offshore branch), the other one penetrates deep into the shelf (inshore branch). The offshore branch is characteristic of an inviscid inertial flow, while the frictional effect due to the presence of a lateral boundary is of importance for the inshore branch.

For a highly inertial case, the inshore branch does not exist and meandering is amplified. Consequently, the on-shelf transport in the middle section diminishes if compared with the moderately inertial case, although the maximum transport increases.

Other factors affecting the on-shelf transport were investigated using the linear bottom friction model. The amount of penetration depends on the depth of the shelf , location of the shelf on a β-plane, and the latitudinal length of the shelf.

Csanady (1978) presented a simple linear model for the frictionally damped steady depth-averaged flow driven over a sloping shelf by a uniform alongshore pressure gradient externally imposed at the shelf break. He concluded that the open ocean imposed the mean pressure gradient along the outer edge of the MAB that was required to drive the observed mean southwestward flow on the shelf. His suggestion has been further supported by Beardsley and Winant (1979). Su and Pan (1987) also used a similar linear model to account for the observed feature of the TWC in the region of north of Taiwan. As we showed the inertial effects are of little importance for the MAB case so that a linear model may be applicable. However, a linear model will significantly underestimate the amount and scale of penetration for the ECS case.

Despite the simplicity of the model there are some similarities between the model results and observed feature in the ECS such as the meandering of the Kuroshio in the ECS (Sugimoto et al., 1988 ; Qiu et al., 1990) and two (inshore and offshore) branches of the TWC (Yuan and Su, 1988 ; Su and Pao, 1987). The model result indicates that the

frictional effect due to the presence of the lateral boundary is important for the inshore branch. In a real ocean, the Taiwan Island may support this inshore branch (Qiu and Imasato, 1990).

In conclusion, the inertial effects and the bottom friction exerted on the shallow continental shelf seem to be two indispensable factors in studying the shelf circulation driven by the subtropical WBC in this steady, barotropic model.

Fig. 4-1. Temporal variation of (A) free surface and (B) meridional velocity in the upper layer at two points in the western (solid lines) and eastern (dotted lines) boundaries. The results are obtained from the deep channel model of the SWEM. Scales of solid and dotted lines are indicated to the left and right sides of the vertical axes respectively.

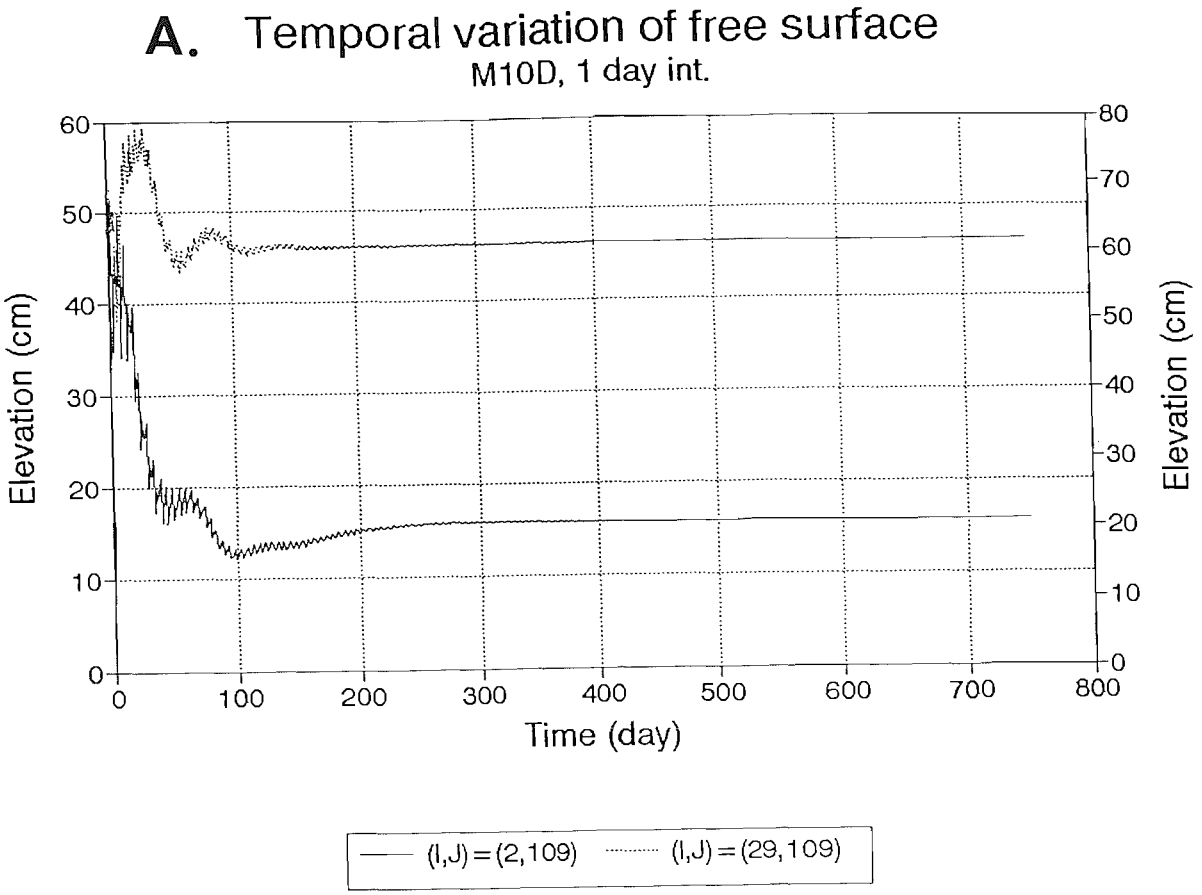
A. Temporal variation of free surface
M10D, 1 day int.
Elevation (cm)
Elevation (cm)
Time (day)
0
100
200
300
400
500
600
700
800
0
10
20
30
40
50
60
70
80
(I,J)=(2,109)
(I,J)=(29,109)

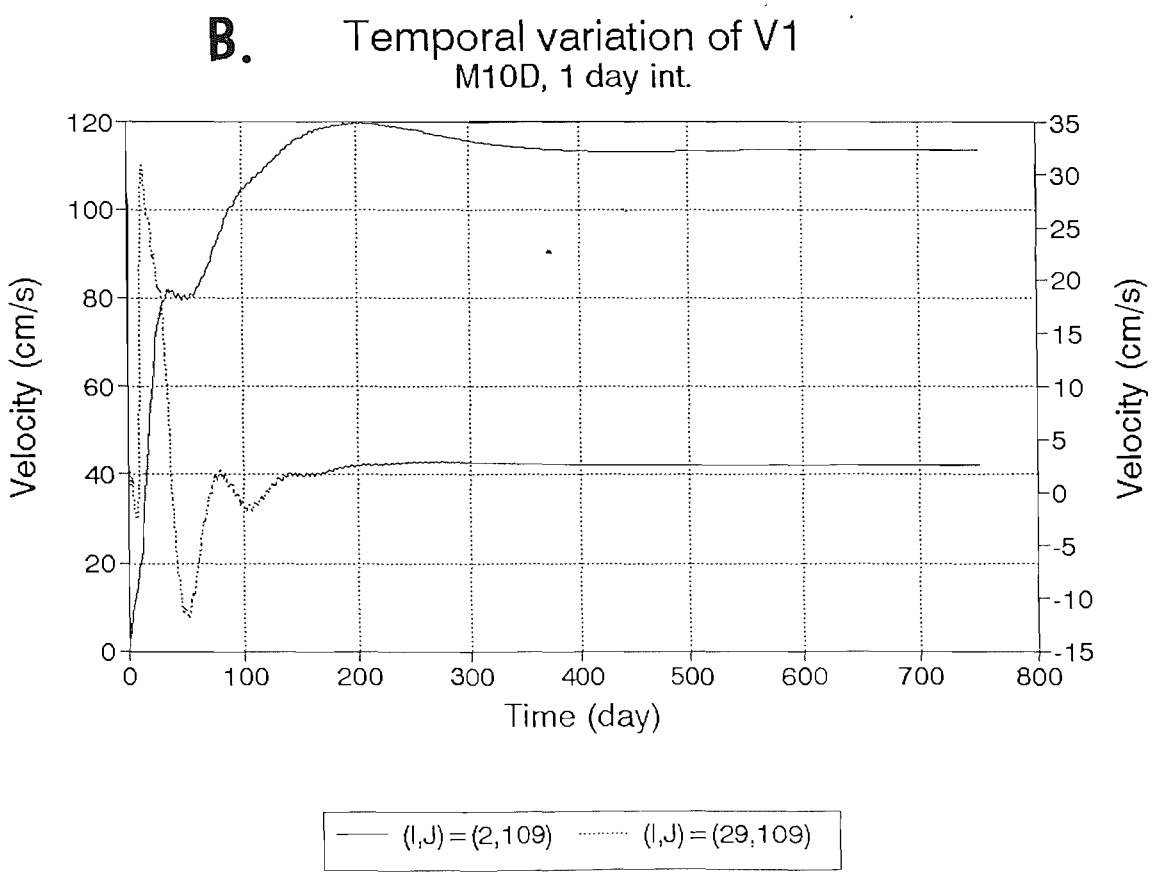
B. Temporal variation of V1
M10D, 1 day int.
Velocity (cm/s)
Velocity (cm/s)
Time (day)
0
100
200
300
400
500
600
700
800
0
20
40
60
80
100
120
-15
-10
-5
0
5
10
15
20
25
30
35
(I,J)=(2,109)
(I,J)=(29,109)

Fig. 4-2. (Upper panel) Contours of (A) free surface, (B) interface perturbation, and (C) meridional velocity in the upper layer at an equilibrium state of the deep channel model of the SWEM.

(Lower panel) Profiles of free surface (solid line) and meridional velocity in the upper layer (dotted line) along (A) a zonal section (J=120 in the above figure) and (B) the western boundary (I=2 in the above figure).

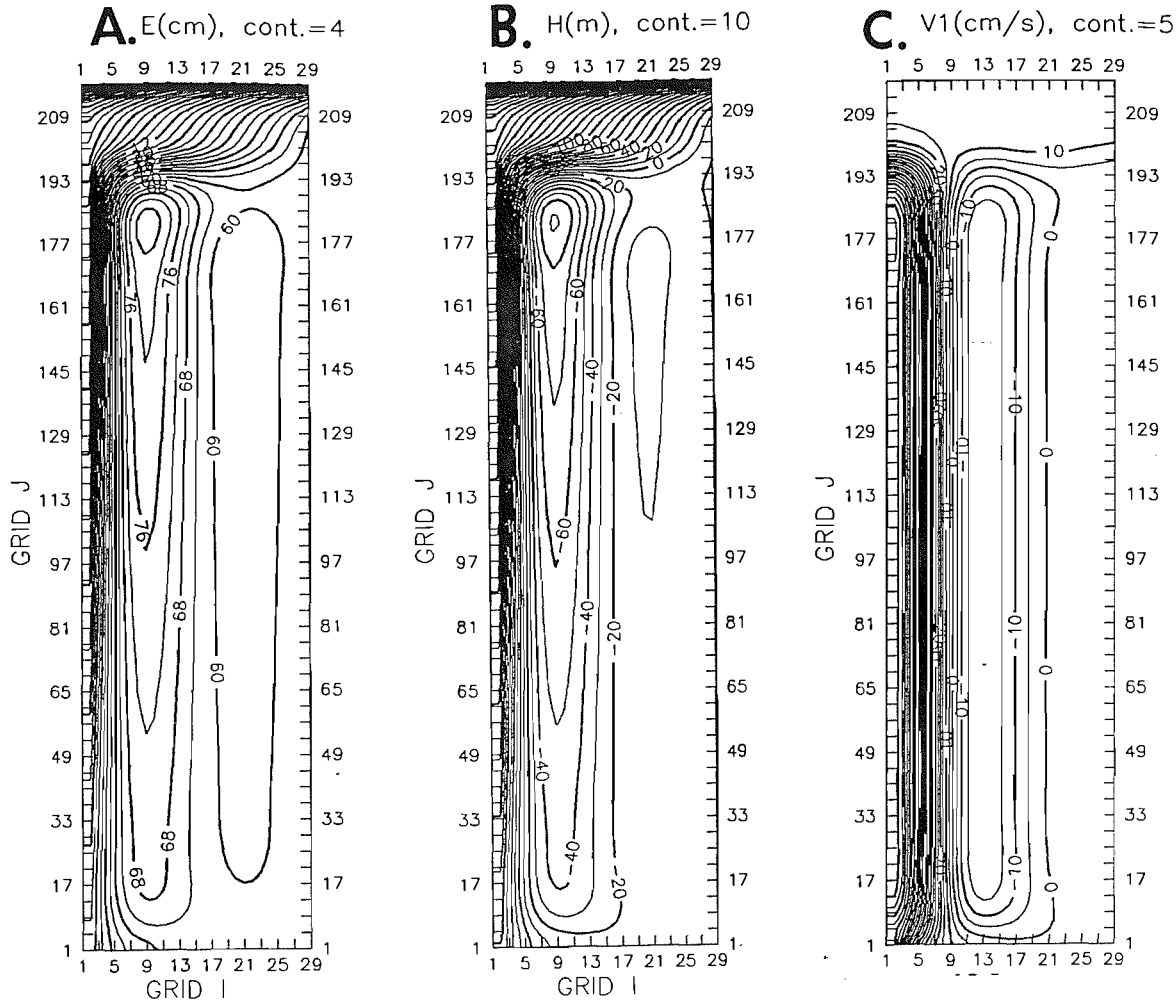
A. E(cm), cont.=4
B. H(m), cont.=10
C. V1(cm/s), cont.=5
GRID J
GRID I
1 5 9 13 17 21 25 29
1 17 33 49 65 81 97 113 129 145 161 177 193 209

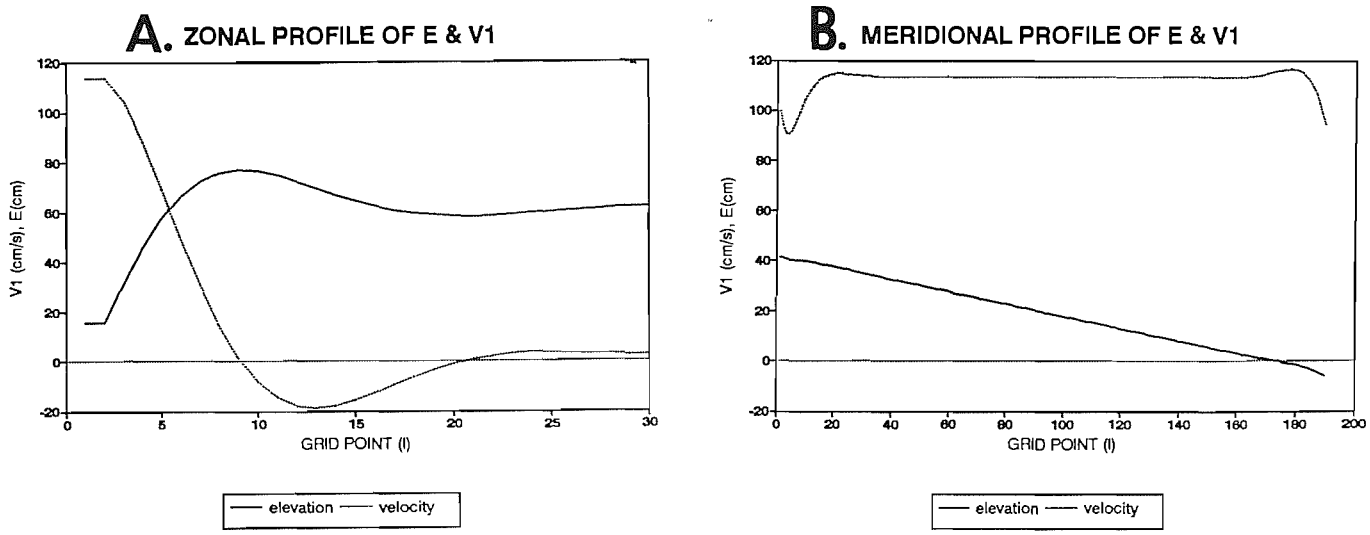
A. ZONAL PROFILE OF E & V1
B. MERIDIONAL PROFILE OF E & V1
V1 (cm/s), E(cm)
GRID POINT (I)
elevation
velocity

Fig. 4-3. Temporal variation of (A) free surface and (B) meridional velocity at two points in the western boundary of the shelf (solid lines, I=2 in the legend) and near the shelf-edge (dotted lines, I=20 in the legend). The results are obtained from the standard shelf model of the SWEM. Scales of solid and dotted lines are indicated to the left and right sides of the vertical axes respectively.

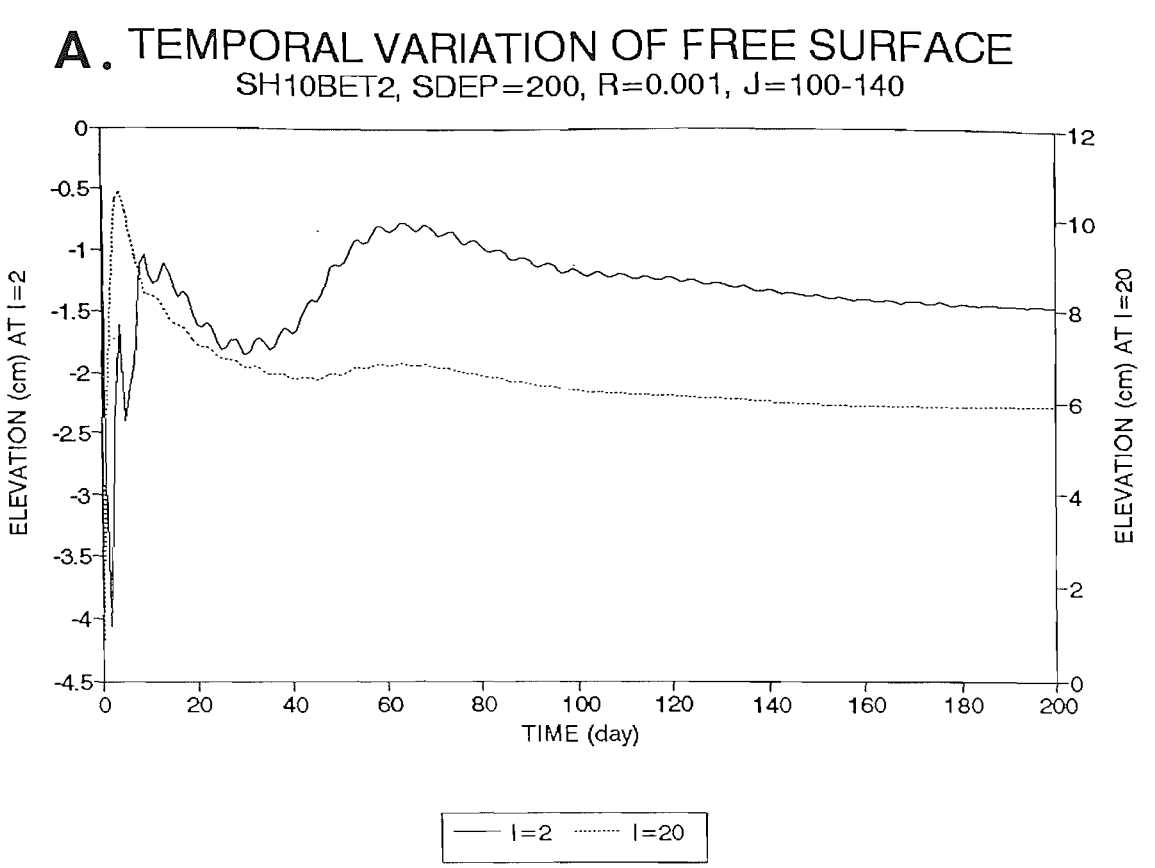
A. TEMPORAL VARIATION OF FREE SURFACE
SH10BET2, SDEP=200, R=0.001, J=100-140
ELEVATION (cm) AT I=2
ELEVATION (cm) AT I=20
TIME (day)
I=2
I=20

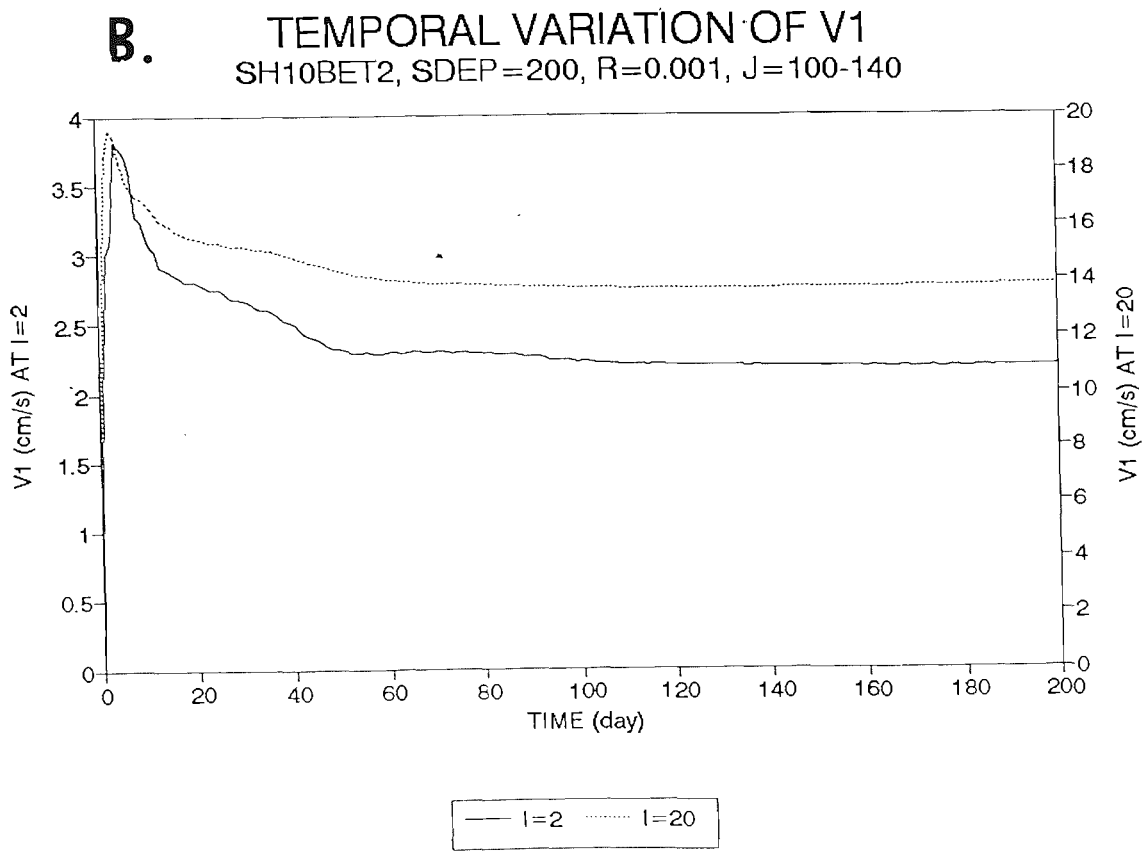
B. TEMPORAL VARIATION OF V1
SH10BET2, SDEP=200, R=0.001, J=100-140
V1 (cm/s) AT I=2
V1 (cm/s) AT I=20
TIME (day)
I=2
I=20

Fig. 4-4. Contours of free surface at an equilibrium state of the standard shelf model of the SWEM (A) in the whole domain, (B) in the shelf and adjacent deep channel area, and (C) only in the shelf. Continental slope lies between grid points I=21 (depth=200 m) and I=22 (depth=400 m). As the staggered grid was used (Fig. A-1), the depth of u-points at I=21 is 300 m. The zonal velocity along the shelf-edge referred to in the text indicates the zonal velocity along I=20 (depth=200 m).

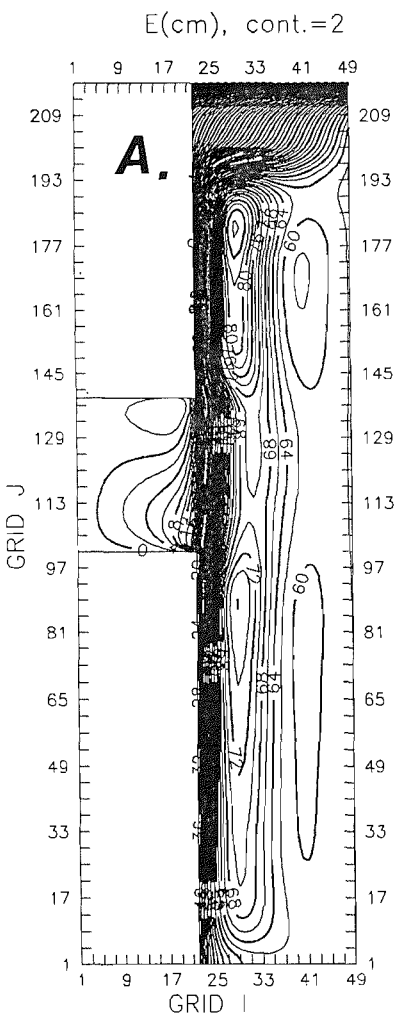
E(cm), cont.=2
A.
GRID J
GRID I

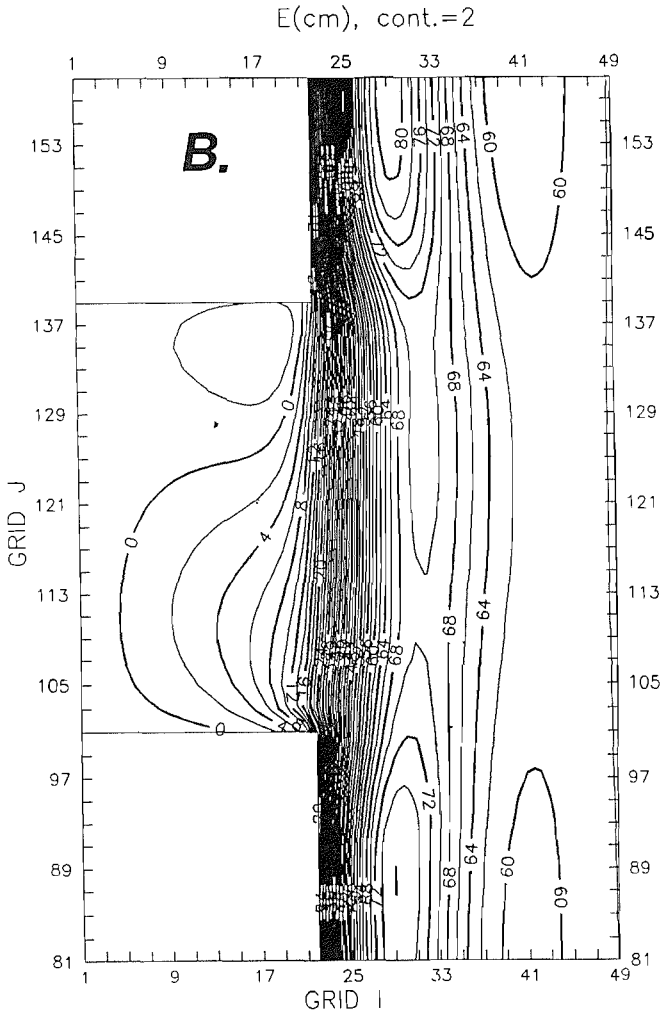
E(cm), cont.=2
B.
GRID J
GRID I

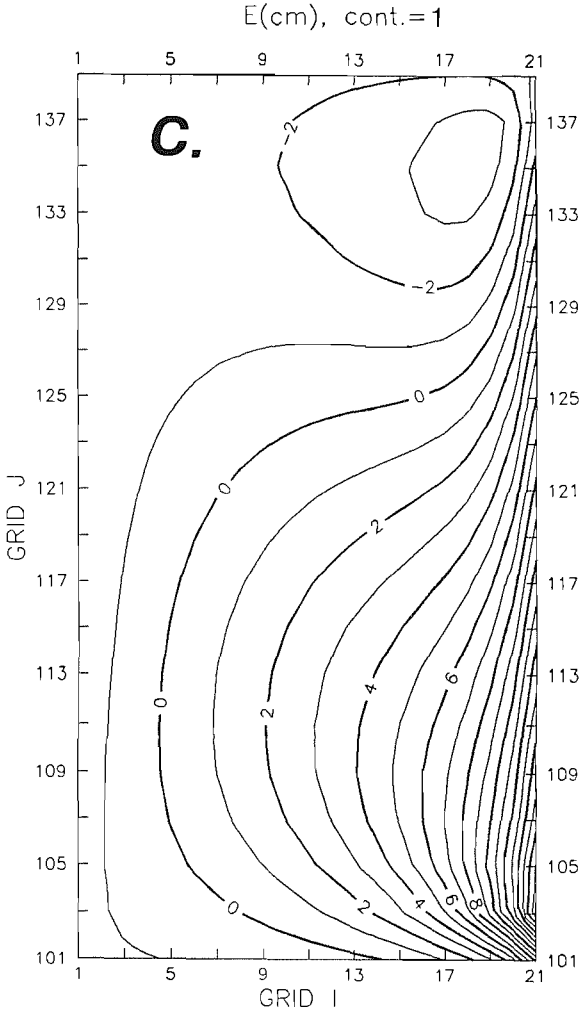
E(cm), cont.=1
C.
GRID J
GRID I

Fig. 4-5. (A) Zonal velocity profile along the southern wall of the shelf (J=101 in Fig. 4-4). The distance is measured westwards from the shelf-edge (I=20). Dotted arrow indicates the ZPS as defined in the text. (B) Zonal velocity profile along the shelf-edge (I=20 in Fig. 4-4). The distance is measured northwards from the southernmost point (I=20 and J=101). Dotted arrow indicates the length scale of the SBL as defined in the text.

(A) U1 along the southern wall

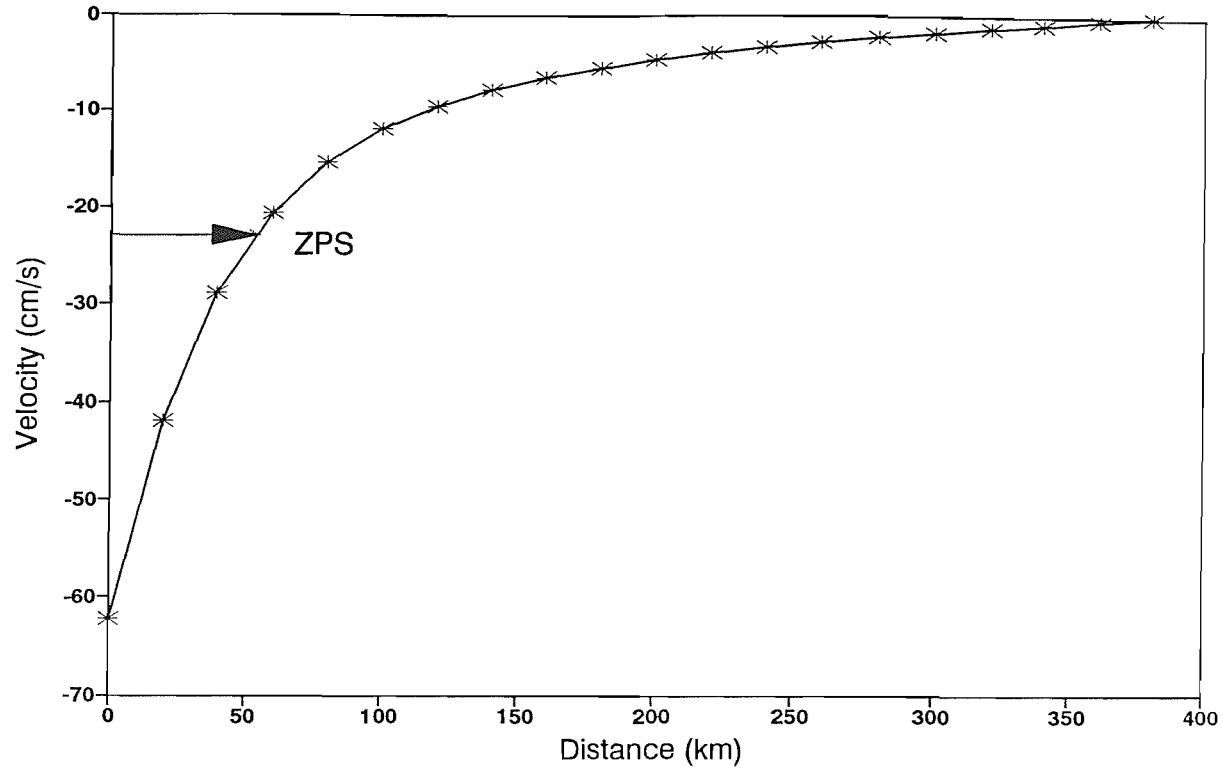

(B) U1 along the shelf-edge

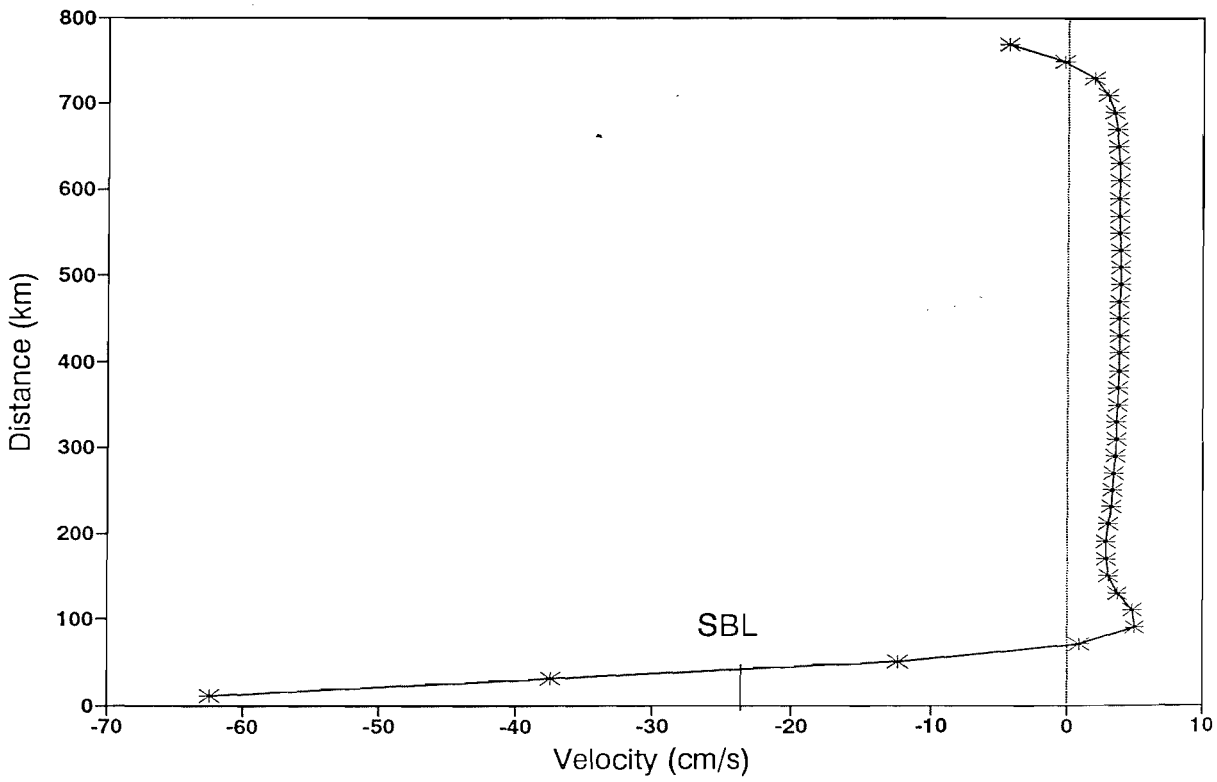

Fig. 4-5. (C) Meridional velocity profile along the western wall of the shelf (I=2 in Fig. 4-4). The distance is measured northwards from the southernmost point (I=2, J=101). Dotted arrow indicates the MPS as defined in the text. (D) Ratio between the on-shelf volume transport and the WBC transport along meridional sections as a function of the distance measured westwards from the shelf-edge (I=20 in Fig. 4-4).

(C) V1 along the western wall

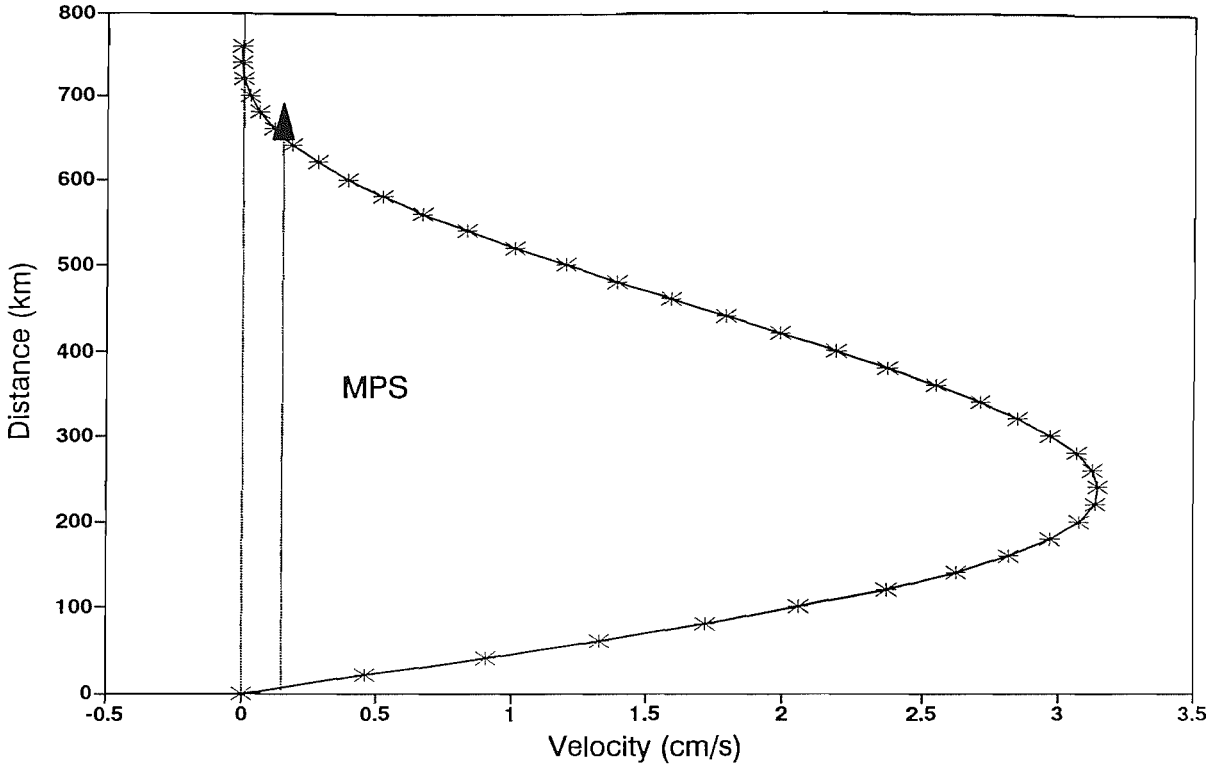

(D) On-shelf volume transport

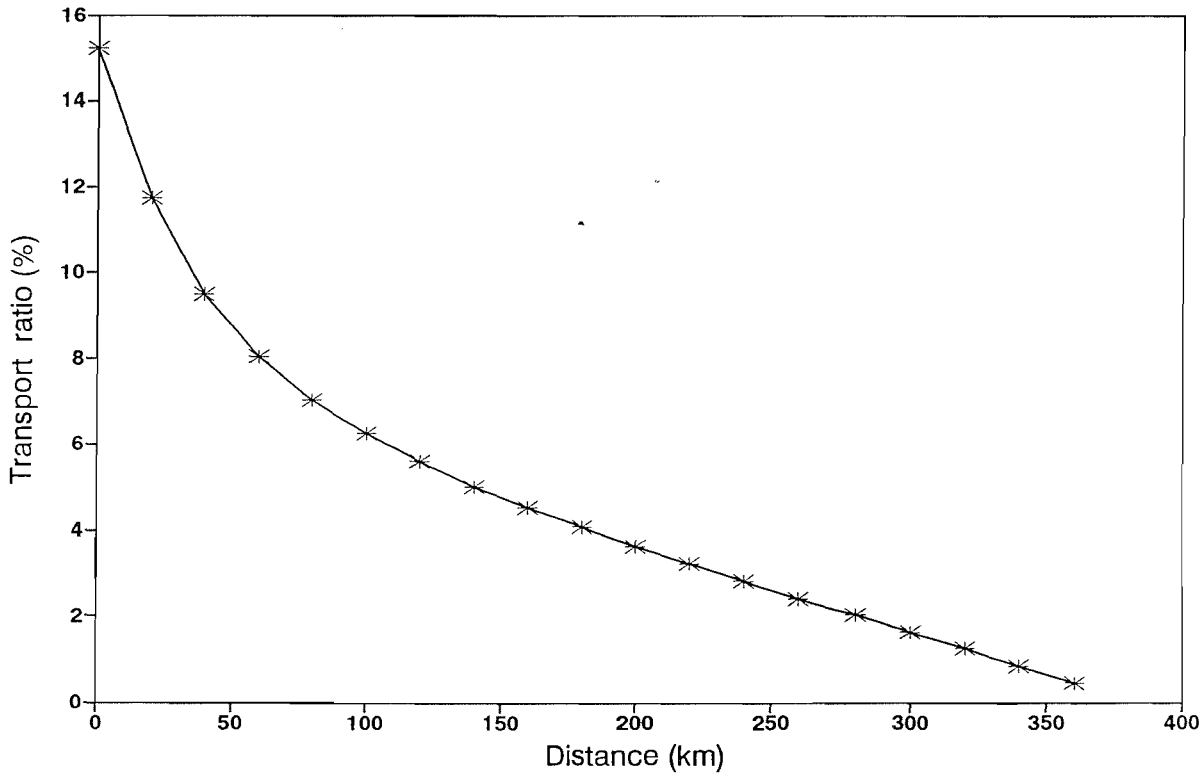

Fig. 4-6. Contours of streamlines at an equilibrium state of the standard SPEM experiment (A) in the whole domain, (B) in the shelf and adjacent deep ocean area, and (C) only in the shelf. Contour intervals in (B) are 0.4 Sv in the shelf and 2.0 Sv in the deep ocean.

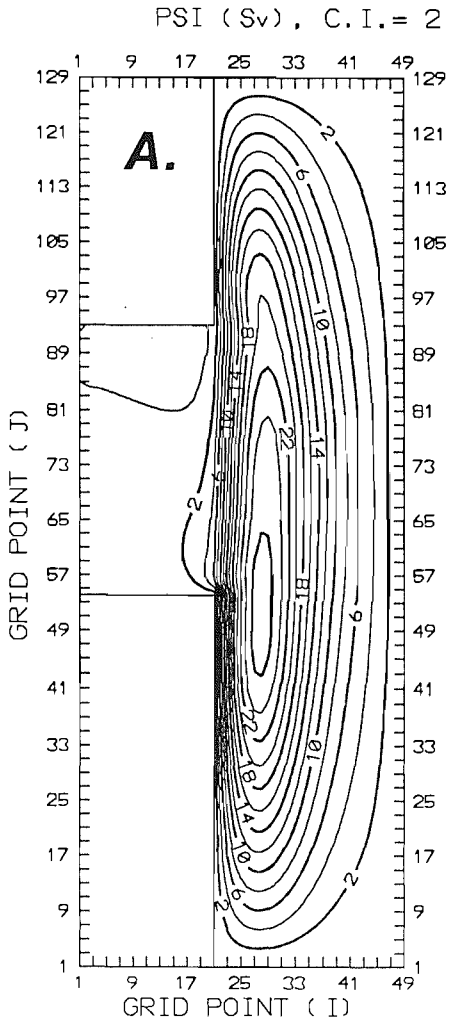
PSI (Sv), C.I.= 2
A.
GRID POINT (J)
GRID POINT (I)

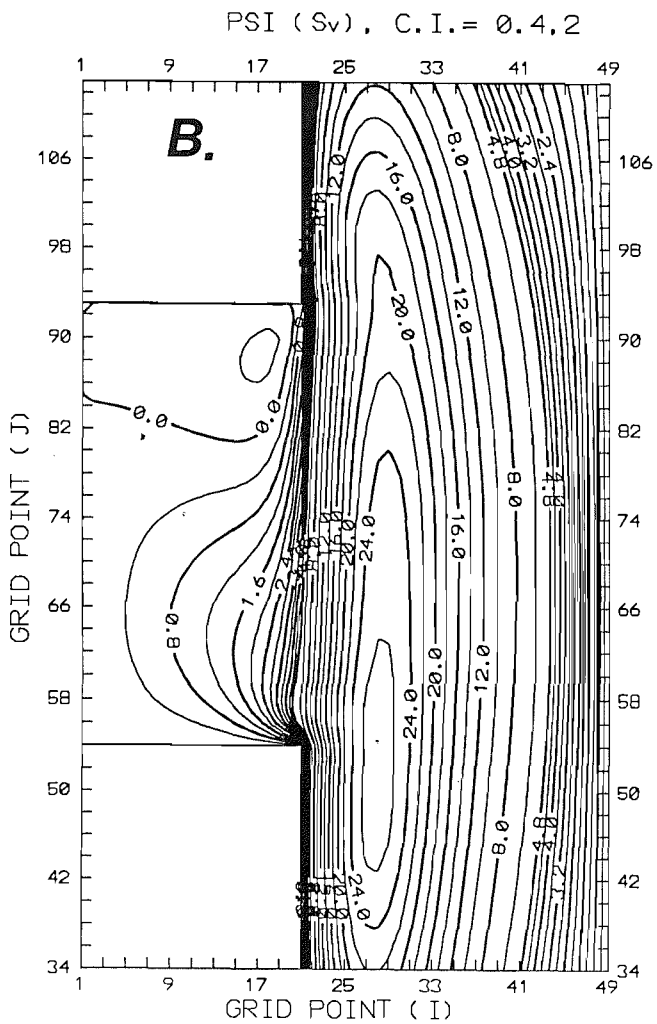
PSI (Sv), C.I.= 0.4,2
B.
GRID POINT (J)
GRID POINT (I)

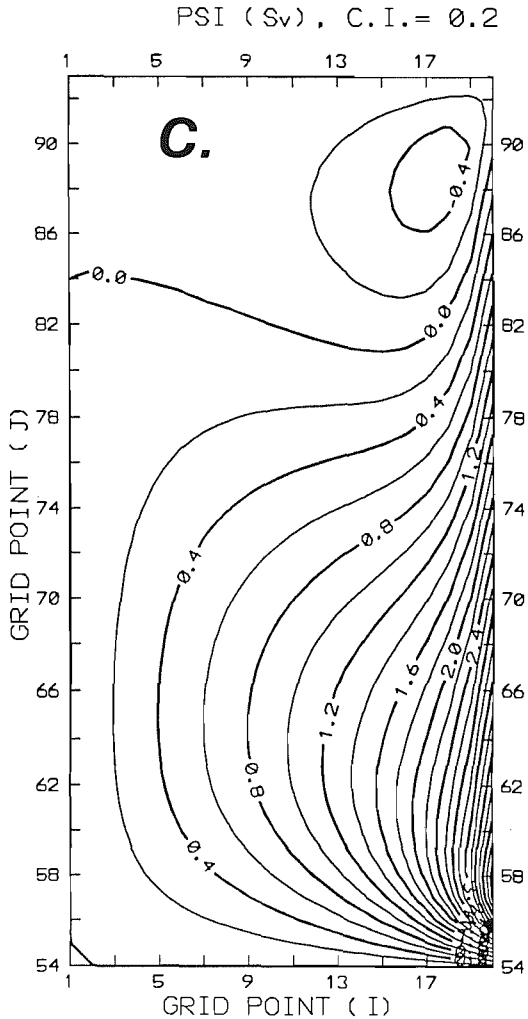
PSI (Sv), C.I.= 0.2
C.
GRID POINT (J)
GRID POINT (I)

Fig. 4-7. Comparisons of (A) zonal velocity profile along the southern wall of the shelf (J=101 in Fig. 4-4 for the SWEM, and J=54 in Fig. 4-6 for the SPEM), and (B) zonal velocity profile along the shelf-edge (I=20 in Fig. 4-4 for the SWEM, and I=19 in Fig. 4-6 for the SPEM) between the standard case of the SWEM and the SPEM.

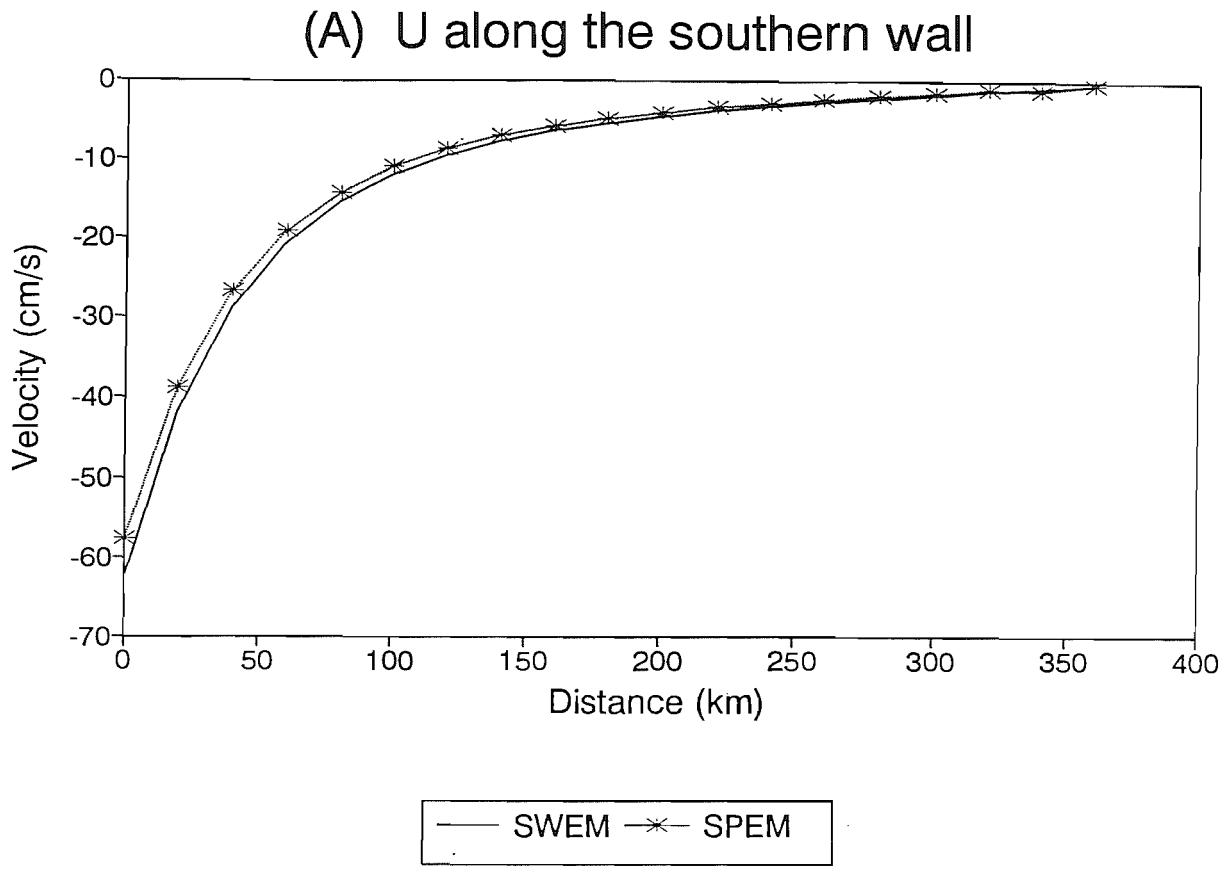
(A) U along the southern wall
Velocity (cm/s)
0
-10
-20
-30
-40
-50
-60
-70
0
50
100
150
200
250
300
350
400
Distance (km)
SWEM
SPEM

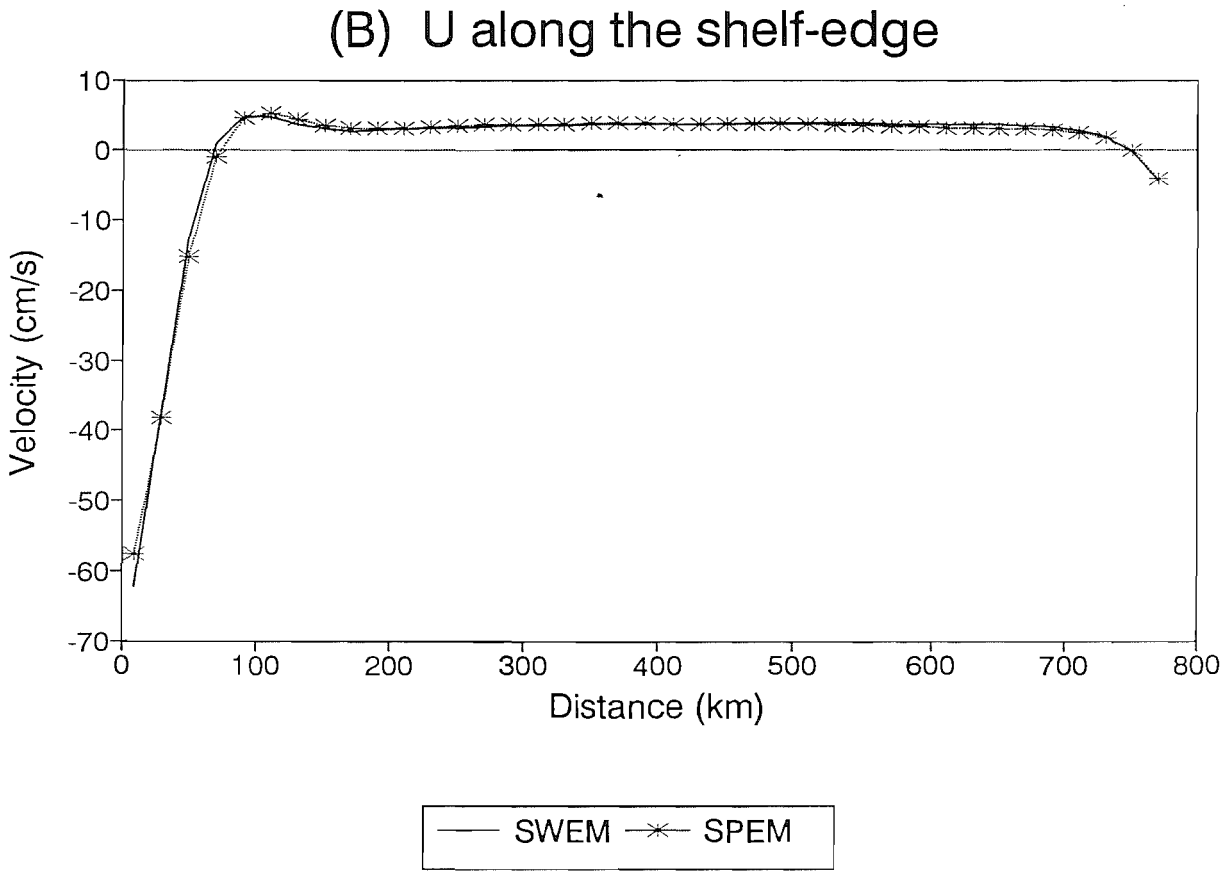
(B) U along the shelf-edge
Velocity (cm/s)
10
0
-10
-20
-30
-40
-50
-60
-70
0
100
200
300
400
500
600
700
800
Distance (km)
SWEM
SPEM

Fig. 4-7. Comparisons of (C) meridional velocity profile along the western wall of the shelf (I=2 in Fig. 4-4 for the SWEM, and I=2 in Fig. 4-6 for the SPEM), and (D) meridional distribution of on-shelf volume transport between the standard case of the SWEM and the SPEM. The distance is measured from the southern wall to the north in (C), and measured from the shelf-edge to the west in (D).

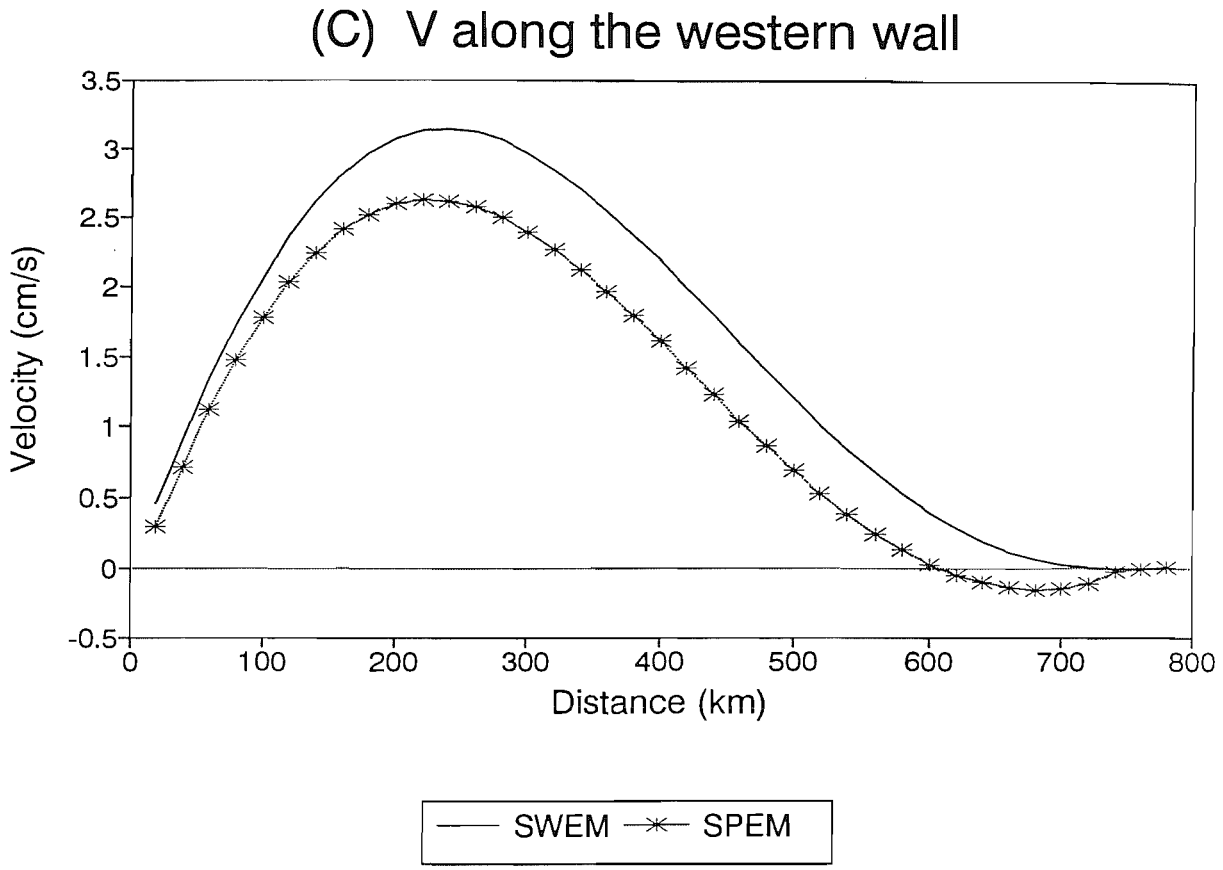
(C) V along the western wall
Velocity (cm/s)
3.5
3
2.5
2
1.5
1
0.5
0
-0.5
0
100
200
300
400
500
600
700
800
Distance (km)
SWEM
SPEM

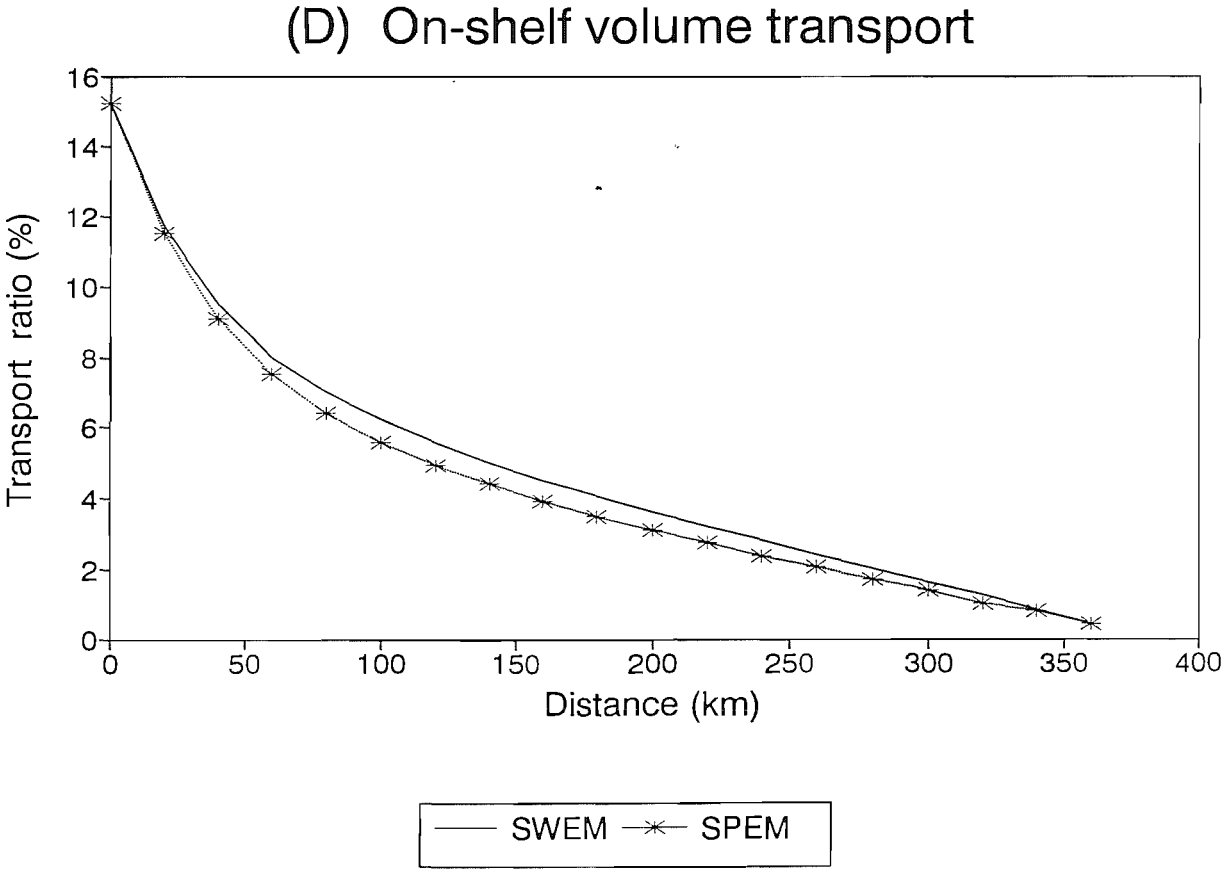
(D) On-shelf volume transport
Transport ratio (%)
16
14
12
10
8
6
4
2
0
0
50
100
150
200
250
300
350
400
Distance (km)
SWEM
SPEM

Fig. 4-8. Selected sections along which the local vorticity balance was examined, superimposed on the contours of free surface in the shelf and adjacent deep channel region at an equilibrium state for the standard SWEM experiment.

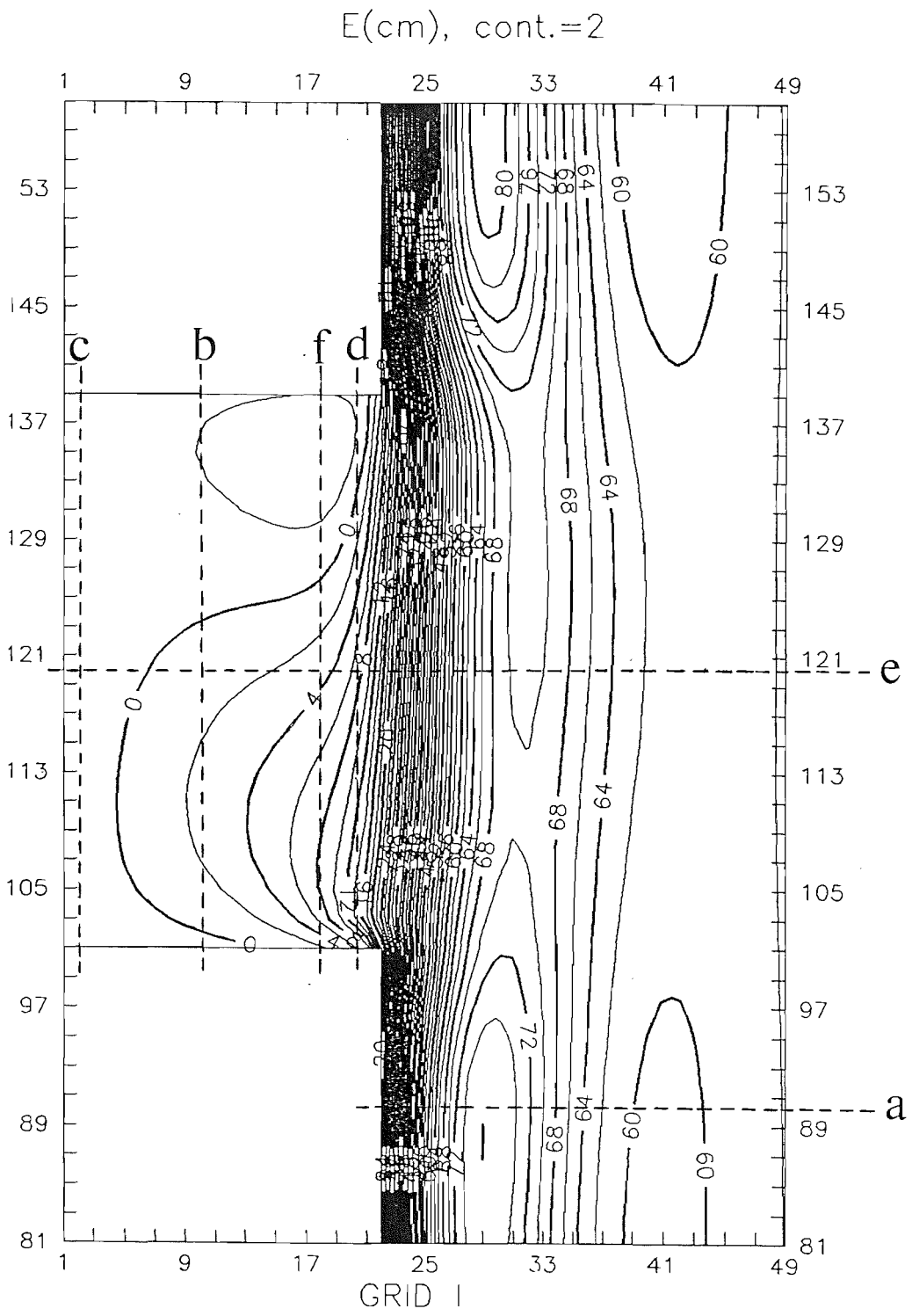
E(cm), cont.=2
1
9
17
25
33
41
49
53
145
137
129
121
113
105
97
89
81
153
c
b
f
d
e
a
0
60
64
68
72
GRID 1

Fig. 4-9. Zonal distribution of terms in the vorticity equation IV-2-7 at section a in Fig. 4-8. DIVE, BETA, BOTF, and LATF represent the topographic vorticity tendency, the planetary vorticity tendency, the dissipation of vorticity due to bottom friction, and the vorticity diffusion term respectively.

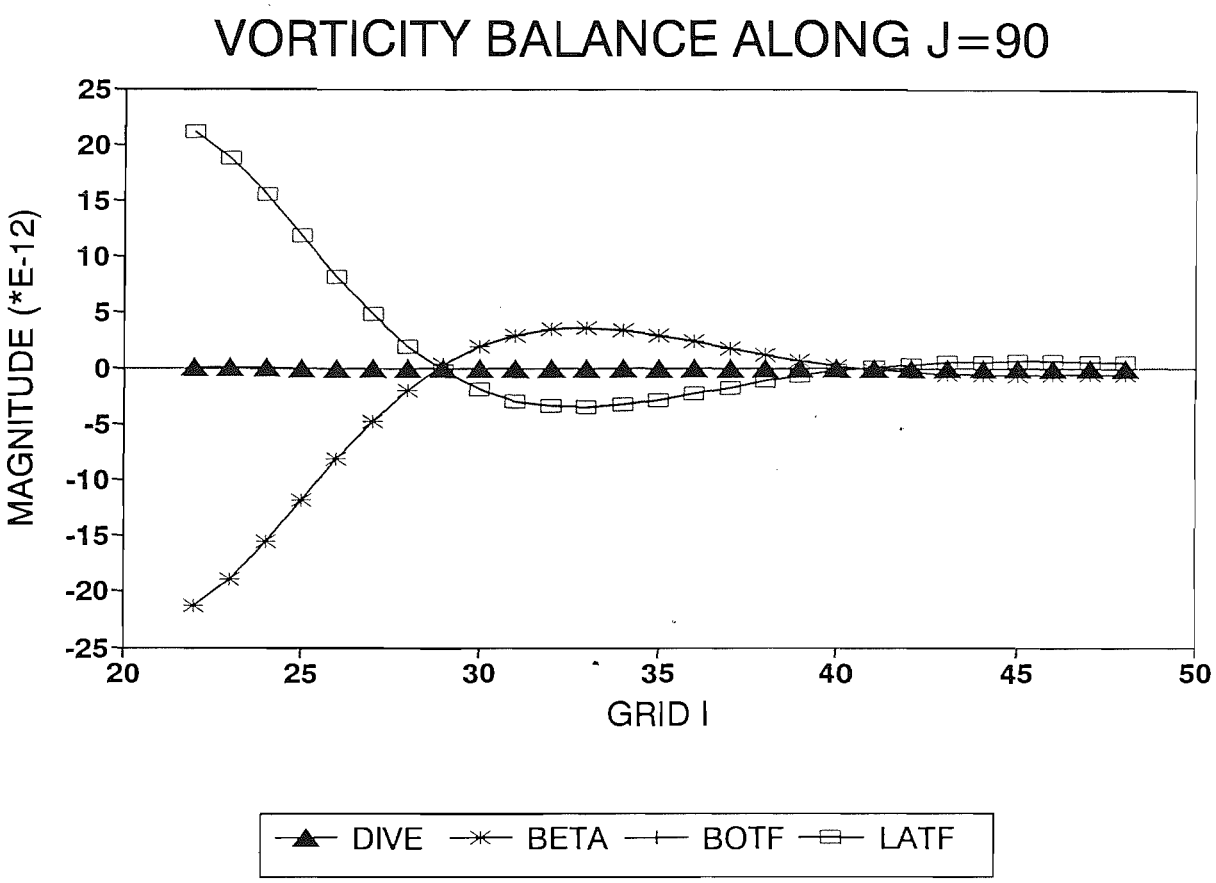
VORTICITY BALANCE ALONG J=90
MAGNITUDE (*E-12)
25
20
15
10
5
0
-5
-10
-15
-20
-25
20
25
30
35
40
45
50
GRID I
DIVE
BETA
BOTF
LATF

Fig. 4-10. Meridional distribution of terms in the vorticity equation IV-2-7 (A) at section c, and (B) at section b in Fig. 4-8. Legends are the same as in Fig. 4-9.

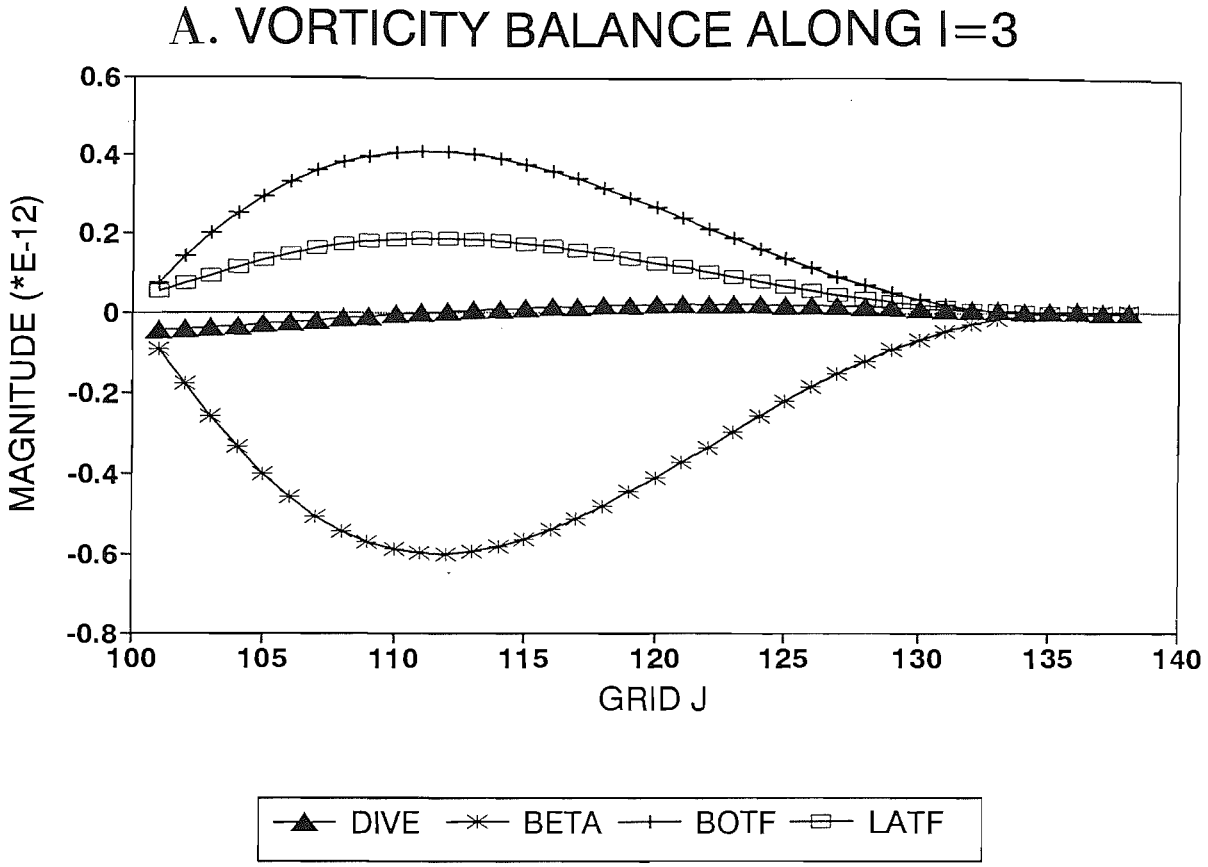
A. VORTICITY BALANCE ALONG I=3
MAGNITUDE (*E-12)
0.6
0.4
0.2
0
-0.2
-0.4
-0.6
-0.8
100
105
110
115
120
125
130
135
140
GRID J
DIVE
BETA
BOTF
LATF

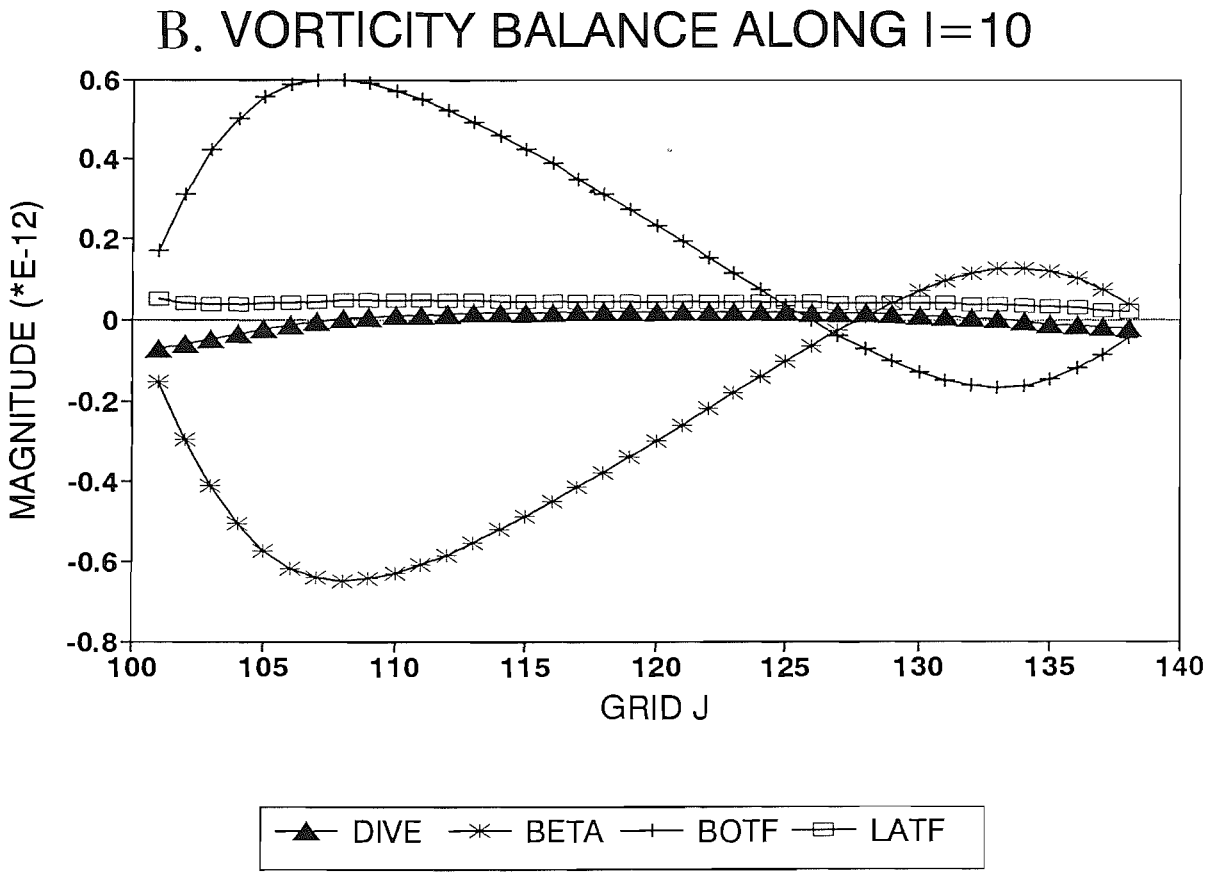
B. VORTICITY BALANCE ALONG I=10
MAGNITUDE (*E-12)
0.6
0.4
0.2
0
-0.2
-0.4
-0.6
-0.8
100
105
110
115
120
125
130
135
140
GRID J
DIVE
BETA
BOTF
LATF

Fig. 4-11. Meridional distribution of terms in the vorticity equation IV-2-7 (A) along the shelf-edge (at section d in Fig. 4-8), and (B) at the same section as (A) but only in the off-shelf flow region.

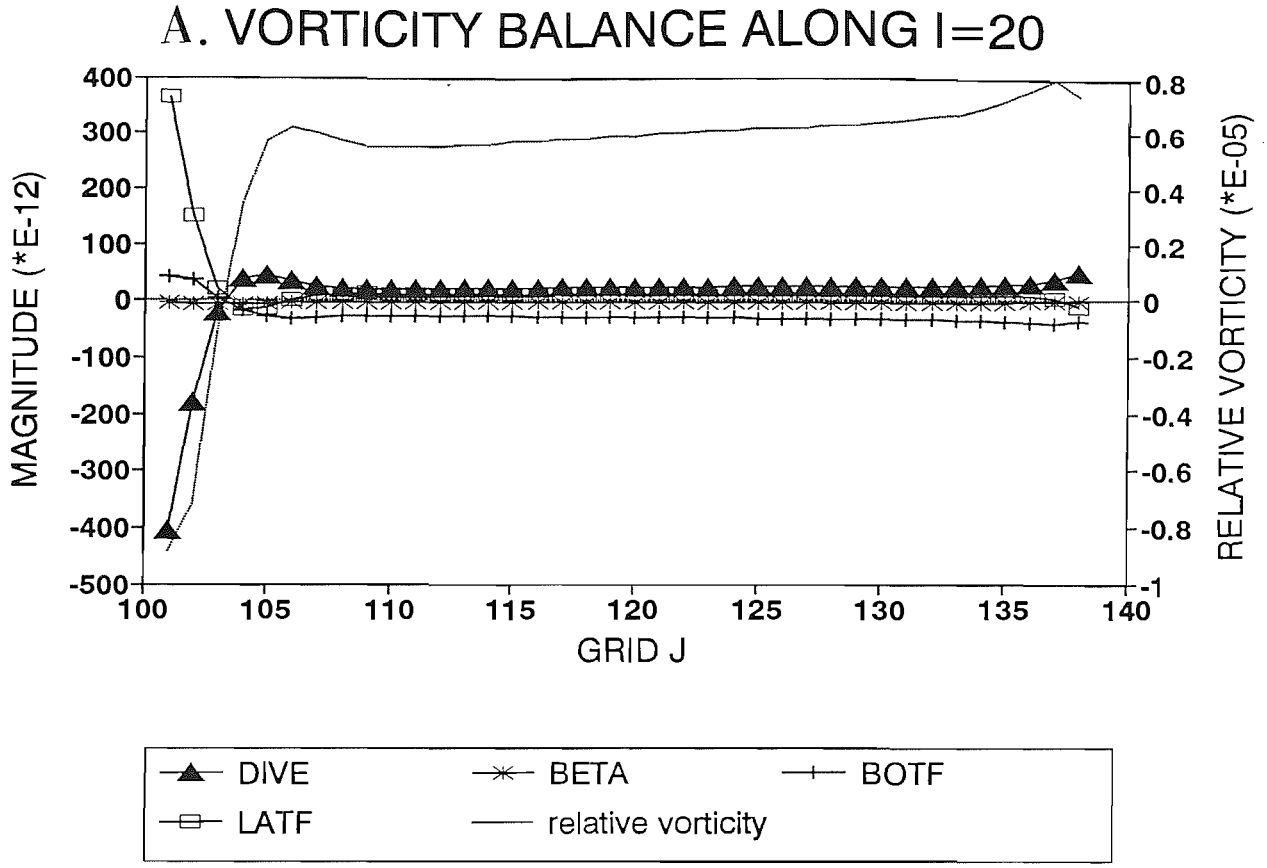
A. VORTICITY BALANCE ALONG I=20
MAGNITUDE (*E-12)
RELATIVE VORTICITY (*E-05)
GRID J
400
300
200
100
0
-100
-200
-300
-400
-500
0.8
0.6
0.4
0.2
0
-0.2
-0.4
-0.6
-0.8
-1
100
105
110
115
120
125
130
135
140
DIVE
BETA
BOTF
LATF
relative vorticity

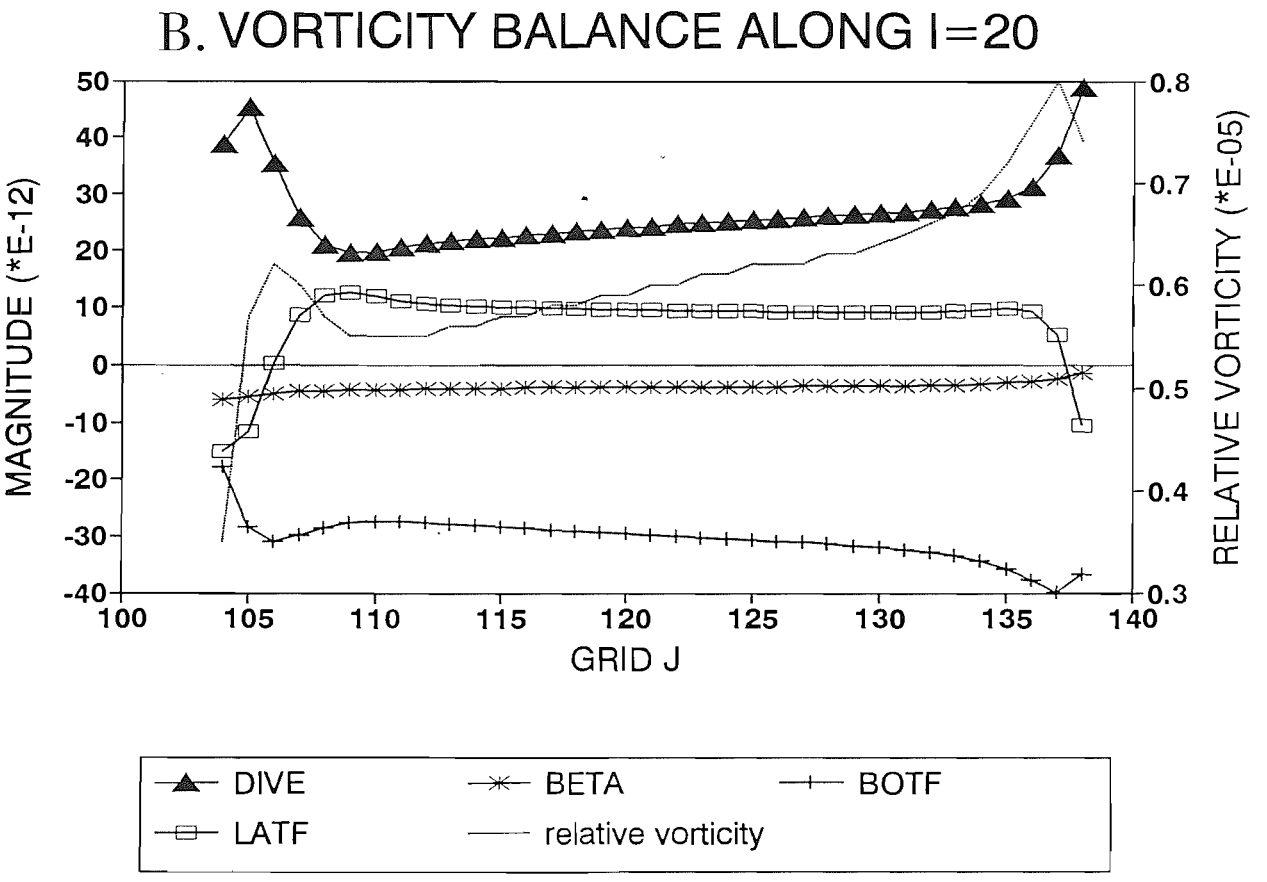
B. VORTICITY BALANCE ALONG I=20
MAGNITUDE (*E-12)
RELATIVE VORTICITY (*E-05)
GRID J
50
40
30
20
10
0
-10
-20
-30
-40
0.8
0.7
0.6
0.5
0.4
0.3
100
105
110
115
120
125
130
135
140
DIVE
BETA
BOTF
LATF
relative vorticity

Fig. 4-12. Meridional profile of the relative vorticity in the shelf boundary layer (SBL). The distance is measured from the southern wall of the shelf to north.

Fig. 4-13. Zonal profile of upper layer meridional velocity and relative vorticity at section e in Fig. 4-8.

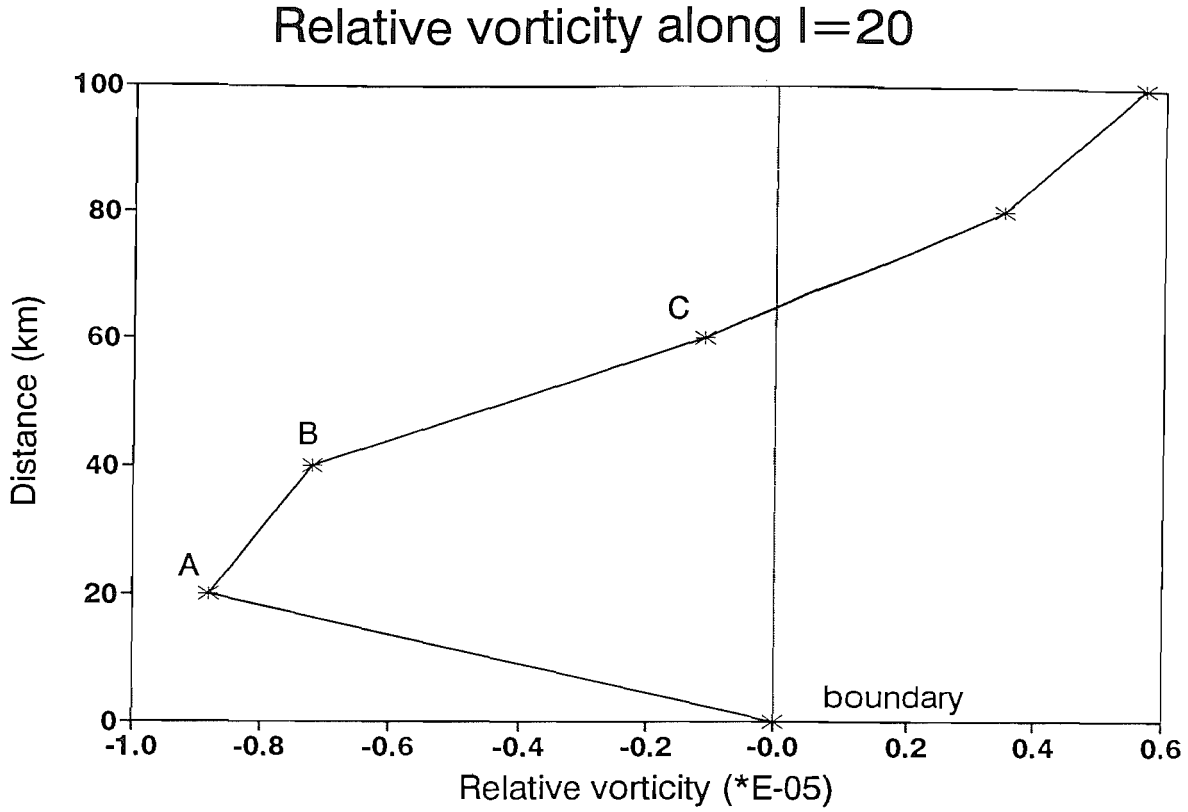
Relative vorticity along I=20
Distance (km)
100
80
60
40
20
0
A
B
C
boundary
-1.0
-0.8
-0.6
-0.4
-0.2
-0.0
0.2
0.4
0.6
Relative vorticity (*E-05)

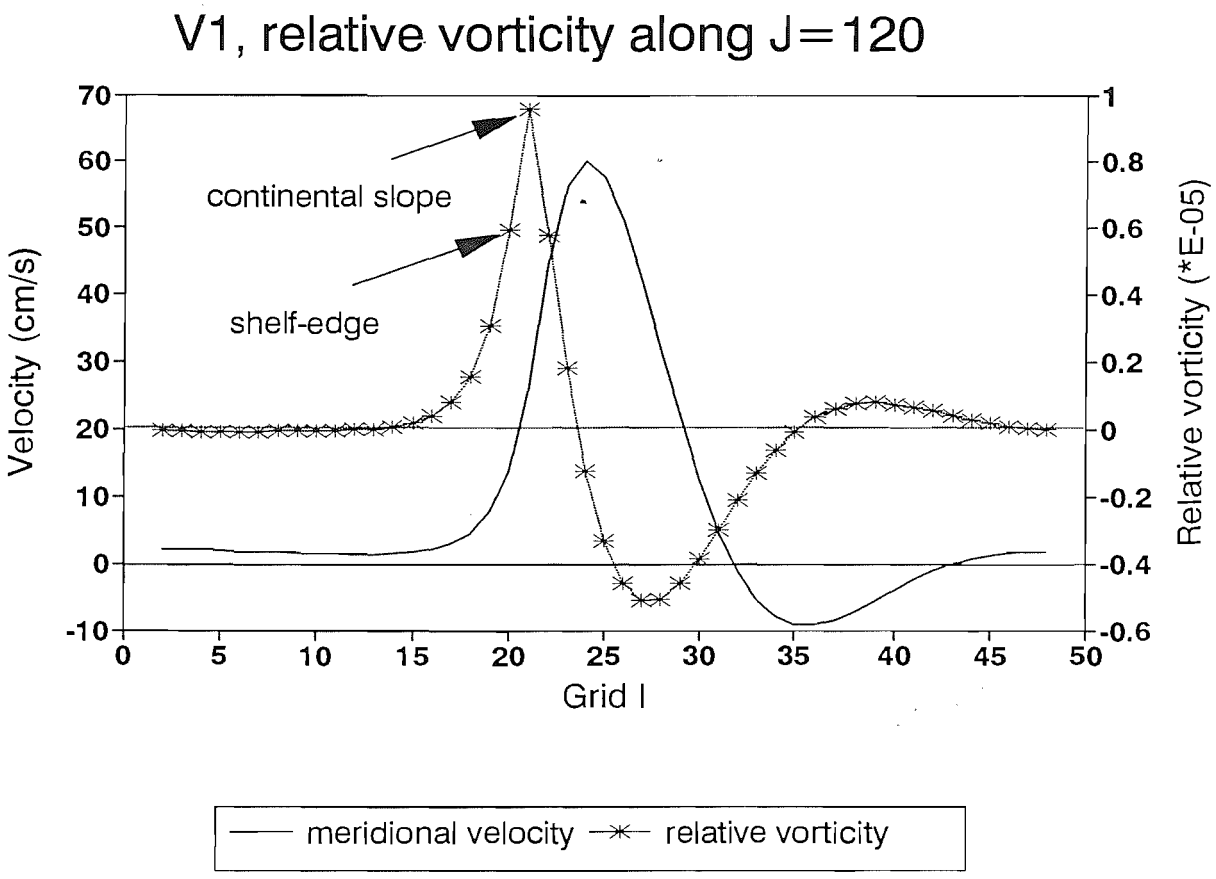
V1, relative vorticity along J=120
Velocity (cm/s)
70
60
50
40
30
20
10
0
-10
continental slope
shelf-edge
0
5
10
15
20
25
30
35
40
45
50
Grid I
1
0.8
0.6
0.4
0.2
0
-0.2
-0.4
-0.6
Relative vorticity (*E-05)
meridional velocity
relative vorticity

Fig. 4-14. Meridional distribution of terms in the vorticity equation IV-2-8 at section f in Fig. 4-8.

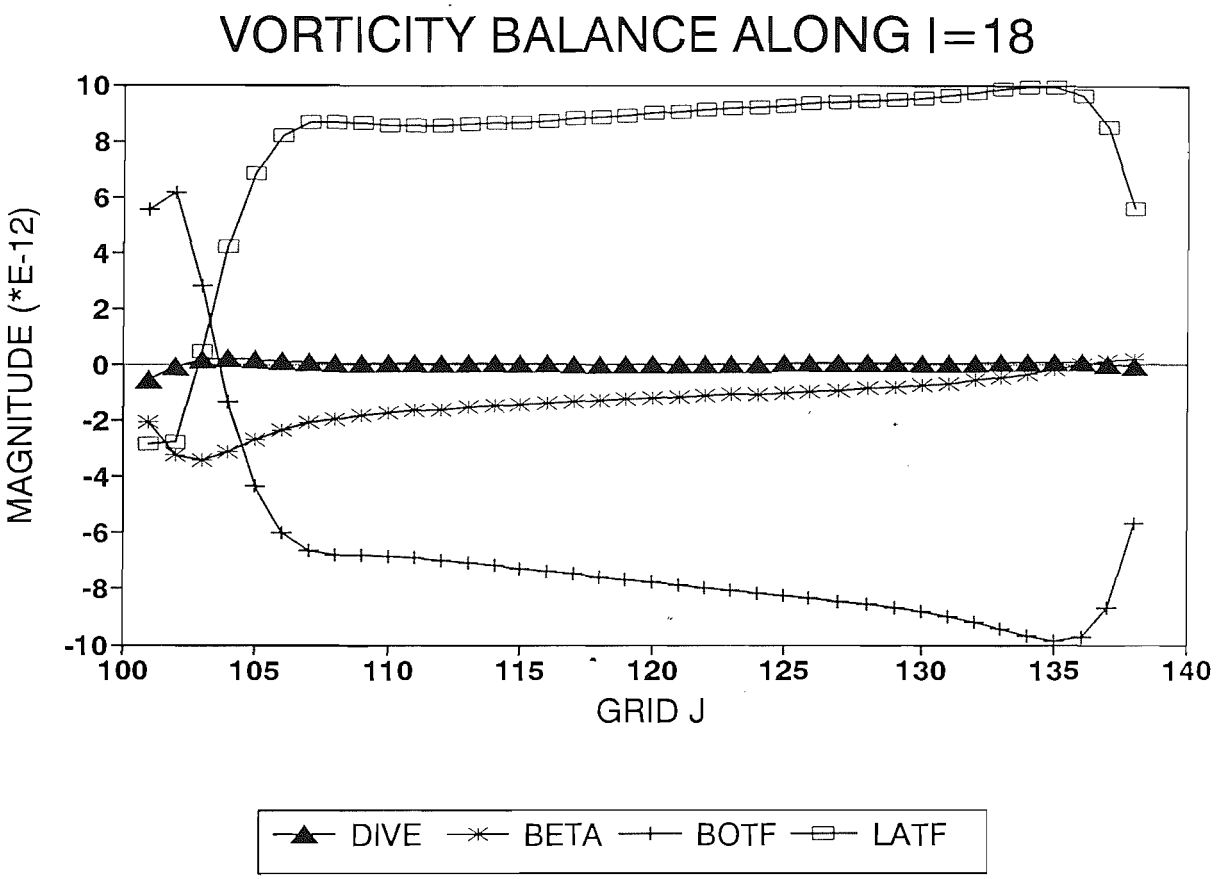
VORTICITY BALANCE ALONG I=18
MAGNITUDE (*E-12)
10
8
6
4
2
0
-2
-4
-6
-8
-10
100
105
110
115
120
125
130
135
140
GRID J
DIVE
BETA
BOTF
LATF

Fig. 4-15. Zonal distribution of terms in the vorticity equation IV-2-7 at section e in Fig. 4-8, (A) from grid point I=2 to I=17, and (B) from I=18 to I=25.

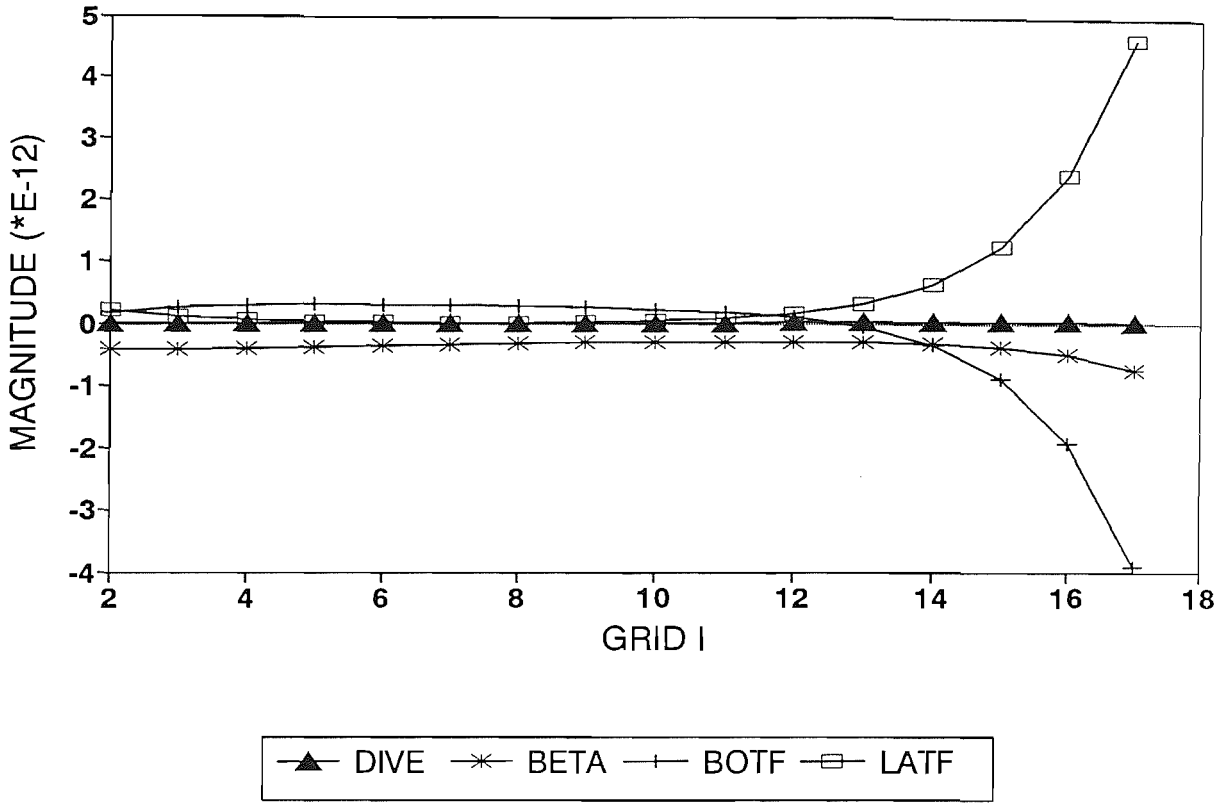
A.VORTICITY BALANCE ALONG J=120
MAGNITUDE (*E-12)
5
4
3
2
1
0
-1
-2
-3
-4
2
4
6
8
10
12
14
16
18
GRID I
DIVE
BETA
BOTF
LATF

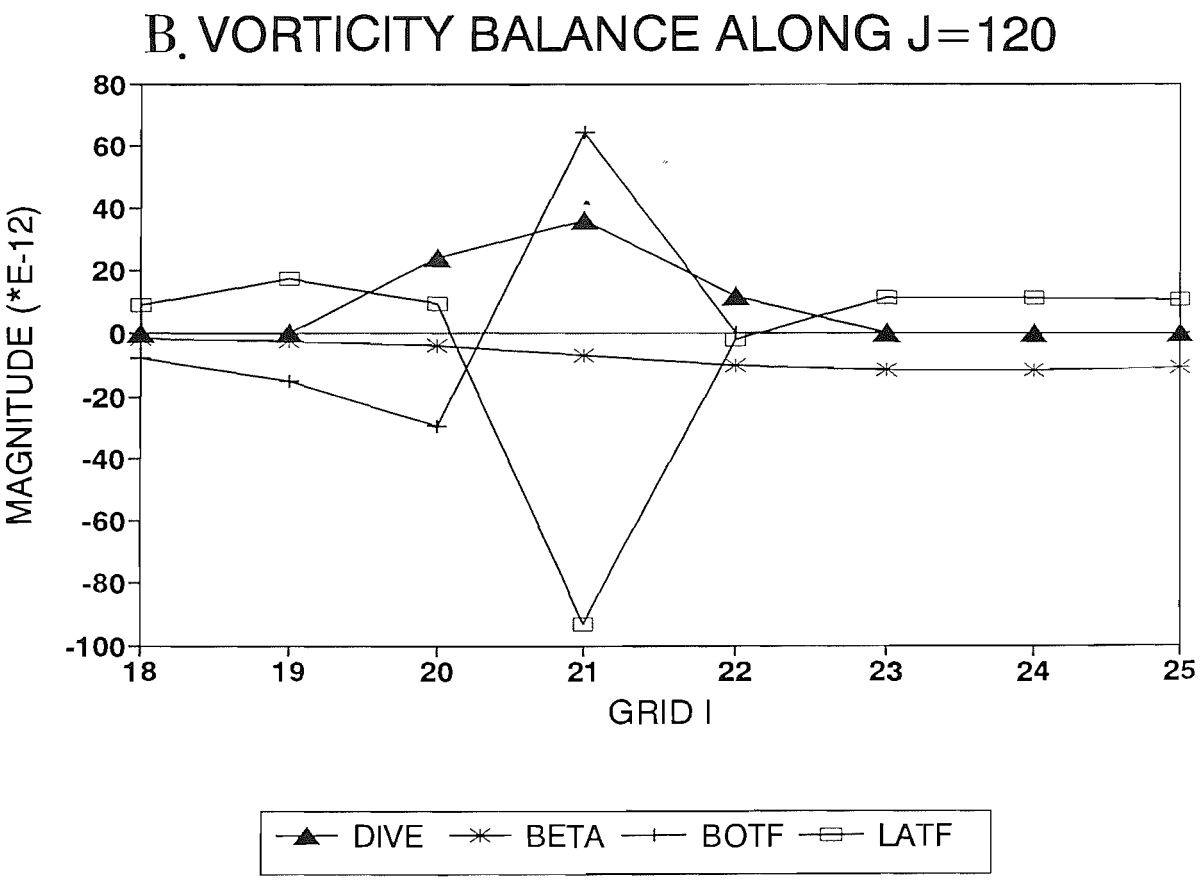
B. VORTICITY BALANCE ALONG J=120
MAGNITUDE (*E-12)
80
60
40
20
0
-20
-40
-60
-80
-100
18
19
20
21
22
23
24
25
GRID I
DIVE
BETA
BOTF
LATF

Fig. 4-16. Distribution of terms in the momentum equations (A) (IV-2-4), and (B) (IV-2-5) along a meridional section in the western boundary layer (I=2 in the upper panel of Fig. 4-2) before introducing the shelf.

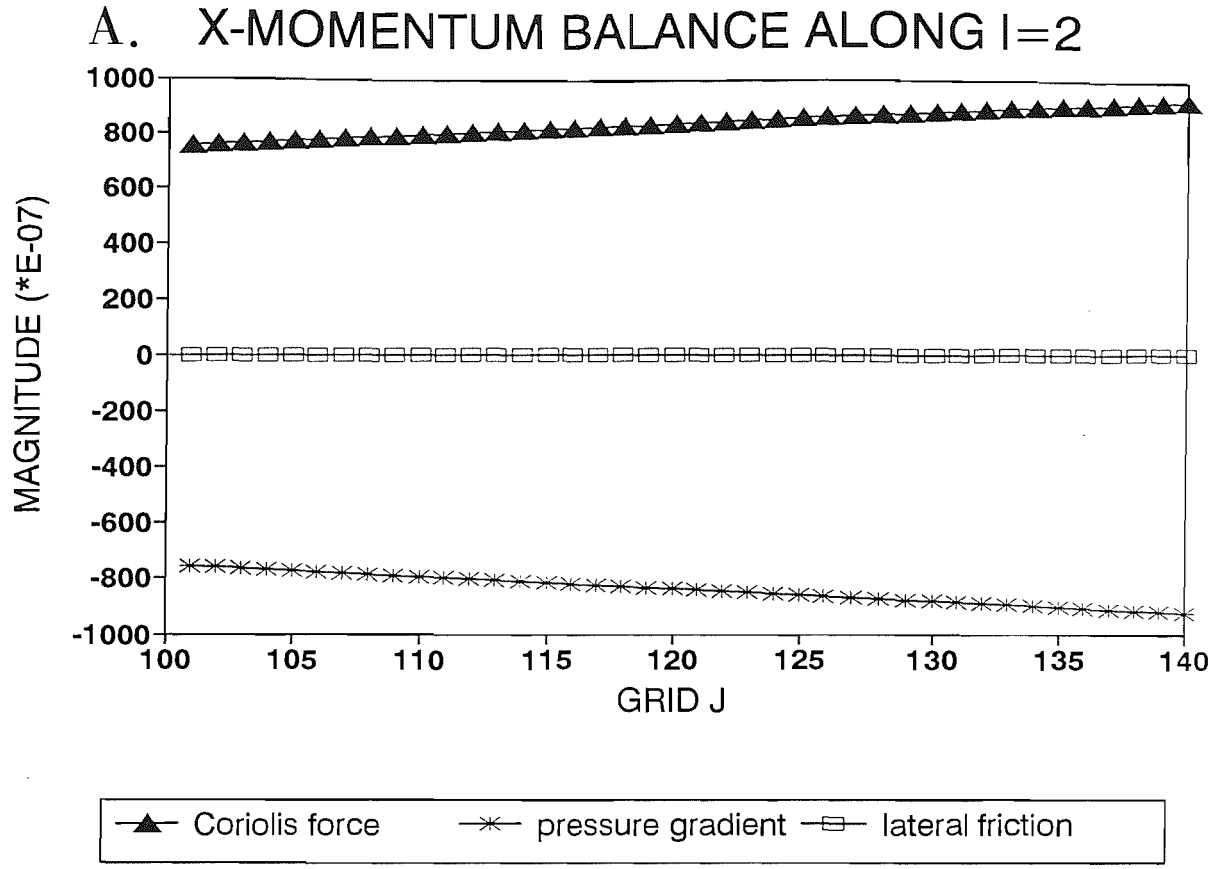
A. X-MOMENTUM BALANCE ALONG I=2
MAGNITUDE (*E-07)
1000
800
600
400
200
0
-200
-400
-600
-800
-1000
100
105
110
115
120
125
130
135
140
GRID J
Coriolis force
pressure gradient
lateral friction

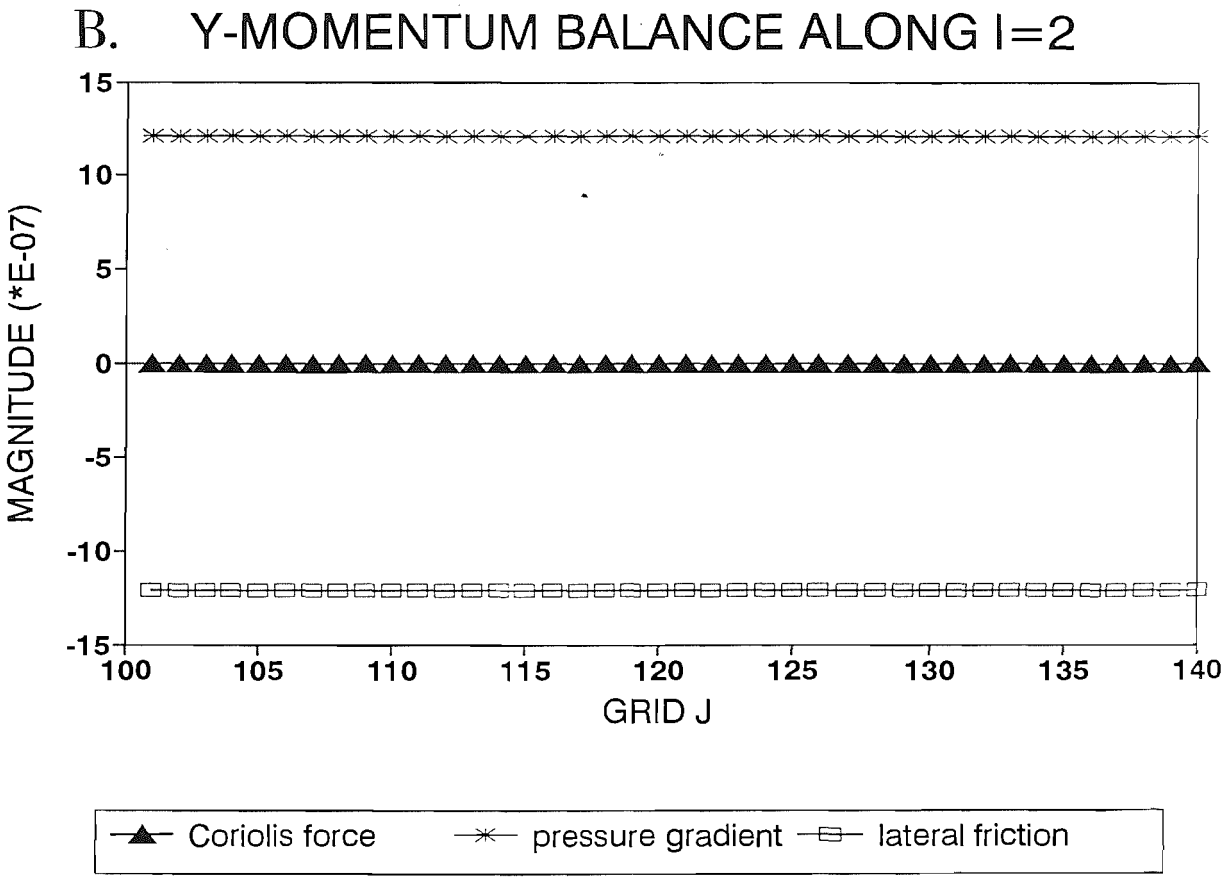
B. Y-MOMENTUM BALANCE ALONG I=2
MAGNITUDE (*E-07)
15
10
5
0
-5
-10
-15
100
105
110
115
120
125
130
135
140
GRID J
Coriolis force
pressure gradient
lateral friction

Fig. 4-17. Distribution of terms in the momentum equation (A) (IV-2-4), and (B) (IV-2-5) along the same section as in Fig. 4-16 (I=22 in Fig. 4-8) after introducing the shelf.

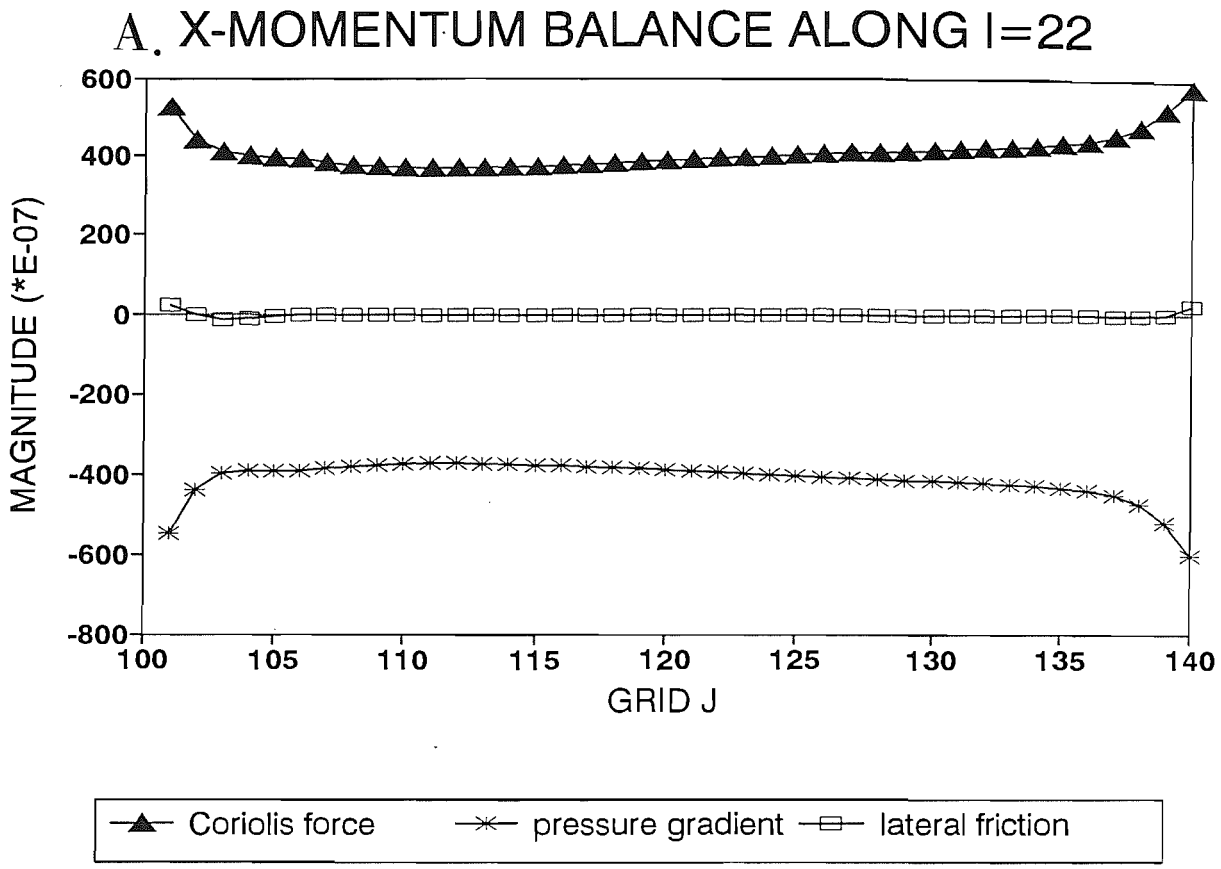
A. X-MOMENTUM BALANCE ALONG I=22
MAGNITUDE (*E-07)
600
400
200
0
-200
-400
-600
-800
100
105
110
115
120
125
130
135
140
GRID J
Coriolis force
pressure gradient
lateral friction

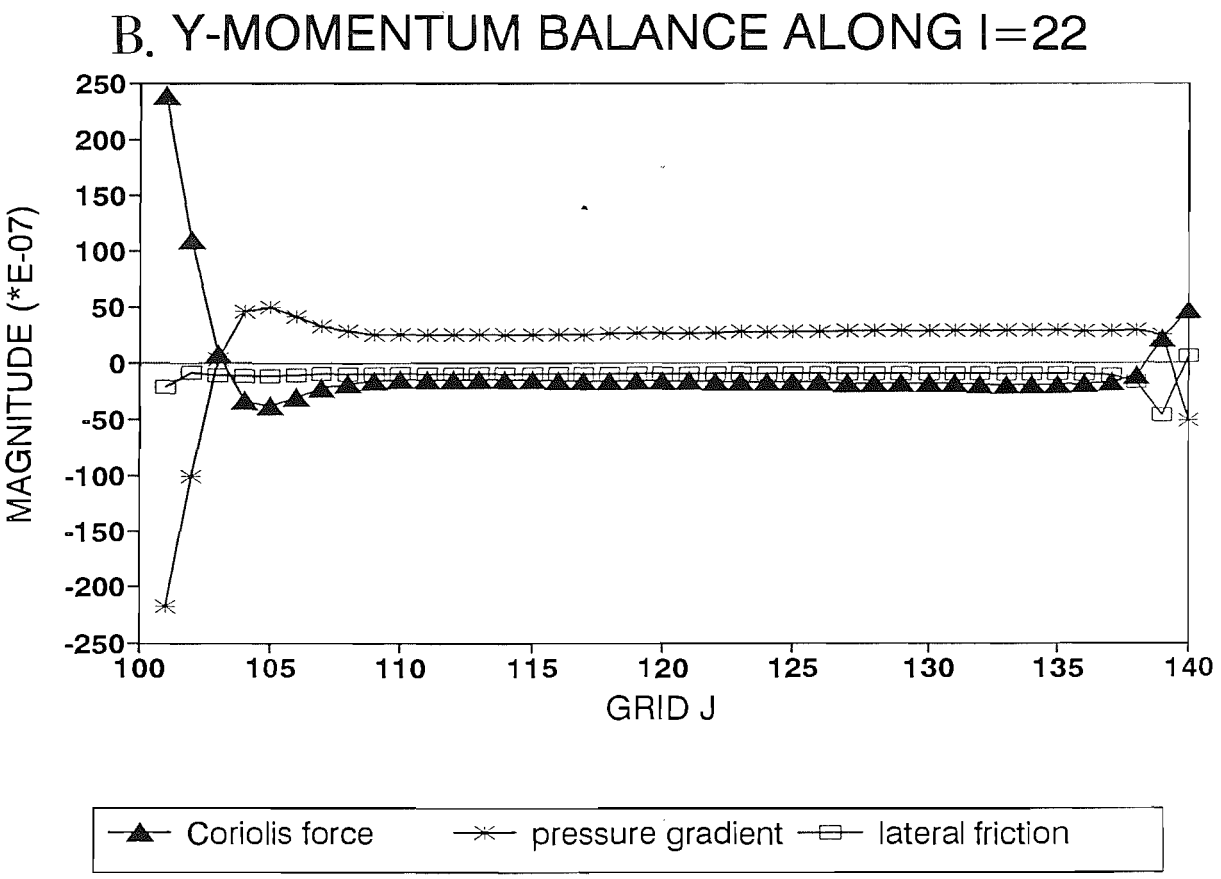
B. Y-MOMENTUM BALANCE ALONG I=22
MAGNITUDE (*E-07)
250
200
150
100
50
0
-50
-100
-150
-200
-250
100
105
110
115
120
125
130
135
140
GRID J
Coriolis force
pressure gradient
lateral friction

Fig. 4-18. Same as in Fig. 4-17 (B), but only shows the distribution of terms in the off-shelf flow region.

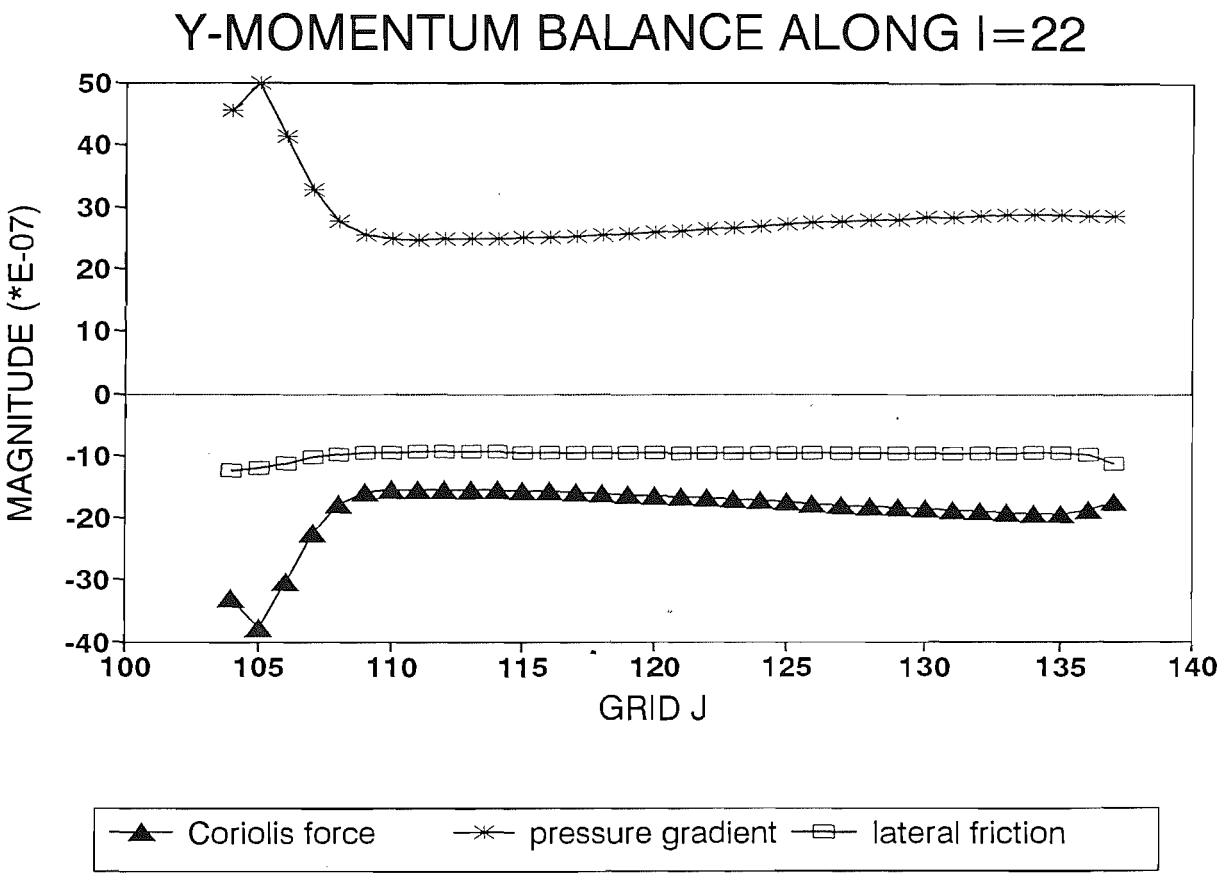
Y-MOMENTUM BALANCE ALONG I=22
MAGNITUDE (*E-07)
50
40
30
20
10
0
-10
-20
-30
-40
100
105
110
115
120
125
130
135
140
GRID J
Coriolis force
pressure gradient
lateral friction

Fig. 4-19. Meridional distribution of terms in the momentum equation (A) (IV-2-4) , and (B) (IV-2-5) at section b in Fig. 4-8.

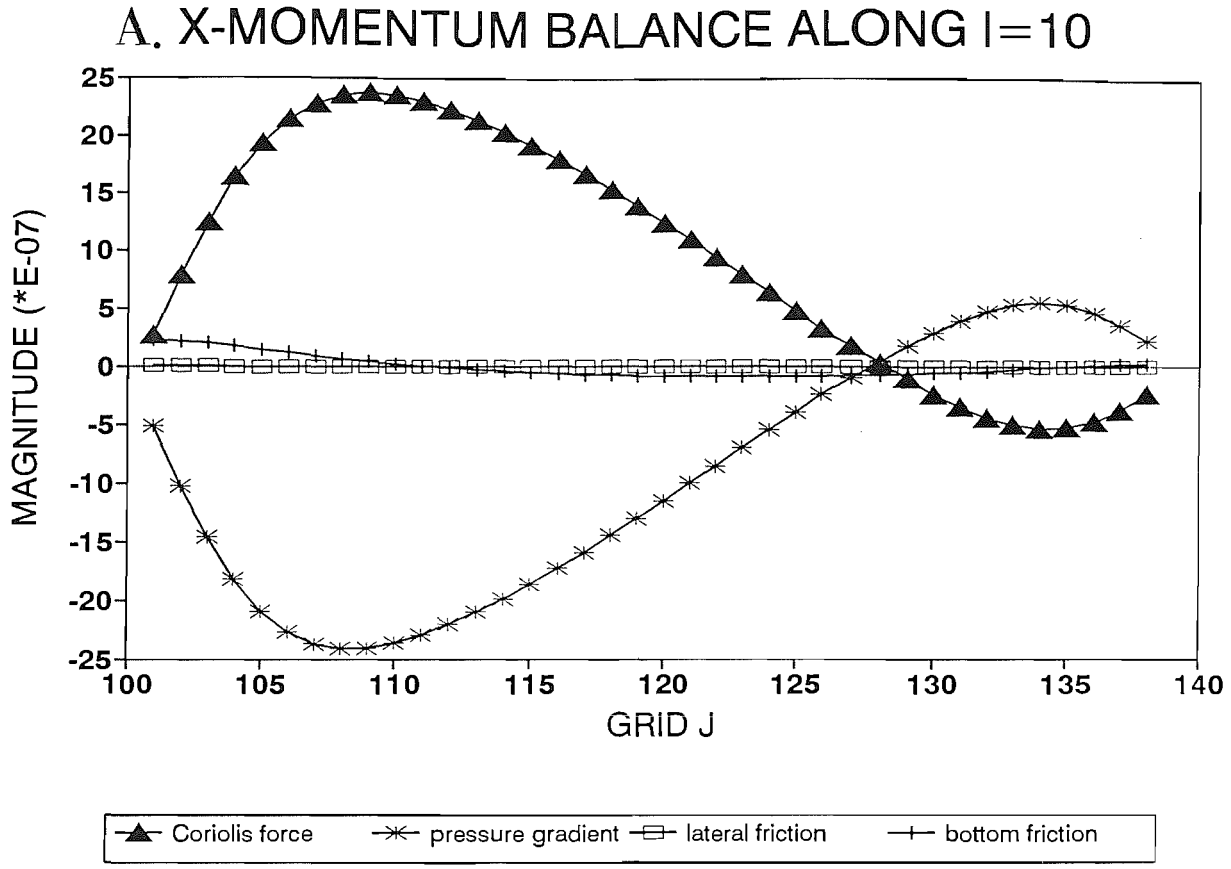
A. X-MOMENTUM BALANCE ALONG I=10
MAGNITUDE (*E-07)
25
20
15
10
5
0
-5
-10
-15
-20
-25
100
105
110
115
120
125
130
135
140
GRID J
Coriolis force
pressure gradient
lateral friction
bottom friction

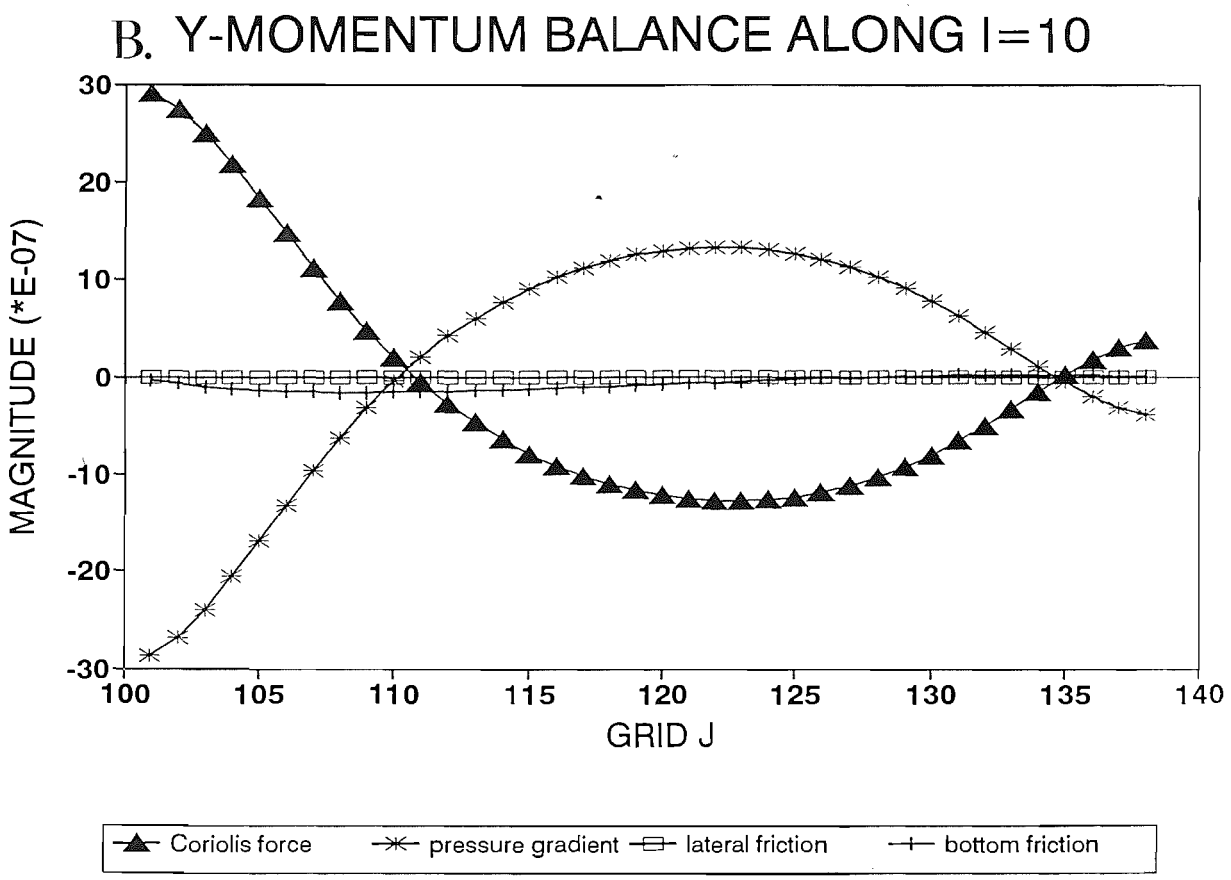
B. Y-MOMENTUM BALANCE ALONG I=10
MAGNITUDE (*E-07)
30
20
10
0
-10
-20
-30
100
105
110
115
120
125
130
135
140
GRID J
Coriolis force
pressure gradient
lateral friction
bottom friction

Fig. 4-20. Contours of free surface at an equilibrium state for the four experiments (A) $r = 0.0$, (B) $r = 10^{-4}$, (C) $r = 5 \times 10^{-4}$, and (D) $r = 10^{-3}$ (standard case), where r is the coefficient of bottom friction. All other parameters are the same as those in Table 4-1.

A. BET2R0, E(cm), C.I=2

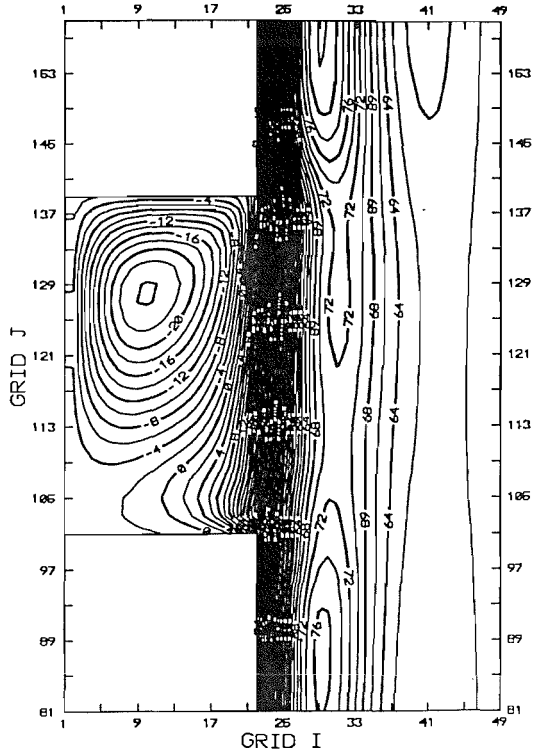

B. BET2R2, E (cm), C.I.= 2

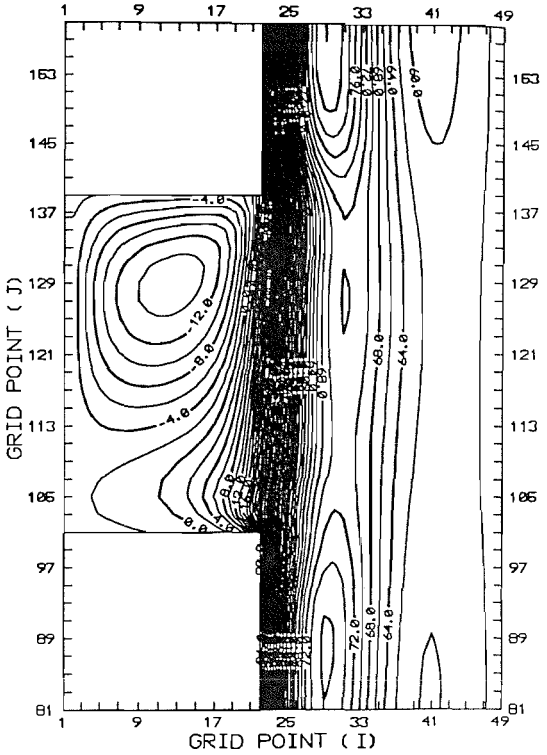

C. BET2R1, E (cm), C.I.= 2

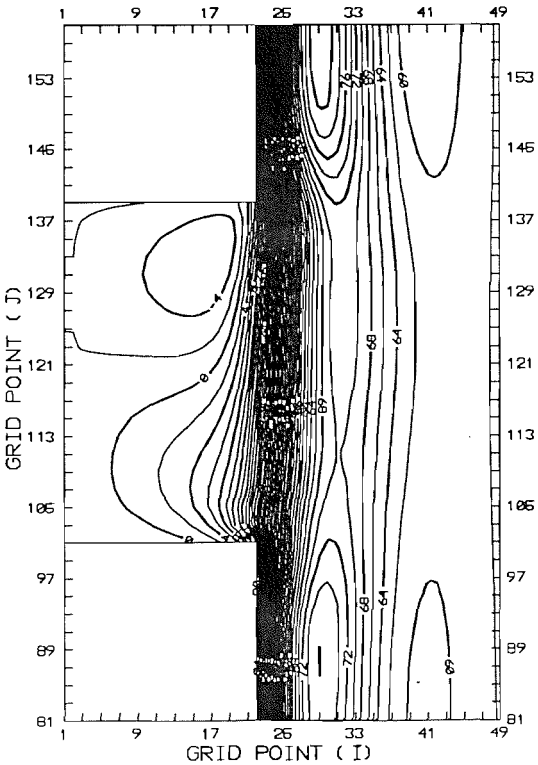

D. B2F200, E(cm), cont.=2

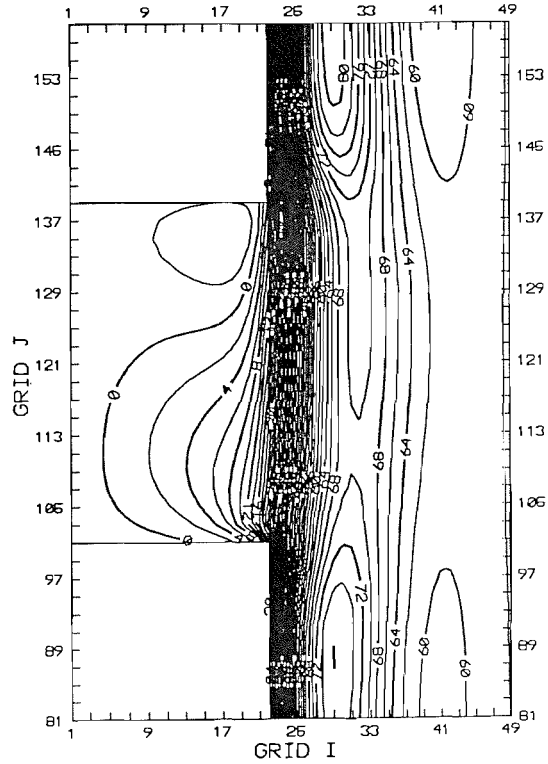

Fig. 4-21. Comparisons of (A) meridional velocity profile along the western wall of the shelf (I=2 in Fig. 4-20), (B) zonal velocity profile along the shelf-edge (I=20 in Fig. 4-20) for the four experiments with different coefficient of bottom friction. The distance is measured northward from the southernmost point in (A), and measured from the southern wall to the north in (B).

A. V1 along the western wall

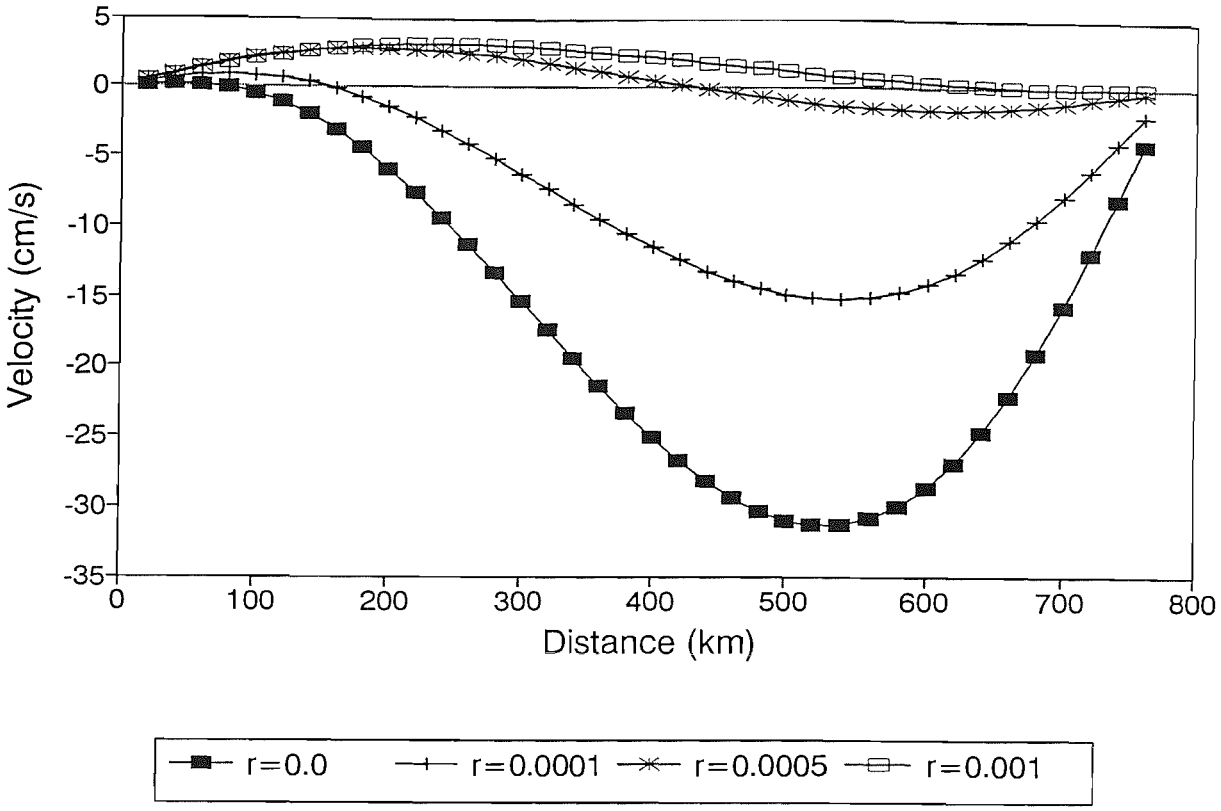

B. U1 along the shelf-edge

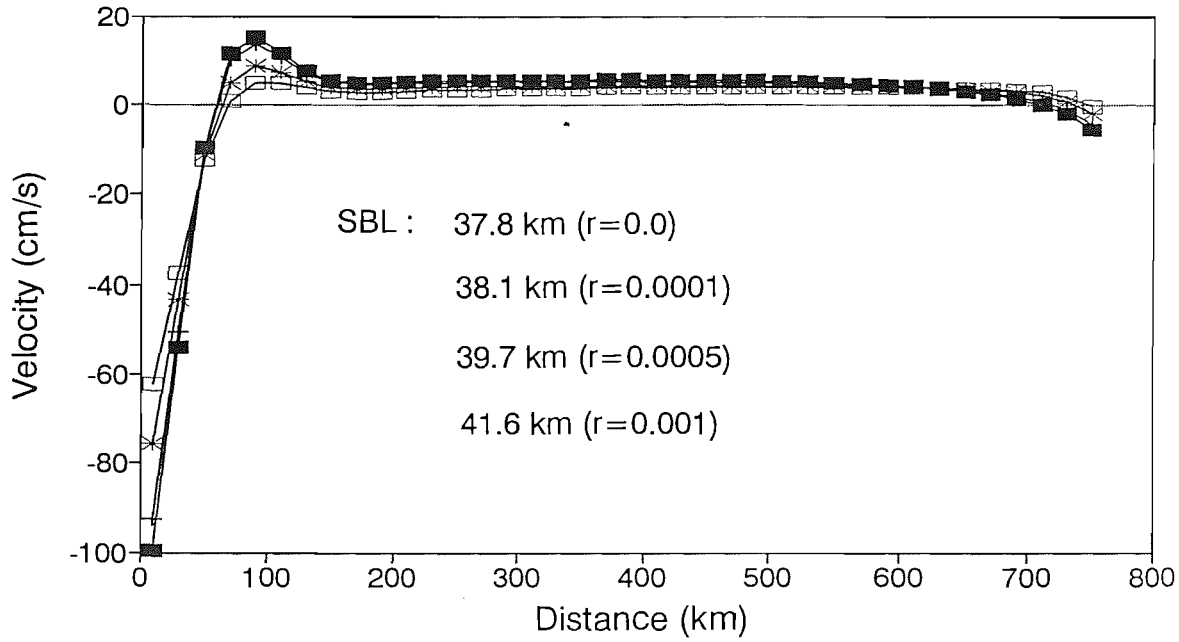

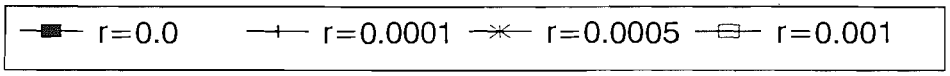

Fig. 4-21. Comparisons of (C) zonal velocity profile along the southern wall of the shelf (J=101 in Fig. 4-20), and (D) longitudinal distribution of the volume transport ratio between the WBC and the on-shelf flow with different coefficient of bottom friction. The distance is measured from the shelf-edge to the west.

C. U1 along the southern wall

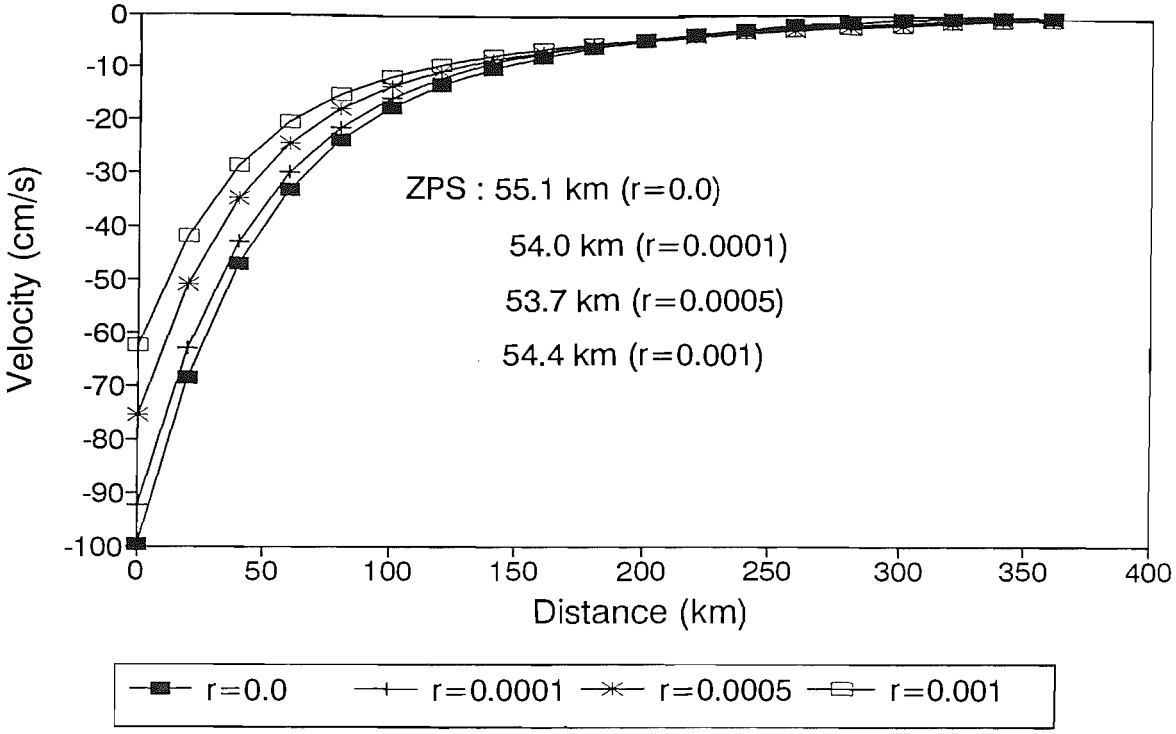

D. On-shelf volume transport

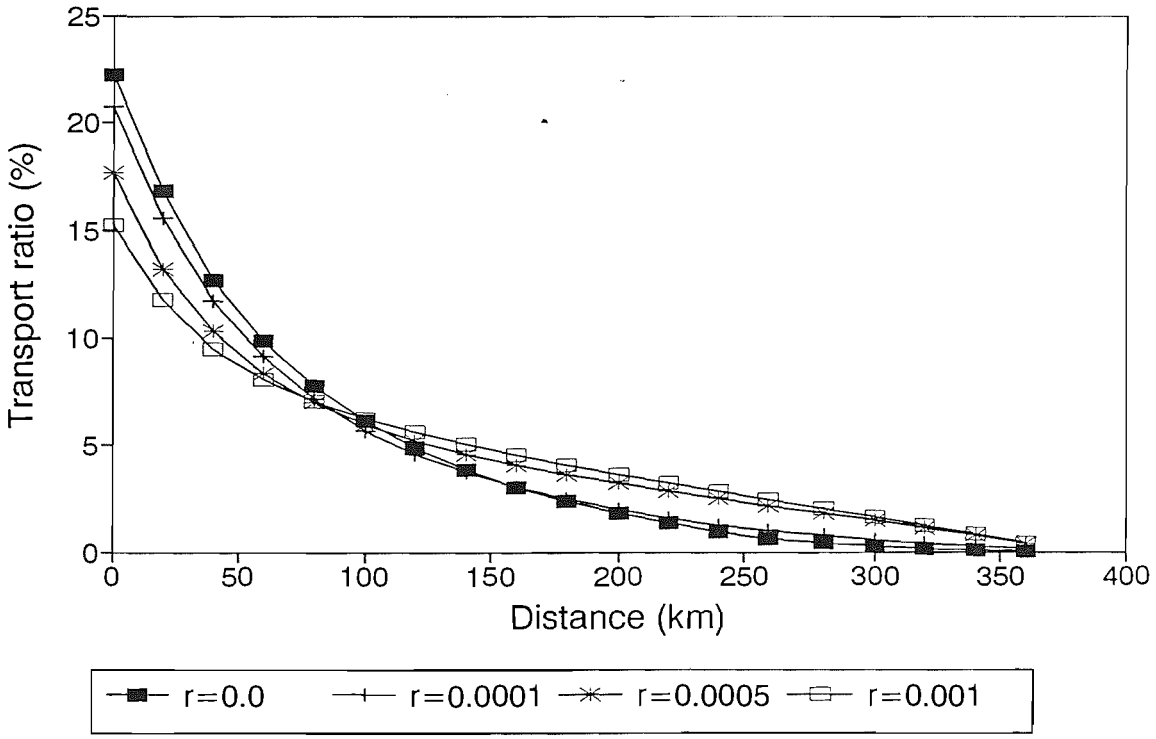

Fig. 4-22. A comparison of terms in the vorticity equation IV-2-7 at section f in Fig. 4-8 (A) for the standard case with the coefficient of bottom friction $r = 10^{-3}$, and (B) for the lateral friction model without bottom friction.

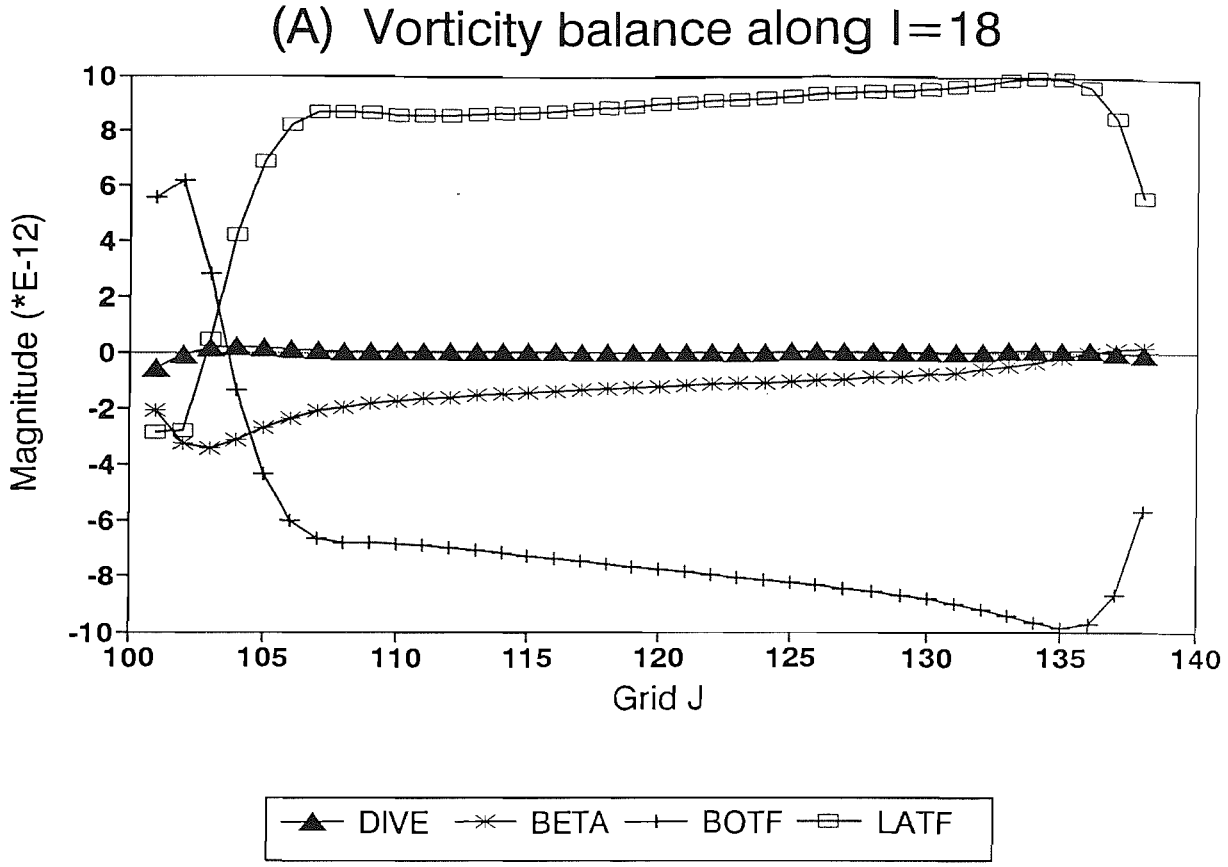
(A) Vorticity balance along I=18
Magnitude (*E-12)
10
8
6
4
2
0
-2
-4
-6
-8
-10
100
105
110
115
120
125
130
135
140
Grid J
DIVE
BETA
BOTF
LATF

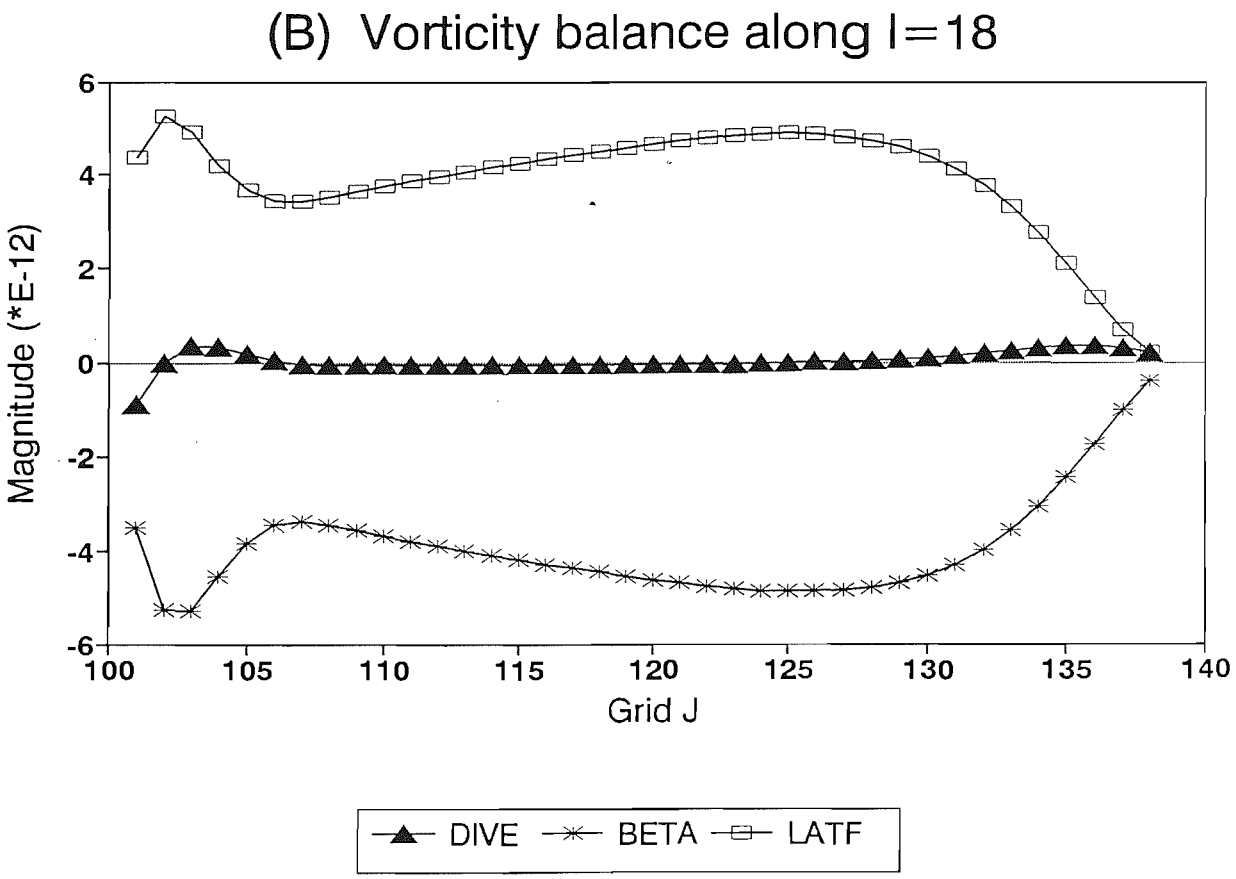
(B) Vorticity balance along I=18
Magnitude (*E-12)
6
4
2
0
-2
-4
-6
100
105
110
115
120
125
130
135
140
Grid J
DIVE
BETA
LATF

Fig. 4-23. Comparisons of (A) meridional velocity components, and (B) relative vorticities at section e in Fig. 4-8 between the standard case with the coefficient of bottom friction $r = 10^{-3}$, and the lateral friction model without bottom friction.

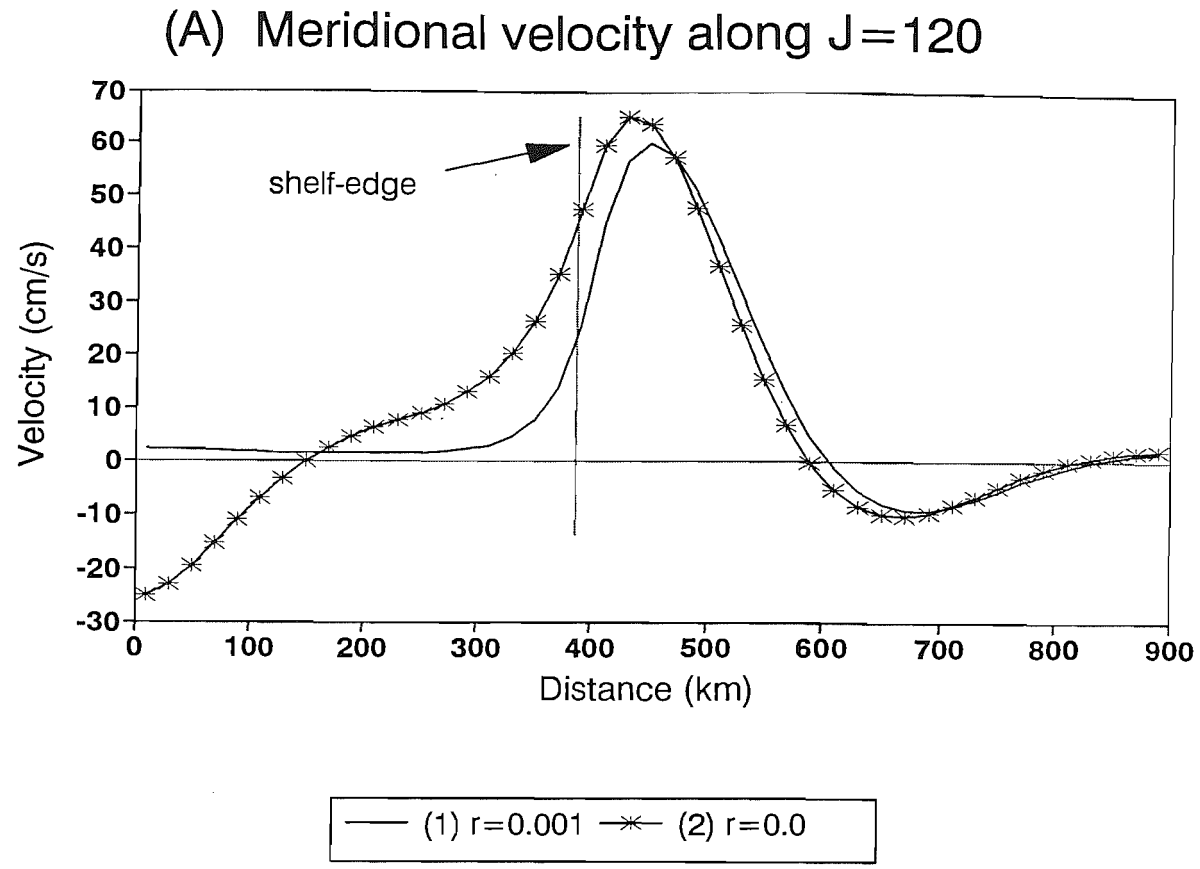
(A) Meridional velocity along J=120
shelf-edge
Velocity (cm/s)
70
60
50
40
30
20
10
0
-10
-20
-30
0
100
200
300
400
500
600
700
800
900
Distance (km)
(1) r=0.001
(2) r=0.0

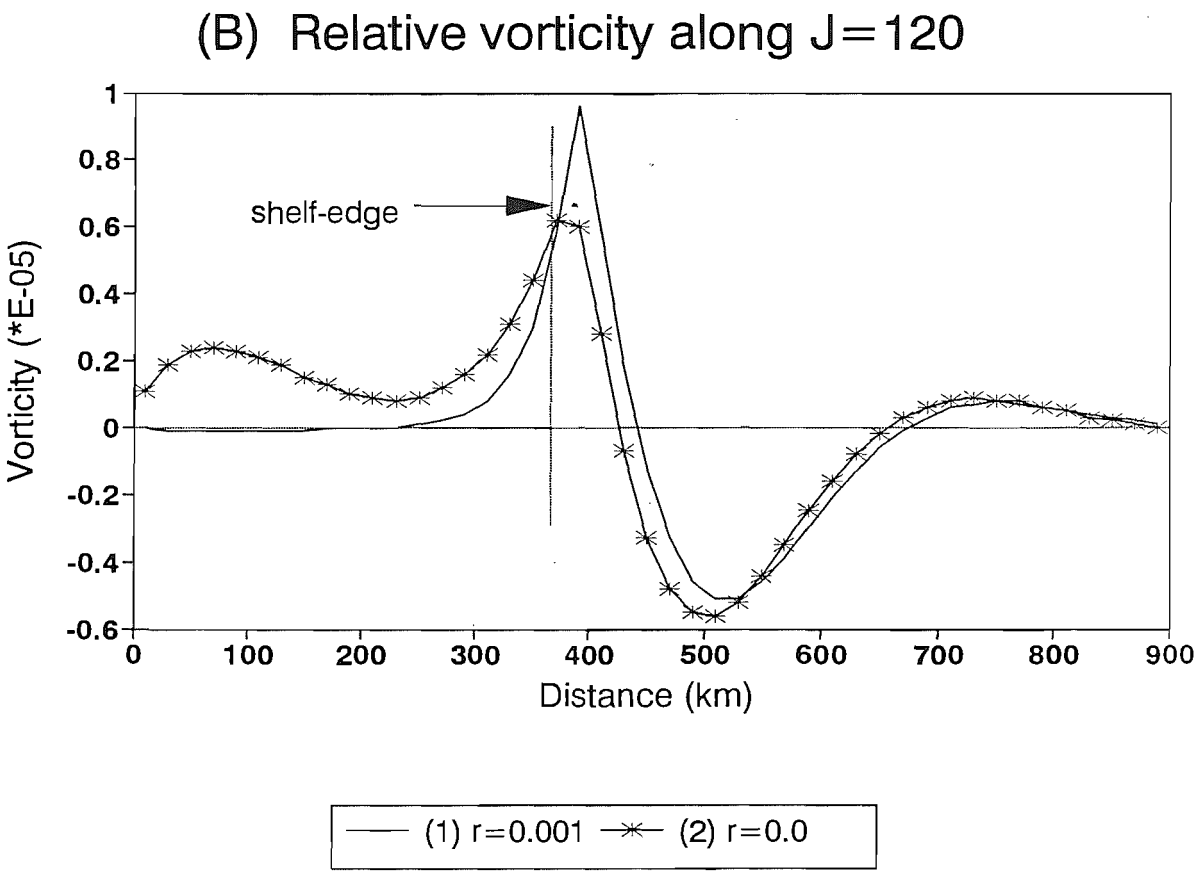
(B) Relative vorticity along J=120
shelf-edge
Vorticity (*E-05)
1
0.8
0.6
0.4
0.2
0
-0.2
-0.4
-0.6
0
100
200
300
400
500
600
700
800
900
Distance (km)
(1) r=0.001
(2) r=0.0

Fig. 4-24. (Upper panel) Contours of streamlines at an equilibrium state in the shelf and adjacent deep ocean region (upper panel), and **(Lower panel)** only in the shelf (lower panel) for the three experiments with different eddy viscosity. For clarity, streamlines of negative values are not plotted in the upper panel. The coefficient of eddy viscosity increases from left ($A_M = 10^3$ m^2s^{-1}) to right ($A_M = 10^4$ m^2s^{-1}). All other parameters are the same as those for the standard SPEM experiment in Table 4-1.

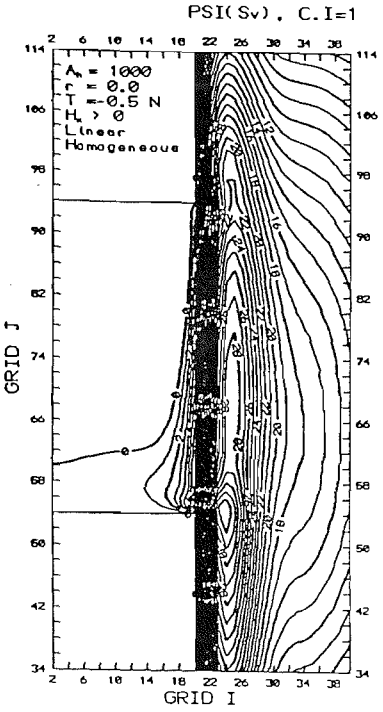
PSI(Sv) , C.I=1
A_h = 1000
c = 0.0
T =-0.5 N
H_L > 0
Linear
Homogeneous
GRID J
GRID I

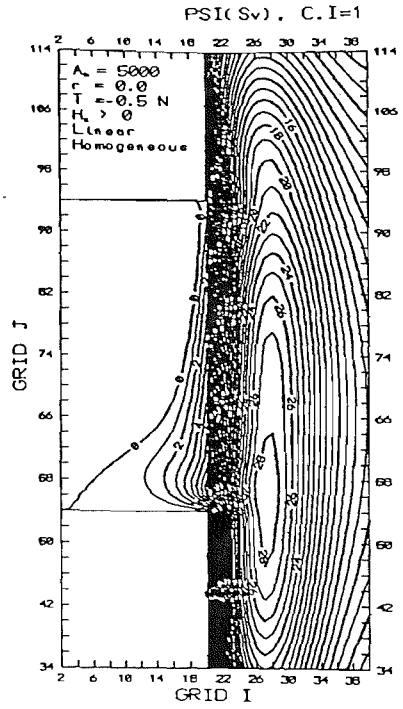
PSI(Sv) , C.I=1
A_h = 5000
c = 0.0
T =-0.5 N
H_L > 0
Linear
Homogeneous
GRID J
GRID I

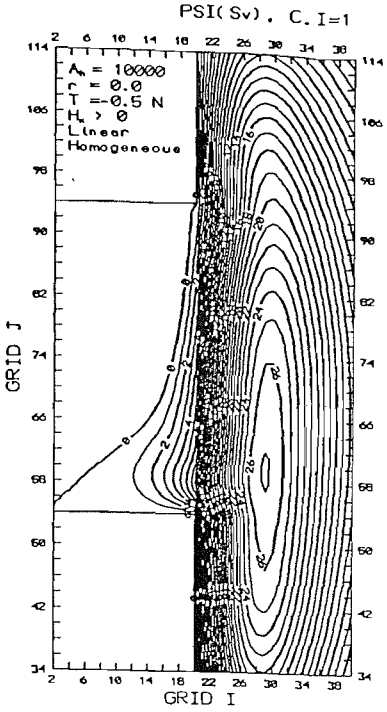
PSI(Sv) , C.I=1
A_h = 10000
c = 0.0
T =-0.5 N
H_L > 0
Linear
Homogeneous
GRID J
GRID I

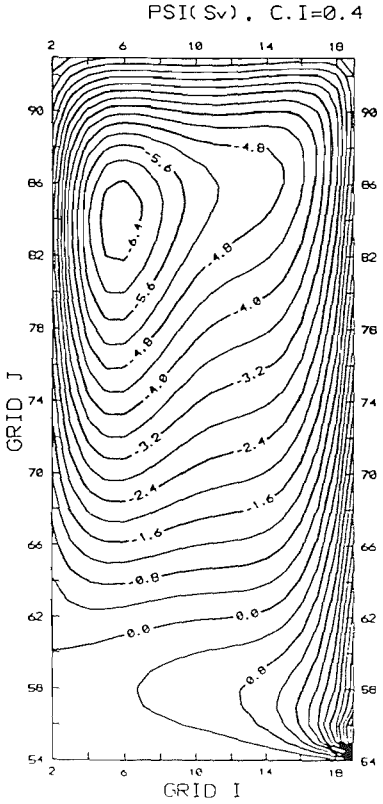
PSI(Sv) , C.I=0.4
GRID J
GRID I

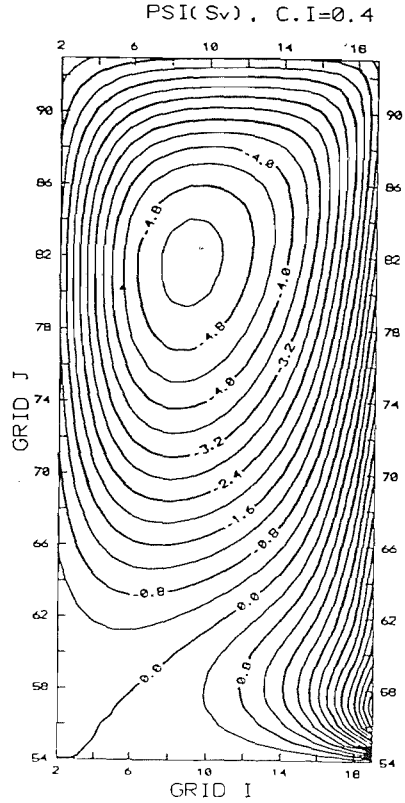
PSI(Sv) , C.I=0.4
GRID J
GRID I

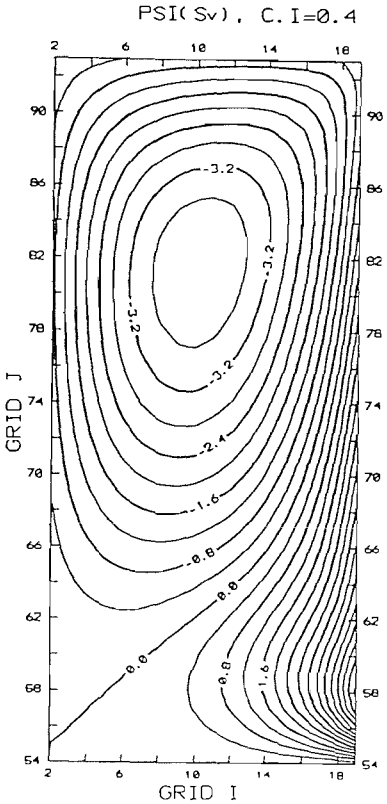
PSI(Sv) , C.I=0.4
GRID J
GRID I

Fig. 4-25. Comparisons of (A) zonal velocity profile along the shelf-edge (I=19 in Fig. 4-24), and (B) longitudinal distribution of on-shelf volume transports for the three experiments with different values for the eddy viscosity. The distance is measured (A) from the southern wall to the north, and (B) from the shelf-edge to the west.

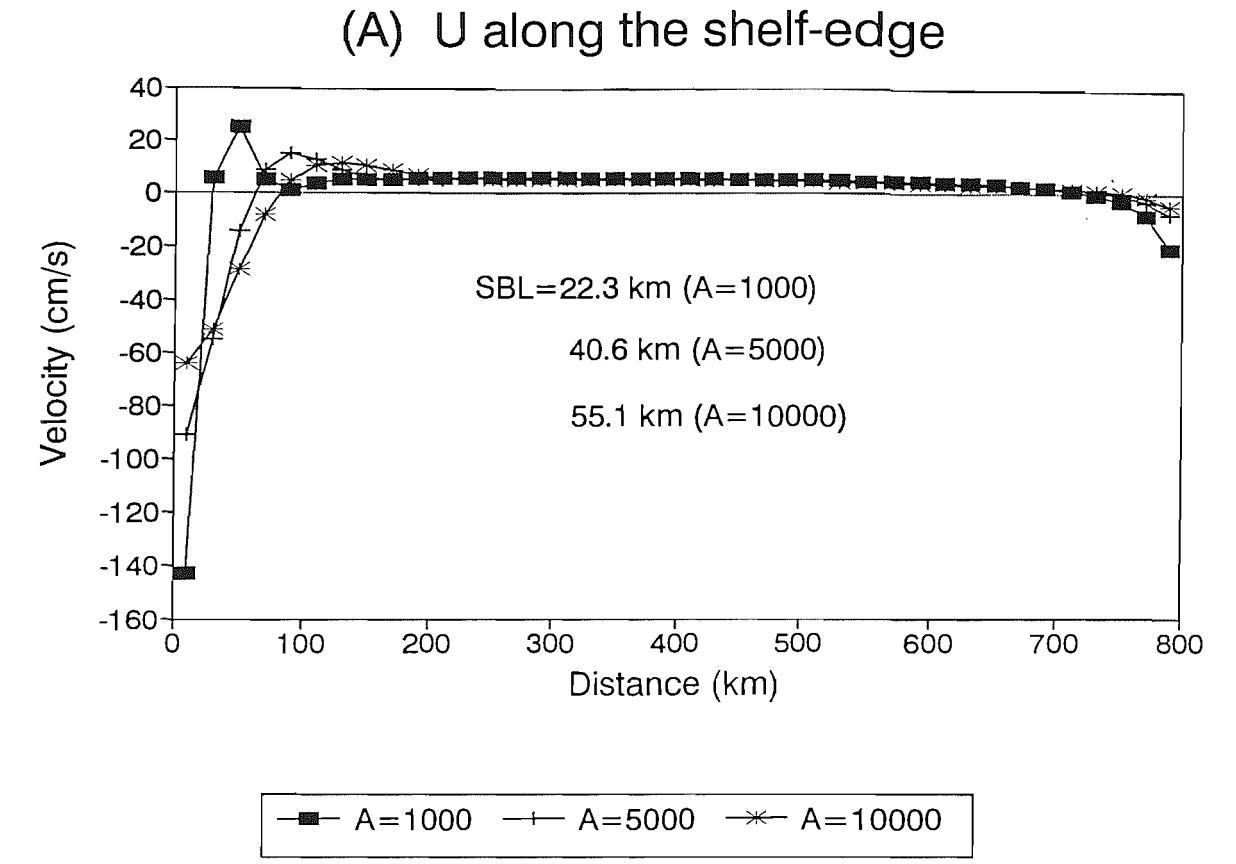
(A) U along the shelf-edge
Velocity (cm/s)
40
20
0
-20
-40
-60
-80
-100
-120
-140
-160
0
100
200
300
400
500
600
700
800
Distance (km)
SBL=22.3 km (A=1000)
40.6 km (A=5000)
55.1 km (A=10000)
A=1000
A=5000
A=10000

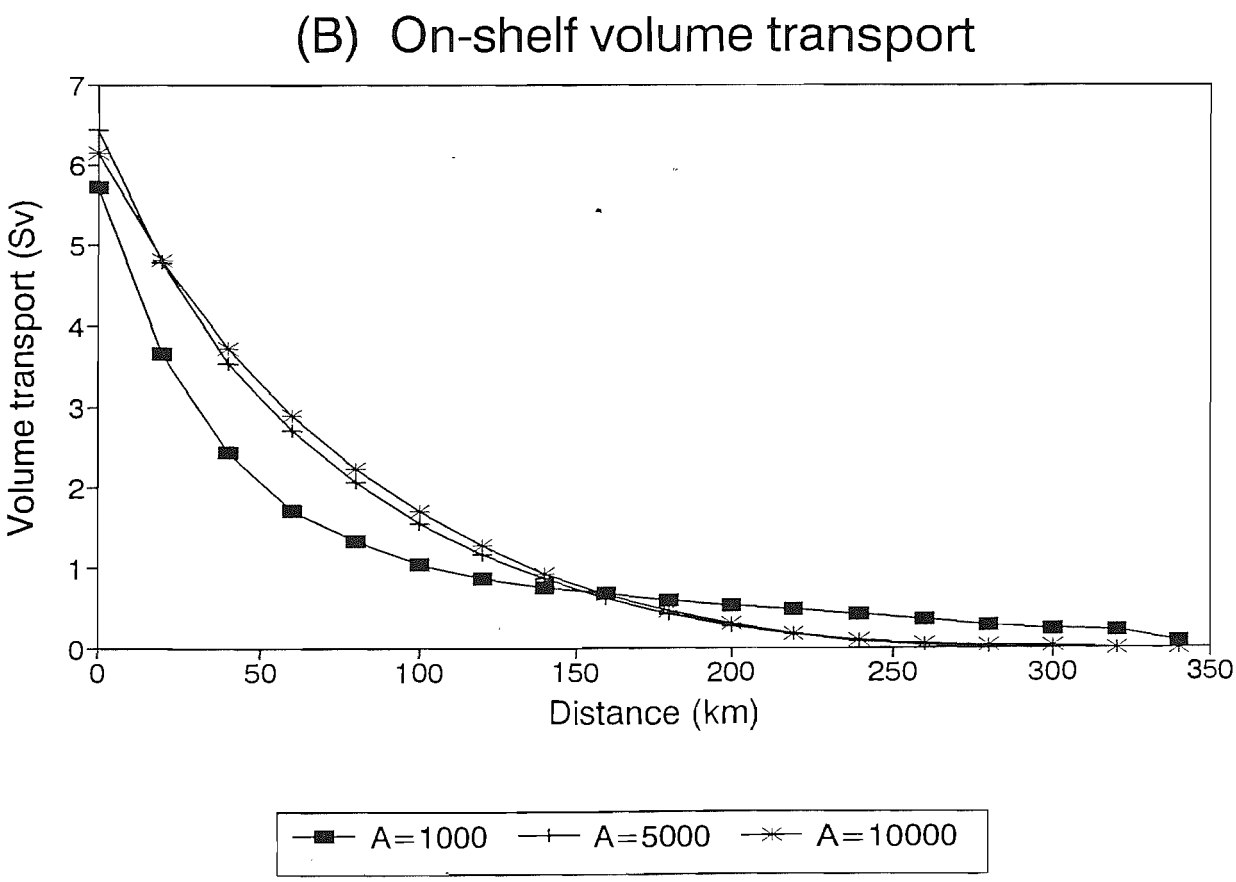
(B) On-shelf volume transport
Volume transport (Sv)
7
6
5
4
3
2
1
0
0
50
100
150
200
250
300
350
Distance (km)
A=1000
A=5000
A=10000

Fig. 4-26. Dependence of the ratio between the maximum on-shelf transport and the WBC transport on five factors; 1. ratio between the shelf depth (d) and unperturbed upper layer depth in the deep ocean (h); 2. coefficient of bottom friction (r, m s^{-1}); 3. latitude of southern boundary of the shelf (θ); 4. coefficient of eddy viscosity (A_M, m^2 s^{-1}); 5. latitudinal size of the shelf (ℓ_y, km).

Relative importance of various factors

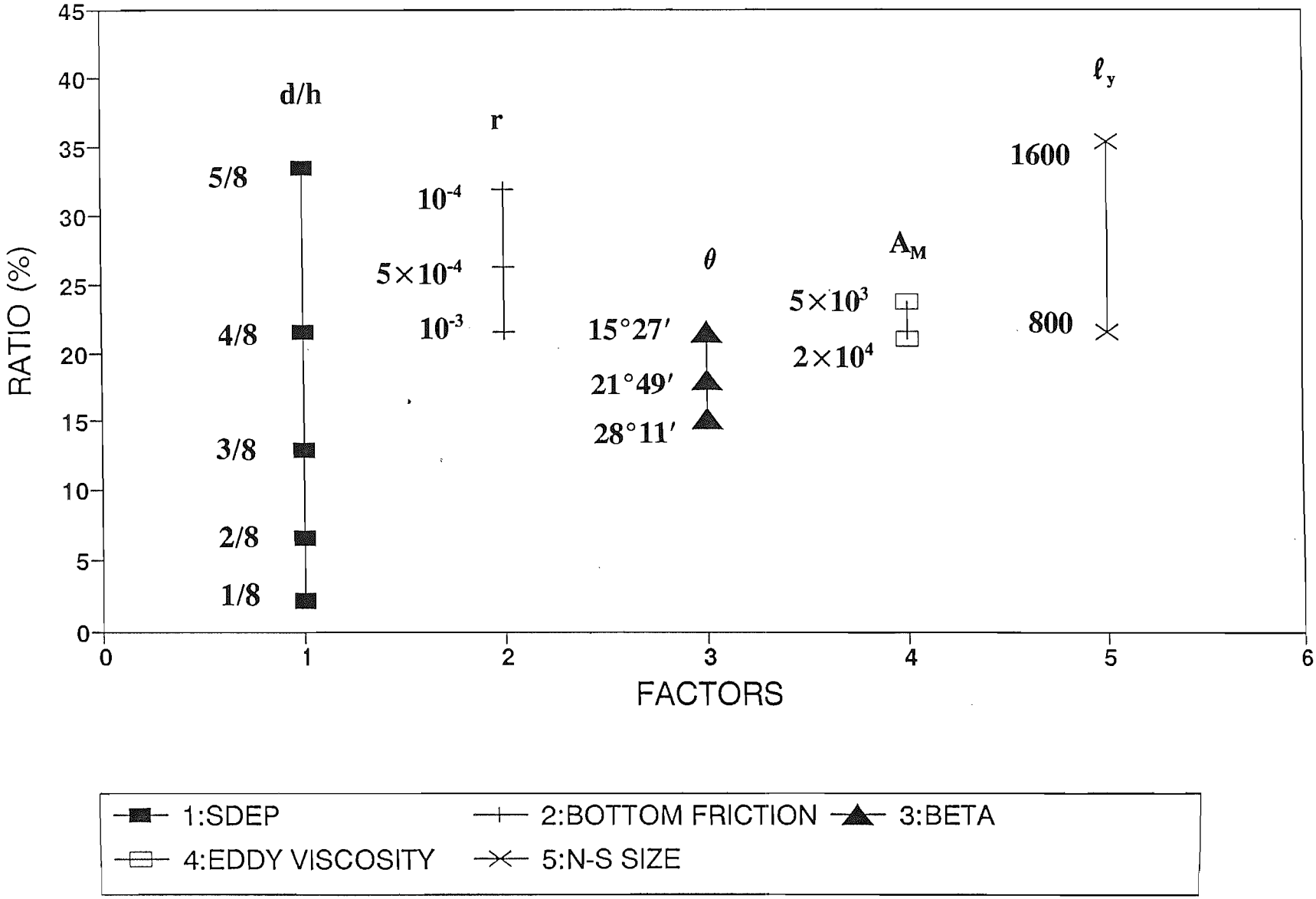

Fig. 4-27. Contours of free surface for three experiments where the southern boundaries of the shelf are placed at (A) 15°27', (B) 21°49', and (C) 28°11' on a β-plane.

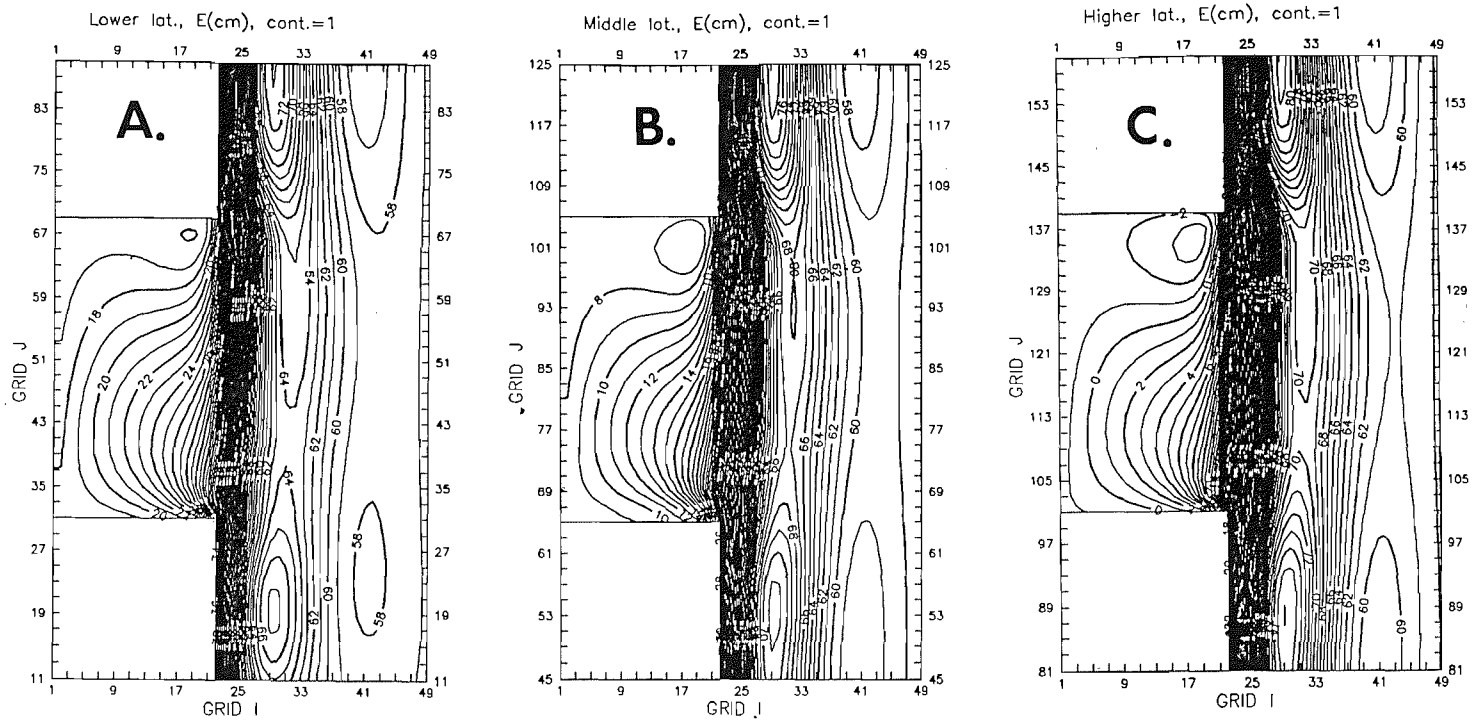
Lower lat., E(cm), cont.=1
A.
Middle lat., E(cm), cont.=1
B.
Higher lat., E(cm), cont.=1
C.
GRID J
GRID I

Fig. 4-28 Contours of free surface for five experiments where depths of the shelf are (A) 50 m, (B) 100 m, (C) 150 m, (D) 200 m, and (E) 250 m. The unperturbed upper layer thickness of the deep channel is 400 m for all the experiments.

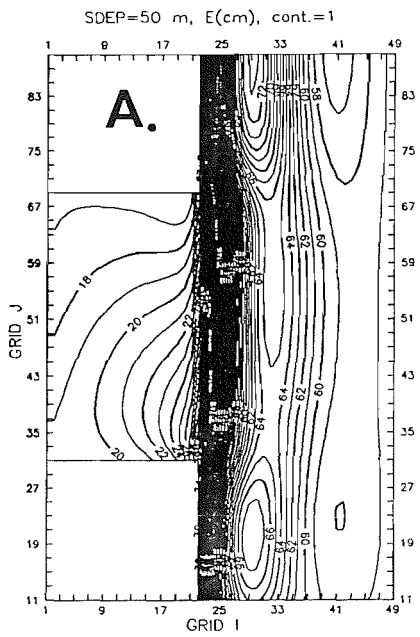
SDEP=50 m, E(cm), cont.=1
A.
GRID J
GRID I

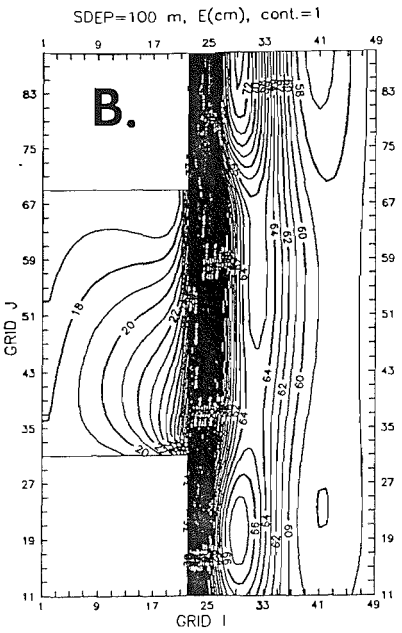
SDEP=100 m, E(cm), cont.=1
B.
GRID J
GRID I

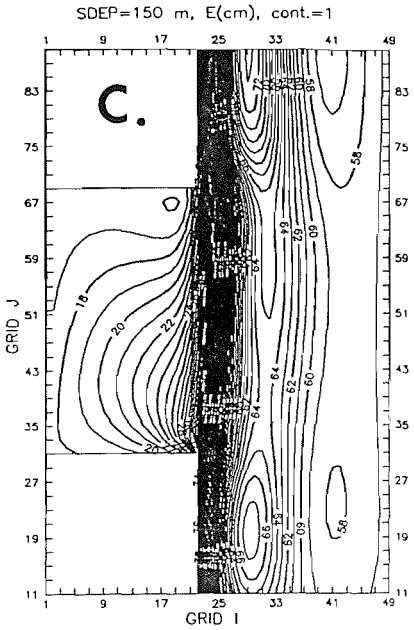
SDEP=150 m, E(cm), cont.=1
C.
GRID J
GRID I

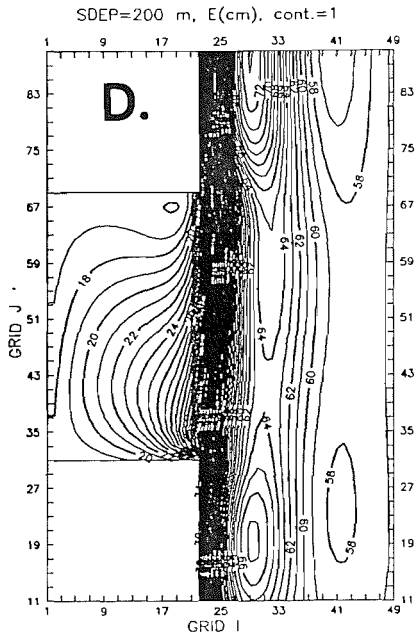
SDEP=200 m, E(cm), cont.=1
D.
GRID J
GRID I

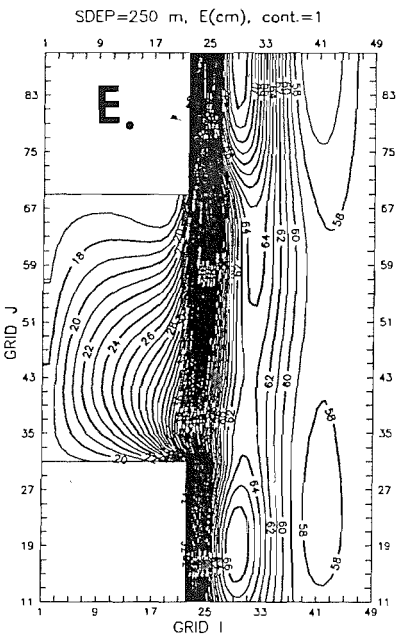
SDEP=250 m, E(cm), cont.=1
E.
GRID J
GRID I

Fig. 4-29. Log-log plot of the ratio between the maximum on-shelf transport along the shelf-edge and the prescribed transport of the WBC along the southern boundary of the deep channel as a function of the shelf depth.

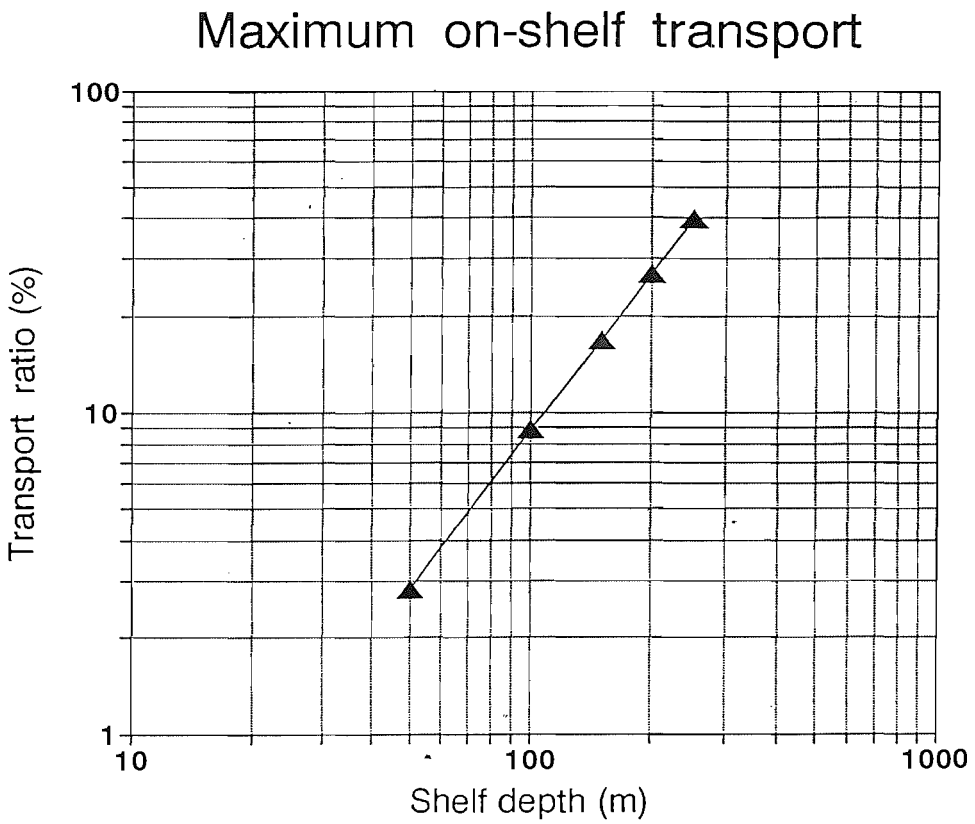
Maximum on-shelf transport
100
10
1
Transport ratio (%)
10
100
1000
Shelf depth (m)

Fig. 4-30. (Upper panel) Contours of free surface for two experiments of different longitudinal size of the shelf.

(Lower panel) Contours of free surface for two experiments of different latitudinal size of the shelf.

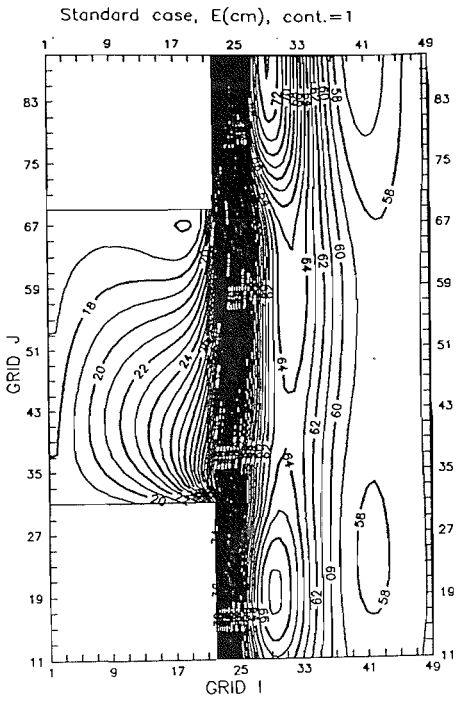
Standard case, E(cm), cont.=1
GRID J
GRID I

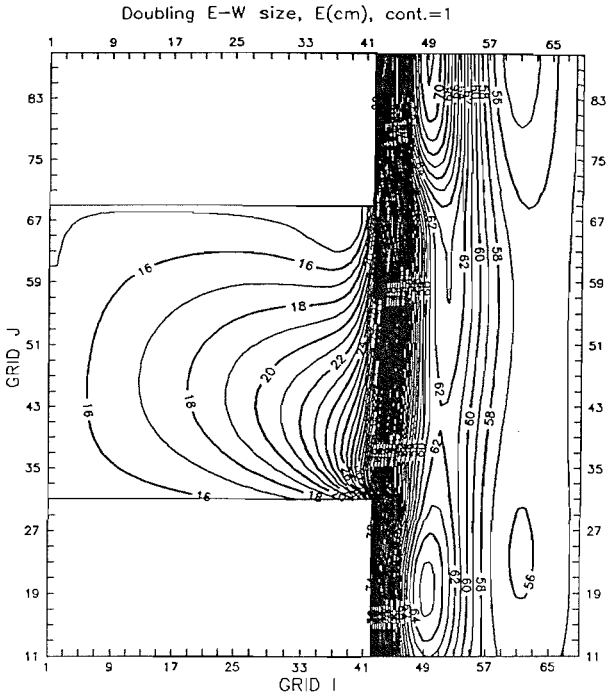
Doubling E-W size, E(cm), cont.=1
GRID J
GRID I

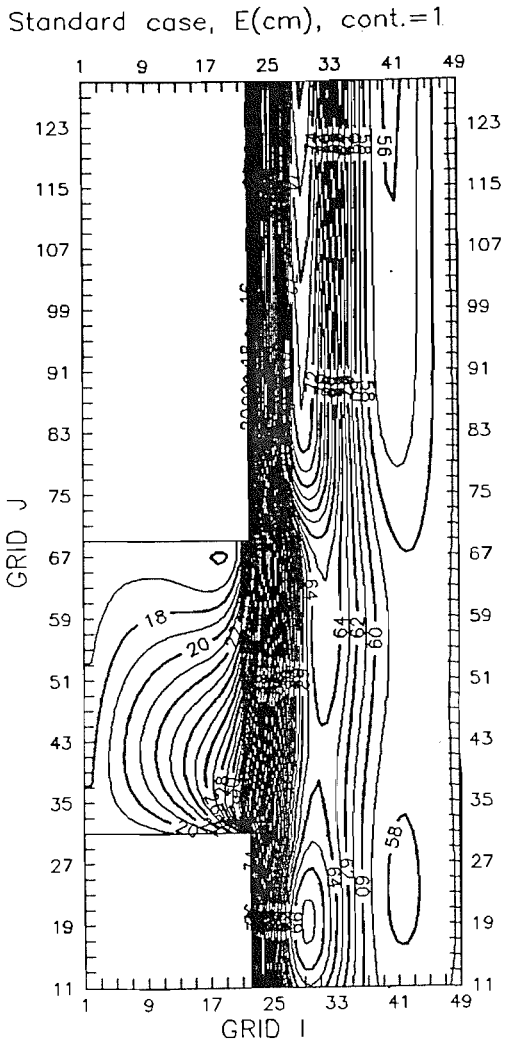
Standard case, E(cm), cont.=1
GRID J
GRID I

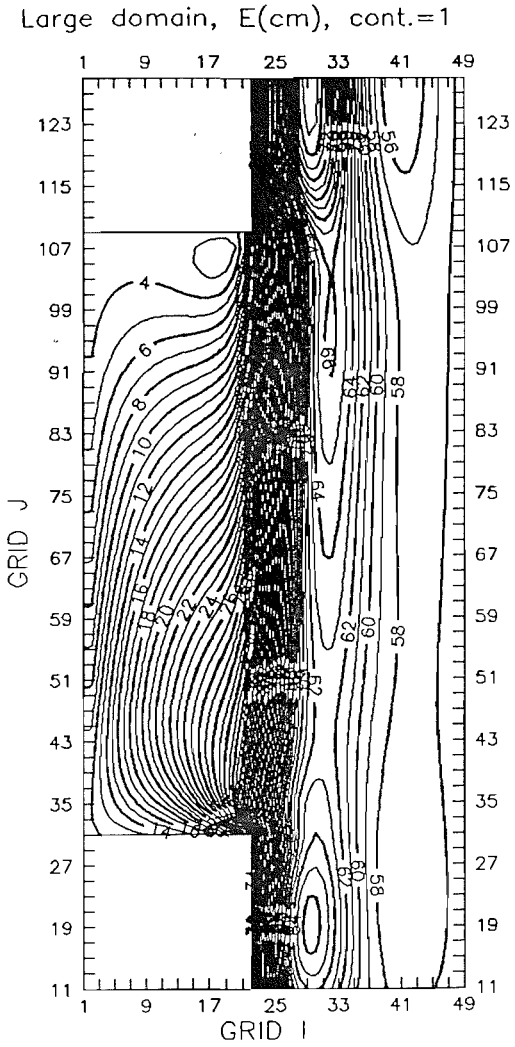
Large domain, E(cm), cont.=1
GRID J
GRID I

Fig. 4-31. Contours of streamlines in the whole domain for four experiments where the applied Sverdrup transports in the deep ocean are (A) 13.5 Sv, (B) 27.0 Sv, (C) 40.4 Sv, and (D) 53.9 Sv.

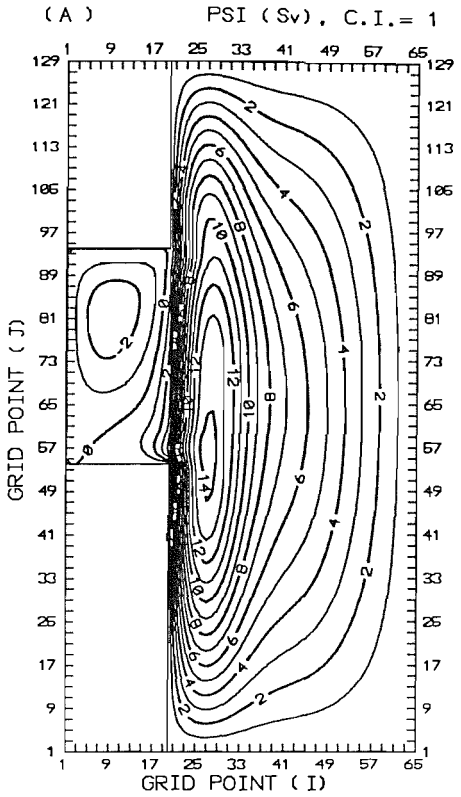
(A)
PSI (Sv), C.I.= 1
GRID POINT (J)
GRID POINT (I)

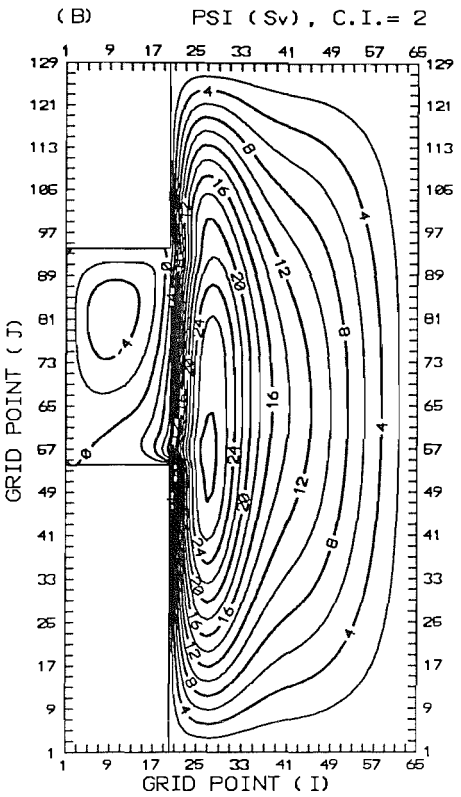
(B)
PSI (Sv), C.I.= 2
GRID POINT (J)
GRID POINT (I)

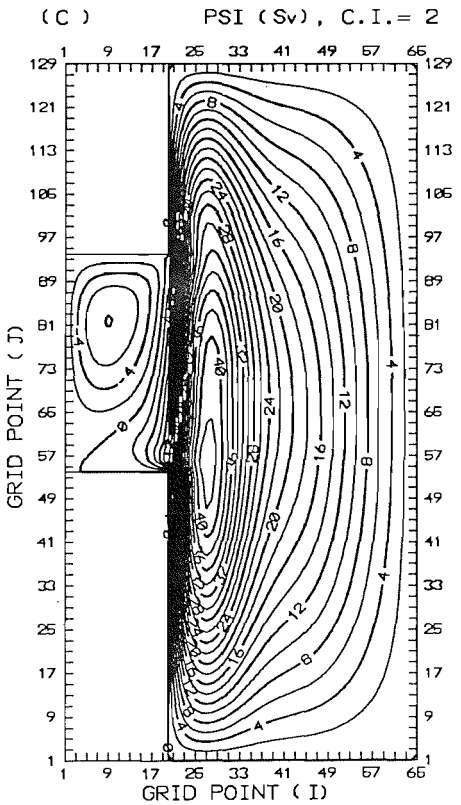
(C)
PSI (Sv), C.I.= 2
GRID POINT (J)
GRID POINT (I)

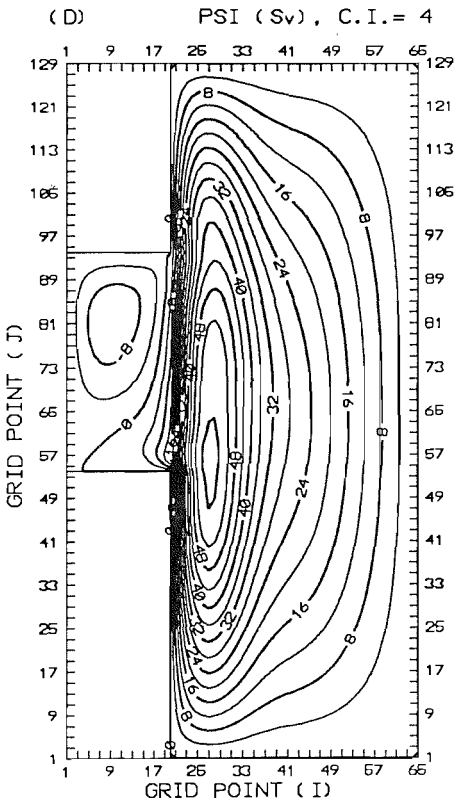
(D)
PSI (Sv), C.I.= 4
GRID POINT (J)
GRID POINT (I)

Fig. 4-31. Contours of streamlines in the shelf and continental slope area for four experiments where the applied Sverdrup transports in the deep ocean are (A) 13.5 Sv, (B) 27.0 Sv, (C) 40.4 Sv, and (D) 53.9 Sv.

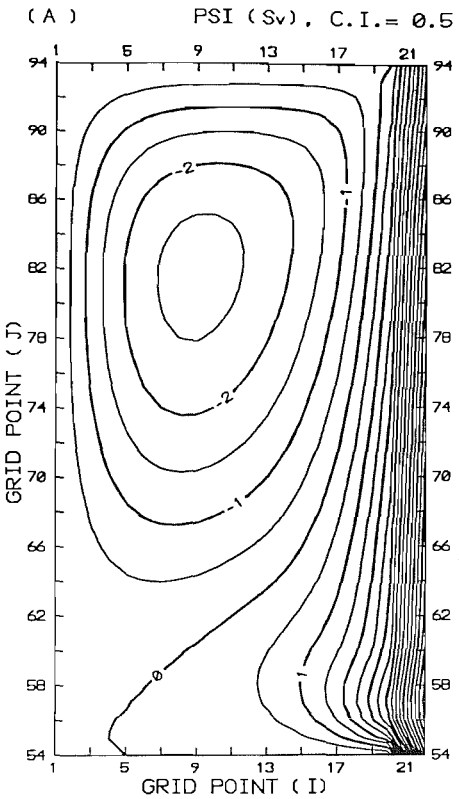
(A) PSI (Sv), C.I.= 0.5
GRID POINT (J)
GRID POINT (I)

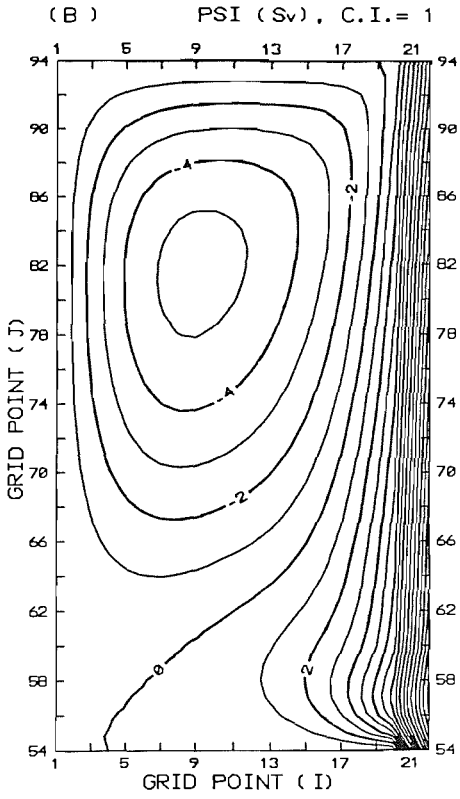
(B) PSI (Sv), C.I.= 1
GRID POINT (J)
GRID POINT (I)

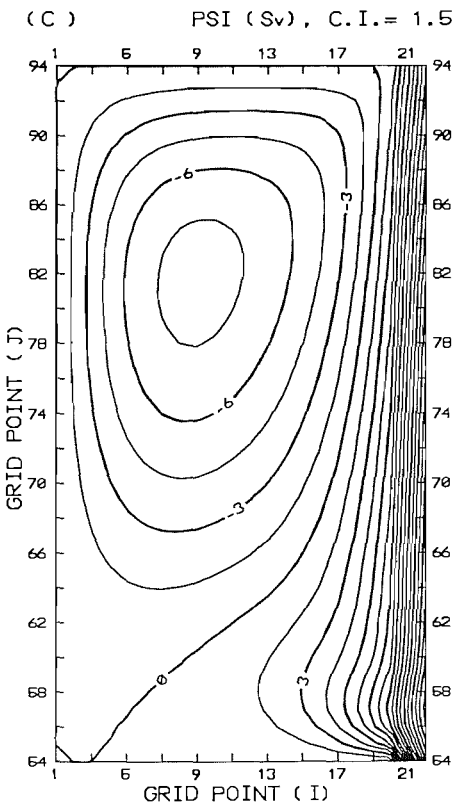
(C) PSI (Sv), C.I.= 1.5
GRID POINT (J)
GRID POINT (I)

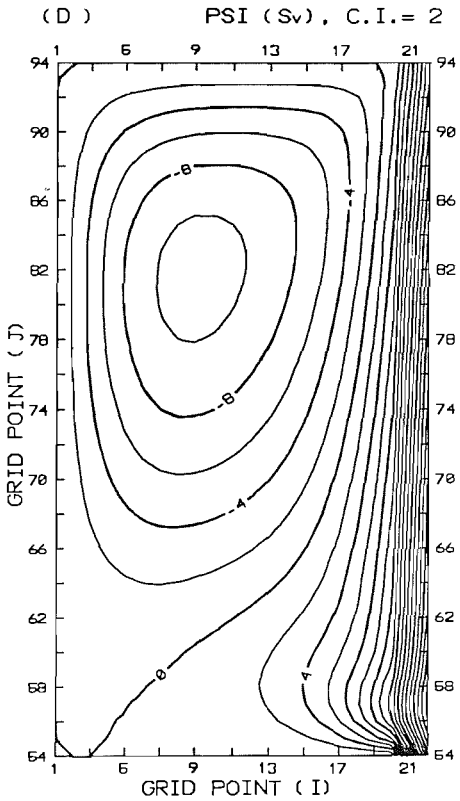
(D) PSI (Sv), C.I.= 2
GRID POINT (J)
GRID POINT (I)

Fig. 4-32. (Upper panel) Contours of free surface in the shelf and continental slope area for two experiments with different lateral boundary conditions, (A) free-slip boundary condition, and (B) no-slip boundary condition.
(Lower panel) Longitudinal variation of the ratio between the on-shelf transport and the prescribed WBC transport along the southern boundary of the deep channel for the above two experiments.

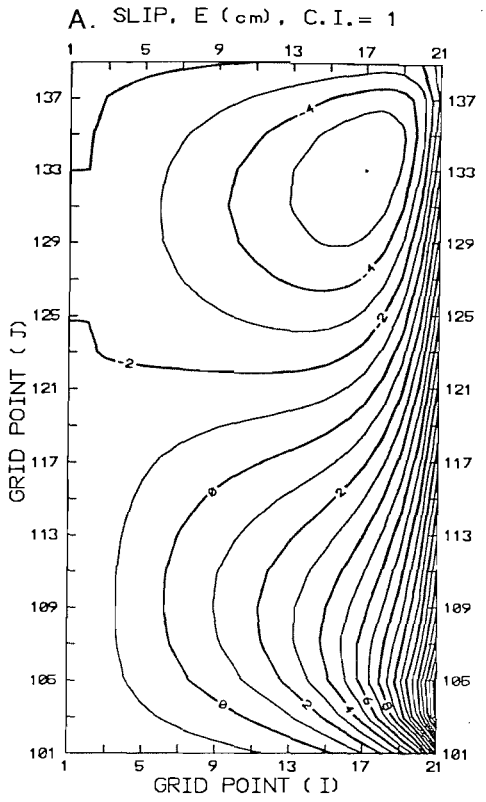
A. SLIP, E (cm), C.I.= 1
GRID POINT (J)
GRID POINT (I)

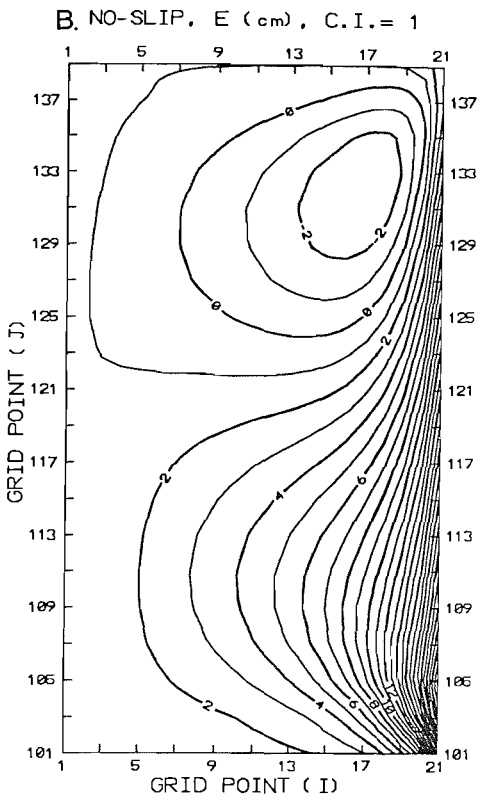
B. NO-SLIP, E (cm), C.I.= 1
GRID POINT (J)
GRID POINT (I)

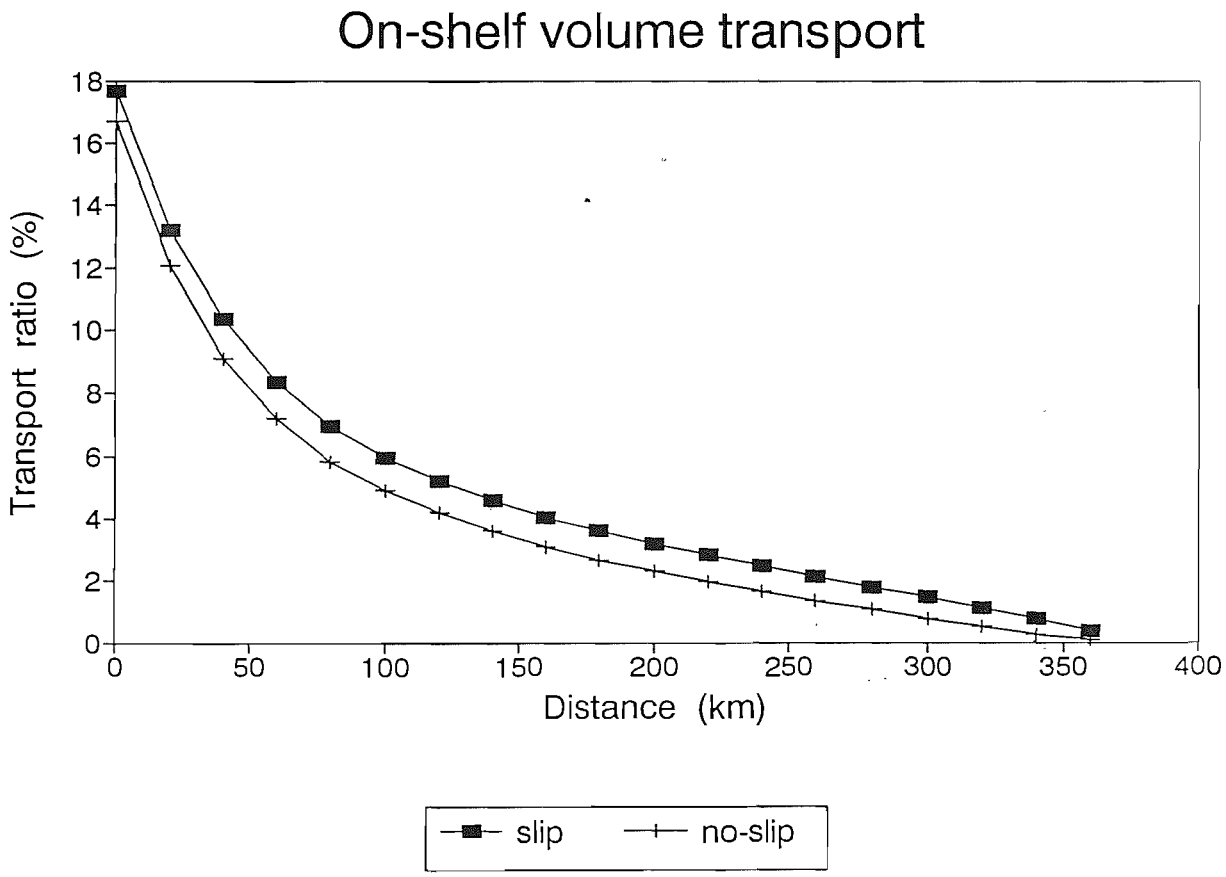
On-shelf volume transport
Transport ratio (%)
Distance (km)
slip
no-slip

Fig. 4-33. (Upper panel) Contours of streamlines in the shelf area for two experiments with different grid resolution, (A) 20 km, and (B) 10 km.
(Lower panel) Longitudinal variation of the ratio between the on-shelf transport and the applied Sverdrup transport in the deep ocean for three experiments with different grid resolution (d in the legend).

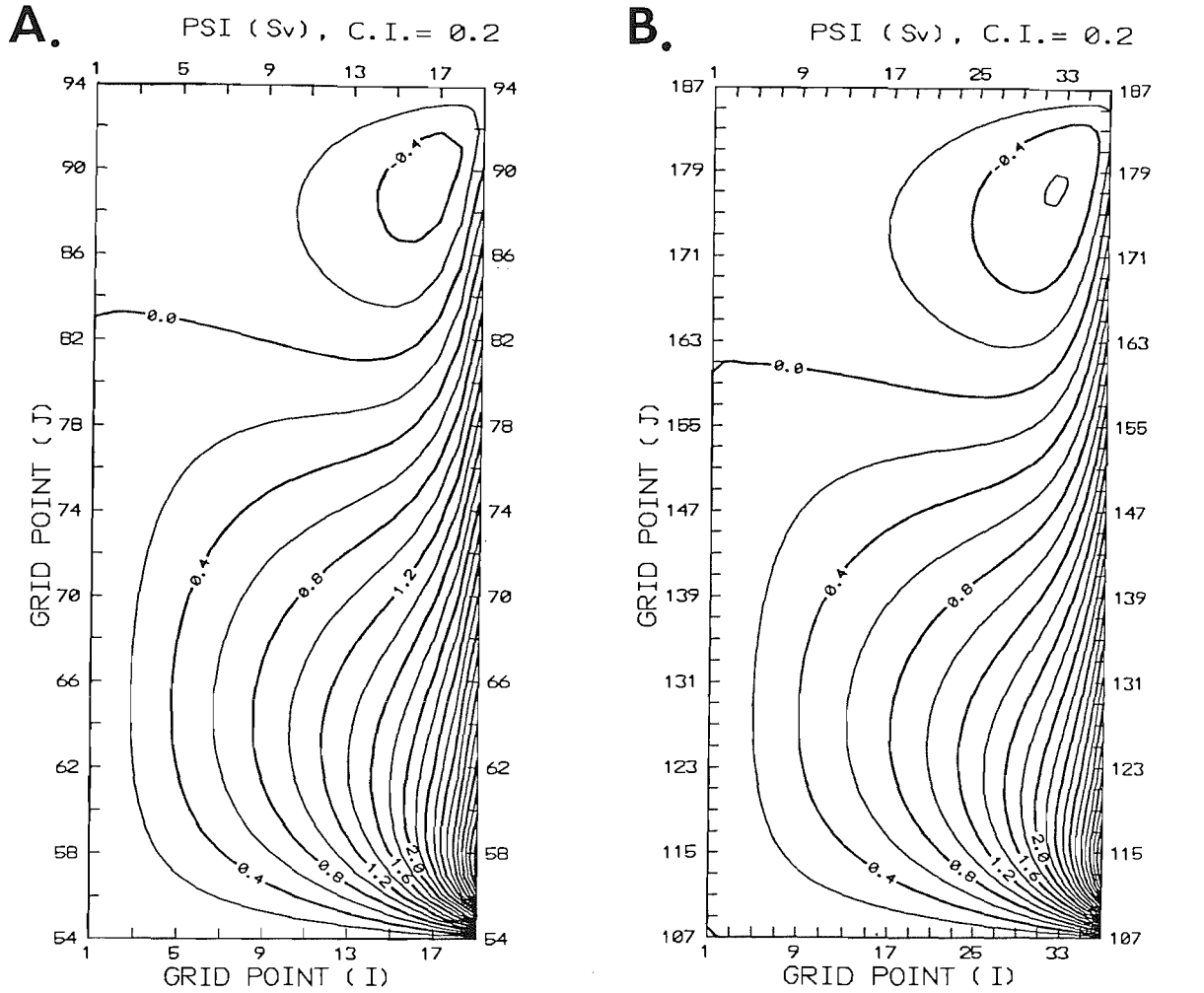
A.
PSI (Sv), C.I.= 0.2
B.
PSI (Sv), C.I.= 0.2
GRID POINT (J)
GRID POINT (I)
0.0
0.4
0.8
1.2
1.6
2.0

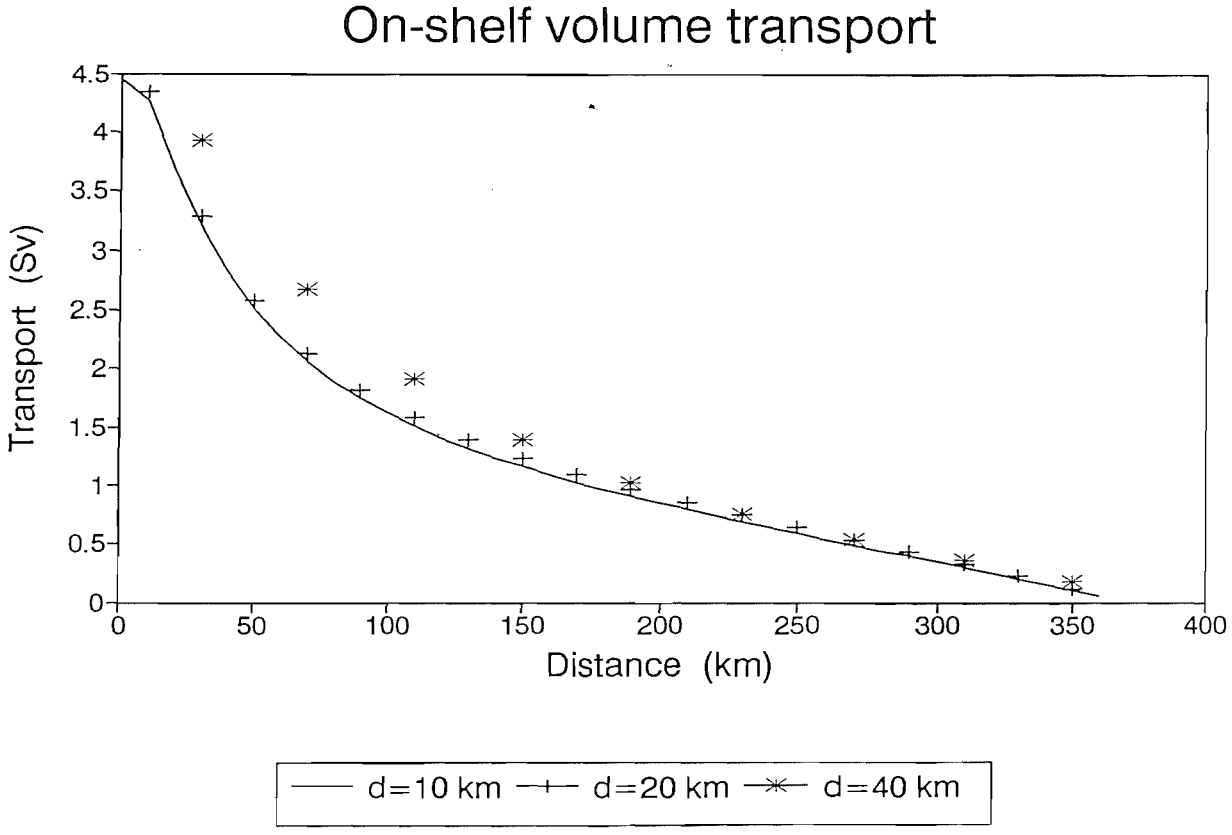
On-shelf volume transport
Transport (Sv)
Distance (km)
d=10 km
d=20 km
d=40 km

Fig. 4-34. (Upper panel) Contours of streamlines in the shelf and adjacent deep ocean area for two experiments, (A) standard case, and (B) smoothed sharp corner. **(Lower panel)** Longitudinal variation of the ratio between the on-shelf transport and the applied Sverdrup transport in the deep ocean for the above two experiments.

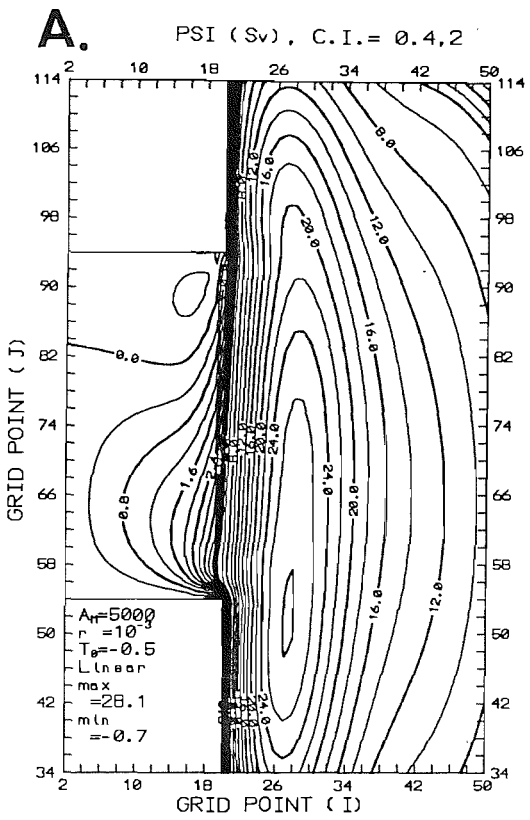
A.
PSI (Sv), C.I.= 0.4,2
GRID POINT (J)
GRID POINT (I)
A_H=5000
r =10^{-3}
T_θ=-0.5
Linear
max
=28.1
min
=-0.7

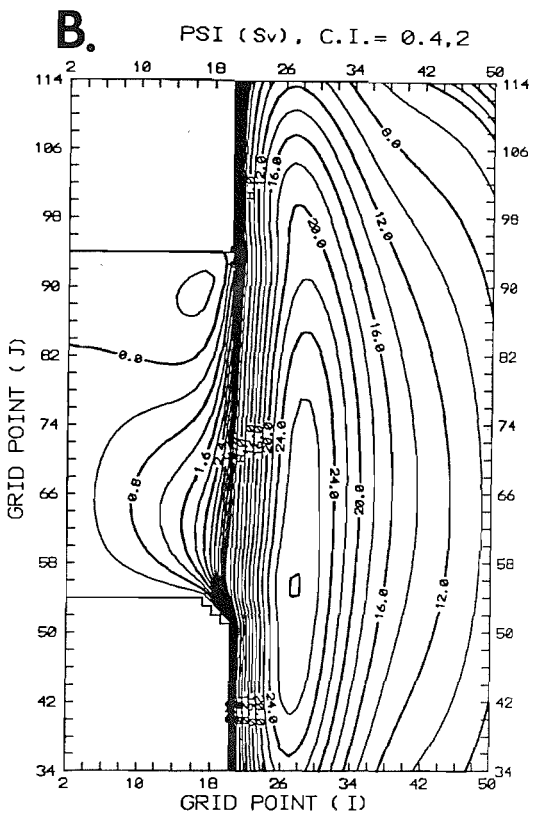
B.
PSI (Sv), C.I.= 0.4,2
GRID POINT (J)
GRID POINT (I)

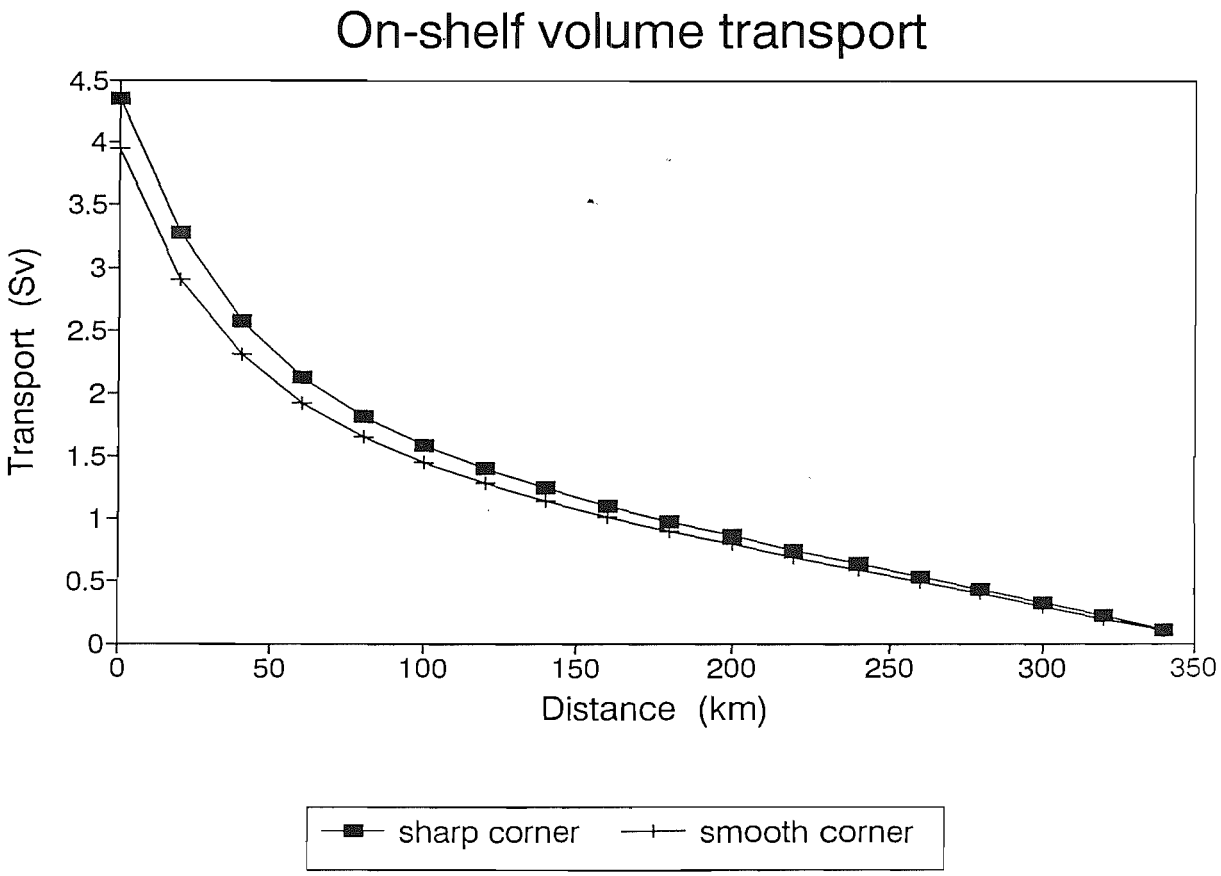
On-shelf volume transport
Transport (Sv)
Distance (km)
sharp corner
smooth corner

Fig. 4-35. Contours of streamlines in the shelf and adjacent deep ocean area for two experiments with different longitudinal size of the deep ocean, (A) narrower case, and (B) wider case.

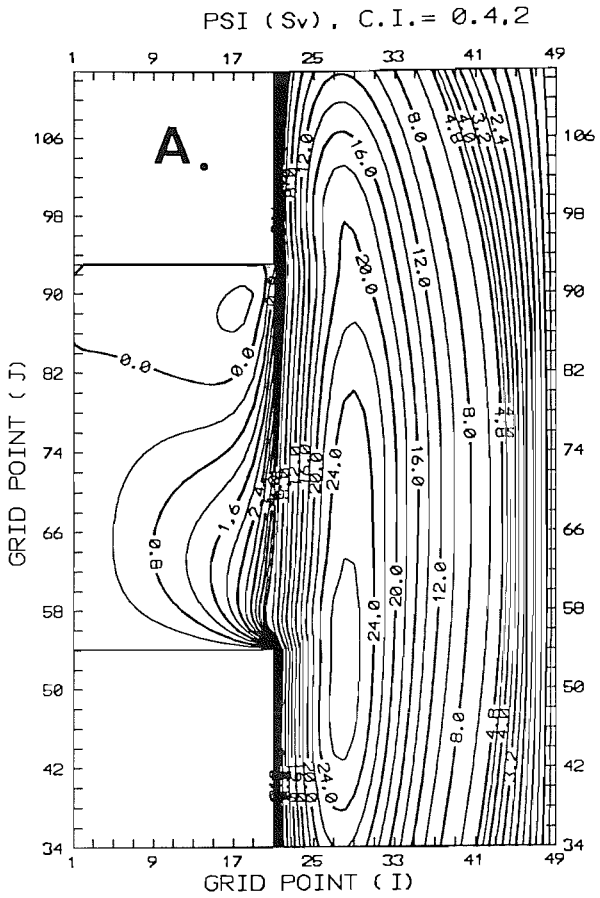
PSI (Sv), C.I.= 0.4,2
A.
GRID POINT (J)
GRID POINT (I)

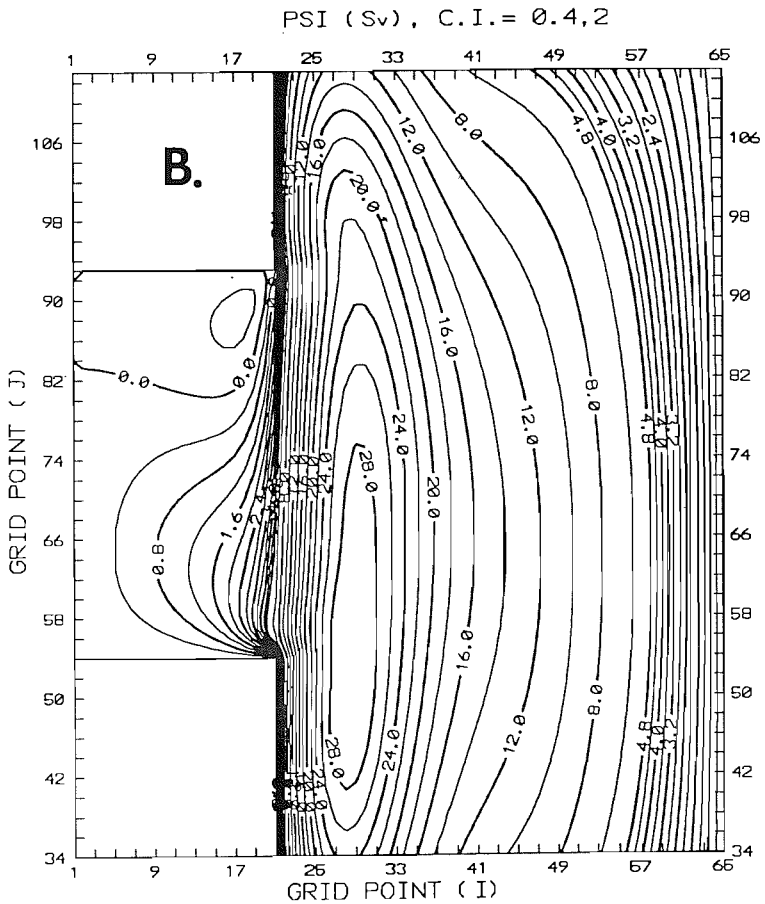
PSI (Sv), C.I.= 0.4,2
B.
GRID POINT (J)
GRID POINT (I)

Fig. 4-36. (A) Profiles of meridional velocity along the western wall of the shelf (I=2 in Fig. 4-35) for the two experiments in Fig. 4-35. (B) Longitudinal variation of the ratio between the on-shelf transport and the applied Sverdrup transport in the deep ocean for the two experiments in Fig. 4-35.

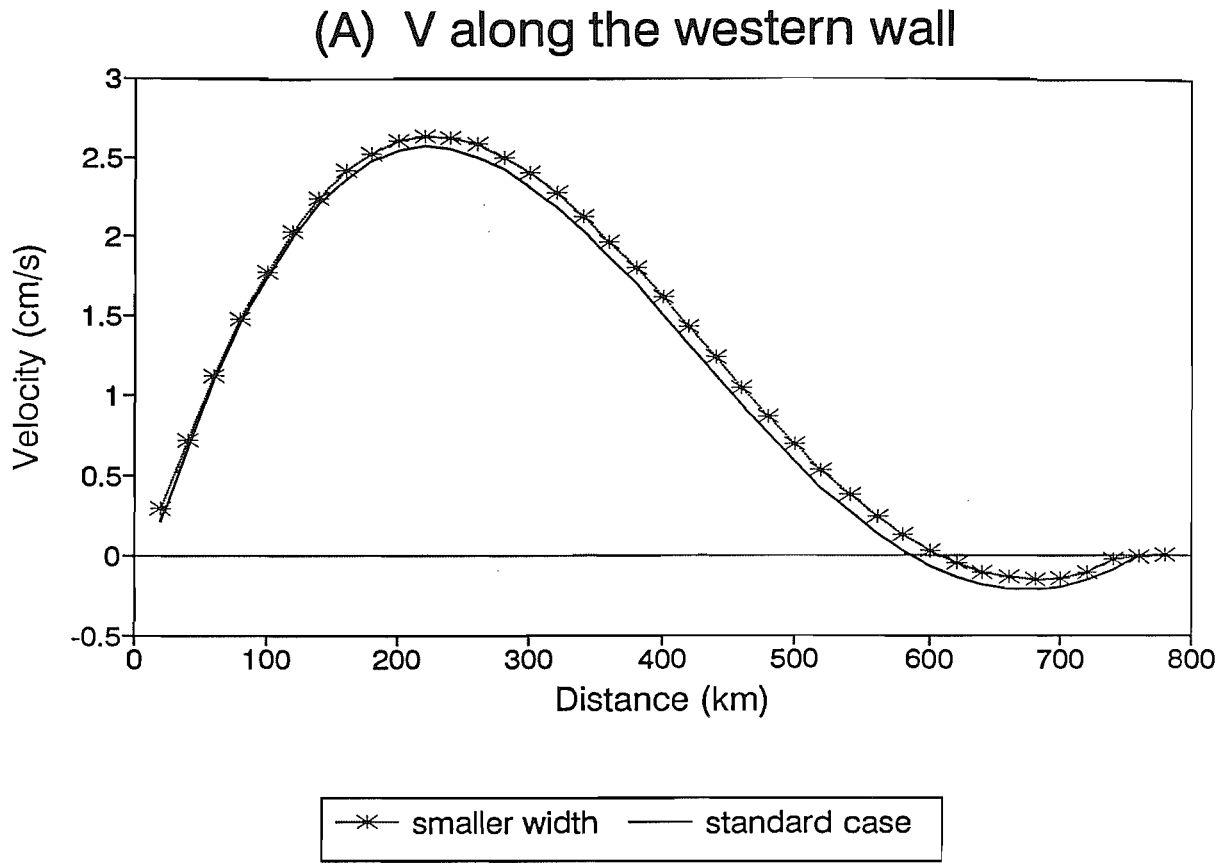
(A) V along the western wall
Velocity (cm/s)
3
2.5
2
1.5
1
0.5
0
-0.5
0
100
200
300
400
500
600
700
800
Distance (km)
smaller width
standard case

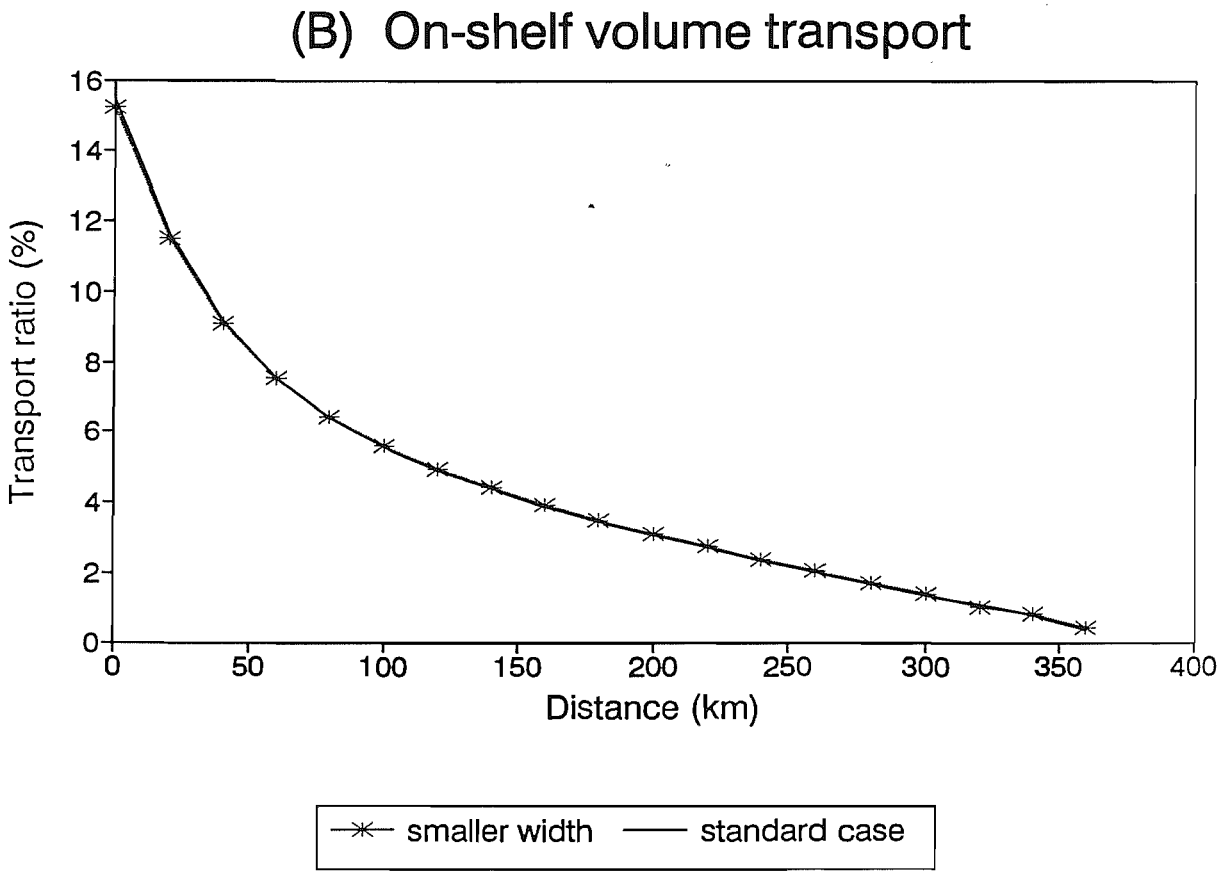
(B) On-shelf volume transport
Transport ratio (%)
16
14
12
10
8
6
4
2
0
0
50
100
150
200
250
300
350
400
Distance (km)
smaller width
standard case

Fig. 4-37. (Upper panel) Contours of streamlines for two linear experiments (A) $p_y < 0$, $h_x > 0$ (ECS case), and (B) $p_y > 0$, $h_x > 0$ (MAB case).
(Lower panel) Contours of streamlines for two linear experiments (A) $p_y < 0$, $h_x < 0$, and (B) $p_y > 0$, $h_x < 0$. The p_y and h_x denote the meridional pressure gradient along the WBC and the zonal gradient of topography respectively. Applied Sverdrup transports are the same for both cases.

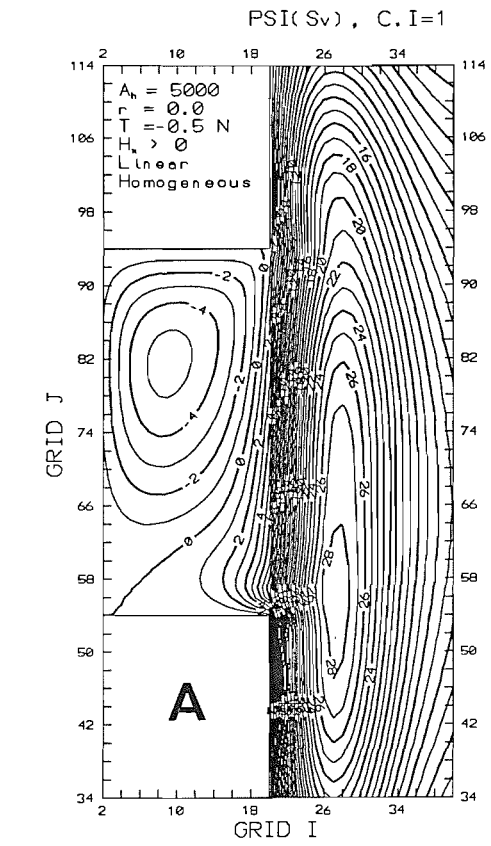
PSI(Sv), C. I=1
A_h = 5000
r = 0.0
T =-0.5 N
H_x > 0
Linear
Homogeneous
A
GRID J
GRID I

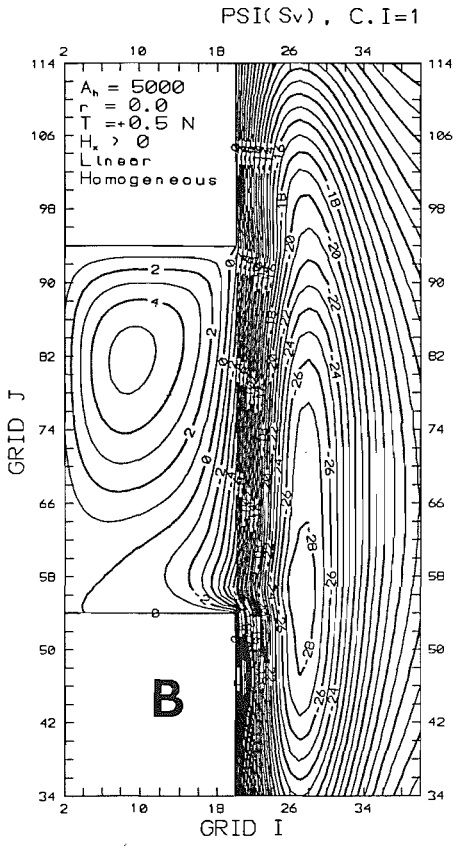
PSI(Sv), C. I=1
A_h = 5000
r = 0.0
T =+0.5 N
H_x > 0
Linear
Homogeneous
B
GRID J
GRID I

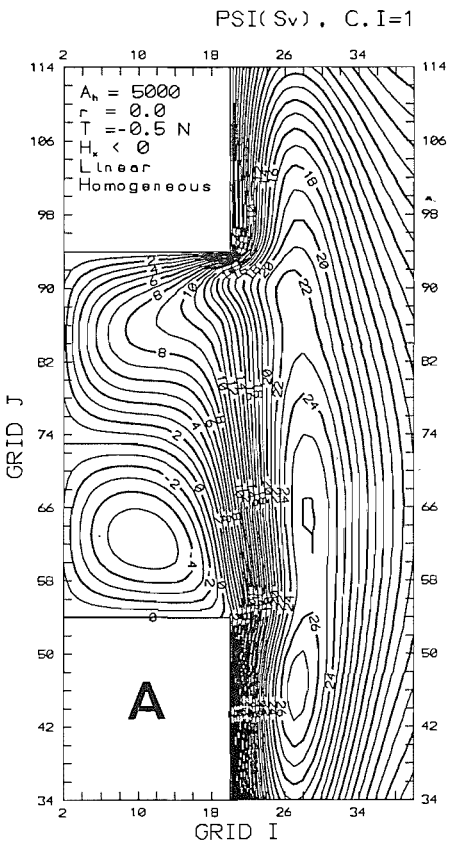
PSI(Sv), C. I=1
A_h = 5000
r = 0.0
T =-0.5 N
H_x < 0
Linear
Homogeneous
A
GRID J
GRID I

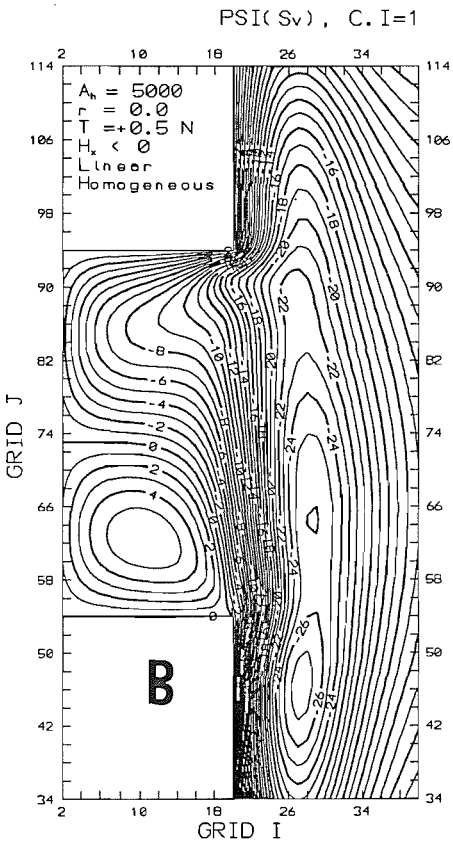
PSI(Sv), C. I=1
A_h = 5000
r = 0.0
T =+0.5 N
H_x < 0
Linear
Homogeneous
B
GRID J
GRID I

Fig. 4-38. (Upper panel) Contours of streamlines in the whole domain for (A) a linear, and (B) a non-linear experiments.
(Lower panel) Contours of streamlines only in the shelf and adjacent deep ocean area for (A) a linear, and (B) a non-linear experiments.

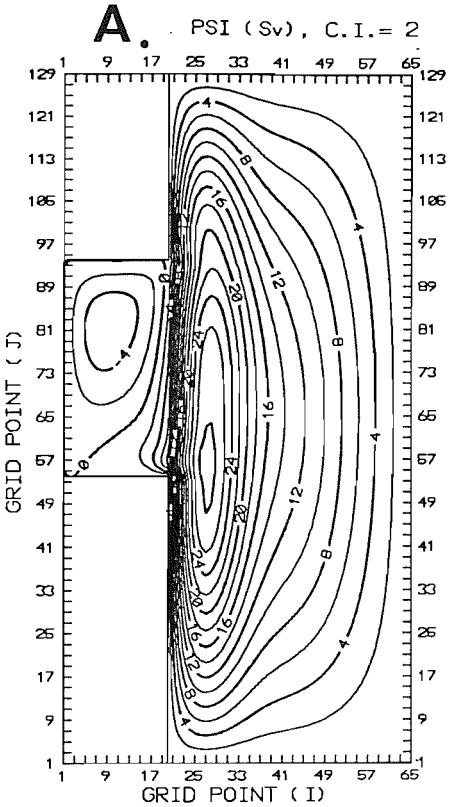
A.
PSI (Sv), C.I.= 2
GRID POINT (J)
GRID POINT (I)

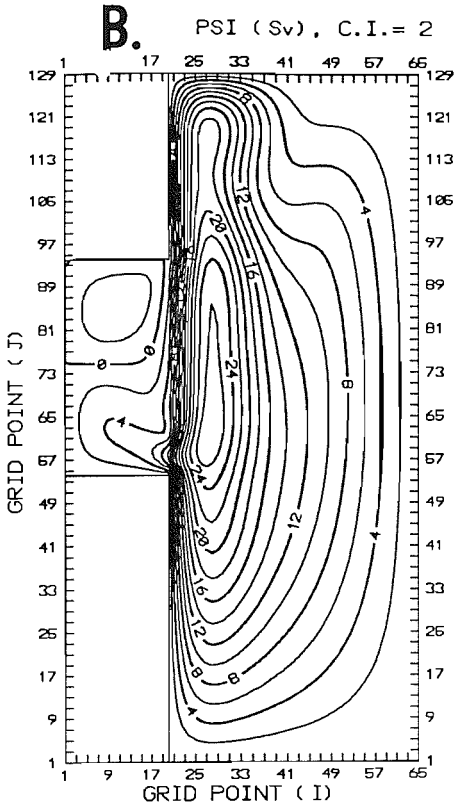
B.
PSI (Sv), C.I.= 2
GRID POINT (J)
GRID POINT (I)

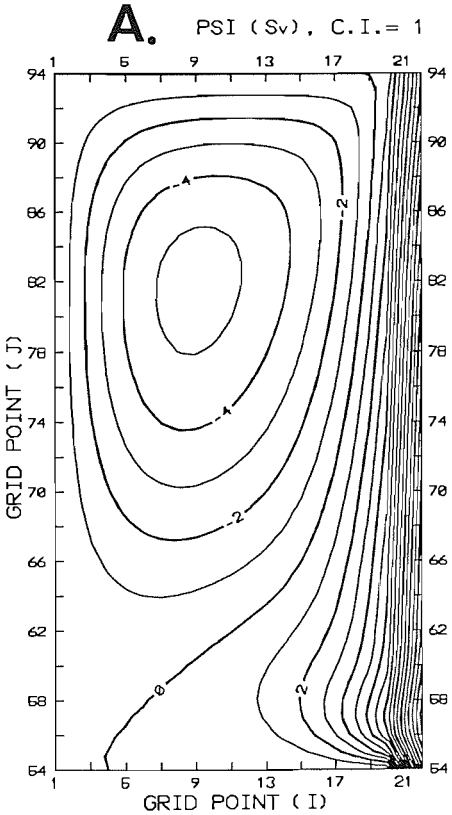
A.
PSI (Sv), C.I.= 1
GRID POINT (J)
GRID POINT (I)

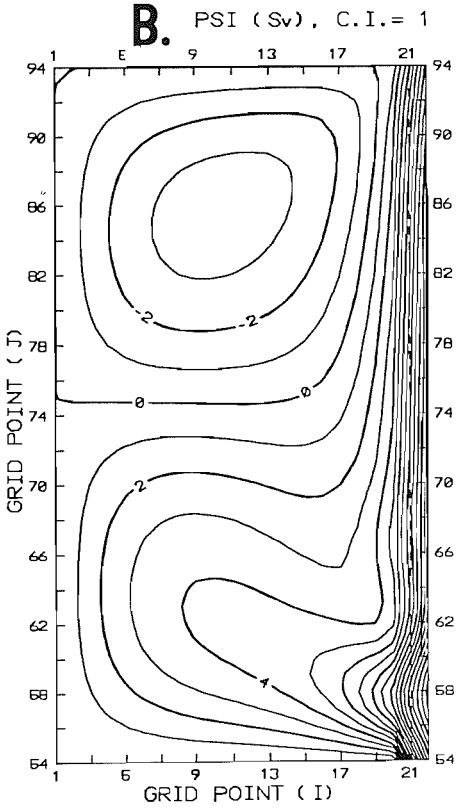
B.
PSI (Sv), C.I.= 1
GRID POINT (J)
GRID POINT (I)

Fig. 4-39. Comparisons of (A) zonal velocity profile along the southern wall of the shelf (J=55 in Fig. 4-38), and (B) zonal velocity along the shelf-edge (I=19 in Fig. 4-38) between the linear and non-linear experiments in Fig. 4-38.

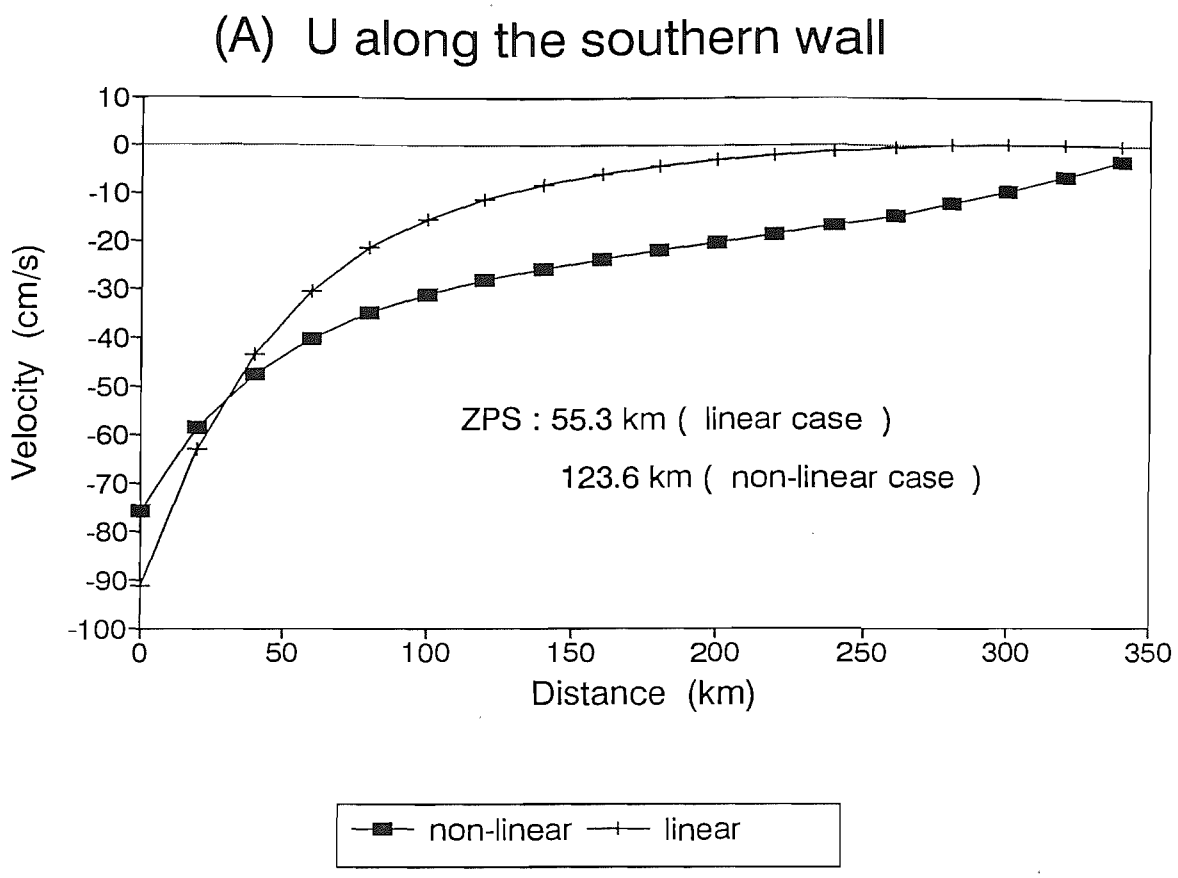
(A) U along the southern wall
Velocity (cm/s)
10
0
-10
-20
-30
-40
-50
-60
-70
-80
-90
-100
0
50
100
150
200
250
300
350
Distance (km)
ZPS : 55.3 km (linear case)
123.6 km (non-linear case)
non-linear
linear

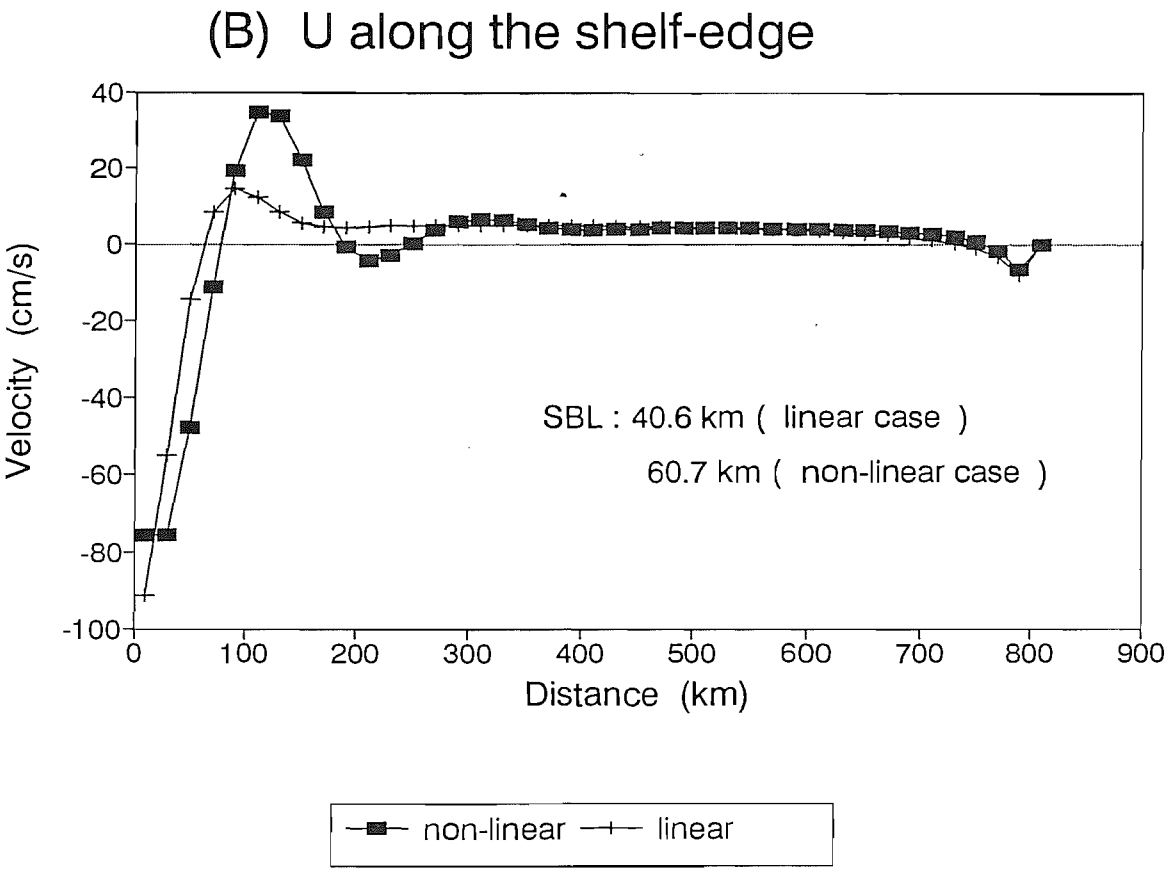
(B) U along the shelf-edge
Velocity (cm/s)
40
20
0
-20
-40
-60
-80
-100
0
100
200
300
400
500
600
700
800
900
Distance (km)
SBL : 40.6 km (linear case)
60.7 km (non-linear case)
non-linear
linear

Fig. 4-39. Comparisons of (C) meridional velocity profile along the western wall of the shelf (I=2 in Fig. 4-38), and (D) Longitudinal variation of the ratio between the on-shelf transport and the applied Sverdrup transport in the deep ocean between the linear and non-linear experiments in Fig. 4-38.

(C) V along the western wall

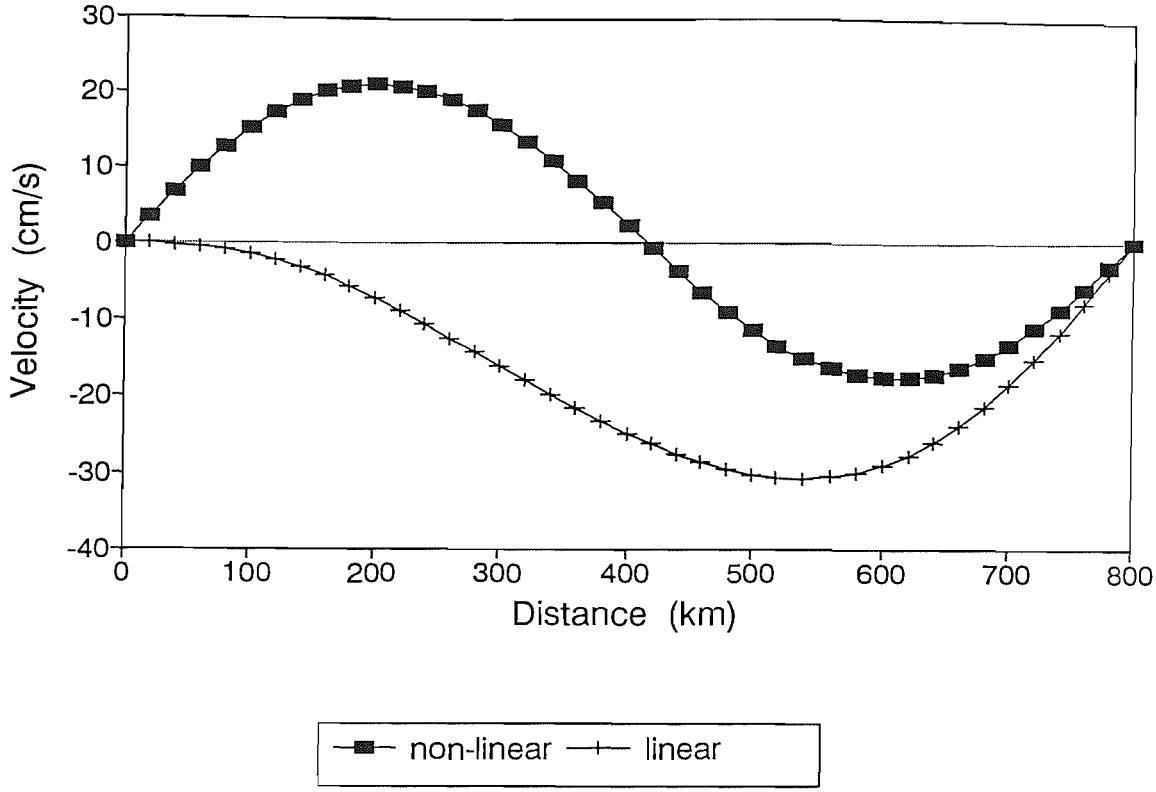

(D) On-shelf volume transport

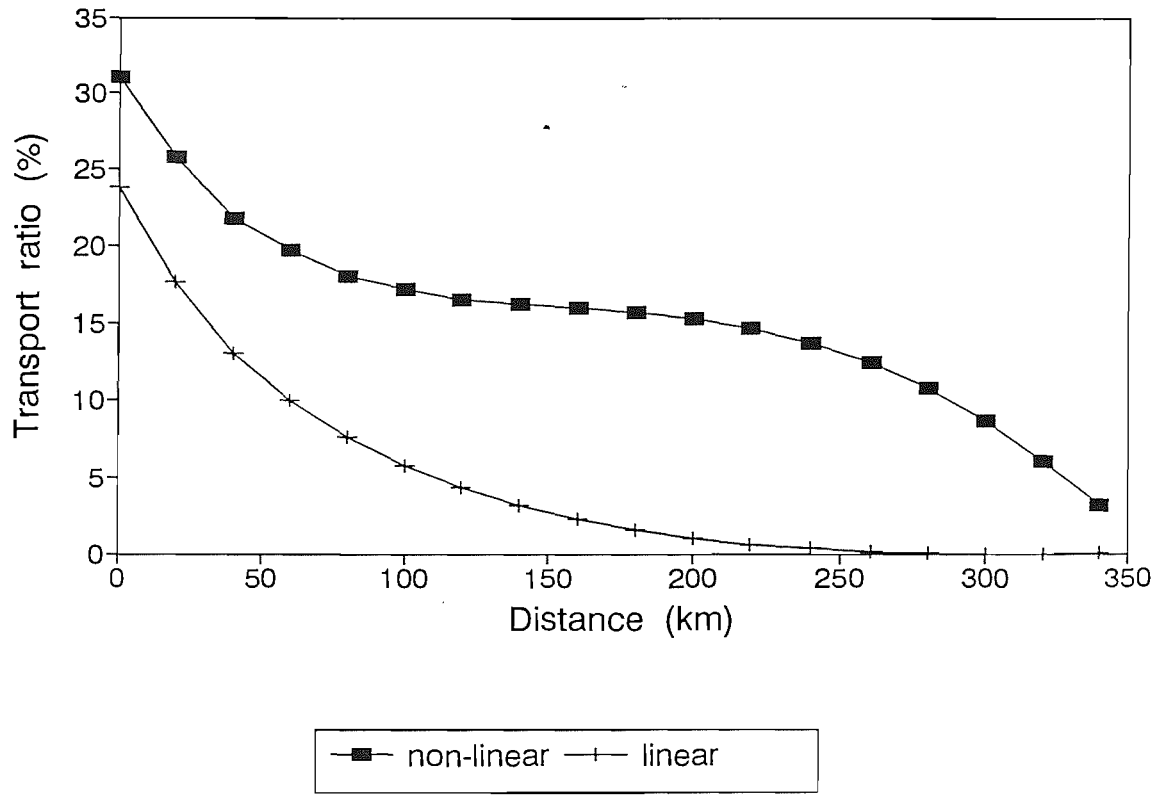

Fig. 4-40. Contours of streamlines for two non-linear experiments (A) $p_y < 0$, $h_x > 0$ (ECS case), and (B) $p_y > 0$, $h_x > 0$ (MAB case). The p_y and h_x represent the meridional pressure gradient along the WBC and the zonal gradient of topography respectively. Applied Sverdrup transports are the same for both cases.

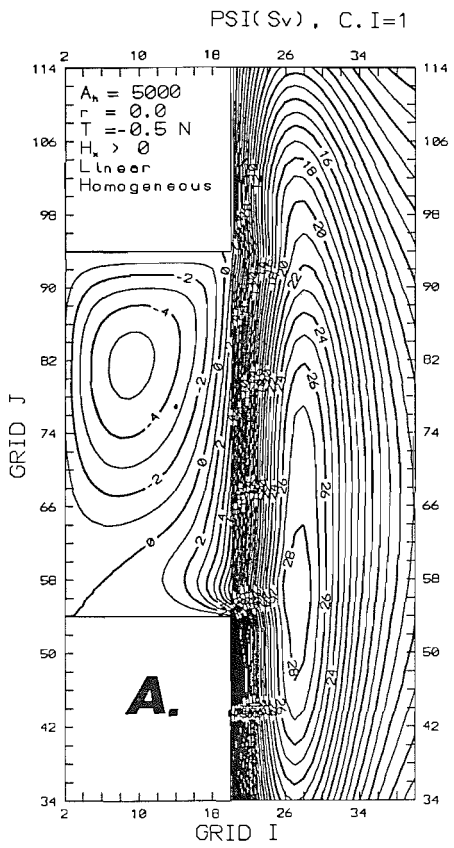
PSI(Sv) , C. I=1
A_h = 5000
r = 0.0
T =-0.5 N
H_x > 0
Linear
Homogeneous
A.
GRID J
GRID I

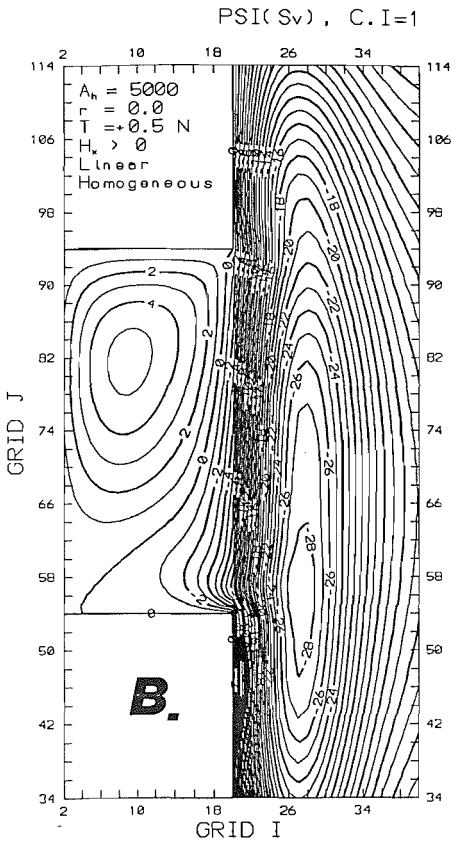
PSI(Sv) , C. I=1
A_h = 5000
r = 0.0
T =+0.5 N
H_x > 0
Linear
Homogeneous
B.
GRID J
GRID I

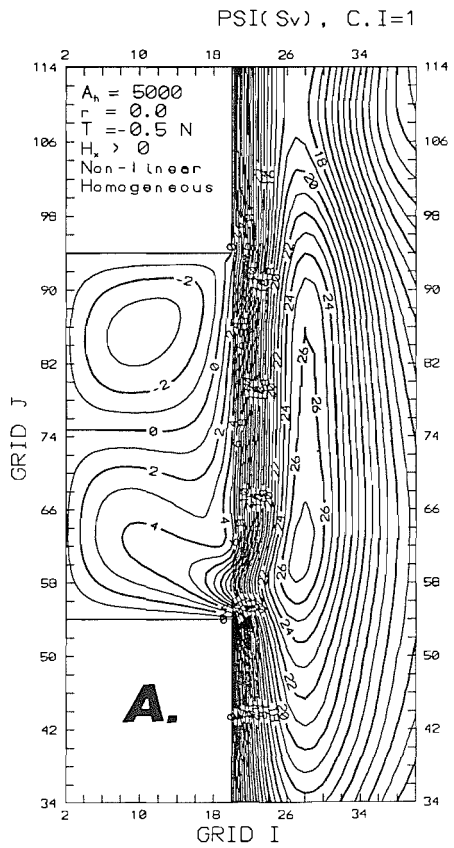
PSI(Sv) , C. I=1
A_h = 5000
r = 0.0
T =-0.5 N
H_x > 0
Non-Linear
Homogeneous
A.
GRID J
GRID I

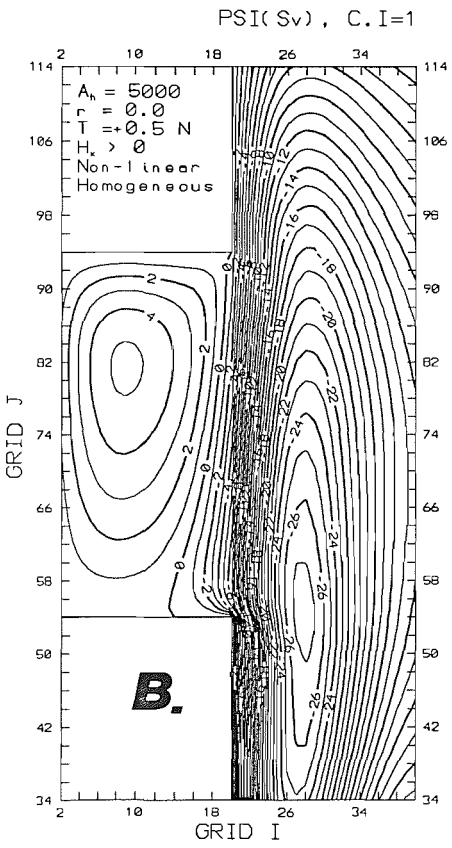
PSI(Sv) , C. I=1
A_h = 5000
r = 0.0
T =+0.5 N
H_x > 0
Non-Linear
Homogeneous
B.
GRID J
GRID I

Fig. 4-41. Contours of streamlines from the barotropic lateral friction model of Böning (1986) for the case (A) $\delta_I / \delta_L = 0.2$, (B) $\delta_I / \delta_L = 0.5$, (C) $\delta_I / \delta_L = 0.8$, (D) $\delta_I / \delta_L = 1.0$, and (E) $\delta_I / \delta_L = 1.5$. δ_I and δ_L represent the non-dimensional inertial and diffusive scales of western boundary layer respectively, defined by the equation (II-3-8) in the text.

A.

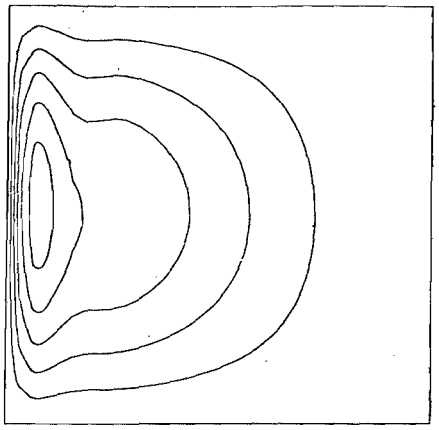

B.

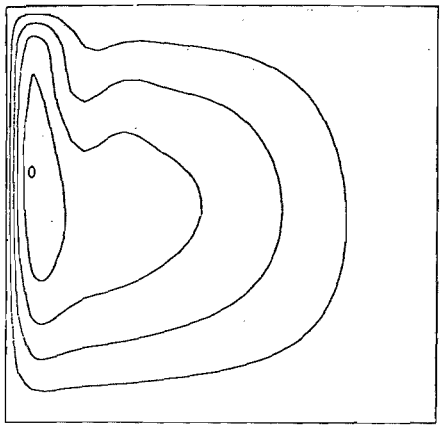

C.

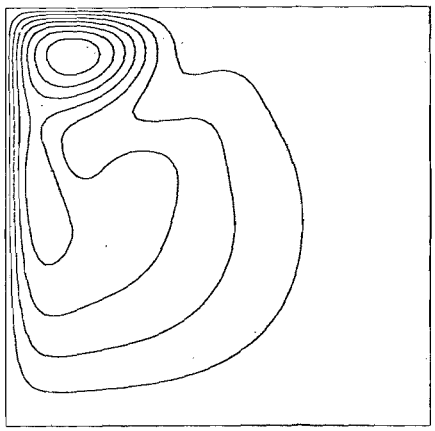

D.

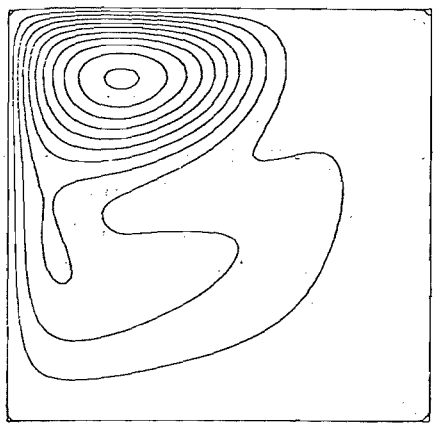

E.

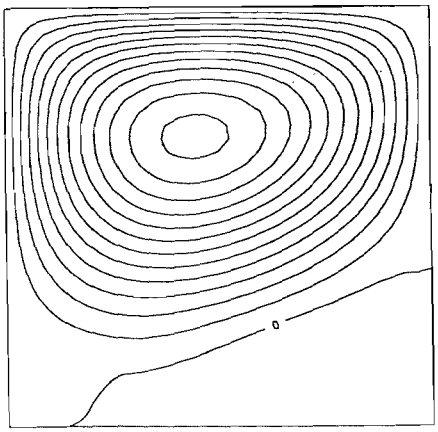

Fig. 4-42. Ratio between the maximum on-shelf transport along the shelf-edge and the applied Sverdrup transport for the linear experiments in Table 4-2, and the non-linear experiments in Table 4-4. ϵ in the figure indicates the ratio between the inertial boundary layer scale and the diffusive boundary layer scale (δ_I / δ_L).

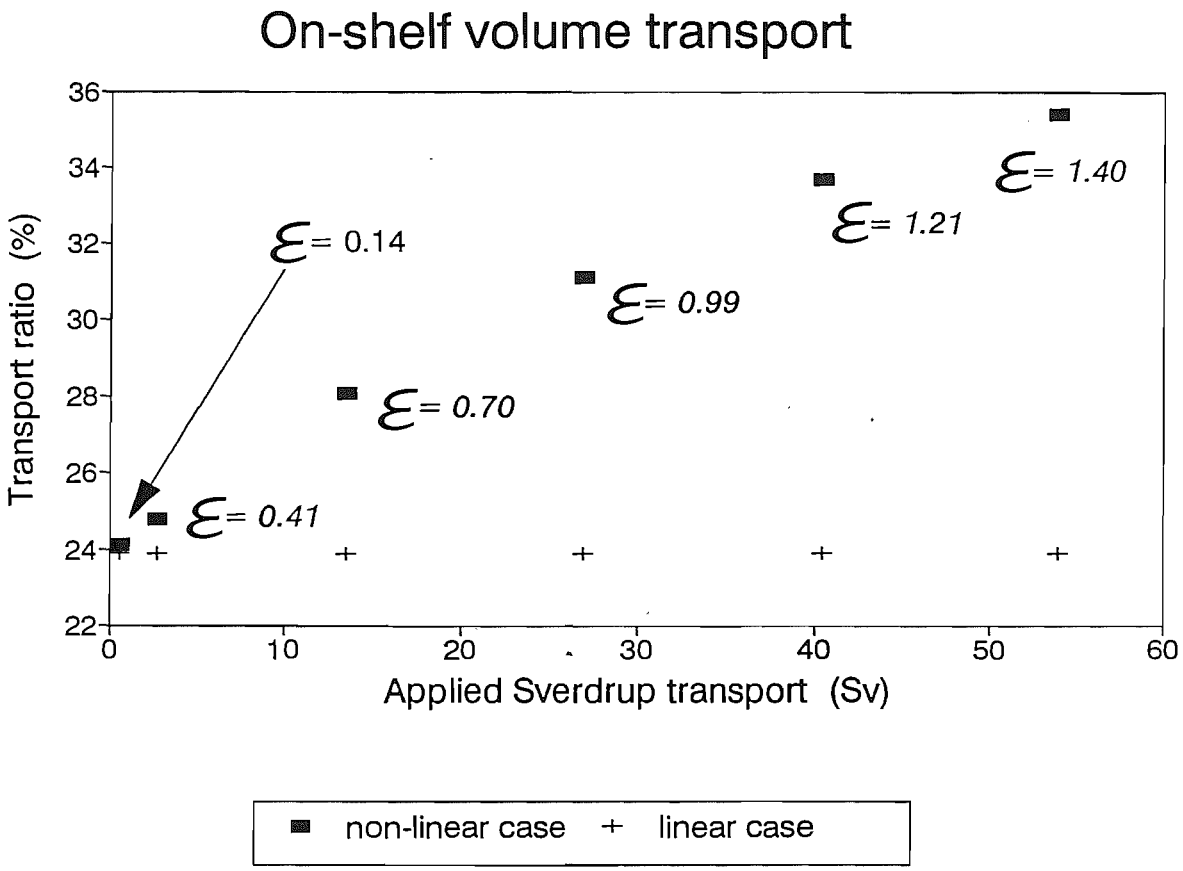
On-shelf volume transport
Transport ratio (%)
36
34
32
30
28
26
24
22
0
10
20
30
40
50
60
Applied Sverdrup transport (Sv)
ε= 0.14
ε= 0.41
ε= 0.70
ε= 0.99
ε= 1.21
ε= 1.40
non-linear case
linear case

Fig. 4-43. Contours of streamlines in the whole domain for the case (A) $\epsilon = 0.14$, (B) $\epsilon = 0.31$, and (C) $\epsilon = 0.70$.

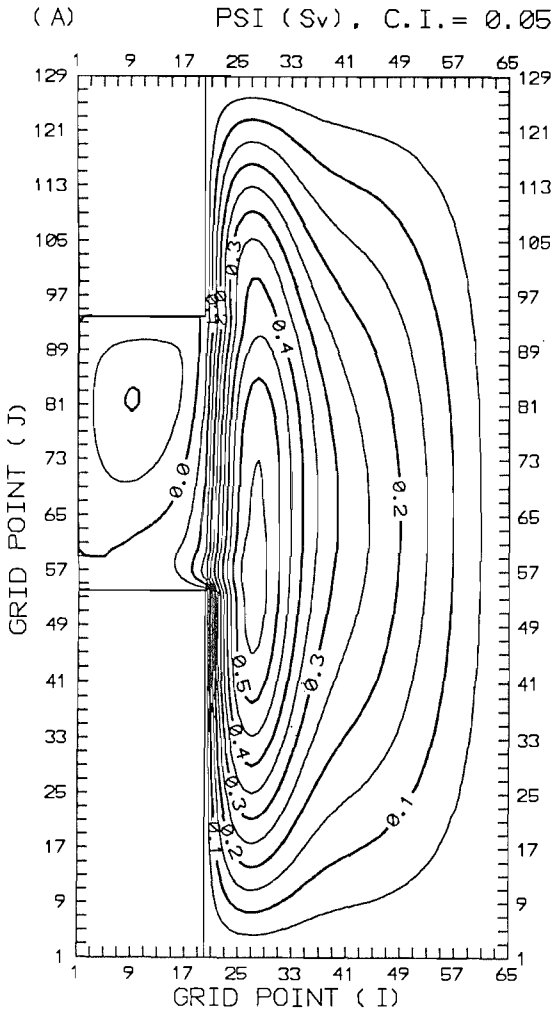
(A)
PSI (Sv), C.I.= 0.05
GRID POINT (J)
GRID POINT (I)

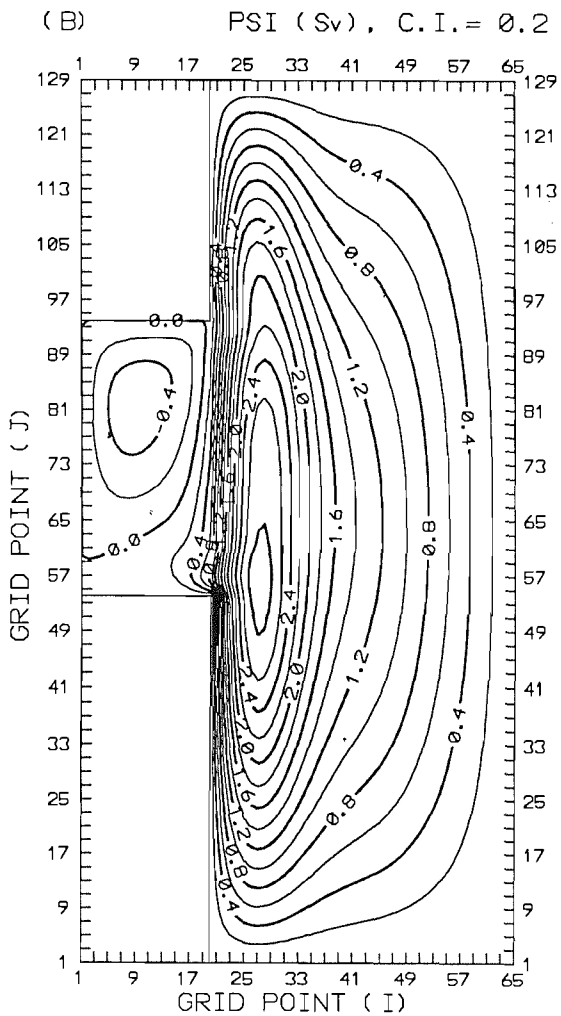
(B)
PSI (Sv), C.I.= 0.2
GRID POINT (J)
GRID POINT (I)

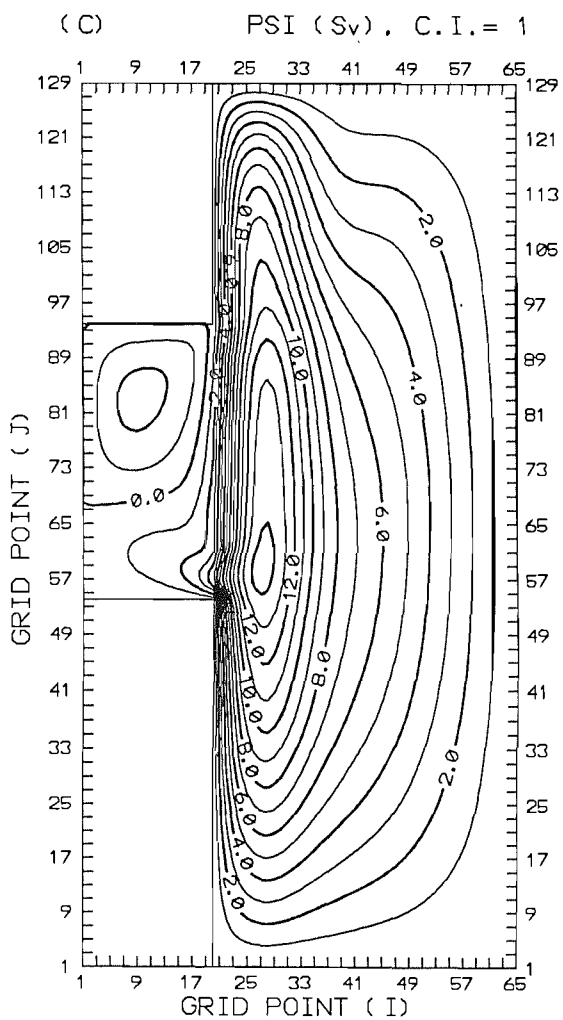
(C)
PSI (Sv), C.I.= 1
GRID POINT (J)
GRID POINT (I)

Fig. 4-43. Contours of streamlines in the whole domain for the case (D) $\epsilon = 0.99$, (E) $\epsilon = 1.21$, and (F) $\epsilon = 1.40$.

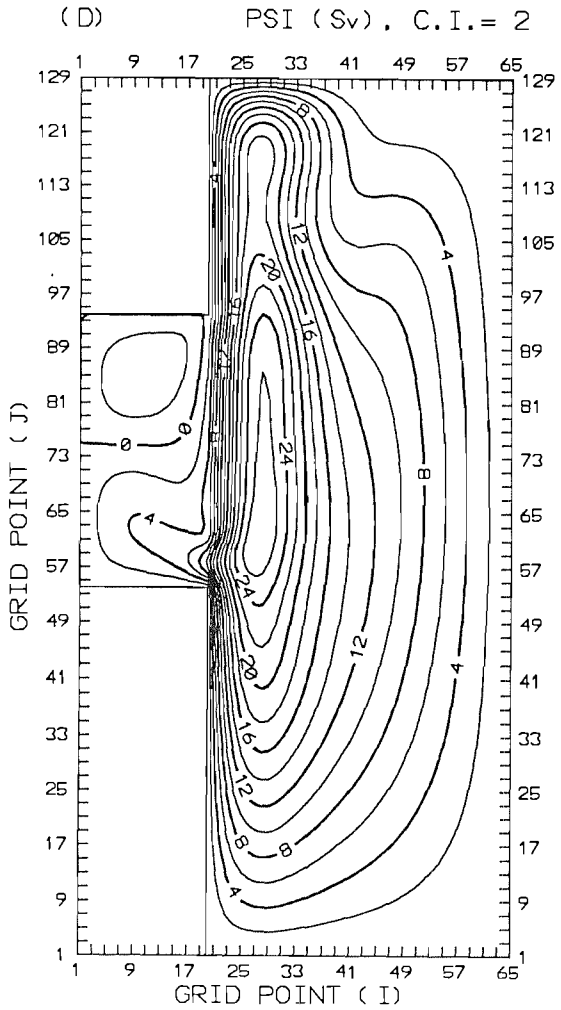
(D) PSI (Sv), C.I.= 2
GRID POINT (J)
GRID POINT (I)

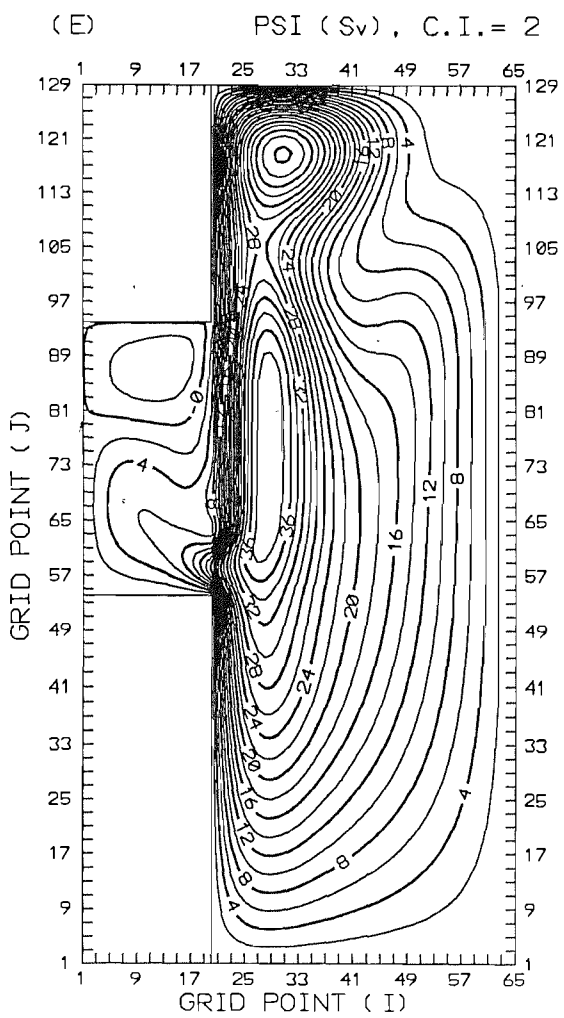
(E) PSI (Sv), C.I.= 2
GRID POINT (J)
GRID POINT (I)

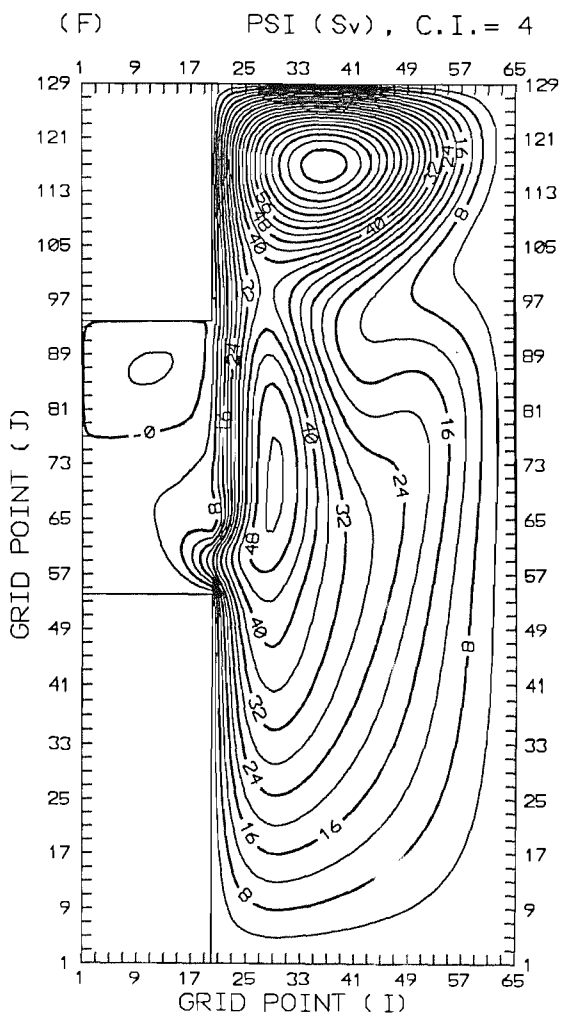
(F) PSI (Sv), C.I.= 4
GRID POINT (J)
GRID POINT (I)

Fig. 4-44. Contours of streamlines in the shelf and adjacent deep ocean for the case (A) $\epsilon = 0.14$, (B) $\epsilon = 0.31$, and (C) $\epsilon = 0.70$.

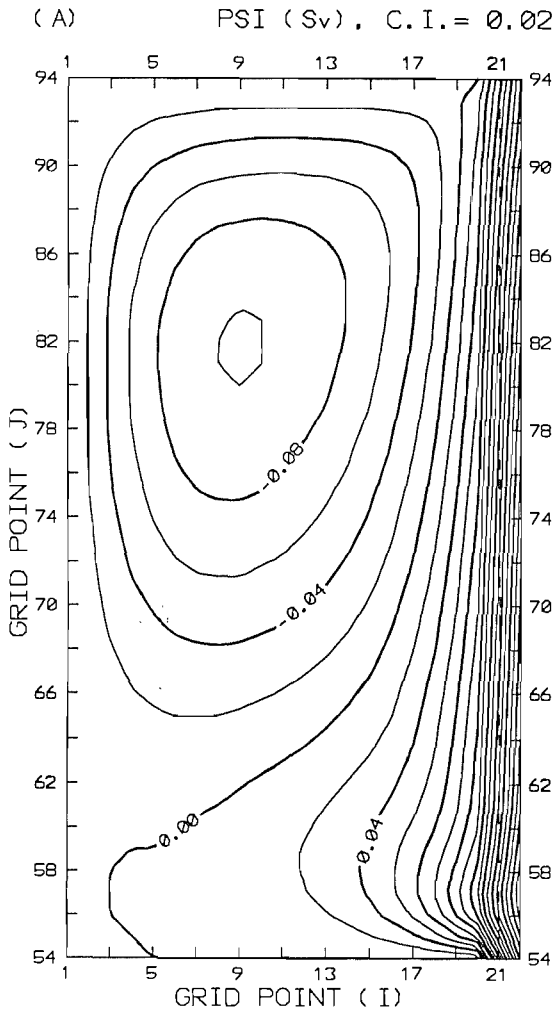
(A) PSI (Sv), C.I.= 0.02
GRID POINT (J)
GRID POINT (I)
-0.08
-0.04
0.00
0.04

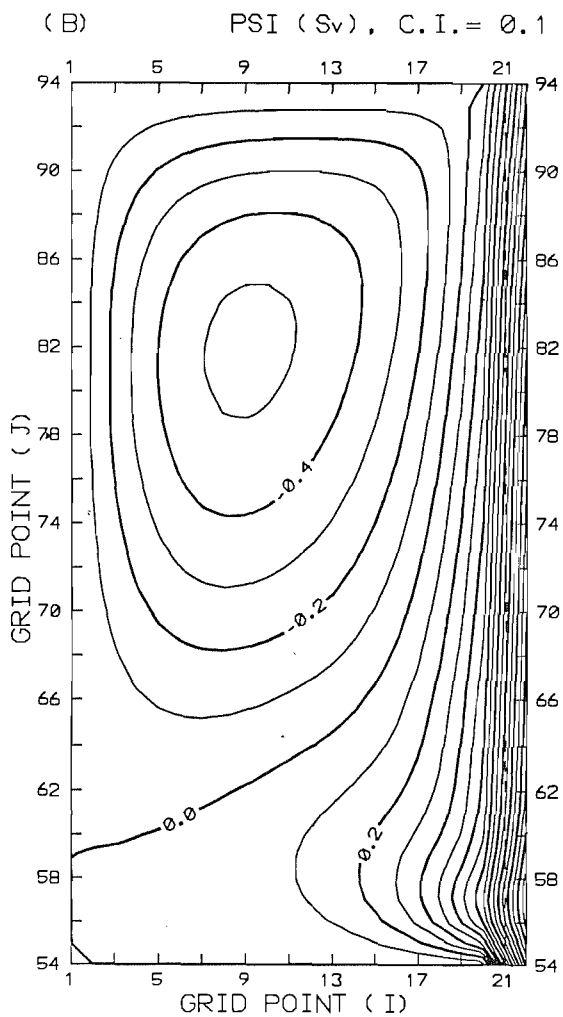
(B) PSI (Sv), C.I.= 0.1
GRID POINT (J)
GRID POINT (I)
-0.4
-0.2
0.0
0.2

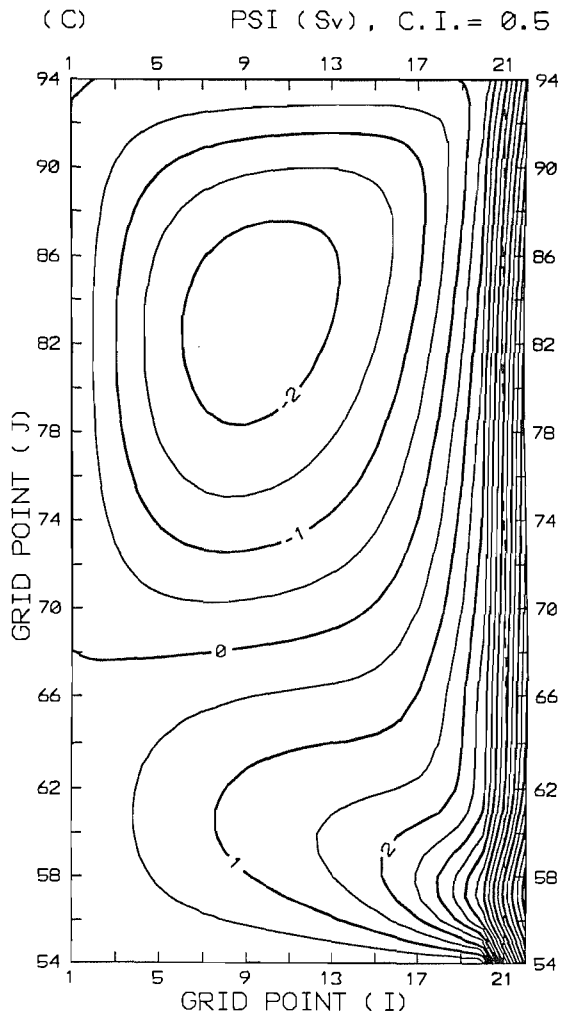
(C) PSI (Sv), C.I.= 0.5
GRID POINT (J)
GRID POINT (I)
-2
-1
0
1
2

Fig. 4-44. Contours of streamlines in the shelf and adjacent deep ocean for the case (D) $\epsilon = 0.99$, (E) $\epsilon = 1.21$, and (F) $\epsilon = 1.41$.

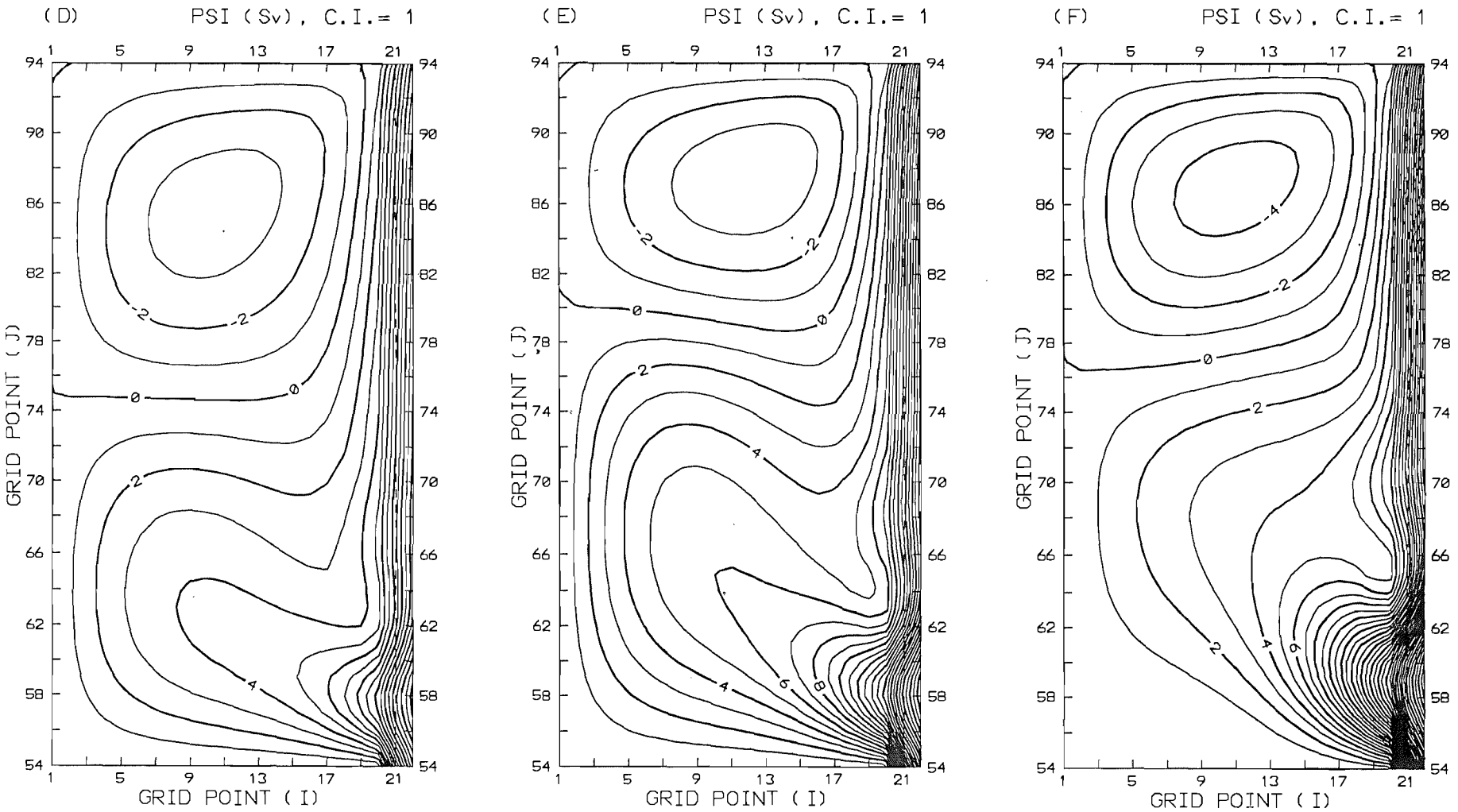
(D) PSI (Sv), C.I.= 1
(E) PSI (Sv), C.I.= 1
(F) PSI (Sv), C.I.= 1
GRID POINT (J)
GRID POINT (I)
1
5
9
13
17
21
54
58
62
66
70
74
78
82
86
90
94
0
2
4
6
8

Fig. 4-45. (A) Zonal velocity profiles along the southern wall (J=55 in Fig. 4-44), and (B) meridional velocity profiles along the western wall (I=2 in Fig. 4-44) for the all experiments in Table 4-4.

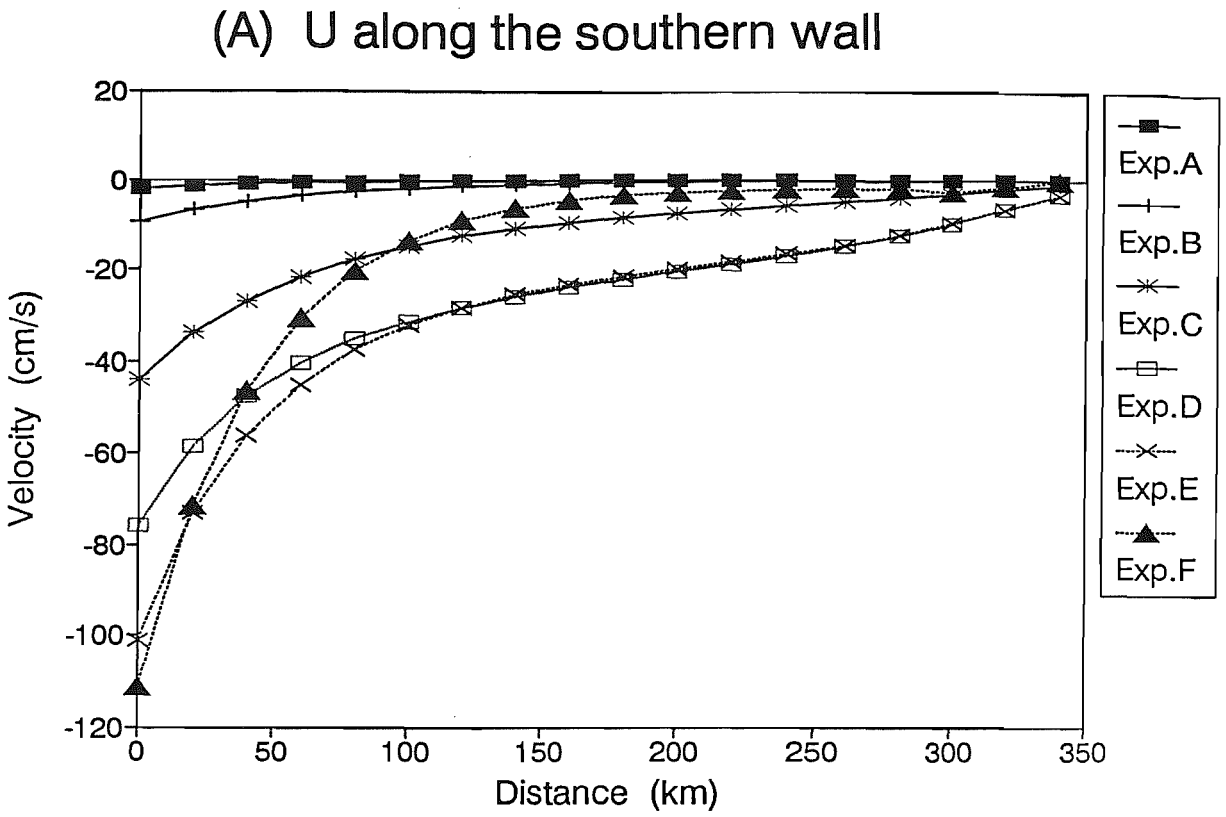
(A) U along the southern wall
Velocity (cm/s)
20
0
-20
-40
-60
-80
-100
-120
0
50
100
150
200
250
300
350
Distance (km)
Exp.A
Exp.B
Exp.C
Exp.D
Exp.E
Exp.F

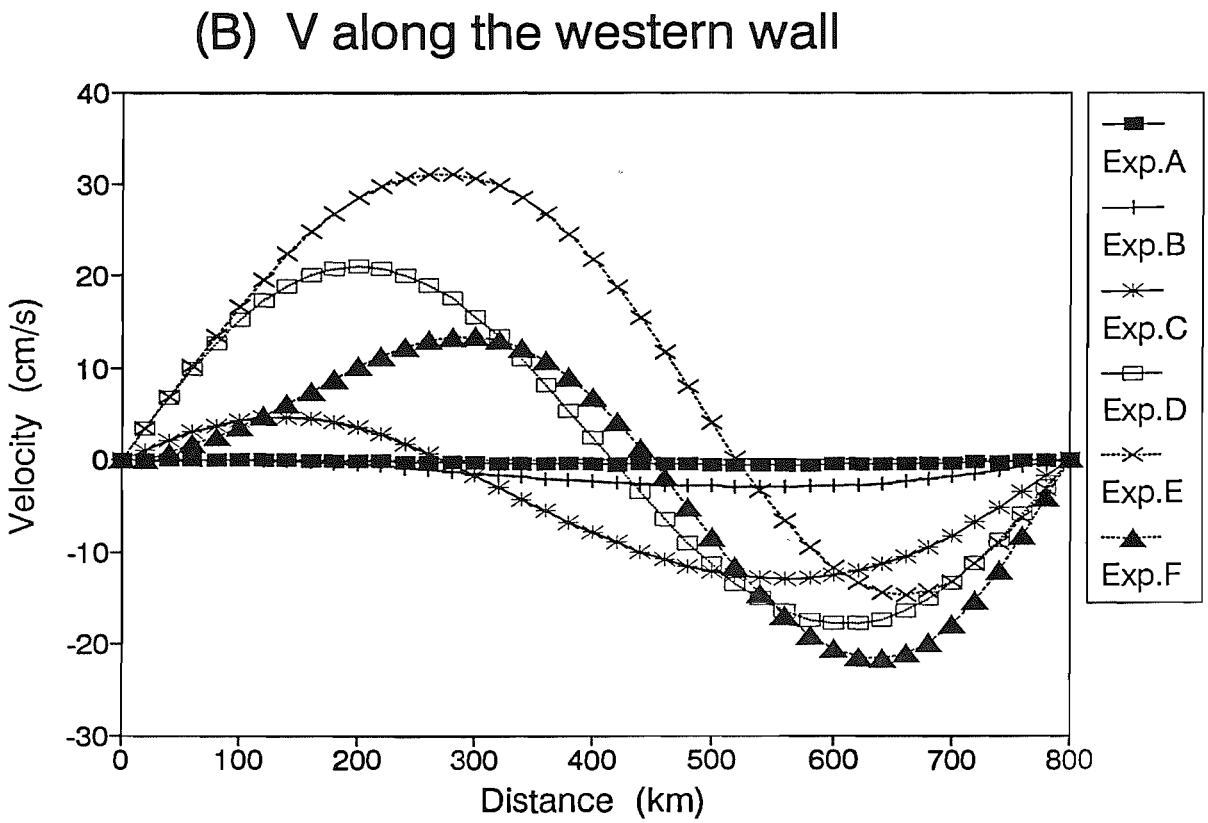
(B) V along the western wall
Velocity (cm/s)
40
30
20
10
0
-10
-20
-30
0
100
200
300
400
500
600
700
800
Distance (km)
Exp.A
Exp.B
Exp.C
Exp.D
Exp.E
Exp.F

Fig. 4-45. (C) Zonal velocity profiles along the shelf-edge (I=19 in Fig. 4-44), and (D) longitudinal variation of the ratio between the on-shelf transport and the applied Sverdrup transport in the deep ocean for the all experiments in Table 4-4.

(C) U along the shelf-edge

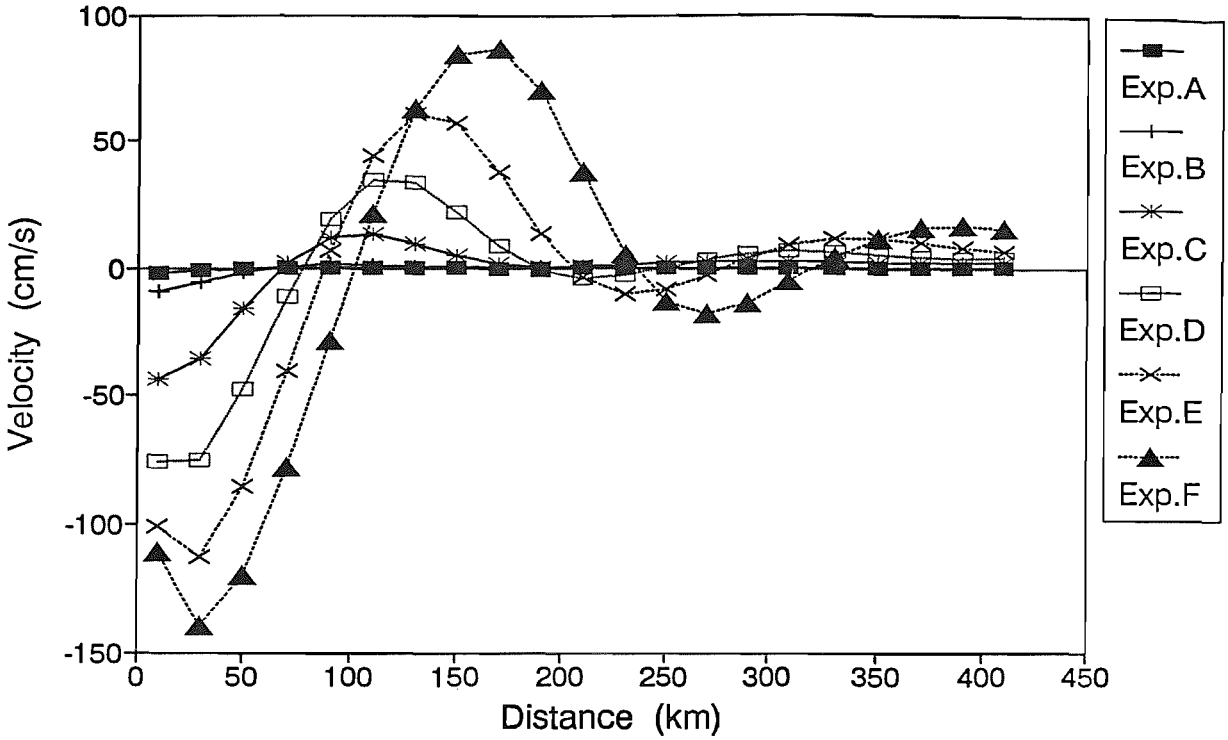

(D) On-shelf volume transport

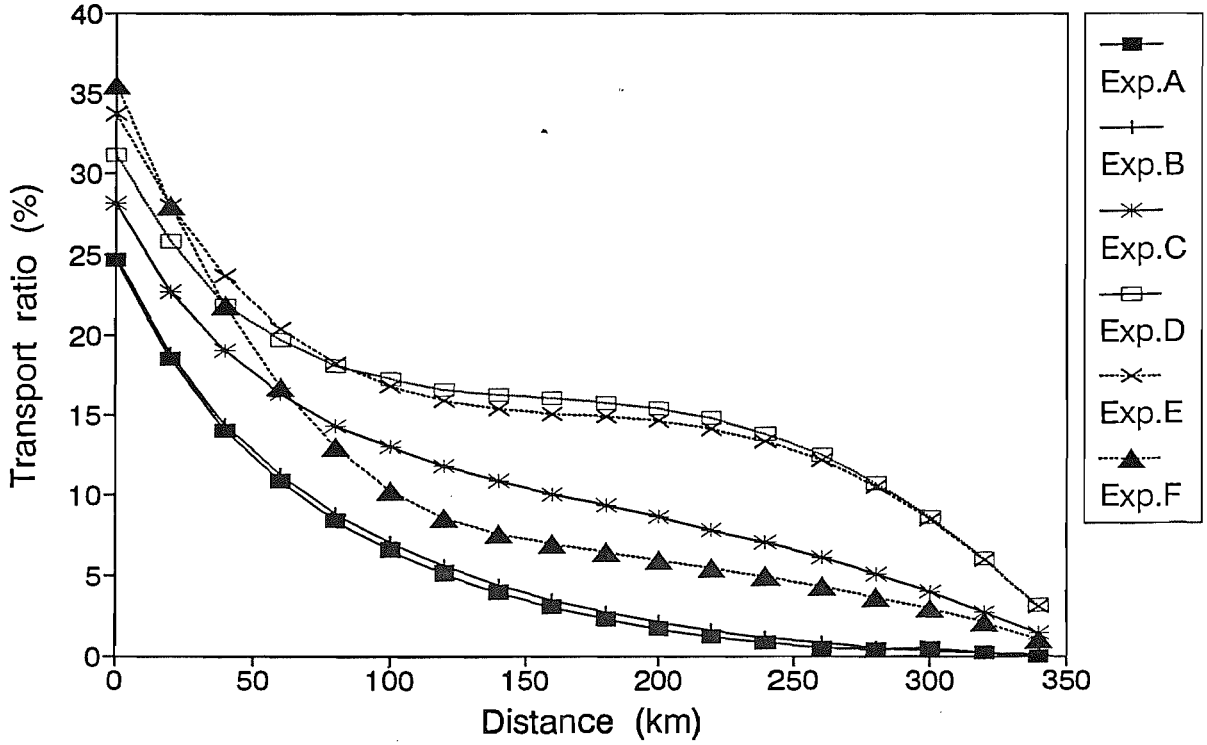

Fig. 4-46. Meridional distribution of terms in the vorticity equation (II-2-13) (A) along the shelf-edge (I=19 and J=55~93 in Fig. 4-44), and (B) along the same section as (A), but J=65~93. DIVE, ADVE, LATF, and BETA represent the topographic vorticity tendency, relative vorticity advection, vorticity diffusion, and planetary vorticity tendency respectively.

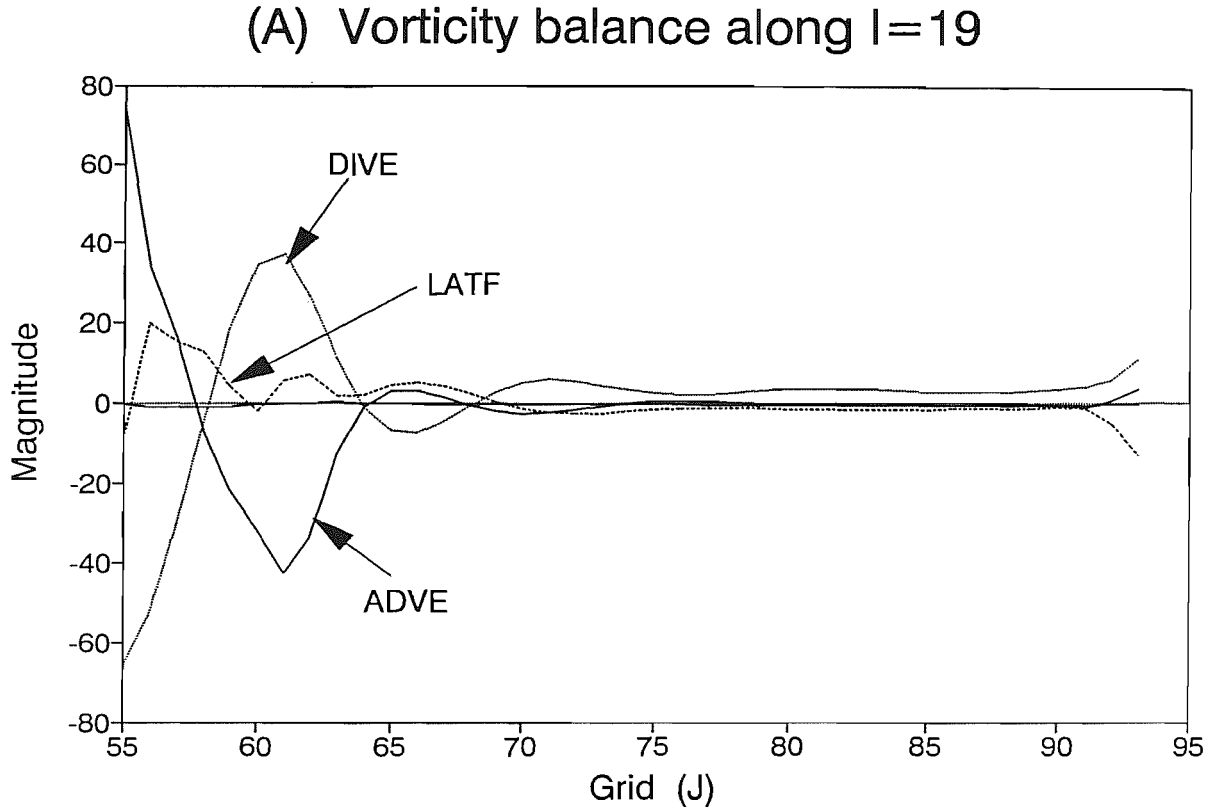
(A) Vorticity balance along I=19
80
60
40
20
0
-20
-40
-60
-80
Magnitude
DIVE
LATF
ADVE
55
60
65
70
75
80
85
90
95
Grid (J)

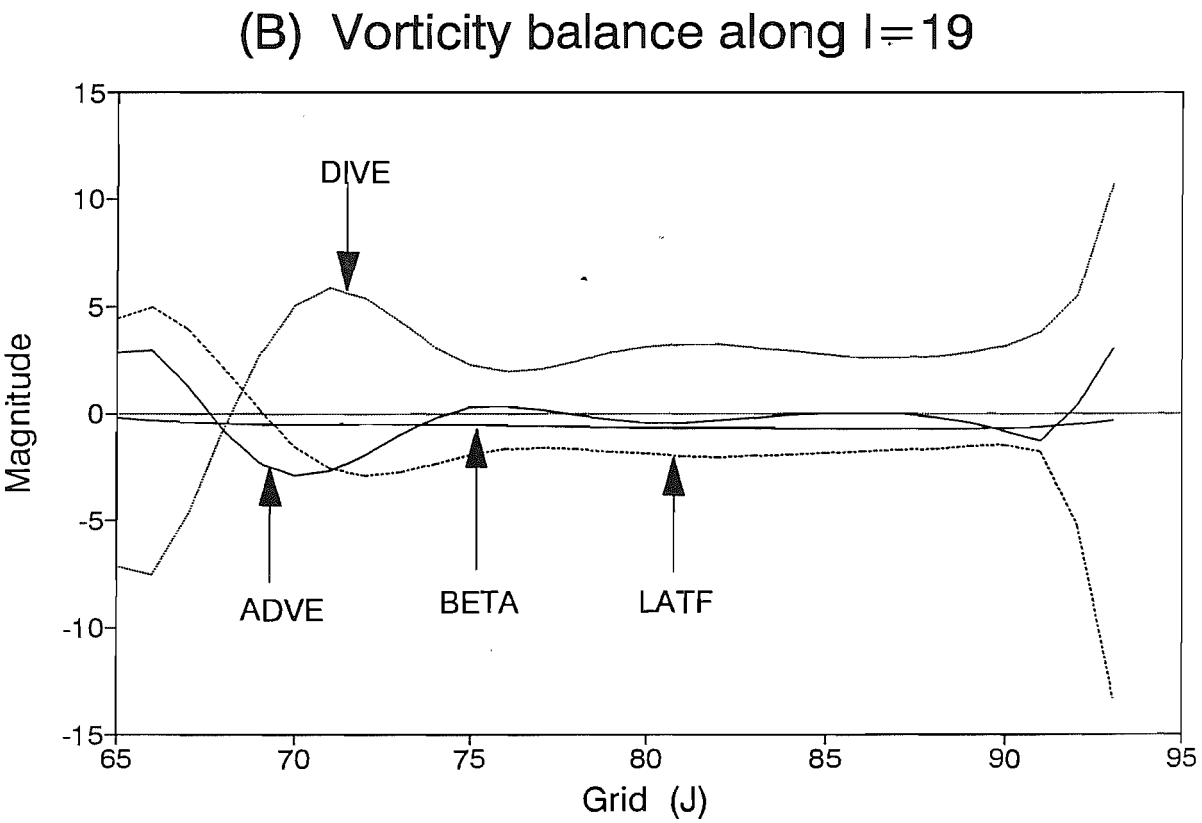
(B) Vorticity balance along I=19
15
10
5
0
-5
-10
-15
Magnitude
DIVE
ADVE
BETA
LATF
65
70
75
80
85
90
95
Grid (J)

Fig. 4-47. Distribution of relative vorticity near the southern part of the shelf (A) for a linear case (experiment C in Table 4-2), and for two non-linear cases of (B) $\epsilon = 1.2$ (experiment E in Table 4-4), and (C) $\epsilon = 1.4$ (experiment F in Table 4-4). Dotted areas represent the region of positive relative vorticity.

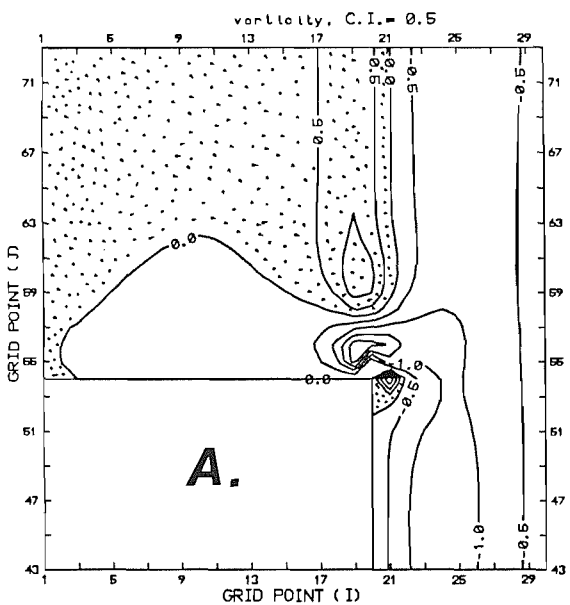
vorticity, C.I.= 0.5
GRID POINT (J)
GRID POINT (I)
A.

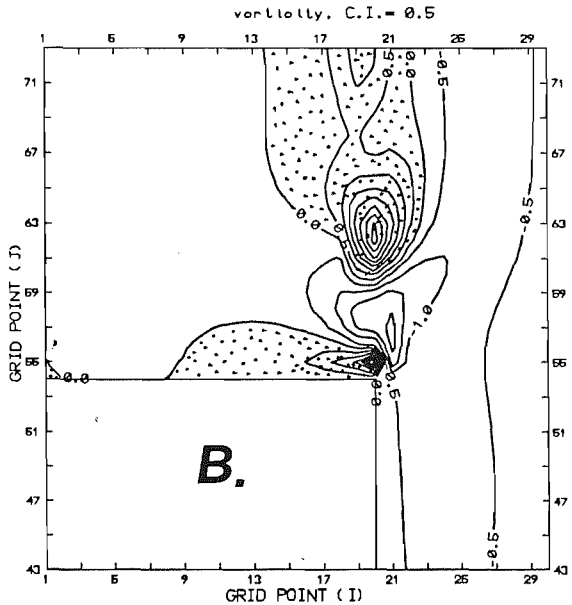
vorticity, C.I.= 0.5
GRID POINT (J)
GRID POINT (I)
B.

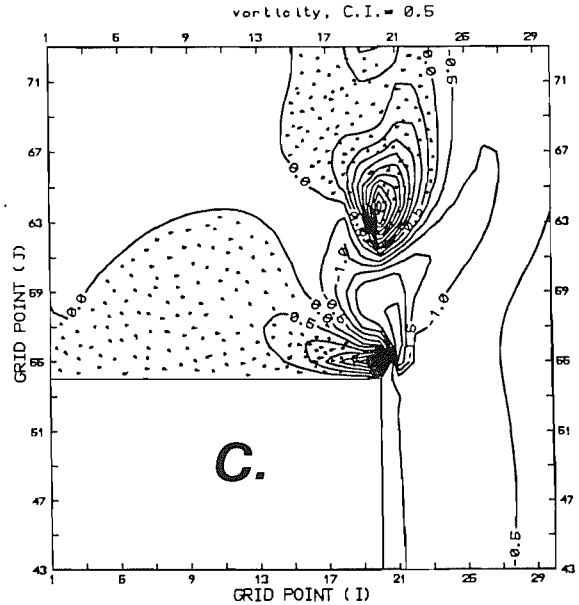
vorticity, C.I.= 0.5
GRID POINT (J)
GRID POINT (I)
C.

Fig. 4-48. Zonal distribution of terms in the vorticity equation (II-2-13) (A) along the southern wall of the shelf (J=56 and I=3~12 in Fig. 4-44), and (B) along the same section as (A), but I=13~19.

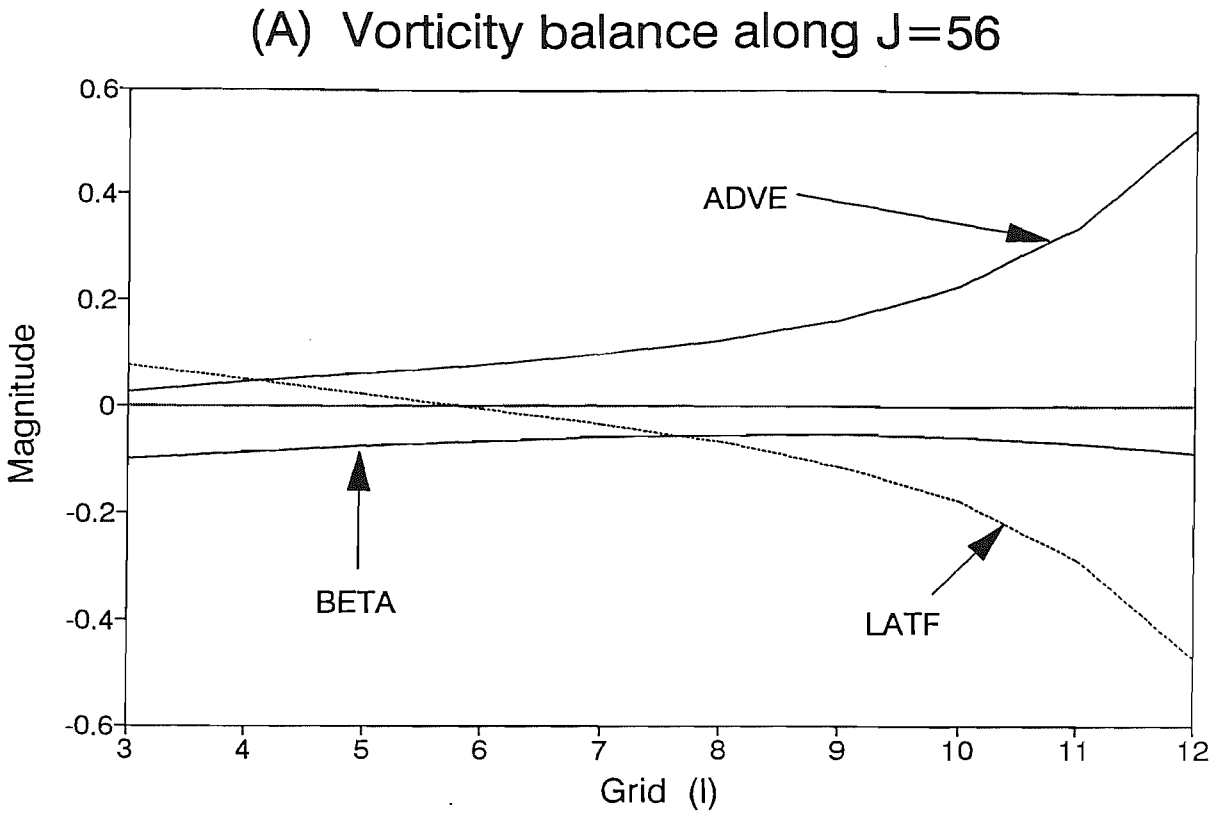
(A) Vorticity balance along J=56
0.6
0.4
0.2
0
-0.2
-0.4
-0.6
Magnitude
ADVE
BETA
LATF
3
4
5
6
7
8
9
10
11
12
Grid (I)

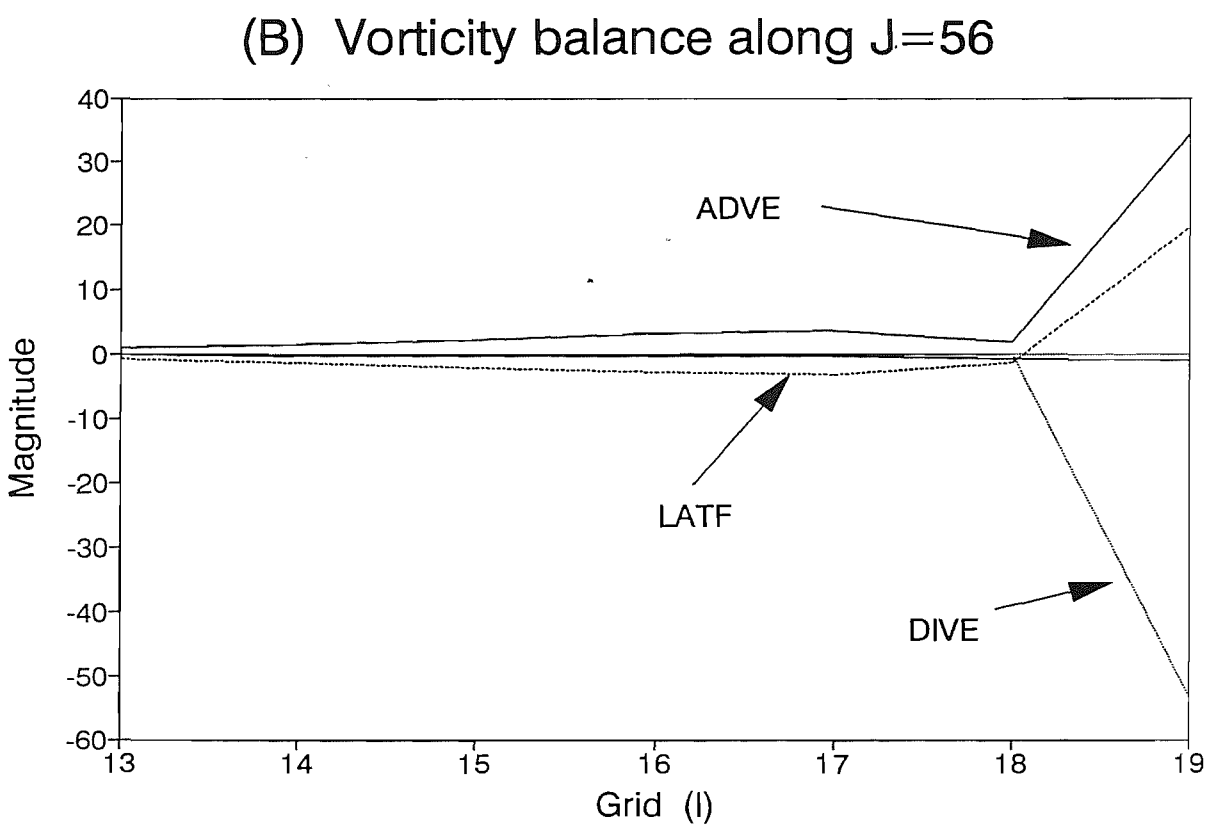
(B) Vorticity balance along J=56
40
30
20
10
0
-10
-20
-30
-40
-50
-60
Magnitude
ADVE
LATF
DIVE
13
14
15
16
17
18
19
Grid (I)

Fig. 4-49. Meridional distribution of terms in the vorticity equation (II-2-13) (A) along the western wall of the shelf (I=3 and J=55 ~ 93 in Fig. 4-44), and (B) along the mid-longitude of the shelf (I=10 and J=55 ~ 93 in Fig. 4-44).

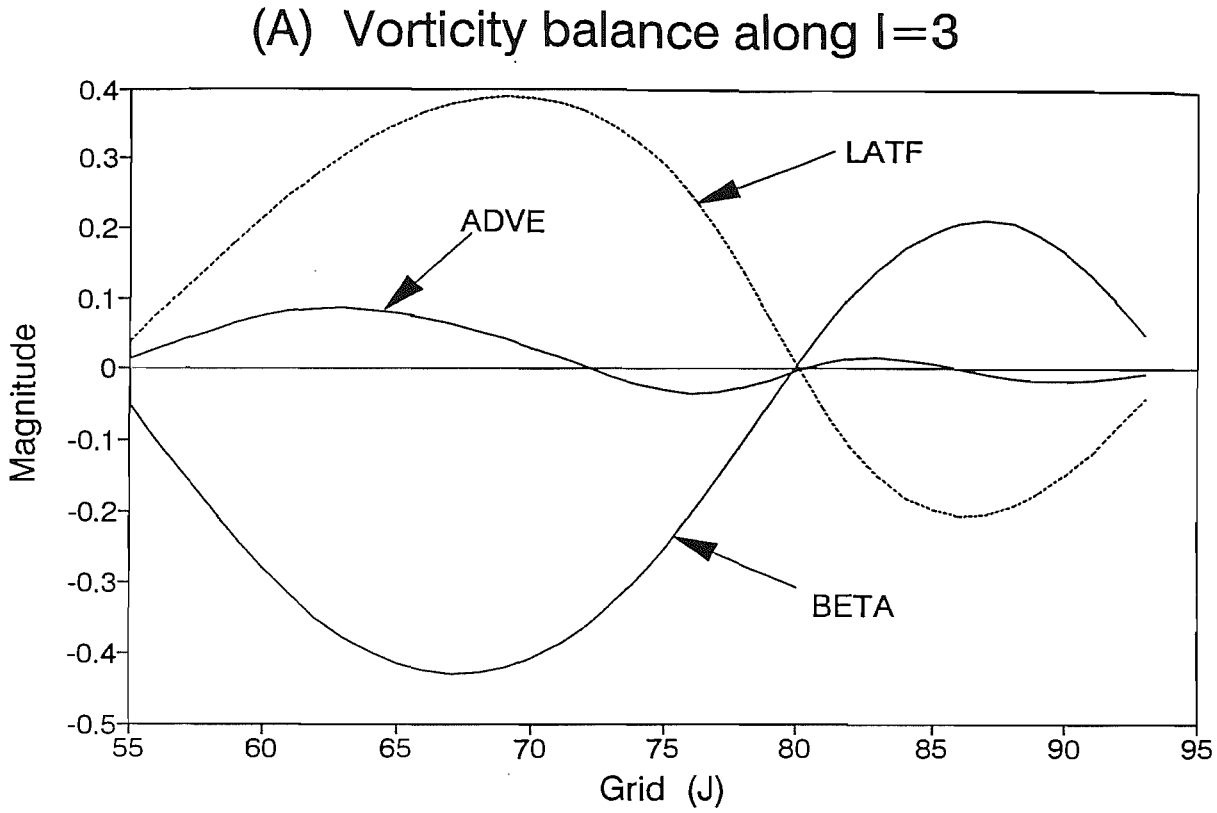
(A) Vorticity balance along I=3
LATF
ADVE
BETA
Magnitude
Grid (J)
0.4
0.3
0.2
0.1
0
-0.1
-0.2
-0.3
-0.4
-0.5
55
60
65
70
75
80
85
90
95

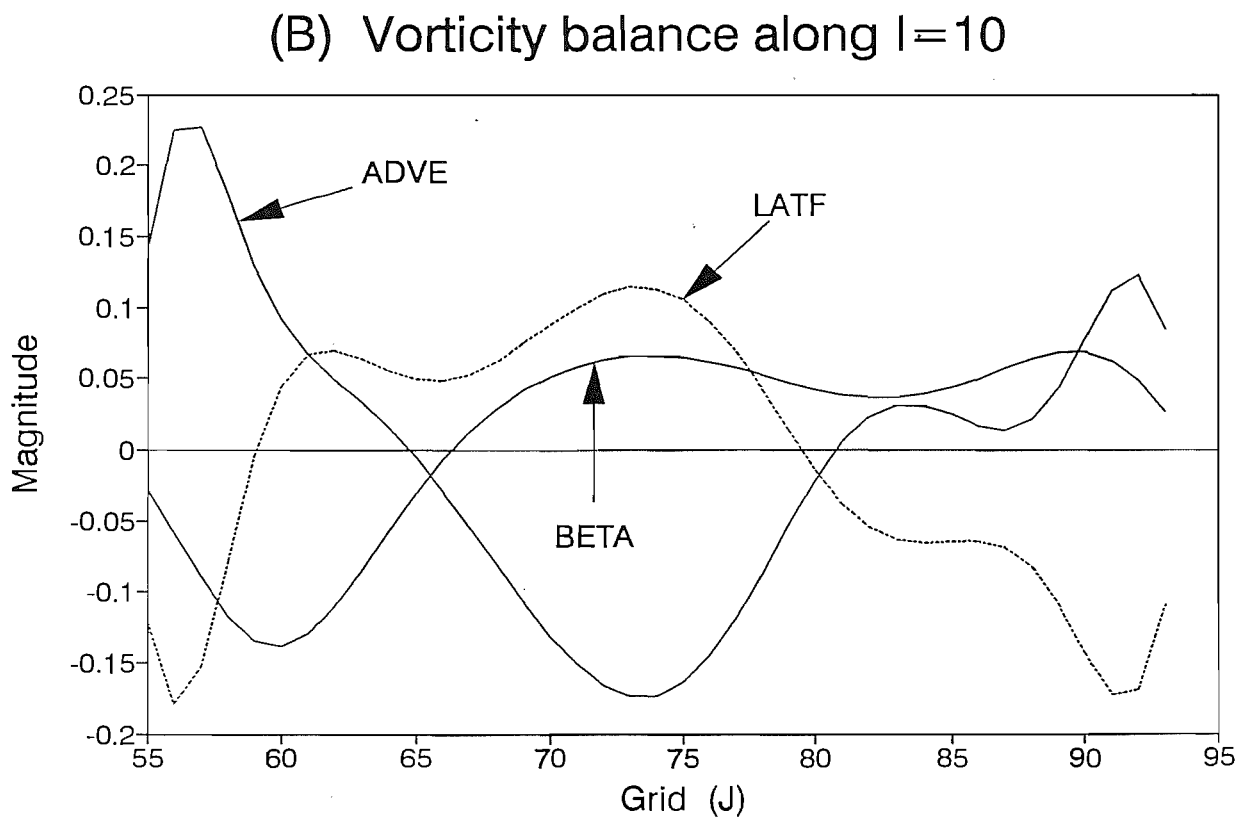
(B) Vorticity balance along I=10
ADVE
LATF
BETA
Magnitude
Grid (J)
0.25
0.2
0.15
0.1
0.05
0
-0.05
-0.1
-0.15
-0.2
55
60
65
70
75
80
85
90
95

CHAPTER V. RESULTS - MARGINAL SEA MODELS

V-1. INTRODUCTION

Warm and saline equatorial water is supplied to the Japan Sea (JS) through the Korea Strait (KS) by a branch of the Kuroshio called the Tsushima Current (TC). Most of the TC (~ 70 %) flows out of the JS through the Tsugaru Strait (TS) as shown in Fig. 1-1. As was reviewed in chapter I, the annual cycle of the volume transport of the TC has a minimum in spring and maximum in autumn which is almost 180° out of phase with the baroclinic transport of the Kuroshio in the ECS, but in phase with that of the Kuroshio Current System. The maximum volume transport of the TC is reported to be about 2 Sv, which is less than 10 % of the Kuroshio in the ECS, whilst the minimum value is only a few percent of the Kuroshio. Some factors controlling the influx to the JS which have been proposed were also reviewed in chapter I.

This chapter investigates factors controlling the influx to the Japan Sea mainly in an idealised configuration and topography shown in Fig. 3-1 (b), and also in a more realistic domain. In particular, we investigate the effects of the large scale circulation in the Pacific on the variation of the influx to the JS such as the separation latitude of the Kuroshio and the strength of the subpolar gyre. This examination was motivated by the facts that the TS, through which the TC exits to the North Pacific, is located in the southwestern part of the subpolar gyre and the separation latitude of the Kuroshio changes in time as well as the transport of the Kuroshio. Cross-gyre transport, therefore, takes place through the JS although it is small.

V-2. A SIMPLE MARGINAL SEA MODEL

Minato and Kimura (1980) estimated the amount of penetration of the WBC into

a marginal sea located at the western part of the subtropical gyre analytically in a simple model ocean shown in Fig. 1-13. They investigated the various factors affecting the influx to the marginal sea. In their model ocean the influx to the marginal sea was assumed to be caused by the pressure difference between two straits associated with the Stommel-type wind-driven single gyre circulation in the deep ocean, but they did not examine the effects of a varying circulation pattern in the deep ocean on the influx.

Before describing the results obtained from a more complicated model configuration, it is useful to approach the problem in a simpler domain like the model ocean of Minato and Kimura (1980) but with a double gyre system. After establishing a stable antisymmetric double gyre circulation in a flat-bottomed deep ocean (Fig. 5-1 (A)), shallow rectangular ocean basins which are connected with the deep ocean through two narrow (100 km) and short (40 km) straits were introduced to the various parts of the western boundary as shown in Fig. 5-2. The Sverdrup value of each gyre in the deep ocean is 54 Sv. The depth of the deep ocean and the shallow basins are 400 m and 200 m respectively, and the depth change between them takes place over one grid spacing. There is no bottom friction and the eddy viscosity coefficient of 5000 m^2s^{-1} is used for the all experiments. As there is no wind stress applied in the shallow basins, the resulting circulation in the shallow basins is expected to be driven by the pressure distribution along the western boundary of the deep ocean.

Fig. 5-1 (B) shows a meridional profile of the pressure along the western boundary of the deep ocean before introducing the shallow ocean basins. Note that the separation latitude of the western boundary currents coincides exactly with the latitude of vanishing wind stress curl as the linear model was used. The pressure increases from the southernmost point to the grid point J=20 where a local pressure maximum occurs. From the J=20 northward the pressure decreases along the western boundary of the subtropical gyre. A pressure minimum occurs to the north of the separation latitude, in the southern part of the subpolar gyre at the grid point J=106. The pressure gradient across the zero wind stress curl line is necessary to maintain the separated eastward flow in the northern (southern) part of the subtropical (subpolar) gyre. The pressure increases northwards from the J=106 along the western boundary of the subpolar gyre.

Table 5-1 summarises the model parameters and the amount of influx to the shallow basins for four experiments in Fig. 5-2. In the experiment 2 where two shallow basins are located at the western part of the subtropical and subpolar gyres, a part of the boundary current penetrates into the shallow basins through the strait located at the high pressure region. Even when the northern strait is located in the southern part of the subpolar gyre (experiment 3), the penetration takes place through the southern strait in so far as the northern strait is placed to the south of the pressure minimum latitude in Fig. 5-1 (B). The amount of penetration for experiment 3, however, is only one third of that for experiment 2 in spite of the larger pressure difference between two straits for experiment 3.

Table 5-1. Volume transport of the boundary currents penetrating onto the shallow basins for four experiment 2 ~ 5.

Experiment	1	2	3	4	5
ℓ_y (km)	100	100	100	100	40
influx (Sv)		-2.1*	1.4	-3.0	-2.1
		4.7**			
Remarks	deep ocean model	two marginal seas			narrow straits

where,

ℓ_y : width of straits

* : influx to the northern basin

** : influx to the southern basin.

Positive (negative) influx indicates that the penetration onto the shallow basins takes place through the southern (northern) straits of each basin.

When the northern strait is placed north of the latitude where the pressure minimum occurs (experiment 4), the circulation in the shallow basin changes radically. The penetration now takes place through the northern strait even though the undisturbed pressure is lower than that at the southern strait. Reducing the width of

both straits (experiment 5) from 100 km (5 grid points) to 40 km (2 grid points) results in a reduction of the influx by about 30 %, but the penetration still takes place through the northern strait.

The above simple model results indicate that penetration of the boundary currents into the MS takes place through the straits located at the high pressure region after opening the straits when the pressure gradients across the both straits of each basin have the same sign (experiments 2 and 4). For experiment 4 the southern strait is placed at the outflow-favouring location and the northern strait at the inflow-favouring location in a geostrophic sense. For this case the on- and off-MS flows are directly implied by the cross strait pressure gradient rather than the pressure difference between two straits. However, it should be mentioned that the pressure inside the northern strait for experiment 4 is higher than that inside the southern strait after the on- and off-MS flows being established (not shown).

The reason for the reduced influx in experiment 3 compared with the influx to the southern basin in experiment 2 is unclear, in spite of the larger pressure difference between the two straits in experiment 3 than that for the southern basin in experiment 2.

In the real ocean the latitudinal length between the KS and the TS is fixed but the gyral system of the north Pacific changes so that the relative position of the TS to the separation latitude of the boundary current varies. The implication of the above simple experiments is that the variation of the large scale circulation can be an important factor in determining the influx to the JS.

Exhaustive experiments with the above simple configuration have not been performed. Instead, a series of experiments has been done with a configuration shown in Fig. 3-1 (b) which comprises both the idealised ECS and the JS as the continuation of the previous modelling investigation.

V-3. A SIMPLE SHELF-MARGINAL SEA MODEL

A shallow basin representing the JS is introduced in the northern part of the previous SSM (Fig. 3-1 (b)). For convenience, the basin will be referred to as a marginal sea (MS). The model domain now consists of the deep ocean, the shelf, and the MS, which will be referred to as a simple marginal sea model (SMSM). The marginal sea is connected with the deep ocean to the east and with the shelf to the south through two narrow straits (100 km wide). The southern and eastern straits will be referred to as the Korea Strait (KS) and the Tsugaru strait (TS) respectively. There is no topography within the marginal sea and the depth of the marginal sea is set to be the same as that of the shelf. We are interested in the amount of influx to the MS rather than a detailed circulation pattern within the MS. The model ocean was spun-up by a specified zonal wind stress only in the deep ocean as before. The resulting circulation of the shelf and the MS is, therefore, purely driven by the WBC established in the deep ocean.

V-3-1. A case experiment

A non-linear marginal sea model result without bottom friction is presented in this section. The SPEM was configured to the SMSM in which the northern land area of the previous SSM domain is replaced by the MS. Model parameters of the experiment is the same as those of the experiment D in Table 4-4.

Fig. 5-3 shows streamlines without and with the MS at an equilibrium state. Most of the water penetrating onto the shelf (~ 8.4 Sv) rejoins the WBC. At the southeastern part of the KS the penetrated water bifurcates, and a part of it (~ 1.1 Sv) enters the MS mainly through the eastern part of the KS. The planetary β-effect deflects the streamlines to the west within the MS, and the flow separates from the western wall at nearly the same location as the latitude of the TS and rejoins the WBC through the TS. Direct inflow from the WBC through the KS does not occur.

The SMSM result shows an increase in the maximum on-shelf transport by the same amount as the influx to the MS. The meridional penetration scale of the WBC onto the shelf is increased and the strength and scale of the northern recirculation cell in the shelf are reduced.

V-3-2. Factors affecting the influx to the MS

V-3-2-1. Non-linearity and bottom friction

Table 5-2 shows the model parameters for three experiments to examine the effects of the non-linearity and bottom friction on the amount of influx. Figs 5-4 and 5-5 show the streamlines of the three experiments at an equilibrium state.

As was examined in the previous chapter the shelf circulation is dominated by a strong and large recirculation cell in the linear lateral friction model. The linear model (Exp. 2) shows a decrease of the maximum on-shelf transport by 25 % compared to the non-linear model. Inclusion of the bottom friction (Exp. 3) leads to a broad circulation pattern with a 30 % reduction of the maximum on-shelf transport. The influx to the MS, however, is relatively less sensitive to the presence of the advective and bottom friction terms in the model equations. Both the linear lateral friction and the non-linear bottom friction models predict a decrease of the influx to the MS by 10 % compared to the influx in the non-linear lateral friction model.

V-3-2-2. Depth of the shelf

To investigate the effect of the shelf depth on the influx to the MS, six experiments were performed varying the depth of the shelf and the MS from 50 m to 300 m with other parameters set to be equal. The depth of the deep ocean is 400 m.

Fig. 5-6 shows the streamlines only in the shelf and the MS areas for the six experiments, and Fig. 5-7 shows both the maximum on-shelf transport and the influx

to the MS as a function of the shelf depth. Both the transports increase as the shelf depth increases. The influx to the MS tends to be more sensitive to the changes in the shelf depth. The maximum on-shelf transport tends to increase linearly, while the influx to the MS tends to be proportional to the square of the shelf depth.

Table 5-2. Model parameters for the three experiments.

Experiment	1	2	3
$\nabla\times\tau$ (Sv)	27.0	27.0	27.0
A_M (m^2 s^{-1})	5000	5000	5000
r (m s^{-1})	0.0	0.0	10^{-3}
SVT (Sv)	9.43	7.29	6.43
MVT (Sv)	1.08	0.98	0.98
Remarks	non-linear lateral friction model	linear lateral friction model	non-linear bottom friction model

where
$\nabla\times\tau$: applied Sverdrup transport
A_M : coefficient of eddy viscosity
r : coefficient of bottom friction
SVT : maximum on-shelf transport
MVT : influx to the marginal sea.

Fig. 5-9 shows the pressure along a path indicated in Fig. 5-8 (A). As the shelf depth increases the cross-strait pressure gradient in the KS increases implying an increase in the along-strait flow. The pressure gradient in the TS shows the same tendency.

To understand the driving mechanism of the inflow to the MS, the pressure along the path B in Fig. 5-8 was examined when there is no MS. Fig. 5-10 shows the pressure along path B for two cases with a shelf depth of 50 m and 200 m, respectively. From the WBC (grid point I=19 in Fig. 5-10) the pressure sharply decreases towards the west and smoothly decreases towards the north. The pressure in the region where the KS is located in the marginal sea model is actually lower than that in the TS region. However, the penetration takes place through the KS. Note that

the pressure gradient along the KS and TS regions tends to favour inflow and outflow respectively. For this case the inflow and outflow are expected to take place through the straits having a inflow-favouring and a outflow-favouring cross-strait pressure gradients, respectively, irrespective of the pressure difference between two straits as was already examined in Fig. 5-2. However, when the KS is placed further west where the pressure gradient favours outflow as the pressure gradient along the TS does, the penetration also takes place through the KS (not shown) with a reduction of the influx by about 10 %. It appears, therefore, that the pressure difference between the two regions just outside the straits or the local pressure gradient cross the KS do not drive the inflow to the MS.

Fig. 5-11 shows the pressure along the inshore part of the WBC (path C in Fig. 5-8) without the MS for two cases again with shelf depths of 50 m and 200 m. A sharp increase in the pressure from the grid point J=54 is a manifestation of the on-shelf flow. Along the off-shelf flow region, the pressure slopes downward to the north. The sign of this pressure gradient is the same as that along the region where the TS is located is SMSM (marked by TS in Fig. 5-11). As predicted by the simple model results in section V-2, the inflow to the MS, then, takes place through the high pressure region. The inflow to the MS is not directly from the WBC but an extension of the WBC water already penetrated onto the shelf. As shown before, the off-shelf flow bifurcates near the KS and part of it enters the MS. Therefore, it may be concluded that the inflow to the MS is driven by the pressure difference between the inshore part of the WBC and the TS region. The results obtained from double gyre experiments which will be shown later also clearly indicate that penetration takes place through the TS when the subpolar gyre is strong enough for the cross-strait pressure gradient along the TS to be reversed.

The amount of influx is also related with the pressure difference between the inshore part of the WBC and the TS region as shown in Fig. 5-12. As the shelf depth increases, a larger pressure is built up due to the increase in the on-shelf transport. This results in a larger pressure difference between the shelf and the southern part of the TS where the pressure changes little.

V-3-2-3. Separation latitude of the WBC

The effects of changes in the separation latitude of the WBC and the strength of the subpolar gyre on the amount of influx to the MS are investigated. The latitudinal length of the model domain was extended from 2560 km to 3200 km. The meridional size of the MS was also extended so that the latitudinal distance between the two model straits is approximately the same as that of the real straits. The non-linear lateral friction model with the eddy viscosity coefficient of 5000 m^2s^{-1} was used for all of the experiments. The depth of the deep ocean, and the shelf and the MS are set to be 400 m and 200 m respectively. The wind, which is applied only to the deep ocean, has a purely zonal structure. First, the results with a zero northern (subpolar) gyre are presented in this section. The latitude of vanishing wind stress curl was made to change, while the Sverdrup transport of the southern (subtropical) gyre was kept constant (54 Sv). In the next section the latitude of vanishing wind stress curl was fixed and the transport of the northern gyre was raised from zero until it has the same value as the southern gyre.

Fig. 5-13 shows meridional profiles of the zonal wind stress used for the experiments. The functional form of the applied zonal wind stress is given by equation (5-1). The latitude of vanishing wind curl was made to change by varying L in equation (5-1). The wind stress was held constant in the north of the latitude of vanishing wind curl. The amplitude T_0 in equation (5-1) was also made to change for the Sverdrup transport of the subtropical gyre to be kept constant. Table 5-3 shows the results of six experiments for zero northern gyre transport in the deep ocean.

$$\tau^x = -T_0 \cos\left(\frac{\pi y}{L}\right) \qquad (5\text{-}1)$$

where T_0 is the amplitude of the zonal wind stress and L is the meridional length of the subtropical gyre.

Model equations were integrated until 200 days. Fig. 5-14 gives the time series of the kinetic energy (KE) for experiment 4 in Table 5-3 both over the whole domain

and over the deep ocean area. The period of oscillation in the initial total KE fluctuation is about 25 days, the same as those observed in the highly inertial shelf model which are mainly associated with the basin mode 1 Rossby wave (see Appendix D). The total KE shows little change after 100 days, while the small amplitude oscillation of the KE in the ocean persists until 200 days. Temporal variation of the KE within the MS is in phase with that in the ocean as shown in Fig. 5-15. The amplitude of the fluctuation, however, is large (~ 20 % of the mean KE), so the circulation within the MS can be said to reach an equilibrium state only in a statistical sense.

Table 5-3. Influx to the marginal sea and maximum on-shelf transport for the six experiments with zero northern gyre.

Experiment		1	2	3	4	5	6
$\nabla \times \tau_S$ (Sv)		54.0	54.0	54.0	54.0	54.0	54.0
$\nabla \times \tau_N$ (Sv)		0.0	0.0	0.0	0.0	0.0	0.0
d (km)		690	300	- 100	- 200	- 300	- 500
SVT (Sv)	mean	21.81	21.48	19.68	19.43	18.98	18.19
	std	0.46	0.23	0.94	1.08	1.02	0.66
MVT (Sv)	mean	6.87	5.52	2.28	1.51	0.84	-0.20
	std	0.41	0.19	0.30	0.36	0.23	0.27

where
$\nabla \times \tau_N$: the applied Sverdrup transport of the northern gyre
$\nabla \times \tau_S$: the applied Sverdrup transport of the southern gyre
d : the distance between the centre of the TS and the latitude of vanishing wind stress curl, the positive sign indicates that the latter locates at the north of the TS
SVT : maximum on-shelf transport
MVT : the influx to the MS
mean : the mean transport values for final 30 days of the total integration periods
std : the standard deviation of the mean transport value.

Fig. 5-16 shows a time series of the maximum on-shelf transport and the influx

to the MS. Oscillations having the periods of about 27 days are evident after 100 days in both of the transports. The fluctuation of the KE within the MS is closely related with the influx to the MS as shown in Fig. 5-17. Fig. 5-18 shows streamlines at selected times marked on Fig. 5-16. The location of zero wind stress curl is at grid J=116 for this case. Due to the inertial effects the WBC extends up into the region of zero curl. There is a strong recirculation region together with a spatially oscillatory behaviour (or meandering) of the separated boundary current. A weak cyclonic vortex appears and disappears at times between the crests of the meandering jet. When the influx to the MS shows its minimum (Fig. 5-18 (A) and (E)), the second crest of the meandering jet is amplified and the vortex between the crests is elongated in an approximately N-S direction. When the influx to the MS shows its maximum (Fig. 5-19 (C) and (G)), the second crest of the meandering jet is diminished and the vortex between the crests becomes stronger and is triangular in shape.

Together with these changes of the meandering jet the recirculation cell in the offshore side of the WBC changes with time. When the influx has a minimum value, a recirculation cell, where the maximum transport of the gyre occurs, is located at the same latitude as the KS (Fig. 5-18 (A) and (E)). The recirculation cell splits into two as the cyclonic vortex in the north weakens. One of the cell migrates southwards. The southern cell becomes stronger and the influx has a maximum value when the maximum transport of the entire gyre occurs in the southern cell, which is located close to the penetration latitude of the WBC onto the shelf. During this stage the northern cell weakens with time.

Fig. 5-19 shows the pressure along the inshore part of the WBC (path C in Fig. 5-8). Associated with the changes in the strength and position of the recirculation cells, the pressure field also changes between the shelf region (J=44 ~ 84 in the figure) and the southern part of the TS. The TS is located between J=124 and J=129. The pressure changes little in the northern part of the TS. As the southern cell becomes stronger the pressure drops along the shelf because of the larger pressure gradient across the WBC associated with the stronger flow (day 131 in Fig. 5-19). Together with the strengthening of the southern cell, the northern cell weakens and the pressure

along the island, which separates the MS from the deep ocean, rises (grid J=84 ~ 124). The maximum influx to the MS takes place when the pressure drops along the shelf and rises from the southern tip of the island to the south of the TS. The variation of the influx to the MS, thus, seems to be related with the variation of the pressure difference between the southern tip of the island and the northern part of the TS, not between the continental slope and the TS region.

In presenting the transports onto the shelf and the MS, the mean value of the final 30 days was used. The standard deviation of the mean value (std in Table 5-4) is also presented. Note that the period of oscillation of the transports is about 27 days. Other variables such as the pressure and streamlines presented below are those at times when the influx is nearly the same as its mean values.

Fig. 5-20 shows snapshots of streamlines for the six experiments. Fig. 5-21 shows the influx to the MS and the maximum on-shelf transport as a function of the distance (d) between the TS and the latitude of vanishing wind stress curl (see also Table 5-3). As d decreases, both the transports decrease. The ratio of the reduction of the influx is about 30 ~ 45 % / 100 km when the separation latitude of the WBC locates in the south of the TS (experiments 3 ~ 5), while it becomes approximately halved when the separation latitude locates in the north of the TS (experiments 1 and 2). When d=-500 km, the direction of flow in the MS reverses with a weak southward flow through the KS. The ratio between the stds and mean values of the influx to the MS becomes larger as d decreases or the region of quiescent water in the north of the deep ocean, which is not directly forced, becomes broader as shown in Table 5-3. The variation of the influx to the MS is more sensitive to d compared with that of the maximum on-shelf transport.

Fig. 5-22 (A) shows the pressure along the inshore part of the WBC for experiments 2 and 4 when there are no marginal seas. The on-shelf transport characterised by a large pressure gradient sloping up to north from the grid J=44 shows little change between the two cases. Along the broad off-shelf flow region, the pressure is higher for the case of higher latitude of vanishing curl (Exp. 2). After

opening the straits the influx to the MS, which takes place through the KS, shows a higher value. In other areas the pressure changes little between the two cases. We need to understand why the pressure rises along the inshore part of the WBC in the shelf region as the latitude of vanishing curl retreats to the south. We have shown that the pressure rises along this part for a fixed location of the vanishing curl in section V-3-2-2 as the shelf depth increases mostly due to a larger on-shelf transport.

Fig. 5-23 shows streamlines for the experiments 2 and 4 but without the MS at an equilibrium state. As we mentioned in chapter IV-3-3 two recirculating flows emerge in the deep ocean when there is a shallow shelf area. As we can see in the figure, the recirculation cells retreat to the south as the latitude of vanishing curl does. The maximum gyre transports which occurs at the southern cell remains nearly the same for both cases as we applied the same amount of Sverdrup transports. As a consequence of the southward migration of the cells, the maximum on-shelf transport slightly increases for experiment 4. The maximum on-shelf transports are 16.78 Sv and 17.63 Sv for experiments 2 and 4 respectively. As the southern cell having the maximum gyre transport migrates southward, the pressure along the inshore part of the WBC in the shelf area drops to support a stronger flow (Fig.5-22 (A)). Therefore, the pressure difference between the off-shelf flow and the TS regions is greater for experiment 2 resulting in an increases influx to the MS compared with that for experiment 4 after opening the straits.

Fig. 5-22 (B) shows the pressure along the inshore part of the WBC (path C in Fig. 5-8) for the six experiments in Table 5-3. The pressure along the off-shelf flow region (grid J=54 ~ 84) further increases after introducing the MS since the on-shelf transport increases nearly the same amount as the influx to the MS. The pressure along the eastern part of the island also increases as more influx to the MS takes place, while it remains the same for the cases without the MSs shown in Fig. 5-22 (A). The short period fluctuation of the influx, however, seems to be more consistently related with the pressure difference between the southern and northern parts of the TS rather than the difference between the off-shelf flow and the TS regions as mentioned before.

It should be noted that if the influx to the MS is subtracted from the on-shelf transport in Table 5-3, the on-shelf transport increases as the separation latitude moves to the south, which is opposite to the tendency of the changes of the influx to the MS. The flow pattern on the shelf is also affected by the presence of the MS as shown in Fig. 5-20. The meandering mode is dominant when there is a negligible influx to the MS and the gyre centre is placed close to the penetration latitude (Fig. 5-20 (F)), while the inshore branch is intensified as the influx to the MS increases.

V-3-2-4. Strength of subpolar gyre

An unsymmetric double gyre system was established by applying the sinusoidal wind stress shown in Fig. 5-24 over the whole deep ocean area. The applied Sverdrup value of the subtropical gyre and the latitude of vanishing curl are exactly the same as those of experiment 4 in Table 5-3. The only difference is that the water in the north is no longer quiescent but is now forced directly by the wind. The applied wind stress over the northern portion of the gyre has the form,

$$\tau^x = -t_0 \cos\left(\frac{\pi}{l}(y-L)+\pi\right) + T_0 - t_0 \quad (y \geq L) , \qquad (5\text{-}2)$$

where t_0 and T_0 are the amplitude of the wind stress applied to the subpolar and subtropical gyres respectively, and l and L are the meridional lengths of subpolar and subtropical gyres respectively. The equation (5-2) was used to match the wind stress over the northern portion of the gyre smoothly to that over the southern portion of the gyre given by the equation (5-1) and to give a zero wind stress curl at the northern boundary.

Table 5-4 summarises the results of four experiments with non-zero subpolar gyre. For comparison the result of the experiment 4 in Table 5-3 is also presented. Model equations were integrated until 200 days for the experiments 7~9 and 360 days for the experiment 10. The observed influx to the MS was dominated by the oscillation having a period of about 25 days for the experiments 7~9. For the experiment 10, a lower frequency oscillation (~180 days) superimposed on the ~25 days oscillation

exists, which is associated with the longer period evolution of the subtropical gyre. The mean values of the influx and the maximum on-shelf transport for the experiment 10 in Table 5-4 are those for the whole integration period.

Fig. 5-25 shows snapshots of streamlines for the five experiments in Table 5-4. As the subpolar gyre strengthens, the separation latitude of the WBC retreats to the south. Fig. 5-21 (B) shows the influx to the MS and the maximum on-shelf transport as a function of the ratio between the transports of subtropical and subpolar gyres. As the ratio increases, both the transports decreases almost linearly. When the subpolar gyre has the half strength of the subtropical gyre there is no virtual influx to the Ms. If the subpolar gyre becomes even stronger, the model predicts penetration through the TS as also shown in Fig. 5-25 (D) and (E).

Fig. 5-26 shows the pressure along the inshore part of the WBC for experiments 4, 7, 9, and 10 when there are no marginal seas. The pressure along the off-shelf flow region changes little. When the subpolar gyre has a zero transport, the pressure decreases almost linearly from the off-shelf flow region to the northern boundary of the model domain. When the subpolar gyre is set up, the pressure minimum occurs at some latitude and the pressure increases further north of the pressure minimum position. As the transport of the subpolar gyre increases, the position of the pressure minimum retreats to the south. When the marginal sea model predicts inflow through the TS, the position of the pressure minimum is located to the south of the TS and the local meridional pressure along the TS region slopes downward to south (experiments 9 and 10 in Fig. 5-27) which is opposite to the zero subpolar gyre case. The pressure itself near the TS region for these cases is lower than either the off-shelf region or the eastern part of the island. The pressure near the KS is also higher than the pressure near the TS region when the penetration takes place through the TS. The amount of penetration through the TS increases as the meridional pressure gradient along the TS region increases.

Table 5-4. Influx to the marginal sea and maximum on-shelf transport for the four experiments with non-zero northern gyre.

Experiment		4	7	8	9	10
$\nabla \times \tau_S$ (Sv)		54.0	54.0	54.0	54.0	54.0
$\nabla \times \tau_N$ (Sv)		0.0	13.5	27.0	40.5	54.0
d (km)		- 200	- 200	- 200	- 200	- 200
SVT (Sv)	mean	19.43	18.75	18.03	17.40	16.38*
	std	1.08	1.07	0.58	0.29	1.73
MVT (Sv)	mean	1.51	0.64	-0.10	-0.60	-1.57*
	std	0.36	0.37	0.21	0.08	1.01

where
$\nabla \times \tau_N$: the applied Sverdrup transport of the northern gyre
$\nabla \times \tau_S$: the applied Sverdrup transport of the southern gyre
d : the distance between the centre of the TS and the latitude of vanishing wind stress curl
SVT : maximum on-shelf transport
MVT : the influx to the MS
mean : the mean transport values for final 30 days of the total integration periods
std : the standard deviation of the mean transport value.
* : The values are the means of total integration periods.

V-3-2-5. Lateral eddy viscosity

Effects of the lateral eddy viscosity on the influx to the MS are examined by increasing the value by two and four times of the standard value of A_M=5000 m^2s^{-1}. Fig. 5-27 shows snapshots of streamlines for the three lateral friction models with different values for the eddy viscosity. All other parameters are the same as experiment 4 in Table 5-3. Table 5-5 summarises the results of the three experiments.

As the eddy viscosity increases, the separation latitude of the WBC retreats to the south slightly, and the northern recirculation cell disappears. The influx to the MS increases, as the eddy viscosity increases, while the on-shelf transport decreases. Four

Table 5-5. Effect of varying lateral eddy viscosity on transports into the shelf and the marginal sea.

Experiment		4	11	12
$\nabla \times \tau_S$ (Sv)		54.0	54.0	54.0
$\nabla \times \tau_N$ (Sv)		0.0	0.0	0.0
A_M (m^2s^{-1})		5000	10000	20000
d (km)		- 200	- 200	- 200
SVT (Sv)	mean	19.43	17.66	15.80
	std	1.08	0.06	0.0
MVT (Sv)	mean	1.51	1.53	1.67
	std	0.36	0.01	0.0

where
A_M : lateral eddy viscosity.
Other notations are the same as those in Table 5-4.

Table 5-6. Effect of longitudinal size of the deep ocean on transports into the shelf and the marginal sea.

Experiment		2	2-1	4	4-1
$\nabla \times \tau_S$ (Sv)		54.0	54.0	54.0	54.0
$\nabla \times \tau_N$ (Sv)		0.0	0.0	0.0	0.0
L^x (km)		890	2170	890	2170
d (km)		690	690	- 200	- 200
SVT (Sv)	mean	21.48	21.83	19.43	19.93
	std	0.23	1.21	1.08	0.84
MVT (Sv)	mean	5.52	5.48	1.51	1.53
	std	0.19	0.20	0.36	0.16

where
L^x : the longitudinal distance of deep ocean basin.
Other notations are the same as those in Table 5-4.

times increase in the eddy viscosity leads to ~10 % increase in the influx to the MS and ~ 20% decrease in the on-shelf transport.

V-3-2-6. Width of the deep ocean

Any effect of the longitudinal distance of the deep ocean on the influx to the MS was examined by increasing the widths of the deep ocean basins by 2.4 times for experiments 2 and 4 in Table 5-3. Fig. 5-28 shows streamlines for the two experiments with extended widths of the deep ocean basins. Table 5-6 summarises the results of the two experiments together with those of experiment 2 and 4 in Table 5-3. The amount of influx to the MS and the on-shelf transport is insensitive to the longitudinal distance of the deep ocean basins.

V-4. A MORE REALISTIC MODEL

V-4-1. Introduction

The bottom topography and the coastlines of the previous simple models were highly simplified so that the possible influence of the topography on the influx to the MS could not be examined. This might be important since the deeper region in the sea area west of Kyushu (see Fig. 1-3) has long been thought as a source region of the TC (Uda, 1934; Nitani, 1972). This influence is examined in this section with a more realistic topography.

The simple model results in section V-3 indicate that the influx to the marginal sea is dependent on features of the large scale circulation in the deep ocean such as the separation latitude of the WBC and the strength of subpolar gyre. It has been shown that a change of the separation latitude of 100 km leads to a change of influx of 30 ~ 45 % when the separation latitude is located in the south of the TS. The meridional variation of the separation latitude of the Kuroshio is about 200 ~ 300 km as reviewed in chapter I (see Fig. 1-12), which appears large enough to result in the whole annual range of the

TC. It will be also further examined in this section.

The influx to the JS is also expected to be dependent on the Kuroshio transport. The annual range of the volume transport of the Kuroshio Extension and the Kuroshio in the ECS is less than 20 % and 40 % of the mean transport respectively according to Clifford and Horton (1992) and Ichikawa and Beardsley (1993). This section investigates the relative importance of the both factors affecting the influx to the JS; the change in the separation latitude of the Kuroshio and the change in the Kuroshio transport itself.

V-4-2. Design of the model

Since this section investigates the effects of large scale circulation on the influx to the JS in an unsymmetric double gyre system, an inflow-outflow limited area model is inappropriate. A basin scale model covering the whole North Pacific is ideal for the present purpose. However, the computing facilities to hand and the time available for this study do not permit use of such a large model. Instead, a closed basin limited area model (SPEM) was used for this study.

Figs. 1-1 and 1-3 show the complex geometry and bathymetry of the ECS area. The area to be modelled is approximately 122°E ~ 152°E, 20°N ~ 43°N and is shown in Fig. 5-29. The model ocean covers the whole ECS from the east of Taiwan, and Yellow Sea. Inflow through the Taiwan Strait is not included, and detailed coastline of China is omitted and are simply represented by a straight coast. As most of the TC exits from the JS to the North Pacific through the TS, the latitude of which is about 41°N, the region north of 43°N is not included. Ryukyu Islands are also excluded. The Korea peninsular and the Japanese Islands are simplified.

Bottom topography in the ECS area where the water depth is less than 400 m is realistically incorporated to the model domain by digitising isobaths of 50 m ~ 400 m for every 50 m interval from the map of bathymetry in Fig. 1-3. Water depths less than 50 m are set to be 50 m. Topographies deeper than 400 m are filtered out by assuming implicitly that the 400 m depth represents the mean thermocline depth above which the

wind-driven currents are concentrated. Bottom topographies south and east of Japan, and within the JS are not realistic.

Slip boundary conditions are applied at all solid walls and along the boundaries of the land area. A 20 km grid is used, the same as that of the previous simple models. The longitudinal and latitudinal distances of the model ocean are 3200 km and 2560 km (161 × 129 points) respectively. The model ocean is forced by the wind stress applied only to the deep ocean (from I=100 to I=161 in Fig. 5-29) and damped by lateral friction. A non-linear model is used since a linear model has been shown to restrict the amount and scale of the penetration of the boundary current onto the shelf over the topography as examined in chapter IV.

V-4-3. Model results

V-4-3-1. A standard case

Model parameters for the standard case are summarised in Table 5-7. The applied Sverdrup transport for the subtropical gyre is 70 Sv, which is approximately a mean value of the baroclinic transport of the Kuroshio Extension relative to 200 dbar (Horton and Clifford, 1992; see Fig. 1-7(D)). The strength and variability of the Oyashio Current, a western boundary current of the subpolar gyre in the North Pacific, has not been well documented, but it is expected to be much weaker than the Kuroshio. The transport of the model subpolar gyre is set to be 10 % of that of the subtropical gyre. The latitude of vanishing wind stress curl is set to be 35°55' N so that the model Kuroshio separates from the coast around this latitude. This latitude corresponds approximately to the lower limit of the northern limit of the Kuroshio Extension according to Kawai (1972) (see Fig. 1-12).

Model equations were integrated for 200 days, by which time an equilibrium state was achieved. Fig. 5-30 shows plots of the total kinetic energy of the system and the influx to the JS as a function of time for every one day interval. The initial oscillation is damped down by the action of lateral friction and the system has converged

to its steady state values at 200 days.

Fig. 5-31 shows streamlines at an equilibrium state. Fig. 5-32 (A) shows profiles of topography along the line P in Fig. 5-31 and velocity component perpendicular to the line. The strong currents representing the model Kuroshio flow northeastward almost parallel to the isobaths. The maximum velocity core of ~ 1 m/s is found to the east of the continental slope region. The width of the strong core (> 0.6 m/s) is about 150 km. The speed of along-slope current sharply decreases from the core toward the southeast and northeast, and the speed of the current over the area, whose depth is less than 200 m, is about 0.1 m/s or less.

Table 5-7. Model parameters for the standard case of the realistic model.

PARAMETERS		Exp.2
$\nabla \times \tau_N$ (Sv)	applied Sverdrup transport of the subtropical gyre	70
$\nabla \times \tau_S$ (Sv)	applied Sverdrup transport of the subpolar gyre	7
f_0 (s^{-1})	Coriolis parameter at a central latitude	7.51×10^{-5}
β_0 (m^{-1} s^{-1})	latitudinal variation of Coriolis parameter	1.98×10^{-11}
L^x, L^y (km)	size of the model domain	3200, 2560
A_M (m^2 s^{-1})	lateral eddy viscosity	5000
r (m s^{-1})	bottom friction coefficient	0
Δx, Δy (km)	grid spacings	20, 20
Δt	timestep length	20 min

Fig. 5-32 (B) shows profiles of topography and meridional velocity component along the western wall of the model domain (I=2). The maximum meridional velocity of ~1.4 m/s along the western wall was found at a depth of about 180 m. It decreases sharply to the north, and the velocity is nearly zero in the north of J=54, about 300 km away from the maximum velocity core as shown in Fig. 5-32 (B). As the model Kuroshio impinges on the sloping topography, most of its transport follows isobaths northeastward. However, a part of it overruns the continental slope and reaches the

continental shelf region along the western wall of the model domain. This part of the branch of the Kuroshio is similar to the TWC which is generated in the northeast of Taiwan. This branch sharply turns anticyclonically over the shelf and eventually returns back to the main stream over the continental slope, the behaviour of which corresponds to that of the TWC as shown in Fig. 5-31. This branch meanders along the inshore part of the main stream of the Kuroshio while flowing northward.

According to the present model result, a part of this branch enters the JS to become the TC. For the standard case, the influx to the JS is 0.5 Sv. There is no direct intrusion of the Kuroshio in the west of Kyushu. On the other hand the streamlines turn anticyclonically around the topographic hump in the west of Kyushu following the isobaths. Consequently, the flow is southward in the vicinity of Kyushu. Attempts have been made to find a northward current in the sea west of Kyushu, but no prominent northward current has been observed. Instead, southward currents are rather predominant according to the surface current fields deduced from a long-term GEK measurements (Ichiye, 1984). The existence of the southward currents in the west of Kyushu can be further supported by trajectories of three satellite tracking surface drifters which were released in July 1991 at three locations along 32° N (KORDI, 1992) as shown in Fig. 5-33. Only the drifter released at 32° N, 127° E, where the water depth is about 100 m, entered the JS. The other two drifters moved to the east or south. The drifter released in the vicinity of Kyushu moved to the southeast for the first 10 days and turned to the northeast in the south of Kyushu.

The model TC flows northeastward along the west coast of Japan, and exits to the deep ocean through the TS. In the simple shelf-MS model, the inflow to the flat-bottomed MS was deflected to the west due to the planetary β-effect. In the realistic model with a topography it is deflected to the east indicating that the vortex stretching balances the vorticity diffusion due to lateral friction. The outflow through the TS also turns eastward and flows southward along the east coast of Japan suggesting that a similar vorticity balance may hold for the outflow. The flow pattern of the model outflow through the TS is similar to that actually observed in the east of the strait (see Fig. 1-1).

V-4-3-2. Effects of the Kuroshio

This section investigates the relative importance of two factors affecting the influx to the JS; changes in the transport of the Kuroshio and the separation latitude of the Kuroshio. Table 5-8 summarises the parameters for the three experiments for the investigation together with the subsequent influx to the JS. The total transports of the subtropical and subpolar gyres are made to increase by 20 % of those for the standard case for experiment 3. The applied Sverdrup transport for experiment 3 is 84 Sv which is approximately the same value of the annual maximum baroclinic transport of the Kuroshio Extension relative to 200 dbar surface according to Clifford and Horton (1992) (see Fig. 1-7 (D)). The latitude of vanishing wind stress curl is made to change so that the separation latitude of the Kuroshio is located 200 km north of the standard case (J=100) for experiment 1 in Table 5-7.

Table 5-8. Effects of the separation latitude of the Kuroshio and the Kuroshio transport on the influx to the Japan Sea.

Experiment	1	2	3
$\nabla \times \tau_S$ (Sv)	70.0	70.0	84.0
$\nabla \times \tau_N$ (Sv)	7.0	7.0	8.4
Lat. (N)	37°44′	35°55′	35°55′
J	100	90	90
MVT (Sv)	1.10	0.48	0.83

where
Lat. : latitude of vanishing wind stress curl
J : grid point of vanishing wind stress curl.
Other notations are the same as those in Table 5-4.

Figs. 5-34 (A) and (B) show streamlines for experiments 1 and 3 at an equilibrium state. As the gyre transport increases, the meridional penetration scale of the Kuroshio along the western wall increases. The maximum along-slope current reaches 1.2 m/s for experiment 3, but there is no direct intrusion of the Kuroshio in the area

west of Kyushu even in this experiment. The influx to the JS also increases by 0.35 Sv. The influx to the JS also increases as the Kuroshio separates from the coast further north. The 200 km increase in the separation latitude leads to the increase in the influx to the JS by 0.62 Sv. The model results indicate that the change in the separation latitude by 100 km corresponds to the change in the Kuroshio transport by 20 %, suggesting that the former is as important as or more important than the latter in determining the influx to the JS.

V-5. SUMMARY AND DISCUSSION

Penetration of the WBC into the marginal sea was investigated with the SPEM in the two kinds of idealised model domains and in a more realistic domain. The investigation was mainly focused on the effects which changes in the large scale circulation of the deep ocean have on the amount of influx to the MS with an unsymmetric double gyre system. This has not previously been described. It has not been intended to make any detailed comparison between the model results and in situ data as this research is a process-oriented one. However, the results give a clue to explaining the observed large fluctuation in the volume transport of the TC and highlight the importance of studying the through flow in connection with the large scale circulation.

Model results indicate that the flow and the transport through the marginal sea are very dependent on the structure of the deep ocean. The results of the simple MS model (section V-2) indicate that the direction of the on- and off-MS flows is determined by the local cross-strait pressure gradient set by the circulation in the deep ocean as well as the pressure difference between two straits. When the local pressure gradients across two straits have the same signs, penetration of the boundary currents takes place through the strait which is located in the high pressure region (referred to as case I). When the signs are changed to be opposite to each other, the on- and off-MS flows are directly implied by the local pressure gradients rather than the pressure difference between two straits (referred to as case II). For the case II, penetration and exit from the MS of the

boundary current take place through the straits whose local pressure gradients tends to favour the inflow (pressure sloping downward to the south) and outflow (pressure sloping downward to the north) respectively in a geostrophic sense.

In the SMSM in section V-3, the meridional pressure gradients along the inshore part of the Kuroshio and the TS are important in driving the inflow to the MS. The same analogy with the simple MS model can be drawn from these two pressure gradients. When the transport of the subpolar gyre is much weaker than the subtropical gyre transport, the above two pressure gradients have the same sign, just as the case I. A part of the WBC water which has already penetrated onto the shelf, then, enters the MS. If the subpolar gyre is strong enough to modify the pressure gradient of the TS from an outflow-favouring one to an inflow-favouring one, penetration of the subpolar water takes place through the TS as the case II. It has been shown from the SMSM that penetration of the subpolar gyre into the MS takes place when the strength of the subpolar gyre is more than 50 % of that of the subtropical gyre in terms of the volume transport.

There is also an indication that the amount of the influx is related to the pressure difference between the off-shelf flow region (high pressure) along the inshore part of the WBC and the TS region (low pressure) either for the zero subpolar gyre or single gyre cases. However, it has not been explained satisfactorily why the influx is reduced for the case of the weak subpolar gyre even though the pressure difference between the above two regions increases (experiments 4 and 7 in Fig. 5-26 or experiments 2 and 3 in Fig. 5-2). It would appear that the flow condition outside the outflow strait (TS) affects the through flow to the MS.

Short period fluctuations of the influx observed from the model results are related to the pressure change along the WBC to the south of the TS. The pressure change was shown to be associated with the strengthening and weakening of the recirculation cells east of the WBC. It should be pointed out that, according to the model results, a small perturbation in the deep ocean area can cause a large fluctuation of the influx to the MS.

The amount of the influx decreases as the shelf depth decreases, and the influx to the MS is more sensitive to the shelf depth than the maximum on-shelf transport. As the shelf depth increases, more penetration onto the shelf occurs and the pressure in the shelf region rises, resulting in a larger influx to the MS caused by a larger pressure difference between the shelf and the TS region.

When the subpolar gyre has a zero transport, the influx to the MS decreases as the latitude of vanishing curl retreats to the south. It was shown that the recirculation cells on the offshore side of the WBC retreats to the south as the latitude of vanishing curl does. This retreat causes a further intensification of the WBC along the offshore side of the shelf. The pressure drops to support the intensified flow resulting in a reduced influx to the MS due to the decrease in the meridional pressure difference.

In conclusion, the influx to our simple MS is very dependent on the following three factors; i) the depth of the shelf; ii) the separation latitude of the WBC; and iii) the strength of the subpolar gyre.

The variation of the Kuroshio transport is also expected to affect the amount of the influx to the MS. The relative importance of two factors affecting the influx to the JS, namely the changes in the transport of the Kuroshio and the separation latitude of the Kuroshio, were examined in section V-4 with a realistic model, to which the realistic topography in the ECS is incorporated. The possible role of the topographic hump in the sea west of Kyushu was also investigated. The main results obtained from the realistic model are ; i) a 100 km change in the separation latitude of the Kuroshio amounts to a 20 % change of the Kuroshio transport; ii) a direct intrusion of the Kuroshio in the area west of Kyushu does not occur. Instead, southward flowing currents are dominant in the vicinity of Kyushu, which is evidenced by the recent direct observation of the current in the area; iii) the model TC is shown to be a continuation of a part of the model TWC, which is generated by an inertial overshooting of the Kuroshio over the topography in the area northeast of Taiwan.

The whole Kuroshio system and its variability is not fully understood. There is

some discrepancy in the annual cycle of the Kuroshio in the ECS. The long-term baroclinic transport (Guan, 1983b) and surface velocity of the Kuroshio (Guan, 1980) have a spring-maximum and a fall-minimum trend, which are almost 180° out of phase with that of the TC. On the other hand, the absolute transport of the Kuroshio in the ECS (Ichikawa and Beardsley, 1993) and the transport of the Kuroshio through the Tokara Strait inferred from the sea level difference (Blaha and Reed, 1982) reach their maximum in summer. The volume transport of the Kuroshio Extension, inferred from both the cross-stream sea level difference and the hydrographic measurements, however, consistently reach a maximum in autumn (Qiu et al., 1991; Clifford and Horton, 1992), which is in phase with that of the TC. The separation latitude of the Kuroshio also relates to the amount of the transport of the Kuroshio Extension (Qiu et al., 1991) so that it is expected that the Kuroshio separates from the coast further north when the transport of the Kuroshio Extension is large in autumn. While it is likely that the variability of the TC is more closely related to that of the Kuroshio Extension, this needs to be confirmed by re-examining the existing data. An important finding of the present study is that the change in the separation latitude of the Kuroshio is as important as the change in the Kuroshio transport, so that the former should be considered in studying the variability of the TC.

The changes in the separation latitude of the boundary current result in a weakening or strengthening of the recirculation cells in the model, which then cause the variation of the influx to the MS. They are, therefore, very much a consequence of the limited model domain. However, there exist a localised recirculation zone called the Kuroshio countercurrent between the Kuroshio and the Ryukyu Island (Nitani, 1972) and a large scale recirculation gyre in the North Pacific (see Fig. 1-2). There have been no attempts to relate the strengthening and the weakening of the countercurrent or recirculating gyre with the variation of the volume transport of the TC.

The generation of the TC by the meridional pressure gradient along the Kuroshio has been challenged simply because the TS is actually located at the western part of the subpolar gyre. However, the pressure minimum position is actually located further north than the separation latitude of the WBC, about 200 km ~ 600 km north of the latitude

of vanishing curl depending on the strength of the subpolar gyre, as the model results showed. Consequently, the influx to the MS takes place through the KS even though the model WBC separates to the south of the TS, and the amount of the influx changes according to the strength of the subpolar gyre.

The annual cycle of meridional sea level difference on the offshore side of the Kuroshio (between 30° N and 50° N), determined from the observed wind fields and the Sverdrup relation, has its maximum in winter and minimum in summer (Ichiye, 1984). As this trend is opposite to the seasonal cycle of the TC, Ichiye argued intuitively that the pressure difference along the Kuroshio may be irrelevant in the generation of the TC. However, the Sverdrup relation does not account for the observed variability of the Kuroshio as pointed out by Blaha and Reed (1982). Our model results also show that the influx to the MS decreases as the subpolar gyre strengthens and the pressure difference increases. The reason for this must be further examined.

Application of even the results of the realistic model to the real ocean is necessarily limited because of the reduced physics and the restricted model domain. The model results in this chapter need to be confirmed by a re-examination of the existing data as well as through a basin scale model covering the whole north Pacific. A major conclusion of this chapter is, however, that changes of the large scale circulation of the North Pacific may affect the flow through the Japan Sea. The relative importance of the large scale circulation compared to local forcings such as the effect of monsoon wind (Huh, 1982a; Ichiye, 1984; Kang, 1984) and the density difference between the ECS and the TS region (Toba et al., 1982) needs also to be studied.

Fig. 5-1 (A) Contours of streamlines for an antisymmetric double gyre circulation at an equilibrium state (left) driven by the applied antisymmetric zonal wind stress (right). The model ocean is homogeneous and flat with a depth of 400 m. **(B)** Locations of straits of each shallow basin for the experiments 2~4 in Table 5-1 superimposed on the meridional distribution of the surface pressure along the western boundary of the double gyre circulation before introducing the shallow basins. The surface pressure is computed assuming that the pressure at the southwestern corner is zero.

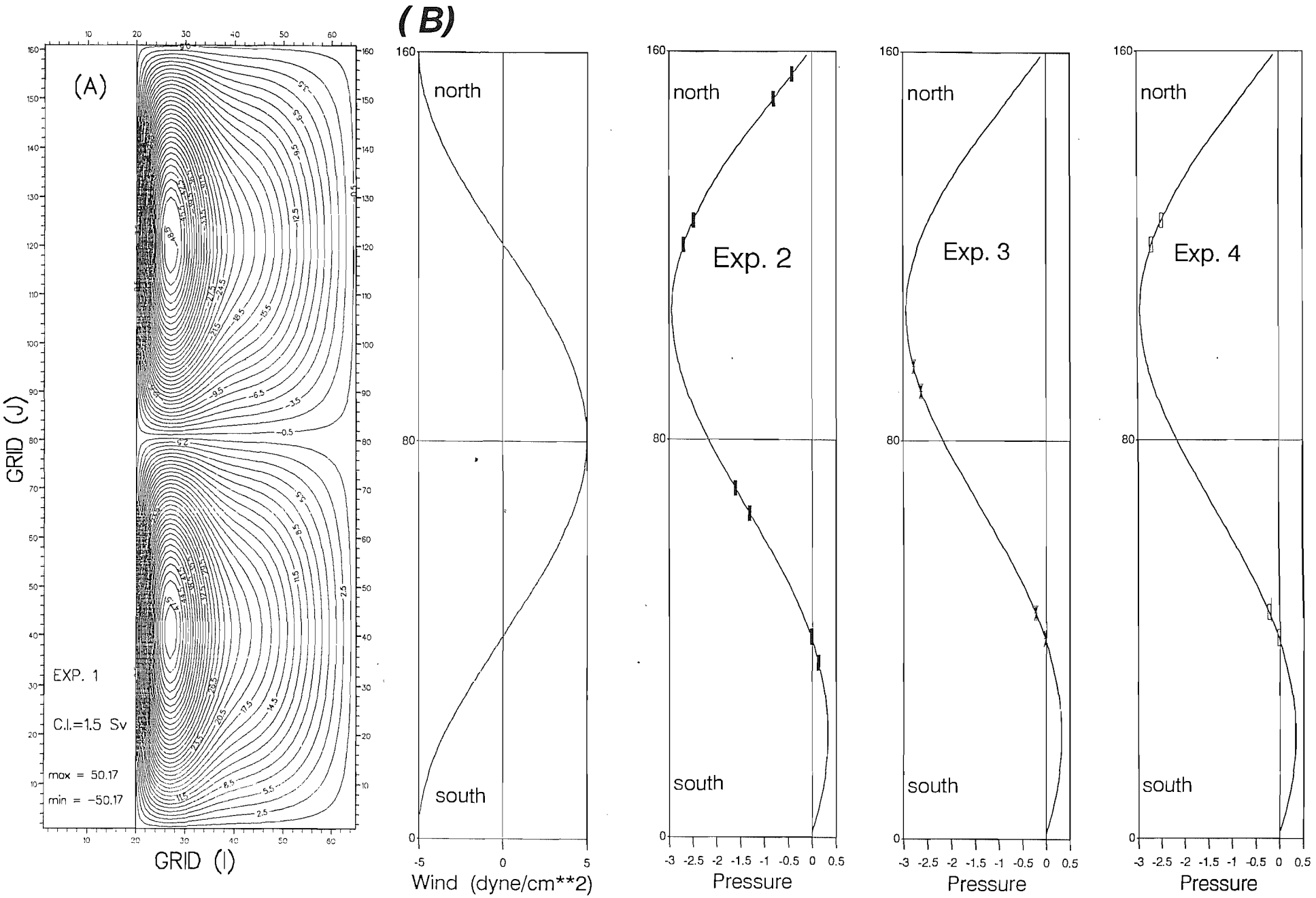
(A)
EXP. 1
C.I.=1.5 Sv
max = 50.17
min = -50.17
GRID (J)
GRID (I)
(B)
north
south
Wind (dyne/cm**2)
Exp. 2
Exp. 3
Exp. 4
Pressure

Fig. 5-2. Contours of streamlines for the experiments 2~4 from left to right (see Table 5-1). Positive and negative values of the streamlines within the shallow basins indicate that the penetration of the boundary currents takes place through the southern and northern straits of each basin respectively.

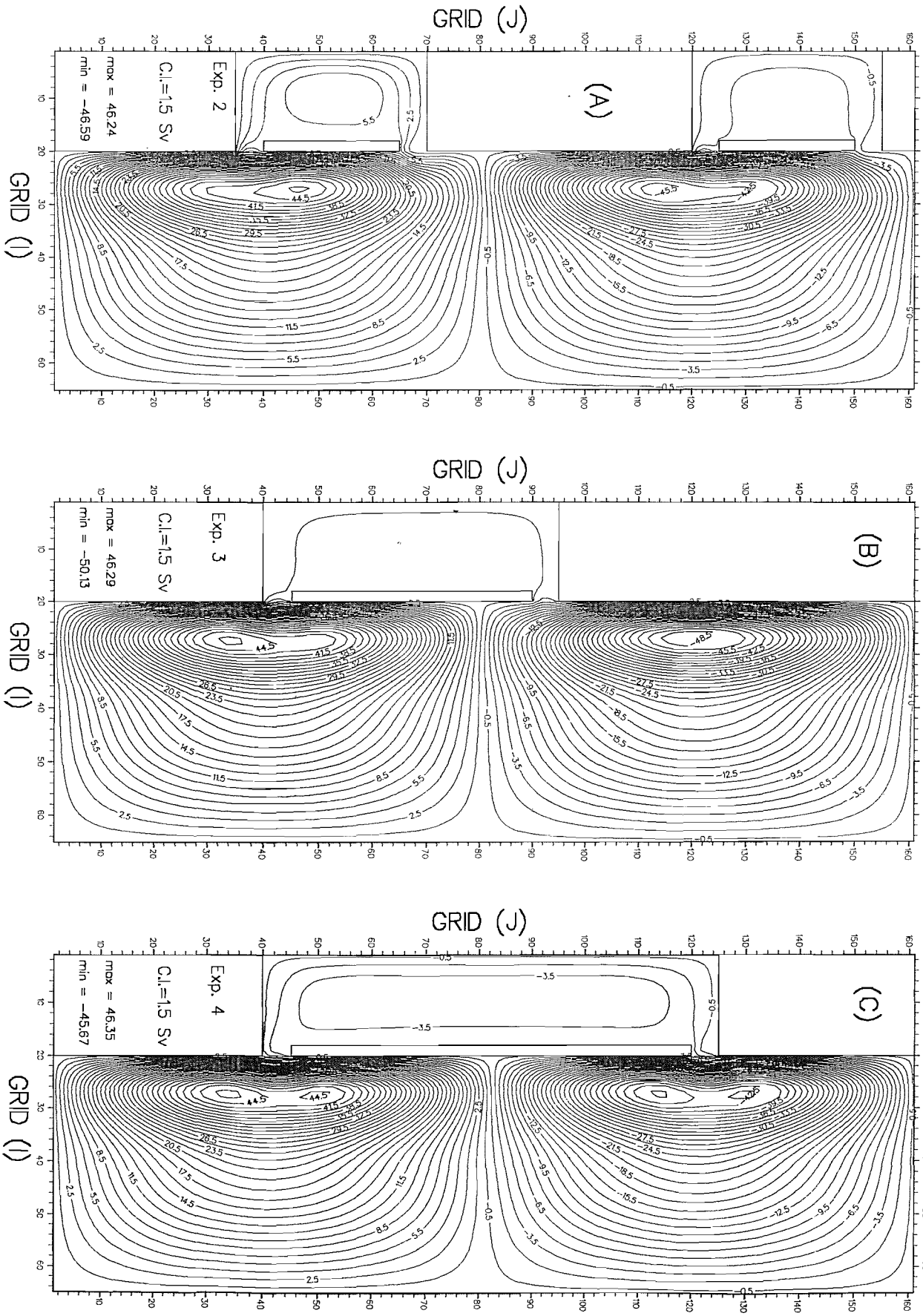
GRID (J)
GRID (I)
(A)
Exp. 2
C.I.=1.5 Sv
max = 46.24
min = −46.59
(B)
Exp. 3
C.I.=1.5 Sv
max = 46.29
min = −50.13
(C)
Exp. 4
C.I.=1.5 Sv
max = 46.35
min = −45.67

Fig. 5-3. Contours of streamlines for the two cases **(A)** without the MS, and **(B)** with the MS. Model parameters for both of the experiments are the same as those of experiment D in Table 4-3.

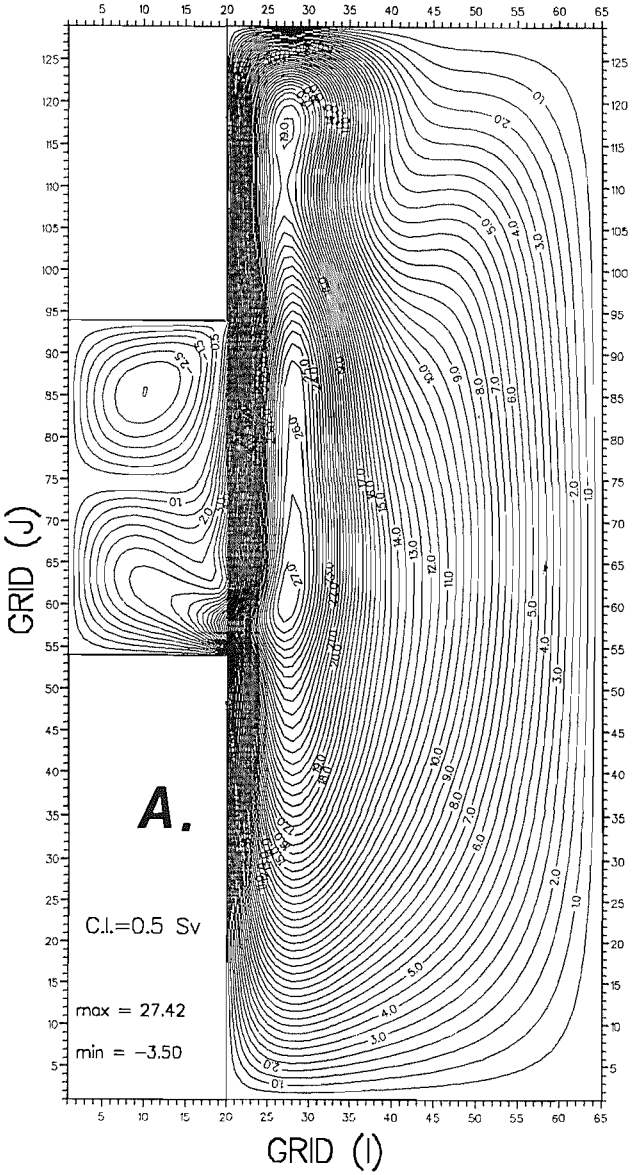
A.
C.I.=0.5 Sv
max = 27.42
min = −3.50
GRID (J)
GRID (I)

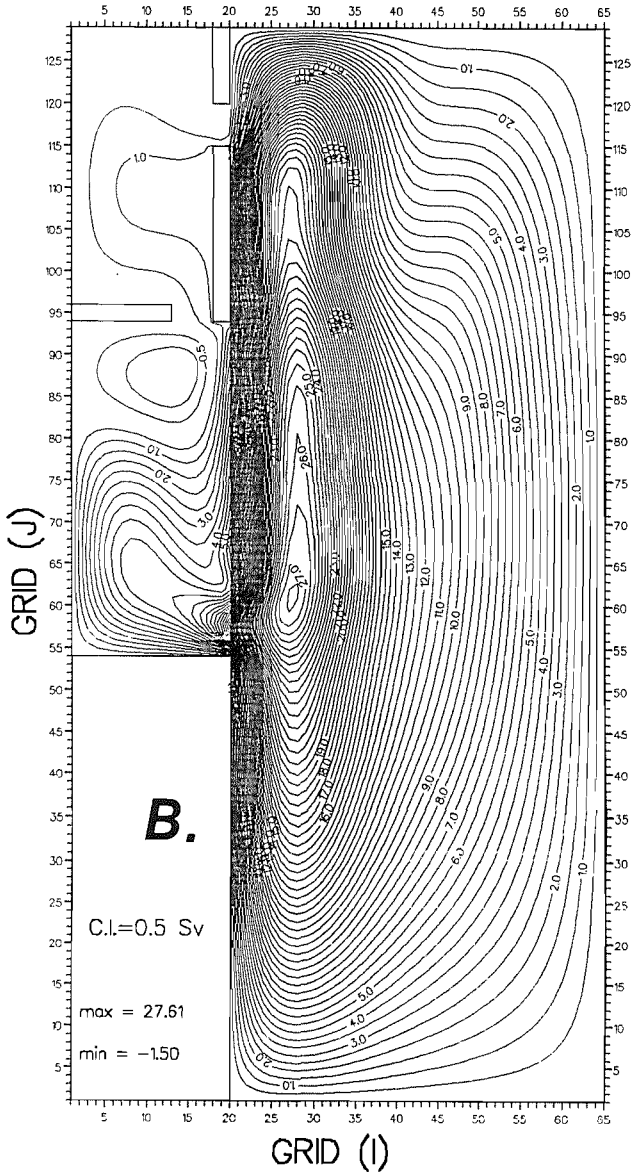
B.
C.I.=0.5 Sv
max = 27.61
min = −1.50
GRID (J)
GRID (I)

Fig. 5-4. A comparison of three model results ; **(A)** non-linear lateral friction model, **(B)** linear lateral friction model, and **(C)** non-linear bottom friction model. The applied Sverdrup transports are the same for the three experiments.

A.
C.I.=0.5 Sv
max = 27.61
min = −1.50
GRID (J)
GRID (I)

B.
C.I.=0.5 Sv
max = 28.88
min = −3.50
GRID (J)
GRID (I)

C.
C.I.=0.5 Sv
max = 27.38
min = −0.12
GRID (J)
GRID (I)

Fig. 5-5. As in Fig. 5-4 except the circulation in the shelf and the MS regions only with a contour interval of 0.2 Sv.

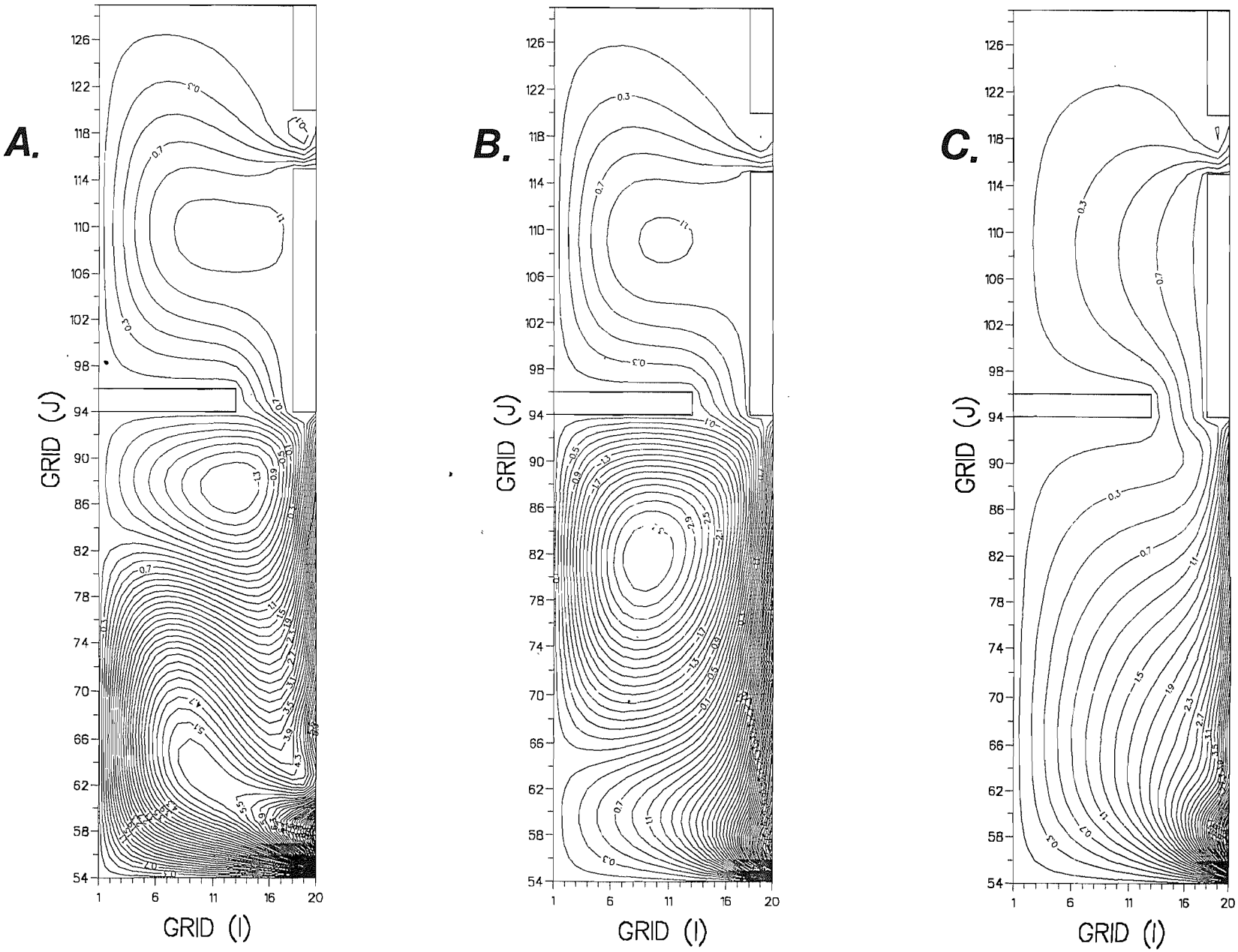
A.
B.
C.
GRID (J)
GRID (I)
126
122
118
114
110
106
102
98
94
90
86
82
78
74
70
66
62
58
54
1
6
11
16
20

Fig. 5-6. Contours of streamlines in the shelf and the MS regions for the six experiments with the depth of the shelf and the MS varying from 50 m (top left) to 300 m (bottom right) at 50 m intervals. The depth of the deep ocean is 400 m.

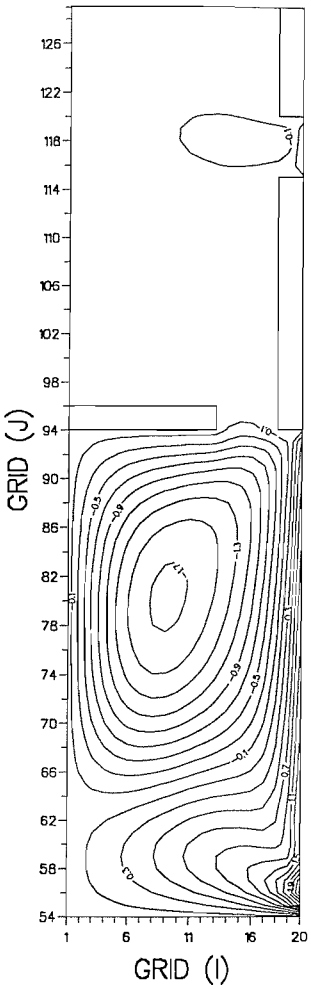
GRID (J)
GRID (I)

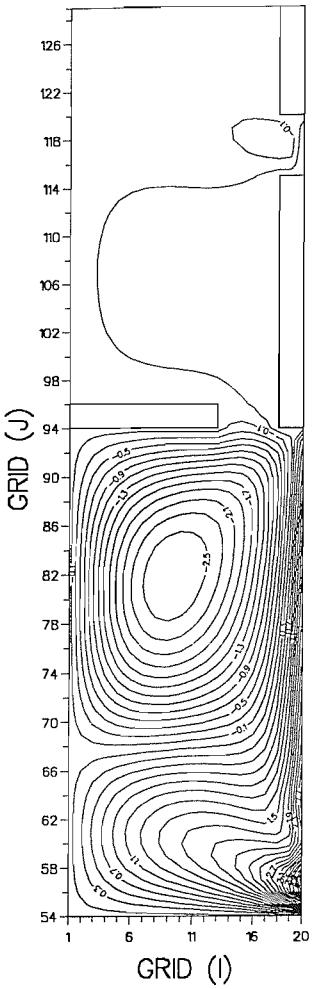
GRID (J)
GRID (I)

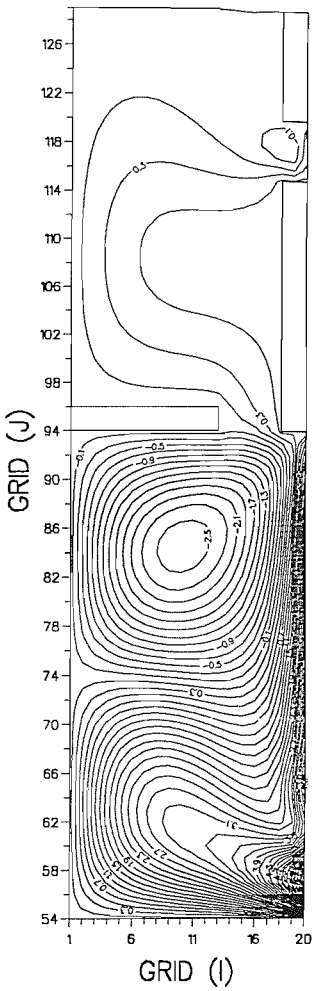
GRID (J)
GRID (I)

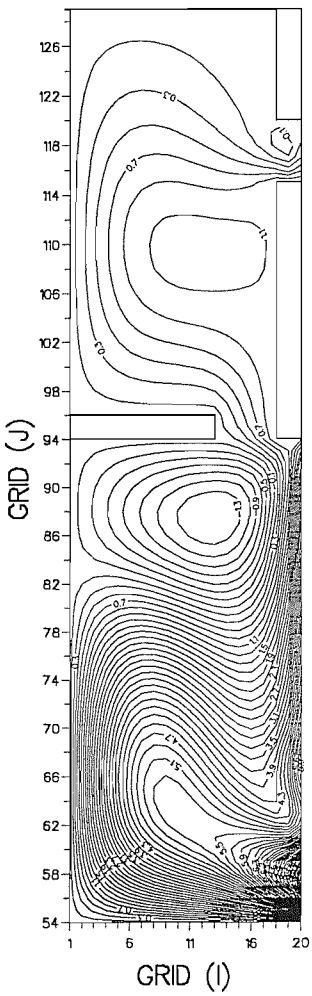
GRID (J)
GRID (I)

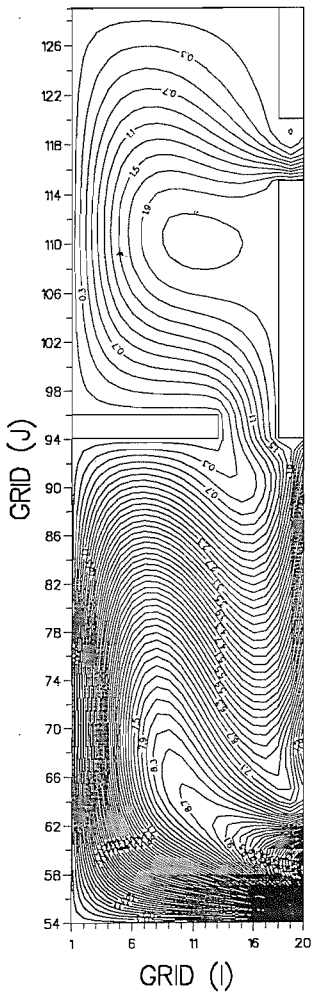
GRID (J)
GRID (I)

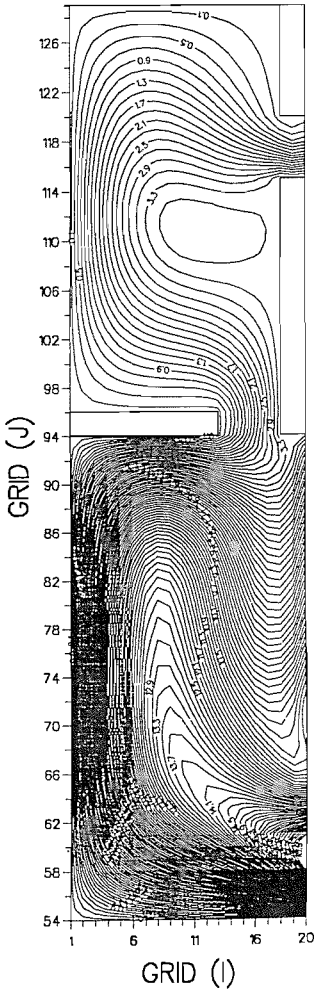
GRID (J)
GRID (I)

Fig. 5-7. The maximum on-shelf transport and the influx to the MS as a function of the shelf depth. Two solid lines having a slope of 1 and 2 are also drawn.

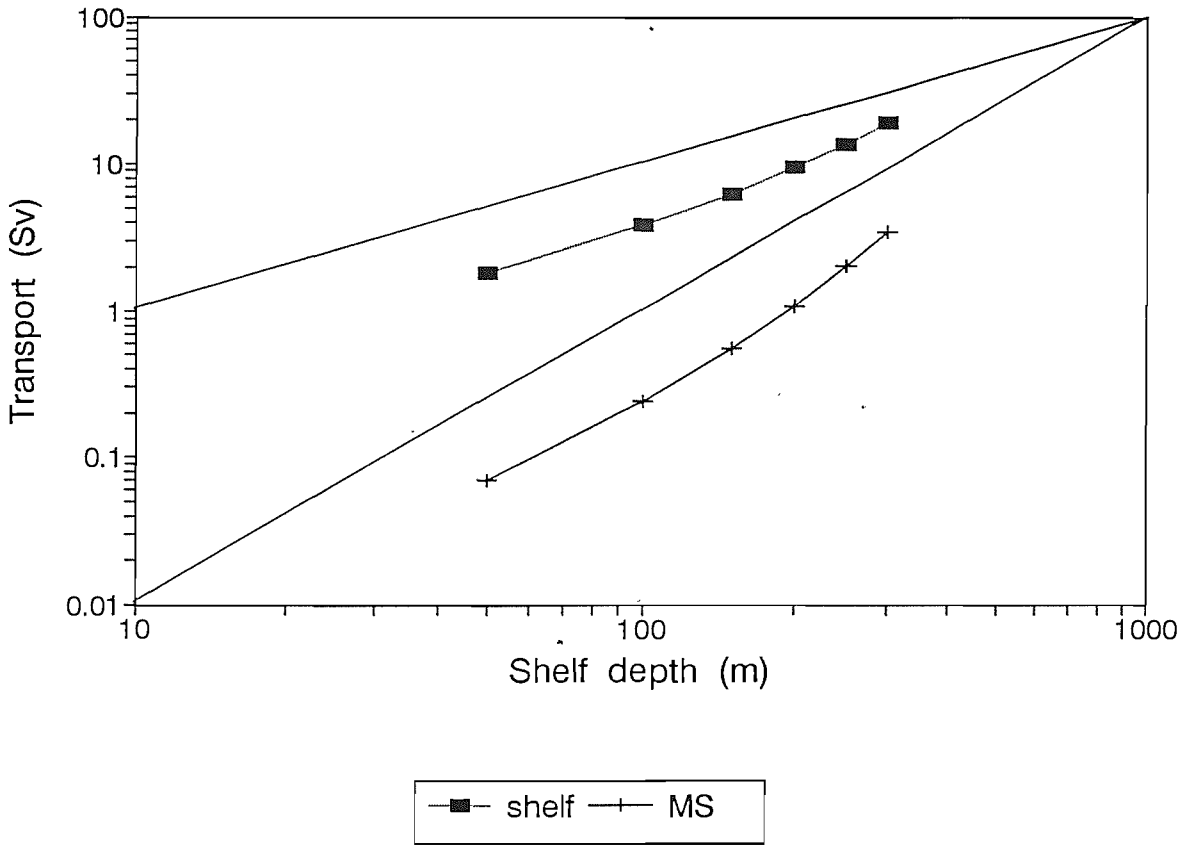
100
10
1
0.1
0.01
Transport (Sv)
10
100
1000
Shelf depth (m)
shelf
MS

Fig. 5-8. Three paths (thick solid lines) along which the pressure is calculated , superimposed on the contours of streamlines for the experiment 1 in Table 5-2. Contour intervals of the streamlines are arbitrary.

PATH A
GRID (J)
GRID (I)

PATH B
GRID (J)
GRID (I)

PATH C
GRID (J)
GRID (I)

Fig. 5-9. The pressure along the path A in Fig. 5-8 for the six experiments with different depths of the shelf and the MS. Numerals denote the shelf depth, and locations of the two straits of the MS are also marked (KS and TS in the figure).

Fig. 5-10. The pressure along the path B in Fig. 5-8 for the two experiments with different depths of the shelf and without the MS. Numerals denote the shelf depth, and locations of the two straits of the MS in the marginal sea model are also marked (KS and TS in the figure).

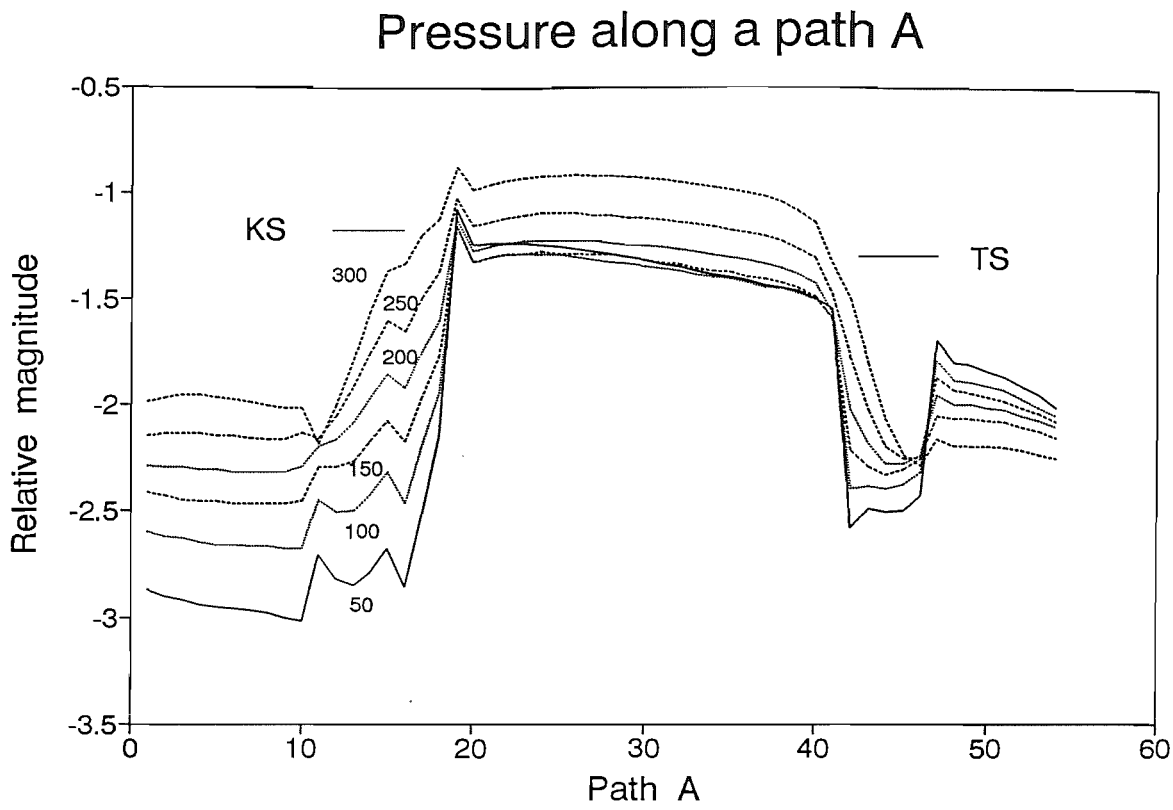
Pressure along a path A
Relative magnitude
-0.5
-1
-1.5
-2
-2.5
-3
-3.5
KS
TS
300
250
200
150
100
50
0
10
20
30
40
50
60
Path A

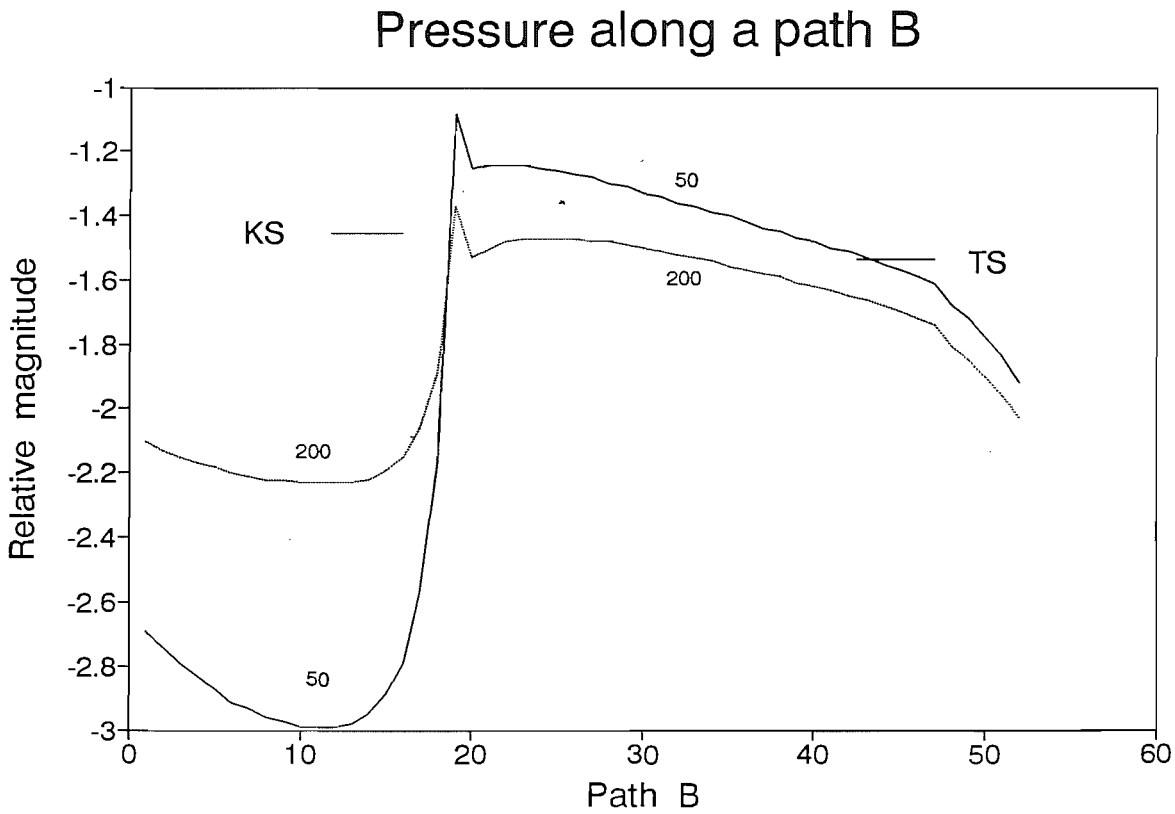
Pressure along a path B
Relative magnitude
-1
-1.2
-1.4
-1.6
-1.8
-2
-2.2
-2.4
-2.6
-2.8
-3
KS
TS
50
200
200
50
0
10
20
30
40
50
60
Path B

Fig. 5-11. The pressure along the inshore part of the western boundary current (path C in Fig. 5-8) for the two experiments with different depths of the shelf and without the MS. Numerals denote the shelf depth, and the locations of the shelf is indicated inside the figure. The location of the TS in the marginal sea model is also marked (TS in the figure).

Fig. 5-12. The pressure along the inshore part of the western boundary current (path C in Fig. 5-8) for the six experiments with different depths of the shelf and the MS. Numerals denote the shelf depth, and locations of the shelf and the TS are indicated.

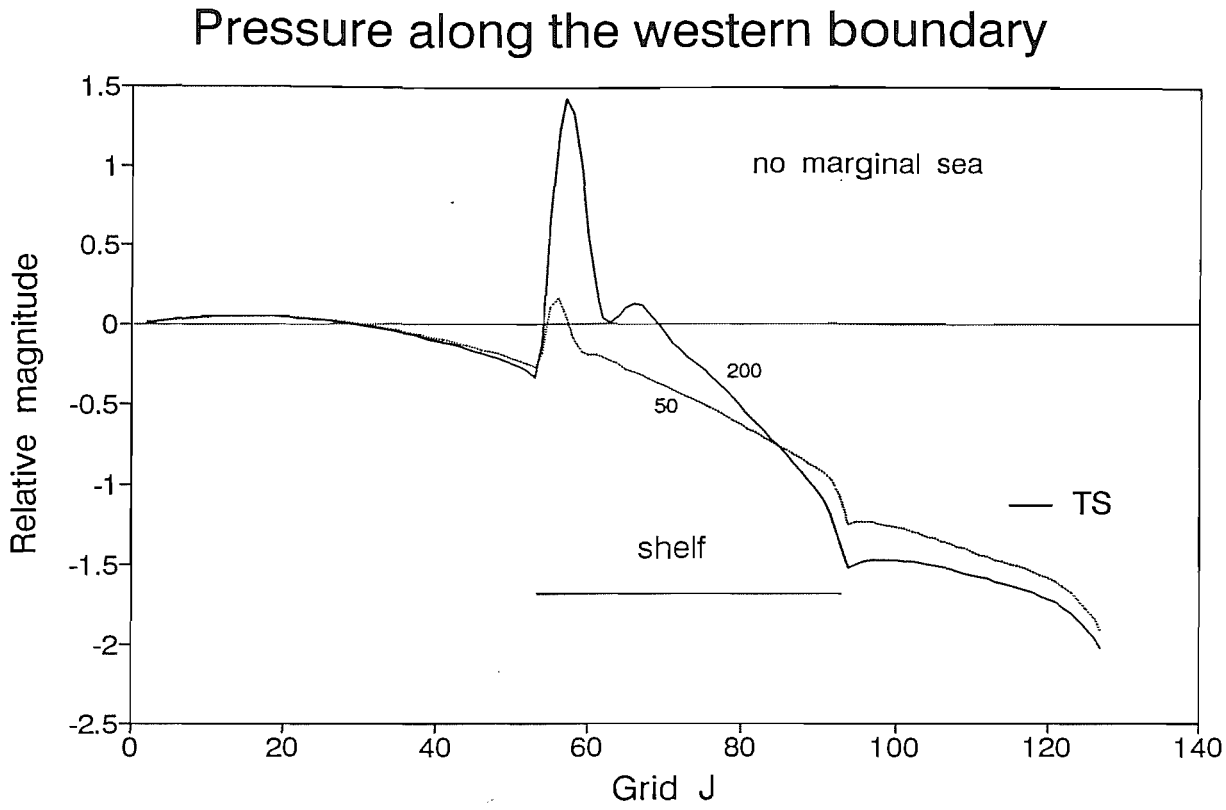
Pressure along the western boundary
Relative magnitude
1.5
1
0.5
0
-0.5
-1
-1.5
-2
-2.5
0
20
40
60
80
100
120
140
Grid J
no marginal sea
200
50
TS
shelf

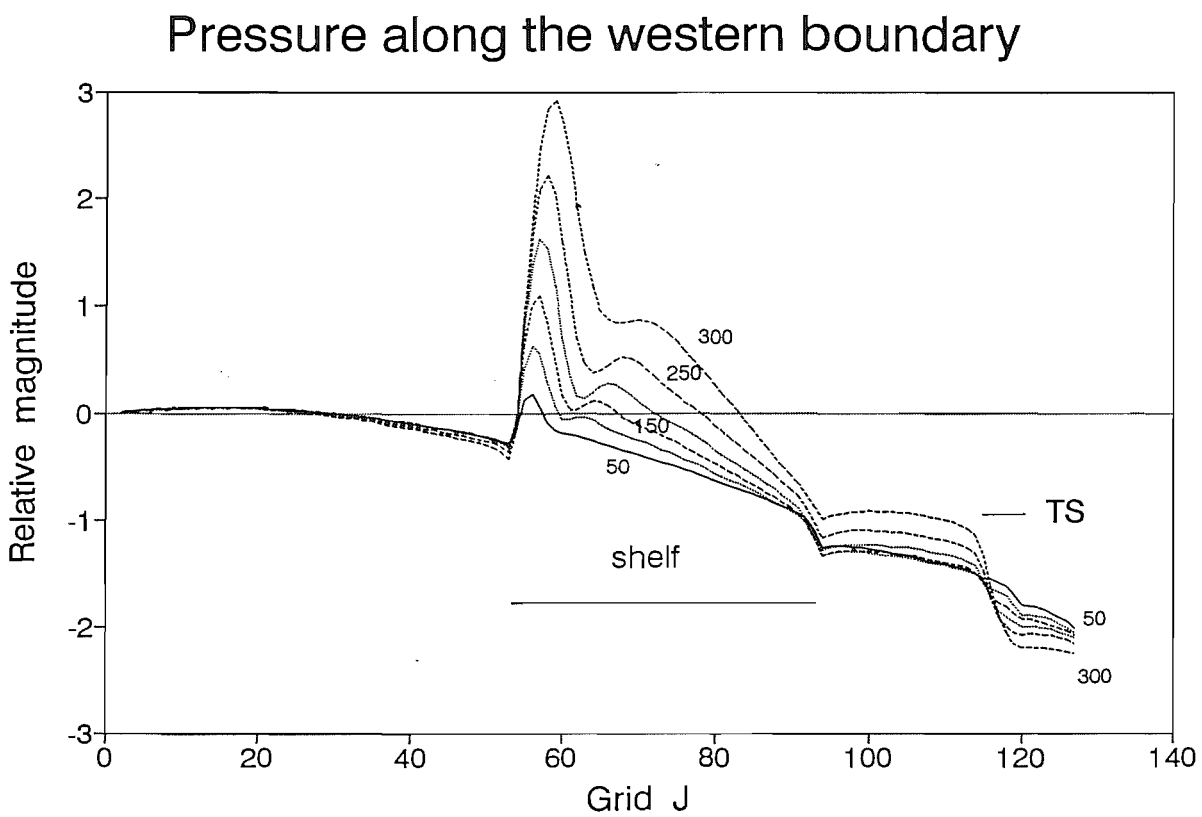
Pressure along the western boundary
Relative magnitude
3
2
1
0
-1
-2
-3
0
20
40
60
80
100
120
140
Grid J
300
250
150
50
TS
shelf
50
300

Fig. 5-13. Meridional profiles of the zonal wind stress used for the spin-up of the six experiments in Table 5-3. The y-axes represent the latitudinal grid points (grid J), and the location of the TS is indicated. Note that the location of vanishing curl of the wind stress moves to the south from left to right. The amplitude of the wind stress also decreases from left to right since the Sverdrup value is fixed.

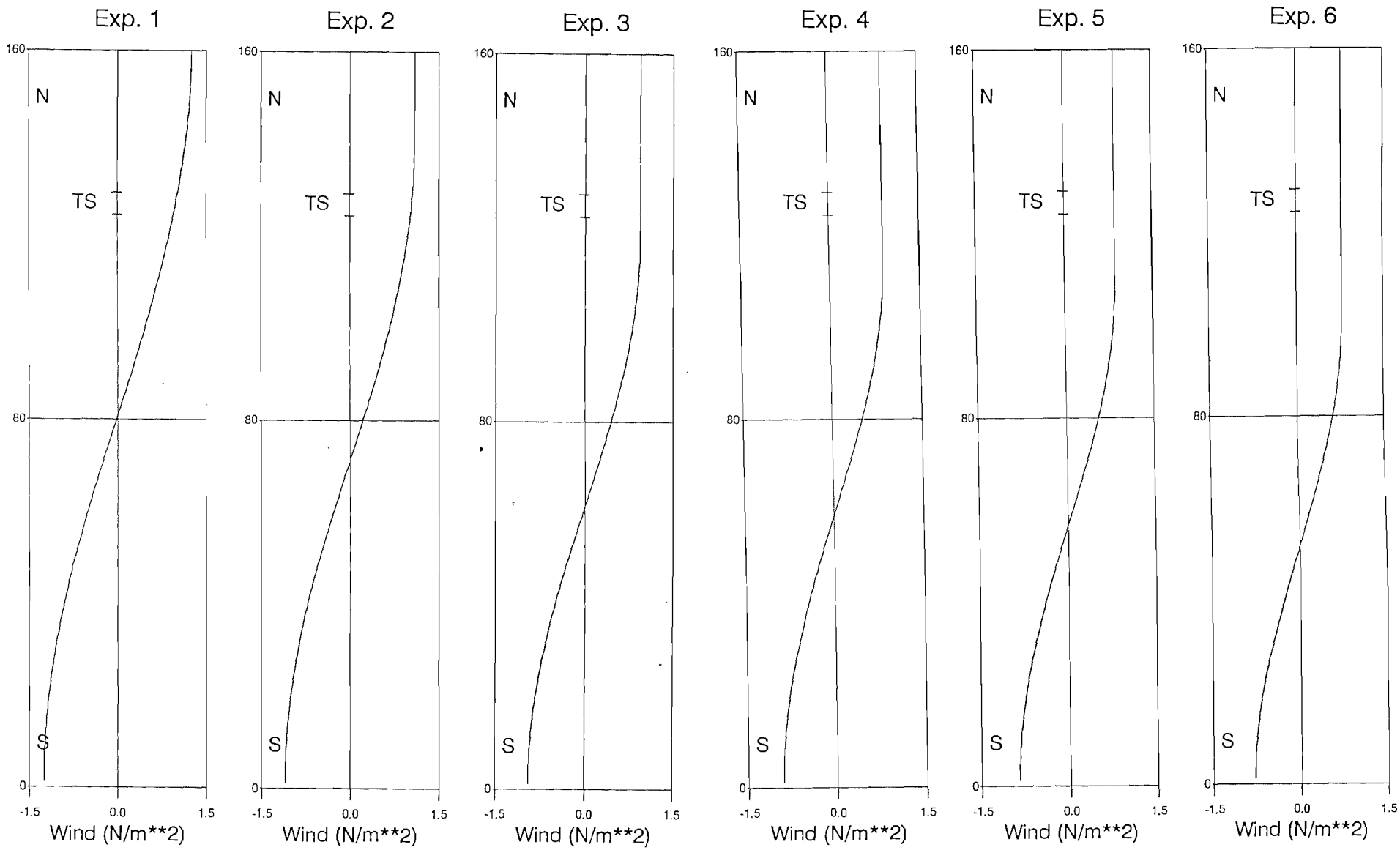
Exp. 1
Exp. 2
Exp. 3
Exp. 4
Exp. 5
Exp. 6
160
80
0
N
TS
S
-1.5
0.0
1.5
Wind (N/m**2)

Fig. 5-14. Plots of model kinetic energy as a function of time for the experiment 4 in Table 5-3 in the whole domain (labelled total), and in the deep ocean area from the offshore side of the WBC (grid J=30 in Fig. 5-18) to the eastern boundary (labelled ocean).

Fig. 5-15. As in Fig. 5-14 except in the ocean and the MS areas from 100 days to 200 days.

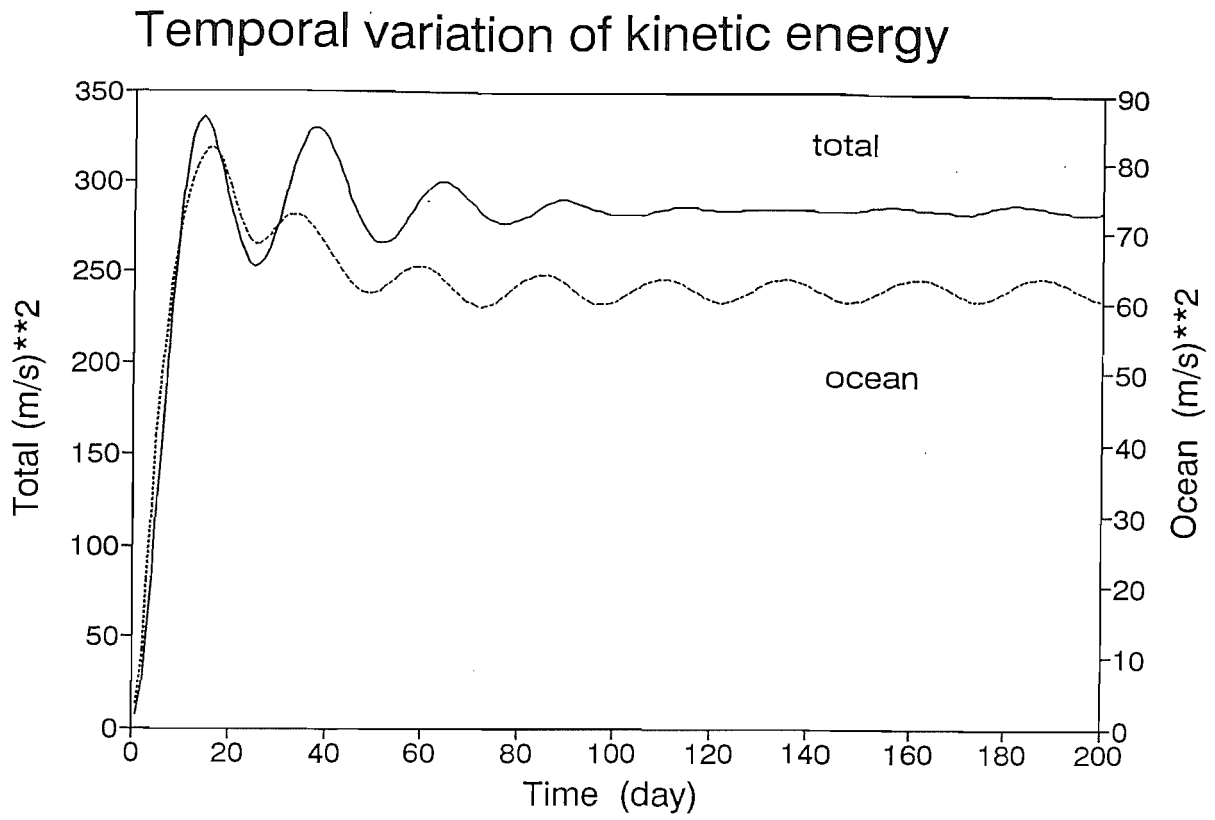
Temporal variation of kinetic energy
total
ocean
Total (m/s)**2
Ocean (m/s)**2
Time (day)
0
50
100
150
200
250
300
350
0
10
20
30
40
50
60
70
80
90
0
20
40
60
80
100
120
140
160
180
200

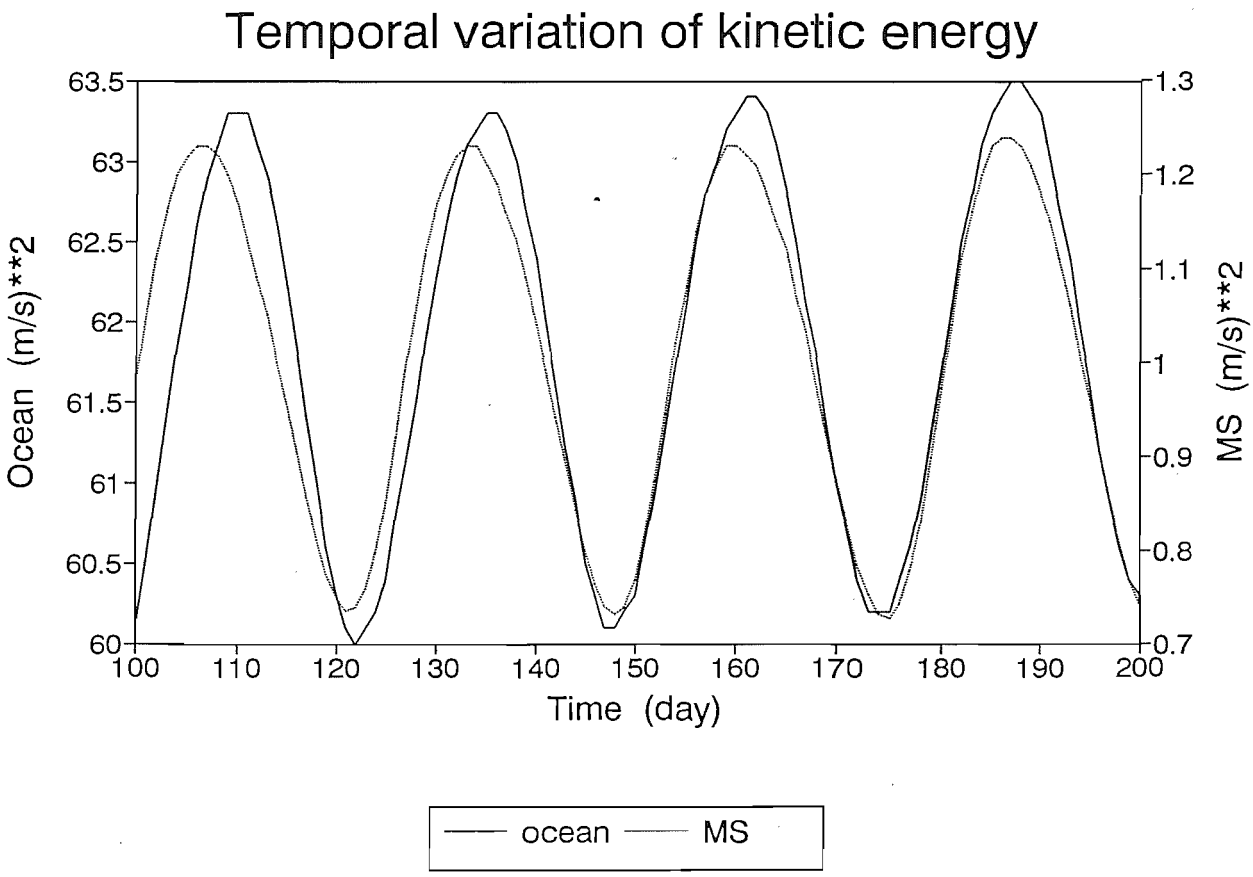
Temporal variation of kinetic energy
Ocean (m/s)**2
MS (m/s)**2
Time (day)
60
60.5
61
61.5
62
62.5
63
63.5
0.7
0.8
0.9
1
1.1
1.2
1.3
100
110
120
130
140
150
160
170
180
190
200
ocean
MS

Fig. 5-16. Plots of the maximum on-shelf transport and the influx to the MS as a function of time. Marked on the solid line are the days of maximum or minimum influx to the MS.

Fig. 5-17. Plots of the influx to the MS and the kinetic energy in the MS as a function of time.

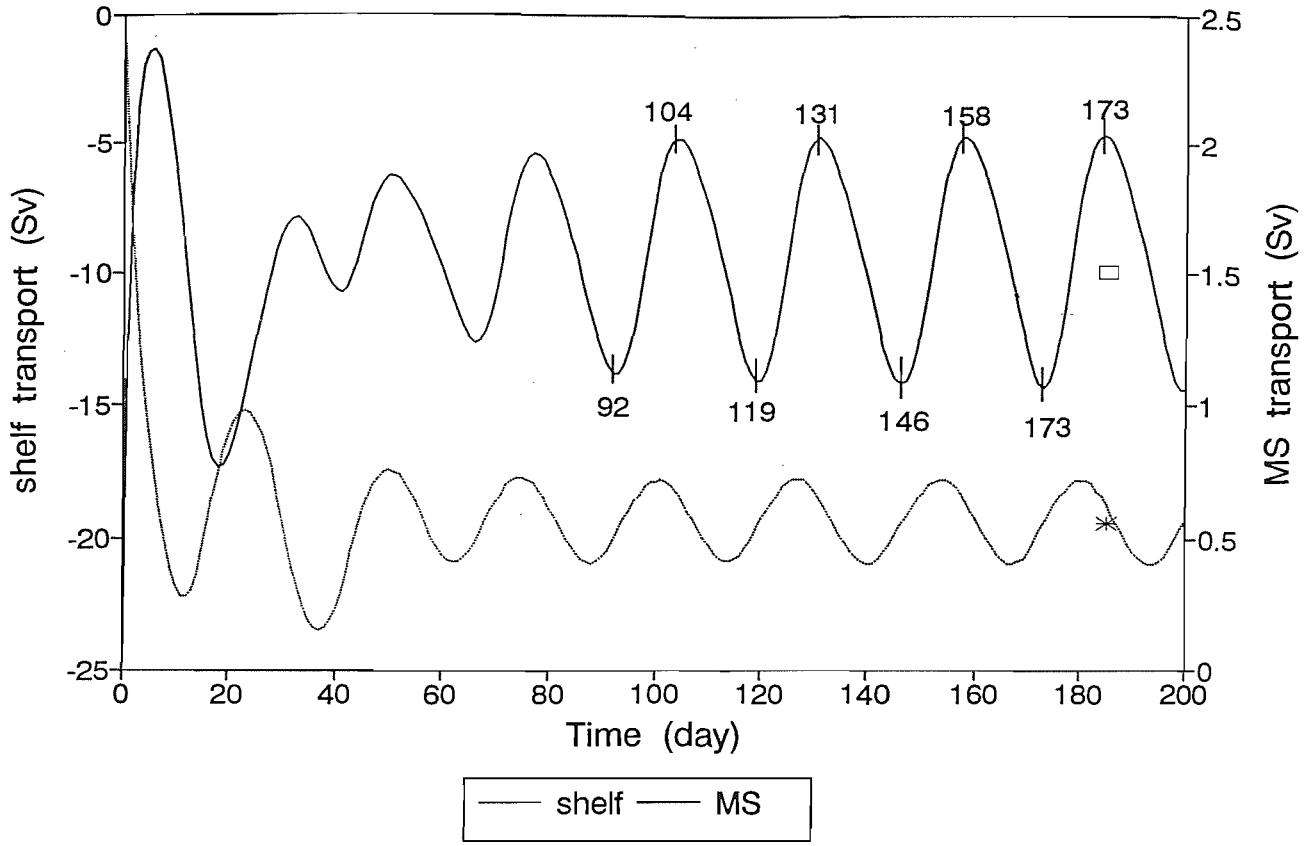
shelf transport (Sv)
MS transport (Sv)
Time (day)
104
131
158
173
92
119
146
173
shelf
MS

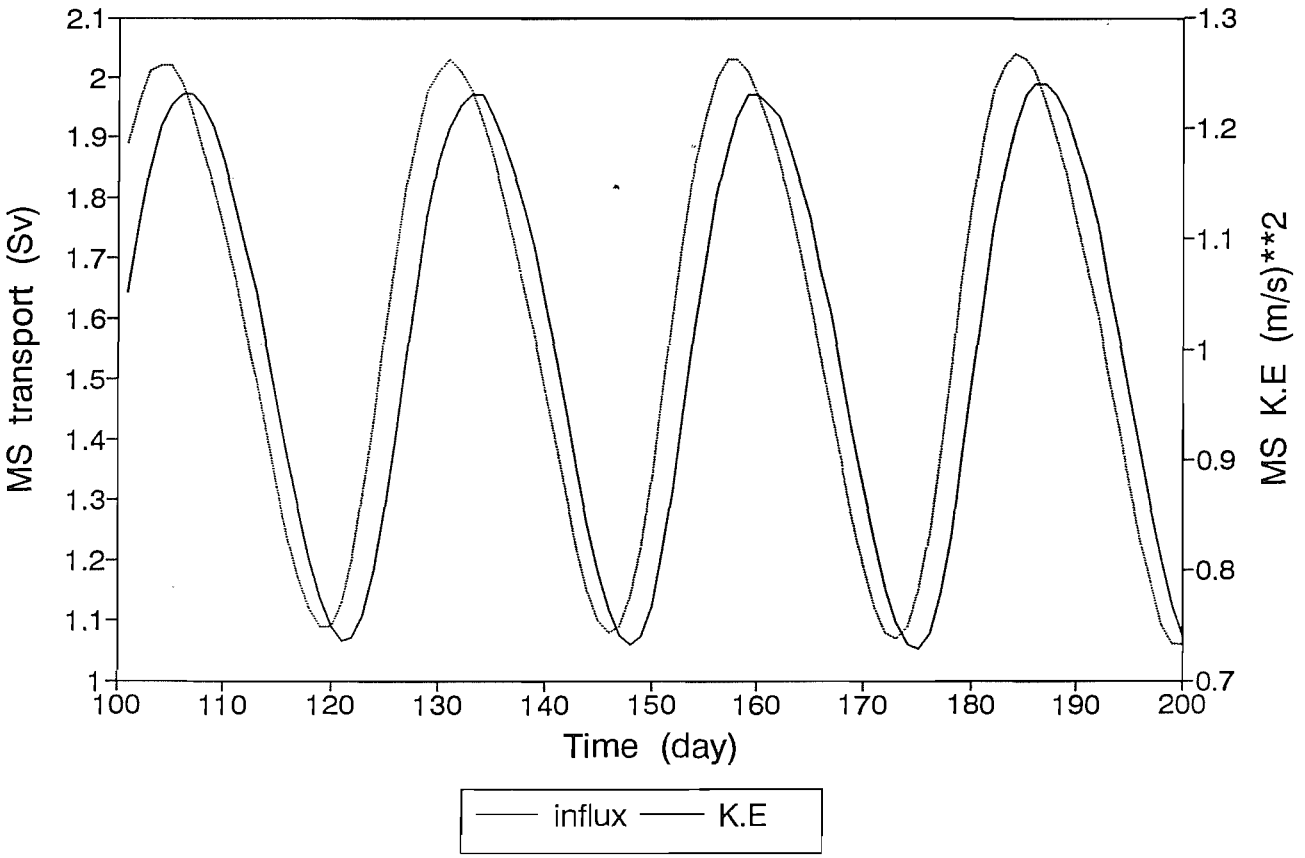
MS transport (Sv)
MS K.E (m/s)**2
Time (day)
influx
K.E

Fig. 5-18. Snapshots of streamlines for the experiment 4 in Table 5-3 at days 120, 125, 131, 138, 146, 152, and 158 plotted on Fig. 5-16. The influx to the MS showed its minimum at (A) and (E) , and its maximum at (C) and (G).

(A)
doy=120
C.I.=1.0 Sv
max = 36.90
min = -0.94
(B)
doy=125
C.I.=1.0 Sv
max = 51.51
min = -0.35
(C)
doy=131
C.I.=1.0 Sv
max = 51.29
min = -1.60
(D)
doy=138
C.I.=1.0 Sv
max = 58.43
min = -2.67
(E)
doy=146
C.I.=1.0 Sv
max = 57.50
min = -1.08
(F)
doy=152
C.I.=1.0 Sv
max = 51.26
min = -0.44
(G)
doy=158
C.I.=1.0 Sv
max = 51.99
min = -1.78
GRID (I)
GRID (J)

Fig. 5-19. The pressure along the inshore part of the western boundary current (path C in Fig. 5-8) at the different times plotted on Fig. 5-16. The influx to the MS showed its minimum at day 120, and its maximum at day 131. The southern and northern boundaries of the shelf are located at grid J=44 and J=84 respectively. The TS is located between the grid points J=124 and J=129.

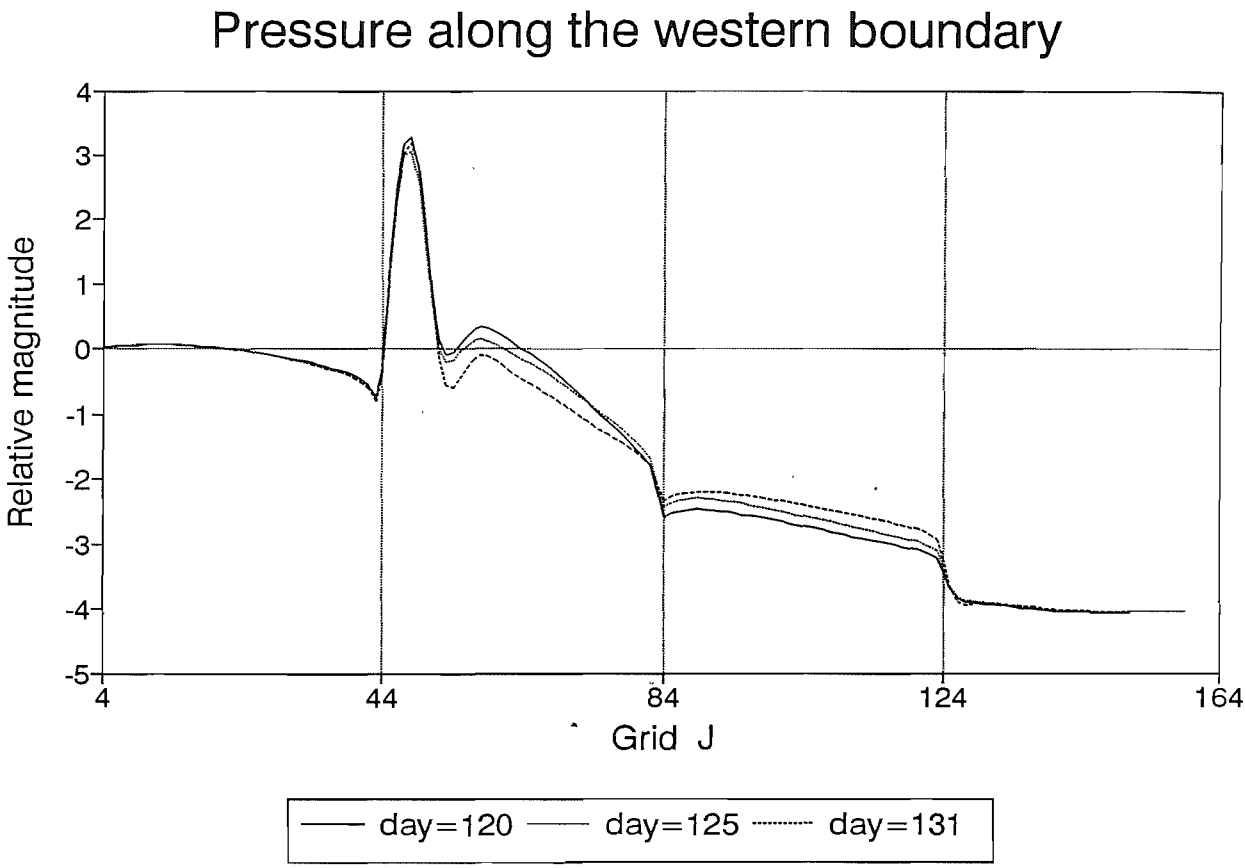
Pressure along the western boundary
Relative magnitude
4
3
2
1
0
-1
-2
-3
-4
-5
4
44
84
124
164
Grid J
day=120
day=125
day=131

Fig. 5-20. Contours of streamlines for the experiments 1 ~ 6 in Table 5-3 from (A) to (G) at the times when the influx to the MS for each case is nearly the same as its mean value.

(A)
Exp. 1
C.I.=1.0 Sv
max = 54.12
min = −0.85
GRID (J)
GRID (I)

(B)
Exp. 2
C.I.=1.0 Sv
max = 48.95
min = −1.50
GRID (J)
GRID (I)

(C)
Exp. 3
C.I.=1.0 Sv
max = 47.47
min = −0.95
GRID (J)
GRID (I)

Fig. 5-20. (continued)

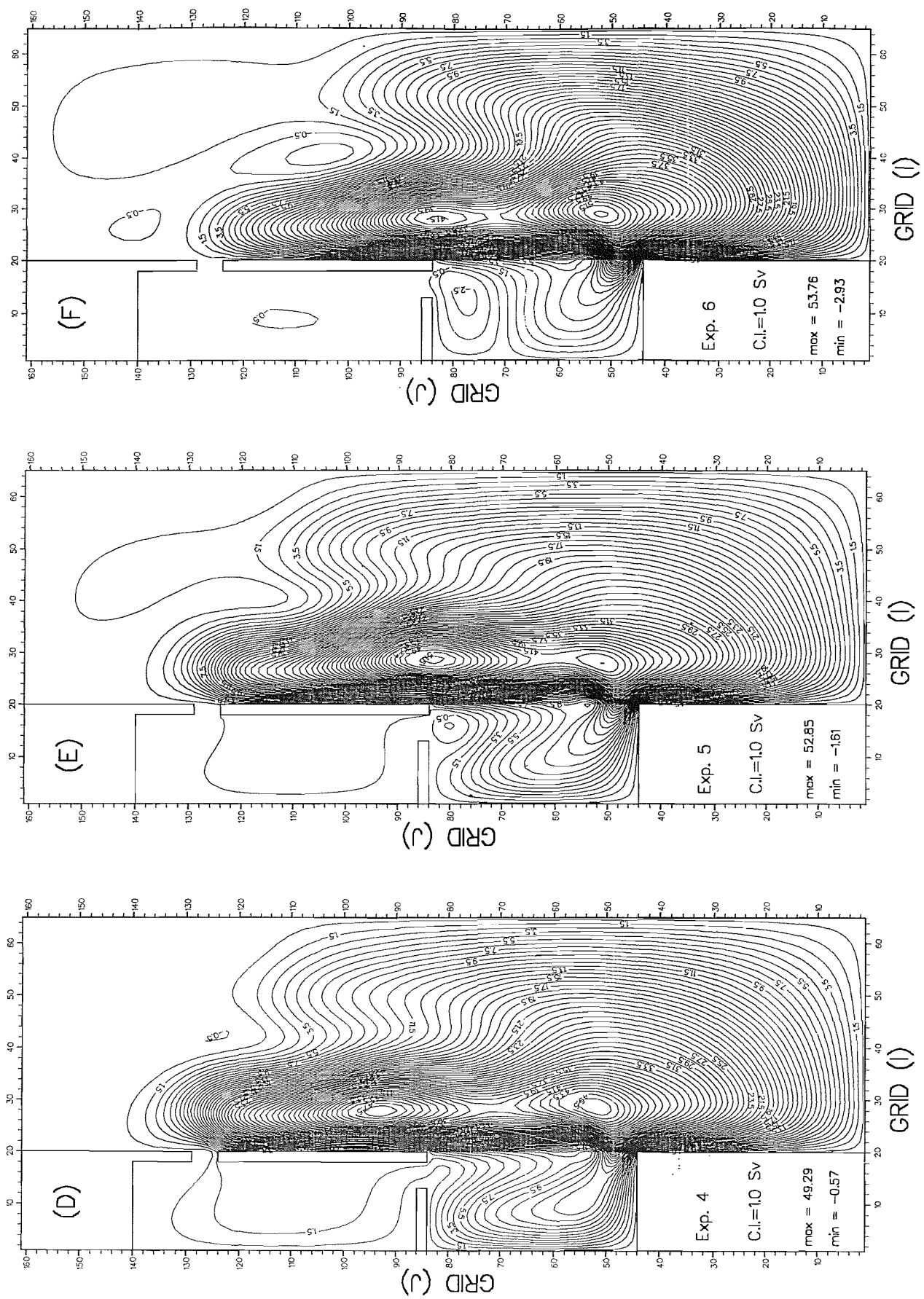
(D)
Exp. 4
C.I.=1.0 Sv
max = 49.29
min = -0.57
(E)
Exp. 5
C.I.=1.0 Sv
max = 52.85
min = -1.61
(F)
Exp. 6
C.I.=1.0 Sv
max = 53.76
min = -2.93
GRID (I)
GRID (J)

Fig. 5-21 (A). The maximum on-shelf transport and the influx to the MS as a function of the distance between the centre of the TS and the latitude of vanishing curl.

Fig. 5-21 (B). The maximum on-shelf transport and the influx to the MS as a function of the ratio between the transports of the subtropical and subpolar gyres in the deep ocean.

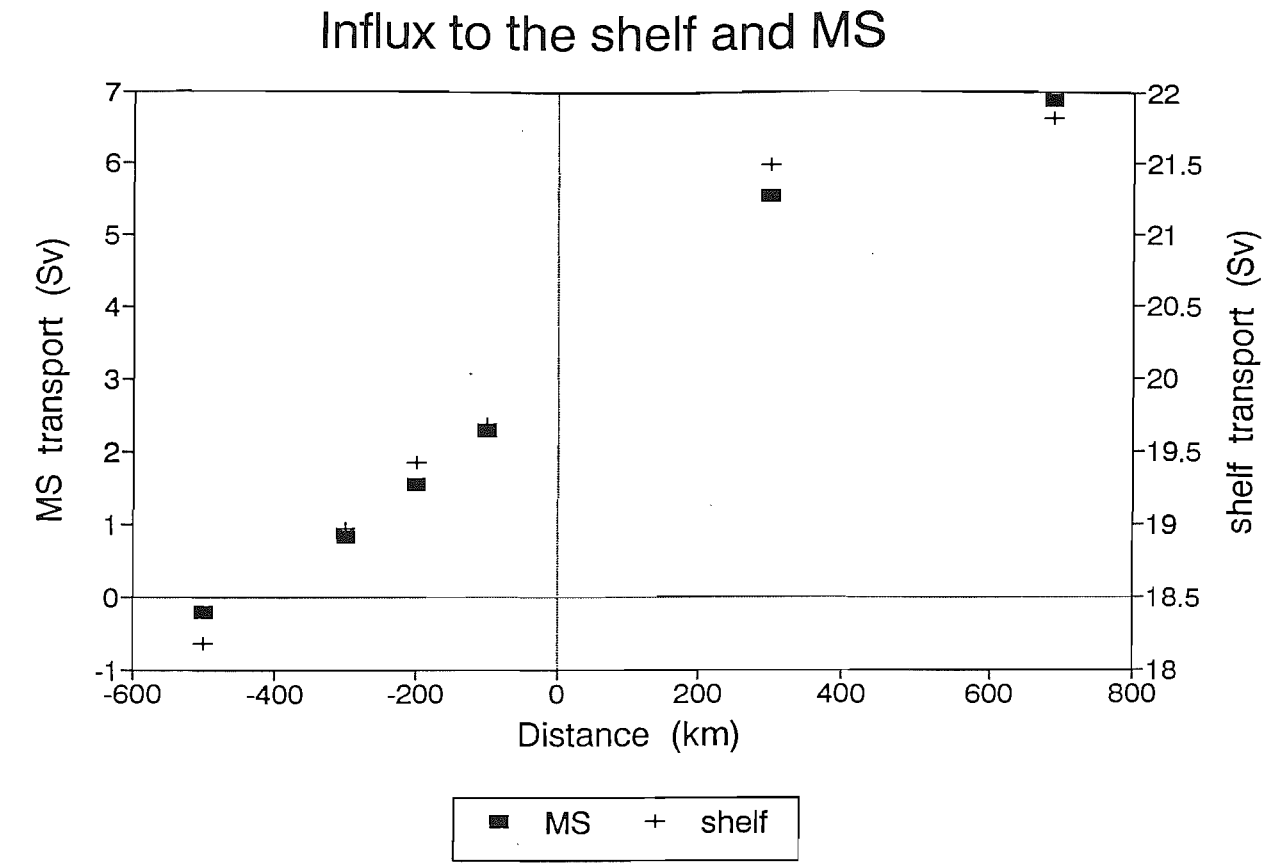
Influx to the shelf and MS
MS transport (Sv)
shelf transport (Sv)
Distance (km)
MS
shelf

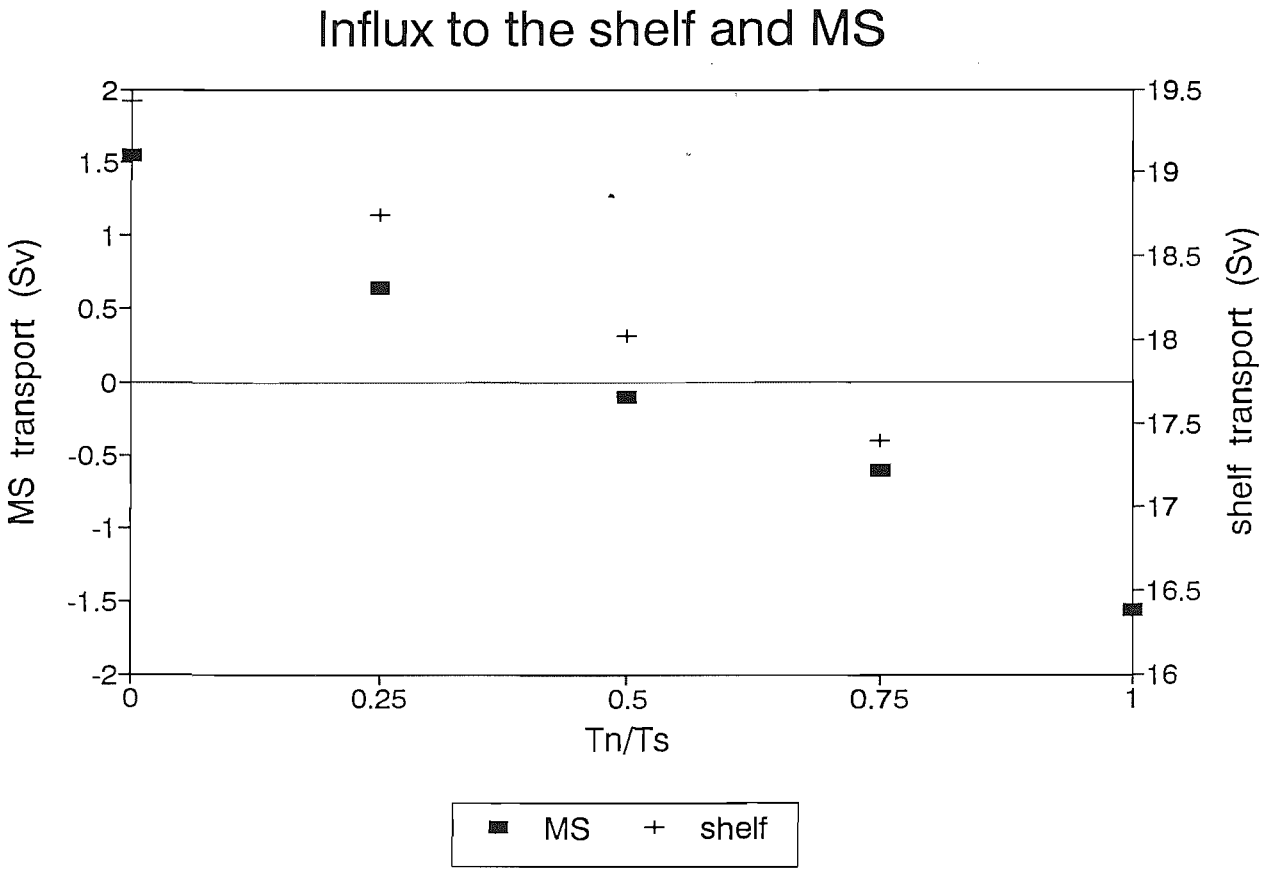
Influx to the shelf and MS
MS transport (Sv)
shelf transport (Sv)
Tn/Ts
MS
shelf

Fig. 5-22 (A). The pressure along the inshore part of the western boundary current (path C in Fig. 5-8) for the experiments 2 and 4 in Table 5-3, but without the MS. The location of the TS in the marginal sea model is indicated (TS in the figure).

Fig. 5-22 (B). The pressure along the inshore part of the western boundary current (path C in Fig. 5-8) for the six experiments in Table 5-3. Numerals denote the number of the experiments in Table 5-3.

(A) Pressure along the western boundary

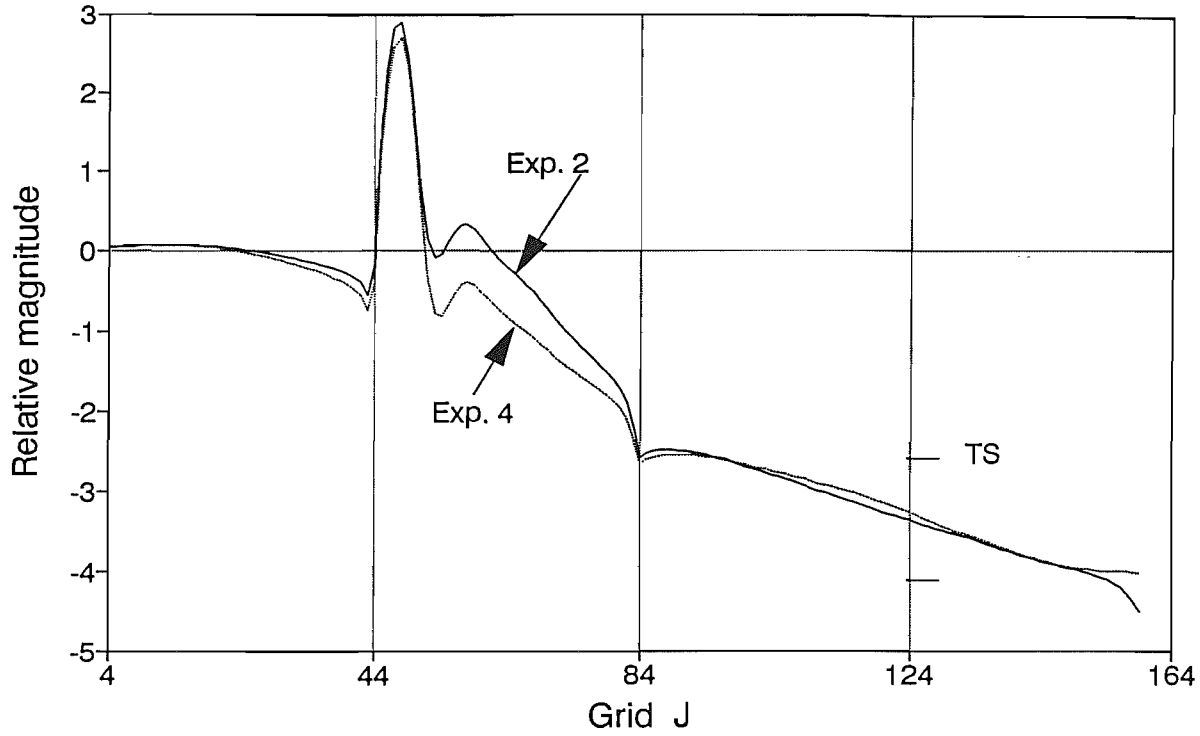

(B) Pressure along the western boundary

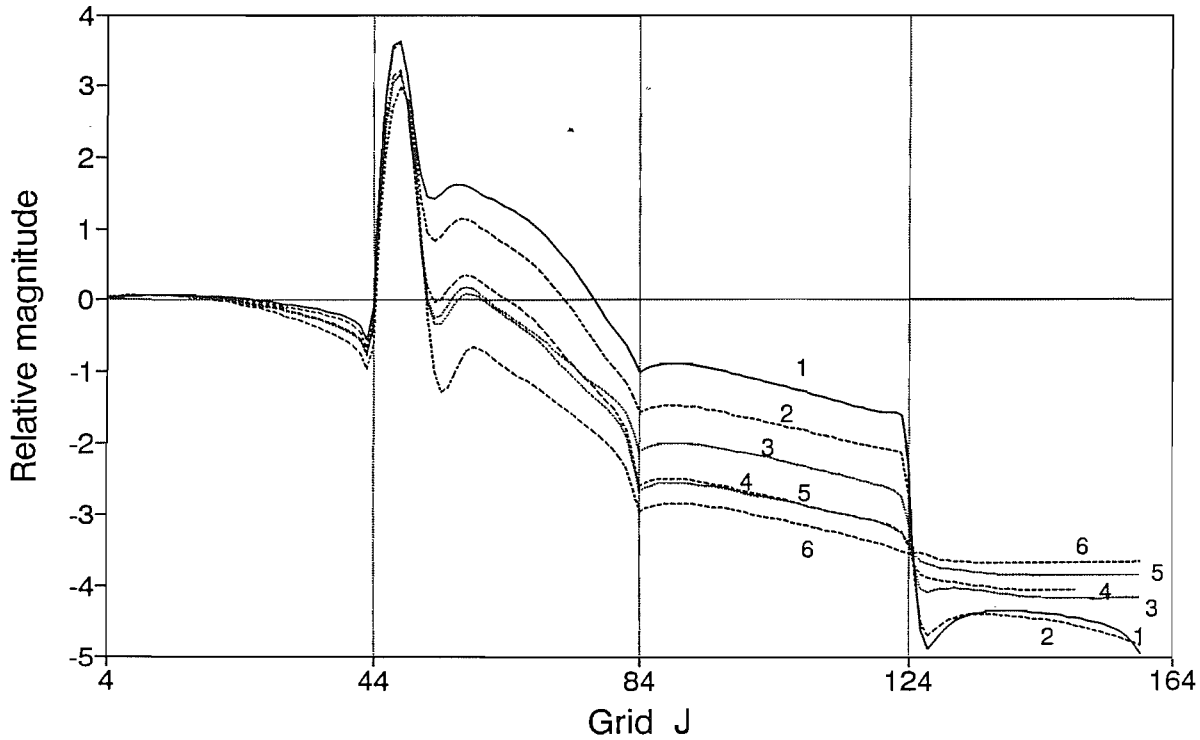

Fig. 5-23. Contours of streamlines for (A) experiment 2, and (B) experiment 4 in Table 5-3, but without MSs.

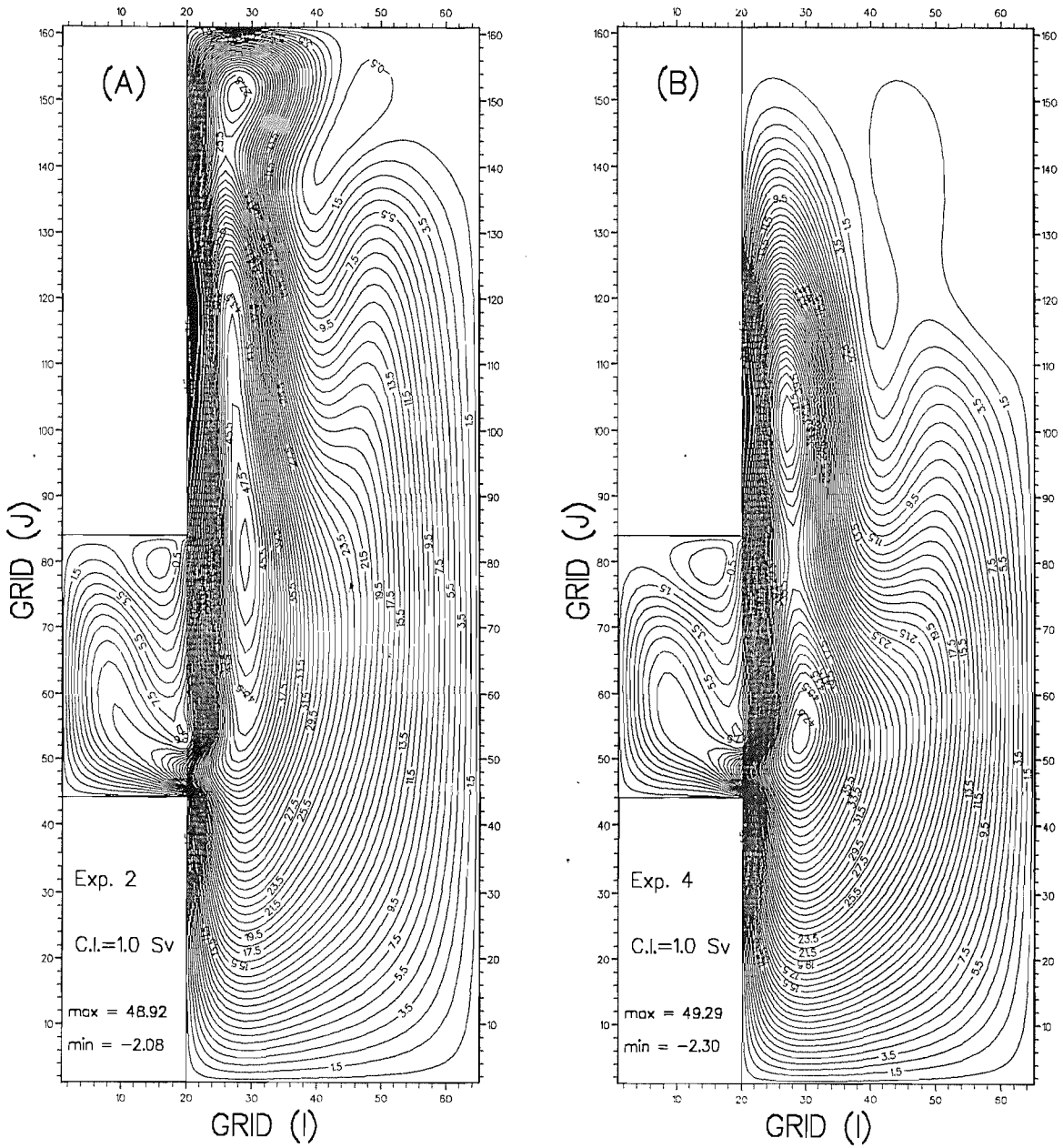
(A)
Exp. 2
C.I.=1.0 Sv
max = 48.92
min = −2.08
GRID (J)
GRID (I)
(B)
Exp. 4
C.I.=1.0 Sv
max = 49.29
min = −2.30
GRID (J)
GRID (I)

Fig. 5-24. Meridional profiles of the zonal wind stress used for the spin-up of the five experiments in Table 5-4. The y-axes represent the latitudinal grid points (grid J), and the location of the TS is indicated. Note that the location of vanishing curl of the wind stress is fixed. The amplitude of the wind stress of the subpolar gyre is intensified from left to right.

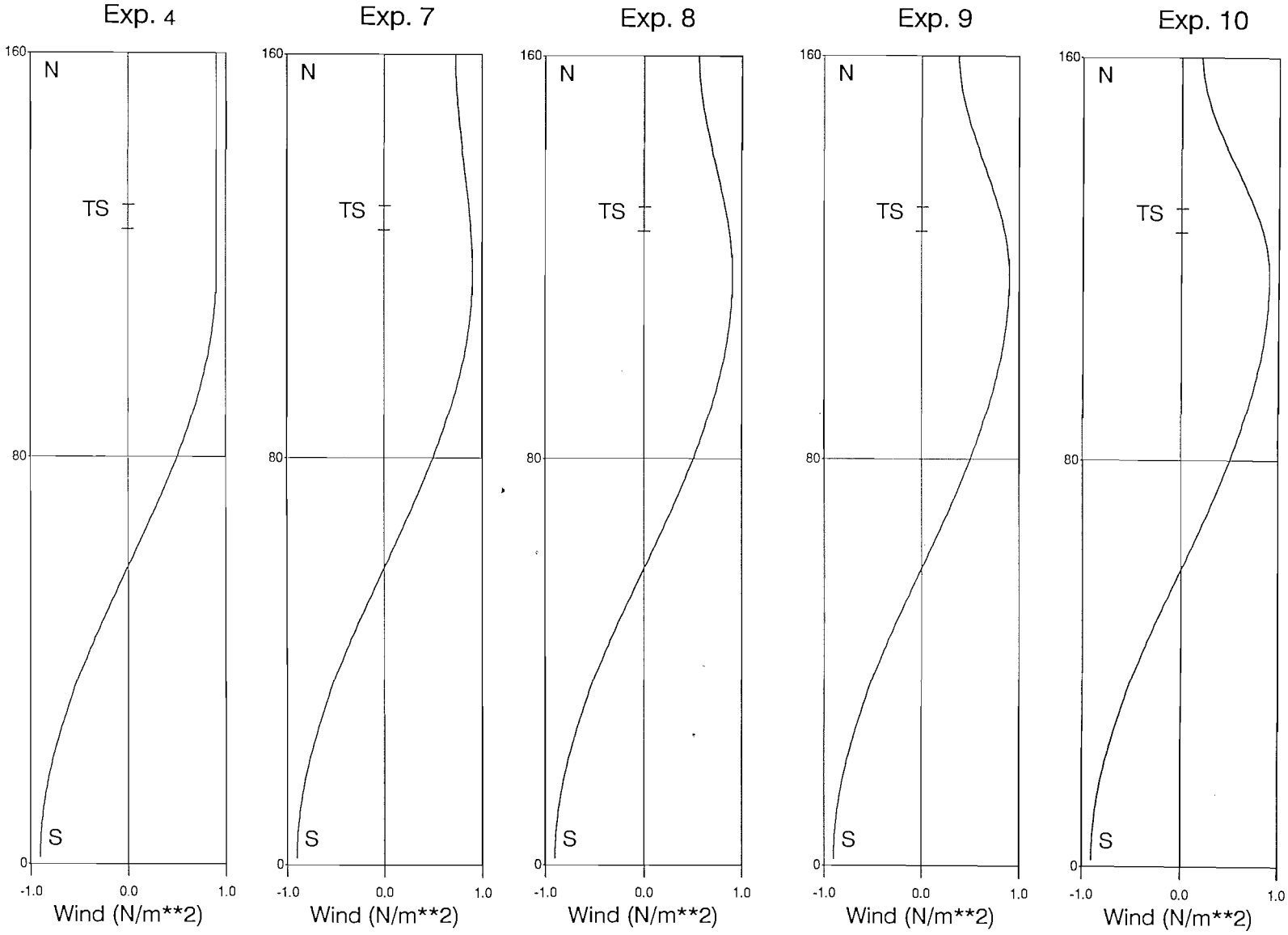
Exp. 4
Exp. 7
Exp. 8
Exp. 9
Exp. 10
160
80
0
N
TS
S
-1.0
0.0
1.0
Wind (N/m**2)

Fig. 5-25. Contours of streamlines for the experiments 4, and 7 ~ 10 in Table 5-4 from (A) to (E) at the times when the influx to the MS for each case is nearly the same as its mean value.

(A)
Exp. 4
C.I.=2.0 Sv
max = 57.37
min = −2.40
GRID (J)
GRID (I)

(B)
Exp. 7
C.I.=2.0 Sv
max = 48.42
min = −15.85
GRID (J)
GRID (I)

(C)
Exp. 8
C.I.=2.0 Sv
max = 55.43
min = −31.31
GRID (J)
GRID (I)

Fig. 5-25. (continued)

(D)
Exp. 9
C.I.=2.0 Sv
max = 62.44
min = −50.51
GRID (J)
GRID (I)
(E)
Exp. 10
C.I.=2.0 Sv
max = 109.21
min = −101.41
GRID (J)
GRID (I)

Fig. 5-26. The pressure along the inshore part of the western boundary current (path C in Fig. 5-8) for the experiments 4, 7, 9, and 10 in Table 5-4, but without the MS. The location of the TS in the marginal sea model is indicated (horizontal bar near the grid J=124 in the figure).

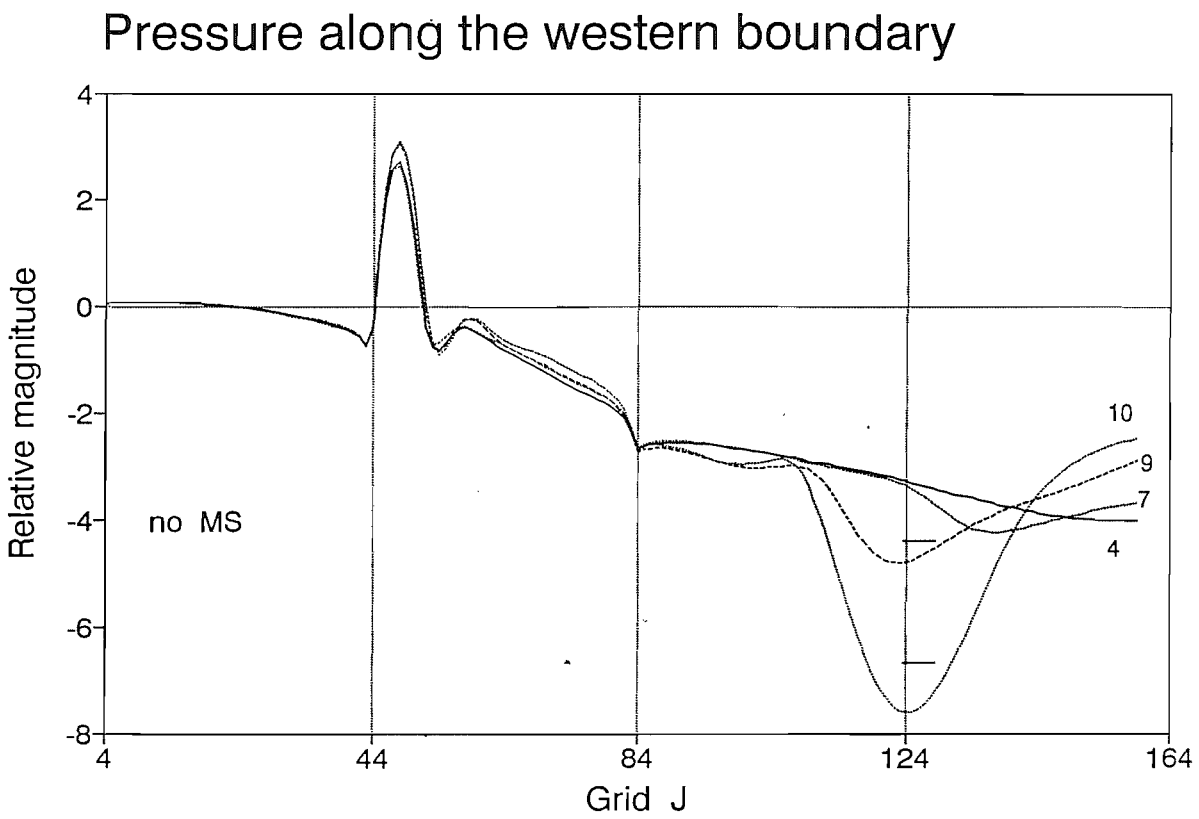
Pressure along the western boundary
Relative magnitude
4
2
0
-2
-4
-6
-8
4
44
84
124
164
Grid J
no MS
10
9
7
4

Fig. 5-27. Contours of streamlines for the three experiments in Table 5-5. The value for the lateral eddy viscosity are (A) 5000 m^2s^{-1}, (B) 10000 m^2s^{-1}, and (C) 20000 m^2s^{-1}.

(A)
A=5000
C.I.=1.0 Sv
max = 49.29
min = −0.57
GRID (J)
GRID (I)

(B)
A=10000
C.I.=1.0 Sv
max = 48.70
min = −1.41
GRID (J)
GRID (I)

(C)
A=20000
C.I.=1.0 Sv
max = 47.73
min = −1.62
GRID (J)
GRID (I)

Fig. 5-28. Contours of streamlines for experiments 2-1, and 4-1 in Table 5-6. The longitudinal distances of the deep ocean basins are extended to 2.4 times of those of experiments 2 and 4 in Table 5-3.

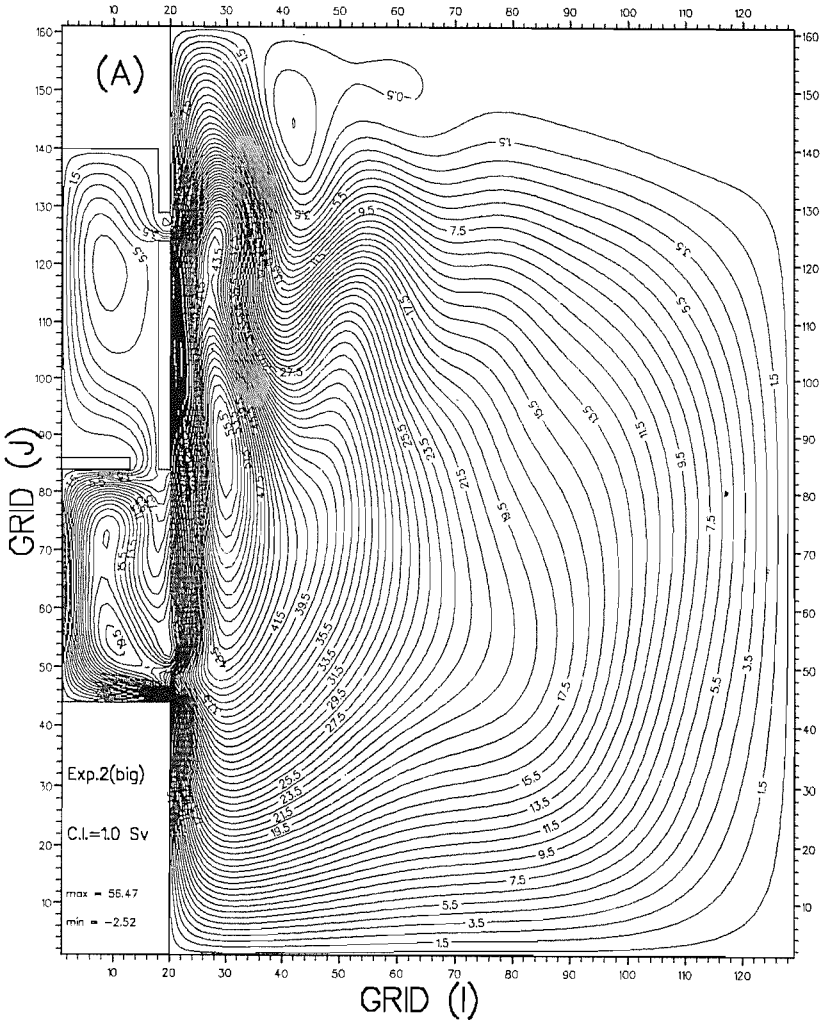
(A)
Exp.2(big)
C.I.=1.0 Sv
max = 56.47
min = -2.52
GRID (J)
GRID (I)

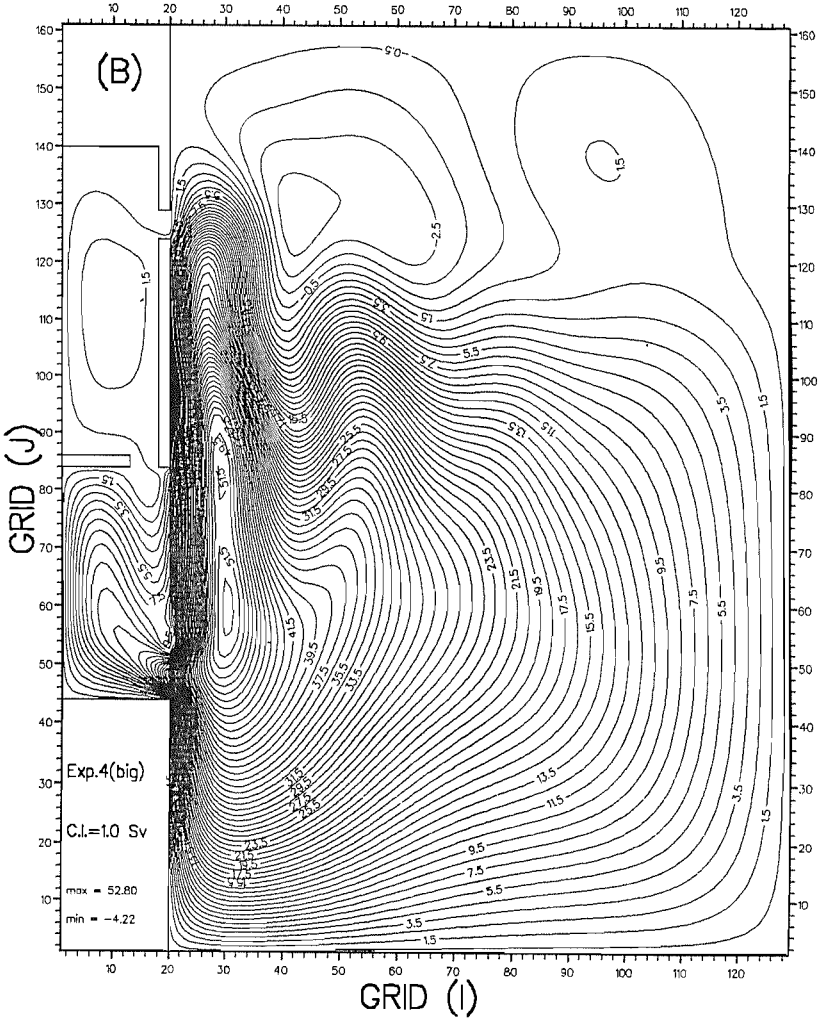
(B)
Exp.4(big)
C.I.=1.0 Sv
max = 52.80
min = -4.22
GRID (J)
GRID (I)

Fig. 5-29. Plan view of the realistic model domain with bottom topography. Contour intervals between isobaths are 20 m. The ECS, JS, KS, and TS denote the East China Sea, the Japan Sea, Korea Strait, and Tsugaru Strait respectively.

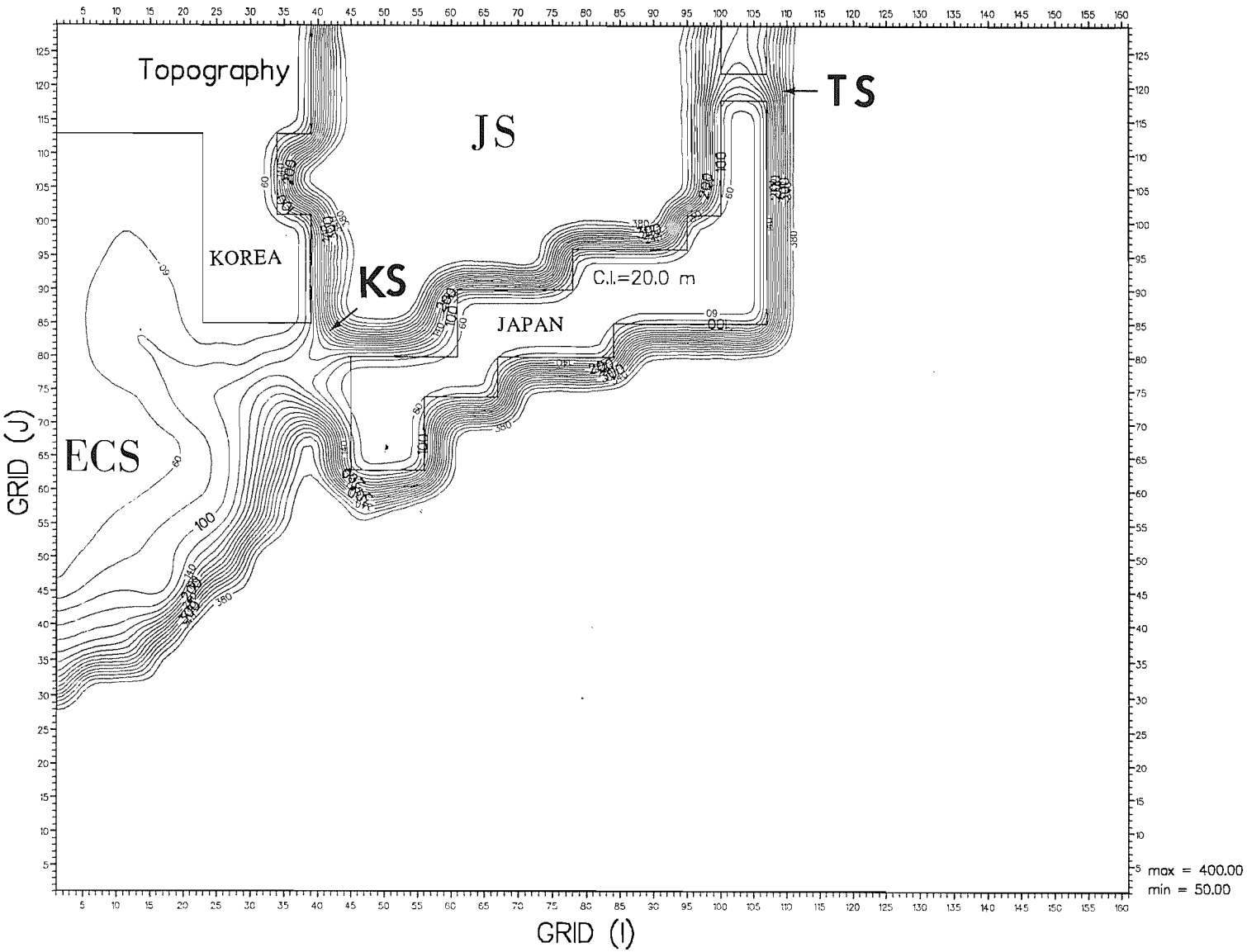
Topography
JS
TS
KOREA
KS
C.I.=20.0 m
JAPAN
ECS
GRID (J)
GRID (I)
max = 400.00
min = 50.00

Fig. 5-30. Time series of the total kinetic energy and the influx to the Japan Sea obtained for every one day interval from the standard case in Table 5-7.

Fig. 5-31. Contours of streamlines for the standard case at an equilibrium state. Contour intervals are 2 Sv from a streamline 58.5 to a streamline 102.5, and the intervals of other streamlines are 1 Sv. The 1.0 Sv streamline is also marked. The thick solid line indicates a section on which the velocity component perpendicular to the line is plotted together with the topographic profile along the line in Fig. 32 (A).

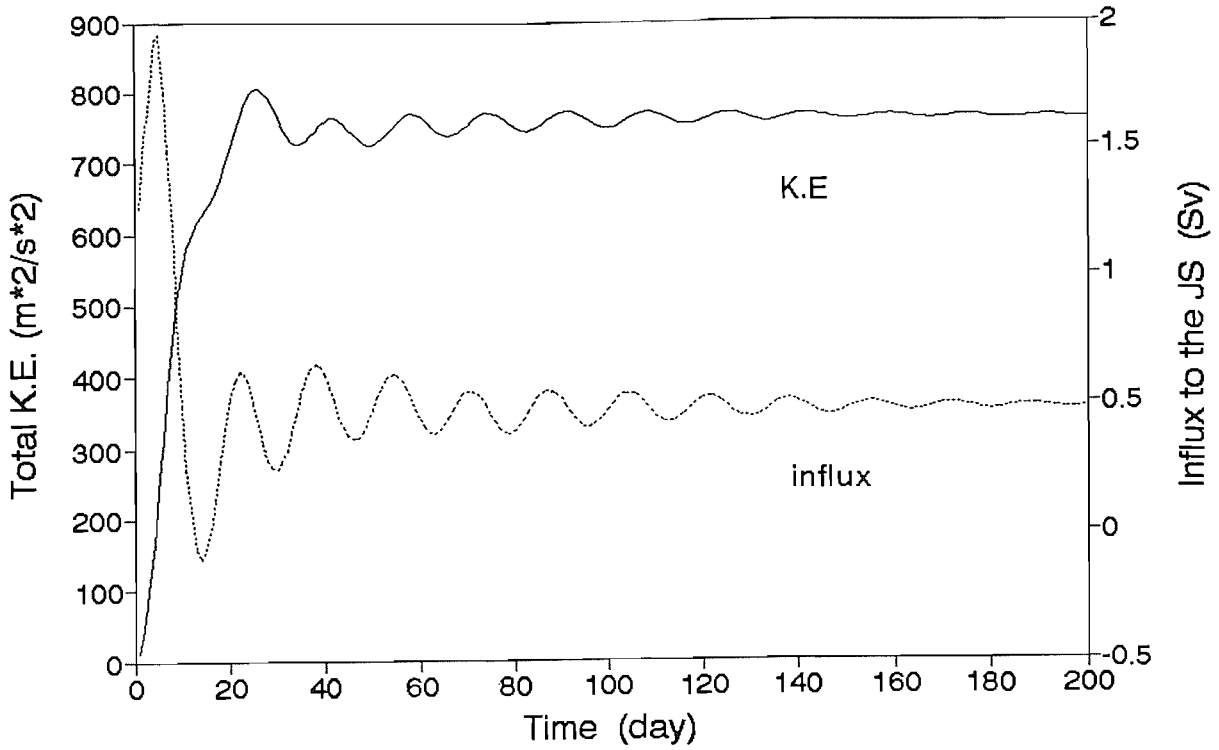
Kinetic energy and influx to the JS
Total K.E. (m*2/s*2)
Influx to the JS (Sv)
K.E
influx
Time (day)
0
100
200
300
400
500
600
700
800
900
-0.5
0
0.5
1
1.5
2
0
20
40
60
80
100
120
140
160
180
200

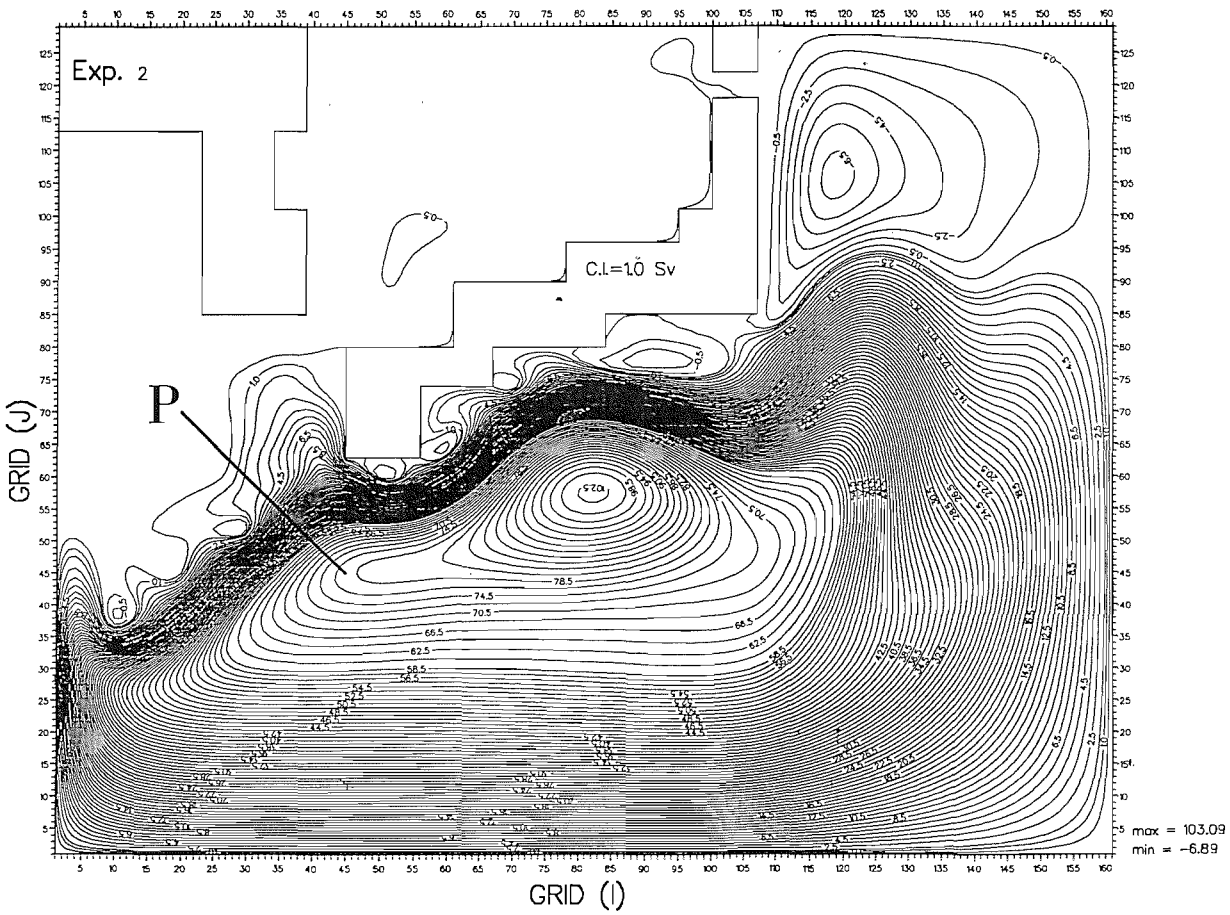
Exp. 2
C.I=1.0 Sv
P
GRID (J)
GRID (I)
max = 103.09
min = -6.89

Fig. 5-32 (A). Profiles of the velocity component perpendicular to the line P in Fig. 5-31, and bottom topography along the line. **(B).** Profiles of the meridional velocity component, and bottom topography along the western wall (I=2 in Fig. 5-31).

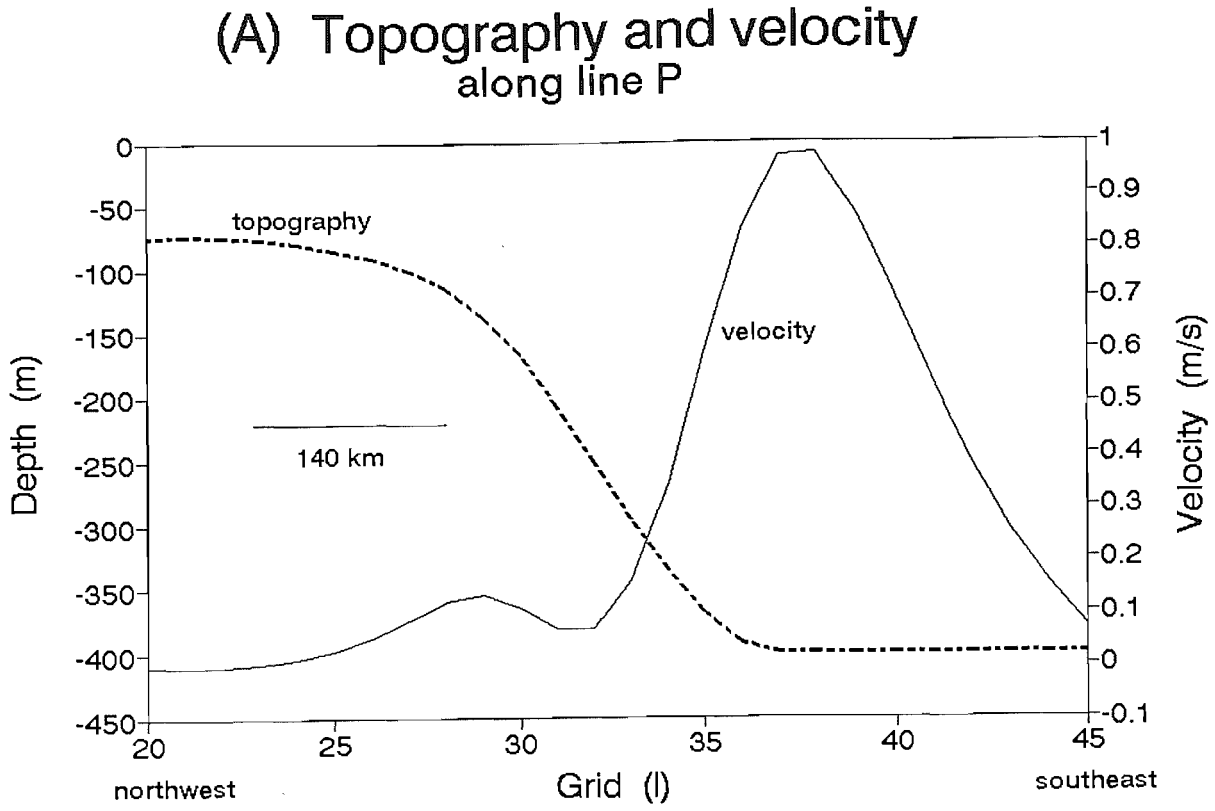
(A) Topography and velocity
along line P
topography
velocity
140 km
Depth (m)
Velocity (m/s)
0
-50
-100
-150
-200
-250
-300
-350
-400
-450
1
0.9
0.8
0.7
0.6
0.5
0.4
0.3
0.2
0.1
0
-0.1
20
25
30
35
40
45
northwest
Grid (I)
southeast

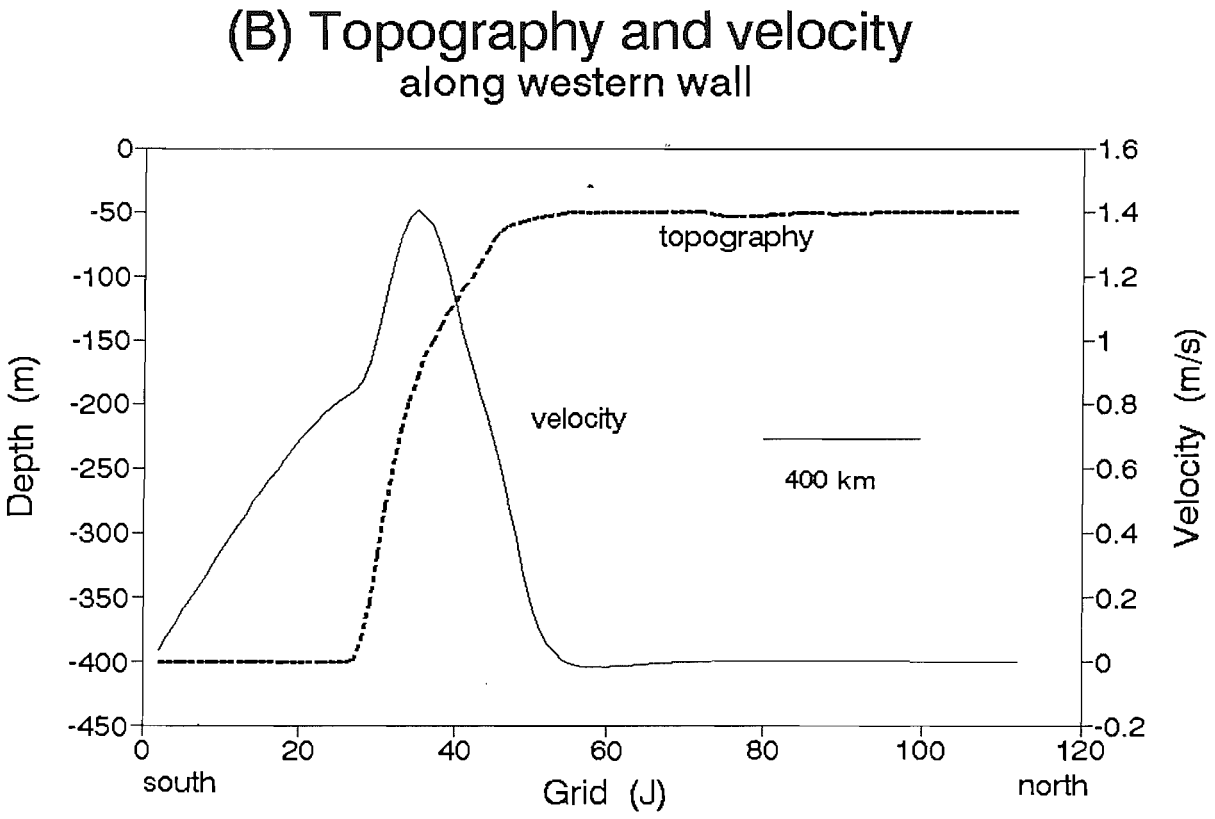
(B) Topography and velocity
along western wall
topography
velocity
400 km
Depth (m)
Velocity (m/s)
0
-50
-100
-150
-200
-250
-300
-350
-400
-450
1.6
1.4
1.2
1
0.8
0.6
0.4
0.2
0
-0.2
0
20
40
60
80
100
120
south
Grid (J)
north

Fig. 5-33. Trajectories of three satellite tracking surface drifters released in July 17, 1991 in the area west of Kyushu (from KORDI, 1992).

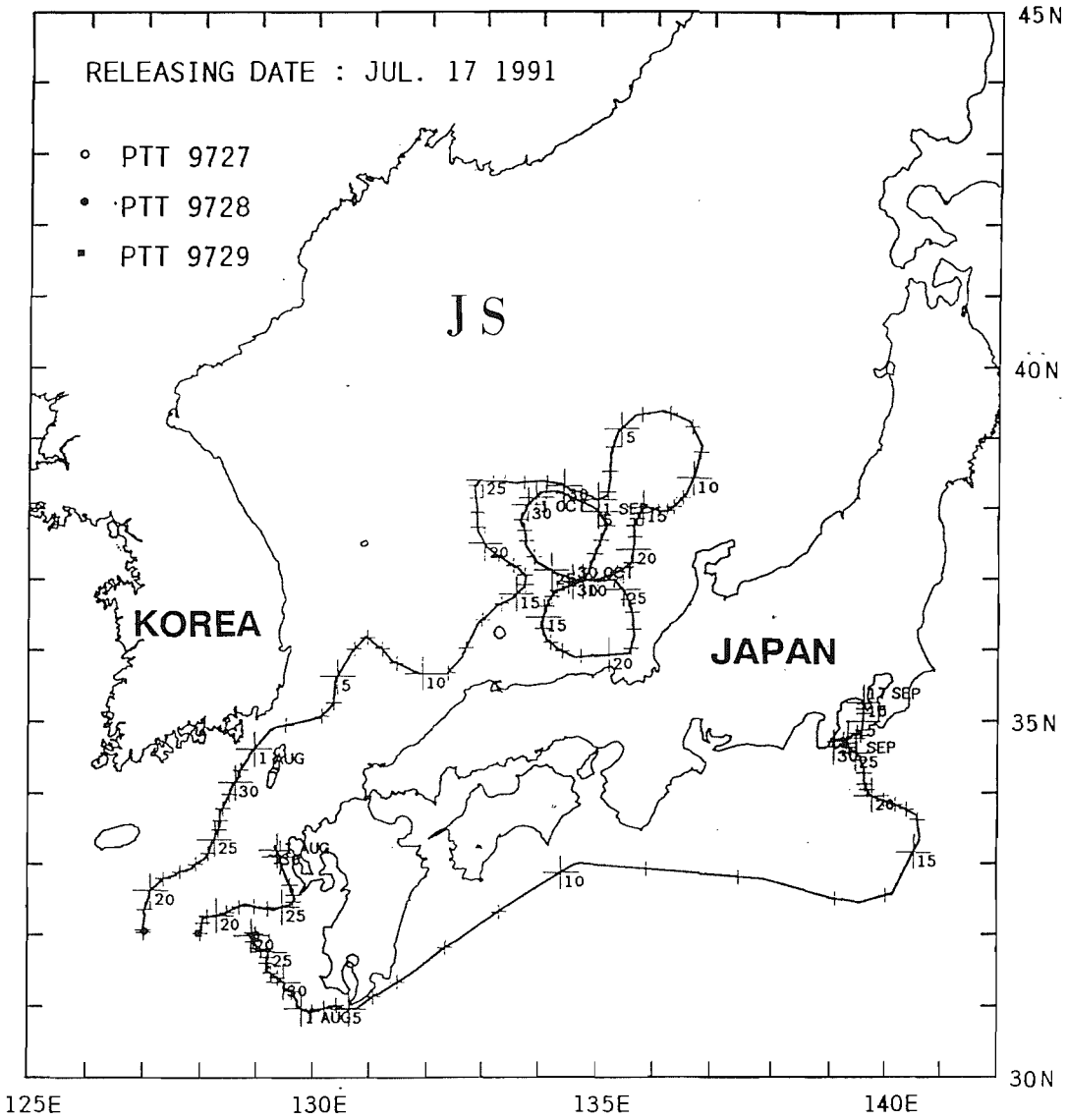
RELEASING DATE : JUL. 17 1991
PTT 9727
PTT 9728
PTT 9729
JS
KOREA
JAPAN
45N
40N
35N
30N
125E
130E
135E
140E

Fig. 5-34. Contours of streamlines for (A) experiment 1, and (B) experiment 3 in Table 5-8 at an equilibrium state. Contour intervals are 2 Sv from a streamline 58.5 to a streamline 102.5 for experiment 1, and from a streamline 49.5 to a streamline 130.5 for experiment 3. The intervals of other streamlines are 1 Sv. The 1.0 Sv streamline is also marked.

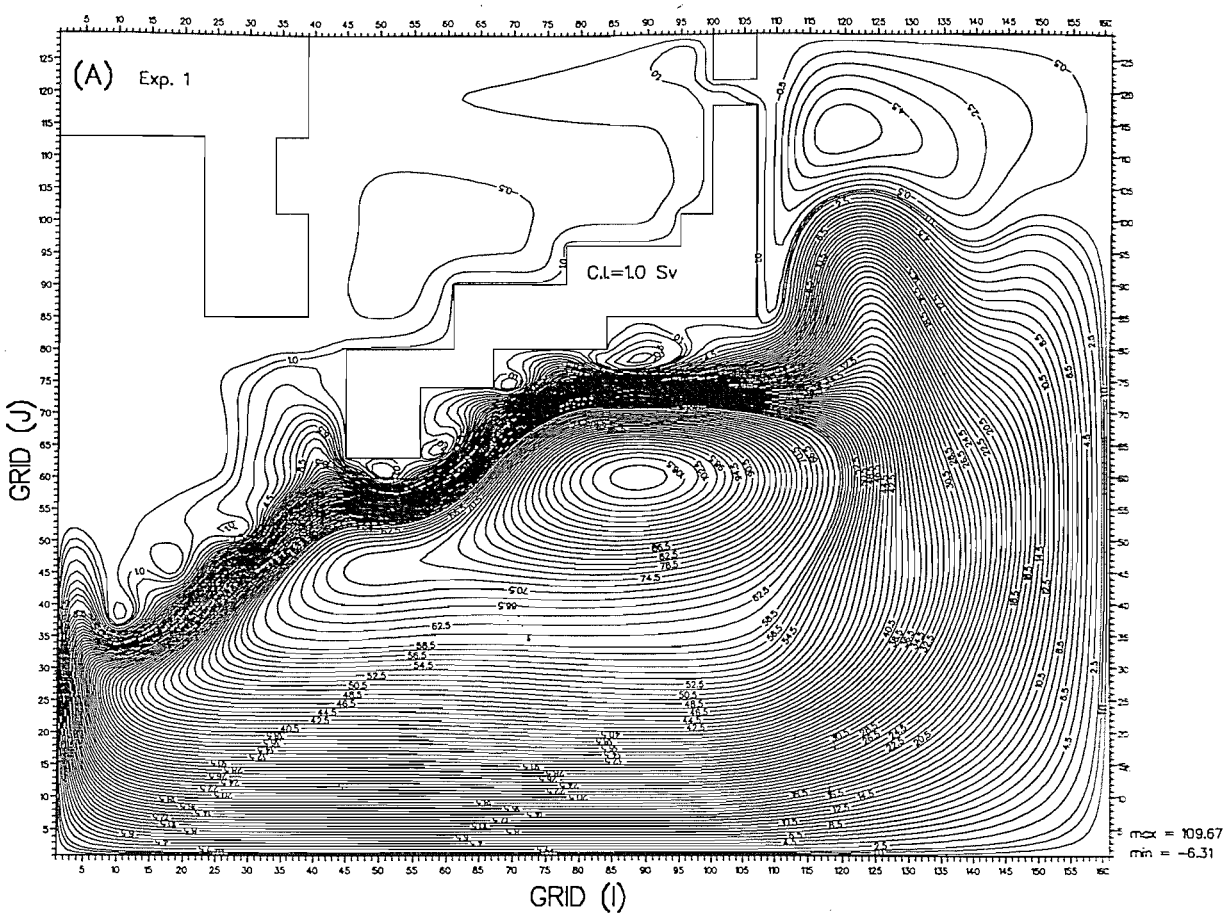
(A) Exp. 1
C.I.=1.0 Sv
GRID (J)
GRID (I)
max = 109.67
min = -6.31

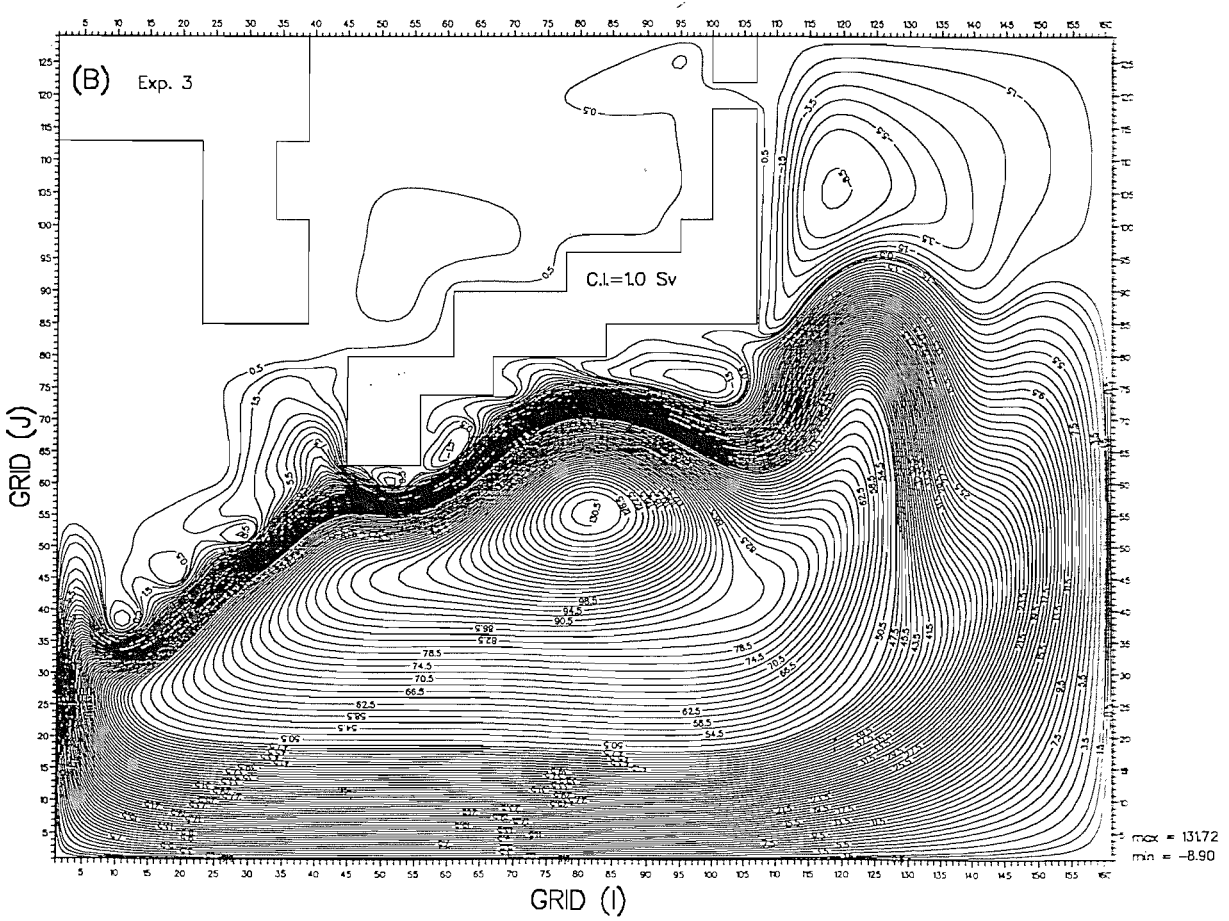
(B) Exp. 3
C.I.=1.0 Sv
GRID (J)
GRID (I)
max = 131.72
min = -8.90

CHAPTER VI. CONCLUSION

The work described in this thesis has two main aspects; shelf circulation driven by the western boundary current (chapter IV), and penetration of the western boundary current into a marginal sea (chapter V). These two aspects were investigated numerically in two simple model domains; a simple shelf model domain, and a simple shelf-marginal sea model domain. At a final stage, a realistic model domain was used, into which salient topographic features of the East China Sea are incorporated. A few experiments were performed with the realistic model to confirm some of the results obtained from the simple models.

In this chapter, a summary and discussion of the result will be presented followed by suggestions for future work.

VI-1. SHELF CIRCULATION DRIVEN BY THE WESTERN BOUNDARY CURRENT

The basic system under investigation consists of a shallow continental shelf connected to a deep ocean with a step-like cross-section. The deep ocean was either stratified or homogeneous. Effects of stratification on the shelf have not been considered. Two models were used.

The models predict an anticyclonic penetration of the subtropical western boundary current onto the shelf (East China Sea case), and the penetration was confined to a narrow boundary layer, formed at a southern part of the shelf. The above fundamental features were shown to be insensitive to the model assumptions made including different boundary conditions as well as the particular choice of model parameters. It was also shown that the presence of a passive lower layer is of little significance in determining the amount of penetration.

Analysis of the linear model results showed that the shelfward penetration of the western boundary current is driven by the meridional pressure gradient inherent in the western boundary current, and the southward intensification of the on-shelf flow is due to a vorticity constraint (section IV-2-3).

The meridional pressure sloping downward to the north drives a broad off-shelf flow along the inshore part of the WBC. Continuity then requires shelfward penetration of the western boundary current to compensate for this off-shelf transport. A study of the momentum balance along the inshore part of the western boundary current shows that the meridional pressure gradient balances both the Coriolis and the frictional forces with the primary importance of the former for the off-shelf flow. The on-shelf flow was shown to be highly correlated with the free surface sloping downward to the south.

With the parameters used in the linear models, a vorticity diffusion term due to the lateral friction was a dominant vorticity sink term in the boundary layer. For the frictionally dominated flow, the negative vorticity acquired by fluid particles entering the shelf is diffused from the boundary by the action of the vorticity diffusion. A southward intensification of the on-shelf flow takes place for the vorticity diffusion term to act as a source of positive vorticity and to balance the topographic vorticity tendency term, which acts as a source of negative vorticity.

Two poorly known parameters in most of numerical models are the coefficient of bottom friction and lateral eddy viscosity. Effects of these two parameters were examined using a realistic range of values for the two parameters (sections IV-2-4 and IV-2-5).

In a lateral friction model without bottom friction, the shelf circulation is dominated by large cyclonic recirculation cell in the northern part of the shelf, and the anticyclonic penetration of the western boundary current is confined only to the southeastern part of the shelf. This cyclonic cell was shown to be formed by the diffusion of positive vorticity from the inshore part of the western boundary current. Inclusion of bottom friction results in a broad spreading of the on-shelf flow and a

destruction of the recirculation cell.

The eddy viscosity has a twofold effect; an increase in the eddy viscosity results in an increase in the length scale of the SBL and a decrease in the magnitude of on-shelf flow. The effect of the eddy viscosity on the amount of penetration, therefore, is less important than that of the bottom friction, an increase of which results in a decrease in the magnitude of on-shelf flow but a negligible change of the length scale of the boundary layer. The linear model predicted that a ten fold increase in the coefficient of bottom friction leads to approximately a 10 % decrease in the ratio between the on-shelf transport and the WBC transport.

Although the general circulation pattern of the shelf driven by the subtropical western boundary current is independent of the particular choice of model parameters, the amount of penetration depends on various parameters (section IV-2-6). The ratio between the on-shelf transport and the transport of the western boundary current increases as the depth and the latitudinal size of the shelf increase. More penetration takes place onto a shelf located in a lower latitude. According to the linear model results, about 20 % of the Kuroshio water penetrates onto the East China Sea with values for parameters relevant to the East China Sea. This ratio is insensitive to changes in the transport of the western boundary current for the linear model.

The longitudinal size of the shelf and deep ocean was shown to be of little significance in determining the amount of penetration. The quantitative model results are also insensitive to the grid resolution used, and lateral boundary condition.

Non-linear effects significantly increase the amount and scale of penetration. Zonal and meridional penetration scales for a non-linear lateral friction model became more than two times larger than those for a linear one (section IV-3-2). The ratio between the maximum on-shelf transport and the transport of the western boundary current also increases by about 7%. The maximum westward on-shelf flow speed in the SBL is larger for the linear case than for the non-linear case, but the length scale of the SBL is about 1.5 times larger for the non-linear case resulting in a larger on-shelf

transport. The ratio between the on-shelf transport and the transport of the western boundary current also increases as the transport of the western boundary current increases (section IV-3-3).

The local vorticity balance in the boundary layer shows that the vorticity advection term acts to reduce the size of the vorticity diffusion term by balancing part of the stretching term (section IV-3-4). Inertial effects, therefore, weaken the flow in the boundary layer by broadening the length scale of the boundary layer. The increase in the maximum on-shelf transport is associated with the broadening of the SBL.

As the inertial effects increase, on-shelf flow splits into two distinct regimes : one rejoins the western boundary current in a tight anticyclonic turn and meanders along the inshore part of the western boundary current (offshore branch), the other one penetrates deep into the shelf (inshore branch). The offshore branch is characteristic of an inviscid inertial flow, while the frictional effect due to the presence of a lateral boundary is of importance for the inshore branch. For a highly inertial case where the non-dimensional inertial boundary layer scale is about 1.4 times the diffusive scale, the meandering of the offshore branch is a dominant feature of the shelf circulation.

With information about the meridional pressure gradient and the vorticity constraint, it is possible to predict the direction of shelf currents induced by boundary currents and the location of the intensification of the on-shelf flow. It has been shown that the direction of shelf currents induced by either a subtropical or subpolar western boundary current is determined by the meridional pressure gradient along the boundary current, and the intensification of the on-shelf current takes place either to the south or to the north depending upon the sign of the depth change between the adjacent seas and ocean. In particular, in contrast to the shelf located to the western boundary of the subtropical gyre, the shelf current flows southward in the shelf region, which is located to the western boundary of the subpolar gyre (Middle Atlantic Bight case) since the meridional pressure along the boundary current is now sloping downward to the south, which drives broad southward on-shelf flow, and the off-shelf flow is confined to a narrow boundary layer (section IV-2-7).

For the linear case, the flow patterns for the East China Sea and Middle Atlantic Bight cases are symmetric in that only the sign of streamlines is reversed, and the amount of penetration is same for the both cases. Inclusion of non-linear terms, however, result in a radical change of the flow pattern for the East China Sea case, while the circulation remains the same for the Middle Atlantic Bight case (section IV-3-2). The differences are due to the structure of the on-shelf flow. Inertial effects are of little importance for the Middle Atlantic Bight case since the on-shelf flow is sluggish and extends over a broad area. On the other hand, they are important for the East China Sea case since the strong on-shelf flow is confined to a narrow boundary layer.

It can be inferred from the inertial model results that the amount of penetration of either the eastern or the western boundary current onto the shelf is greatest, in terms of the ratio between the on-shelf transport and the transport of the boundary current, for a shelf located to the western boundary of a subtropical gyre (e.g. East China Sea in the North Pacific and the South Atlantic Bight in the North Atlantic) with other parameters being the same.

Numerical results described in this part of the thesis can be applied to the East China Sea area. As the Kuroshio flow northeastward along the continental slope, the pressure along the inshore of the Kuroshio slopes downward to the northeast. The meridional pressure gradient, then, induces broad entrainment of shelf waters to the Kuroshio, and a part of the Kuroshio is expected to penetrate onto the East China Sea at the southwestern end of the continental slope, north of Taiwan. The existence of this branch current, called the Taiwan Warm Current, has been observed (section I-7-1). The realistic model results further indicates that the Taiwan Warm Current is a source of other branch currents in the East China Sea. The amount of penetration predicted by the non-linear model results is, then, about 20 % ~ 30 % of the Kuroshio transport depending upon the coefficients of bottom friction for the depth ratio between the East China Sea shelf break and the upper layer depth of deep ocean of 0.5. This amount of penetration of the Kuroshio onto the northeast of Taiwan is comparable to that obtained from a inviscid reduced-gravity model by Hsueh et al. (1992).

Other qualitative similarities between the model results and observed feature in the ECS are the meandering of the Kuroshio in the ECS (Sugimoto et al., 1988; Qiu et al., 1990) and two (inshore and offshore) branches of the TWC (Yuan and Su, 1988; Su and Pan, 1987). Although any comparisons between the linear and non-linear models were not made with the realistic model, it is expected that the sloping topography in the ECS restricts the penetration scale of the Kuroshio for the linear model. It is the inertial effects that make the branch current overrun the topography and to generate a deep reaching branch of the Kuroshio (inshore branch of the TWC).

An important question remains as to how the above results are modified by stratification. Observations have shown a three dimensional structure of the Kuroshio intrusion in the northeast of Taiwan such as a persistent shelf break upwelling of the subsurface Kuroshio water (Su and Pan, 1987; Liu et al., 1992). This needs to be further studied.

VI-2. PENETRATION OF THE WESTERN BOUNDARY CURRENT INTO A MARGINAL SEA

Penetration of the western boundary current into the Japan Sea was investigated in the two kinds of idealised model domains and in a more realistic domain. The investigation was mainly focused on the effects, that changes in the large scale circulation of the deep ocean have, on the amount of influx to the Japan Sea .

Model results suggest that the Tsushima Current, a branch of the Kuroshio entering the Japan Sea, is generated by the pressure difference between the inshore part of the Kuroshio in the East China Sea and the Tsugaru Strait region, and that the Tsushima Current is a continuation of the Taiwan Warm Current generated in the northeast of Taiwan. A direct intrusion of the Kuroshio in the area west of Kyushu was not obtained in this barotropic model. Instead, southward flowing currents are dominant in the vicinity of Kyushu, which is evidenced by the recent direct observation of

currents in the area (KORDI, 1992).

The model results also indicate that the influx to the JS is dependent on the separation latitude of the Kuroshio and the strength of the Oyashio Current as well as the strength of the Kuroshio.

As the separation latitude retreats to the south, a recirculating gyre also retreats to the south resulting in an intensification of the WBC along the offshore side of the shelf. The pressure, then, drops on this side to support the intensified flow resulting in a reduced influx to the JS due to the decrease in the meridional pressure difference.

It was also shown that as the Oyashio Current strengthens, the influx to the JS decreases. The simple model results indicated that penetration of the Oyashio Current onto the JS would take place through the TS rather than the penetration of the Kuroshio through the KS when the strength of the Oyashio Current is more than 50 % of that of the Kuroshio in terms of the volume transport. This occurs due to the changes in the pressure gradient across the TS from an outflow-favouring one to an inflow-favouring one.

Comparing between model and observed transport of the Tsushima Current, model results show a connection between the strength of the Tsushima Current and the separation latitude of the Kuroshio. Based on the observational evidences of the Kuroshio reviewed in chapter I, it can be inferred that the Kuroshio separates from the coast further north in autumn when the transport of the Kuroshio Extension shows its annual maximum. If the separation latitude of the Kuroshio is 37°44′, then the influx to the Japan Sea would be about 1.5 Sv with a maximum baroclinic transport of the Kuroshio Extension based on a long-term climatology (Clifford and Horton, 1992), which is comparable to the maximum transport of the TC in autumn ($\sim$ 2 Sv). The variation of Kuroshio transport does not seem to account for the observed large annual range of the volume transport of the TC. The observed annual variation in the Tsushima Current may well be related with the observed annual migration of the separation latitude of the Kuroshio.

While the model results described in the thesis are illuminating, the conclusions drawn from them need to be validated by further comparing with observation and by performing numerical experiments in a basin scale model covering the whole North Pacific. Effects of stratification also remain to be investigated. The relative importance of the large scale circulation in controlling the transport through the Japan Sea compared to local forcings such as the effect of monsoon wind (Huh, 1982a; Ichiye, 1984), the density difference between the ECS and the TS region (Toba et al., 1982), and the topographic effects (Oye and Chen, 1991) needs to be further studied.

LIST OF REFERENCES

Atkinson, L.P., T.N. Lee, J.O. Blanton, and W.S. Chandler (1983) Climatology of the southeastern United States continental shelf waters. *Journal of Geophysical Research, 88(C8), 4705-4718.*

Atkinson, L.P., D.W. Menzel, and K.A. Bush, editors (1985) *Oceanography of the Southeastern U.S. Continental Shelf.* Coastal Estuarine Sciences, 2 AGU, Washington, D.C., 156 pp.

Beardsley, R.C., and W.C. Boicourt (1981) On estuarine and continental-shelf circulation in the middle Atlantic Bight. In: *Evolution of Physical Oceanography,* Warren, B.A., and C. Wunch, Eds., The MIT Press, 198-233.

Beardsley, R.C., R. Limeburner, H. Yu, and G.A. Cannon (1985) Discharge of the Changjiang (Yangtze River) into the East China Sea. *Continental Shelf Research, 4, 57-76.*

Beardsley, R.C., and C.D. Winant (1979) On the mean circulation in the Mid-Atlantic Bight. *Journal of Physical Oceanography, 9, 612-619.*

Blaha, J., and R. Reed (1982) Fluctuations of sea level in the western North Pacific and inferred flow of the Kuroshio. *Journal of Physical Oceanography, 12, 669-678.*

Blumberg, A.F., and G.L. Mellor (1983) Diagnostic and prognostic numerical calculation studies of the South Atlantic Bight. *Journal of Geophysical Research, 88(C8), 4579-4592.*

Böning, C.W. (1986) On the influence of frictional parameterization in wind-driven ocean circulation models. *Dynamics of Atmospheres and Oceans, 10, 63-92.*

Bryan, K. (1969) A numerical method for the study of the circulation of the world ocean. *Journal of Computational Physics, 4, 347-376.*

Camerlengo, A.L., and J.J. O'Brien (1980) Open boundary condition in rotating fluids. *Journal of Computational Physics, 35, 12-35.*

Chang, K.I. (1983) Structure and dynamics of currents in the Cheju Strait. *M.Sc Thesis, Seoul National University, 62 pp.*

Chao, S.-Y. (1991) Circulation of the East China Sea, A numerical study. *Journal of the Oceanographical Society of Japan, 46, 273-295.*

Chapman, D.C. (1985) Numerical treatment of cross-shelf open boundaries in a barotropic coastal ocean model. *Journal of Physical Oceanography, 15, 1060-1075.*

Chapman, D.C., and D.B. Haidvogel (1992) Formation of Taylor caps over a tall isolated seamount in a stratified ocean. *Geophysical and Astrophysical Fluid Dynamics, 64, 31-65.*

Chen, C., R.C. Beardsley, and R. Limeburner (1992) The structure of the Kuroshio southwest of Kyushu: velocity, transport and potential vorticity fields. *Deep-Sea Research, 39, 245-268.*

Chern, C.-S., and J. Wang (1990) On the Kuroshio branch current north of Taiwan. *Acta Oceanographica Taiwanica, 25, 55-64.*

Chern, C.-S., J. Wang, and D.-P. Wang (1990) The exchange of Kuroshio and East China Sea shelf water. *Journal of Geophysical Research, 95, 16017-16023.*

Choi, B.H. (1982) Note on currents driven by a steady uniform wind stress on the Yellow Sea and the East China Sea. *La Mer, 20, 65-74.*

Clifford, M.A., and C.W. Horton (1992) Baroclinic transport of the Kuroshio Extension between 141°E and 165°E. *Journal of Geophysical Research, 97, 12527-12533.*

Csanady, G.T. (1978) The arrested topographic wave. *Journal of Physical Oceanography, 8, 47-62.*

Davey, M.K., W.W. Hsieh, and R.C. Wajsowicz (1983) The free Kelvin wave with lateral and vertical viscosity. *Journal of Physical Oceanography, 13, 2182-2191.*

Dearnaley, M.P. (1990) Throughflow from the Pacific to the Indian Ocean through south east Asian waters. *Ph.D. thesis, Dept. of Oceanography, Southampton University, 215 pp.*

Dengg, J. (1992) The problem of Gulf Stream separation - A barotropic approach. *Journal of Physical Oceanography, 23, 2182-2200.*

Foreman, M.G.G., and A.F. Bennett (1989) On calculating vorticity balances in primitive equation models. *Journal of Physical Oceanography, 19, 1407-1411.*

Gawarkiewicz, G., and D.C. Chapman (1991) Formation and maintenance of shelfbreak fronts in an unstratified flow. *Journal of Physical Oceanography, 21, 1225-1239.*

Gill, A.E. (1982) *Atmosphere-Ocean Dynamics.* Academic Press, New York, 662 pp.

Greatbatch, R.J., and A. Goulding (1990) On the seasonal variation of transport through the Tokara Strait. *Journal of the Oceanographical Society of Japan. 46, 9-20.*

Guan, B. (1980) Some results from the study of the variation of the Kuroshio in the East China Sea. *The Kuroshio IV - Proc. 4th Symp. Coop. Study Kuroshio Adj. Reg., 879-911.*

Guan, B. (1983a) A sketch of the current structure and eddy characteristics in the East

China Sea. In: *Sedimentation on the continental shelf, with special reference to the East China Sea, Acta Oceanologia Sinica, Ed., China Ocean Press, Beijing, 52-73.*

Guan, B. (1983b) Analysis of the variations of volume transport of the Kuroshio in the East China Sea. *Chinese Journal of Oceanology and Limnology, 1(2), 156-165.*

Guan, B. (1984) Major features of the shallow water hydrography in the East China Sea and Huanghai Sea. In: *Ocean Hydrodynamics of the Japan and East China Sea, T. Ichiye, Ed., Elsevier, Amsterdam, 1-13.*

Guan, B., and H. Mao (1982) A note on circulation of the East China Sea. *Chinese Journal of Oceanology and Limnology, 1(1), 5-16.*

Guo, B., K. Lin, and J. Lu (1987) Characteristics of circulation in the continental shelf area of the East China Sea in winter. *Acta Oceanologica Sinica, 6, 51-60.*

Haidvogel, D.B., J.L. Wilkin, and R. Young (1991a) A semi-spectral primitive equation ocean circulation model using vertical sigma and orthogonal curvilinear horizontal coordinates. *Journal of Computational Physics, 94, 151-185.*

Haidvogel, D.B., A. Beckmann, and K.S. Hedström (1991b) Dynamical simulations of filament formation and evolution in the Coastal Transition Zone. *Journal of Geophysical Research, 96(C8), 15017-15040.*

Haidvogel, D.B., J.C. McWilliams, and P.R. Gent (1992) Boundary current separation in a quasigeostrophic, eddy-resolving ocean circulation model. *Journal of Physical Oceanography, 22, 882-902.*

Heburn, G.W., T.H. Kinder, J.H. Allender, and H.E. Hurlburt (1982) A numerical model of eddy generation in the southeastern Caribbean Sea. In: *Hydrodynamics of Semi-Enclosed Seas. J.C.J. Nihoul, Ed., Elsevier, Amsterdam, 299-327.*

Hedström, K.S. (1990) User's manual for a semi-spectral primitive equation regional ocean - circulation model version 3.0. *Technical Report SR-1, Institute for Naval Oceanography, 82 pp.*

Hendershott, M.C. (1981) Long waves and ocean tides. In: *Evolution of Physical Oceanography, Warren, B.A., and C. Wunch, Eds., The MIT Press, 292-341.*

Holland, W.R. (1967) On the wind-driven circulation in an ocean with bottom topography. *Tellus, 19, 582-599.*

Holland, W.R. (1973) Baroclinic and topographic influences on the transport in western boundary currents. *Geophysical Fluid Dynamics, 4, 187-210.*

Holland, W.R., and L.B. Lin (1975) On the generation of mesoscale eddies and their contribution to the oceanic general circulation. I. A preliminary numerical

experiment. *Journal of Physical Oceanography, 5, 642-657.*

Holton, J.R. (1979) *An Introduction To Dynamical Meteorology.* Academic Press, New York, 391 pp.

Hsieh, W.W., M.K. Davey, and R.C. Wajsowicz (1983) The free Kelvin wave in finite-difference numerical models. *Journal of Physical Oceanography, 13, 1383-1397.*

Hsueh, Y. (1988) Recent current observations in the eastern Yellow Sea. *Journal of Geophysical Research, 93(C6), 6875-6884.*

Hsueh, Y. (1992) The intrusion of the Kuroshio across the continental shelf northeast of Taiwan. *Journal of Geophysical Research, 97(C9), 14323-14330.*

Huh, O.K. (1982a) Satellite observations and the annual cycle of surface circulation in the Yellow Sea and Korea Strait. *La Mer, 20, 210-222.*

Huh, O.K. (1982b) Spring season flow of the Tsushima Current and its separation from the Kuroshio: Satellite evidence. *Journal of Geophysical Research, 87, 9687-9693.*

Hurlburt, H.E., and J.D. Thompson (1980) A numerical study of Loop Current intrusion and eddy shedding. *Journal of Physical Oceanography, 10, 1611-1651.*

Huthnance, J.M. (1981) Waves and currents near the continental shelf edge. *Progress in Oceanography, 10, 193-226.*

Ichikawa, H., and R.C. Beardsley (1993) Temporal and spatial variability of volume transport of the Kuroshio in the East China Sea. *Deep Sea Research, 40(3), 583-605.*

Ichiye, T. (1984) Some problems of circulation and hydrography of the Japan Sea and the Tsushima Current. In: *Ocean Hydrodynamics of the Japan and East China Sea, T. Ichiye, Ed., Elsevier, Amsterdam, 15-54.*

Ichiye, T., and L. Li (1984) A numerical study of circulation in a northeastern part of the East China Sea. In: *Ocean Hydrodynamics of the Japan and East China Sea, T. Ichiye, Ed., Elsevier, Amsterdam, 187-207.*

Kaneko, A. (1990) Observation methods of ocean currents by Doppler Sonars (in Japanese). *Hydrological Engineering Series, 90-B-6, 1-22.*

Kaneko, A., W. Koterayama, H. Honji, S. Mizuno, K. Kawatate, and R.L. Gordon (1990) Cross-stream survey of the upper 400 *m* of the Kuroshio by an ADCP on a towed fish. *Deep-Sea Research, 37(5), 875-889.*

Kaneko, A., S. Mizuno, W. Koterayama, and R.L. Gordon (1992) Cross-stream velocity structures and their downstream variation of the Kuroshio around Japan. *Deep-Sea Research, 39(9), 1583-1594.*

Kang, Y.Q. (1984) An analytical model of wind-driven currents in the Yellow, the East China and South China Seas. In: *Ocean Hydrodynamics of the Japan and East China Sea, T. Ichiye, Ed., Elsevier, Amsterdam, 187-207.*

Kantha, L., G.L. Mellor, and A.F. Blumberg (1982) A diagnostic calculation of the general circulation in the South Atlantic Bight. *Journal of Physical Oceanography, 12(8), 805-819.*

Kawabe, M. (1988) Variability of Kuroshio velocity assessed from the sea-level difference between Naze and Nishinoomote. *Journal of Oceanographical Society of Japan, 44(6), 293-304.*

Kawai, H. (1972) Hydrography of the Kuroshio Extension. In: *Kuroshio - Physical Aspects of the Japan Current, Stommel, H., and K. Yoshida, Eds., University of Washington Press, 235-352.*

Kim, K., and S.H. Lee (1982) Vertically homogeneous water along the west coast of Jeju Island. *Journal of the Oceanological Society of Korea, 17, 59-68.*

Kim, K., H.K. Rho, and S.H. Lee (1991) Water masses and circulation around Cheju-Do in summer (Korean with English abstract). *Journal of the Oceanological Society of Korea, 26(3), 262-277.*

Kitano, K. (1975) Some properties of the warm eddies generated in the confluence zone of the Kuroshio and Oyashio Currents. *Journal of Physical Oceanography, 5, 245-252.*

Korea Ocean Research and Development Institute (1992) Study on oceanographic variability in the formation area of Tsushima Current - KORDI program for World Ocean Circulation Experiment / Surface Velocity Program (Second year). *Report BSPG00168-473-1, 122 pp.*

Kutsuwada, K., and T. Teramoto (1987) Monthly maps of surface wind stress fields over the North Pacific during 1961-1984. *Bulletin of the Ocean Research Institute of the University of Tokyo, 24, 1-100.*

Leblond, P.H., and L.A. Mysak (1978) *Waves in the Ocean.* Elsevier Scientific Publishing Company, 602 pp.

Lee, T.N., L.P. Atkinson (1983) Low frequency current and temperature variability from Gulf Stream frontal eddies and atmospheric forcing along the southeast U.S. outer continental shelf. *Journal of Geophysical Research, 88, 4539-4567.*

Lee, T.N., L.P. Atkinson, and R. Legeckis (1981) Observations of a Gulf Stream frontal eddy on the Georgia continental shelf, April 1977. *Deep-Sea Research, 28, 347-378.*

Lie, H.J. (1986) Summertime hydrographic features in the southeastern Hwanghae. *Progress in Oceanography, 17, 229-242.*

Lim, D.B. (1971) On the origin of the Tsushima Current water. *Journal of the Oceanological Society of Korea, 6(2), 85-91.*

Liu, C.-T., and S.-C. Pai (1987) As Kuroshio turns: (II) The oceanic front north of Taiwan. *Acta Oceanographica Taiwanica, 18, 49-61.*

Liu, K.-K., G.-C. Gong, C.-Z. Shyu, S.-C. Pai, C.-L. Wei, and S.-Y. Chao (1992) Response of Kuroshio upwelling to the onset of the northeast monsoon in the sea north of Taiwan: Observations and a numerical simulation. *Journal of Geophysical Research, 97(C8), 12511-12526.*

Liu, Z. (1990) On the influence of the continental slope on the western boundary layer: The enhanced transport and recirculation. *Journal of Marine Research, 48, 255-285.*

Lorenzzetti, J.A., J.D. Wang, and T.N. Lee (1988) Two-layer model of summer circulation on the southeast U.S. continental shelf. *Journal of Physical Oceanography, 18, 591-608.*

Masuzawa, J. (1972) Water characteristics of the North Pacific central region. In: *Kuroshio - Physical Aspects of the Japan Current, Stommel, H., and K. Yoshida, Eds., University of Washington Press, 95-127.*

Middleton, J.H. (1987) Steady coastal circulation due to alongshore pressure gradients. *Journal of Physical Oceanography, 17, 604-612.*

Miller, M.J., and A.J. Thorpe (1981) Radiation conditions for the lateral boundaries of limited-area numerical models. *Quarterly Journal of the Royal Meteorological Society, 107, 615-628.*

Minato, S., and R. Kimura (1980) Volume transport of the western boundary current penetrating into a marginal sea. *Journal of Oceanographical Society of Japan, 36, 185-195.*

Mizuno, S., A. Kaneko, T. Nagahama, and K. Kawatate (1991) A long-term measurements of the Kuroshio currents in the East China Sea. *Abstracts submitted to the sixth Japan and East China Seas Study Workshop, 32.*

Mizuno, K., and W.B. White (1983) Annual and interannual variability in the Kuroshio Current System. *Journal of Physical Oceanography, 13, 1847-1867.*

Moriyasu, S. (1972) The Tsushima Current. In: *Kuroshio - Physical Aspects of the Japan Current, Stommel, H., and K. Yoshida, Eds., University of Washington Press, 353-369.*

Munk, W.H. (1950) On the wind-driven ocean circulation. *Journal of Meteorology, 7, 79-93.*

Nishizawa, J., E. Kamihira, K. Komura, R. Kumabe., and M. Miyazaki (1982) Estimation of the Kuroshio mass transport flowing out of the East China Sea to the North Pacific. *La Mer, 20, 55-59.*

Nitani, H. (1972) Beginning of the Kuroshio. In: *Kuroshio - Physical Aspects of the Japan Current, Stommel, H., and K. Yoshida, Eds., University of Washington Press, 129-163.*

Oey, L.-Y, and P. Chen (1991) Frontal waves upstream of a diabathic blocking: A model study. *Journal of Physical Oceanography, 21, 1643-1663.*

Orlanski, I. (1976) A simple boundary condition for unbounded hyperbolic flows. *Journal of Computational Physics, 21, 251-269.*

Park, Y.H. (1986) Water characteristics and movements of the Yellow Sea Warm Current in summer. *Progress in Oceanography, 17, 243-254.*

Pedlosky, J. (1979) *Geophysical Fluid Dynamics.* Springer-Verlag, New York, 624 pp.

Power, S.B., J.H. Middleton, and R.H.J. Grimshaw (1989) Frictionally modified continental shelf waves and the subinertial response to wind and deep ocean forcing. *Journal of Physical Oceanography, 19, 1486-1506.*

Qiu, B. (1992) Recirculation and seasonal change of the Kuroshio from altimetry observations. *Journal of Geophysical Research, 97(C11), 17801-17811.*

Qiu, B., and N. Imasato (1990) A numerical study on the formation of the Kuroshio Counter Current and the Kuroshio Branch Current in the East China Sea. *Continental Shelf Research, 10(2), 165-184.*

Qiu, B., K.A. Kelly, and T.M. Joyce (1991) Mean flow and variability in the Kuroshio Extension from Geosat altimetry data. *Journal of Geophysical Research, 96(C10), 18491-18507.*

Qiu, B., T. Toda, and N. Imasato (1990) On Kuroshio front fluctuations in the East China Sea using satellite and in situ observational data. *Journal of Geophysical Research, 95(C10), 18191-18204.*

Røed, L.P., and C.K. Cooper (1986) Open boundary conditions in numerical ocean models. In: *Advanced Physical Oceanographic Numerical Modelling,* J.J. O'Brien Ed., NATO Advanced Science Institutes Series, Kluwer Academic Publishers, Dordrecht, Boston, and London, 411-436.

Salmon, R. (1992) A two-layer Gulf Stream over a continental slope. *Journal of Marine Research, 50, 341-365.*

Sawara, T., and Y. Hanzawa (1979) Distribution of water type in the East China Sea (in Japanese with English abstract). *Umi to Sora, 54(4), 13-26.*

Sekine, Y. (1988) On the seasonal variation in- and Outflow volume transport of the Japan Sea. *Progress in Oceanography, 21, 269-279.*

Semtner, A.J. (1986) Finite-difference formulation of a world ocean model. In: *Advanced Physical Oceanographic Numerical Modelling,* J.J. O'Brien Ed., NATO Advanced Science Institutes Series, Kluwer Academic Publishers, Dordrecht, Boston, and London, 187-202.

Stommel, H. (1948) The westward intensification of wind-driven ocean currents. *Transactions of the American Geophysical Union, 29, 202-206.*

Su J., and Y. Pan (1987) On the shelf circulation north of Taiwan. *Acta Oceanologica Sinica, 6, 1-20.*

Sugimoto, T. (1990) A review of recent physical investigations on the straits around the Japanese Islands. In: *The Physical Oceanography of Sea Straits,* L.J. Pratt Ed., NATO Advanced Science Institutes Series, Kluwer Academic Publishers, Dordrecht, Boston, and London, 191-209.

Sugimoto, T., S. Kimura, and K. Miyaji (1988) Meander of the Kuroshio front and current variability in the East China Sea. *Journal of Oceanographical Society of Japan, 44, 125-135.*

Sverdrup, H.U., M.W. Johnson, and R.H. Fleming (1942) *The Oceans; Their Physics, Chemistry and General Biology,* Englewood Cliffs, NY ; Prentice-Hall, 1060 pp,

Thomson, J.D., and W.J. Schmitz, Jr. (1989) A limited-area model of the Gulf Stream: Design, initial experiments, and model-data intercomparison. *Journal of Physical Oceanography, 19, 791-814.*

Toba, Y., K. Tomizawa, Y. Kurasawa, and K. Hanawa (1982) Seasonal and year-to-year variability of the Tsushima-Tsugaru Warm Current system with its possible cause. *La Mer, 20, 41-51.*

Uda, M. (1934) The result of simultaneous oceanographical investigations in the Japan Sea and its adjacent waters in May and June, 1932 (in Japanese). *Japan Imp. Fish. Exp. Stations, 5, 57-190.*

Veronis, G. (1966) Wind-driven ocean circulation - Part 2. Numerical solution of the non-linear problem. *Deep-Sea Research, 13, 31-55.*

Veronis, G. (1981) Dynamics of large-scale ocean circulation. In: *Evolution of Physical Oceanography,* Warren, B.A., and C. Wunch, Eds., The MIT Press, 140-183.

Walsh, J.J., P.E. Biscaye, and T. Csanady (1988) The 1983-1984 Shelf Edge Exchange Processes (SEEP)-I experiment: hypotheses and highlights. *Continental Shelf Research, 8(5-7), 435-456.*

Walsh, J.J., G.T. Rowe, R.L. Iverson, and C.P. McRoy (1981) Biological export of shelf carbon is a sink in the global CO_2 cycle. *Nature, 291, 196-201.*

Wang, D.P. (1982) Effects of continental slope on the mean shelf circulation. *Journal of Physical Oceanography, 12, 1524-1526.*

Wang, Y., and D.G. Aubrey (1987) The characteristics of the China coastline. *Continental Shelf Research, 7(4), 329-349.*

Wang, W., and J. Su (1987) A barotropic model of the Kuroshio system and eddy phenomena in the East China Sea. *Acta Oceanologica Sinica, 6, 21-35.*

Wells, N. (1986) *The Atmosphere and Ocean: A Physical Introduction.* Taylor & Francis, London and Philadelphia, 347 pp.

Wroblewski, J.S., and E.E. Hofmann (1989) U.S. interdisciplinary modeling studies of coastal-offshore exchange processes: Past and future. *Progress in Oceanography, 23, 65-99.*

Yi, S.K. (1966) Seasonal and secular variation of the water column transport across the Korea Strait. *Journal of the Oceanological Society of Korea, 1, 7-13.*

Yi, S.K. (1970) Variation of oceanic condition and mean sea level in the Korea Strait. In: *Kuroshio, Marr, J.C., Ed., East-West Center Press, Honolulu.*

Yuan, Y., and J. Su (1983) A two-layer circulation model of the East China Sea In: *Sedimentation on the continental shelf, with special reference to the East China Sea, Acta Oceanologia Sinica, Ed., China Ocean Press, Beijing, 335-345.*

Yuan, Y., and J. Su (1984) Numerical modelling of the circulation in the East China Sea. In: *Ocean Hydrodynamics of the Japan and East China Sea, T. Ichiye, Ed., Elsevier, Amsterdam, 167-186.*

Yuan, Y., and J. Su (1988) The calculation of Kuroshio current structure in the East China Sea-Early summer 1986. *Progress in Oceanography, 21, 343-361.*

Zheng, Q.A., and V. Klemas (1982) Determination of winter temperature pattern, front and surface currents in the Yellow Sea and East China Sea from satellite imagery. *Remote Sensing of Environment, 12, 201-215.*

APPENDIX A.

THE FINITE DIFFERENCE EQUATIONS (SWEM)

The continuous equations (III-3-1) ~ (III-3-2) and (III-3-4) ~ (III-3-10) are to be solved by finite difference methods. The staggered grid system (Arakawa C-grid) used is shown in Fig. A-1. The zonal velocity u is placed at a distance $\Delta/2$ (Δ being the uniform grid interval in both the x and y directions) to the east and west of the η_1 (free surface elevation) and η_2 (interface perturbation). The meridional velocity v is placed at the same distance to the north and south of η_1 and η_2. The Coriolis parameter f is defined at u points as a linear function of y.

The boundaries of the basin are so chosen that a north-south boundary coincides with a line of u points and an east-west boundary coincides with v points. This choice of boundaries permits a simple specification of the kinematic boundary condition of having no normal flow across the lateral walls. An extra array of grid points is introduced outside each boundary at a distance $\Delta/2$ away. These fictitious points allow the same computing algorithm to be used for points adjacent to the boundary as for points of the interior. They also provide a way for specifying the dynamic boundary condition. For a slip boundary condition, the tangential velocity outside the boundary is set equal to that of just inside the boundary. For a no-slip condition, the tangential velocity ouside the boundary is set equal, but opposite in sign, to that just inside the boundary. The value of free surface η_1 and interface perturbation η_2 at the outside points can be set arbitrarily because they are never used in calculating the variables of the interior. The η and h values outside the boundary are set to be equal to those just inside the boundary.

Defining a operator,

$$\delta_x s(x) = \frac{1}{\Delta}\left[s\left(s+\frac{\Delta}{2}\right) - \left(s-\frac{\Delta}{2}\right)\right],$$

$$\overline{s(x)}^{x} = \frac{1}{2}\left[s\left(x+\frac{\Delta}{2}\right)+s\left(x-\frac{\Delta}{2}\right)\right],$$

where s(x) is any function of the discrete variable, the finite difference form of the model equations in the deep ocean is

$$(u_1)^{n+1} = (u_1)^{n-1} - 2\Delta t\left[\left(-\overline{f\overline{v_1}^{y}}^{x} + g\,\delta_x \eta_1\right)^{n} - A_M\left(\delta_{xx}u_1 + \delta_{yy}u_1\right)^{n-1}\right] \tag{A1}$$

$$(v_1)^{n+1} = (v_1)^{n-1} - 2\Delta t\left[\left(\overline{f\overline{u_1}^{y}}^{x} + g\,\delta_y \eta_1\right)^{n} - A_M\left(\delta_{xx}v_1 + \delta_{yy}v_1\right)^{n-1}\right] \tag{A2}$$

$$(\eta_1)^{n+1} = (\eta_1)^{n-1} - 2\Delta t\left[\delta_x\left(u_1\overline{H_1}^{x} + u_2\overline{H_2}^{x}\right) + \delta_y\left(v_1\overline{H_1}^{y} + v_2\overline{H_2}^{y}\right)\right]^{n} \tag{A3}$$

$$(u_2)^{n+1} = (u_2)^{n-1} - 2\Delta t\left[\left(-\overline{f\overline{v_2}^{y}}^{x} + \frac{\rho_1}{\rho_2}g\,\delta_x\eta_1 + g'\delta_x\eta_2\right)^{n} - A_M\left(\delta_{xx}u_2 + \delta_{yy}u_2\right)^{n-1}\right] \tag{A4}$$

$$(v_2)^{n+1} = (v_2)^{n-1} - 2\Delta t\left[\left(\overline{\overline{fu_2}^{y}}^{x} + \frac{\rho_1}{\rho_2}g\,\delta_y\eta_1 + g'\delta_y\eta_2\right)^{n} - A_M\left(\delta_{xx}v_2 + \delta_{yy}v_2\right)^{n-1}\right] \tag{A5}$$

$$(\eta_2)^{n+1} = (\eta_2)^{n-1} - 2\Delta t\left[\delta_x\left(u_2\overline{H_2}^{x}\right) + \delta_y\left(v_2\overline{H_2}^{y}\right)\right]^{n}. \tag{A6}$$

In the shelf area,

$$(u_1)^{n+1} = (u_1)^{n-1} - 2\Delta t\left[\left(-\overline{\overline{fv_1}^{y}}^{x} + g\,\delta_x \eta_1\right)^n - A_M\left(\delta_{xx}u_1 + \delta_{yy}u_1\right)^{n-1} + \left(\frac{rv_1}{\overline{H_1}^{y}}\right)^{n-1}\right] \tag{A7}$$

$$(v_1)^{n+1} = (v_1)^{n-1} - 2\Delta t\left[\left(\overline{\overline{fu_1}^{y}}^{x} + g\,\delta_y \eta_1\right)^n - A_M\left(\delta_{xx}v_1 + \delta_{yy}v_1\right)^{n-1} + \left(\frac{ru_1}{\overline{H_1}^{x}}\right)^{n-1}\right] \tag{A8}$$

$$(\eta_1)^{n+1} = (\eta_1)^{n-1} - 2\Delta t\left[\delta_x\left(u_1\overline{H_1}^{x}\right) + \delta_y\left(v_1\overline{H_1}^{y}\right)\right]^n . \tag{A9}$$

The superscripts n-1 and n+1 indicate the time level. That is, if n represents the present time level, the n-1 is one time step in the past and n+1 is one time step in the future. Equations (A1) and (A4) are written with reference to a u point and equations (A2) and (A5) with reference to a v point. Equations (A3) and (A6) are written with reference to an η_1 and η_2 points. The Holland and Lin (1975) scheme is used for the Coriolis force.

Fig. A1. Horizontal arrangements of variables on an Arakawa C-grid. ● denotes free surface (η_1), interface perturbation (η_2), and depth points, × meridional velocity points, and ◇ zonal velocity points. Δ denotes horizontal grid spacing, and dotted lines indicate the placement of horizontal boundary.

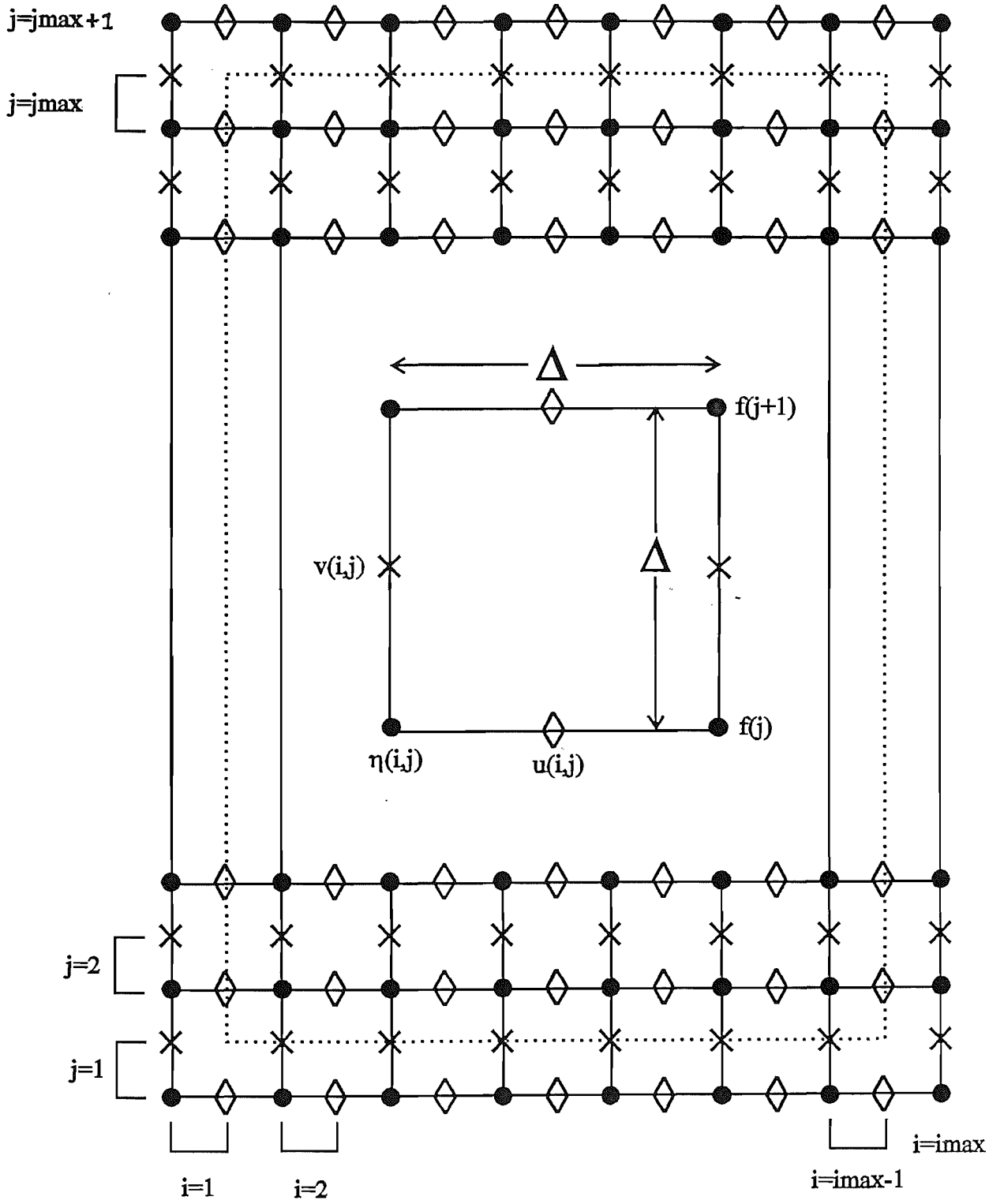
j=jmax+1
j=jmax
Δ
f(j+1)
v(i,j)
Δ
f(j)
η(i,j)
u(i,j)
j=2
j=1
i=1
i=2
i=imax-1
i=imax

APPENDIX B.

OPEN BOUNDARY CONDITION FOR THE SWEM

B-1. Introduction

Limited area numerical models inevitably include the treatment of open boundaries. If we had enough observational data sets at the open boundaries, we would be able to prescribe these values. If not, the appropriate form of open boundary conditions (OBCs) should be necessary.

Attempts have been made to develop an inflow-outflow model driven with a specified velocity field with outflow self-determined. A pragmatic approach was adopted to find an appropriate OBC for a stable integration of model equations (equations A1 ~ A9) rather than mathematically vigorous treatment of the OBC. The accuracy of the selected OBC was then tested by twin experiments using a different OBC.

B-2. Numerical model

The model domain used for examining various OBC specifications is a flat-bottomed meridional channel with rectangular cross-section located on a mid-latitude β-plane. Three different OBC specifications (Table B-1) were tested and their results will be presented. Horizontal grid spacings in both directions are 20 km which is about the half of the internal deformation radius of the system. Numerical methods are the same as described in section III-2-2.

The eastern and western boundaries are solid and slippery walls, while the northern and southern boundaries are open. The flow in the model domain is driven by the prescribed exponential profile of velocity at the southern boundary. The inflow boundary condition is steady except for a spin-up with some time constant (typically one

day). The outflow at the northern boundary needs to be determined with an appropriate OBC.

B-3. Open boundary conditions

Ideal open boundaries are transparent to motions which are generated within the computational domain and which are felt at the open boundaries. Therefore, radiation boundary conditions of the appropriate form are necessary. Most of the OBCs are basically Sommerfeld radiation condition of the following form with a different prescription for the phase speed,

$$\phi_t + C\phi_n = 0 \ , \tag{B-1}$$

where ϕ represents any variable and C the phase speed, n is in the normal direction to the boundary. A widely used numerical implemetation of this condition was presented by Orlanski (1976). Camerlengo and O'Brien (1980) presented a simplification of Orlanski's implemetation and showed an improvement for outgoing Rossby waves. Miller and Thorpe (1981) showed that the Orlanski radiation condition, which involved a leapfrog in time, could be made more accurate by use of the upstream method. In a wind-driven barotropic coastal ocean model the Orlanski radiation condition (ORC) was shown to give the best performance and to be adequate at transmitting wave energy (Chapman, 1985). Various methods for implementing the above condition were reviewed and tested by Chapman (1985) and Røed and Cooper (1986).

Although an OBC may give a good performance in a specific experiment, it cannot be guaranteed to be equally well-behaved under different physical condition. We have tested the ORC extensively since other OBCs are modified or simplified versions of the most sophisticated original Orlanski's implementation (Orlanski, 1976).

The phase speed at which ϕ is approaching the boundary is evaluated at each time step from values of ϕ at previous times close to the boundary. The computed phase speed is then used at the boundary. An explicit form for the phase speed was used (Orlanski, 1976; Chapman, 1985).

Writing (B-1) in the finite difference form at j=jmax-1 which is just inside the zonal boundary (Fig. A-1) yields,

$$\frac{\phi^{n}_{ij-1} - \phi^{n-2}_{ij-1}}{2\Delta t} + C\,\frac{\phi^{n-1}_{ij-1} - \phi^{n-1}_{ij-2}}{\Delta y} = 0 \,. \tag{B-2}$$

If the following expression is used to avoid artificial time splitting which leapfrog scheme can produce

$$\phi^{n-1}_{ij-1} = \frac{1}{2}(\phi^{n}_{ij-1} + \phi^{n-2}_{ij-1}) \,,$$

then equation (B-2) becomes

$$\frac{\phi^{n}_{ij-1} - \phi^{n-2}_{ij-1}}{2}\Delta t + C\,\frac{\phi^{n}_{ij-1} + \phi^{n-2}_{ij-1} - 2\phi^{n-1}_{ij-2}}{2\Delta y} = 0 \,. \tag{B-3}$$

Manipulation yields

$$C = -\,\frac{\phi^{n}_{ij-1} - \phi^{n-2}_{ij-1}}{\phi^{n}_{ij-1} + \phi^{n-2}_{ij-1} - 2\,\phi^{n-1}_{ij-2}}\,\frac{\Delta y}{\Delta t} = M_{\phi}\frac{\Delta y}{\Delta t} \,. \tag{B-4}$$

The phase speed C is estimated from values of variables at previous times close to the boundary. The variable at the boundary point at the next timestep can then be determined after writing equation (B-2) at n+1 and substituting (B-4) into the resulting equation,

$$\phi^{n+1}_{ij} = \frac{(1-M_{\phi})\phi^{n-1}_{ij} + 2\,M_{\phi}\,\phi^{n}_{ij-1}}{1 + M_{\phi}} \,. \tag{B-5}$$

In this expression it is required that,
$0 < M_{\phi} < 1$ or $0 < C < \Delta y/\Delta x$.

If $M_{\phi} \geq 1$ or $c \geq \Delta y/\Delta x$, then

$$\phi^{n+1}_{ij} = \phi^{n}_{ij-1} \,,$$

which is the condition for the phase speed to be equal to the numerical maximum of the grid spacing divided by the timestep.

If $M_\phi \leq 0$ or $c \leq 0$, then

$$\phi_{ij}^{n+1} = \phi_{ij}^{n-1} ,$$

which means that if no information has come from the interior, the variable is prescribed at the boundary by a value at a previous timestep.

At the southern open boundary (j=1 in Fig. A1), the normal velocity components in the upper and lower layers were prescribed . A steady exponential shape of current profile was specified only in the upper layer. The model was spun-up with an e-folding time of one day. The velocity in the lower layer was set to be zero in all experiments. The model calculations for the normal velocity components take place for rows from j=2 to j=jmax-1, while for the tangential velocity components, free surface, and interface perturbation for rows from j=2 to j=jmax.

The tangential velocity at grid points just outside the domain is assumed to be zero for calculating the lateral friction term. This specification showed better results than to specify it to be equal to the value just inside the boundary.

It is useful to briefly mention the transients in the system to monitor the performance of each OBC specification. Major concern is focused on the establishment of the western boundary current associated with the slow internal mode of Rossby and Kelvin waves. The mechanism of the establishment of the WBC was explained in detail in section II-4-2 in terms of long wave theory.

To obtain a steady state solution the model equations need to be integrated for order of hundred days since it will take those time scales for the internal Rossby wave to cross the model ocean basin. The relatively fast external mode of each wave and gravity waves as well as their reflection within the domain therefore are expected to be

insignificant in the establishment of the WBC and unlikely to contaminate the steady state solution.

Table B1. Model partameters to test OBC specifications

	case I	case II	case III
L^x, L^y	600 km,1100 km	300 km,1100 km	300 km,1100 km
H_1, H_2	300 m, 1200 m	300 m, 1200 m	300 m, 1200 m
A_M	5000 m^2s^{-1}	5000 m^2s^{-1}	5000 m^2s^{-1}
$\Delta x, \Delta y$	20 km	20 km	20 km
Δt	50 sec	50 sec	50 sec
OBC	ORC	ORC + IC	ORC + IC + SL

where,

L^x : width of the domain
L^y : length of the domain
H_1 : unperturbed upper layer thickness
H_2 : unperturbed lower layer thickness
A_M : lateral viscosity
$\Delta x, \Delta y$: grid spacings
Δt : timestep length
ORC : Orlanski radiation condition
IC : Integral Constraint
SL : Sponge Layer.

Initially the internal Kelvin wave is expected to propagate northwards along the eastern wall. The displacements of the free surface and interface formed in the eastern wall associated with the propagation of the internal Kelvin wave are then carried westwards by internal Rossby waves. The western boundary layer is then established by the internal Rossby wave motion. The incident long internal Rossby waves are reflected at the western wall as short Rossby waves whose group speed in the zonal direction is eastward. The reflected short Rossby waves are, however, damped and trapped at the western boundary due to the effect of friction.

The theoretical value of phase speed of internal Kelvin wave of the system considered is 2.84 m/s and the phase and group speeds of internal Rossby wave in the mid-latitude (equation II-4-6) are 4.4 cm/s. It takes about 79 and 158 days for the Rossby wave to cross the model basin for the case II and III, and case I respectively in the Table B-1.

Space-time plot of variables are presented to monitor the propagation of the Kelvin wave (Figs. B2 and B3) and Rossby wave (Fig. B4), and to check whether the free surface reaches an equilibrium state (Fig. B1).

B-3-1. Orlanski radiation condition (ORC)

The Orlanski radiation condition is applied for the calculation of the normal velocity components at the northern boundary.

Propagation of Kelvin and Rossby waves can be seen in the space-time plot of interface and upper layer meridional velocity (Figs. B2 and B4) leading to the establishment of the western boundary layer (Fig. B5). However, free surface decreases until day 150 and then increases until day 500 (Fig. B1). It rises up to 37 m at day 500. With these type of OBC, the mass in the system is not to be conserved, resulting in the filling-up of the model basin even after long time integration. Although the reason for this is not clear, it may be due to the effect of the external mode in the system. Applying the ORC alone to a one and half layer model with a rigid lid on the top showed to give a resonable performance (Jacyra Soares, personal communication).

We tried to apply the ORC to all the variables at the northern boundary rather than only to the normal velocity component to the boundary as other alternatives. The results are unsuccessful, however, since the filling-up of the basin also occurred.

B-3-2. ORC and integral constraint

To avoid this undesirable result, another type of OBC specification was used. All

the procedures for calculating the variables are the same as before except for using an additional constraint for the normal velocity components at the outflow boundary.

After applying the Orlanski radiation condition for the calculation of normal velocity components, they were uniformly accelerated or decelerated such that total prescribed inflow volume transport for the each layer is matched by total outflow transport for every timestep (integral constraint).

The integral constraint was originally used as an OBC by Hurlburt and Thompson (1980) in their Gulf of Mexico modelling and later used by Heburn et al (1982). Most recently Thompson and Schmitz (1989) used the ORC and integral constraint in their Gulf Stream modelling.

The free surface reached steady state in a statistical sense although a small amplitude oscillation persisted until day 500 (Fig. B1(B)). The maximum amplitude of this oscillation is less than 1 % of the mean free surface value. All other variables also reached a steady state after the Rossby wave arrives at the western wall (Fig. B4(B)) and strong jet seems to pass through cleanly (Fig. B6(A)).

Kelvin waves can, however, bridge the open portion of the boundary via the integral constraint. Also the integral constraint applied at the northern boundary resulted in the generation of another Kelvin wave. Initial response is, therefore, dominated by the propagation of Kelvin waves originating from both southern and northern boundaries (Fig. B2(B)). The internal Kelvin wave signal fell into decay within 70 days due to the action of lateral friction (Fig. B3(C)).

Lateral and vertical viscous effects on free Kelvin waves were investigated both in a continuous model and in a finite-difference model by Davey et al. (1983) and Hsieh et al. (1983). In the numerical model with lateral viscosity two main non-dimensional parameters emerge determining the longshore phase speed and temporal decay scale : 1) Δ, defined as the ratio between offshore grid spacing and the Rossby radius, 2) ϵ (= A_M / f L^2 l) the offshore lateral viscous effect, where A_M is the lateral viscosity, f is the

constant Coriolis parameter, and l is the positive longshore wavenumber. The effect of Δ and ϵ on the phase speed and decay scale is shown in Fig. B11 for a C-grid with free-slip boundary condition. Increasing the viscosity (increasing ϵ) decreases the phase speed of the Kelvin wave and increases the temporal decay scale (quickly decaying). The poor resolution (increasing Δ) greatly reduces the decay factor resulting in long temporal oscillation although the slowdown of the phase speed by lateral viscosity is cancelled by poor resolution.

The estimated phase speed of the internal Kelvin wave from the model result agrees well with that of the theoretical inviscid wave on a f-plane. The calculated values of ϵ and Δ (refer to Fig. B11) are 0.26 and 0.5 respectively. The dominant alongshore wavelength was chosen as the meridional size of the model domain ($\sim$1000 km) and the values of L (Rossby radius), f, and A_M are 40 km, 5×10^{-5} s^{-1}, and 5000 s m^{-2} respectively. With these values of ϵ and Δ, the phase speed of the internal Kelvin wave with the presence of lateral friction is nearly the same as the theoretical value of the inviscid Kelvin wave as shown in Fig. B11. The temporal decay scale for the barotropic and baroclinic waves due to lateral friction is inversely proportional to the square of the Rossby radius of each wave and proportional to the frictional coefficient. According to Hsieh et al. (1983) the temporal decay scale of the internal Kelvin wave for the above values of ϵ and Δ is about 70 days. For the external mode, the ϵ value greatly reduces due to the large Rossby radius resulting in a much reduced decay factor (Fig. B11) and persistent oscillation of the free surface observed in the model results.

B-3-3. ORC, integral constraint, and sponge layer

A viscous boundary layer, sponge layer, was applied near the northern boundary in an effort to damp the free surface oscillations due to the integral constraint. The sponge layer employs a linear drag law proportional to velocity. The drag coefficient varies exponentially from zero at 160 km (8 grid points) from the northern boundary to a maximum of 10^{-3} at the boundary.

Free surface oscillations are quickly damped out (Fig. B1(C)). Internal Kelvin

waves originating from both boundaries are quickly damped out also (Fig. B3(C)). However, a number of grid points are wasted and contours are spreading out in the northern boundary region causing the jet structure to be disintegrated to a more uniform flow (Fig. B6(B)).

All the numerical experiments (SWEM) used in chapter IV are the inflow-outflow models driven with a specified velocity field with outflow determined using both ORC and the integral constraint at the outflow boundary. A sponge layer near and at the outflow boundary was also introduced to damp out any undesirable persistent oscillations, although many grid points are wasted as a trade-off.

B-4. Twin experiments

Stable numerical integration does not guarantee that the numerical solution is an accurate representation of true solution. A strict mathematical proof demonstrating that a given OBC together with the governing equations forms a properly posed problem is impossible for most practical problems. Alternatively, the model may be suitably simplified so that analytical solution exists, thus allowing a quantitative comparison of numerical results with analytical solutions. However, there is still a difficulty to assess the performance of the same OBC in the complicated numerical model since the simplifications may eliminate essential features of the model.

The accuracy of previously described inflow-outflow model results was tested by comparing them with results of other kind of stable numerical scheme with different boundary conditions.

Using the two-stage modelling approach mentioned at section III-2-4, shelf circulation driven by the western boundary current was examined with the two shallow water models with different boundary conditions (Table B2). The model scheme and all of the physical parameters are the same for both models including the location of the shelf on a β-plane except the length of deep channel and the unperturbed depths of upper and lower layers. The ratio of shelf depth to the unperturbed depth of the upper layer in

the deep channel, however, was set to be equal for both models. The resulting shelf circulation is expected to be little influenced by the meridional size of deep channel.

B-4-1. Closed basin model

The other model used for the comparison is also a shallow water equation model developed by Dearnaley (1990). The model domain is a closed one and a slip condition is applied at all of the walls. The flow is driven by a north-south pressure gradient which was imposed by the surface elevation via the continuity equation. A simple relaxation condition is added to the continuity equation to relax the free surface to the prescribed value:

$$\frac{\partial \eta}{\partial t} = \alpha \, (\eta_b - \eta) \, ,$$

where η_b is the prescribed value and α is some suitably chosen positive time constant. To generate a northward flowing western boundary current, the free surface is forced to η_b on a time scale of α in the southern forcing region extending over 200 km (10 grid points). In the northern forcing region (10 grid points) the free surface and interface are forced to their unperturbed state on some time scales. In this model the effects of disturbances or reflected waves generated at the southern and northern boundaries are confined to the forcing regions due to the relaxation condition imposed on the boundary regions. The mass in the system was conserved for this model and steady state was attained.

B-4-2. Comparisons

Figs. B7 and B8 show both model results of deep channel model for both cases at an equlibrium state. Two disadvantages of the relaxation boundary condition in a closed basin are that firstly, more grid points near the boundaries are wasted and secondly, a desired WBC transport can only be achieved by a process of trial and error since the prescribed variable is not the velocity but the elevation.

Table 2. Model parameters for a twin experiment

	open channel model	closed basin model
L^x, L^y	600 km , 2200 km	600 km , 4400 km
ℓ^x, ℓ^y	400 km , 800 km	400 km , 800 km
H_1, H_2	300 m , 1200 m	400 m , 1100 m
D	150 m	200 m
A_M	5000 m^2 s^{-1}	5000 m^2 s^{-1}
r	10^{-3} m s^{-1}	10^{-3} m s^{-1}
f^*	22 °	22 °
$\Delta x, \Delta y$	20 km , 20 km	20 km , 20 km
Δt	50 sec	50 sec

where,
L^x : width of the deep channel
L^y : length of the deep channel
ℓ^x : width of the shelf
ℓ^y : length of the shelf
H_1 : unperturbed upper layer thickness of deep channel
H_2 : unperturbed lower layer thickness of deep channel
D : unperturbed shelf depth
A_M : lateral viscosity
r : bottom friction coefficient
f^* : latitude of the southern boundary of the shelf
$\Delta x, \Delta y$: grid spacings
Δt : timestep length.

The meridional velocity profile along a zonal section is shown in Fig. B9. Quantitative comparison was also made by comparing the ratio (T_t / T_s) between the total northward volume transport from the western wall of the shelf to the first zero-crossing point of the meridional velocity (T_t) and northward transport in the shelf region (T_s) at all latitudes where the shelf is introduced. T_t and T_s represent the total WBC transport and on-shelf transport respectively. Fig. B10 shows the latitudinal variation of

the ratio from the southern wall to the northern wall of the shelf. Both model results show a good agreement not only qualitatively but also quantitatively.

Fig. B1. Time-latitude plot of free surface along the western boundary with open boundary conditions (A) case I, (B) case II, and (C) case III from initial state to 250 days (left panel) and from 250 days to 500 days (right panel). The direction of increasing grid point is due north. Contour intervals are 1 m (case I), and 0.5 cm (case II and case III).

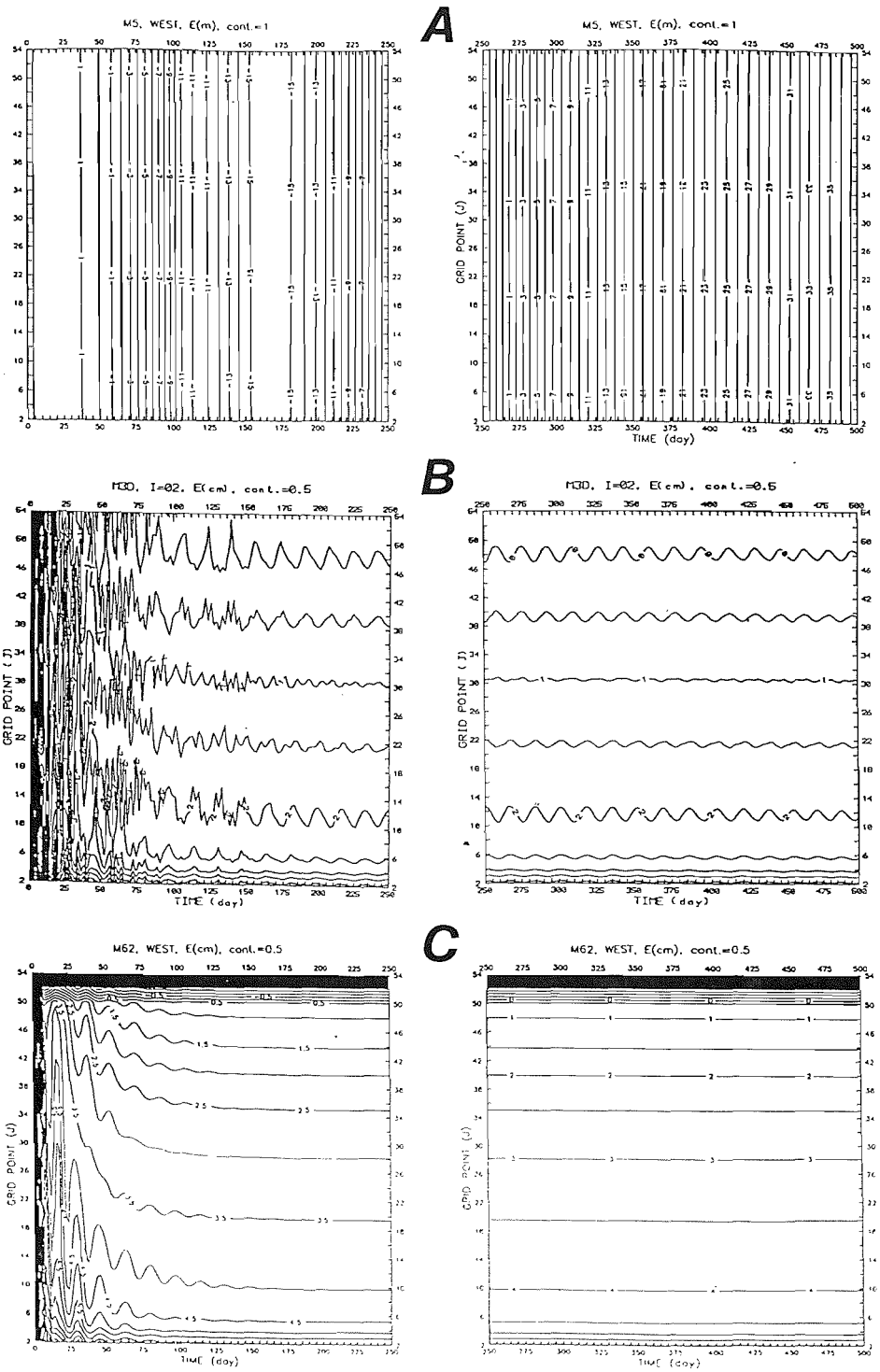
A
M5, WEST, E(m), cont.=1
M5, WEST, E(m), cont.=1
GRID POINT (J)
TIME (day)
B
M3D, I=02, E(cm), cont.=0.5
M3D, I=02, E(cm), cont.=0.5
GRID POINT (J)
TIME (day)
C
M62, WEST, E(cm), cont.=0.5
M62, WEST, E(cm), cont.=0.5
GRID POINT (J)
TIME (day)

Fig. B2. Time-latitude plot of upper layer meridional velocity along the eastern boundary with open boundary conditions (A) case I, (B) case II, and (C) case III from initial state to 50 days. The direction of increasing grid point is due north. Contour intervals are 1 cm/s. Dotted lines show the theoretical path of the inviscid internal Kelvin wave.

A.

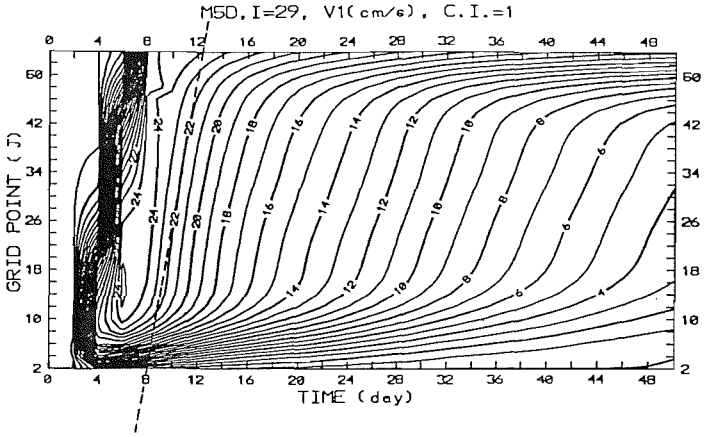
M5D, I=29, V1(cm/s), C.I.=1
GRID POINT (J)
TIME (day)

B.

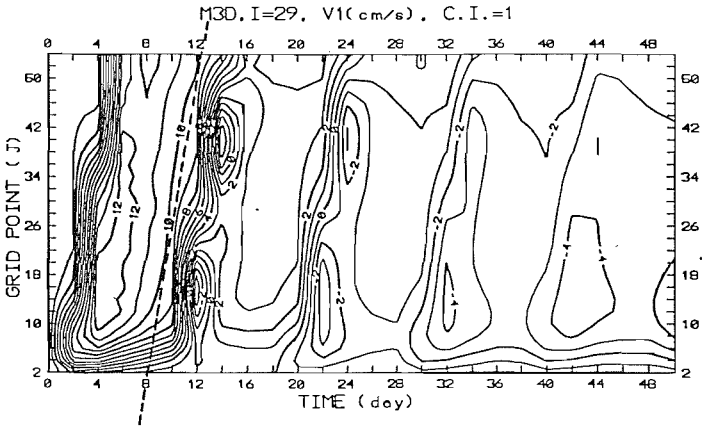
M3D, I=29, V1(cm/s), C.I.=1
GRID POINT (J)
TIME (day)

C.

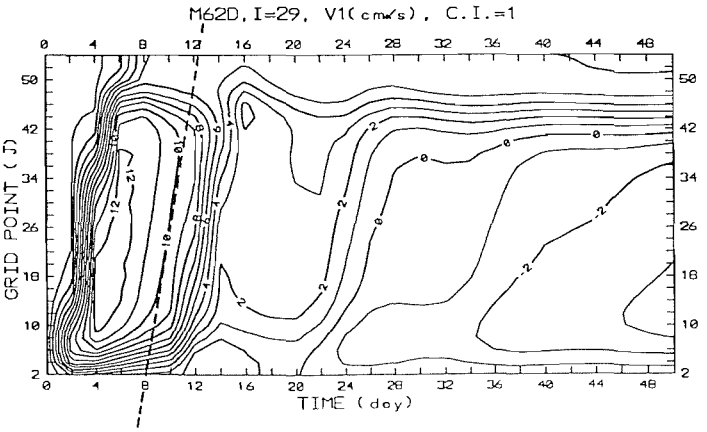
M62D, I=29, V1(cm/s), C.I.=1
GRID POINT (J)
TIME (day)

Fig. B3. Time-latitude plot of upper layer meridional velocity along the eastern boundary with open boundary conditions (A) case I, (B) case II, and (C) case III from initial state to 250 days. The direction of increasing grid point is due north. Contour intervals are 1 cm/s.

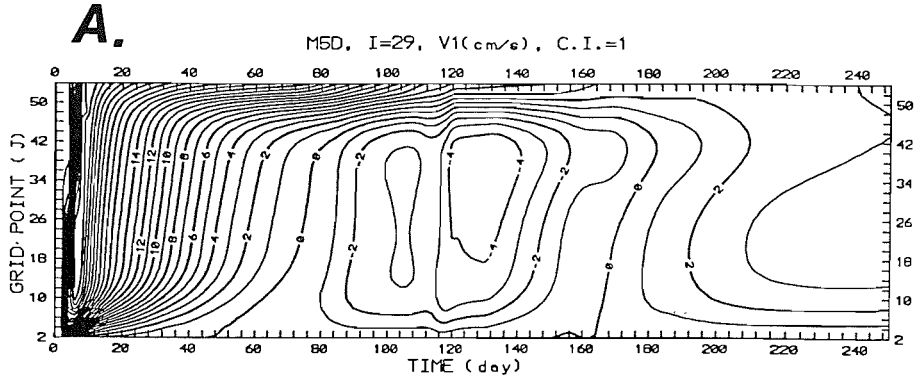
A.
M5D, I=29, V1(cm/s), C.I.=1
GRID POINT (J)
TIME (day)

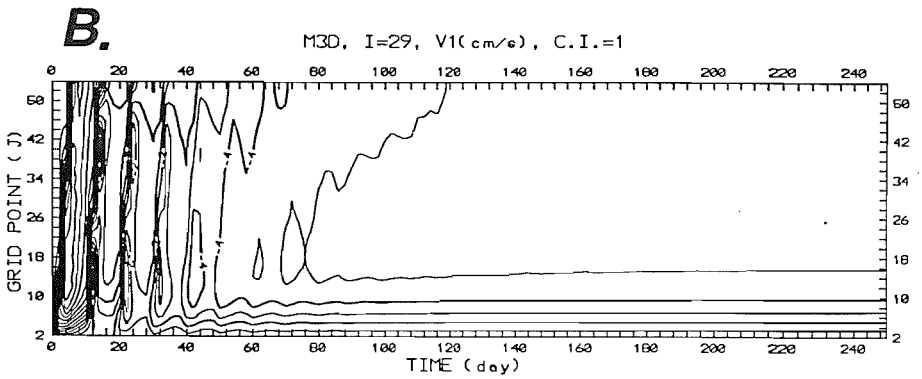
B.
M3D, I=29, V1(cm/s), C.I.=1
GRID POINT (J)
TIME (day)

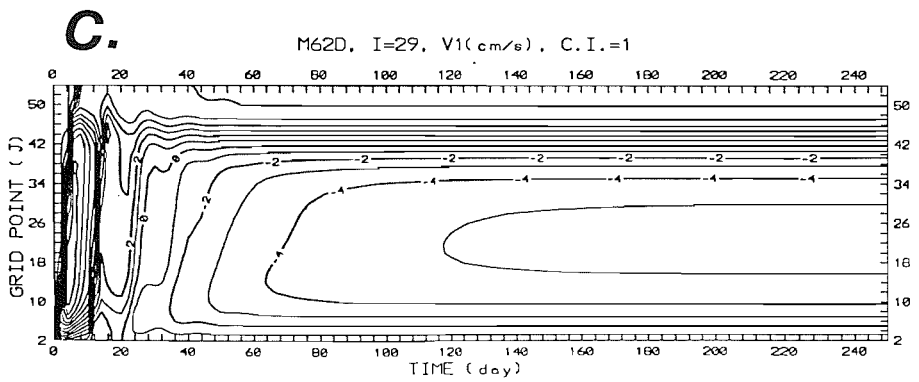
C.
M62D, I=29, V1(cm/s), C.I.=1
GRID POINT (J)
TIME (day)

Fig. B4. Time-longitude plot of interface perturbation along the middle section with open boundary conditions (A) case I, (B) case II, and (C) case III from initial state to 250 days. The direction of increasing grid point is due east. Contour intervals are 4 m (case I), and 2 m (case II and case III). Dotted lines show the theoretical path of the long Rossby wave whose phase and group speeds are given by equation (II-4-6).

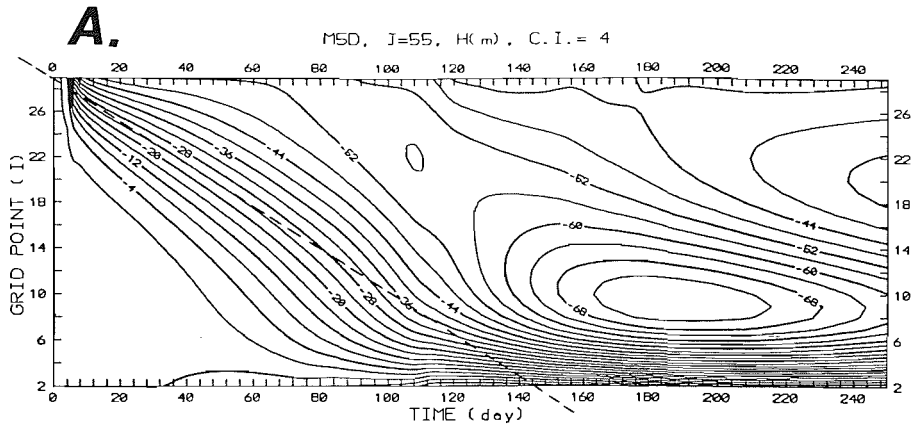
A.
M5D, J=55, H(m), C.I.= 4
GRID POINT (I)
TIME (day)

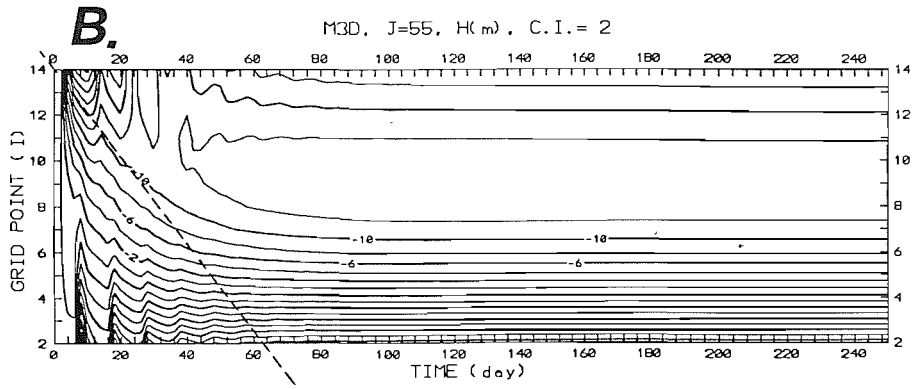
B.
M3D, J=55, H(m), C.I.= 2
GRID POINT (I)
TIME (day)

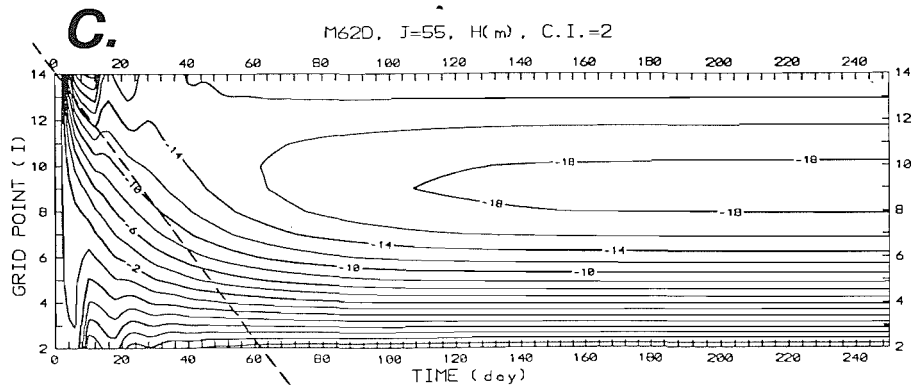
C.
M62D, J=55, H(m), C.I.=2
GRID POINT (I)
TIME (day)

Fig. B5. Contours of (A) free surface, (B) interface perturbation, and (C) upper layer meridional velocity after 500 days for the case I. Contour intervals are (a) 1 m, (b) 2 m, and (c) 2 cm/s.

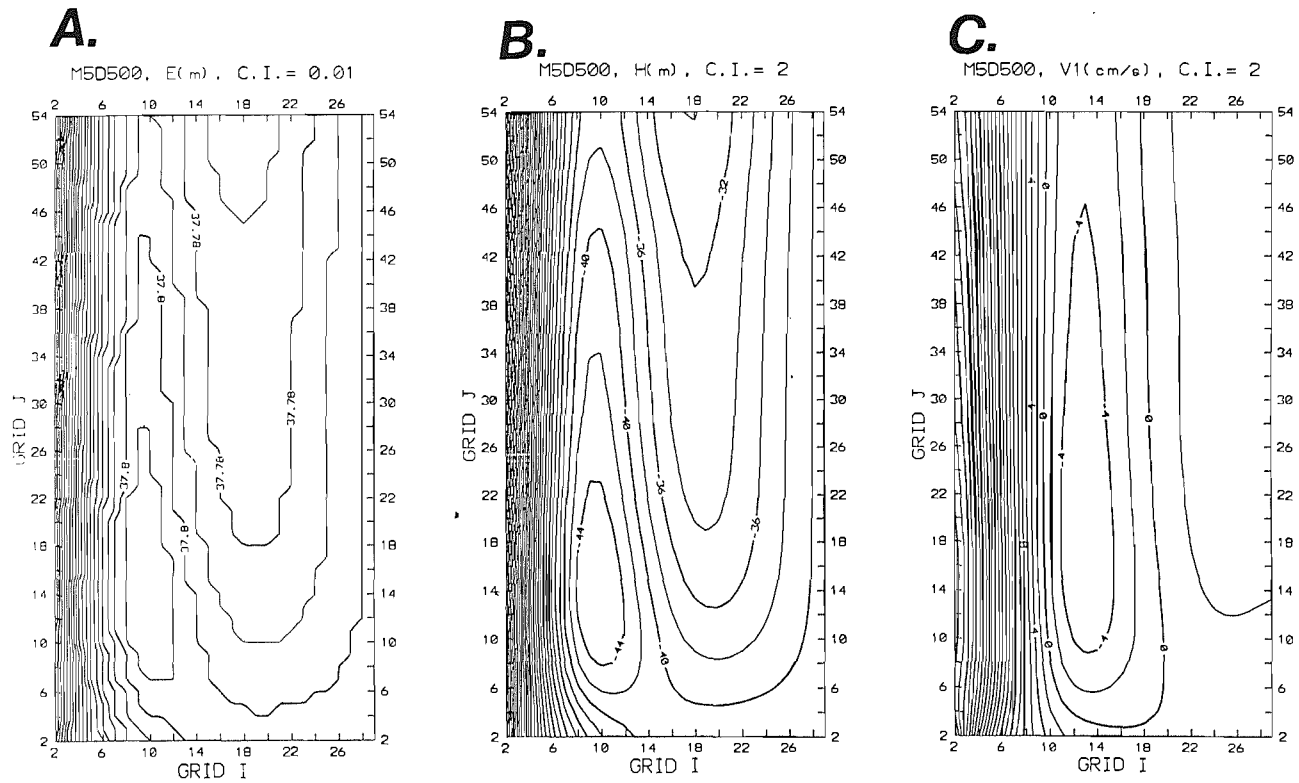
A.
M5D500, E(m), C.I.= 0.01
37.78
37.8
GRID J
GRID I
B.
M5D500, H(m), C.I.= 2
GRID J
GRID I
C.
M5D500, V1(cm/s), C.I.= 2
GRID J
GRID I

Fig. B6. Contours of (A) free surface, (B) interface perturbation, and (C) upper layer meridional velocity after 500 days for the case II **(upper panel)**, and case III **(lower panel)**. Contour intervals are (A) 1 m, (B) 2 m, and (C) 2 cm/s.

A.

M3D500, E(cm), C.I.= 1

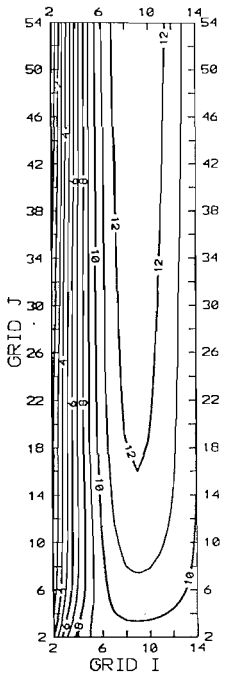

B.

M3D500, H(m), C.I.= 2

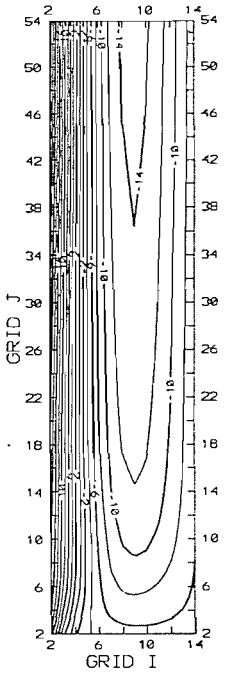

C.

M3D500, V1(cm/s), C.I.= 2

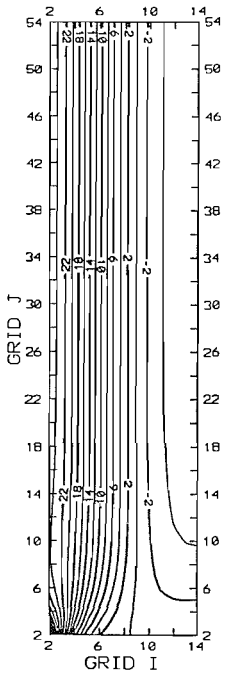

M62D500, E(cm), C.I.= 1

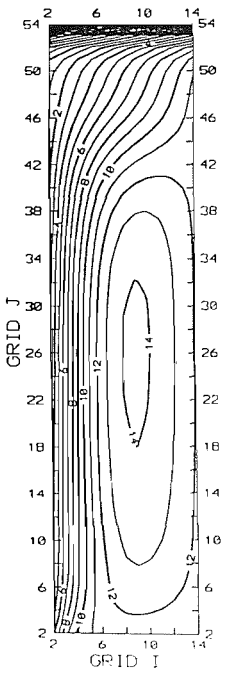

M62D500, H(m), C.I.= 2

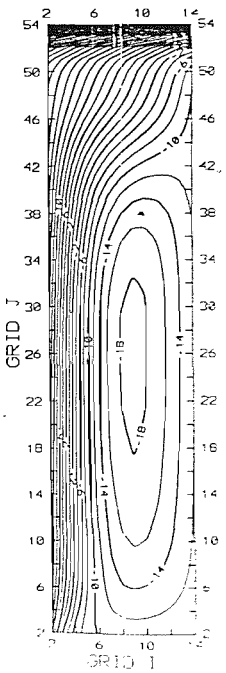

M62D500, V1(cm/s), C.I.= 2

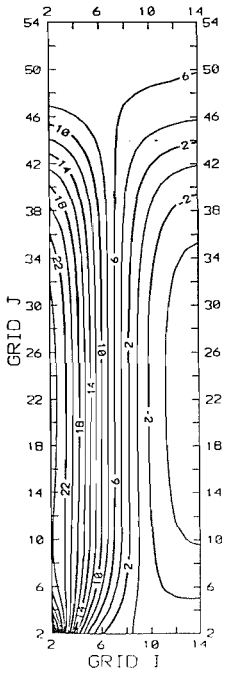

Fig. B7. Contours of free surface at an equilibrium state for the closed basin model covering the (A) whole domain, (B) shelf and adjacent deep ocean area, and (C) shelf area. Contour intervals are 2 cm (A and B), and 1 cm (C).

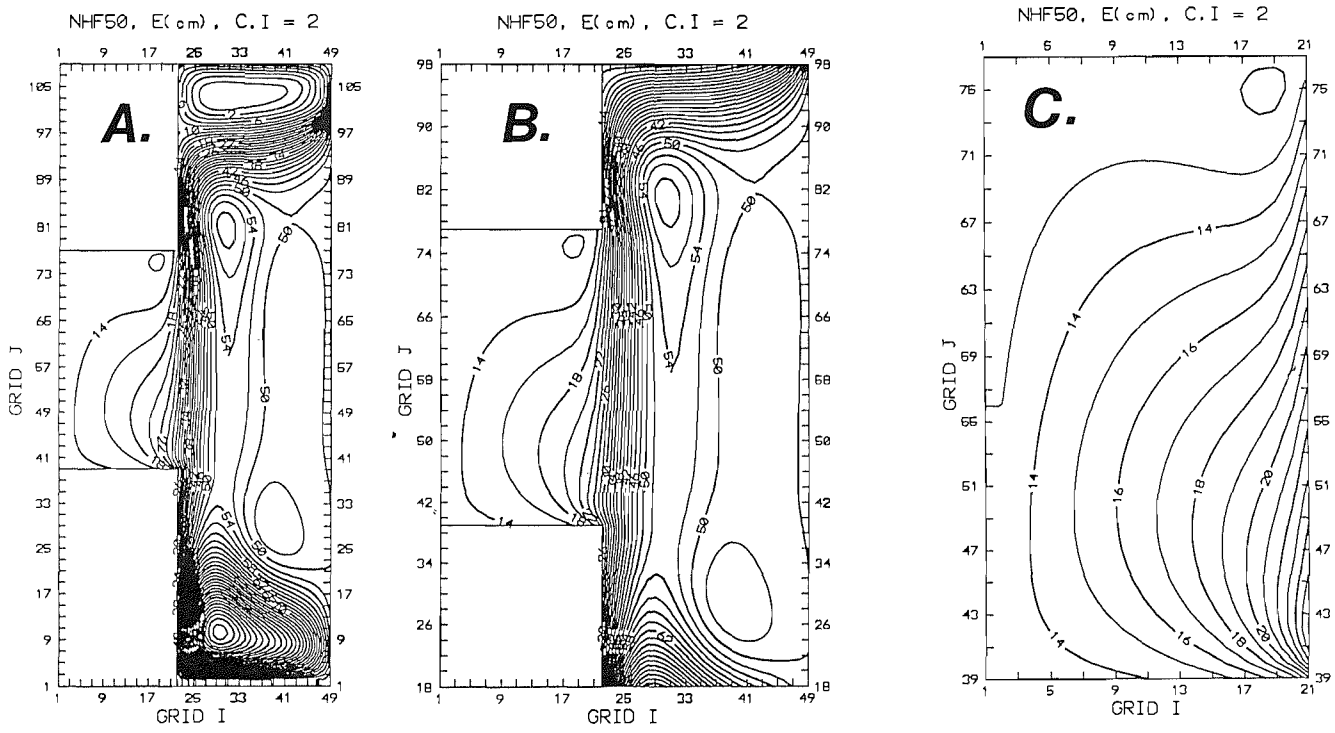
NHF50, E(cm), C.I = 2
A.
GRID J
GRID I
NHF50, E(cm), C.I = 2
B.
GRID J
GRID I
NHF50, E(cm), C.I = 2
C.
GRID J
GRID I

Fig. B8. Contours of free surface at an equilibrium state for the open channel model covering the (A) whole domain, (B) shelf and adjacent deep ocean area, and (C) shelf area. Contour intervals are 2 cm (A and B), and 1 cm (C).

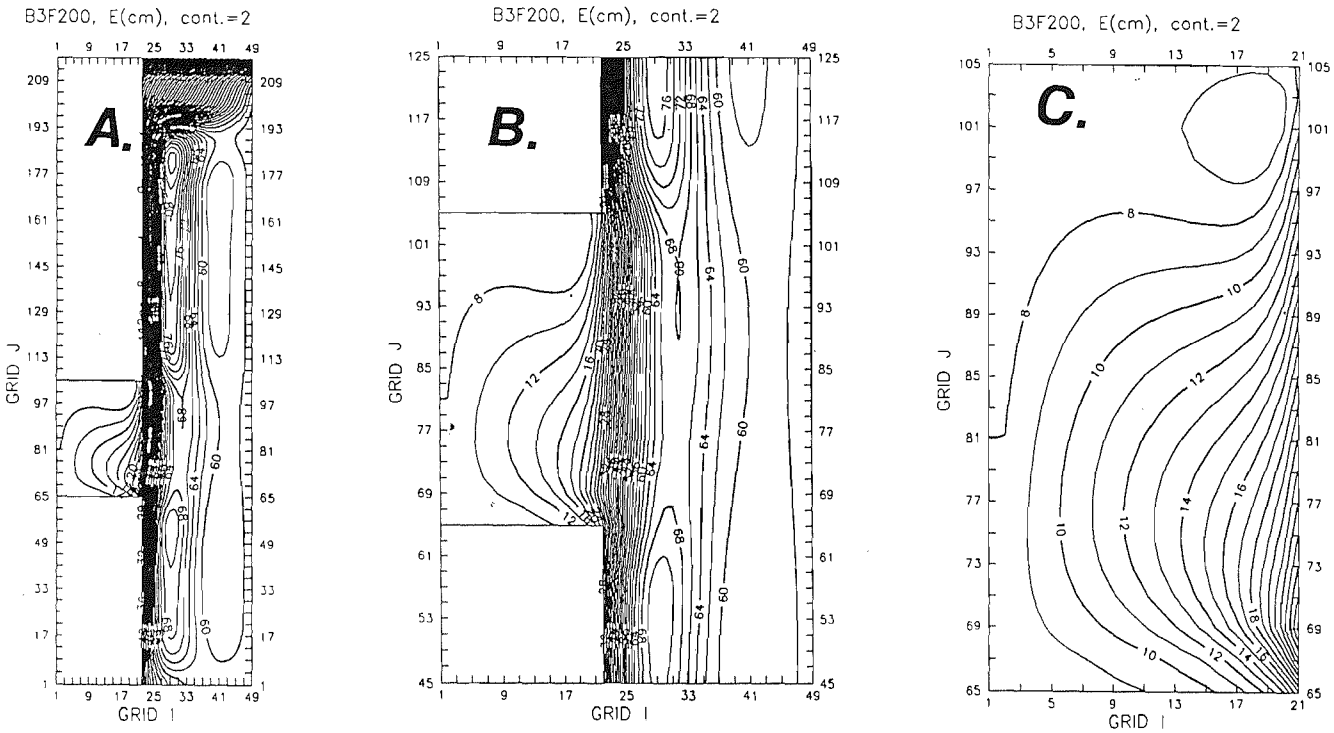
B3F200, E(cm), cont.=2
A.
GRID J
GRID I
B3F200, E(cm), cont.=2
B.
GRID J
GRID I
B3F200, E(cm), cont.=2
C.
GRID J
GRID I

Fig. B9. Meridional velocity profile along a zonal section (J=70 in Fig. B8).

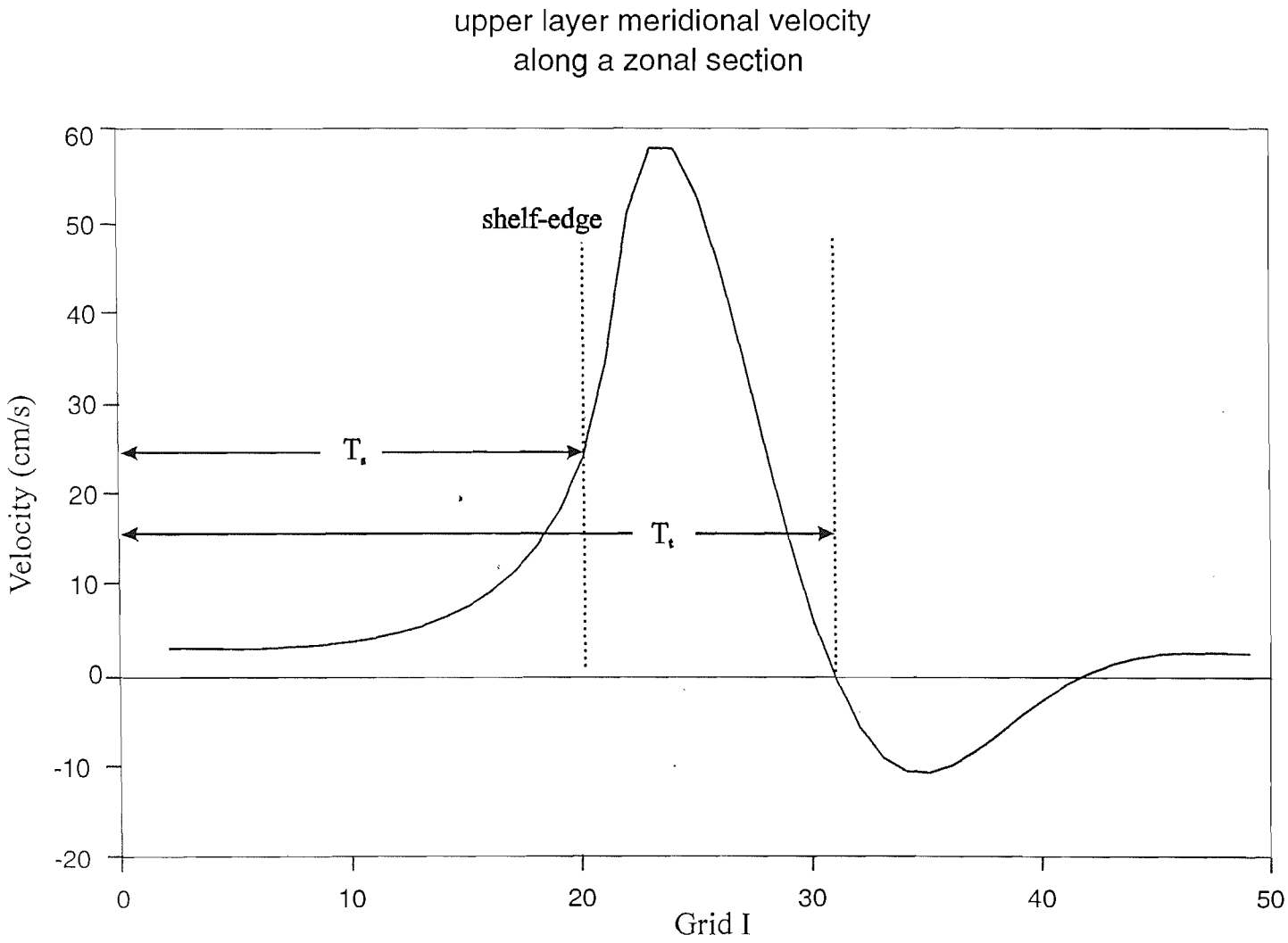
upper layer meridional velocity
along a zonal section
shelf-edge
T_s
T_t
Velocity (cm/s)
60
50
40
30
20
10
0
-10
-20
0
10
20
30
40
50
Grid I

Fig. B10. Latitudinal variation of northward volume transport ratio for the closed basin and open channel cases from the southern wall (left to the horizontal axis) to the northern wall (right to the horizontal axis) of the shelf.

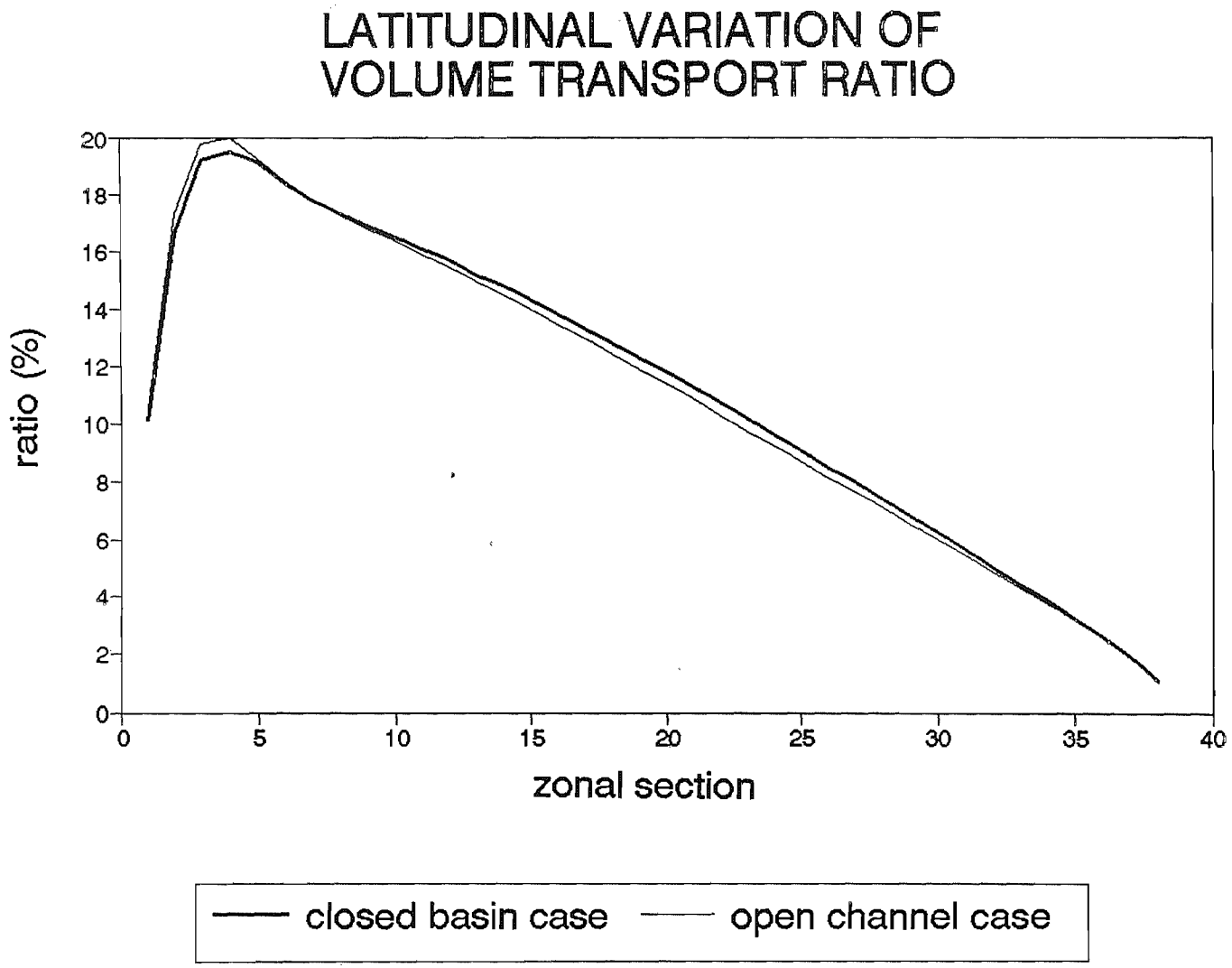
LATITUDINAL VARIATION OF
VOLUME TRANSPORT RATIO
ratio (%)
0
2
4
6
8
10
12
14
16
18
20
0
5
10
15
20
25
30
35
40
zonal section
closed basin case
open channel case

Fig. B11. (A) Alongshore phase speed (Re(c)) and (B) temporal decay factor (-Im(c)) for the Kelvin wave versus Δ at selected values of ϵ for the C-grid with free-slip boundary (from Hsieh et al., 1983). Increasing Δ and ϵ implies worsening resolution and higher viscosity respectively. Re(c)=1 means the phase speed of the inviscid Kelvin wave in a continuum. The e-folding decay scale t_d is given by $t_d = (-\mathrm{Im}(c) \times \ell)$, where ℓ is the longshore wavenumber.

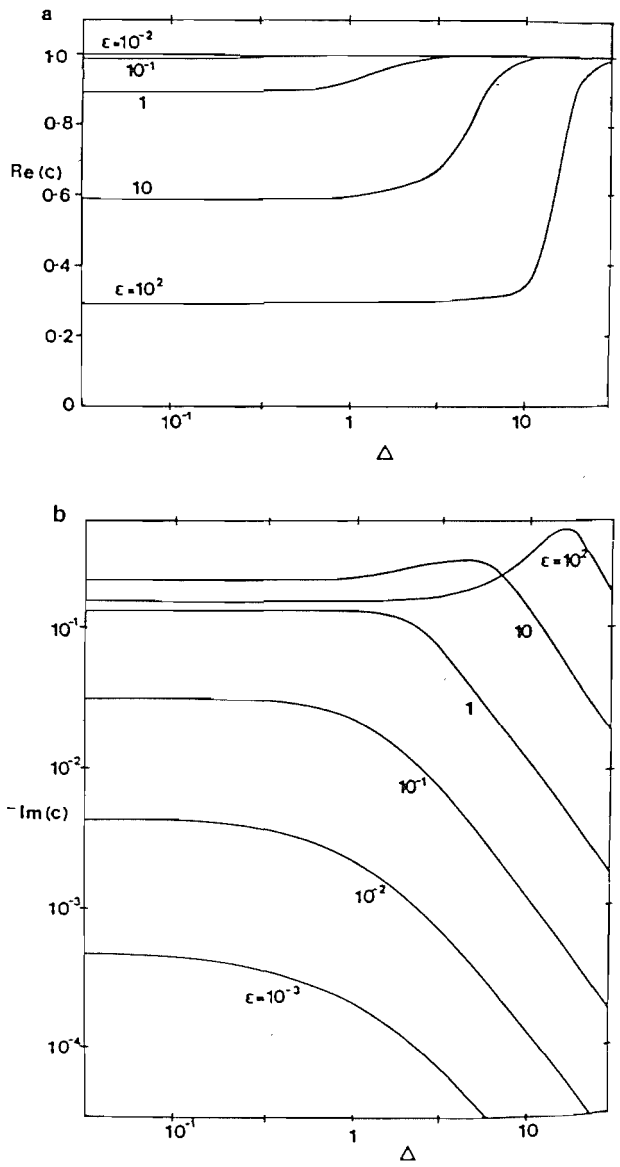
a
ε=10^-2
10^-1
1
10
ε=10^2
Re (c)
1·0
0·8
0·6
0·4
0·2
0
10^-1
1
10
Δ
b
ε=10^2
10
1
10^-1
10^-2
ε=10^-3
-Im (c)
10^-1
10^-2
10^-3
10^-4
10^-1
1
10
Δ

APPENDIX C.

SIGMA-COORDINATE TRANSFORMATION

A general expression for the horizontal gradient of variables such as pressure which is applicable to any vertical coordinate s = s(x,y,z,t) can be obtained using a chain rule (Holton, 1979),

$$\left(\frac{\partial}{\partial \xi}\right)_s = \left(\frac{\partial}{\partial \xi}\right)_z + \frac{\partial s}{\partial z}\left(\frac{\partial z}{\partial \xi}\right)_s \frac{\partial}{\partial s}, \tag{C.1}$$

where ξ can be x, y, or t.

The σ-coordinate is a stretched vertical coordinate system which conforms to the variable bottom at z = - h(x,y),

$$\sigma = 1 + 2\left(\frac{z}{h}\right), \quad -1 \le \sigma \le 1 . \tag{C.2}$$

From (C.2)

$$\frac{\partial \sigma}{\partial z} = \frac{2}{h}, \quad \left(\frac{\partial z}{\partial \xi}\right)_\sigma = \frac{\sigma - 1}{2}\frac{\partial h}{\partial \xi},$$

so that (C.1) becomes

$$\left(\frac{\partial}{\partial \xi}\right)_\sigma = \left(\frac{\partial}{\partial \xi}\right)_z + \frac{\sigma - 1}{h}\frac{\partial h}{\partial \xi}\frac{\partial}{\partial \sigma} . \tag{C.3}$$

The primitive equations in Cartesian coordinates can be written :

$$u_t + \vec{v}\cdot\nabla u - fv = -\phi_x + F_u + D_u \tag{C.4}$$

$$v_t + \vec{v}\cdot\nabla v + fu = -\phi_y + F_v + D_v \tag{C.5}$$

$$\phi_z = -\frac{g\rho}{\rho_0} \tag{C.6}$$

$$\rho_t + \vec{v}\cdot\nabla\rho = F_\rho + D_\rho \tag{C.7}$$

$$u_x + v_y + w_z = 0 \,, \tag{C.8}$$

where

$$\vec{v}\cdot\nabla = u\frac{\partial}{\partial x} + v\frac{\partial}{\partial y} + w\frac{\partial}{\partial z} \tag{C.9}$$

Other notations are the same as in chapter III-3-1.

The above equations are tranformed into those in σ-coordinates as follows,

Hydrostatic equation (III-4-4) :

From (C.3)

$$\left(\frac{\partial\phi}{\partial z}\right)_\sigma = \left(\frac{\partial\phi}{\partial z}\right)_z + \frac{\sigma-1}{h}\frac{\partial h}{\partial z}\frac{\partial\phi}{\partial\sigma} = \left(\frac{\partial\phi}{\partial z}\right)_z \,,$$

since h = h(x,y). Then the hydrostatic equation in σ-coordinates is obtained from the relation

$$\left(\frac{\partial\phi}{\partial z}\right)_\sigma = \frac{\partial\sigma}{\partial z}\frac{\partial\phi}{\partial\sigma} = \frac{2}{h}\frac{\partial\phi}{\partial\sigma} \,,$$

and (C.6) becomes III-4-4.

Vertical velocity (Ω) :

Vertical velocity in Cartesian-coordinates is given by

$$w = \frac{Dz}{Dt} \,, \; where \; \frac{D}{Dt} = u\frac{\partial}{\partial x} + v\frac{\partial}{\partial y} + w\frac{\partial}{\partial z} \,.$$

From (C.2)

$$\frac{Dz}{Dt} = \left(\frac{\sigma - 1}{2}\right)\frac{Dh}{Dt} + h\frac{D}{Dt}\left(\frac{\sigma - 1}{2}\right)$$

$$= \frac{\sigma - 1}{2}\left(u\frac{\partial h}{\partial x} + v\frac{\partial h}{\partial y}\right) + \frac{h}{2}\frac{D\sigma}{Dt}$$

Therefore,

$$\Omega(x,y,\sigma,t) = \frac{D\sigma}{Dt} = \frac{1}{h}\left[(1-\sigma)u\frac{\partial h}{\partial x} + (1-\sigma)v\frac{\partial h}{\partial y} + 2w\right]. \qquad \text{(C.10)}$$

Continuity equation (III-4-6) :

Using the chain rule (C.3), the horizontal gradient of velocity components can be found,

$$\left(\frac{\partial u}{\partial x}\right)_z = \left(\frac{\partial u}{\partial x}\right)_\sigma - \frac{\sigma - 1}{h}\frac{\partial h}{\partial x}\frac{\partial u}{\partial \sigma} \qquad \text{(C.11)}$$

$$\left(\frac{\partial v}{\partial y}\right)_z = \left(\frac{\partial v}{\partial y}\right)_\sigma - \frac{\sigma - 1}{h}\frac{\partial h}{\partial y}\frac{\partial v}{\partial \sigma}, \qquad \text{(C.12)}$$

From (C.10)

$$w = \frac{h}{2}\Omega + \frac{\sigma - 1}{2}\left(u\frac{\partial h}{\partial x} + v\frac{\partial h}{\partial y}\right).$$

Hence,

$$\frac{\partial w}{\partial z} = \frac{\partial \sigma}{\partial z}\frac{\partial w}{\partial \sigma} = \frac{2}{h}\left[\frac{h}{2}\frac{\partial \Omega}{\partial \sigma} + \frac{1}{2}\left(u\frac{\partial h}{\partial x} + v\frac{\partial h}{\partial y}\right) + \frac{\sigma - 1}{2}\left(\frac{\partial u}{\partial \sigma}\frac{\partial h}{\partial x} + \frac{\partial v}{\partial \sigma}\frac{\partial h}{\partial y}\right)\right]. \qquad \text{(C.13)}$$

From (C.11), (C.12), and (C.13) the continuity equation in σ-coordinates is obtained.

Momentum equations (III-4-2 and III-4-3) :

The local derivative and Coriolis terms remain unchanged in σ-coordinates. Using (C.3) and equation III-4-4, the horizontal pressure gradient in σ-coordinates can be found,

$$\left(\frac{\partial \phi}{\partial x}\right)_z = \left(\frac{\partial \phi}{\partial x}\right)_\sigma + \frac{\sigma - 1}{h}\frac{\partial h}{\partial x}\frac{h}{2}\frac{\rho g}{\rho_0}$$

$$= \left(\frac{\partial \phi}{\partial x}\right)_\sigma + \frac{\sigma - 1}{2}\frac{\partial h}{\partial x}\frac{\rho g}{\rho_0}$$

$$\left(\frac{\partial \phi}{\partial y}\right)_z = \left(\frac{\partial \phi}{\partial y}\right)_\sigma + \frac{\sigma - 1}{h}\frac{\partial h}{\partial y}\frac{h}{2}\frac{\rho g}{\rho_0}$$

$$= \left(\frac{\partial \phi}{\partial y}\right)_\sigma + \frac{\sigma - 1}{2}\frac{\partial h}{\partial y}\frac{\rho g}{\rho_0}$$

The advection term in the x-momentum equation in σ-coordinates can be found using (C.11) and the following two relations

$$\frac{\partial u}{\partial z} = \frac{\partial u}{\partial \sigma}\frac{\partial \sigma}{\partial z} = \frac{2}{h}\frac{\partial u}{\partial \sigma}$$

$$\left(\frac{\partial u}{\partial y}\right)_z = \left(\frac{\partial u}{\partial y}\right)_\sigma - \frac{\sigma - 1}{h}\frac{\partial h}{\partial y}\frac{\partial u}{\partial \sigma}$$

Manipulation yields

$$\vec{v}\cdot\nabla u = u\frac{\partial u}{\partial x} + v\frac{\partial u}{\partial y} + w\frac{\partial u}{\partial z} = u\frac{\partial u}{\partial x} + v\frac{\partial u}{\partial y} + \Omega\frac{\partial u}{\partial \sigma} .$$

APPENDIX D.

SPIN-UP OF THE SPEM

Possible waves in the SPEM configuration are the barotropic Rossby wave and topographic wave. There are no gravity and Kelvin waves since the rigid-lid approximation was used and the model ocean is homogeneous. Fig. D-1. gives an example of a time series of kinetic energy (KE) spatially averaged in four different regions over the SSM domain: the main deep ocean basin (labelled ocean), the WBC, the shelf, and their sum (labelled total). Oscillations having periods of twenty-eight days are evident in all of the regions. The period of oscillation in the shelf region is slightly shorter than those in other regions.

Four experiments were conducted to identify the nature of this oscillation. Table D.1 summarises the parameters of the four experiments. The model ocean is spun-up by the applied steady wind-stress and all other model parameters are set to be equal for all the experiments. The configuration of the experiment 4 is the normal SSM domain.

There are neither topography nor coastal promontories for experiments 1 and 2. The only difference between them is the width (L^x) of the model domain. The only possible wave for the two cases is the barotropic Rossby wave. The frequency of the basin mode 1 Rossby waves is obtained using the equation (II-4-7) after dropping the last term in the denominator since the flow is non-divergent due to the rigid-lid approximation. The periods of oscillations in the total kinetic energy for two cases correspond to those of the basin mode 1 Rossby waves as shown in Fig. D-2.

Two coastal promontories are introduced in experiment 3, the same as the normal SSM domain but without topography. As there is no topography the WBC fills the area in between the two promontories as shown in Fig. D-3. The period of oscillation in the total kinetic energy is 25 days for this case which lies in between the periods of two cases of the experiments 1 and 2.

When both the topography and the coastal promontories are present (experiment 4), most of the WBC flows along the continental slope and only a part of the WBC penetrates onto the shelf as shown in Fig. D-3. The period of oscillation in the total kinetic energy is 28 days as shown in Fig. D-1 corresponding to the basin mode 1 Rossby wave of 28 days, if the longitudinal size of the basin is taken as the width of the deep ocean basin. Fig. D-4 shows streamline patterns obtained at the different times marked on Fig. D-1. The presence of the basin mode 1 Rossby wave superimposed on the general circulation is clearly seen. The oscillatory motions are effectively damped by the lateral friction within 150 days.

Table D-1. Model parameters for the four experiments.

Experiment	1	2	3	4
L^x (km)	1280	900	1280	1280
L^y (km)	2560	2560	2560	2560
topography	X	X	X*	O
promontories	X	X	O*	O
T (days)	20	28	25	28
BRT (days)	20	28		

where
L^x : longitudinal size of the model domain
L^y : latitudinal size of the model domain
T : periods of oscillation obtained from model results
BRT : calculated periods of basin model 1 Rossby waves.
O (X) indicates that there is either (no) topography or (no) coastal promontories.

Table 4-4 in chapter IV-3-3 summarises six non-linear experiments using the SPEM. The width and length of the model domain are the same as those of the experiment 4 in Table D-1. Fig. D-5 shows plots of the normalised kinetic energy in the whole basin and only on the shelf as a function of time for all cases in Table 4-4.

For the moderately inertial case ($\epsilon < 1$), the periods of oscillations are 27 ~ 28

days similar to the period of oscillation for the linear case. As the inertial effects become more prominent, the period of the oscillation tends to be reduced. For a highly inertial case (experiment F in Table 4-4), an oscillation having a period of 25 days dominates in the initial kinetic energy fluctuation. It has been found that the period of oscillation changes to be 27 ~ 28 days without advection terms in experiment F.

The initial oscillations are damped by the action of lateral friction and the system has converged to its steady state value at 150 days. For the experiment F the kinetic energy for the entire flow is still increasing at 150 days of integration. This was observed to be caused mainly by the strengthening of a recirculating flow in the northern part of the deep ocean (see Fig. 4-43 (F)). The kinetic energy for the flow in the shelf region exhibits more pronounced oscillatory behaviour as the inertial effects in the deep ocean become more prominent. For the highly inertial case (experiment F in Table 4-3) the oscillation persists until 150 days of integration, but the amplitude is greatly reduced from the initial stage. The system can be said to reach an equilibrium state in a statistical sense even for this highly inertial case. A temporal average of model results was not taken and all the results presented in chapter IV-3-3 are based on the results at 150 days.

As this study is mainly concerned with the final steady state results, details of transients have not been investigated. It may be concluded cautiously that the transients are dominated by the basin mode 1 Rossby waves in the early stage of SPEM integration although the knowledge of the topographic waves is totally lacking. It is unlikely that any topographic wave signal affects the total kinetic energy in the system. It is yet to be explained why the period of oscillation becomes reduced as the inertial effects become prominent .

Fig. D-1. Plots of kinetic energies averaged over four different regions of the model domain of the experiment 4 in Table D-1 as a function of time. Numerals denote the times when the total kinetic energy shows its maximum or minimum values.

Fig. D-2. Plots of total kinetic energies for the three experiments in Table D-1 as a function of time. Observed periods of oscillation are marked for each experiment. Numerals denote the times when the total kinetic energy shows its maximum or minimum values.

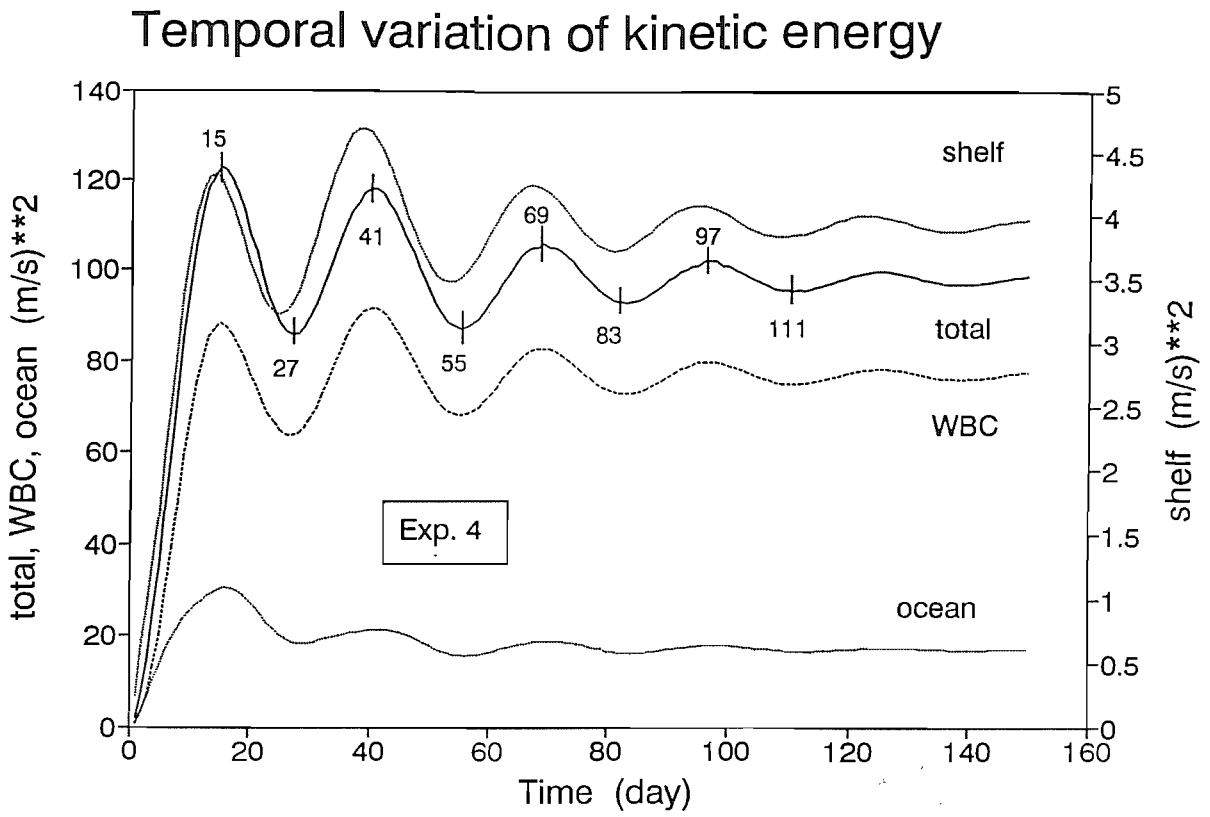
Temporal variation of kinetic energy
total, WBC, ocean (m/s)**2
shelf (m/s)**2
Time (day)
shelf
total
WBC
ocean
Exp. 4
15
27
41
55
69
83
97
111

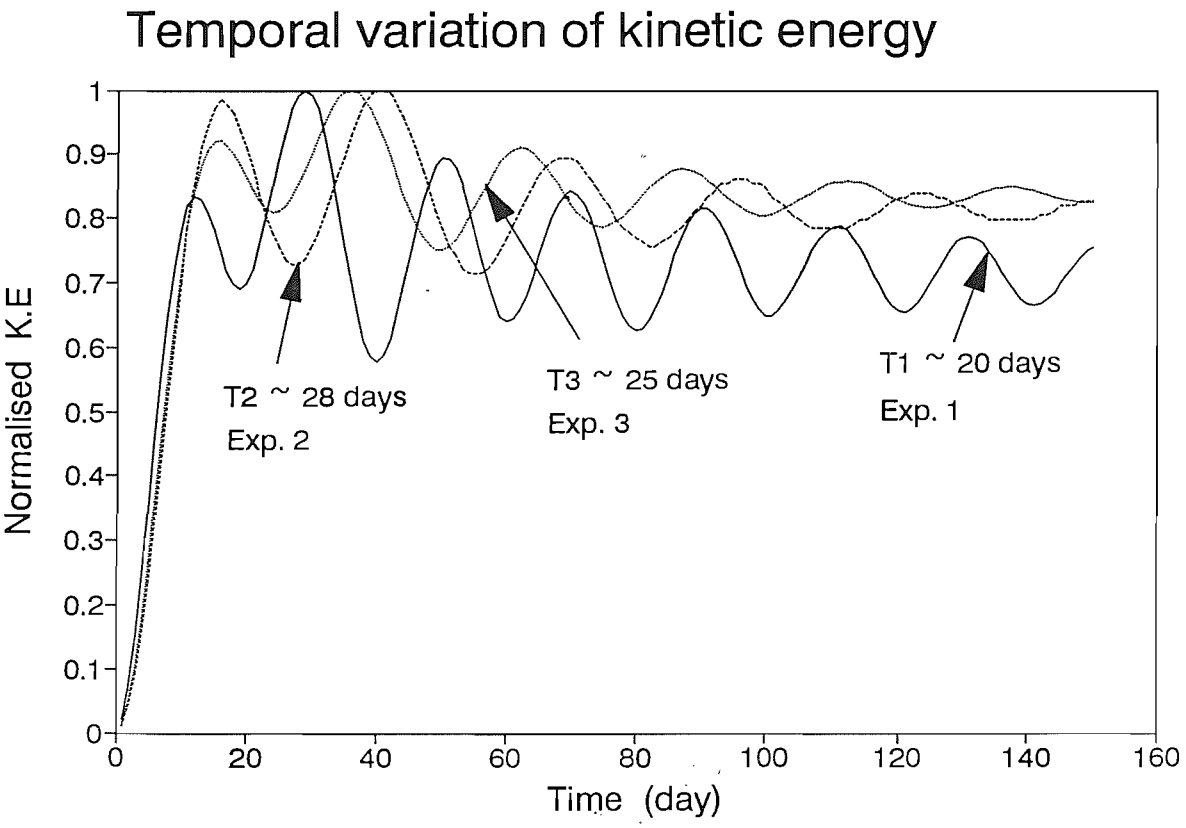
Temporal variation of kinetic energy
Normalised K.E
Time (day)
T2 ~ 28 days
Exp. 2
T3 ~ 25 days
Exp. 3
T1 ~ 20 days
Exp. 1

Fig. D-3. Contours of streamlines at 150 days for the three experiments in Table D-1.

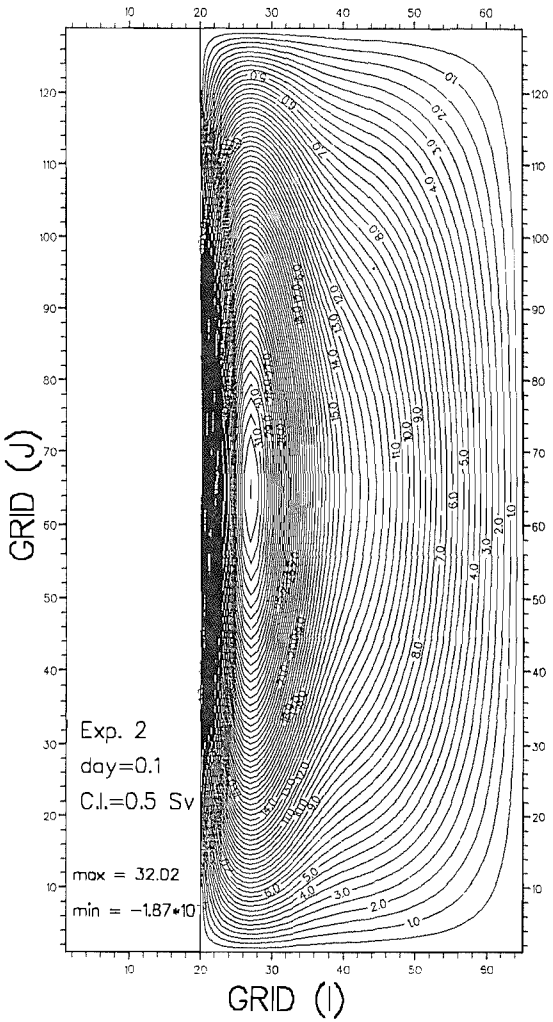
Exp. 2
day=0.1
C.I.=0.5 Sv
max = 32.02
min = −1.87*10
GRID (J)
GRID (I)

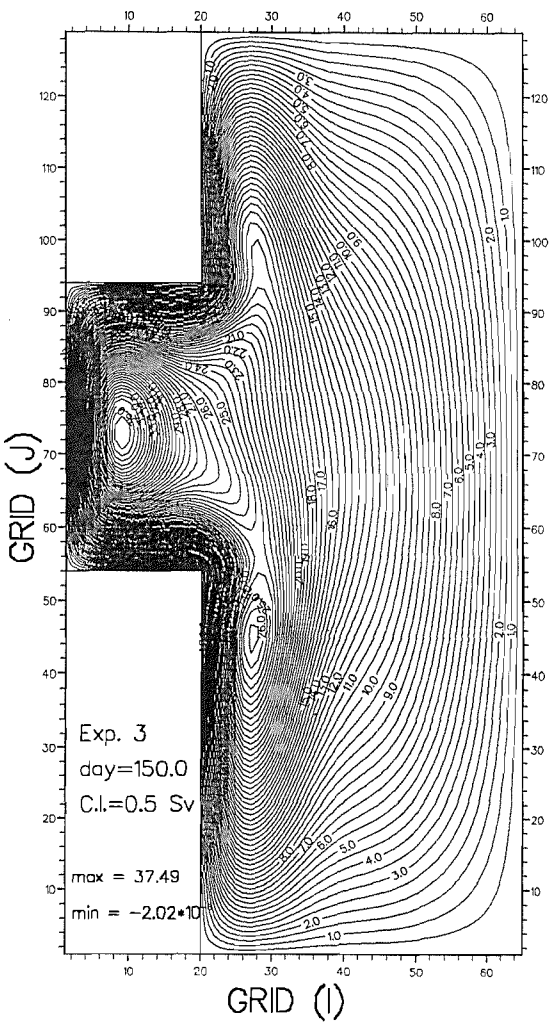
Exp. 3
day=150.0
C.I.=0.5 Sv
max = 37.49
min = −2.02*10
GRID (J)
GRID (I)

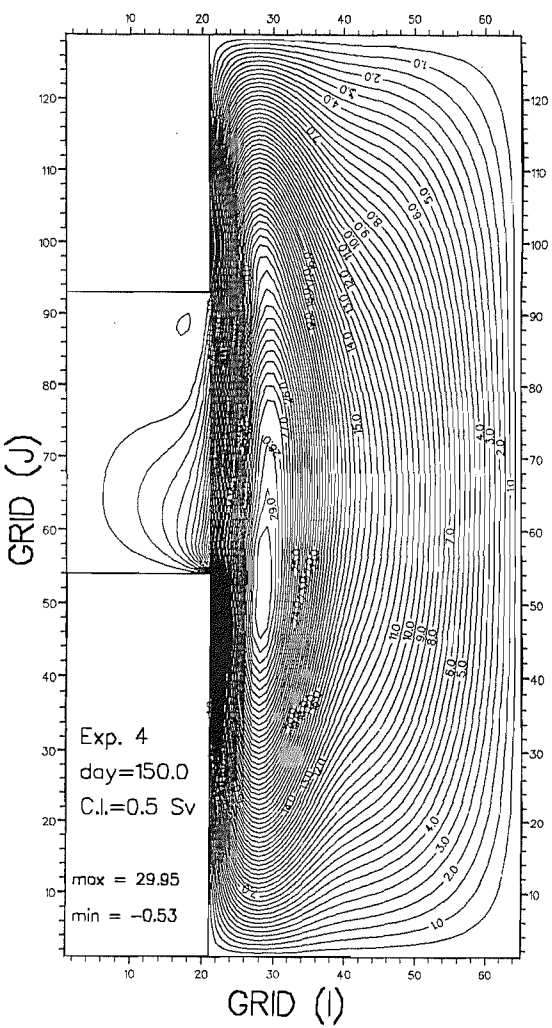
Exp. 4
day=150.0
C.I.=0.5 Sv
max = 29.95
min = −0.53
GRID (J)
GRID (I)

Fig. D-4. Contours of streamlines at the different times of day 15, day 27, and day 41 (from left to right) marked in Fig. D-1.

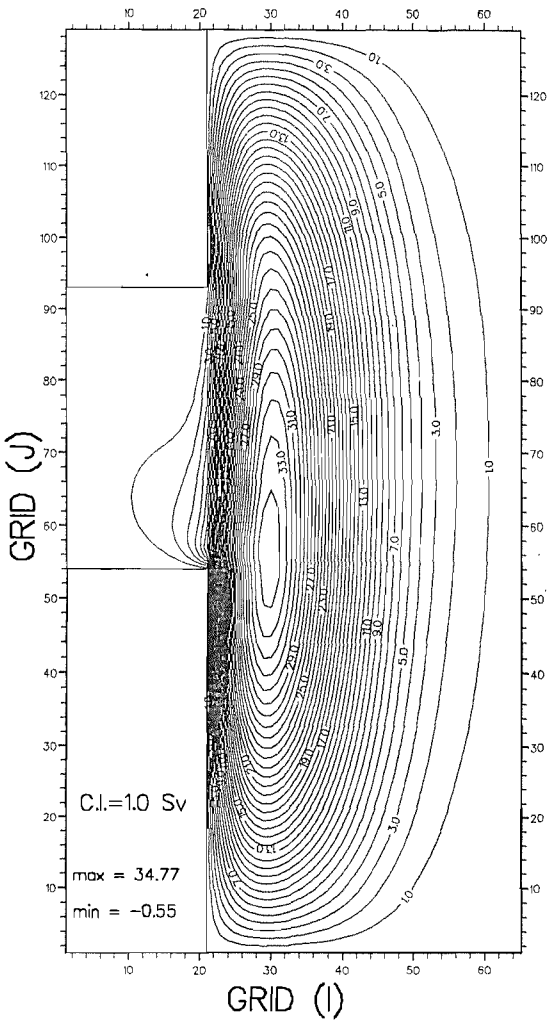
GRID (J)
GRID (I)
C.I.=1.0 Sv
max = 34.77
min = -0.55

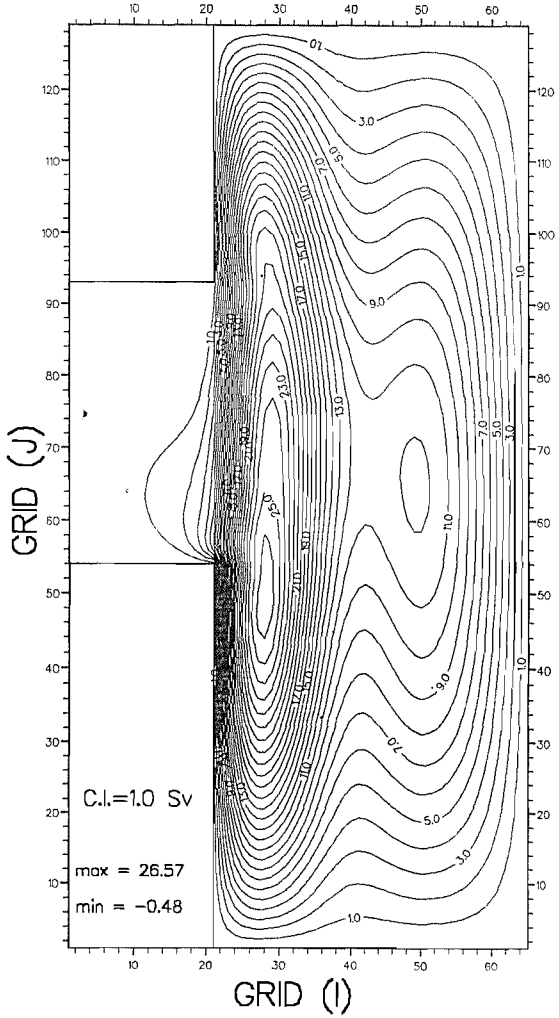
GRID (J)
GRID (I)
C.I.=1.0 Sv
max = 26.57
min = -0.48

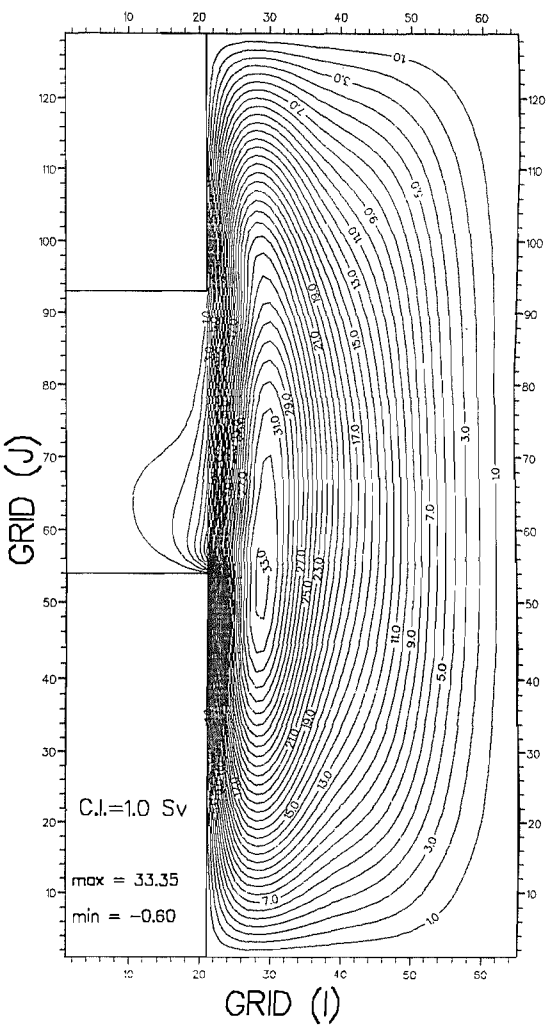
GRID (J)
GRID (I)
C.I.=1.0 Sv
max = 33.35
min = -0.60

Fig. D-4. Contours of streamlines at the different times of day 55, and day 69 (from left to right) marked in Fig. D-1.

GRID (J)
GRID (I)
C.I.=1.0 Sv
max = 27.61
min = −0.51

GRID (J)
GRID (I)
C.I.=1.0 Sv
max = 31.38
min = −0.59

Fig. D-5. Plots of normalised kinetic energies for the six experiments in Table 4-4 as a function of time **(A)** in the whole domain, and **(B)** only in the shelf. T=10.0 in the figure indicates the kinetic energy for the highly inertial case (experiment F in Table 4-4).

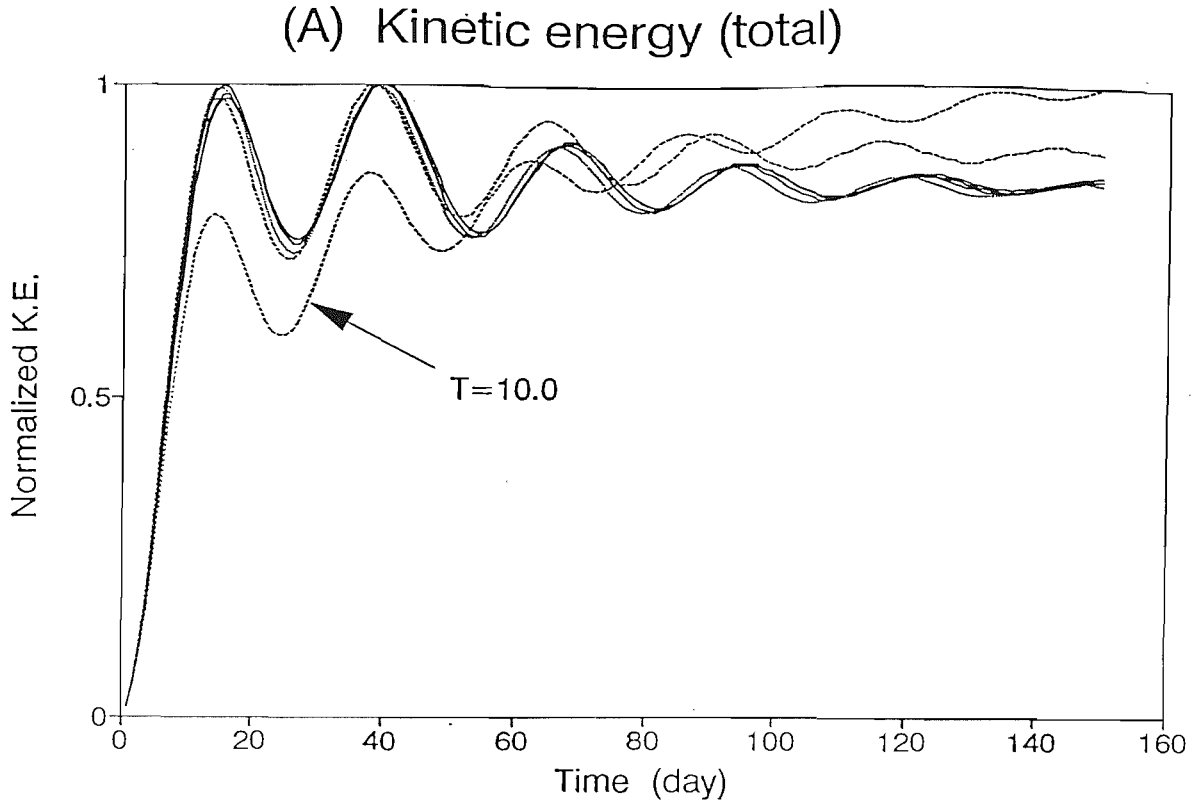
(A) Kinetic energy (total)
Normalized K.E.
1
0.5
0
T=10.0
0
20
40
60
80
100
120
140
160
Time (day)

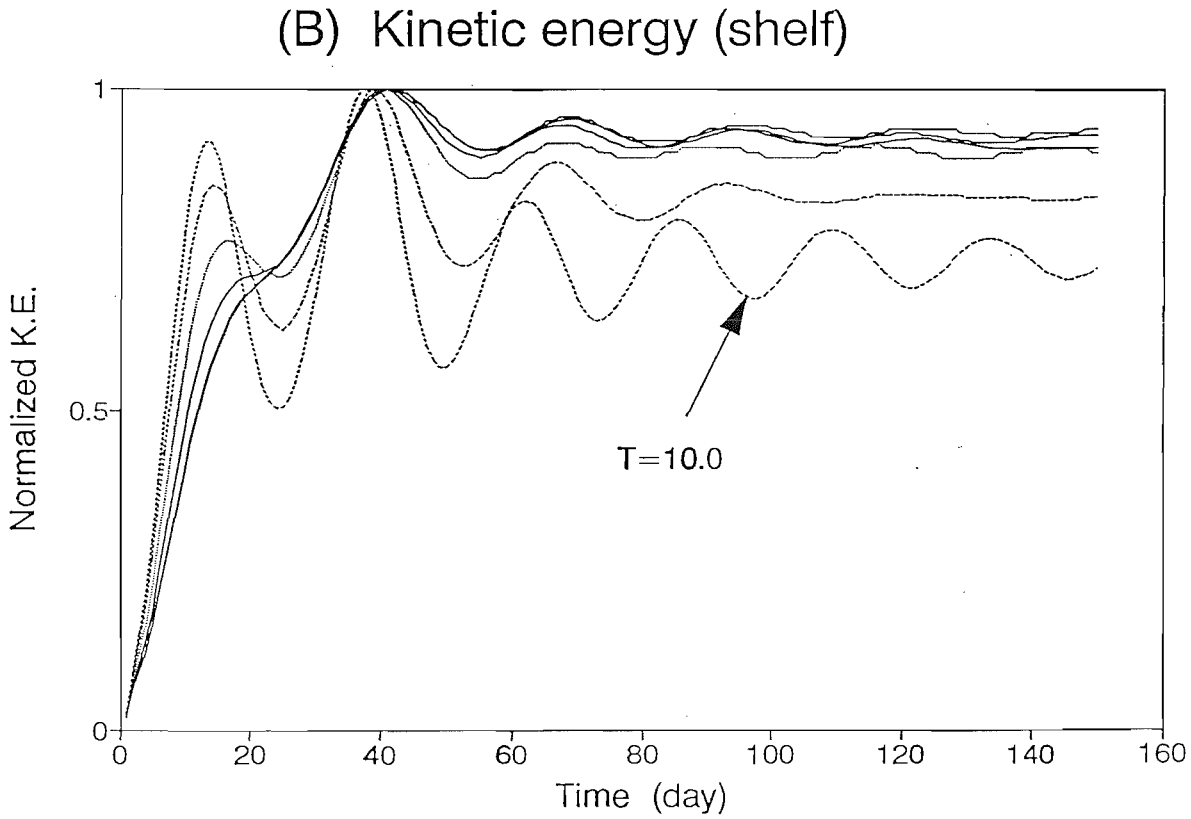
(B) Kinetic energy (shelf)
Normalized K.E.
1
0.5
0
T=10.0
0
20
40
60
80
100
120
140
160
Time (day)

APPENDIX E.

FINITE DIFFERENCE FORM OF VORTICITY EQUATION (SWEM)

The vertical component of the relative vorticity is defined as $\zeta = \delta_x v - \delta_y u$ and placed at a distance $\Delta/2$ to the east of the meridional velocity in Fig. A-1. From the finite difference form of momentum equations the vorticity tendency equation at grid point (i,j) is now derived for the steady flow.

From equations (A7) and (A8) the finite difference form of the momentum equations at grid point (i,j) for the steady flow is,

$$U^s(i,j) = -\frac{g}{\Delta x}[\eta_1(i+1,j)-\eta_1(i,j)] + \frac{f(j)}{4}[v_1(i,j)+v_1(i+1,j)+v_1(i,j-1)+v_1(i+1,j+1)]$$
$$+ A_M\left[\frac{u_1(i+1,j)-2\times u_1(i,j)+u_1(i-1,j)}{(\Delta x)^2} + \frac{u_1(i,j+1)-2\times u_1(i,j)+u_1(i,j-1)}{(\Delta y)^2}\right]$$
$$- \frac{2\times r\, u_1(i,j)}{[H_1(i,j)+H_1(i+1,j)]} = 0 \,, \tag{D1}$$

$$V^s(i,j) = -\frac{g}{\Delta y}[\eta_1(i+1,j)-\eta_1(i,j)] - \frac{1}{4}[f(j)[u_1(i,j)+u_1(i-1,j)]+f(j+1)[u_1(i,j+1)+u_1(i-1,j+1)]]$$
$$+ A_M\left[\frac{v_1(i+1,j)-2\times v_1(i,j)+v_1(i-1,j)}{(\Delta x)^2} + \frac{v_1(i,j+1)-2\times v_1(i,j)+v_1(i,j-1)}{(\Delta y)^2}\right]$$
$$- \frac{2\times r\, v_1(i,j)}{[H_1(i,j)+H_1(i,j+1)]} = 0 \,, \tag{D2}$$

where Δx and Δy are grid intervals in both x and y directions. The vorticity equation, thus, can be obtained from equations (D1) and (D2) by calculating the curl of these equations,

$$\delta_x V^s(i,j) - \delta_y U^s(i,j) = \left[V^s(i+1,j) - V^s(i,j)\right] - \left[U_s(i,j+1) - U^s(i,j)\right] = 0 .$$

Pressure gradient terms are eliminated by the curl operation and manipulation yields,

i) planetary vorticity term

$$-\frac{[f(j+1) - f(j)]}{2\Delta y}\ [v_1(i,j) + v_1(i+1,j)] = -\beta\, \overline{v_1}^{x} ,$$

ii) divergence term

$$-\frac{1}{4\Delta x}\left[f(j)\,[u_1(i+1,j) - u_1(i-1,j)] + f(j+1)\,[u_1(i+1,j+1) - u_1(i-1,j+1)]\right]$$

$$-\frac{1}{4\Delta y}\left[f(j+1)[v_1(i,j+1) + v_1(i+1,j+1) - v_1(i,j) - v_1(i+1,j)]\right]$$

$$-\frac{1}{4\Delta y}\left[f(j)[v_1(i,j) + v_1(i+1,j) - v_1(i,j-1) - v_1(i+1,j-1)]\right]$$

$$= -\delta_x \overline{\overline{f u_1}^{x}}^{y} - \overline{f \delta_y \overline{v_1}^{x}}^{y}$$

iii) lateral dissipation term

$$A_M\left[\frac{\zeta(i+1,j) - 2\times\zeta(i,j) + \zeta(i-1,j)}{(\Delta x)^2} + \frac{\zeta(i,j+1) - 2\times\zeta(i,j) + \zeta(i,j-1)}{(\Delta y)^2}\right]$$

$$= A_M(\delta_{xx} + \delta_{yy})\,\zeta$$

iv) bottom dissipation term

$$-\frac{2r\zeta(i,j)}{H_1(i,j)+H_1(i+1,j)} + r\left[\frac{H_1(i+1,j)-H_1(i,j)}{\Delta x}\right]\left[\frac{\frac{v_1(i,j)}{H_1(i,j)}+\frac{v_1(i+1,j)}{H_1(i+1,j)}}{H_1(i,j)+H_1(i+1,j)}\right]$$

$$= -\frac{r\zeta}{\overline{H_1}^x} + r\,\delta_x H_1 \frac{\overline{\left(\frac{v}{H_1}\right)}^x}{\overline{H_1}^x}$$

In the above manipulation, $H_1(i,j) = H_1(i,j+1)$, and friction terms are not lagged in time since the balance at a steady state is investigated.